COLLECTIVE PHENOMENA IN QUANTUM GASES

A Dissertation

Presented to the Faculty of the Graduate School

of Cornell University

in Partial Fulfillment of the Requirements for the Degree of

Doctor of Philosophy

by

Shovan Dutta

August 2018

COLLECTIVE PHENOMENA IN QUANTUM GASES

Shovan Dutta, Ph.D.

Cornell University 2018

Motivated by rapid experimental progress in the fields of ultracold atoms and quantum optics, I present a series of theoretical studies which explore collective phenomena in quantum gases of atoms and photons. In Chapter 1, I highlight the major developments in the research field and identify the overarching themes and motivations. I also provide a roadmap for the rest of the thesis and summarize the main results. The remaining eight chapters contain original studies, organized along three broad motifs. In Chapters 2 through 5, I investigate how the nature of collective excitations and quasiparticles can be explored in modern experiments. More specifically, I model the dynamics of a spin impurity in a Bose lattice gas, develop a protocol for observing fractionalized excitations or anyons in an optical cavity, and characterize the collective dynamics of Bogoliubov quasiparticles and domain walls in a Fermi superfluid. In Chapters 6 and 7, I examine unconventional superfluid phases in spin-imbalanced Fermi gases. In particular, I propose a novel technique for engineering the long-sought-after Fulde-Ferrell-Larkin-Ovchinnikov (FFLO) phase and study the relative stability of exotic phases across a dimensional crossover. Finally, Chapters 8 and 9 are devoted to studies of kinetics in out-of-equilibrium systems. I model the formation of a Bose-Einstein condensate in a dimple trap and characterize the approach to thermal equilibrium in quasi-one-dimensional geometries.

BIOGRAPHICAL SKETCH

Shovan Dutta appeared as a human on earth in a hospital located in India during the festive month of October, 1990. He remembers being incredibly docile as a child. In Shishu Tirtha kindergarten, he would remain seated on the bench even after wetting his pants. He is happy to report that he doesn't remain seated now. While still in kindergarten, his parents, Soma and Goutam, enrolled him in music classes where he learned to sing melodies and play the harmonium. To this day, he can be seen happily humming tunes and listening to music.

At the grand age of seven, when he had morphed into a full human being, he was transferred to Howrah Zilla School, where he would stay for the next ten years and form many happy memories. He was quite good in studies and did well in exams, although he doesn't seem to remember most of what he learned. One year, when he didn't do so well, he was given the "best student of the year" award, to satisfy his ego. Quite early on, he developed a liking for mathematics, playing with numbers and equations more than reading literature. These symptoms worsened in high school, when he would engage in heated debates over math problems with his friends and teachers, who were kind enough to pay attention. Suffice it to say, he is rather inept in social interactions.

You must be wondering then why he wrote a thesis in physics and not math. Well, that anomaly can be largely attributed to a book he read in high school, called "Concepts of Physics" by H. C. Verma, which disclosed how one could use imagination and mathematical reasoning to understand things in nature. Some thought-provoking science documentaries are also partly to blame. Come the summer of 2008, his eyes were set on studying physics in college.

But there is a twist to the story. Our protagonist would, in fact, be enrolled in electronics and telecommunications engineering at Jadavpur University, after a

surprisingly good result in engineering entrance exams, much to his regret and everyone else's delight. There were more jobs in engineering and he came from a middle-class family, so after much prodding from elders, he relented.

But there was a little rebel in him which no one knew about. He kept learning new things about physics by reading wonderful books, particularly the ones by Feynman. As his friends confirm[1], he chased the library more than chasing girls. He even got hold of physics professors and did some research on random walks, dynamical systems, and quantum mechanics. Moreover, the engineering faculty did nothing to stop this aberration. Some even encouraged and helped. Because of this multi-faceted conspiracy, he topped several physics exams for research fellowships, all the while getting decent grades in college and riding overcrowded buses. This is widely regarded as one of the greatest achievements of humanity.[2] No wonder he got accepted at Cornell for a physics PhD.[3]

He flew through the air and landed in Ithaca, without any phone or laptop, which is an incredible feat in itself. To his amusement, he found there was broad daylight even though it was 8:30 PM, and the cars would stop for him to cross the roads, not the other way around. Later, much like Columbus, he discovered there were people living here as well, notably some friendly graduate students and professors. After meeting them and measuring the lifetime of a muon, he was sure he wanted to work with Prof. Erich Mueller on ultracold atoms.

Days turned into months turned into years. Braving the fierce cold to get to Clark Hall, he kept working, oblivious to the passage of time, and published many outstanding papers.[4] He also taught several courses and got rave reviews from his students, something he is particularly proud of. Further, he traveled

[1] Although it seems unlikely, he did have some friends.
[2] The writer couldn't verify this claim. Citations needed.
[3] The protagonist is unwilling to admit that he also got some rejections.
[4] The writer couldn't verify this claim either.

to places, impressed people from all over the world, walked through woods, and talked to himself[5], canoed on Beebe lake, played tennis with competitive coworkers[6], went to the cinema, and watched youtube. To this day, he remains the only student for whom Erich cooked dinner. On the historic day of April 27, 2018, he defended his thesis. After receiving PhD, he will join the Theory of Condensed Matter group at Cambridge University as a postdoctoral fellow.

Shovan has many other fascinating anecdotes to share, but he won't tell them now, as he wants you to read his thesis instead.

[5]Upon further inspection, it has been confirmed that he is not technically a lunatic.
[6]He likes playing cricket and tennis. Beware of inviting him though—he is not very good.

To my parents

To Erich

To my late aunt

ACKNOWLEDGEMENTS

First and foremost, I am deeply indebted to my advisor, Erich Mueller, for all the help and guidance throughout my stay at Cornell. I cannot express in words how incredibly lucky and thankful I feel to have him as my mentor. Interacting with him and learning from him have been the best part of my grad school experience, which I will cherish for a lifetime. He is smart, knowledgeable, creative, fun to be around, and has a delightful laughter which everyone in the department knows about! At the same time, he is down-to-earth and accommodating. His infectious enthusiasm (on research, teaching, and woodwork!) and positive outlook have been a great source of inspiration for me. He has devoted valuable time to my progress, spending countless hours on the blackboard, patiently answering my questions, discussing new ideas, and showing "slick" ways of breaking down a complex problem into simple tractable units. Most of what I am as a physicist stems from these discussions. Further, he taught me how to write more efficient codes, improve the narrative in manuscripts, and make better presentations, most notably by stating the "punchline" at the beginning! I'm thankful to him for being flexible and letting me work at my own pace. It always seemed that, above all, he wanted me to have a good time. He drove me for long hours to conferences and even cooked (delicious) dinner! I'm also grateful to him for providing excellent guidance when I was applying for postdoc positions, and writing a letter of recommendation. Most importantly, he is one of the nicest individuals I've ever met. I'll never forget what he once said, "You never lose by helping others." Thank you for everything, Erich!

I would like to thank the faculty at Jadavpur University who helped me pursue a PhD in physics despite being enrolled as an engineering undergrad. In particular, I owe special thanks to Profs. Subhankar Ray and Jaya Shamanna

for guiding me through my first research experience, suggesting me wonderful physics books, and writing letters of recommendation for graduate school applications. I am also indebted to Prof. Chayanika Bose and Dr. Manas Bose for encouraging me to study physics and kindly supervising my final year project on photoemission. I owe many thanks to Profs. Chayanika Bose, Bhaskar Gupta, and Saikat Ghosh for writing letters of reference on my behalf. I would also like to thank Dr. Baisakhi Mal, Prof. Ananda Shankar Chowdhury and Prof. Mrinal Kanti Naskar for their help and encouragement.

I learned a great deal from the amazing physics faculty at Cornell. I would especially like to thank Prof. Veit Elser for serving on my special committee, recommending me in postdoc applications, teaching thought-provoking courses on statistical mechanics and "RRR," and honoring me with colored squares for writing "exemplary homework solutions!" I owe my thanks to Prof. Mukund Vengalattore for serving on my committee, stimulating my research on dimple traps and thermalization, and sharing valuable insights as a cold atom experimentalist. I owe special thanks to Prof. Jeevak Parpia for agreeing to serve on my committee on a short notice and for drawing my attention to very interesting and mysterious phenomena in liquid helium. I thank Profs. Tomas Arias, Liam McAllister, and Dan Ralph for serving on my temporary committee. I would like to thank the LASSP theory faculty for teaching the very useful modules in "basic training," Liam for teaching the most awesome electrodynamics course, and Profs. Chris Henley, Jim Sethna, Paul McEuen, Eun-Ah Kim, Dave Rubin, Tom Hartman, and Itai Cohen for teaching other wonderful courses. I also thank Prof. Vinay Ambegaokar for encouraging me to join Erich's group and having interesting conversations on Indian music.

I am grateful to Prof. Jon Simon for several illuminating discussions on the

exciting physics of polaritons, as well as for serving as a reference in my postdoc applications. Besides, it was a great pleasure to meet such a delightfully funny and curious character! I also thank Prof. Randy Hulet and Dr. Ben Olsen for fruitful discussions and for sharing their data on imbalanced Fermi gases.

Grad school experience would be incomplete without the amazing friends and colleagues in the physics department. In particular, I owe special thanks to all other students and visitors in Erich's group—Bhuvanesh, Matthew, Ran, Junjun, Sayan, Nur, Mehmet, Yariv, Kristina, Daniel, Junkai, and Ipsita. Shoutout to Yi-Ting, Kyungmin, and Yogesh as well. We spent some great times together, discussing physics (and non-physics) problems, having lunch, going to movies, playing games, or just hanging out. I am especially thankful to Bhuvanesh, for being my first contact and mentor in Ithaca, introducing me to the group, inviting me for paddling and a home-cooked dinner, asking puzzles, playing tennis and squash, failing to teach me rock climbing, transporting my luggage when I changed apartments, and sharing rooms in conferences. I thank Matthew for being consumed by politics, and still talking to me after I broke his glasses in a tennis match and debated over the existence of free will. I thank Nur for being worse than me in tennis (but better in rock climbing) and for sharing Turkish delights. I thank Junjun for accompanying me for lunch at Northstar, Ran for being so down-to-earth, and Sayan for being so laid back.

One of my most rewarding and enjoyable experiences at Cornell has been to teach a number of undergraduate physics courses. A special shoutout to all my students, especially the ones in PHYS 1116, 2208, and 3327, you were awesome! I'd like to thank all the instructors and other TAs as well, for arranging food (if you did!) and sharing the pain during grading sessions. I had great fun making demos with the help of Jenny Wurster, so a big thank you to Jenny! I would also

thank Prof. Natasha Holmes and the Cornell Center for Teaching Innovation for organizing PER journal clubs and other useful teaching related events.

I owe many thanks to the administrative staff at Cornell. From day one, they have ensured everything runs smoothly, which have enabled me to fully focus on studies. My special thanks to Caroline, Kacey, Lawrence, Debra, John, Rosemary, Vince, Mark, and Judy, for helping me so many times. I also thank Linda Glaser and Tom Fleischman for advertising our research on Chronicle.

I would like to thank the cold-atom community at large for laying the groundwork of my thesis and inspiring budding physicists like me with their discoveries. I owe thanks to the editors and referees of the American Physical Society (APS) for providing constructive comments on my papers and publishing my work in their journals. I also thank the organizers of various workshops and conferences that I've attended—DAMOP, ARO MURI, and ITAMP.

For the first four years of grad school, I shared an apartment with wonderful roommates—Omar, Ruitong, Varun, Kang, Alex, and Peter. Thank you so much for putting up with me and giving me company. I also owe my thanks to the friendly housing communities at Maplewood and Hasbrouck apartments. I am particularly grateful to the GCAs—Natalia, Hao, Prateek, Bo, Anne, Sergio, and many others whose names I have forgotten—for organizing community events, which were a great opportunity to meet people from all different backgrounds. I am also grateful for the friendly and informal atmosphere in the physics department, which was like a second home to me.

I wholeheartedly thank the people of Ithaca for being so warm, inclusive, and welcoming. Coming from a foreign land, I have never felt alienated. I have thoroughly enjoyed the scenic campus, local festivals, cultural events, cinemas and theaters, and delicious cuisine! It is certainly one of the best places to live.

I owe the greatest of thanks to my parents for their love and support. Coming from a humble background, it was hard for them to let go of their only child to a distant land, but they did. To this day, they wait anxiously for my Skype call, the only reason they have an internet connection, and warn me of all possible dangers I'm about to get into. I am glad we get to talk everyday, especially because I can remind my cousin how awful she looks. I'm also thankful to them for treating me like a prince whenever I go back!

I am grateful to my school teachers for nurturing my interest in science and mathematics at an early age, and for still keeping in touch. I am also very lucky to be in touch with several friends from high school and college, who always cheer me up and happily acknowledge my godlike status.

Finally, I would like to thank my funding sources. The work presented here was supported by the National Science Foundation grants PHY-1068165 and PHY-1508300, the ARO-MURI Non-equilibrium Many-body Dynamics grants 63834-PH-MUR and W9111NF-14-1-0003, and the Dr. V. Ramachandra Rao Summer Fellowship. I also received DAMOP Travel Grants from the APS.

I apologize to anyone whom I forgot to acknowledge. Please blame my negligence on the stress of writing a thesis on a deadline, any not on any malice.

TABLE OF CONTENTS

LIST OF FIGURES

CHAPTER 1

INTRODUCTION AND OVERVIEW

1.1 Motivation and themes

"*If, in some cataclysm, all of scientific knowledge were to be destroyed, and only one sentence passed on to the next generations of creatures, what statement would contain the most information in the fewest words? I believe it is that all things are made of atoms—little particles that move around in perpetual motion, attracting each other when they are a little distance apart, but repelling upon being squeezed into one another. In that one sentence, you will see, there is an enormous amount of information about the world, if just a little imagination and thinking are applied.*"— Feynman, 1963.

In this thesis, I will be uncovering some of that information about the quantum world, where simple interactions between the particles can give rise to an amazingly rich variety of complex collective phenomena [1]. I will theoretically explore a subset of these phenomena in quantum gases of atoms and photons, using a blend of analytical and numerical techniques to model their behavior.

Such studies are motivated in part by the remarkable experimental progress in trapping, cooling, and manipulating atoms that has taken place over the past two decades [2–6]. In June 1995, experimentalists used lasers and magneto-optical traps to cool rubidium atoms down to near absolute zero temperatures, producing the first Bose-Einstein condensate [7–11]. Since then, ultracold-atom setups have rapidly emerged as one of the most versatile playgrounds for exploring novel quantum phenomena [12, 13]. The features which make these systems so effective are reduced thermal fluctuations, isolation from sources of

decoherence, and a high degree of control over the atomic degrees of freedom. Experimentalists routinely cool down bosonic [14] and fermionic [15] atoms to nanokelvin temperatures, tune their interactions via Feshbach resonance [16], control their spin states with microwaves and radio waves [17, 18], and control their motional states through optical traps of varying shape and dimensionality [19, 20]. They also project arbitrary time-dependent potentials [21, 22], apply synthetic magnetic fields [23–27], address single atoms with high-resolution microscopes [28–32], and measure the atom distribution and equation of state through advanced imaging and spectroscopy [33–35]. Such capabilities offer unprecedented access to the behavior of interacting quantum systems, inspiring both theoretical and experimental investigations.

There are several broad themes underlying this exciting field of research, which overlap with one another. Below we highlight three major research directions and two other significant motivators:

Quantum simulation: The highly controllable experimental setting provides an ideal testbed to simulate iconic many-body Hamiltonians over a wide range of parameters [36–38]. This "quantum simulation" [39, 40] has, most notably, been implemented by loading cold atoms in optical lattices to mimic the behavior of electrons in solids [41, 42], thus realizing various Hubbard models which yield valuable insights into quantum magnetism and superconductivity [43–53].

Novel quantum states: Another theme is to observe and engineer new states of matter. A major success of this endeavor was the creation of the first fermionic condensate in 2003 [54], which led to the first experimental demonstration of the long-predicted BEC-BCS crossover in a Fermi gas [55–60]. The ability to tune parameters has enabled the generation of strongly correlated [61–66] and

topological [67–72] phases. We have seen exotic many-body states arising from an interplay of two competing orders, such as superfluidity and magnetism [73–77], or interactions and disorder [78–80]. We have also seen novel few-body physics [81], such as Efimov states [82–85] and ultracold molecules [86–88].

Nonequilibrium physics: A third motif is the characterization of quantum dynamics in systems out of equilibrium [89]. Here, one group of studies have focused on quench experiments which reveal the spontaneous generation of domain walls and topological defects following a sudden change of parameters [90–101]. Others have examined the relaxation to thermal equilibrium in isolated quantum systems [102–107], motivated by striking demonstrations like the quantum Newton's cradle [108–110]. Further insights into dynamics have come from studying periodically driven systems [111], leading to observations of such dramatic phenomena as time crystals [112, 113] and Bose fireworks [114].

Cavity QED: An expanding frontier is to look for new physics at the intersection of quantum optics and cold atoms [115–118]. Advances along this line date back to the turn of the century, when experimentalists could slow down [119] and stop [120] light by coupling photons with atoms. Optical cavities provide an ideal platform to enhance this coupling [121] and have been used, in conjunction with Rydberg atoms [122, 123], to mediate strong photon-photon interactions, paving the way for multi-photon quantum states [124–128]. Similarly, experiments have designed photon-mediated atom-atom interactions who strength and range are both tunable [129, 130]. Further, since cavities are open to the environment, they provide a natural setting to explore novel many-body states by engineering drive, dissipation, measurement, and feedback [131–134].

Technological applications: The ability to prepare and manipulate nontriv-

ial quantum states makes these systems ideally suited for developing future quantum technologies. Optical atomic clocks are already at the forefront of measurement science, with a record precision of 2.5×10^{-19} [135]. They can have wide-ranging applications in sensors, navigation, communications, metrology, and fundamental physics [136]. Atom-cavity systems [137–139], Rydberg gases [140–142], and optical lattices [143–147] are leading platforms for realizing large-scale entanglement and quantum information processing [148–152], and even a quantum internet [153]. A complementary approach is the generation of the still elusive non-Abelian anyons [154], such as Majorana zero modes [155], which could enable topological quantum computation [156–158].

Needless to say, it is an active, diverse, and interdisciplinary field which is firmly grounded in experimental reality [159]. A hallmark of its rapid progress in the first two decades has been a fruitful collaboration between theory and experiment. Despite this progress, so far we've only had a glimpse at the strange world of interacting quantum systems and there are many things to discover, which presents many opportunities for a theorist to explore this landscape and understand experiments. In this thesis, I will present a series of such explorations which touch on several of the aforementioned themes.

1.2 Outline

The studies I will describe are like points on a map. There are several ways one could traverse them, but certain routes are more natural than others. Thus, instead of simply presenting them in the chronological order, I have decided to arrange them into broadly defined groups having common themes, as follows.

1.2.1 Quasiparticles and collective excitations

These two terms are often used interchangeably and represent elementary excitations of an interacting system [160]. Ever since the time of Landau [161], the concept of quasiparticles has proven incredibly useful to obtain a better understanding of complex many-body phenomena [162, 163]. In Chapters 2–5, I investigate the properties of various quasiparticles arising in quantum gases.

Chapter 2: Polarons and bipolarons

Adapted from S. Dutta and E. J. Mueller, Phys. Rev. A **88**, *053601 (2013)*

A polaron is formed when a quantum impurity in a medium is "dressed" by the excitations which result from the impurity-bath interactions [164–167]. They arise in a wide range of physical systems [168–172]. Here, we model the dynamics of a spin impurity in a one-dimensional (1D) Bose lattice gas [173]. The study was motivated by an experiment [174] where Fukuhara *et al.* prepared an array of spin-polarized ^{87}Rb atoms and then flipped one of the spins (see Fig. 1.1). They measured how fast this impurity spreads through the gas as a function of the interaction strength, finding its motion to be strongly influenced by the gas. We use a variational wave function which captures the binding of the impurity with a hole, explaining the main features observed in the experiment. We find a stable polaron both in the Mott-insulating regime and the strongly-interacting superfluid regime. Below a critical interaction strength, the polaron becomes unstable over a finite range of momentum, decaying into uncorrelated particle-hole pairs. We show how this instability can be detected in future experiments by measuring the impurity-hole correlation.

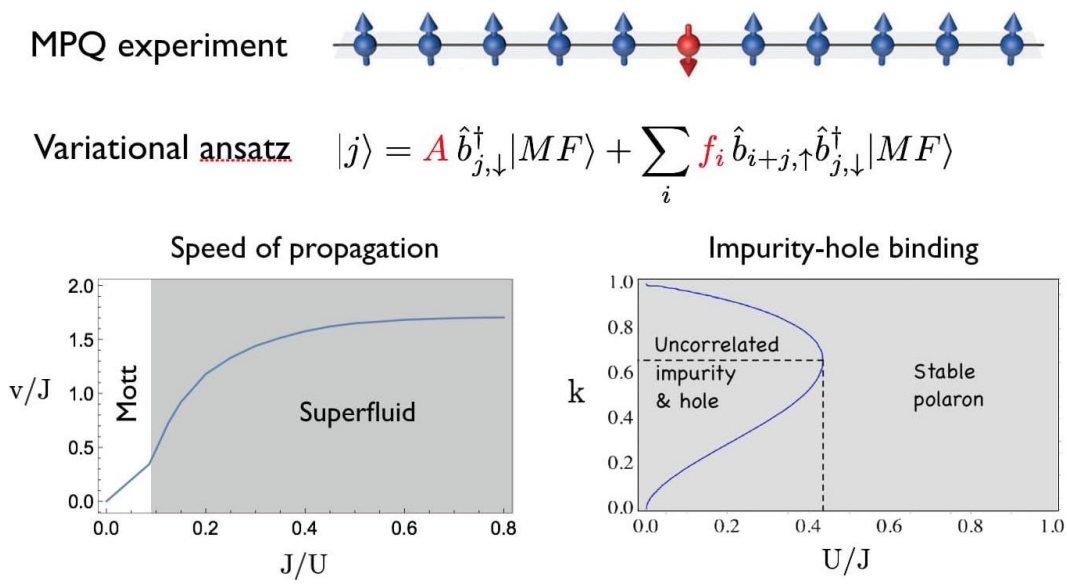

Figure 1.1: A picture summary of Chapter 2. From top to bottom, one sees a schematic of the experiment, the main variational *ansatz*, and two of the central results. On the left is the speed v of the impurity as a function of the hopping parameter J and on-site interaction U. On the right is a phase diagram showing the stability of a polaron as a function of its momentum k and U/J.

Multiple quantum impurities can attract one another through their interactions with the medium. This attraction can lead to a two-impurity bound state, or a bipolaron [165, 175]. We generalize our variational *ansatz* to incorporate two spin impurities, finding bipolarons for sufficiently strong interactions.

Chapter 3: Polaritons and anyons

Adapted from S. Dutta and E. J. Mueller, Phys. Rev. A **97**, *033825 (2018)*

When light is strongly coupled with a matter excitation, the resulting hybrid quasiparticle is called a polariton [127]. Depending on the type of matter excitation, there can be multiple flavors of polaritons [176]. The ability to tune the polaritonic properties by engineering the light-matter coupling could enable all-optical quantum information processing in the near future [122, 177]. A major

breakthrough in this direction has come from coupling photons with metastable Rydberg excitations of cold atomic ensembles [116, 122–124]. These Rydberg polaritons are both long lived [178] and strongly interacting [179], which are necessary to prepare and manipulate nontrivial photonic states. Here, we build on these advances to develop a protocol for creating fractional quantum Hall states of polaritons in a cavity and probe their topological excitations [180].

The fractional quantum Hall effect was first observed in a two-dimensional (2D) electron gas in a semiconductor placed in a magnetic field [181]. They are described by many-body wave functions with topological order, the simplest of which is the Laughlin state [182]. Such states are known to possess quantized vortex-like excitations with fractional statistics, called anyons [183], which can be used to implement fault-tolerant quantum computation [156–158]. Directly observing and controlling anyons in experiments is one of the most important challenges of contemporary physics. We show how one can produce anyonic excitations and measure their statistics in the proposed experiment.

We envision an optical cavity built by carefully aligning a set of high-quality mirrors, as shown in Fig. 1.2. The anyons are formed in a transverse plane of the cavity where photons are coupled to atoms to form Rydberg polaritons. The mirrors are not in the same plane, which gives rise to an effective magnetic field for the polaritons, as already demonstrated in Ref. [184]. We show how one can drive the cavity with lasers to sequentially inject photons, building up a many-particle Laughlin state. One produces anyonic quasihole excitations in such a state by moving additional lasers in from the edge of the cloud. One then stirs these pinning lasers to move the quasiholes around, extracting their anyonic statistics by interferometry. We carefully model all stages of the protocol,

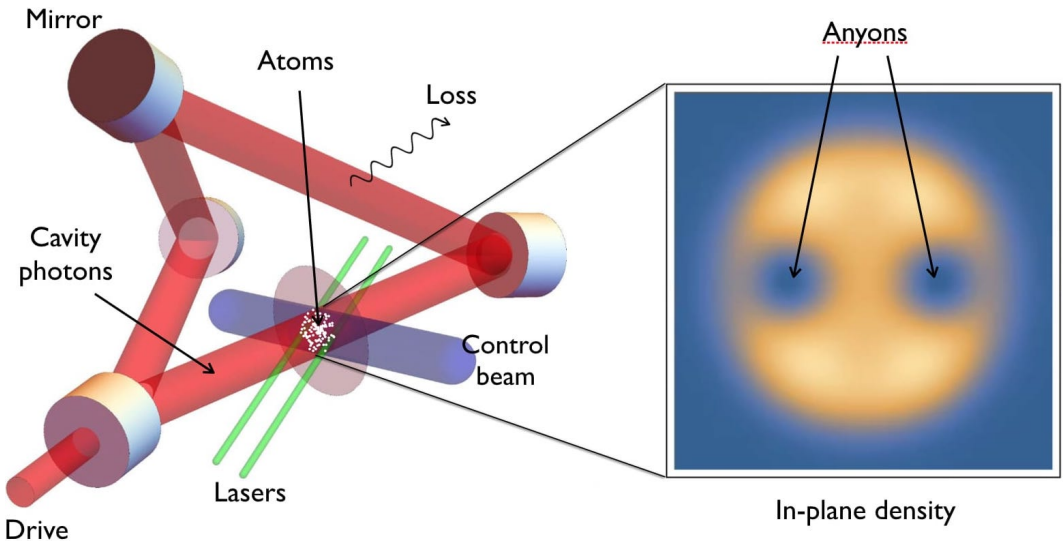

Figure 1.2: A picture summary of Chapter 3. On the left is a schematic of the proposed experiment for observing anyons in an optical cavity. The noncoplanar arrangement of the mirrors yields an effective magnetic field for the cavity photons, which are coupled with atoms to form strongly interacting Rydberg polaritons. We show how one can drive these polaritons to generate fractional quantum Hall states. Additional lasers are used to produce localized repulsive potentials and bind anyonic quasihole excitations, as shown on the right.

identifying potential challenges and how to overcome them.

Chapter 4: Bogoliubov quasiparticles

Bardeen, Cooper, and Schrieffer showed in 1957 that an attractively interacting Fermi gas with equal number of ↑- and ↓-spins has an instability whereby an ↑-spin forms a pair with a ↓-spin and these Cooper pairs Bose condense to form a superfluid [185, 186]. Shortly thereafter, Bogoliubov [187] and Valatin [188], and later de Gennes [189], showed that the excitation spectrum of a superfluid is composed of quasiparticle modes that are linear combinations of particles and holes with opposite spin. These modes are known as Bogoliubov quasiparticles. Here, we briefly review the well-established Bogoliubov–de Gennes (BdG) for-

malism [190] in the context of ultracold Fermi gases with spin imbalance. In particular, we summarize two competing conventions for the Bogoliubov modes that are found in the literature. We use the formalism in the next three chapters to explore domain-wall dynamics and unconventional superfluidity.

Chapter 5: Solitons or domain walls

Adapted from S. Dutta and E. J. Mueller, Phys. Rev. Lett. **118**, *260402 (2017)*

Solitons are persistent nonlinear waves—"pulses" which travel without changing shape [191]. They are ubiquitous in nature [192–199] and have a number of technological applications [200–203]. Matter-wave solitons manifest as domain walls in superfluids, i.e., sharp changes in the Cooper pair wave function, $\Delta(x)$ [197]. Soliton trains are spontaneously generated in quench experiments in Bose-Einstein condensates [90–96]. They can also be created in a controlled manner by phase imprinting, where one shines off-resonant light on selected regions of a superfluid to rotate the local phase by π [204]. Recently, Fermi gas experiments have used phase imprinting and advanced imaging to produce single solitons and directly observe their motion [205–207]. Here, we model the collective dynamics of a train of solitons in a quasi-1D Fermi superfluid [208].

We linearize the dynamics of a soliton train, finding a rich set of collective modes, as illustrated in Fig. 1.3. The soliton train spontaenously breaks gauge- and translational symmetries, which gives rise to two Goldstone modes [209]: a "phonon" mode describing phase twists and an "elastic" mode describing oscillations in the spacing between solitons. We find a mode of amplitude oscillations, which is the remnant of the "Higgs" mode in a uniform Fermi superfluid [210, 211]. In addition to these expected modes, we discover novel collective

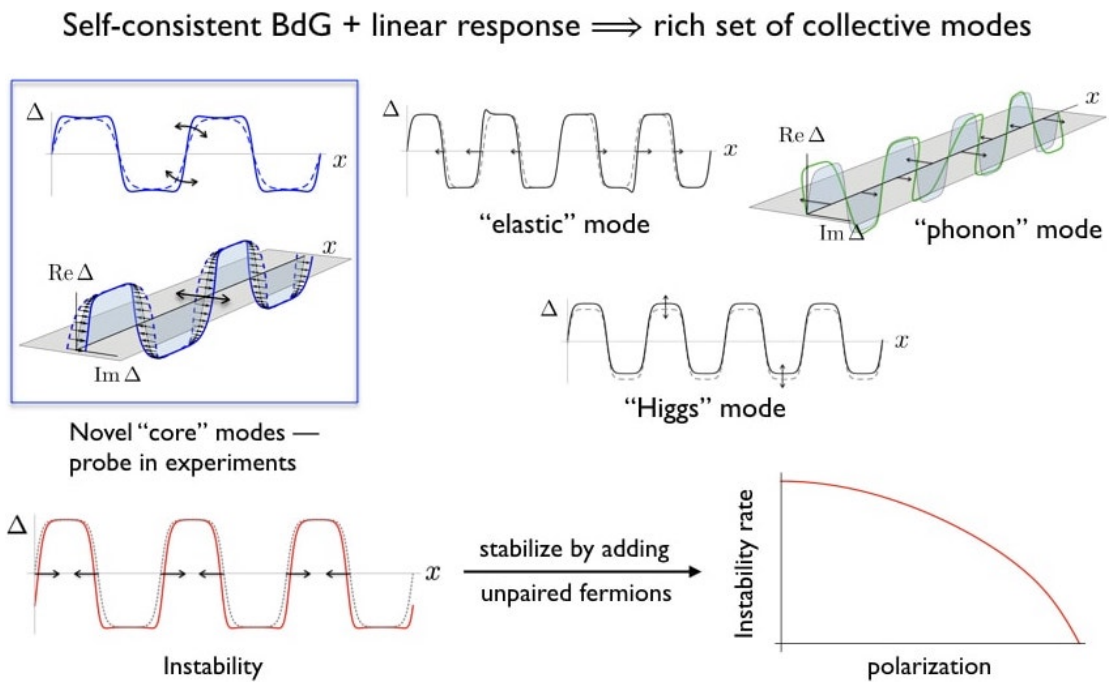

Figure 1.3: A picture summary of Chapter 5. On top, we see various collective oscillations of a soliton train in a Fermi superfluid. Here, $\Delta(x)$ denotes the superfluid order parameter. In addition to the expected Goldstone- and "Higgs" modes, there are novel "core" modes describing oscillations in the width and grayness of each soliton. Below, we see a dynamical instability where pairs of neighboring solitons collide and annihilate. The instability rate decreases with polarization and vanishes when each soliton is filled with one excess fermion.

oscillations of the soliton cores, which are not found in a Bose superfluid. Another distinctive feature of the dynamics is an instability where pairs of adjacent solitons collide and annihilate. The instability rate is sensitive to the separation of solitons and the interaction between atoms, both of which can be tuned in experiments. Further, the instability is prevented by polarizing the gas, which realizes a spin-imbalanced spatially modulated superfluid, a long-sought-after phase of condensed matter physics [73, 212, 213]. This result provides a way to directly engineer such a phase in cold Fermi gases, as we describe in Chapter 6. We also discuss how the various modes can be detected in experiments and how our results generalize to other physical systems.

1.2.2 Superfluidity in spin-imbalanced Fermi gases

In an attractively interacting cold Fermi gas with equal number of ↑- and ↓-spins, each ↑-spin is paired with a ↓-spin, forming a Bardeen-Cooper-Schrieffer (BCS) superfluid [185]. Unbalancing the spin populations, through a magnetic field or a radio-frequency pulse, frustrates the Cooper pairs, which can lead to unconventional superfluid phases with exotic pairing mechanisms [73–76]. The most studied example of such phases is the Fulde-Ferrell-Larkin-Ovchinnikov (FFLO) state, which was first proposed in 1964 in the context of superconductors with magnetic impurities [214, 215]. In this state, pairing occurs at a finite momentum, leading to periodic spatial domains in the order parameter where the unpaired fermions reside. Despite much effort, experimental evidence of FFLO pairing has been rather elusive and mostly indirect [216, 217]. In Chapters 6–7, we explore the creation and stability of such phases in cold Fermi gases.

Chapter 6: Engineering FFLO states in a quasi-1D Fermi gas

Adapted from S. Dutta and E. J. Mueller, Phys. Rev. A **96**, *023612 (2017)*

Past attempts to observe FFLO states in Fermi gases have centered on searching for parameters which minimize the free energy, so that the system can be cooled to an FFLO phase [74–76]. Although thermodynamic evidence has been found in a few experiments [77, 217], the nature of the superfluid pairing could not be ascertained. Here, we develop a protocol which circumvents thermodynamics and directly drives a quasi-1D Fermi gas into an FFLO state [218].

Our protocol stems from the results in Chapter 5, where we found that it is possible to stabilize a train of solitons in a quasi-1D Fermi gas by filling each

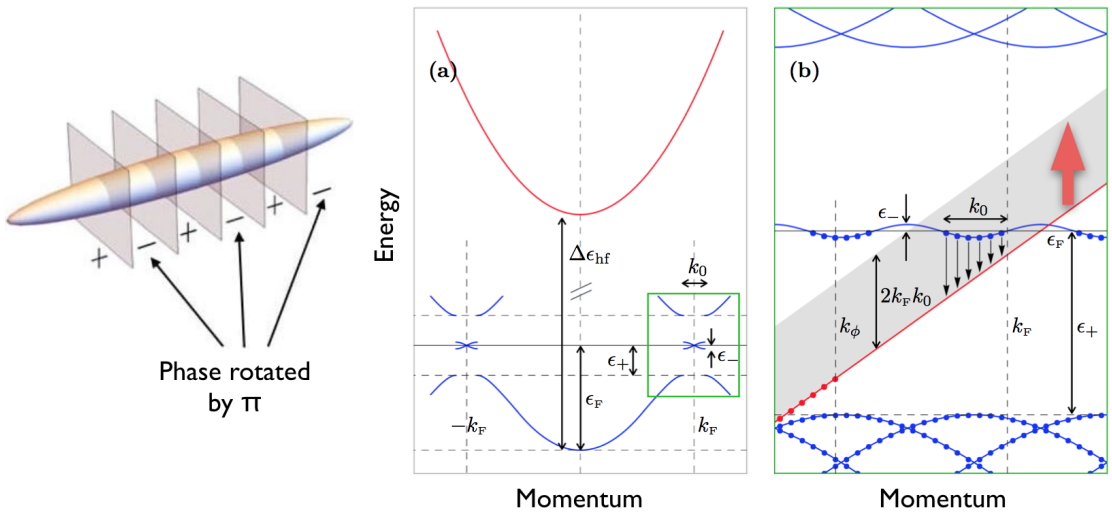

Figure 1.4: A picture summary of Chapter 6. The sketch on the left shows how a soliton train can be generated by phase imprinting. Figures (a) and (b) illustrate a rapid adiabatic passage protocol for polarizing the soliton train. A detailed explanation of the protocol and the various symbols can be found in Sec. 6.5. Roughly, the blue curves show the Bogoliubov spectrum of a soliton train composed of spin-↑ and spin-↓ atoms, and the red curves show the dispersion of a third noninteracting spin state $|\phi\rangle$. A controlled radio-frequency sweep (red arrow) couples the spin-↑ state with $|\phi\rangle$, thus altering the Bogoliubov mode occupations in such a way that each soliton is left with an unpaired spin-↓ atom.

domain wall with one unpaired fermion. This partially polarized state is nothing but an FFLO phase. Since the separation of the domains can be controlled by phase imprinting [204], this result offers a route to generating stable FFLO states of a given period. Here, we propose a two-step protocol to achieve this goal (Fig. 1.4). First, one employs phase imprinting to produce a train of domain walls in a balanced superfluid, with equal number of spin-↑ and spin-↓ atoms. Second, one applies a controlled radio-frequency sweep to selectively break Cooper pairs near the domain walls and transfer the spin-↑ atoms to a third noninteracting spin state, leaving behind an FFLO state with exactly one unpaired ↓-spin per domain wall. We carefully model this creation process and show that the protocol can be implemented with high fidelity for a wide range of parameters in present-day experimental conditions.

Chapter 7: Dimensional crossover in a spin-imbalanced Fermi gas

Adapted from S. Dutta and E. J. Mueller, Phys. Rev. A **94**, *063627 (2016)*

The FFLO phases are more stable in lower dimensions due to enhanced Fermi surface nesting [219]. Calculations have shown that they occupy a large part of the phase diagram in 1D but require extensive finetuning in three dimensions (3D) [74, 220]. However, since long-range order is absent in 1D [221, 222], they are also more susceptible to fluctuations. Nonetheless, experiments have seen indirect evidence of FFLO in elongated 1D tubes [77, 217]. Further modeling of an array of weakly-coupled tubes indicate that such phases will be most robust in quasi-1D regimes, where the dynamics are largely 1D but the residual transverse degrees of freedom help establish long-range order [223]. Here, we study this 1D-to-3D crossover in a trapped spin-imbalanced Fermi gas [224].

First, we consider a Fermi gas in a transverse harmonic confinement, where the crossover from 1D to 3D occurs when multiple transverse channels become accessible as a result of increased density or strong interactions. We calculate the phase diagram as a function of density, imbalance, interaction strength, and temperature (Fig. 1.5), finding large parameter regions where the FFLO phase is stable. For weak interactions and low density, we find 1D-like islands which repeat as a function of the chemical potential, eventually giving way to 3D-like behavior once sufficiently many channels are occupied. Stronger atom-atom interactions mix the energy levels of the trap, which changes the nature of this crossover, yielding a more 3D-like phase diagram for all densities. For strong interactions and high density, we also find a stable breached-pair (BP) superfluid phase, where pairs exist with a Fermi surface [225–227]. We discuss the prospects of observing these exotic phases in cold-atom experiments.

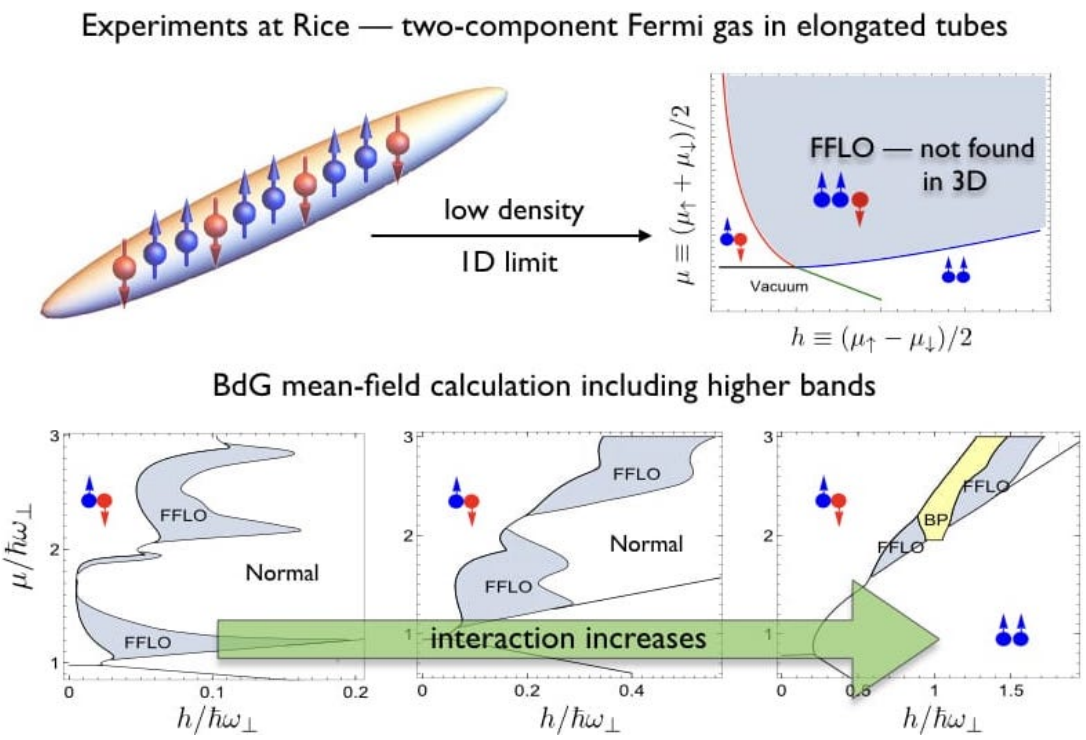

Figure 1.5: A picture summary of Chapter 7. On the top left is a sketch of a spin-imbalanced Fermi gas in a quasi-1D trap. Experiments performed in such traps in the low-density limit agree with the 1D phase diagram calculated from Bethe *Ansatz*, which is shown to the right. Here, μ and h are the average chemical potential and the chemical potential difference of the two spins, respectively. At the bottom are mean-field phase diagrams for a spin-imbalanced Fermi gas in a transverse harmonic trap of frequency $\omega_\perp$. The nature of the phase diagram changes from 1D-like to 3D-like as interactions are increased.

In the Supplement, we consider the more general case of Fermi gases in a 2D optical lattice. For large lattice depths, the gas splits into 1D tubes at individual lattice sites. By tuning the lattice depth, one can control the coupling between sites and induce a 1D-to-3D crossover [217]. We investigate how this crossover occurs by studying the phase diagrams as a function of the lattice depth.

1.2.3 Kinetics of Bose condensation and thermalization

The exquisite control and long coherence times available in cold-atom setups have enabled direct observations of out-of-equilibrium dynamics [103], stimulating intense theoretical activity to understand such processes [89, 102]. Central to this pursuit is a proper modeling of the kinetic processes at the single-particle level. In Chapters 8–9, we use quantum Boltzmann master equations [228, 229] to model the kinetics of Bose condensation and thermalization in trapped gases.

Chapter 8: Bose-Einstein condensation in a dimple trap

Adapted from S. Dutta and E. J. Mueller, Phys. Rev. A **91**, *013601 (2015)*

Designing efficient cooling schemes is a prerequisite for creating novel many-body quantum states [230]. One effective paradigm is to divide the system into a high-entropy reservoir, which can be readily cooled, and a low-entropy subsystem where the interesting phase will develop [231, 232]. Dimple traps implement this strategy for producing Bose-Einstein condensates [233]. They consist of a large but shallow reservoir trap with a strongly attractive "dimple" at the center (see Fig. 1.6). In experiments, precooled thermal atoms are loaded in the reservoir before turning on the dimple with a focused laser beam. The subsequent dynamics cause a rapid growth of phase space density inside the dimple, yielding a Bose-Einstein condensate [234]. Here, we model the loading and equilibration of weakly-interacting bosons in a dimple trap [235].

We construct rate equations incorporating two-body elastic- and three-body inelastic collisions. The two-body processes populate the dimple and lead to loss when one of the atoms is ejected from the trap. The three-body processes

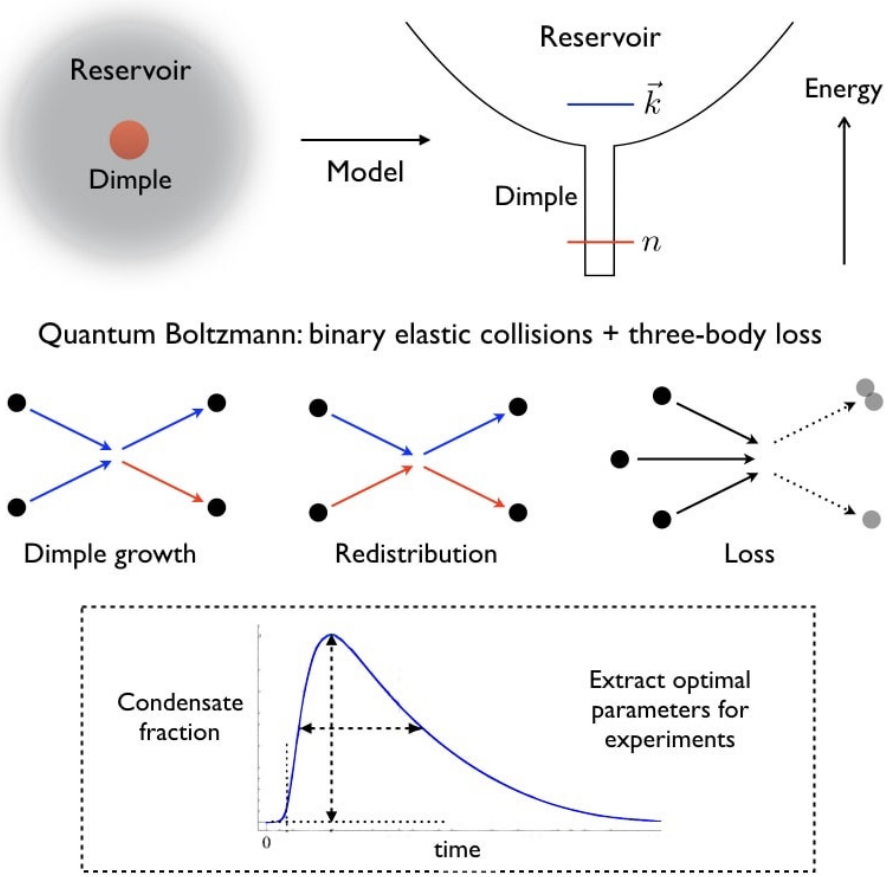

Figure 1.6: A picture summary of Chapter 8. On the top left is a sketch of the dimple trap, showing a large resevoir region and a tight "dimple" at the center. The reservoir is modeled by a shallow harmonic trap and the dimple is modeled by a deep square well, as shown to the right. The single-particle states in the reservoir and the dimple are labeled by momentum $\vec{k}$ and quantum number n, respectively. Below, we sketch the two-body and three-body processes which govern the occupation of these states. Here, the blue arrows denote atoms in the reservoir and the red ones denote atoms in the dimple. The lower panel shows the how the condensate fraction in the dimple evolves with time.

cause heating and loss. We study the resulting dynamics, providing quantitative estimates for condensate yields, lifetimes, thermalization timescales, and temperature variations. We study the variation of these quantities with the trap parameters and the initial conditions, explaining the trends in physical terms and extracting optimal parameters for future experiments.

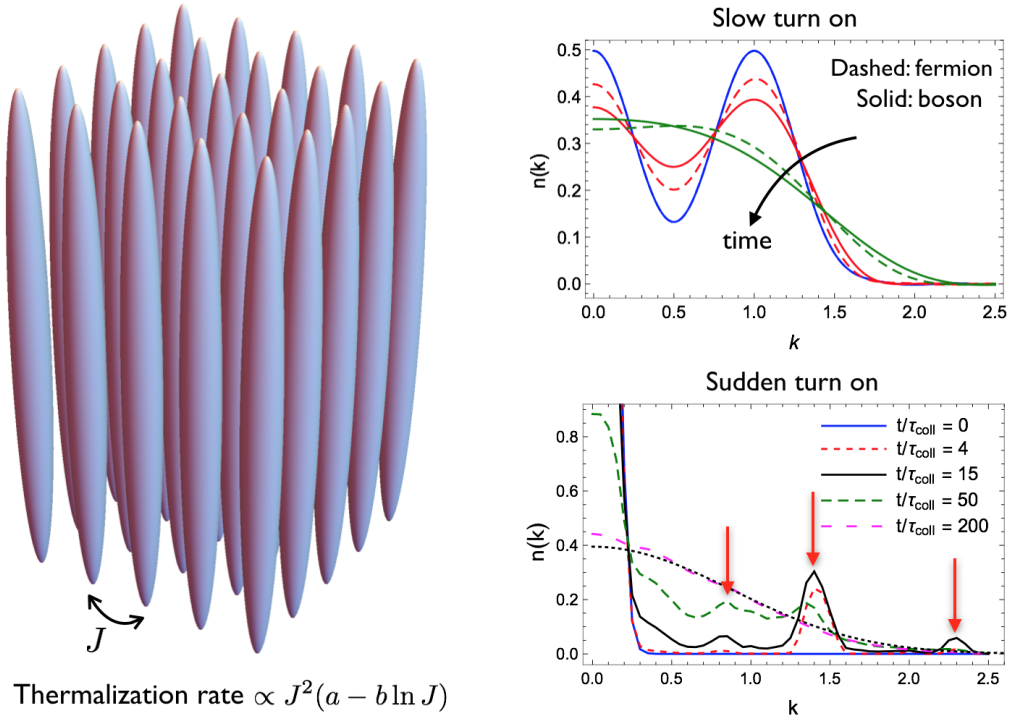

Figure 1.7: A picture summary of Chapter 9. On the left is a schematic of a typical experiment, where atoms are loaded into an array of coupled tubes by turning on a lattice in the horizontal plane. The intertube tunneling is denoted by J. On the right are plots showing the time evolution of the quasimomentum distribution $n(k)$ for a slow (above) and sudden (below) turn on of the lattice.

Chapter 9: Thermalization in a quasi-1D trap

A major frontier of contemporary physics is understanding the mechanisms of thermalization in a closed many-body quantum system [102, 103]. Much of the recent progress in this field has been fueled by pioneering experiments probing the dynamics of near-integrable cold atomic gases in quasi-1D traps [108, 109]. It is known that purely 1D systems cannot reach thermal equilibrium due to kinematic constraints [89, 236]. However, in quasi 1D, there are leftover transverse degrees of freedom which can redistribute momenta, causing thermalization. Here, we use rate equations for binary elastic collisions to characterize the approach to thermal equilibrium in such a system.

In a typical quasi-1D experiment, atoms are loaded into an array of weakly-coupled "tubes" by turning on an optical lattice in the transverse plane [64, 77]. If the lattice is turned on slowly compared to the rate of collisions, which is the situation in most experiments, we find the quasimomentum distribution evolves smoothly into a thermal profile (Fig. 1.7). We show that for small inter-tube tunneling J, the rate of equilibration grows as $J^2 \ln J$, which is consistent with the hugely different timescales observed in Refs. [64, 77]. Conversely, for a sudden turn on of the lattice, the momentum distribution develops multiple isolated peaks, which later merge and eventually reach a thermal profile. These nonequilibrium peaks originate from the exchange of particles between different energy bands of the lattice and can be resolved for about 50 collision times.

BIBLIOGRAPHY FOR CHAPTER 1

[1] P. Coleman, "Many body physics: Unfinished revolution," Ann. Henri Poincaré **4**, 559 (2003).

[2] H. J. Metcalf and P. van der Straten, *Laser Cooling and Trapping of Neutral Atoms* (Wiley, New York, 2007).

[3] C. E. Wieman, D. E. Pritchard, and D. J. Wineland, "Atom cooling, trapping, and quantum manipulation," Rev. Mod. Phys. **71**, S253 (1999).

[4] W. D. Phillips, "Nobel Lecture: Laser cooling and trapping of neutral atoms," Rev. Mod. Phys. **70**, 721 (1998).

[5] C. N. Cohen-Tannoudji, "Nobel Lecture: Manipulating atoms with photons," Rev. Mod. Phys. **70**, 707 (1998).

[6] S. Chu, "Nobel Lecture: The manipulation of neutral particles," Rev. Mod. Phys. **70**, 685 (1998).

[7] M. H. Anderson, J. R. Ensher, M. R. Matthews, C. E. Wieman, and E. A. Cornell, "Observation of Bose-Einstein condensation in a dilute atomic vapor," Science **269**, 198 (1995).

[8] K. B. Davis, M.-O. Mewes, M. R. Andrews, N. J. Van Druten, D. S. Durfee, D. M. Kurn, and W. Ketterle, "Bose-Einstein condensation in a gas of sodium atoms," Phys. Rev. Lett. **75**, 3969 (1995).

[9] C. C. Bradley, C. A. Sackett, J. J. Tollett, and R. G. Hulet, "Evidence of Bose-Einstein condensation in an atomic gas with attractive interactions," Phys. Rev. Lett. **75**, 1687 (1995).

[10] E. A. Cornell and C. E. Wieman, "Nobel Lecture: Bose-Einstein condensation in a dilute gas, the first 70 years and some recent experiments," Rev. Mod. Phys. **74**, 875 (2002).

[11] W. Ketterle, "Nobel Lecture: When atoms behave as waves: Bose-Einstein condensation and the atom laser," Rev. Mod. Phys. **74**, 1131 (2002).

[12] I. Bloch, J. Dalibard, and W. Zwerger, "Many-body physics with ultracold gases," Rev. Mod. Phys. **80**, 885 (2008).

[13] I. Bloch and M. Greiner, "Exploring quantum matter with ultracold atoms in optical lattices," Adv. At. Mol. Opt. Phys. **52**, 1 (2005).

[14] C. J. Pethick and H. Smith, *Bose-Einstein Condensation in Dilute Gases* (Cambridge University Press, Cambridge, 2002).

[15] S. Giorgini, L. P. Pitaevskii, and S. Stringari, "Theory of ultracold atomic Fermi gases," Rev. Mod. Phys. **80**, 1215 (2008).

[16] C. Chin, R. Grimm, P. Julienne, and E. Tiesinga, "Feshbach resonances in ultracold gases," Rev. Mod. Phys. **82**, 1225 (2010).

[17] F. Gerbier, A. Widera, S. Fölling, O. Mandel, and I. Bloch, "Resonant control of spin dynamics in ultracold quantum gases by microwave dressing," Phys. Rev. A **73**, 041602(R) (2006).

[18] G. B. Partridge, W. Li, R. I. Kamar, Y.-a. Liao, and R. G. Hulet, "Pairing and phase separation in a polarized Fermi gas," Science **311**, 503 (2006).

[19] I. Bloch, "Ultracold quantum gases in optical lattices," Nat. Phys. **1**, 23 (2005).

[20] M. Greiner and S. Fölling, "Condensed-matter physics: Optical lattices," Nature (London) **453**, 736 (2008).

[21] K. Henderson, C. Ryu, C. MacCormick, and M. G. Boshier, "Experimental demonstration of painting arbitrary and dynamic potentials for Bose–Einstein condensates," New J. Phys. **11**, 043030 (2009).

[22] P. Zupancic, P. M. Preiss, R. Ma, A. Lukin, M. E. Tai, M. Rispoli, R. Islam, and M. Greiner, "Ultra-precise holographic beam shaping for microscopic quantum control," Opt. Express **24**, 13881 (2016).

[23] Y.-J. Lin, R. L. Compton, K. Jimenez-Garcia, J. V. Porto, and I. B. Spielman, "Synthetic magnetic fields for ultracold neutral atoms," Nature (London) **462**, 628 (2009).

[24] J. Dalibard, F. Gerbier, G. Juzeliūnas, and P. Öhberg, "Colloquium: Artificial gauge potentials for neutral atoms," Rev. Mod. Phys. **83**, 1523 (2011).

[25] N. Goldman, G. Juzeliūnas, P. Öhberg, and I. B. Spielman, "Light-induced gauge fields for ultracold atoms," Rep. Prog. Phys. **77**, 126401 (2014).

[26] V. Galitski and I. B. Spielman, "Spin–orbit coupling in quantum gases," Nature (London) **494**, 49 (2013).

[27] H. Zhai, "Degenerate quantum gases with spin–orbit coupling: A review," Rep. Prog. Phys. **78**, 026001 (2015).

[28] W. S. Bakr, J. I. Gillen, A. Peng, S. Fölling, and M. Greiner, "A quantum gas microscope for detecting single atoms in a Hubbard-regime optical lattice," Nature (London) **462**, 74 (2009).

[29] J. F. Sherson, C. Weitenberg, M. Endres, M. Cheneau, I. Bloch, and S. Kuhr, "Single-atom-resolved fluorescence imaging of an atomic Mott insulator," Nature (London) **467**, 68 (2010).

[30] C. Weitenberg, M. Endres, J. F. Sherson, M. Cheneau, P. Schauß, T. Fukuhara, I. Bloch, and S. Kuhr, "Single-spin addressing in an atomic Mott insulator," Nature (London) **471**, 319 (2011).

[31] L. W. Cheuk, M. A. Nichols, M. Okan, T. Gersdorf, V. V. Ramasesh, W. S. Bakr, T. Lompe, and M. W. Zwierlein, "Quantum-gas microscope for fermionic atoms," Phys. Rev. Lett. **114**, 193001 (2015).

[32] E. Haller, J. Hudson, A. Kelly, D. A. Cotta, B. Peaudecerf, G. D. Bruce, and S. Kuhr, "Single-atom imaging of fermions in a quantum-gas microscope," Nat. Phys. **11**, 738 (2015).

[33] P. Törmä and K. Sengstock, eds., *Quantum Gas Experiments: Exploring Many-Body States* (Imperial College Press, London, 2015).

[34] P. Törmä, "Physics of ultracold Fermi gases revealed by spectroscopies," Phys. Scr. **91**, 043006 (2016).

[35] S. Nascimbene, N. Navon, F. Chevy, and C. Salomon, "The equation of state of ultracold Bose and Fermi gases: A few examples," New J. Phys. **12**, 103026 (2010).

[36] I. Bloch, J. Dalibard, and S. Nascimbene, "Quantum simulations with ultracold quantum gases," Nat. Phys. **8**, 267 (2012).

[37] C. Gross and I. Bloch, "Quantum simulations with ultracold atoms in optical lattices," Science **357**, 995 (2017).

[38] M. Lewenstein, A. Sanpera, and V. Ahufinger, *Ultracold Atoms in Optical Lattices: Simulating Quantum Many-Body Systems* (Oxford University Press, Oxford, 2012).

[39] R. P. Feynman, "Simulating physics with computers," Int. J. Theor. Phys. **21**, 467 (1982).

[40] I. M. Georgescu, S. Ashhab, and F. Nori, "Quantum simulation," Rev. Mod. Phys. **86**, 153 (2014).

[41] M. Lewenstein, A. Sanpera, V. Ahufinger, B. Damski, A. Sen, and U. Sen, "Ultracold atomic gases in optical lattices: Mimicking condensed matter physics and beyond," Adv. Phys. **56**, 243 (2007).

[42] D. Jaksch and P. Zoller, "The cold atom Hubbard toolbox," Ann. Phys. **315**, 52 (2005).

[43] D. Jaksch, C. Bruder, J. I. Cirac, C. W. Gardiner, and P. Zoller, "Cold bosonic atoms in optical lattices," Phys. Rev. Lett. **81**, 3108 (1998).

[44] M. Greiner, O. Mandel, T. Esslinger, T. W. Hänsch, and I. Bloch, "Quantum phase transition from a superfluid to a Mott insulator in a gas of ultracold atoms," Nature (London) **415**, 39 (2002).

[45] W. S. Bakr, A. Peng, M. E. Tai, R. Ma, J. Simon, J. I. Gillen, S. Foelling, L. Pollet, and M. Greiner, "Probing the superfluid–to–Mott insulator transition at the single-atom level," Science **329**, 547 (2010).

[46] S. Trotzky, P. Cheinet, S. Fölling, M. Feld, U. Schnorrberger, A. M. Rey, A. Polkovnikov, E. A. Demler, M. D. Lukin, and I. Bloch, "Time-resolved observation and control of superexchange interactions with ultracold atoms in optical lattices," Science **319**, 295 (2008).

[47] J. Struck, C. Ölschläger, R. Le Targat, P. Soltan-Panahi, A. Eckardt, M. Lewenstein, P. Windpassinger, and K. Sengstock, "Quantum simulation of frustrated classical magnetism in triangular optical lattices," Science **333**, 996 (2011).

[48] T. Esslinger, "Fermi-Hubbard physics with atoms in an optical lattice," Annu. Rev. Condens. Matter Phys. **1**, 129 (2010).

[49] J. Simon, W. S. Bakr, R. Ma, M. E. Tai, P. M. Preiss, and M. Greiner, "Quantum simulation of antiferromagnetic spin chains in an optical lattice," Nature (London) **472**, 307 (2011).

[50] D. Greif, T. Uehlinger, G. Jotzu, L. Tarruell, and T. Esslinger, "Short-range quantum magnetism of ultracold fermions in an optical lattice," Science , 1236362 (2013).

[51] R. A. Hart, P. M. Duarte, T.-L. Yang, X. Liu, T. Paiva, E. Khatami, R. T. Scalettar, N. Trivedi, D. A. Huse, and R. G. Hulet, "Observation of antiferromagnetic correlations in the Hubbard model with ultracold atoms," Nature (London) **519**, 211 (2015).

[52] A. Mazurenko, C. S. Chiu, G. Ji, M. F. Parsons, M. Kanász-Nagy, R. Schmidt, F. Grusdt, E. Demler, D. Greif, and M. Greiner, "A cold-atom Fermi–Hubbard antiferromagnet," Nature (London) **545**, 462 (2017).

[53] P. T. Brown, D. Mitra, E. Guardado-Sanchez, P. Schauß, S. S. Kondov, E. Khatami, T. Paiva, N. Trivedi, D. A. Huse, and W. S. Bakr, "Spin-imbalance in a 2D Fermi-Hubbard system," Science **357**, 1385 (2017).

[54] C. A. Regal, M. Greiner, and D. S. Jin, "Observation of resonance condensation of fermionic atom pairs," Phys. Rev. Lett. **92**, 040403 (2004).

[55] C. A. R. Sá de Melo, "When fermions become bosons: Pairing in ultracold gases," Physics Today **61**, 45 (2008).

[56] M. W. Zwierlein, J. R. Abo-Shaeer, A. Schirotzek, C. H. Schunck, and W. Ketterle, "Vortices and superfluidity in a strongly interacting Fermi gas," Nature (London) **435**, 1047 (2005).

[57] A. J. Leggett, "Cooper pairing in spin-polarized Fermi systems," J. Phys. Colloq. **41**, C7–19 (1980).

[58] P. Nozieres and S. Schmitt-Rink, "Bose condensation in an attractive fermion gas: From weak to strong coupling superconductivity," J. Low Temp. Phys. **59**, 195 (1985).

[59] Y. Ohashi and A. Griffin, "BCS-BEC crossover in a gas of Fermi atoms with a Feshbach resonance," Phys. Rev. Lett. **89**, 130402 (2002).

[60] Q. Chen, J. Stajic, S. Tan, and K. Levin, "BCS–BEC crossover: From high temperature superconductors to ultracold superfluids," Phys. Rep. **412**, 1 (2005).

[61] K. M. O'hara, S. L. Hemmer, M. E. Gehm, S. R. Granade, and J. E. Thomas, "Observation of a strongly interacting degenerate Fermi gas of atoms," Science **298**, 2179 (2002).

[62] M. Randeria and E. Taylor, "Crossover from Bardeen-Cooper-Schrieffer to Bose-Einstein condensation and the unitary Fermi gas," Annu. Rev. Condens. Matter Phys. **5**, 209 (2014).

[63] B. Paredes, A. Widera, V. Murg, O. Mandel, S. Fölling, I. Cirac, G. V. Shlyapnikov, T. W. Hänsch, and I. Bloch, "Tonks–Girardeau gas of ultracold atoms in an optical lattice," Nature (London) **429**, 277 (2004).

[64] T. Kinoshita, T. Wenger, and D. S. Weiss, "Observation of a one-dimensional Tonks-Girardeau gas," Science **305**, 1125 (2004).

[65] P. Makotyn, C. E. Klauss, D. L. Goldberger, E. A. Cornell, and D. S. Jin, "Universal dynamics of a degenerate unitary Bose gas," Nat. Phys. **10**, 116 (2014).

[66] A. Adams, L. D. Carr, T. Schaefer, P. Steinberg, and J. E. Thomas, "Strongly correlated quantum fluids: Ultracold quantum gases, quantum chromodynamic plasmas and holographic duality," New J. Phys. **14**, 115009 (2012).

[67] N. Goldman, J. C. Budich, and P. Zoller, "Topological quantum matter with ultracold gases in optical lattices," Nat. Phys. **12**, 639 (2016).

[68] N. R. Cooper, "Rapidly rotating atomic gases," Adv. Phys. **57**, 539 (2008).

[69] Y.-J. Lin, K. Jiménez-García, and I. B. Spielman, "Spin–orbit-coupled Bose–Einstein condensates," Nature (London) **471**, 83 (2011).

[70] M. Aidelsburger, M. Atala, M. Lohse, J. T. Barreiro, B. Paredes, and I. Bloch, "Realization of the Hofstadter Hamiltonian with ultracold atoms in optical lattices," Phys. Rev. Lett. **111**, 185301 (2013).

[71] M. Aidelsburger, M. Lohse, C. Schweizer, M. Atala, J. T. Barreiro, S. Nascimbene, N. Cooper, I. Bloch, and N. Goldman, "Measuring the Chern number of Hofstadter bands with ultracold bosonic atoms," Nat. Phys. **11**, 162 (2015).

[72] S. Nakajima, T. Tomita, S. Taie, T. Ichinose, H. Ozawa, L. Wang, M. Troyer, and Y. Takahashi, "Topological Thouless pumping of ultracold fermions," Nat. Phys. **12**, 296 (2016).

[73] R. Casalbuoni and G. Nardulli, "Inhomogeneous superconductivity in condensed matter and QCD," Rev. Mod. Phys. **76**, 263 (2004).

[74] L. Radzihovsky and D. E. Sheehy, "Imbalanced Feshbach-resonant Fermi gases," Rep. Prog. Phys. **73**, 076501 (2010).

[75] F. Chevy and C. Mora, "Ultra-cold polarized Fermi gases," Rep. Prog. Phys. **73**, 112401 (2010).

[76] K. B. Gubbels and H. T. C. Stoof, "Imbalanced Fermi gases at unitarity," Phys. Rep. **525**, 255 (2013).

[77] Y.-a. Liao, A. S. C. Rittner, T. Paprotta, W. Li, G. B. Partridge, R. G. Hulet, S. K. Baur, and E. J. Mueller, "Spin-imbalance in a one-dimensional Fermi gas," Nature (London) **467**, 567 (2010).

[78] M. Schreiber, S. S. Hodgman, P. Bordia, H. P. Lüschen, M. H. Fischer, R. Vosk, E. Altman, U. Schneider, and I. Bloch, "Observation of many-body localization of interacting fermions in a quasi-random optical lattice," Science **349**, 842 (2015).

[79] J.-y. Choi, S. Hild, J. Zeiher, P. Schauß, A. Rubio-Abadal, T. Yefsah, V. Khemani, D. A. Huse, I. Bloch, and C. Gross, "Exploring the many-body localization transition in two dimensions," Science **352**, 1547 (2016).

[80] R. Nandkishore and D. A. Huse, "Many-body localization and thermalization in quantum statistical mechanics," Annu. Rev. Condens. Matter Phys. **6**, 15 (2015).

[81] C. H. Greene, P. Giannakeas, and J. Perez-Rios, "Universal few-body physics and cluster formation," Rev. Mod. Phys. **89**, 035006 (2017).

[82] F. Ferlaino and R. Grimm, "Forty years of Efimov physics: How a bizarre prediction turned into a hot topic," Physics **3**, 9 (2010).

[83] P. Naidon and S. Endo, "Efimov physics: A review," Rep. Prog. Phys. **80**, 056001 (2017).

[84] V. Efimov, "Energy levels arising from resonant two-body forces in a three-body system," Phys. Lett. B **33**, 563 (1970).

[85] T. Kraemer, M. Mark, P. Waldburger, J. Danzl, C. Chin, B. Engeser, A. Lange, K. Pilch, A. Jaakkola, H.-C. Nägerl, *et al.*, "Evidence for Efimov quantum states in an ultracold gas of caesium atoms," Nature (London) **440**, 315 (2006).

[86] C. A. Regal, C. Ticknor, J. L. Bohn, and D. S. Jin, "Creation of ultracold molecules from a Fermi gas of atoms," Nature (London) **424**, 47 (2003).

[87] G. Quemener and P. S. Julienne, "Ultracold molecules under control!" Chem. Rev. **112**, 4949 (2012).

[88] L. D. Carr, D. DeMille, R. V. Krems, and J. Ye, "Cold and ultracold molecules: Science, technology and applications," New J. Phys. **11**, 055049 (2009).

[89] A. Polkovnikov, K. Sengupta, A. Silva, and M. Vengalattore, "Colloquium: Nonequilibrium dynamics of closed interacting quantum systems," Rev. Mod. Phys. **83**, 863 (2011).

[90] K. E. Strecker, G. B. Partridge, A. G. Truscott, and R. G. Hulet, "Formation and propagation of matter-wave soliton trains," Nature (London) **417**, 150 (2002).

[91] S. L. Cornish, S. T. Thompson, and C. E. Wieman, "Formation of bright matter-wave solitons during the collapse of attractive Bose-Einstein condensates," Phys. Rev. Lett. **96**, 170401 (2006).

[92] J. J. Chang, P. Engels, and M. A. Hoefer, "Formation of dispersive shock waves by merging and splitting Bose-Einstein condensates," Phys. Rev. Lett. **101**, 170404 (2008).

[93] C. Hamner, J. J. Chang, P. Engels, and M. A. Hoefer, "Generation of dark-bright soliton trains in superfluid-superfluid counterflow," Phys. Rev. Lett. **106**, 065302 (2011).

[94] J. H. V. Nguyen, D. Luo, and R. G. Hulet, "Formation of matter-wave soliton trains by modulational instability," Science **356**, 422 (2017).

[95] P. J. Everitt, M. A. Sooriyabandara, M. Guasoni, P. B. Wigley, C. H. Wei, G. D. McDonald, K. S. Hardman, P. Manju, J. D. Close, C. C. N. Kuhn, *et al.*, "Observation of a modulational instability in bose-einstein condensates," Phys. Rev. A **96**, 041601(R) (2017).

[96] G. Lamporesi, S. Donadello, S. Serafini, F. Dalfovo, and G. Ferrari, "Spontaneous creation of Kibble–Zurek solitons in a Bose–Einstein condensate," Nat. Phys. **9**, 656 (2013).

[97] T. W. B. Kibble, "Topology of cosmic domains and strings," J. Phys. A **9**, 1387 (1976).

[98] W. H. Zurek, "Cosmological experiments in superfluid helium?" Nature (London) **317**, 505 (1985).

[99] L. E. Sadler, J. M. Higbie, S. R. Leslie, M. Vengalattore, and D. M. Stamper-Kurn, "Spontaneous symmetry breaking in a quenched ferromagnetic spinor Bose–Einstein condensate," Nature (London) **443**, 312 (2006).

[100] C. N. Weiler, T. W. Neely, D. R. Scherer, A. S. Bradley, M. J. Davis, and B. P. Anderson, "Spontaneous vortices in the formation of Bose–Einstein condensates," Nature (London) **455**, 948 (2008).

[101] N. Fläschner, D. Vogel, M. Tarnowski, B. S. Rem, D.-S. Lühmann, M. Heyl, J. C. Budich, L. Mathey, K. Sengstock, and C. Weitenberg, "Observation of dynamical vortices after quenches in a system with topology," Nat. Phys. **14**, 265 (2018).

[102] J. Eisert, M. Friesdorf, and C. Gogolin, "Quantum many-body systems out of equilibrium," Nat. Phys. **11**, 124 (2015).

[103] T. Langen, R. Geiger, and J. Schmiedmayer, "Ultracold atoms out of equilibrium," Annu. Rev. Condens. Matter Phys. **6**, 201 (2015).

[104] M. Rigol, V. Dunjko, V. Yurovsky, and M. Olshanii, "Relaxation in a completely integrable many-body quantum system: An *ab initio* study of the dynamics of the highly excited states of 1D lattice hard-core bosons," Phys. Rev. Lett. **98**, 050405 (2007).

[105] M. Rigol, V. Dunjko, and M. Olshanii, "Thermalization and its mechanism for generic isolated quantum systems," Nature (London) **452**, 854 (2008).

[106] S. Trotzky, Y.-A. Chen, A. Flesch, I. P. McCulloch, U. Schollwöck, J. Eisert, and I. Bloch, "Probing the relaxation towards equilibrium in an isolated strongly correlated one-dimensional Bose gas," Nat. Phys. **8**, 325 (2012).

[107] M. Gring, M. Kuhnert, T. Langen, T. Kitagawa, B. Rauer, M. Schreitl, I. Mazets, D. A. Smith, E. Demler, and J. Schmiedmayer, "Relaxation and prethermalization in an isolated quantum system," Science **337**, 1318 (2012).

[108] T. Kinoshita, T. Wenger, and D. S. Weiss, "A quantum Newton's cradle," Nature (London) **440**, 900 (2006).

[109] S. Hofferberth, I. Lesanovsky, B. Fischer, T. Schumm, and J. Schmiedmayer, "Non-equilibrium coherence dynamics in one-dimensional Bose gases," Nature (London) **449**, 324 (2007).

[110] M. Greiner, O. Mandel, T. W. Hänsch, and I. Bloch, "Collapse and revival of the matter wave field of a Bose–Einstein condensate," Nature (London) **419**, 51 (2002).

[111] A. Eckardt, "Colloquium: Atomic quantum gases in periodically driven optical lattices," Rev. Mod. Phys. **89**, 011004 (2017).

[112] J. Zhang, P. W. Hess, A. Kyprianidis, P. Becker, A. Lee, J. Smith, G. Pagano, I.-D. Potirniche, A. C. Potter, A. Vishwanath, *et al.*, "Observation of a discrete time crystal," Nature (London) **543**, 217 (2017).

[113] S. Choi, J. Choi, R. Landig, G. Kucsko, H. Zhou, J. Isoya, F. Jelezko, S. Onoda, H. Sumiya, V. Khemani, *et al.*, "Observation of discrete time-crystalline order in a disordered dipolar many-body system," Nature (London) **543**, 221 (2017).

[114] L. W. Clark, A. Gaj, L. Feng, and C. Chin, "Collective emission of matter-wave jets from driven Bose–Einstein condensates," Nature (London) **551**, 356 (2017).

[115] R. Miller, T. E. Northup, K. M. Birnbaum, A. D. B. A. Boca, A. D. Boozer, and H. J. Kimble, "Trapped atoms in cavity QED: Coupling quantized light and matter," J. Phys. B **38**, S551 (2005).

[116] M. D. Lukin, "Colloquium: Trapping and manipulating photon states in atomic ensembles," Rev. Mod. Phys. **75**, 457 (2003).

[117] C. Gardiner and P. Zoller, *The Quantum World of Ultra-Cold Atoms and Light. Book II: The Physics of Quantum-Optical Devices* (Imperial College Press, 2015, 2015).

[118] S. Haroche, "Nobel Lecture: Controlling photons in a box and exploring the quantum to classical boundary," Rev. Mod. Phys. **85**, 1083 (2013).

[119] L. V. Hau, S. E. Harris, Z. Dutton, and C. H. Behroozi, "Light speed reduction to 17 metres per second in an ultracold atomic gas," Nature (London) **397**, 594 (1999).

[120] C. Liu, Z. Dutton, C. H. Behroozi, and L. V. Hau, "Observation of coherent optical information storage in an atomic medium using halted light pulses," Nature (London) **409**, 490 (2001).

[121] H. J. Kimble, "Strong interactions of single atoms and photons in cavity QED," Phys. Scr. **1998**, 127 (1998).

[122] O. Firstenberg, C. S. Adams, and S. Hofferberth, "Nonlinear quantum optics mediated by Rydberg interactions," J. Phys. B **49**, 152003 (2016).

[123] J. D. Pritchard, K. J. Weatherill, and C. S. Adams, "Nonlinear optics using cold Rydberg atoms," in *Annual Review of Cold Atoms and Molecules: Volume 1* (World Scientific, 2013) p. 301.

[124] D. E. Chang, V. Vuletić, and M. D. Lukin, "Quantum nonlinear optics—photon by photon," Nat. Photonics **8**, 685 (2014).

[125] M. J. Hartmann, "Quantum simulation with interacting photons," J. Opt. **18**, 104005 (2016).

[126] C. Noh and D. G. Angelakis, "Quantum simulations and many-body physics with light," Rep. Prog. Phys. **80**, 016401 (2016).

[127] I. Carusotto and C. Ciuti, "Quantum fluids of light," Rev. Mod. Phys. **85**, 299 (2013).

[128] D. G. Angelakis, *Quantum Simulations with Photons and Polaritons: Merging Quantum Optics with Condensed Matter Physics* (Springer International Publishing, 2017).

[129] H. Ritsch, P. Domokos, F. Brennecke, and T. Esslinger, "Cold atoms in cavity-generated dynamical optical potentials," Rev. Mod. Phys. **85**, 553 (2013).

[130] V. D. Vaidya, Y. Guo, R. M. Kroeze, K. E. Ballantine, A. J. Kollár, J. Keeling, and B. L. Lev, "Tunable-range, photon-mediated atomic interactions in multimode cavity QED," Phys. Rev. X **8**, 011002 (2018).

[131] H. Mabuchi and A. C. Doherty, "Cavity quantum electrodynamics: Coherence in context," Science **298**, 1372 (2002).

[132] S. Diehl, A. Micheli, A. Kantian, B. Kraus, H. P. Büchler, and P. Zoller, "Quantum states and phases in driven open quantum systems with cold atoms," Nat. Phys. **4**, 878 (2008).

[133] F. Verstraete, M. M. Wolf, and J. I. Cirac, "Quantum computation and quantum-state engineering driven by dissipation," Nat. Phys. **5**, 633 (2009).

[134] M. J. Hartmann, F. G. S. L. Brandao, and M. B. Plenio, "Quantum many-body phenomena in coupled cavity arrays," Laser Photonics Rev. **2**, 527 (2008).

[135] G. E. Marti, R. B. Hutson, A. Goban, S. L. Campbell, N. Poli, and J. Ye, "Imaging optical frequencies with 100 μ Hz precision and 1.1 μ m resolution," Phys. Rev. Lett. **120**, 103201 (2018).

[136] A. D. Ludlow, M. M. Boyd, J. Ye, E. Peik, and P. O. Schmidt, "Optical atomic clocks," Rev. Mod. Phys. **87**, 637 (2015).

[137] S.-B. Zheng and G.-C. Guo, "Efficient scheme for two-atom entanglement and quantum information processing in cavity QED," Phys. Rev. Lett. **85**, 2392 (2000).

[138] J.-M. Raimond, M. Brune, and S. Haroche, "Manipulating quantum entanglement with atoms and photons in a cavity," Rev. Mod. Phys. **73**, 565 (2001).

[139] S. Ritter, C. Nölleke, C. Hahn, A. Reiserer, A. Neuzner, M. Uphoff, M. Mücke, E. Figueroa, J. Bochmann, and G. Rempe, "An elementary quantum network of single atoms in optical cavities," Nature (London) **484**, 195 (2012).

[140] M. D. Lukin, M. Fleischhauer, R. Cote, L. M. Duan, D. Jaksch, J. I. Cirac, and P. Zoller, "Dipole blockade and quantum information processing in mesoscopic atomic ensembles," Phys. Rev. Lett. **87**, 037901 (2001).

[141] M. Saffman, T. G. Walker, and K. Mølmer, "Quantum information with Rydberg atoms," Rev. Mod. Phys. **82**, 2313 (2010).

[142] D. Paredes-Barato and C. S. Adams, "All-optical quantum information processing using Rydberg gates," Phys. Rev. Lett. **112**, 040501 (2014).

[143] D. Jaksch, J. I. Cirac, P. Zoller, S. L. Rolston, R. Côté, and M. D. Lukin, "Fast quantum gates for neutral atoms," Phys. Rev. Lett. **85**, 2208 (2000).

[144] O. Mandel, M. Greiner, A. Widera, T. Rom, T. W. Hänsch, and I. Bloch, "Controlled collisions for multi-particle entanglement of optically trapped atoms," Nature (London) **425**, 937 (2003).

[145] J. J. García-Ripoll, P. Zoller, and J. I. Cirac, "Quantum information processing with cold atoms and trapped ions," J. Phys. B **38**, S567 (2005).

[146] I. Bloch, "Quantum coherence and entanglement with ultracold atoms in optical lattices," Nature (London) **453**, 1016 (2008).

[147] D. S. Weiss and M. Saffman, "Quantum computing with neutral atoms," Physics Today **70**, 44 (2017).

[148] C. Monroe, "Quantum information processing with atoms and photons," Nature (London) **416**, 238 (2002).

[149] D. P. DiVincenzo, "The physical implementation of quantum computation," Fortschr. Phys. **48**, 771 (2000).

[150] P. Zoller, T. Beth, D. Binosi, R. Blatt, H. Briegel, D. Bruss, T. Calarco, J. I. Cirac, D. Deutsch, J. Eisert, *et al.*, "Quantum information processing and communication," Eur. Phys. J. D **36**, 203 (2005).

[151] T. D. Ladd, F. Jelezko, R. Laflamme, Y. Nakamura, C. Monroe, and J. L. O'Brien, "Quantum computers," Nature (London) **464**, 45 (2010).

[152] T. E. Northup and R. Blatt, "Quantum information transfer using photons," Nat. Photonics **8**, 356 (2014).

[153] H. J. Kimble, "The quantum internet," Nature (London) **453**, 1023 (2008).

[154] A. Stern, "Non-Abelian states of matter," Nature (London) **464**, 187 (2010).

[155] S. D. Sarma, M. Freedman, and C. Nayak, "Majorana zero modes and topological quantum computation," Quantum Inf. **1**, 15001 (2015).

[156] S. D. Sarma, M. Freedman, and C. Nayak, "Topological quantum computation," Physics Today **59**, 32 (2006).

[157] A. Y. Kitaev, "Fault-tolerant quantum computation by anyons," Ann. Phys. **303**, 2 (2003).

[158] C. Nayak, S. H. Simon, A. Stern, M. Freedman, and S. D. Sarma, "Non-Abelian anyons and topological quantum computation," Rev. Mod. Phys. **80**, 1083 (2008).

[159] N. P. Proukakis, D. W. Snoke, and P. B. Littlewood, eds., *Universal Themes of Bose-Einstein Condensation* (Cambridge University Press, Cambridge, 2017).

[160] R. D. Mattuck, *A Guide to Feynman Diagrams in the Many-Body Problem* (McGraw-Hill, New York, 1976).

[161] L. D. Landau, "The theory of a Fermi liquid," Sov. Phys. JETP **3**, 920 (1957), [Zh. Eksp. Teor. Fiz. **30**, 1058 (1956)].

[162] L. Venema, B. Verberck, I. Georgescu, G. Prando, E. Couderc, S. Milana, M. Maragkou, L. Persechini, G. Pacchioni, and L. Fleet, "The quasiparticle zoo," Nat. Phys. **12**, 1085 (2016).

[163] P. Wölfle, "Quasiparticles in condensed matter systems," Rep. Prog. Phys. **81**, 032501 (2018).

[164] A. S. Alexandrov and N. Mott, *Polarons and Bipolarons* (World Scientific, Singapore, 1995).

[165] A. S. Alexandrov and J. T. Devreese, *Advances in polaron physics* (Springer, New York, 2010).

[166] D. Emin, *Polarons* (Cambridge University Press, Cambridge, 2013).

[167] C. T. Walker and G. A. Slack, "Who named the -on's?" Am. J. Phys. **38**, 1380 (1970).

[168] I. G. Austin and N. F. Mott, "Polarons in crystalline and non-crystalline materials," Adv. Phys. **18**, 41 (1969).

[169] J. L. Bredas and G. B. Street, "Polarons, bipolarons, and solitons in conducting polymers," Acc. Chem. Res. **18**, 309 (1985).

[170] E. K. H. Salje, A. S. Alexandrov, and W. Y. Liang, *Polarons and Bipolarons in High-T_c Superconductors and Related Materials* (Cambridge University Press, Cambridge, 2005).

[171] A. S. Alexandrov, ed., *Polarons in Advanced Materials* (Springer, Dordrecht, 2007).

[172] P. Massignan, M. Zaccanti, and G. M. Bruun, "Polarons, dressed molecules and itinerant ferromagnetism in ultracold Fermi gases," Rep. Prog. Phys. **77**, 034401 (2014).

[173] S. Dutta and E. J. Mueller, "Variational study of polarons and bipolarons in a one-dimensional Bose lattice gas in both the superfluid and the Mott-insulator regimes," Phys. Rev. A **88**, 053601 (2013).

[174] T. Fukuhara, A. Kantian, M. Endres, M. Cheneau, P. Schauß, S. Hild, D. Bellem, U. Schollwöck, T. Giamarchi, C. Gross, *et al.*, "Quantum dynamics of a mobile spin impurity," Nat. Phys. **9**, 235 (2013).

[175] A. S. Alexandrov and N. F. Mott, "Bipolarons," Rep. Prog. Phys. **57**, 1197 (1994).

[176] D. N. Basov, M. M. Fogler, and F. J. G. de Abajo, "Polaritons in van der Waals materials," Science **354**, aag1992 (2016).

[177] D. Sanvitto and S. Kéna-Cohen, "The road towards polaritonic devices," Nat. Mater. **15**, 1061 (2016).

[178] J. Ningyuan, A. Georgakopoulos, A. Ryou, N. Schine, A. Sommer, and J. Simon, "Observation and characterization of cavity Rydberg polaritons," Phys. Rev. A **93**, 041802 (2016).

[179] N. Jia, N. Schine, A. Georgakopoulos, A. Ryou, L. W. Clark, A. Sommer, and J. Simon, "A strongly interacting polaritonic quantum dot," Nat. Phys. , 1 (2018).

[180] S. Dutta and E. J. Mueller, "Coherent generation of photonic fractional quantum Hall states in a cavity and the search for anyonic quasiparticles," Phys. Rev. A **97**, 033825 (2018).

[181] H. L. Stormer, D. C. Tsui, and A. C. Gossard, "The fractional quantum Hall effect," Rev. Mod. Phys. **71**, S298 (1999).

[182] R. B. Laughlin, "Nobel Lecture: Fractional quantization," Rev. Mod. Phys. **71**, 863 (1999).

[183] A. Stern, "Anyons and the quantum Hall effect—a pedagogical review," Ann. Phys. **323**, 204 (2008).

[184] N. Schine, A. Ryou, A. Gromov, A. Sommer, and J. Simon, "Synthetic Landau levels for photons," Nature (London) **534**, 671 (2016).

[185] J. R. Schrieffer, *Theory of Superconductivity* (Benjamin, New York, 1964).

[186] L. N. Cooper, "Nobel Lecture: Microscopic quantum interference in the theory of superconductivity," Science **181**, 908 (1973).

[187] N. N. Bogoljubov, "On a new method in the theory of superconductivity," Nuovo Cimento **7**, 794 (1958).

[188] J. G. Valatin, "Comments on the theory of superconductivity," Nuovo Cimento **7**, 843 (1958).

[189] P. G. De Gennes, "Boundary effects in superconductors," Rev. Mod. Phys. **36**, 225 (1964).

[190] P. G. De Gennes, *Superconductivity of Metals and Alloys* (Benjamin, New York, 1966).

[191] M. Remoissenet, *Waves called solitons: concepts and experiments* (Springer Science & Business Media, 2013).

[192] E. Infeld and G. Rowlands, *Nonlinear Waves, Solitons and Chaos* (Cambridge University Press, Cambridge, 2000).

[193] Y. S. Kivshar and G. Agrawal, *Optical Solitons: From Fibers to Photonic Crystals* (Academic Press, San Diego, 2003).

[194] Y. Lu, *Solitons and Polarons in Conducting Polymers* (World Scientific, Singapore, 1988).

[195] Y. V. Kartashov, B. A. Malomed, and L. Torner, "Solitons in nonlinear lattices," Rev. Mod. Phys. **83**, 247 (2011).

[196] P. G. Kevrekidis and D. J. Frantzeskakis, "Solitons in coupled nonlinear Schrödinger models: A survey of recent developments," Rev. Phys. **1**, 140 (2016).

[197] P. G. Kevrekidis, D. J. Frantzeskakis, and R. Carretero-González, *Emergent Nonlinear Phenomena in Bose-Einstein Condensates: Theory and Experiment* (Springer, Berlin, 2007).

[198] R. Rajaraman, *Solitons and Instantons* (North Holland, Amsterdam, 1982).

[199] E. J. Weinberg, *Classical Solutions in Quantum Field Theory: Solitons and Instantons in High Energy Physics* (Cambridge University Press, Cambridge, 2012).

[200] L. F. Mollenauer and J. P. Gordon, *Solitons in Optical Fibers: Fundamentals and Applications* (Academic Press, Boston, 2006).

[201] V. E. Zakharov and S. Wabnitz, eds., *Optical Solitons: Theoretical Challenges and Industrial Perspectives* (Springer-Verlag, Berlin, 1999).

[202] G. D. McDonald, C. C. N. Kuhn, K. S. Hardman, S. Bennetts, P. J. Everitt, P. A. Altin, J. E. Debs, J. D. Close, and N. P. Robins, "Bright solitonic matter-wave interferometer," Phys. Rev. Lett. **113**, 013002 (2014).

[203] M. H. Jakubowski, K. Steiglitz, and R. Squier, "Computing with solitons: A review and prospectus," in *Collision-Based Computing*, edited by A. Adamatzky (Springer, London, 2002) p. 277.

[204] J. Denschlag, J. E. Simsarian, D. L. Feder, C. W. Clark, L. A. Collins, J. Cubizolles, L. Deng, E. W. Hagley, K. Helmerson, W. P. Reinhardt, *et al.*, "Generating solitons by phase engineering of a Bose-Einstein condensate," Science **287**, 97 (2000).

[205] T. Yefsah, A. T. Sommer, M. J. Ku, L. W. Cheuk, W. Ji, W. S. Bakr, and M. W. Zwierlein, "Heavy solitons in a fermionic superfluid," Nature (London) **499**, 426 (2013).

[206] M. J. H. Ku, W. Ji, B. Mukherjee, E. Guardado-Sanchez, L. W. Cheuk, T. Yefsah, and M. W. Zwierlein, "Motion of a solitonic vortex in the BEC-BCS crossover," Phys. Rev. Lett. **113**, 065301 (2014).

[207] M. J. H. Ku, B. Mukherjee, T. Yefsah, and M. W. Zwierlein, "Cascade of solitonic excitations in a superfluid Fermi gas: From planar solitons to vortex rings and lines," Phys. Rev. Lett. **116**, 045304 (2016).

[208] S. Dutta and E. J. Mueller, "Collective modes of a soliton train in a Fermi superfluid," Phys. Rev. Lett. **118**, 260402 (2017).

[209] J. Goldstone, A. Salam, and S. Weinberg, "Broken symmetries," Phys. Rev. **127**, 965 (1962).

[210] D. Pekker and C. M. Varma, "Amplitude/Higgs modes in condensed matter physics," Annu. Rev. Condens. Matter Phys. **6**, 269 (2015).

[211] P. W. Anderson, "Superconductivity: Higgs, Anderson and all that," Nat. Phys. **11**, 93 (2015).

[212] Y. Matsuda and H. Shimahara, "Fulde–Ferrell–Larkin–Ovchinnikov state in heavy fermion superconductors," J. Phys. Soc. Jpn. **76**, 051005 (2007).

[213] G. Zwicknagl and J. Wosnitza, "Breaking translational invariance by population imbalance: The Fulde–Ferrell–Larkin–Ovchinnikov states," Int. J. Mod. Phys. B **24**, 3915 (2010).

[214] P. Fulde and R. A. Ferrell, "Superconductivity in a strong spin-exchange field," Phys. Rev. **135**, A550 (1964).

[215] A. I. Larkin and I. U. N. Ovchinnikov, "Nonuniform state of superconductors," Sov. Phys. JETP **20**, 762 (1965), [Zh. Eksp. Teor. Fiz. **47**, 1136 (1964)].

[216] G. Koutroulakis, H. Kühne, J. A. Schlueter, J. Wosnitza, and S. E. Brown, "Microscopic study of the Fulde-Ferrell-Larkin-Ovchinnikov state in an all-organic superconductor," Phys. Rev. Lett. **116**, 067003 (2016).

[217] M. C. Revelle, J. A. Fry, B. A. Olsen, and R. G. Hulet, "1D to 3D crossover of a spin-imbalanced fermi gas," Phys. Rev. Lett. **117**, 235301 (2016).

[218] S. Dutta and E. J. Mueller, "Protocol to engineer Fulde-Ferrell-Larkin-Ovchinnikov states in a cold Fermi gas," Phys. Rev. A **96**, 023612 (2017).

[219] S. B. Dugdale, "Life on the edge: A beginner's guide to the Fermi surface," Phys. Scr. **91**, 053009 (2016).

[220] X.-W. Guan, M. T. Batchelor, and C. Lee, "Fermi gases in one dimension: From Bethe ansatz to experiments," Rev. Mod. Phys. **85**, 1633 (2013).

[221] N. D. Mermin and H. Wagner, "Absence of ferromagnetism or antiferromagnetism in one-or two-dimensional isotropic Heisenberg models," Phys. Rev. Lett. **17**, 1133 (1966).

[222] P. C. Hohenberg, "Existence of long-range order in one and two dimensions," Phys. Rev. **158**, 383 (1967).

[223] M. M. Parish, S. K. Baur, E. J. Mueller, and D. A. Huse, "Quasi-one-dimensional polarized Fermi superfluids," Phys. Rev. Lett. **99**, 250403 (2007).

[224] S. Dutta and E. J. Mueller, "Dimensional crossover in a spin-imbalanced Fermi gas," Phys. Rev. A **94**, 063627 (2016).

[225] W. Yi and L.-M. Duan, "Detecting the breached-pair phase in a polarized ultracold Fermi gas," Phys. Rev. Lett. **97**, 120401 (2006).

[226] E. Gubankova, A. Schmitt, and F. Wilczek, "Stability conditions and Fermi surface topologies in a superconductor," Phys. Rev. B **74**, 064505 (2006).

[227] W. V. Liu and F. Wilczek, "Interior gap superfluidity," Phys. Rev. Lett. **90**, 047002 (2003).

[228] R. Zwanzig, *Nonequilibrium Statistical Mechanics* (Oxford University Press, Oxford, 2001).

[229] L. P. Kadanoff and G. Baym, *Quantum Statistical Mechanics: Green's Function Methods in Equilibrium and Nonequilibrium Problems* (Benjamin, New York, 1962).

[230] D. C. McKay and B. DeMarco, "Cooling in strongly correlated optical lattices: Prospects and challenges," Rep. Prog. Phys. **74**, 054401 (2011).

[231] T.-L. Ho and Q. Zhou, "Universal cooling scheme for quantum simulation," arXiv:0911.5506 .

[232] J.-S. Bernier, C. Kollath, A. Georges, L. De Leo, F. Gerbier, C. Salomon, and M. Köhl, "Cooling fermionic atoms in optical lattices by shaping the confinement," Phys. Rev. A **79**, 061601 (2009).

[233] D. M. Stamper-Kurn, H.-J. Miesner, A. P. Chikkatur, S. Inouye, J. Stenger, and W. Ketterle, "Reversible formation of a Bose-Einstein condensate," Phys. Rev. Lett. **81**, 2194 (1998).

[234] S. Stellmer, B. Pasquiou, R. Grimm, and F. Schreck, "Laser cooling to quantum degeneracy," Phys. Rev. Lett. **110**, 263003 (2013).

[235] S. Dutta and E. J. Mueller, "Kinetics of Bose-Einstein condensation in a dimple potential," Phys. Rev. A **91**, 013601 (2015).

[236] I. E. Mazets and J. Schmiedmayer, "Thermalization in a quasi-one-dimensional ultracold bosonic gas," New J. Phys. **12**, 055023 (2010).

CHAPTER 2

DYNAMICS OF SPIN IMPURITIES IN A ONE-DIMENSIONAL BOSE LATTICE GAS

This chapter was adapted from "Variational study of polarons and bipolarons in a one-dimensional Bose lattice gas in both the superfluid and the Mott-insulator regimes" by Shovan Dutta and Erich J. Mueller, published in Physical Review A **88**, *053601 (2013).*

2.1 Abstract

We use variational methods to study a spin impurity in a one-dimensional Bose lattice gas. Both in the strongly interacting superfluid regime and in the Mott regime we find that the impurity binds with a hole, forming a polaron. Our calculations for the dispersion of the polaron are consistent with recent experiments by Fukuhara *et. al.* [Nat. Phys. **9**, 235 (2013)] and give a better understanding of their numerical simulations. We find that for sufficiently weak interactions there are ranges of momentum for which the polaron is unstable. We propose experimentally studying the stability of the polaron by measuring the correlation between the impurity and the hole. We also study two interacting impurities, finding stable bipolarons for sufficiently strong interactions.

2.2 Introduction

Using single-site imaging techniques [1–6] it is now possible to track the motion of spin impurities in a gas of cold atoms trapped in an optical lattice [7–11]. Such a direct probe is unprecedented in condensed matter physics [12–15], and

has stimulated a rich body of theoretical work [16–21]. These experimental and theoretical studies are motivated in part by connections between the physics of a spin impurity and larger questions in quantum magnetism [22], high-T_c superconductivity [23], and transition-metal oxides [24]. Here we present a theoretical study of the properties of spin impurities in a one-dimensional (1D) Bose lattice gas.

In a typical experiment of this type, one first prepares an array of spin-polarized atoms on a lattice. Then Raman lasers flip one or more of these atomic spins, creating spin impurities. The excitations of the spin-polarized bath can dress such an impurity, producing a composite particle called a polaron [25–30]. In one recent experimental study involving a bosonic spin impurity in ^{87}Rb, Fukuhara *et. al.* found preliminary evidence of polaron like behavior within the superfluid regime [10]. They observed a suppression of the bath density near the impurity, and a strong renormalization of the impurity's hopping rate. In the Mott phase, their results are understood by mapping the system to a Heisenberg chain [31–34], whereas in the superfluid phase, they find good agreement with numerical time-dependent density-matrix renormalization group (t-DMRG) simulations [35]. Here we use simple variational arguments to explain the underlying physics.

We model this system by the two-species Bose-Hubbard Hamiltonian [36–38]. In Sec. 2.3.1, we analytically study the limiting cases of very strong and very weak coupling. Guided by these limiting behaviors, in Sec. 2.3.2, we propose a simple variational model that captures the physics in both limits, extending those descriptions to all interaction strengths. Our model begins with the Gutzwiller mean-field wave function [39–42] and adds correlation between a

single impurity and a hole. We find that our ansatz provides a rich picture of the physics of a spin impurity, and we believe it fully captures all the relevant physics. It is exact in the strongly and weakly interacting limits, but, like the underlying Gutzwiller mean-field theory, we do not believe that it is quantitatively accurate for intermediate coupling [43, 44].

In terms of the single-particle hopping rate J and the on-site interaction U [see Eq. (2.1)], we find stable polarons for all momenta when $J/U \lesssim 2.3$. This agrees with the experimental observation of a stable polaron at $J/U = 0.47$ [10]. We fully characterize the polaron, calculating its energy, spatial structure, and dispersion. From the dispersion we calculate the rate of expansion for a wave packet and find qualitative agreement with experimental and numerical studies in Ref. [10]. At weaker coupling ($J/U \gtrsim 2.3$), our ansatz predicts that the energy for a total momentum k may be lowered by unbinding the hole from the impurity. For $J/U \approx 2.3$, this instability only occurs for $k \approx 2\pi/3a$, where a is the lattice spacing. As J/U is increased, the instability window grows. Future experiments can map out such a "polaron phase diagram" by studying the correlations between the impurity and the density of the bath. We provide detailed predictions for such measurements.

Adding a second impurity to the system admits the possibility of a bound state of two polarons, a bipolaron. Such bound states are of intrinsic interest for a variety of reasons, including their possible role in high-T_c superconductivity [11, 45, 46]. In a recent experiment, two-magnon bound states were observed in the Mott phase [11]. The measurements are consistent with analytical predictions of the Heisenberg model. The study of polaron binding in the superfluid phase is much more challenging [45, 47]. We study a simple generalization of

our original variational model for the case of two impurities with zero total momentum. Our results indicate the formation of stable bipolarons in the superfluid phase for sufficiently strong interactions.

The rest of this article is organized as follows. In Sec. 2.3, we introduce the physical system and describe our proposed variational model. We analyze the system's properties in the Mott and the deep superfluid regime, with emphasis on how the correlation length of the impurity-hole binding changes with interaction strength. In Sec. 2.4, we discuss several physical predictions of our model, and present numerical results. In particular, we identify two qualitatively distinct regions in the superfluid phase, polaronic and "two particle." We show how the crossover can be detected experimentally from correlation measurements. Our variational model is extended to incorporate two impurities in Sec. 2.5, where we infer the existence of stable bipolarons at adequately large interactions. Finally, we summarize our findings and indicate possible directions of future research in Sec. 2.6. The appendices contain derivations of key analytical results.

2.3 Formalism

2.3.1 The Bose lattice gas and its limiting behaviors

We consider a one-dimensional chain of bosonic atoms in an optical lattice with a single spin impurity. Such a system can be experimentally realized by initially preparing the atoms (e.g., ^{87}Rb) in a definite hyperfine state (such as $|F = 1, m_F = -1\rangle$), and then changing the hyperfine state of one atom by the

single-site addressing technique (for example, to $|F = 2, m_F = -2\rangle$) [10]. The system is described by the two-species single-band Bose-Hubbard Hamiltonian at unity filling [36, 37]:

$$\hat{H} = -J \sum_{(l_1,l_2),\sigma} \hat{b}^\dagger_{l_1,\sigma} \hat{b}_{l_2,\sigma} + \frac{U}{2} \sum_{l,\sigma,\sigma'} \hat{n}_{l,\sigma} \hat{n}_{l,\sigma'} - \mu \sum_{l,\sigma} \hat{n}_{l,\sigma} \ . \tag{2.1}$$

Here (l_1, l_2) varies over all neighboring sites l_1 and l_2, σ denotes the spin index ($\uparrow$ or $\downarrow$), J represents the single-particle hopping amplitude, and U is the on-site repulsion energy. As is appropriate for models of ^{87}Rb, the interactions only depend on the total density on a site, and not the density of each spin component. $\hat{b}^\dagger_{l,\sigma}$ ($\hat{b}_{l,\sigma}$) and $\hat{n}_{l,\sigma}$ denote the creation (annihilation) and number operators for the boson of spin σ at site l. The chemical potential μ should be chosen so that the ground state is at unity filling. Although the experiment includes an additional trap along the chain, we do not model it here, as all observations are made near the center of the trap where the potential is roughly constant. The system undergoes a Mott-superfluid phase transition as J/U is increased beyond a critical value, $(J/U)_c \approx 0.086$ within mean-field theory [36]. In comparing with experiments it is useful to note that the Gutzwiller ansatz overestimates the stability of the superfluid, and the Mott transition actually occurs at $J/U \approx 0.29$ [48].

Mott regime

For $J \ll U$, single-particle hopping is energetically expensive, as it changes the on-site populations. This results in an interaction-driven "Mott" insulator. However, the impurity is able to move through a second-order process, and the system can be mapped onto the isotropic spin-1/2 Heisenberg chain [31–34]

$$\hat{H}_{\text{eff}} = -\frac{J_{\text{ex}}}{2} \sum_{(i,j)} (\hat{S}^+_i \hat{S}^-_j + \hat{S}^-_i \hat{S}^+_j) - J_{\text{ex}} \sum_{(i,j)} \hat{S}^z_i \hat{S}^z_j \ , \tag{2.2}$$

where $\hat{S}_i^+ = |\uparrow\rangle_i|\downarrow\rangle_i$ and $\hat{S}_i^- = |\downarrow\rangle_i|\uparrow\rangle_i$ are the spin-flip operators, $\hat{S}_i^z = (\hat{n}_{i,\uparrow} - \hat{n}_{i,\downarrow})/2$, and $J_{\text{ex}} = 4J^2/U$ is the superexchange coupling. Here the impurity has dispersion

$$\varepsilon_{\text{Mott}}(k) = \varepsilon_{\text{Mott}}(0) + J_{\text{ex}}(1 - \cos k) \tag{2.3}$$

corresponding to eigenstates

$$|k_{\text{Mott}}\rangle = \sum_j e^{ikj} \left[|\downarrow\rangle_j + \frac{J}{U}\big\{(1 + e^{ik})|+\rangle_j + (1 + e^{-ik})|-\rangle_j\big\} \right], \tag{2.4}$$

where $|\downarrow\rangle_j$ is the state where the $\downarrow$ impurity is localized at site j, and $|\pm\rangle_j = \hat{b}_{j\pm1,\uparrow}\hat{b}^\dagger_{j,\uparrow}|\downarrow\rangle_j$ (see Appendix 2.7 for a derivation). We see from Eq. (2.4) that the correlation hole is mostly localized at the impurity site, with a spread of order $(J/U)^2$ into the neighboring sites.

Deep superfluid regime

In the weak-coupling limit ($U \ll J$), one can study the system within the Bogoliubov approximation [49–52], where one takes quadratic fluctuations about a state where $\hat{b}_{0,\sigma} = \hat{b}^\dagger_{0,\sigma} = \sqrt{N^\sigma}$, N^σ being the number of particles in the condensate of spin σ. The single-impurity physics emerges in the limit $N^\downarrow \to 1$.

The Bose-Hubbard Hamiltonian [Eq. (2.1)] can be expressed in momentum space as ($\mathcal{N}$ denotes the total number of lattice sites)

$$\hat{H} = -\sum_{p,\sigma} \left(2J\cos p + \mu - \frac{U}{2} \right) \hat{b}^\dagger_{p,\sigma}\hat{b}_{p,\sigma} + \frac{U}{2\mathcal{N}} \sum_{p_1,p_2,q,\sigma_1,\sigma_2} \hat{b}^\dagger_{p_1,\sigma_1}\hat{b}^\dagger_{p2,\sigma_2}\hat{b}_{p1+q,\sigma_1}\hat{b}_{p_2-q,\sigma_2} \ , \tag{2.5}$$

where the momenta are summed over $2\pi m/\mathcal{N}$ with integer m. To quadratic

order in fluctuations (see Appendix 2.8 for derivation),

$$\hat{H} = E_0 + \sum_{p\neq 0} \left[\varepsilon_c(p)\ \hat{c}_p^\dagger \hat{c}_p + \varepsilon_0(p)\ \hat{d}_p^\dagger \hat{d}_p \right] , \tag{2.6}$$

$$\text{where} \quad \varepsilon_0(p) = 2J\ (1 - \cos p) \tag{2.7}$$

$$\text{and} \quad \varepsilon_c(p) = \sqrt{[\varepsilon_0(p)]^2 + 2\ \varepsilon_0(p)\ U\ (n^\uparrow + n^\downarrow)} \tag{2.8}$$

are the excitation spectra, n^σ denote the average particle densities of the condensates, and E_0 is a constant. $\hat{c}_p$ and $\hat{d}_p$ are the annihilation operators of the Bogoliubov quasiparticles, defined by the canonical transformation

$$\hat{b}_{p,\uparrow/\downarrow} = \sqrt{\frac{n^{\uparrow/\downarrow}}{n^\uparrow + n^\downarrow}}\,(u_p \hat{c}_p + v_p \hat{c}_{-p}^\dagger) \mp \sqrt{\frac{n^{\downarrow/\uparrow}}{n^\uparrow + n^\downarrow}}\ \hat{d}_p\ , \tag{2.9}$$

$$\text{with } u_p, v_p = 0.5 \left[\sqrt{\varepsilon_0(p)/\varepsilon_c(p)} \pm \sqrt{\varepsilon_c(p)/\varepsilon_0(p)}\ \right] . \tag{2.10}$$

In the limit $n^\downarrow \to 0$, the $\hat{d}_p$ operators simply correspond to the impurity annihilation operators, and the $\hat{c}_p$'s reduce to the standard single-component Bogoliubov operators. More generically, $\varepsilon_0(p)$ corresponds to the energy of the Goldstone mode associated with the SU(2) rotational symmetry between the $\uparrow$ and $\downarrow$ spins.

In the limit $n^\downarrow \to 0$ and $n^\uparrow \to 1$, we wish to calculate $n_{h,j}$, the hole density at a distance j from the impurity. We relate $n_{h,j}$ to a correlation function by noting that, in the limit of small $n^\downarrow$,

$$C_j \equiv \langle \hat{b}_{j,\uparrow}^\dagger \hat{b}_{j,\uparrow} \hat{b}_{0,\downarrow}^\dagger \hat{b}_{0,\downarrow} \rangle = n^\downarrow (1 - n_{h,j})\ . \tag{2.11}$$

Direct calculation of C_j then yields

$$n_{h,j} = \frac{1}{\mathcal{N}} \sum_{p\neq 0} \left(1 - \frac{\varepsilon_0(p)}{\varepsilon_c(p)} \right) \cos pj\ . \tag{2.12}$$

As shown in Fig. 2.1, there is a strong tendency to have a hole near the impurity.

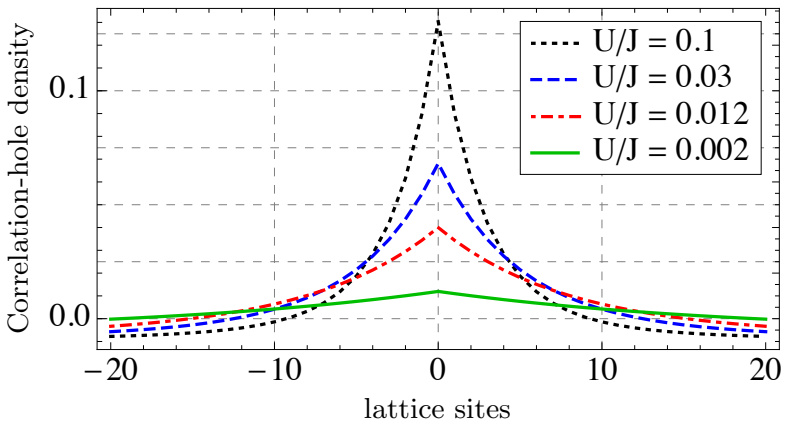

Figure 2.1: Correlation-hole density in the Bogoliubov approximation for zero total momentum, plotted with $\mathcal{N} = 101$. The impurity-hole binding weakens at lower U/J, leading to a flatter profile.

As indicated by the strength of the correlations at short distances, the impurity-hole binding becomes weaker at lower interaction. The areas under the curves in Fig. 2.1 are constant. In fact, summing Eq. (2.12) over all j yields $\sum_j n_{h,j} = 0$. The impurity "pushes away" the bath atoms, causing an excess of particles far away.

2.3.2 The variational wave function

Guided by the limiting properties of the impurity-hole binding discussed above, we propose the following variational wave function for the system with momentum k:

$$|k\rangle = \sum_j |j\rangle\, e^{ikj}, \quad \text{where} \quad |j\rangle = A\, \hat{b}^\dagger_{j,\downarrow}|\text{MF}\rangle + \sum_i f_i\, \hat{b}_{i+j,\uparrow}\hat{b}^\dagger_{j,\downarrow}|\text{MF}\rangle. \tag{2.13}$$

Here $|\text{MF}\rangle = \prod_l \sum_n \beta_n |n\rangle_l$ denotes the Gutzwiller mean-field ground state of the bath, where the amplitudes β_n for having n bath atoms on a site are determined by minimizing the energy. Variational parameters A and f_i encode whether and how strongly the impurity binds with a hole at different distances.

In the Mott phase, the impurity is strongly bound to a localized hole with a small spread, as seen from Eq. (2.4). Thus in this limit we expect $A \to 0$, $f_{\pm 1} \to (J/U)(1 + e^{\pm ik}) f_0$, and $f_i \lesssim O((J/U)^2)$ for $|i| \geq 2$, whereas for weak coupling, the f_i's should approach uniform magnitudes as the interactions are lowered, since the correlation length ought to increase. These conjectures are confirmed in our numerical studies. In the next section, we present several physical predictions of our model. For our numerical calculation we use 101 lattice sites with a maximum of 20 bath atoms at one site. Throughout the remainder we set $\hbar = 1$ and $a = 1$. We label the optimized energy of the variational state as $E_{\text{var}}(J/U, k)$.

2.4 Results

2.4.1 Polarons

We find that the system exhibits stable polaronic excitations for all momenta at sufficiently strong repulsive interactions ($U/J \gtrsim 0.44$). Here the impurity displaces bath atoms around it, as illustrated by the correlations plotted in Fig. 2.2. The polaron becomes more spread out as U/J is lowered. The momentum dependence of the polaron's size is more complicated. For a given U/J, the healing length increases with k for small k, reaches a maximum for $k \approx 2\pi/3$, then decreases rapidly. At finite k we observe decaying oscillations in the correlations with wavelength $\lambda \approx 4\pi/k$.

In Ref. [10] the experimentalists measure the speed of propagation of an initially localized spin impurity. As a first step toward understanding such trans-

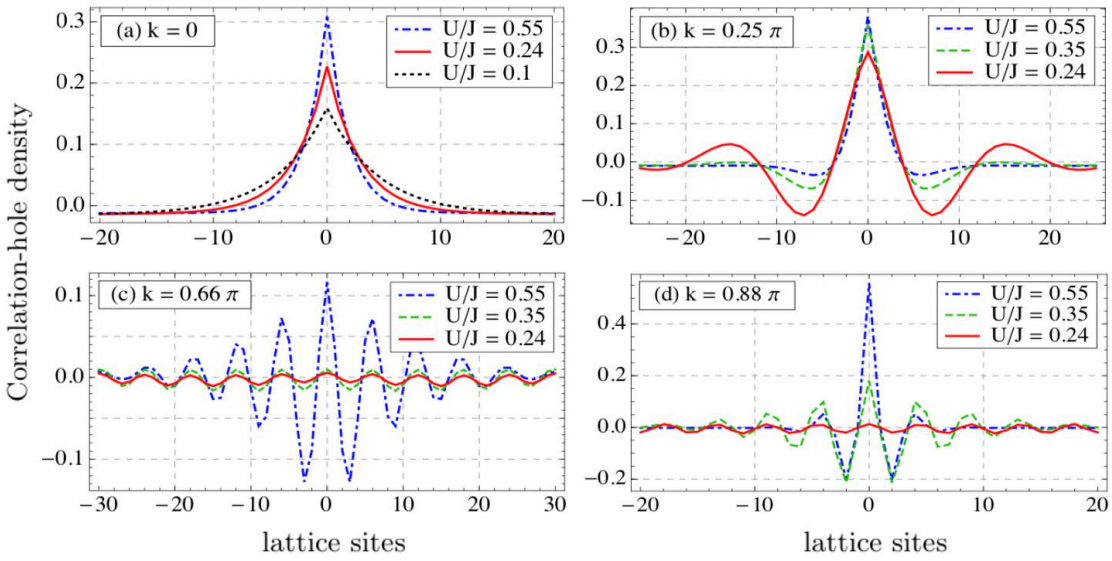

Figure 2.2: Correlation-hole density in the vicinity of the impurity located at 0 for (a) $k = 0$, (b) $k = 0.25\pi$, (c) $k = 0.66\pi$, and (d) $k = 0.88\pi$, from our variational wave function. At strong interactions, we see polaronic excitation for all values of k. Here the impurity displaces nearby bath atoms, creating a (symmetric) bath density oscillation of period $\approx 4\pi/k$ within the healing length. The healing length increases with decreasing U/J and is largest for $k \approx 2\pi/3$. For nonzero k, the system crosses over to the particle-hole continuum below a certain interaction strength, where the bath distribution becomes essentially independent of the impurity location. This crossover occurs at $U/J \approx 0.16$, 0.44, and 0.29 for $k = 0.25\pi$, 0.66π, and 0.88π, respectively. Such a crossover does not happen for $k = 0$ (compare with Fig. 2.1).

port, in Fig. 2.3(a) we plot the polaron group velocity $v_g = \partial E_{\text{var}}(J/U, k)/\partial k$ for several points in the Brillouin zone. We see that the velocities (in units of J) rapidly grow for small J/U, then reach plateaus when $J \gtrsim 0.5\ U$. The maximum velocity is much smaller than the maximum speed of propagation of a free particle with a tight-binding dispersion, $v_f = 2J$.

To model the propagation of an initially localized impurity we project the initial state $|\psi(0)\rangle = \hat{b}_{0,\uparrow}\hat{b}^{\dagger}_{0,\downarrow}|\text{MF}\rangle$ into our variational subspace to find its time evolution:

$$|\psi(t)\rangle = \sum_k \frac{\langle k|\psi(0)\rangle}{\langle k|k\rangle}|k\rangle e^{-iE_{\text{var}}(k)t}\ . \tag{2.14}$$

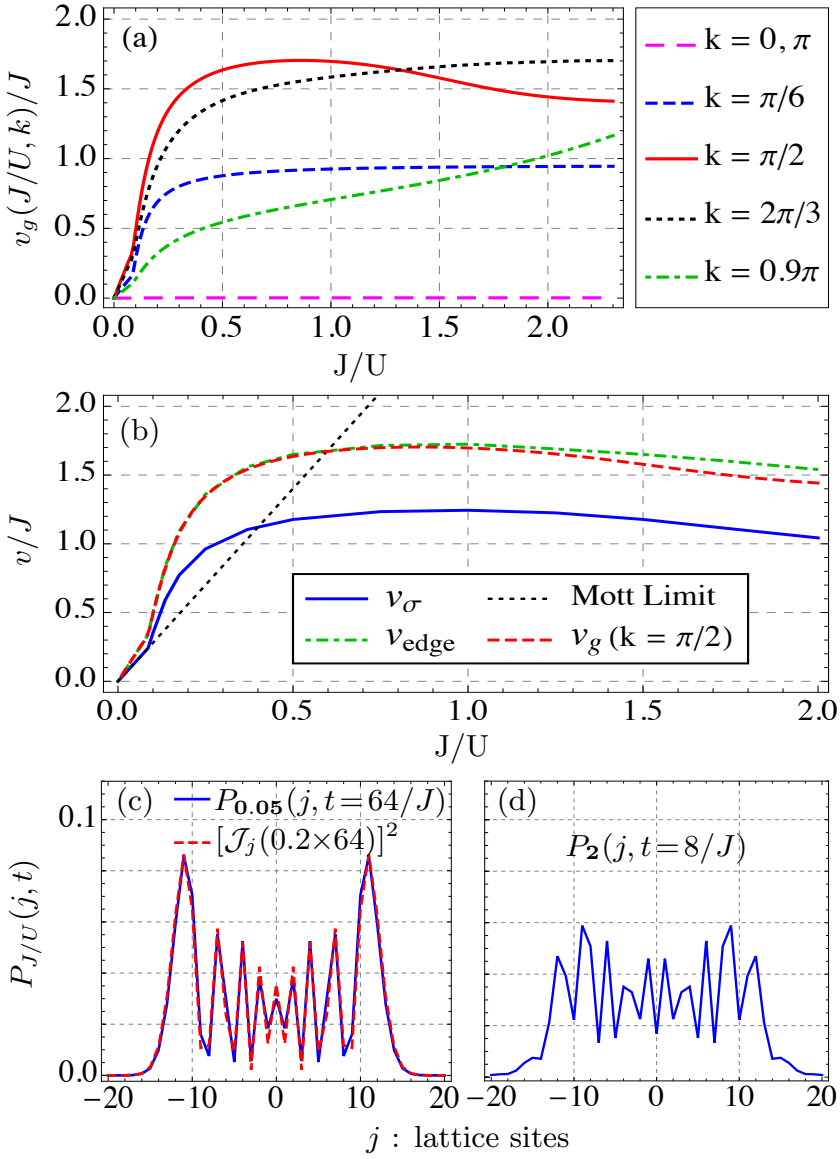

Figure 2.3: (a) Polaron group velocity at different momenta. After a rapid growth for small J/U, these saturate for $J/U \gtrsim 0.5$. (b) Propagation speed of an initially localized impurity in $|\psi(0)\rangle = \hat{b}_{0,\uparrow}\hat{b}^\dagger_{0,\downarrow}|\mathrm{MF}\rangle$ projected into our variational subspace. v_σ and $v_{\rm edge}$ denote expansion speeds of the standard deviation and the leading edges of the impurity distribution, respectively. $v_{\rm edge}$ closely mimics the group velocity at $k = \pi/2$. For $J/U \gtrsim 0.5$, both speeds level off at values much smaller than the free-particle tunneling $2J$. (c, d) Impurity distribution for $J/U = 0.05$ and 2, respectively. In the Mott phase the distribution is described by a squared Bessel function, as predicted by the Heisenberg model, whereas for large J/U it has a distinctly different shape.

The probability distribution of the impurity is calculated as $P(j,t) = \langle\psi(t)|\hat{b}^\dagger_{j,\downarrow}\hat{b}_{j,\downarrow}|\psi(t)\rangle/\langle\psi(t)|\psi(t)\rangle$. In Fig. 2.3(b) we plot the speed of propagation, v_σ, defined by taking the slope of $\sigma(t)$, where $\sigma(t) = \sum_j j^2 P(j,t)$. We find that for sufficiently large t, σ increases linearly, and this speed is well defined. In the Mott phase we find excellent agreement with the Heisenberg model, which predicts $P(j,t) = [\mathcal{J}_j(J_{\text{ex}}t)]^2$, where $\mathcal{J}_j$ denotes the Bessel function of the first kind [53] [see Fig. 2.3(c)]. The distribution deviates more and more from this shape as J/U increases [Fig. 2.3(d)]. In addition to v_σ, we calculate the speed of propagation of the leading edge by fitting a Bessel function to the tail of the wave packet. We plot this speed in Fig. 2.3(b), finding that it closely follows the group velocity of the dispersion at $k = \pi/2$. This correspondence is consistent with the idea that the speed of the edge is constrained by the maximum group velocity (which is approximately the group velocity at $k = \pi/2$) [54]. Both v_σ and v_{edge} grow linearly with J/U in the Mott regime and become fairly flat well inside the superfluid regime, in agreement with the experimental and simulation studies in Ref. [10]. We find a kink at the phase-transition point. We do not know if this kink is an artifact of the mean-field theory. No such feature is seen in the experiments. We find that the localized impurity state has less overlap with the variational subspace at larger J/U. This becomes especially important for $J/U \gtrsim 2.3$ when polarons become unstable for some momenta. Beyond this point the impurity dynamics are not well described by a single velocity.

2.4.2 Crossover to the particle-hole continuum

As illustrated in Fig. 2.2, for weaker interactions the correlations between the impurity and the bath no longer decay. This indicates that the impurity and the

hole are not bound. To investigate this physics we study the wave function

$$|k\,;p\rangle = \hat{b}_{p,\uparrow}\hat{b}^{\dagger}_{p-k,\downarrow}|\mathrm{MF}\rangle\ , \tag{2.15}$$

where p is a variational parameter. This represents an uncorrelated impurity and hole. It is a special case of Eq. (2.13). For a given k, we have a continuum of energies $E_{\text{two}}(k,p)$ found by varying p. In Fig. 2.4 we plot this continuum and our variational ground-state energy for $U/J = 0.37$. For small and large values of k, the ground-state energy is below the continuum, representing a stable polaron. At intermediate k, our variational approach finds the state at the bottom of the continuum, which does not correspond to a polaron. If the polaron exists at these momenta, its energy would be within the continuum. We expect that due to Landau damping it would have a short lifetime [50]. We find that at small and large k, the polaron dispersion $E_{\text{var}}(k)$ is well approximated by the free-particle form $E(k) = E_0 - 2J_{\text{eff}}\cos(k)$, which Fig. 2.4 shows entering the particle-hole continuum.

We denote the bottom of the particle-hole continuum as $E^{\text{min}}_{\text{two}}(J/U,k)$. In Fig. 2.5 we estimate the region of the stability of the polaron by plotting the difference between the energies $E^{\text{min}}_{\text{two}}$ and E_{var}. The unstable region is to the left of the dark contour in Fig. 2.5, where these two energies are nearly equal. The instability window starts from $k \approx 2\pi/3$ at $U/J \approx 0.44$ and grows as the interaction is reduced.

To further illustrate this physics, in Fig. 2.6 we plot $n_{h,0}$, the excess-hole density at the impurity site. We again see two distinct regions: the polaronic regime where $n_{h,0}$ is finite, and a two-particle regime where $n_{h,0}$ vanishes. The crossover location coincides with the dark curve in Fig. 2.5. These correlations could readily be measured in an experiment.

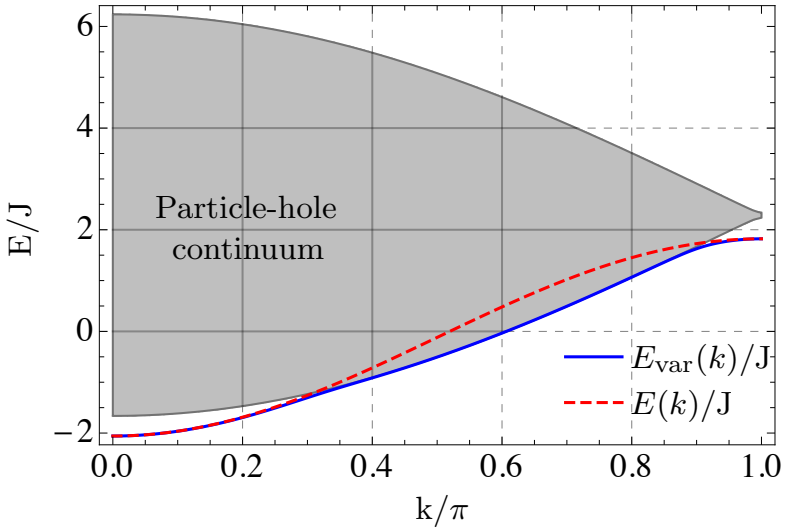

Figure 2.4: Energy of states with one impurity and one excess hole for $U/J = 0.37$. Solid line denotes the variational ground state, $E_{\rm var}(k)$; shaded region denotes the independent particle-hole continuum; dashed line denotes the approximate polaron dispersion $E(k) = E_0 - 2J_{\rm eff}\cos(k)$, where E_0 and $J_{\rm eff}$ are chosen so that $E(0) = E_{\rm var}(0)$ and $E(\pi) = E_{\rm var}(\pi)$. At small and large k, $E_{\rm var}(k)$ describes a stable polaron. For intermediate k, the polaron energy lies within the particle-hole continuum. Thus we expect it to be short lived due to Landau damping.

Throughout the two-particle regime, the lowest-energy continuum state has $p \approx k/2$, leading to the small-amplitude ($\sim 1/\mathcal{N}$) density oscillations of period $4\pi/k$ in Fig. 2.2. We can analytically calculate this optimal p in the limit $U/J \to 0$. Here the Bogoliubov quasiparticle spectra reduce to the free-particle spectrum, $\varepsilon_0(p) = 2J(1 - \cos p)$, and the quasiparticle operators are simply the particle and hole operators [Eqs. (2.7)–(2.10)]. Since $\cos p + \cos(k - p)$ is maximized when $p = k/2$, it becomes energetically favorable to divide the total momentum equally between the impurity and the hole.

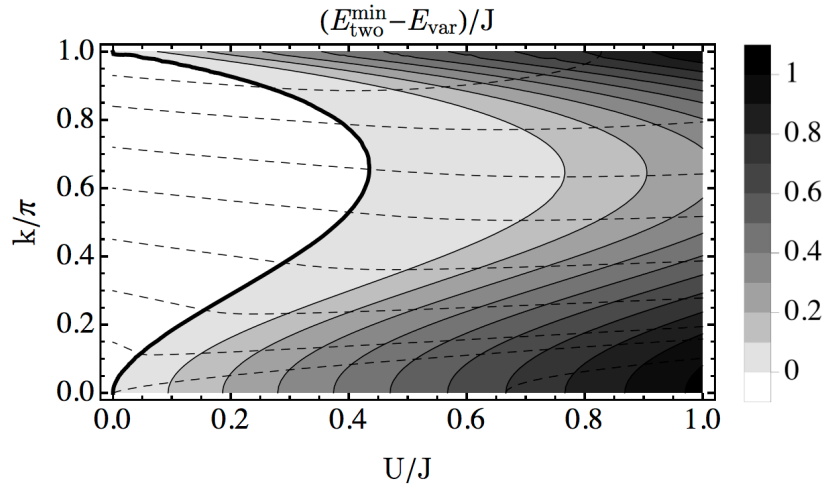

Figure 2.5: Contour plot of the energy difference between our variational state in Eq. (2.13) and the bottom of the uncorrelated particle-hole continuum of states from Eq. (2.15). Dotted lines show constant energy contours for E_{var}. For $U/J \gtrsim 0.44$, the variational ground state is lower in energy and describes a stable polaron. The two energies coincide to the left of the dark contour. Thus at weaker interactions there exists a growing range of momenta where the polaron is unstable, and the ground state belongs to the particle-hole continuum.

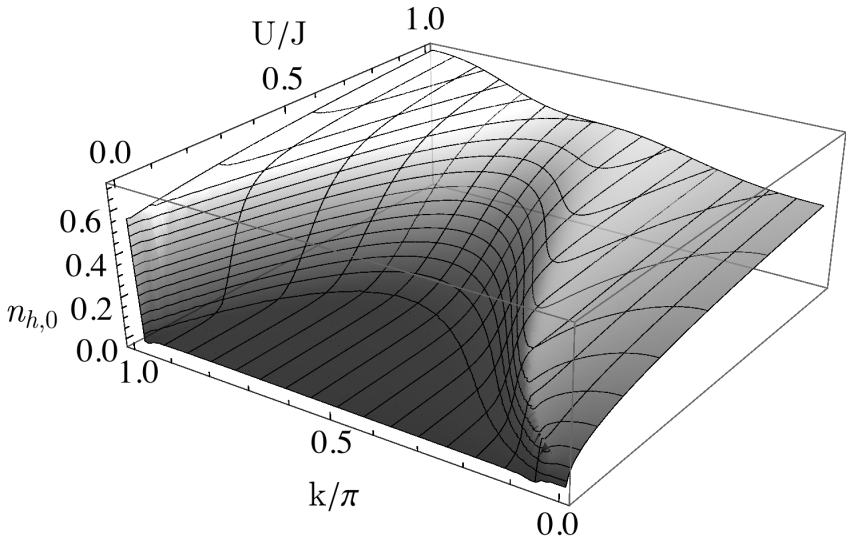

Figure 2.6: Correlation-hole density at the impurity site. As the system crosses over from the polaronic to the two-particle regime, the hole density rapidly falls toward zero. These correlations can be measured in experiments.

2.5 Two impurities and bipolarons

A recent experimental study observed two-magnon bound states in the Mott regime [11]. Here the attraction arises from the fact that two flipped spins lower energy by sitting next to one another in the Heisenberg model. The stability of bipolarons in the superfluid phase is not obvious, though related studies have found regimes of stable bipolarons in superfluids [45, 47]. Here we find that bipolarons are stable for $J/U \lesssim 0.15$, but unstable for weaker interactions.

We study the following variational wave function for the case of zero total momentum, which is a simple extension of our model in Eq. (2.13):

$$|\psi\rangle = \sum_{d\geq 0,\, j} \left[A(d) + \sum_{l} g(d,l)\ \hat{b}_{j+l,\uparrow} \right] \hat{b}^{\dagger}_{j,\downarrow} \hat{b}^{\dagger}_{j+d,\downarrow} |\mathrm{MF}\rangle \ , \tag{2.16}$$

where $A(d)$ and $g(d,l)$ are variational parameters that control how the two impurities bind with holes and with each other. In Fig. 2.7 we plot

$$P(d) = \sum_{j} \langle\psi| \hat{b}^{\dagger}_{j+d,\downarrow} \hat{b}^{\dagger}_{j,\downarrow} \hat{b}_{j,\downarrow} \hat{b}_{j+d,\downarrow} |\psi\rangle / \langle\psi|\psi\rangle \tag{2.17}$$

for optimal parameter values, which gives the separation probability of the two impurities.

For sufficiently strong interactions, the probability peaks at unity separation, falling off rapidly for greater distances. This indicates that the two polarons are bound. As J/U is raised, the distribution becomes flatter, so the average distance between the two polarons grows. For $J/U \gtrsim 0.15$, the average separation scales with the system size. We interpret this to mean that the polarons are no longer bound, and we are studying scattering states. Note that the Mott-superfluid transition occurs at $J/U \approx 0.086$ in our model, and our model gives stable polarons at all k for $J/U \lesssim 2.3$. Thus we have four regions: (i) Mott

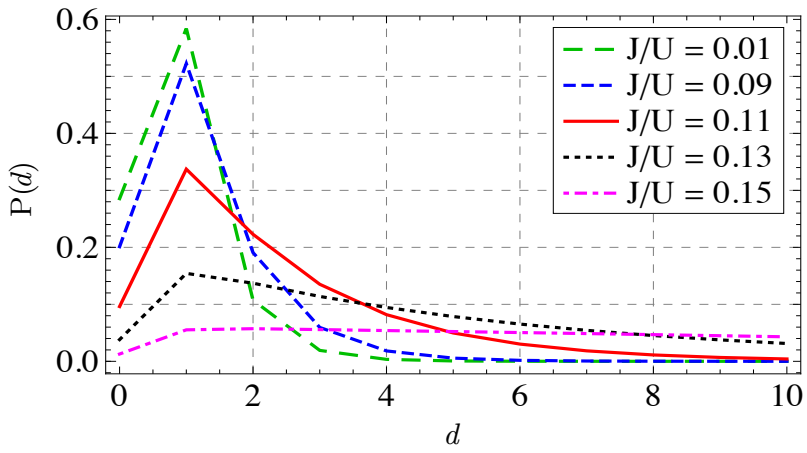

Figure 2.7: Separation probability of the two impurities, as predicted by the variational wave function in Eq. (2.16) on a lattice with 40 sites. In the Mott and the strongly interacting superfluid phase, the most probable separation of the impurities is one site, and the probabilities fall roughly exponentially with distance. For weaker interactions, the probabilities do not decay.

(where polarons and bipolarons are stable), (ii) superfluid with stable polarons and bipolarons, (iii) superfluid with stable polarons but no bipolarons, and (iv) superfluid where polarons are stable only for a narrow momentum range.

2.6 Summary and outlook

In this work we have studied spin impurities in a 1D Bose lattice gas through a computationally tractable variational ansatz. This ansatz provides an intuitive picture of phenomena seen in recent experiments and simulations. Our method reproduces the correct analytic results at strong and weak coupling.

For the case of a single impurity, we find stable polarons for all momenta when $U/J \gtrsim 0.44$. The polaron becomes larger with decreasing U/J. A moving polaron is bigger than a static one, attaining maximum size for $k \approx 2\pi/3$. We find that the impurity-hole correlations oscillate with wavelength $\approx 4\pi/k$.

We calculate the impurity mobility from the polaronic dispersion. In the Mott phase, it increases linearly with J/U, as predicted by the Heisenberg model, whereas well inside the superfluid phase, it saturates at a value much smaller than the free-particle hopping, as was experimentally observed in Ref. [10]. At weaker interactions our model suggests that the polaron energy lies within the particle-hole continuum for intermediate k. Here we expect the polaron to be short lived due to Landau damping. For the two-impurity system with zero total momentum, we find stable bipolarons for $J/U \lesssim 0.15$.

Future experiments can probe the transition from the polaronic to the two-particle regime by studying impurity-hole correlations. As was illustrated in Ref. [10], one can measure the density at the impurity site and compare it with the average density. This crossover should also show up in momentum-resolved radio-frequency spectroscopy or other techniques which probe the single-particle spectral function. The spectrum should be bimodal, with one peak coming from the polaron and the other from the particle-hole continuum. This intuition is confirmed by explicit calculations in related systems [30]. The techniques in Ref. [11] can be extended to study the stability of bipolarons in the superfluid phase. On the theoretical side, it would be interesting to study the system at higher dimensions and at filling factors different from unity [55], as well as the effects of disorder on the polaron dynamics [56]. One of the most intriguing results we find is a kink in the polaron spread velocity when one crosses the Mott transition. It would be valuable to learn if this is an artifact or a real physical feature.

Acknowledgments

We thank Yariv Yanay for discussions. This work was supported by the National Science Foundation Grant PHY-1068165. S.D. was partially supported by the Dr. V. Ramachandra Rao Summer Fellowship.

2.7 Appendix A: Eigenstates of the Hamiltonian in the Mott phase from second-order perturbation theory

For completeness, in this appendix we calculate the polaron states in the Mott limit to leading order in J/U [31–34]. The Bose-Hubbard Hamiltonian in Eq. (2.1) can be expressed as $\hat{H} = \hat{H}_0 - (J/U)\hat{H}_1$, where

$$\hat{H}_0 = \frac{U}{2} \sum_{l,\sigma,\sigma'} \hat{n}_{l,\sigma} \hat{n}_{l,\sigma'} \ , \tag{2.18}$$

$$\hat{H}_1 = U \sum_{(l_1,l_2),\sigma} \hat{b}^\dagger_{l_1,\sigma} \hat{b}_{l_2,\sigma} \ . \tag{2.19}$$

We treat $\hat{H}_1$ as a perturbation. A chemical potential is unnecessary as we are working with states of fixed particle number. The eigenstates of the Heisenberg Hamiltonian [(Eq. (2.2)] are given by $|k_{\text{eff}}\rangle = \sum_j e^{ikj} \ |\downarrow\rangle_j$, where $|\downarrow\rangle_j$ is the state where the impurity is localized at site j, and all other sites have one $\uparrow$ spin. We write the eigenstates of $\hat{H}$ as $|k\rangle = |k_{\text{eff}}\rangle + \sum_\alpha d_\alpha |\alpha\rangle$, where $|\alpha\rangle$ denotes states of the form

$$|\beta\rangle_{ij} \ = \ \hat{b}_{j,\uparrow} \hat{b}^\dagger_{i,\uparrow} |\downarrow\rangle_i \ \ (i \neq j) \ , \tag{2.20}$$

$$|\gamma\rangle_{ijk} \ = \ \hat{b}_{j,\uparrow} \hat{b}^\dagger_{k,\uparrow} |\downarrow\rangle_i \ \ (i \neq j \neq k) \ , \tag{2.21}$$

which are parametrized by indices ij and ijk. From degenerate second-order perturbation theory,

$$\begin{aligned}|k\rangle &= |k_{\text{eff}}\rangle + \frac{J}{U}\sum_j e^{ikj}\sum_\alpha |\alpha\rangle \frac{\langle\alpha|\hat{H}_1|\downarrow\rangle_j}{\langle\alpha|\hat{H}_0|\alpha\rangle - {}_j\langle\downarrow|\hat{H}_0|\downarrow\rangle_j} \\ &= |k_{\text{eff}}\rangle + \frac{J}{U^2}\sum_j e^{ikj}\sum_\alpha |\alpha\rangle\langle\alpha|\hat{H}_1|\downarrow\rangle_j \\ &= \sum_j e^{ikj}\left[|\downarrow\rangle_j + \frac{J}{U}\big\{(1+e^{ik})|+\rangle_j + (1+e^{-ik})|-\rangle_j\big\}\right] \\ &\quad + \sqrt{2}\,\frac{J}{U}\sum_j e^{ikj}\sum_{l\neq j,j-1}\left(|\gamma\rangle_{j(l+1)l} + |\gamma\rangle_{jl(l+1)}\right), \end{aligned} \tag{2.22}$$

where $|\pm\rangle_j = \hat{b}_{j\pm1,\uparrow}\hat{b}^\dagger_{j,\uparrow}|\downarrow\rangle_j$. The k dependence in the dispersion comes from the matrix element of the Hamiltonian between $|k_{\text{eff}}\rangle$ and the states $|\pm\rangle_j$ which represent impurity hopping. The other correction states only contribute a constant term.

2.8 Appendix B: Bogoliubov weak-coupling analysis

In this appendix we calculate the correlation-hole density around an impurity within the Bogoliubov approximation [51, 52]. Using $\hat{b}_{0,\sigma} = \hat{b}^\dagger_{0,\sigma} = \sqrt{N^\sigma}$ in the Bose-Hubbard Hamiltonian [Eq. (2.5)] and retaining quadratic fluctuations, we obtain the mean-field Hamiltonian:

$$\begin{aligned}\hat{H} = H_0 &- \sum_{p\neq0,\sigma}\left(2J\cos p + \tilde{\mu} - U\frac{N}{\mathcal{N}}\right)\,\hat{b}^\dagger_{p,\sigma}\hat{b}_{p,\sigma} \\ &+ \frac{U}{2}\sum_{p\neq0,\sigma_1,\sigma_2}\Big[\sqrt{n^{\sigma_1}n^{\sigma_2}}\,\hat{b}^\dagger_{p,\sigma_1}(\hat{b}_{p,\sigma_2} + \hat{b}^\dagger_{-p,\sigma_2}) + \text{H.c.}\Big], \end{aligned} \tag{2.23}$$

where $n^\sigma = N^\sigma/\mathcal{N}$, $N = \sum_\sigma N^\sigma$, $\tilde{\mu} = \mu - U/2$, and $H_0 = -(2J+\tilde{\mu})N + \frac{U}{2\mathcal{N}}N^2$. The constant H_0 is minimized when

$$\tilde{\mu} = -2J + U(N/\mathcal{N})\,. \tag{2.24}$$

Substituting this back into Eq. (2.23) yields

$$\hat{H} = -\frac{1}{2}\frac{U}{\mathcal{N}}N^2 + \sum_{p\neq 0,\sigma} \varepsilon_0(p)\ \hat{b}^\dagger_{p,\sigma}\hat{b}_{p,\sigma} + \frac{U}{2}\sum_{p\neq 0,\sigma_1,\sigma_2}\Big[\sqrt{n^{\sigma_1}n^{\sigma_2}}\ \hat{b}^\dagger_{p,\sigma_1}(\hat{b}_{p,\sigma_2}+\hat{b}^\dagger_{-p,\sigma_2}) + \text{H.c.}\Big], \tag{2.25}$$

where $\varepsilon_0(p) = 2J(1-\cos p)$. We wish to diagonalize this Hamiltonian to produce

$$\hat{H} = E_0 + \sum_{p\neq 0}\left(\varepsilon_c(p)\ \hat{c}^\dagger_p\hat{c}_p + \varepsilon_d(p)\ \hat{d}^\dagger_p\hat{d}_p\right)\ , \tag{2.26}$$

where the quasiparticle operators $\hat{c}_p$ and $\hat{d}_p$ are related to $\hat{b}_{p,\sigma}$ by a Bogoliubov transformation. A convenient way to find this transformation is to analyze the Heisenberg equations of motion:

$$i\partial_t\hat{b}_{p,\sigma} = \varepsilon_0(p)\,\hat{b}_{p,\sigma} + U\sqrt{n^\sigma}\sum_{\sigma'}\sqrt{n^{\sigma'}}(\hat{b}_{p,\sigma'} + \hat{b}^\dagger_{-p,\sigma'}), \tag{2.27}$$

$$i\partial_t\hat{c}_p = \varepsilon_c(p)\,\hat{c}_p\ , \tag{2.28}$$

$$i\partial_t\hat{d}_p = \varepsilon_d(p)\,\hat{d}_p\ . \tag{2.29}$$

These can be written more succinctly as

$$i\partial_t\hat{B}^+_{p,\sigma} = \varepsilon_0(p)\hat{B}^-_{p,\sigma}\ , \tag{2.30}$$

$$i\partial_t\hat{B}^-_{p,\sigma} = \varepsilon_0(p)\hat{B}^+_{p,\sigma} + 2U\sqrt{n^\sigma}\sum_{\sigma'}\sqrt{n^{\sigma'}}\hat{B}^+_{p,\sigma'}\ , \tag{2.31}$$

$$i\partial_t\hat{C}^\pm_p = \varepsilon_c(p)\hat{C}^\mp_p\ , \tag{2.32}$$

$$i\partial_t\hat{D}^\pm_p = \varepsilon_d(p)\hat{D}^\mp_p\ , \tag{2.33}$$

where $\hat{B}^\pm_{p,\sigma} = \frac{1}{\sqrt{2}}(\hat{b}_{p,\sigma} \pm \hat{b}^\dagger_{-p,\sigma})$, $\hat{C}^\pm_p = \frac{1}{\sqrt{2}}(\hat{c}_p \pm \hat{c}^\dagger_{-p})$, and $\hat{D}^\pm_p = \frac{1}{\sqrt{2}}(\hat{d}_p \pm \hat{d}^\dagger_{-p})$. We define the transformation

$$\hat{B}^\pm_{p,\sigma} = \Gamma^\pm_{p,\sigma}\hat{C}^\pm_p + \Delta^\pm_{p,\sigma}\hat{D}^\pm_p\ . \tag{2.34}$$

From bosonic commutation relations it follows that

$$\Gamma^+_{p,\sigma}\Gamma^-_{p,\sigma} + \Delta^+_{p,\sigma}\Delta^-_{p,\sigma} = 0\ . \tag{2.35}$$

In addition, using Eqs. (2.32)–(2.34) in Eqs. (2.30) and (2.31) yields

$$\Gamma^{+}_{p,\sigma}\ \varepsilon_c(p) = \Gamma^{-}_{p,\sigma}\ \varepsilon_0(p)\ , \tag{2.36}$$

$$\Gamma^{-}_{p,\sigma}\ \varepsilon_c(p) = \Gamma^{+}_{p,\sigma}\ \varepsilon_0(p) + 2U\sqrt{n^{\sigma}}\sum_{\sigma'}\sqrt{n^{\sigma'}}\,\Gamma^{+}_{p,\sigma'}\ , \tag{2.37}$$

and similar equations for Δ. These equations, along with Eq. (2.35), can be solved to obtain (with $f^{\sigma} \equiv N^{\sigma}/N$)

$$\varepsilon_c(p) = \sqrt{(\varepsilon_0(p))^2 + 2\ \varepsilon_0(p)\ U\ (n^{\uparrow} + n^{\downarrow})}\ , \tag{2.38}$$

$$\varepsilon_d(p) = \varepsilon_0(p)\ , \tag{2.39}$$

$$\Gamma^{+}_{p,\uparrow/\downarrow} = \sqrt{f^{\uparrow/\downarrow}\ \varepsilon_0(p)/\varepsilon_c(p)}\ , \tag{2.40}$$

$$\Gamma^{-}_{p,\uparrow/\downarrow} = \sqrt{f^{\uparrow/\downarrow}\ \varepsilon_c(p)/\varepsilon_0(p)}\ , \tag{2.41}$$

$$\Delta^{\pm}_{p,\uparrow/\downarrow} = \mp\sqrt{f^{\downarrow/\uparrow}}\ , \tag{2.42}$$

In the limit $n^{\downarrow} \to 0$ and $n^{\uparrow} \to 1$, we can calculate the correlation-hole density as [see Eq. (2.11)]

$$\begin{aligned} n_{h,j} &= \big(\langle \hat{n}_{j,\uparrow}\rangle\langle \hat{n}_{0,\downarrow}\rangle - \langle \hat{n}_{j,\uparrow}\hat{n}_{0,\downarrow}\rangle\big)/n^{\downarrow} \\ &= \frac{1}{\mathcal{N}^2\, n^{\downarrow}} \sum_{p,q,s,t} \Big[\langle \hat{b}^{\dagger}_{p,\uparrow}\hat{b}_{q,\uparrow}\rangle\langle \hat{b}^{\dagger}_{s,\downarrow}\hat{b}_{t,\downarrow}\rangle - \langle \hat{b}^{\dagger}_{p,\uparrow}\hat{b}_{q,\uparrow}\hat{b}^{\dagger}_{s,\downarrow}\hat{b}_{t,\downarrow}\rangle\Big] e^{i(p-q)j}\ . \end{aligned} \tag{2.43}$$

Replacing the zero-momenta operators by $\sqrt{N^{\sigma}}$ and keeping the quadratic terms, we find

$$\begin{aligned} n_{h,j} &= -\frac{\sqrt{N^{\uparrow}N^{\downarrow}}}{\mathcal{N}^2\, n^{\downarrow}} \sum_{p,q\neq 0} \langle (\hat{b}_{p,\uparrow} + \hat{b}^{\dagger}_{-p,\uparrow})(\hat{b}_{q,\downarrow} + \hat{b}^{\dagger}_{-q,\downarrow})\rangle\ e^{-ipj} \\ &= -\frac{2\sqrt{N^{\uparrow}N^{\downarrow}}}{\mathcal{N}^2\, n^{\downarrow}} \sum_{p,q\neq 0} \langle \hat{B}^{+}_{p,\uparrow}\hat{B}^{+}_{q,\downarrow}\rangle\ e^{-ipj}\ . \end{aligned} \tag{2.44}$$

Substituting Eq. (2.34) in the above equation and using the fact that $\hat{c}_p|\mathrm{MF}\rangle = \hat{d}_p|\mathrm{MF}\rangle = 0$, we get

$$\begin{aligned} n_{h,j} &= -\frac{\sqrt{N^{\uparrow}N^{\downarrow}}}{\mathcal{N}^2\, n^{\downarrow}} \sum_{p\neq 0} \big(\Gamma^{+}_{p,\uparrow}\Gamma^{+}_{p,\downarrow} + \Delta^{+}_{p,\uparrow}\Delta^{+}_{p,\downarrow}\big) \\ &= \big(1/\mathcal{N}\big) \sum_{p\neq 0} \big(1 - \varepsilon_0(p)/\varepsilon_c(p)\big)\cos pj\ . \end{aligned} \tag{2.45}$$

BIBLIOGRAPHY FOR CHAPTER 2

[1] M. Greiner, O. Mandel, T. Esslinger, T. W. Hänsch, and I. Bloch, "Quantum phase transition from a superfluid to a Mott insulator in a gas of ultracold atoms," Nature (London) **415**, 39 (2002).

[2] W. S. Bakr, J. I. Gillen, A. Peng, S. Fölling, and M. Greiner, "A quantum gas microscope for detecting single atoms in a Hubbard-regime optical lattice," Nature (London) **462**, 74 (2009).

[3] W. S. Bakr, A. Peng, M. E. Tai, R. Ma, J. Simon, J. I. Gillen, S. Foelling, L. Pollet, and M. Greiner, "Probing the superfluid–to–Mott insulator transition at the single-atom level," Science **329**, 547 (2010).

[4] J. F. Sherson, C. Weitenberg, M. Endres, M. Cheneau, I. Bloch, and S. Kuhr, "Single-atom-resolved fluorescence imaging of an atomic Mott insulator," Nature (London) **467**, 68 (2010).

[5] C. Weitenberg, M. Endres, J. F. Sherson, M. Cheneau, P. Schauß, T. Fukuhara, I. Bloch, and S. Kuhr, "Single-spin addressing in an atomic Mott insulator," Nature (London) **471**, 319 (2011).

[6] B. Gadway, D. Pertot, J. Reeves, and D. Schneble, "Probing an ultracold-atom crystal with matter waves," Nat. Phys. **8**, 544 (2012).

[7] S. Palzer, C. Zipkes, C. Sias, and M. Köhl, "Quantum transport through a Tonks-Girardeau gas," Phys. Rev. Lett. **103**, 150601 (2009).

[8] A. Schirotzek, C.-H. Wu, A. Sommer, and M. W. Zwierlein, "Observation of Fermi polarons in a tunable Fermi liquid of ultracold atoms," Phys. Rev. Lett. **102**, 230402 (2009).

[9] J. Catani, G. Lamporesi, D. Naik, M. Gring, M. Inguscio, F. Minardi, A. Kantian, and T. Giamarchi, "Quantum dynamics of impurities in a one-dimensional Bose gas," Phys. Rev. A **85**, 023623 (2012).

[10] T. Fukuhara, A. Kantian, M. Endres, M. Cheneau, P. Schauß, S. Hild, D. Bellem, U. Schollwöck, T. Giamarchi, C. Gross, *et al.*, "Quantum dynamics of a mobile spin impurity," Nat. Phys. **9**, 235 (2013).

[11] T. Fukuhara, P. Schauß, M. Endres, S. Hild, M. Cheneau, I. Bloch, and C. Gross, "Microscopic observation of magnon bound states and their dynamics," Nature (London) **502**, 76 (2013).

[12] I. Bloch, "Ultracold quantum gases in optical lattices," Nat. Phys. **1**, 23 (2005).

[13] M. Lewenstein, A. Sanpera, V. Ahufinger, B. Damski, A. Sen, and U. Sen, "Ultracold atomic gases in optical lattices: Mimicking condensed matter physics and beyond," Adv. Phys. **56**, 243 (2007).

[14] I. Bloch, J. Dalibard, and W. Zwerger, "Many-body physics with ultracold gases," Rev. Mod. Phys. **80**, 885 (2008).

[15] I. Bloch and P. Zoller, "Focus on cold atoms in optical lattices," New J. Phys. **8** (2006).

[16] G. E. Astrakharchik and L. P. Pitaevskii, "Motion of a heavy impurity through a Bose-Einstein condensate," Phys. Rev. A **70**, 013608 (2004).

[17] D. M. Gangardt and A. Kamenev, "Bloch oscillations in a one-dimensional spinor gas," Phys. Rev. Lett. **102**, 070402 (2009).

[18] M. A. Cazalilla, R. Citro, T. Giamarchi, E. Orignac, and M. Rigol, "One dimensional bosons: From condensed matter systems to ultracold gases," Rev. Mod. Phys. **83**, 1405 (2011).

[19] T. H. Johnson, S. R. Clark, M. Bruderer, and D. Jaksch, "Impurity transport through a strongly interacting bosonic quantum gas," Phys. Rev. A **84**, 023617 (2011).

[20] Y. Yanay, E. J. Mueller, and V. Elser, "Magnetic polarons in two-component hard-core bosons," Phys. Rev. A **87**, 043622 (2013).

[21] F. Massel, A. Kantian, A. J. Daley, T. Giamarchi, and P. Törmä, "Dynamics of an impurity in a one-dimensional lattice," New J. Phys. **15**, 045018 (2013).

[22] J. Simon, W. S. Bakr, R. Ma, M. E. Tai, P. M. Preiss, and M. Greiner, "Quantum simulation of antiferromagnetic spin chains in an optical lattice," Nature (London) **472**, 307 (2011).

[23] A. Klein and D. Jaksch, "Simulating high-temperature superconductivity model Hamiltonians with atoms in optical lattices," Phys. Rev. A **73**, 053613 (2006).

[24] M. Imada, A. Fujimori, and Y. Tokura, "Metal-insulator transitions," Rev. Mod. Phys. **70**, 1039 (1998).

[25] E. T. Whittaker and G. N. Watson, *Advances in Polaron Physics* (Springer-Verlag, Berlin, 2010).

[26] R. P. Feynman, *Statistical Mechanics* (W. A. Benjamin, London, 1972).

[27] R. P. Feynman, "Slow electrons in a polar crystal," Phys. Rev. **97**, 660 (1955).

[28] F. M. Cucchietti and E. Timmermans, "Strong-coupling polarons in dilute gas Bose-Einstein condensates," Phys. Rev. Lett. **96**, 210401 (2006).

[29] M. Bruderer, W. Bao, and D. Jaksch, "Self-trapping of impurities in Bose-Einstein condensates: Strong attractive and repulsive coupling," Europhys. Lett. **82**, 30004 (2008).

[30] S. P. Rath and R. Schmidt, "Field-theoretical study of the Bose polaron," Phys. Rev. A **88**, 053632 (2013).

[31] J. J. García-Ripoll and J. I. Cirac, "Spin dynamics for bosons in an optical lattice," New J. Phys. **5**, 76 (2003).

[32] T. Giamarchi, *Quantum Physics in One Dimension* (Oxford University Press, Oxford, 2004).

[33] A. B. Kuklov and B. V. Svistunov, "Counterflow superfluidity of two-species ultracold atoms in a commensurate optical lattice," Phys. Rev. Lett. **90**, 100401 (2003).

[34] L.-M. Duan, E. Demler, and M. D. Lukin, "Controlling spin exchange interactions of ultracold atoms in optical lattices," Phys. Rev. Lett. **91**, 090402 (2003).

[35] U. Schollwöck, "The density-matrix renormalization group," Rev. Mod. Phys. **77**, 259 (2005).

[36] S. Sachdev, *Quantum Phase Transitions* (Cambridge University Press, Cambridge, 2001).

[37] D. Jaksch, C. Bruder, J. I. Cirac, C. W. Gardiner, and P. Zoller, "Cold bosonic atoms in optical lattices," Phys. Rev. Lett. **81**, 3108 (1998).

[38] A. Albus, F. Illuminati, and J. Eisert, "Mixtures of bosonic and fermionic atoms in optical lattices," Phys. Rev. A **68**, 023606 (2003).

[39] D. S. Rokhsar and B. G. Kotliar, "Gutzwiller projection for bosons," Phys. Rev. B **44**, 10328 (1991).

[40] W. Krauth, M. Caffarel, and J.-P. Bouchaud, "Gutzwiller wave function for a model of strongly interacting bosons," Phys. Rev. B **45**, 3137 (1992).

[41] M. P. A. Fisher, P. B. Weichman, G. Grinstein, and D. S. Fisher, "Boson localization and the superfluid-insulator transition," Phys. Rev. B **40**, 546 (1989).

[42] K. Sheshadri, H. R. Krishnamurthy, R. Pandit, and T. V. Ramakrishnan, "Superfluid and insulating phases in an interacting-boson model: Mean-field theory and the RPA," Europhys. Lett. **22**, 257 (1993).

[43] W. Zwerger, "Mott–Hubbard transition of cold atoms in optical lattices," J. Opt. B **5**, S9 (2003).

[44] H. Pichler, J. Schachenmayer, A. J. Daley, and P. Zoller, "Heating dynamics of bosonic atoms in a noisy optical lattice," Phys. Rev. A **87**, 033606 (2013).

[45] W. Casteels, J. Tempere, and J. T. Devreese, "Bipolarons and multipolarons consisting of impurity atoms in a Bose-Einstein condensate," Phys. Rev. A **88**, 013613 (2013).

[46] A. S. Alexandrov and N. F. Mott, "Bipolarons," Rep. Prog. Phys. **57**, 1197 (1994).

[47] M. Bruderer, A. Klein, S. R. Clark, and D. Jaksch, "Polaron physics in optical lattices," Phys. Rev. A **76**, 011605 (2007).

[48] J. Zakrzewski and D. Delande, "Accurate determination of the superfluid-insulator transition in the one-dimensional Bose-Hubbard model," AIP Conf. Proc. **1076**, 292 (2008).

[49] N. Bogolubov, "On the theory of superfluidity," J. Phys. (Moscow) **11**, 23 (1947).

[50] G. D. Mahan, *Many-Particle Physics* (Kluwer Academic / Plenum, New York, 2000) Chap. 5.

[51] P. Tommasini, E. J. V. de Passos, A. F. R. de Toledo Piza, M. S. Hussein, and E. Timmermans, "Bogoliubov theory for mutually coherent condensates," Phys. Rev. A **67**, 023606 (2003).

[52] B. Sun and M. S. Pindzola, "Bogoliubov modes and the static structure factor for a two-species Bose–Einstein condensate," J. Phys. B **43**, 055301 (2010).

[53] N. Konno, "Limit theorem for continuous-time quantum walk on the line," Phys. Rev. E **72**, 026113 (2005).

[54] M. Cheneau, P. Barmettler, D. Poletti, M. Endres, P. Schauß, T. Fukuhara, C. Gross, I. Bloch, C. Kollath, and S. Kuhr, "Light-cone-like spreading of correlations in a quantum many-body system," Nature (London) **481**, 484 (2012).

[55] J. P. Ronzheimer, M. Schreiber, S. Braun, S. S. Hodgman, S. Langer, I. P. McCulloch, F. Heidrich-Meisner, I. Bloch, and U. Schneider, "Expansion dynamics of interacting bosons in homogeneous lattices in one and two dimensions," Phys. Rev. Lett. **110**, 205301 (2013).

[56] B. Damski, J. Zakrzewski, L. Santos, P. Zoller, and M. Lewenstein, "Atomic Bose and Anderson glasses in optical lattices," Phys. Rev. Lett. **91**, 080403 (2003).

CHAPTER 3

CREATING PHOTONIC FRACTIONAL QUANTUM HALL STATES AND BRAIDING ANYONS IN AN OPTICAL CAVITY

This chapter was adapted from "Coherent generation of photonic fractional quantum Hall states in a cavity and the search for anyonic quasiparticles" by Shovan Dutta and Erich J. Mueller, published in Physical Review A **97***, 033825 (2018).*

3.1 Abstract

We present and analyze a protocol in which polaritons in a noncoplanar optical cavity form fractional quantum Hall states. We model the formation of these states and present techniques for subsequently creating anyons and measuring their fractional exchange statistics. In this protocol, we use a rapid adiabatic passage scheme to sequentially add polaritons to the system, such that the system is coherently driven from n- to $(n+1)$-particle Laughlin states. Quasiholes are created by slowly moving local pinning potentials in from outside the cloud. They are braided by dragging the pinning centers around one another, and the resulting phases are measured interferometrically. The most technically challenging issue with implementing our procedure is that maintaining adiabaticity and coherence requires that the two-particle interaction energy V_0 be sufficiently large compared to the single-polariton decay rate γ, $V_0/\gamma \gg 10N^2 \ln N$, where N is the number of particles in the target state. While this condition is very demanding for present-day experiments where $V_0/\gamma \sim 50$, our protocol presents a significant advance over the existing protocols in the literature.

3.2 Introduction

Fractional quantum Hall (FQH) states are the iconic examples of strongly correlated topological phases. They arise from a delicate interplay between interactions and magnetic field in a two-dimensional (2D) electron gas [1–3]. Both theory [4–6] and experiments [7–9] suggest that they possess "anyonic" quasiparticle excitations with fractional statistics, which could provide the building blocks for fault-tolerant quantum computation [10, 11]. In recent years, synthetic quantum materials [12–19] have rapidly emerged as a promising platform to engineer FQH states, especially bosonic Laughlin states [20–24]. Two leading platforms are ultracold neutral atoms [21–42] and cavity photons [43–53]. Unfortunately, as we describe below, technical issues have so far prevented the realization of these aspirations. Here we describe a simple protocol which overcomes many of the hurdles. It will allow experimentalists to coherently produce particle-number-resolved $\nu = 1/2$ Laughlin states in a high-finesse optical cavity using techniques that have already been demonstrated [54–58]. We additionally show how one can create quasiholes in a Laughlin state that are bound to external laser potentials. We model a scheme for interferometrically measuring the braiding phase when two such quasiholes are moved around one another [59]. This procedure not only yields the quasiparticle exchange statistics, but is also a prototype of the externally controlled braiding needed for topological quantum computation.

Photonic systems offer unique features particularly suited for quantum information processing—fast dynamics, long coherence times, versatile optical in-out coupling, and ease of transmission over communication channels [60–63]. These features are also useful for preparing interesting many-body states. How-

ever, in conventional nonlinear media, photons interact too weakly with one another to establish strong enough correlation to produce FQH states. Nonetheless, some nontrivial quantum states, such as a thermal Bose-Einstein condensate, have been produced [64–68]. The strong-coupling limit can be reached by resonantly coupling the light to matter and using the matter-matter interactions to mediate the photon-photon interactions [18, 55, 69]. Such mediated interactions have been demonstrated in both optical and microwave domains. Optical experiments have confined the light via macroscopic cavities [57, 70] or photonic structures [71–73]. The interactions have been mediated by atoms [70, 71], quantum dots [72], semiconductor excitons [73, 74], or Rydberg-dressed atoms [57, 75]. Microwave experiments typically use resonating circuits and superconducting qubits [76, 77].

In addition to strong interactions, creating FQH states requires a magnetic field. Generating effective magnetic fields for photons is nontrivial. Nonetheless, by employing clever cavity designs to modify the photon dispersion [54, 78, 79], experiments have created synthetic gauge fields in "twisted" optical cavities [56, 58], microwave cavity arrays [77, 80], radio-frequency circuits [81], and solid-state photonic devices [82–88]. These developments have set the stage to explore FQH physics in a single optical cavity [56–58] or in a lattice of coupled microwave resonators [77, 80].

As in Ref. [51], we consider a near-degenerate cavity setup, similar to the one used to observe photonic Landau levels in Ref. [56] and shown schematically in Fig. 3.1. Because of the noncoplanar mirror geometry in such a twisted cavity, the transverse light field obeys a 2D Schrödinger equation with an effective magnetic field (see Sec. 3.3). One can induce strong photon-photon inter-

actions by loading ^{87}Rb atoms into a transverse plane of the cavity and illuminating them with a control beam that resonantly couples the cavity photons to a long-lived highly excited atomic state [89]. Experiments have demonstrated that the resulting Rydberg polaritons are both long lived [90] and strongly interacting [57].

Initial theoretical proposals to construct FQH phases in single-cavity [47, 48] and coupled-cavity [49, 50] setups employed a monochromatic drive to excite Laughlin states via multiphoton resonances. These proposals produce states with very small overlap with the desired Laughlin state, and the overlaps fall off exponentially with the number of photons in the target state [48]. More sophisticated schemes have been proposed recently which use frequency-selective incoherent pumps [51, 52, 91] or alternate flux insertions and coherent pumping [53]. Unfortunately, even these complex approaches are lacking. For example, the scheme in Ref. [51] yields at best a 70% overlap with the $N = 3$ Laughlin state. Using such a scheme to produce states with more particles seems impractical.

Here we describe a simpler and more effective protocol whereby one can reliably produce N-particle Laughlin states with high fidelity in a twisted optical cavity. As we explain in Sec. 3.4, this is achieved by using rapid adiabatic passage ideas to sequentially transfer the state of the cavity from n- to $(n + 1)$-particle Laughlin states [Fig. 3.5(a)]. For adiabaticity, the duration of each transfer, T, must be large compared to the inverse of the many-body level splittings. These splittings are proportional to the two-particle interaction energy V_0, and, for the Laughlin states, the splittings are nearly independent of the particle number. Thus, one finds that the accumulated error scales as $Ne^{-\xi}$,

where $\xi \propto V_0 T$. For our protocol to be successful, the experiment must also be faster than the coherence time set by polariton loss from the cavity. Hence, the key technical impediment to implementing our scheme, which is also present in the earlier proposals [47, 48, 51], is engineering a sufficiently large ratio between the interaction strength and the single-polariton decay rate γ. In particular, for a high-fidelity generation of the N-particle Laughlin state, we require $V_0/\gamma \gg 10N^2 \ln N$. Since current experimental setups yield $V_0/\gamma \sim 50$ [92], only the smallest N states may be reliably produced. While nontrivial, it is reasonable to expect this figure of merit will increase in the next few years, enabling the creation of higher N states. Despite this limitation, our protocol presents a significant step forward, as the existing protocols either have low fidelity (~ 0.01 for $N = 2$) [47, 48] or require prohibitively large values of V_0/γ ($\sim 3 \times 10^4$ for $N = 3$) [51].

A central motivation for preparing a Laughlin state is to observe anyonic statistics by creating quasiparticles and braiding them [47]. In Sec. 3.5 we show that one can generate quasiholes by adiabatically bringing in localized repulsive potentials through the edge of the cloud. These potentials can be engineered through the dynamical Stark shift from tightly focused lasers [93–95] (see Fig. 3.1). The cavity geometry can be tuned to eliminate the excitation of surface modes (Fig. 3.7). Subsequently, one can drag the pinning potentials around one another to perform quasihole braiding [23], which we discuss in Sec. 3.6. We find that both quasihole generation and braiding can be implemented with high fidelity over much shorter time scales than the preparation of the Laughlin state. In Sec. 3.7 we put forward an interferometric scheme to measure the braiding phase and extract the fractional exchange statistics (Fig. 3.10). We conclude with a summary and outlook in Sec. 3.8.

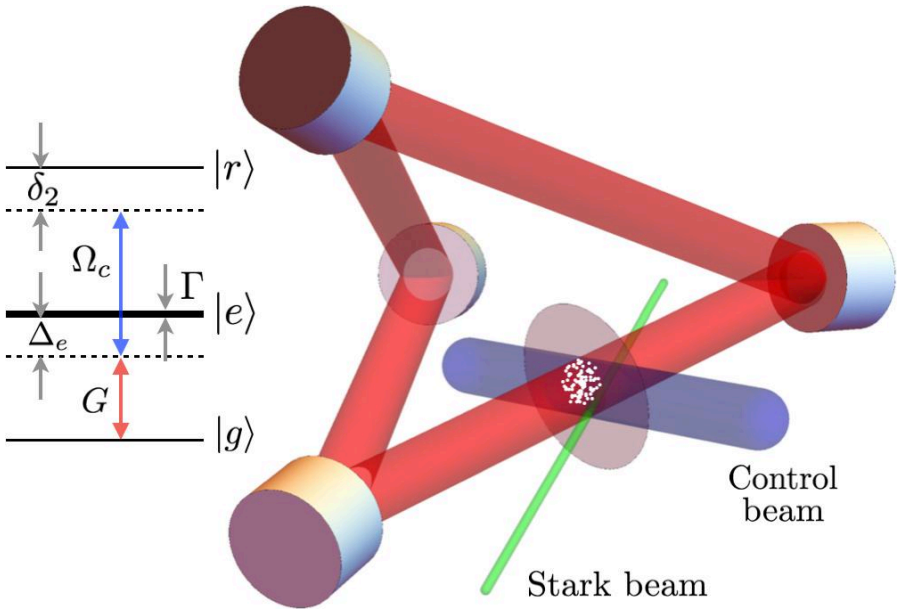

Figure 3.1: Schematic of the proposed cavity experiment. The noncoplanar arrangement of the mirrors gives rise to an effective magnetic field for the transverse dynamics of the cavity photons (red beam). These photons are coupled to atoms (white dots) loaded into a transverse plane (transparent disk) of the cavity. As shown in the energy level diagram, the photons couple the ground state $|g\rangle$ and an excited state $|e\rangle$ of the atoms with a collective Rabi frequency G. The excited state has a single-photon detuning Δ_e and lifetime $1/\Gamma$ and is coupled to a metastable Rydberg level $|r\rangle$ by a control laser (blue beam) with Rabi frequency Ω_c. When the two-photon detuning δ_2 is smaller than a linewidth, long-lived Rydberg polaritons form which inherit the transverse photon dynamics and interact strongly with one another. In Sec. 3.4 we describe how one can drive these polaritons to form $\nu = 1/2$ Laughlin states in the transverse plane. An additional laser (green beam) can be used to produce a localized potential for the polaritons via the ac Stark shift. As we show in Secs. 3.5 and 3.6, by moving such potentials relative to the polariton cloud, one can create and braid anyonic quasihole excitations in a Laughlin state.

While our analysis is focused on Rydberg polaritons in optical cavities, nearly identical modeling applies to exciton-polaritons in semiconductors [16, 17, 51, 73, 74, 96]. Brief estimates of the energy scales suggest that our ideas are readily transferable to that domain.

3.3 The physical system

3.3.1 Overview of polariton dynamics

We envision the "twisted" cavity setup of Ref. [56], shown schematically in Fig. 3.1. The cavity is nearly degenerate; i.e., the transverse dynamics are much slower than the longitudinal dynamics. In this limit, an effective equation can be derived for the transverse field profile within the cavity. This equation is identical to the Schrödinger equation for a 2D harmonically trapped charged particle in a uniform magnetic field. In Ref. [97] they gave an intuitive derivation of this mapping by tracing the coordinates of a light ray as it repeatedly intersects a transverse plane within the cavity. One thereby constructs a dynamical map which describes the stroboscopic evolution of the transverse position and wave vector of a light ray. The latter plays the role of momentum. In the paraxial approximation, this map is linear and is equivalently generated by a 2D quadratic Hamiltonian. Quantizing this Hamiltonian yields the desired Schrödinger equation. In the case of a planar cavity with flat mirrors, the dynamics map onto those of a free particle of mass $m_{\rm ph} = \hbar\omega_0/c^2$ where ω_0 is the frequency of the longitudinal mode and c is the speed of light. The mirror curvature confines the light in the transverse direction, leading to a harmonic trapping potential. The deviation from a planar geometry rotates the light field about the longitudinal axis, which gives rise to Coriolis and centrifugal forces in the transverse plane. The former acts as a uniform magnetic field perpendicular to the plane. Thus, the twisted cavity realizes a Fock-Darwin Hamiltonian [98, 99] describing massive, trapped particles in two dimensions experiencing a uniform magnetic field. The effective photon mass, trap frequency, and

magnetic field strength can be controlled independently by adjusting the cavity geometry.

Strong interactions can be introduced into the system by coupling the photons to an atomic ensemble in a Rydberg electromagnetically induced transparency (EIT) configuration [75, 100], as discussed in detail in Ref. [89] and illustrated in Fig. 3.1. A thin layer of laser-cooled atoms is loaded into the cavity waist. The cavity photons couple the atomic ground state to an intermediate excited state $|e\rangle$ which is in turn coupled to a metastable Rydberg level $|r\rangle$ by a strong control laser. This light-matter coupling yields two "bright" and one "dark" polariton modes [100, 101]. Near EIT resonance, the dark polariton mode has a long lifetime and represents a superposition of a collective Rydberg excitation and a cavity photon. The bright polariton modes, on the other hand, are short lived. For strong coupling, the splitting between the dark and bright modes is large compared to the energy scales of the transverse photon dynamics and Rydberg-Rydberg interactions. Then the problem reduces to describing the motion of dark polaritons in the cavity waist, which inherit the single-particle dynamics of photons and the interactions of Rydberg atoms.

3.3.2 Single-particle Hamiltonian

Projecting the 2D photon Hamiltonian onto the dark-polariton manifold renormalizes the photon mass and trap frequency, yielding the single-particle Hamiltonian

$$\hat{H}_0 = \int d^2r\, \hat{\psi}^\dagger(\vec{r}) \left[\frac{(-i\vec{\nabla} - M\omega_B r\hat{\varphi})^2}{2M} + \frac{1}{2}M\omega_T^2 r^2 \right] \hat{\psi}(\vec{r})\,, \tag{3.1}$$

where $\hat{\psi}(\vec{r})$ denotes the bosonic polariton field operator, M and ω_T are the effective polariton mass and trap frequency, ω_B denotes half the cyclotron frequency, and $\hat{\varphi}$ is the unit vector in the azimuthal direction. Here we have explicitly used a symmetric-gauge vector potential to represent the uniform magnetic field and set $\hbar = 1$. The cyclotron frequency $2\omega_B$ sets the energy gap between Landau levels and is typically a few GHz [56]. This is much faster than the motion of polaritons, so the dynamics are confined to the lowest Landau level. The polariton mass M is related to the photon mass m_{ph} and the collective Rabi frequencies G and Ω_c of the atomic transitions (see Fig. 3.1) via $M = m_{\text{ph}}/\cos^2\theta$, where $\theta \equiv \tan^{-1}(G/\Omega_c)$ [89]. For typical experimental parameters, $m_{\text{ph}} \sim 2 \times 10^{-5} m_e$ [56] and $\theta \approx 60^\circ$ [57, 90], we get $M \sim 10^{-4} m_e$, where m_e is the electron mass. Similarly, the trap frequency seen by polaritons is related to that seen by photons via $\omega_T = \omega_{T,\text{ph}} \cos^2\theta$, where $\omega_{T,\text{ph}}$ is calculated from the cavity geometry [92, 97]. This frequency was varied from zero to several tens of MHz in Ref. [56] by changing the mirror separation. As we will see in Sec. 3.5, one needs a finite ω_T in order to adiabatically produce quasiholes without exciting edge modes.

3.3.3 Interaction Hamiltonian

Rydberg atoms interact through a strong dipole-dipole coupling of the form $V(r) = C_6/r^6$ [102]. This leads to strong polariton-polariton interactions which are most simply modeled by a hard core of radius r_b, known as the "blockade radius" [89, 103]. For typical experimental conditions, r_b is several micrometers and can be varied using the scaling $r_b \propto n^{11/6}$, where n is the principal quantum number of the Rydberg state $|r\rangle$ [75, 104]. For mean polariton separations larger

than r_b, the interaction can be further approximated by a contact potential. In current experiments this regime can be reached for a few tens of polaritons by controlling the cavity waist radius $w \equiv \sqrt{2/(M\omega_B)}$ which sets the average polariton separation [92]. Under this approximation, we can write the interaction Hamiltonian

$$\hat{H}_{\text{int}} = g \int d^2 r \, \hat{\psi}^\dagger(\vec{r}) \hat{\psi}^\dagger(\vec{r}) \hat{\psi}(\vec{r}) \hat{\psi}(\vec{r}) \,, \tag{3.2}$$

where g is the effective interaction strength which depends on C_6 as well as the EIT parameters Ω_c, Δ_e, and Γ, where Ω_c denotes the Rabi frequency of the control laser, Δ_e is the detuning to the excited state $|e\rangle$, and Γ is the decay rate of $|e\rangle$. The Rydberg-Rydberg interactions are generically inelastic, which can be modeled by taking g complex. The imaginary part can, in principle, be made arbitrarily small by increasing both Ω_c and Δ_e while keeping the ratio $\Delta_e/\Omega_c \approx 0.25$ [92]. Thus, we limit ourselves to real values of g in this paper.

3.3.4 Single-particle spectrum

Combining Eqs. (3.1) and (3.2) we find the many-body Hamiltonian $\hat{H} = \hat{H}_0 + \hat{H}_{\text{int}}$. The single-particle spectrum in the absence of a trap consists of degenerate Landau levels separated by the cyclotron frequency $2\omega_B$. The lowest Landau level (LLL) is spanned by angular momentum eigenstates $\phi_m(\vec{r}) \propto r^m e^{im\varphi} \exp(-r^2/w^2)$ with $m = 0, 1, 2, \ldots$. The harmonic trap splits the energies of these states and rescales the wave functions, yielding new eigenstates $\phi_m(\vec{r}) \propto z^m e^{-|z|^2/2}$ with energies $\epsilon_m = \omega_{\text{eff}} + m\varepsilon$, where $z \equiv re^{i\varphi}/l$, $l \equiv 1/\sqrt{M\omega_{\text{eff}}}$, $\omega_{\text{eff}} \equiv \sqrt{\omega_B^2 + \omega_T^2}$, and $\varepsilon \equiv \omega_{\text{eff}} - \omega_B$. Note that $|\phi_m(\vec{r})|^2$ is peaked at $r = \sqrt{m}\, l$ and has a width $\Delta r \sim l$. In the absence of interactions, the energy of a many-body state in the LLL depends only on the total particle number N and

total angular momentum L. A generic noninteracting eigenstate takes the form of a Gaussian times a symmetric polynomial in the coordinates z_1, z_2, ..., z_N representing the positions of the N particles. Interactions split this degeneracy.

3.3.5 Laughlin states

An exact N-particle eigenstate of the Hamiltonian is the $\nu = 1/2$ Laughlin state [22]

$$\Phi_N(z_1, z_2, \ldots, z_N) \propto \prod_{j<k}(z_j - z_k)^2 e^{-\sum_i |z_i|^2/2}, \tag{3.3}$$

which is composed of single-particle states in the LLL with $m = 0, 1, \ldots, 2(N-1)$. It has zero interaction energy since the wave function vanishes whenever two particles coincide. Further, it is an angular momentum eigenstate with $L = N(N-1)$ and has energy $E_N = N\omega_{\text{eff}} + N(N-1)\varepsilon$. As we will see below, the Laughlin state is the lowest-energy N-particle state in the $L = N(N-1)$ manifold. Therefore, one way to excite $|\Phi_N\rangle$ is to pump on the single-particle mode with angular momentum $N-1$ and frequency $\omega_{\text{eff}} + (N-1)\varepsilon$, which is the essence of the multiphoton resonance protocols proposed in Refs. [47, 48]. However, as discussed in Sec. 3.2, this approach produces an exponentially small overlap with $|\Phi_N\rangle$ due to the coupling with other many-body states. Here we circumvent this problem by employing a rapid adiabatic passage protocol which drives the system from $|\Phi_0\rangle \to |\Phi_1\rangle \to \cdots \to |\Phi_N\rangle$ through a sequence of frequency sweeps. Physically, the transition from $|\Phi_n\rangle$ to $|\Phi_{n+1}\rangle$ is implemented by adding a particle with angular momentum $m = 2n$ while maintaining the strong correlation in Eq. (3.3).

3.3.6 Projection to lowest Landau level

The efficiency of our drive mechanism is limited by the energy splittings between the Laughlin states and the neighboring many-body states. To quantify this efficiency, we assume that the dynamics are confined to the LLL, as in Refs. [47, 48, 51], and consider states within that manifold. To ensure that the LLL is spectrally well resolved from the higher Landau levels, we need to take $\varepsilon \ll 2\omega_B/m_{\text{max}}$, where the occupied single-particle states all have $m \leq m_{\text{max}}$. For Laughlin states $|\Phi_N\rangle$, $m_{\text{max}} = 2(N-1)$, so this requirement becomes $N \ll \omega_B/\varepsilon \approx 2(\omega_B/\omega_T)^2$. For typical experiments, $(\omega_B/\omega_T)^2 \gtrsim 10^4$ [56], so this requirement is not particularly limiting. Further, we assume that there is no Landau level mixing from interactions. Typical interaction energies between two particles in the LLL can be estimated from the zeroth Haldane pseudopotential $V_0 = g\langle\phi_0|\delta(\hat{\vec{r}})|\phi_0\rangle = g/(\pi l^2)$ [48, 105]. Hence, our assumption is justified provided $V_0 \ll 2\omega_B$, which is indeed fulfilled in present-day experimental conditions, where V_0 is several MHz and $\omega_B \sim 1$ GHz [92].

We project the dynamics onto the LLL by substituting $\hat{\psi}(\vec{r}) = \sum_{m=0}^{\infty} \phi_m(\vec{r})\,\hat{a}_m$ into Eqs. (3.1) and (3.2), where $\hat{a}_m$ annihilates a particle in the state $|\phi_m\rangle$. Thus, we obtain the restricted Hamiltonian

$$\hat{H}_{\text{LLL}} = \omega_{\text{eff}}\hat{N} + \varepsilon\,\hat{L} + V_0 \sum_{s=0}^{\infty} 2^{-(s+1)}\,\hat{A}_s^\dagger \hat{A}_s\,, \tag{3.4}$$

where $\hat{N} \equiv \sum_{m=0}^{\infty} \hat{a}_m^\dagger \hat{a}_m$ and $\hat{L} \equiv \sum_{m=0}^{\infty} m\hat{a}_m^\dagger \hat{a}_m$ measure the total particle number N and total angular momentum L, respectively, and $\hat{A}_s \equiv \sum_{m=0}^{s} \sqrt{s!/[m!(s-m)!]}\,\hat{a}_m \hat{a}_{s-m}$ annihilates two particles with net angular momentum s.

3.3.7 Many-body spectrum

The eigenstates of $\hat{H}_{\mathrm{LLL}}$ can be labeled by N and L. Figure 3.2(a) shows the spectrum in the $N = 3$ manifold. The lowest-energy state with $L = N(N-1)$ is the Laughlin state $|\Phi_N\rangle$. The lowest-energy eigenstates with $L > N(N-1)$ represent quasihole and edge excitations of the Laughlin state and are degenerate with $|\Phi_N\rangle$ for $\varepsilon = 0$ (no trap) [51]. Each of these states is separated from the excited states with the same L by an energy gap $\Delta_N \sim V_0$ (see Fig. 3.2). As we will see in the next section, it is this gap which sets the maximum speed at which one can drive the system from $|\Phi_n\rangle$ to $|\Phi_{n+1}\rangle$. Any state with $L < N(N-1)$ also has an interaction energy $E_{\mathrm{int}} \geq \Delta_N$. As the trap frequency is increased from zero, the eigenstate energies are simply increased by εL. Consequently, there is a range of ε for which the Laughlin state is the unique N-particle ground state and it costs energy to excite edge modes. As we describe in Sec. 3.5, this energy cost will aid the adiabatic generation of quasiholes by suppressing unwanted edge excitations.

3.3.8 Polariton loss

A number of processes limit the polariton lifetime. First, the cavity has a finite finesse and a photon will eventually escape. Second, the atomic Rydberg states have finite lifetime, reflecting the fact that the atom can decay, emitting a photon into a noncavity mode. Third, as already discussed, the interactions between Rydberg atoms can have inelastic components and cause polariton loss. As we discussed in Sec. 3.3.3, this latter process can be made negligible by carefully choosing parameters. In current experiments, the first two processes yield a net

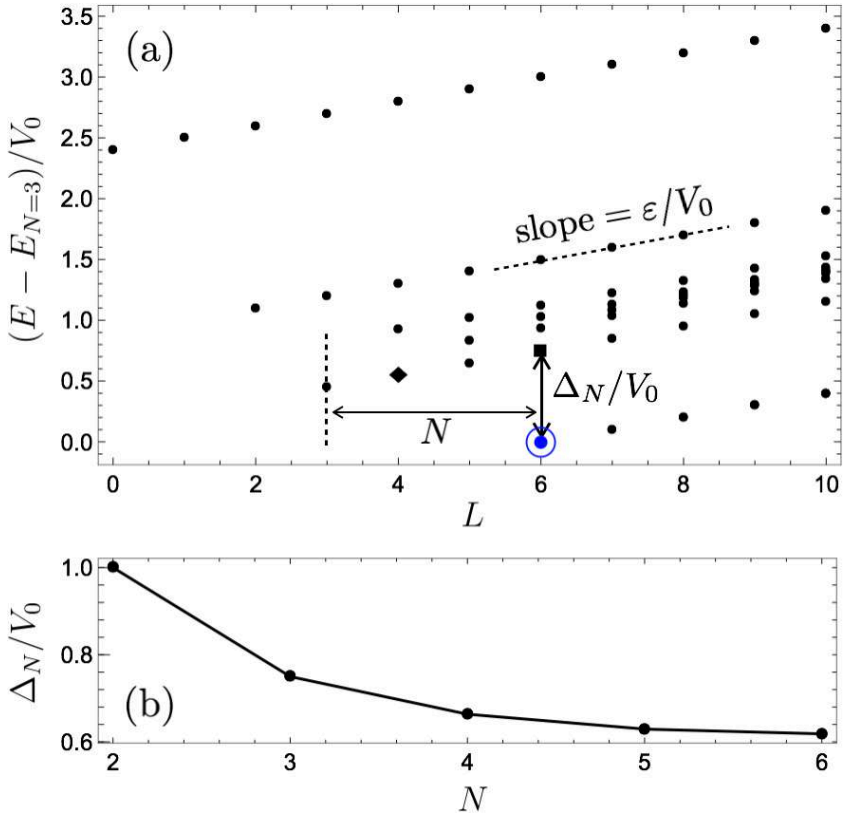

Figure 3.2: **(a)** Spectrum of three polaritons in a twisted optical cavity, described by the Hamiltonian in Eq. (3.4), which illustrates the general features of the N-body spectrum. The ground state, highlighted by the circled blue dot, has total angular momentum $L = N(N-1) = 6$ and corresponds to the $\nu = 1/2$ Laughlin state $|\Phi_N\rangle$. At fixed L, the excitation gap from this state is Δ_N, which arises from polariton-polariton interactions. The lowest-energy excitation with higher angular momentum has energy ε, whereas that with lower angular momentum has energy $\Delta_N - N\varepsilon$, where ε is related to the harmonic confinement and the effective magnetic field. The square- and diamond-shaped dots represent the excited states $|\Phi_N^e\rangle$ and $|\Phi_N^g\rangle$ defined in Sec. 3.4. **(b)** Number dependence of the excitation gap Δ_N. For $N \gtrsim 5$, it saturates at $0.6V_0$, where V_0 is the interaction energy of two particles in the lowest Landau level with zero relative angular momentum (zeroth Haldane pseudopotential).

polariton decay rate $\gamma \sim 0.1$ MHz [92].

Our protocol to create Laughlin states and braid quasiparticles relies on coherent evolution, and losing even a single polariton would be deleterious. Thus, the entire experiment must be conducted on microsecond time scales.

3.4 Laughlin state preparation

3.4.1 Overview

Our protocol for creating the N-particle Laughlin state $|\Phi_N\rangle$ is based on a series of coherent optical drives which transfer the system from $|\Phi_n\rangle$ to $|\Phi_{n+1}\rangle$ via rapid adiabatic passage [106]. Thus, the final state $|\Phi_N\rangle$ is built up by sequentially injecting photons near the outer rim of the cloud. The idea of adding photons sequentially was also used in Ref. [53].

In Sec. 3.3.5 we explained that successive Laughlin states differ in their total angular momentum by $L_{n+1} - L_n = 2n$. Thus, in our protocol, we illuminate the cavity in state $|\Phi_n\rangle$ with a laser that couples strongly to the mode with $m = 2n$ and sweep the detuning of the drive from negative to positive. If such a sweep is performed sufficiently slowly, the system will be adiabatically transferred to the state $|\Phi_{n+1}\rangle$. Our goal is to find the fastest possible sweep rate. We find that adiabaticity requires that the entire process take place over a time $T_L \gtrsim 40(N/V_0)\ln N$. In order to have negligible loss during this time, $T_L \ll 2/N\gamma$, where γ is the single-polariton decay rate.

3.4.2 Sweep protocol

A coherent drive is expressed by the Hamiltonian

$$\hat{H}_{\text{dr}} = \int d^2r\, \lambda(\vec{r},t)\hat{\psi}^\dagger(\vec{r}) + \text{H.c.} = \sum_{m=0}^{\infty} \lambda_m(t)\hat{a}_m^\dagger + \text{H.c.}, \tag{3.5}$$

where $\lambda(\vec{r},t)$ denotes the optical drive field and $\lambda_m(t) \equiv \int d^2r\, \lambda(\vec{r},t)\phi_m^*(\vec{r})$, whereby we have projected $\hat{H}_{\text{dr}}$ onto the LLL (see Sec. 3.3.4). Thus, $\lambda_m(t)$ represents the field component with a phase winding $e^{im\varphi}$. The transition from $|\Phi_n\rangle$ to $|\Phi_{n+1}\rangle$ requires an optical drive with $\lambda_m \neq 0$ only for $m = 2n$. Such helically phased laser beams are readily available [107, 108].

Thus, we consider a drive which couples $|\Phi_n\rangle$ to $|\Phi_{n+1}\rangle$,

$$\hat{H}_{\text{dr}}^{(n)} = \Lambda_n(t)\, \exp\left[-i\int^t dt'[\omega_n + \delta_n(t')]\right]\hat{a}_{2n}^\dagger + \text{H.c.}, \tag{3.6}$$

where ω_n is the resonant frequency, $\omega_n \equiv E_{n+1} - E_n = \omega_{\text{eff}} + 2n\varepsilon$ (see Sec. 3.3.5), $\delta_n(t)$ denotes the detuning which is swept from negative to positive values (or vice versa), and $\Lambda_n(t)$ is the amplitude which is controlled by the laser intensity and can be used to vary the Rabi frequency $\Omega_n(t) = \Lambda_n(t)\langle\Phi_{n+1}|\hat{a}_{2n}^\dagger|\Phi_n\rangle$. This setup is similar to the two-state Landau-Zener problem [109, 110], where the amplitude is constant and the detuning is swept over a finite range $-\delta_{\text{max}}$ to $+\delta_{\text{max}}$ at a constant rate $\nu \equiv \partial_t\delta_n(t)$. In the Landau-Zener problem, the system will transition to the state $|\Phi_{n+1}\rangle$ provided $\delta_{\text{max}} \gg |\Omega_n| \gtrsim \sqrt{\nu}$ [111]. In our case, the transition probability will be modified because the coupling is not restricted to the two Laughlin states. In particular, the drive in Eq. (3.6) couples any pair of states which differ in particle number by 1 and total angular momentum by $2n$. We also somewhat improve the transition probability by sculpting the profiles $\Lambda_n(t)$ and $\delta_n(t)$ [112–115].

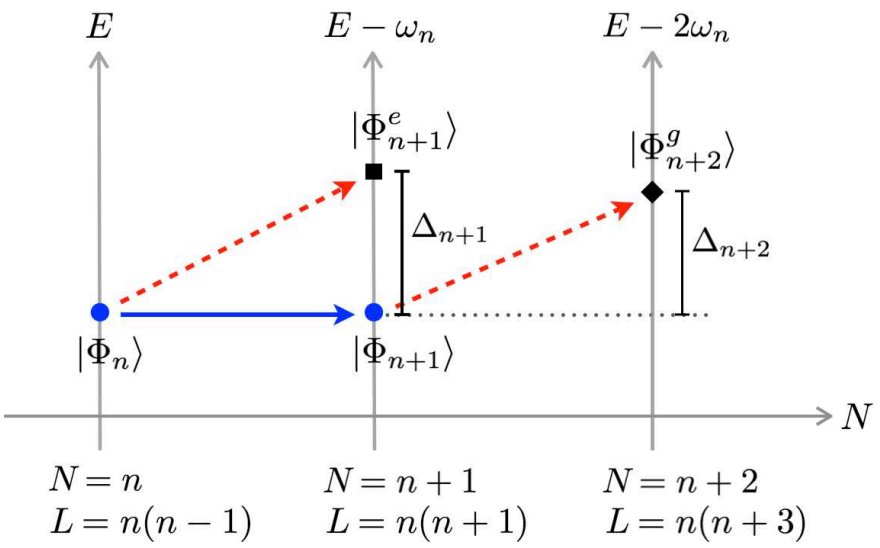

Figure 3.3: Spectrum of states coupled during our driving protocol. The solid blue arrow shows the desired transition from the n-particle Laughlin state $|\Phi_n\rangle$ to the $(n+1)$-particle Laughlin state $|\Phi_{n+1}\rangle$ with a resonant frequency ω_n. Dashed red arrows show possible undesired transitions to the low-lying excited states $|\Phi^e_{n+1}\rangle$ and $|\Phi^g_{n+2}\rangle$. These transitions are off resonant by the many-body gaps Δ_{n+1} and Δ_{n+2}.

The leading correction to the Landau-Zener problem comes from the in-coupled states which are closest to resonance. As sketched in Fig. 3.3, these unwanted states are denoted by $|\Phi^e_{n+1}\rangle$ and $|\Phi^g_{n+2}\rangle$ which are the lowest-energy excited states with quantum numbers $N=n+1$, $L=n(n+1)$ and $N=n+2$, $L=n(n+3)$. The drive in Eq. (3.6) couples $|\Phi_n\rangle$ to $|\Phi^e_{n+1}\rangle$ with Rabi frequency $\Omega^e_n = \Lambda_n\langle\Phi^e_{n+1}|\hat{a}^\dagger_{2n}|\Phi_n\rangle$. Similarly, it couples $|\Phi_{n+1}\rangle$ to $|\Phi^g_{n+2}\rangle$ with Rabi frequency $\Omega^g_{n+1} = \Lambda_n\langle\Phi^g_{n+2}|\hat{a}^\dagger_{2n}|\Phi_{n+1}\rangle$. The energy splittings of these transitions are $\omega^e_n = \omega_n + \Delta_{n+1}$ and $\omega^g_{n+1} = \omega_n + \Delta_{n+2}$, where Δ_n is the bulk excitation gap shown in Fig. 3.2. To suppress these undesired excitations, we must have $\delta_{\max} \lesssim \Delta_{n+1}, \Delta_{n+2} \sim V_0$.

As we discussed earlier, the desired transition from $|\Phi_n\rangle$ to $|\Phi_{n+1}\rangle$ occurs with near-unity probability only if $\delta_{\max} \gg |\Omega_n| \gtrsim \sqrt{\nu}$. Thus, we have a bound on the sweep rate, $\nu \ll \Delta^2_{n+1}, \Delta^2_{n+2}$. Figure 3.2(b) shows that Δ_n varies weakly

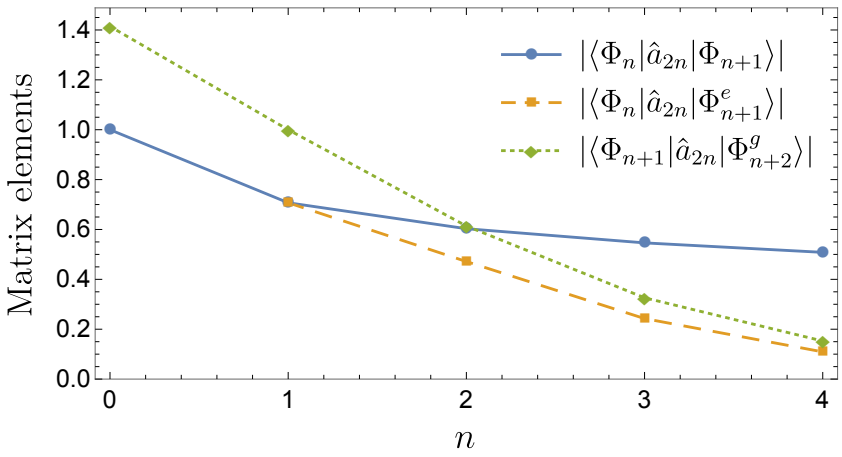

Figure 3.4: Matrix elements of the drive between the coupled many-body states. The operator $\hat{a}_{2n}$ annihilates a particle in the angular momentum mode $m = 2n$.

with n, saturating at $0.6V_0$ for $n \gtrsim 5$. Hence, we can choose the same detuning range and sweep rate for each transfer. Further, as illustrated in Fig. 3.4, $|\Omega_n| \propto |\langle\Phi_{n+1}|\hat{a}^\dagger_{2n}|\Phi_n\rangle|$ is roughly independent of n and therefore roughly the same laser intensity can be used for each transition. We also see that the undesired matrix elements fall off with n. Thus, we do not expect coupling to these states to be a problem even when n is large.

As argued in Refs. [112–114], the adiabaticity requirements are somewhat relaxed if one takes smooth profiles for the laser intensity $\Lambda_n(t)$ and detuning $\delta_n(t)$. Thus, we take

$$\Lambda_n(t) = \frac{\Omega(t-(4n+2)\tau)}{|\langle\Phi_n|\hat{a}_{2n}|\Phi_{n+1}\rangle|}\,,\ \delta_n(t) = \delta(t-(4n+2)\tau)\,, \tag{3.7}$$

$$\text{where}\quad \Omega(t) \equiv \frac{c_\Omega}{\tau}e^{-\frac{t^2}{\tau^2}}\quad\text{and}\quad \delta(t) \equiv \frac{c_\delta}{\tau}\frac{t}{\tau}e^{-\frac{t^2}{3\tau^2}}\,. \tag{3.8}$$

These profiles are characterized by the parameters c_Ω, c_δ, and τ. The first two parameters set the amplitudes of the Rabi frequency and the detuning, and τ sets the time scale of the frequency sweep. The Rabi frequency Ω_n is only

significant in the interval $t = 4n\tau$ to $t = 4(n+1)\tau$, during which the system is transferred from $|\Phi_n\rangle$ to $|\Phi_{n+1}\rangle$. The factor of 4 is chosen so that each sweep is well separated from the others. In the limit $c_\Omega \ll c_\delta$ and $\tau \gg c_\delta/V_0$, the sweep reduces to the original Landau-Zener problem with Rabi frequency c_Ω/τ and sweep rate $\nu = c_\delta/\tau^2$. Then the transition probability is given by $P \approx 1 - \exp(-\pi c_\Omega^2/c_\delta)$ [109, 110]. Generically, we find $P \approx 1$ provided $c_\Omega \lesssim c_\delta \lesssim c_\Omega^2$ and $\tau \gg c_\delta/V_0$. Hence, the drive protocol is optimized by taking c_Ω and c_δ of order unity and τ sufficiently large compared to $1/V_0$.

Figure 3.5(a) shows the creation of the $N = 4$ Laughlin state with $c_\Omega = 4$, $c_\delta = 5.33$, and $\tau = 12.5/V_0$. For $P \approx 1$, the error $1 - P$ in a given sweep is roughly independent of n and falls off exponentially as $V_0\tau$ is increased. Hence, the cumulative error after N sweeps, for large $V_0\tau$, scales as $Ne^{-\xi}$ where $\xi \propto V_0\tau$. This feature is apparent in Fig. 3.5(b), where we plot the cumulative error as a function of $V_0\tau$ for different values of N. As a rough estimate, we find this error is less than 1% for $\tau \gtrsim (10/V_0)\ln N$. Thus, one can prepare $|\Phi_N\rangle$ with such high fidelity in a total time $T_L \gtrsim 40(N/V_0)\ln N$.

In the Supplemental Material [116], we show animations of the polariton density during our driving protocol. If the sweeps are adiabatic, the density is uniform and the radius of the Laughlin puddle grows as $\sqrt{n}$ as more photons are injected into the system. For nonadiabatic sweeps, we see the development of vortices arising from the coupling to other many-body states.

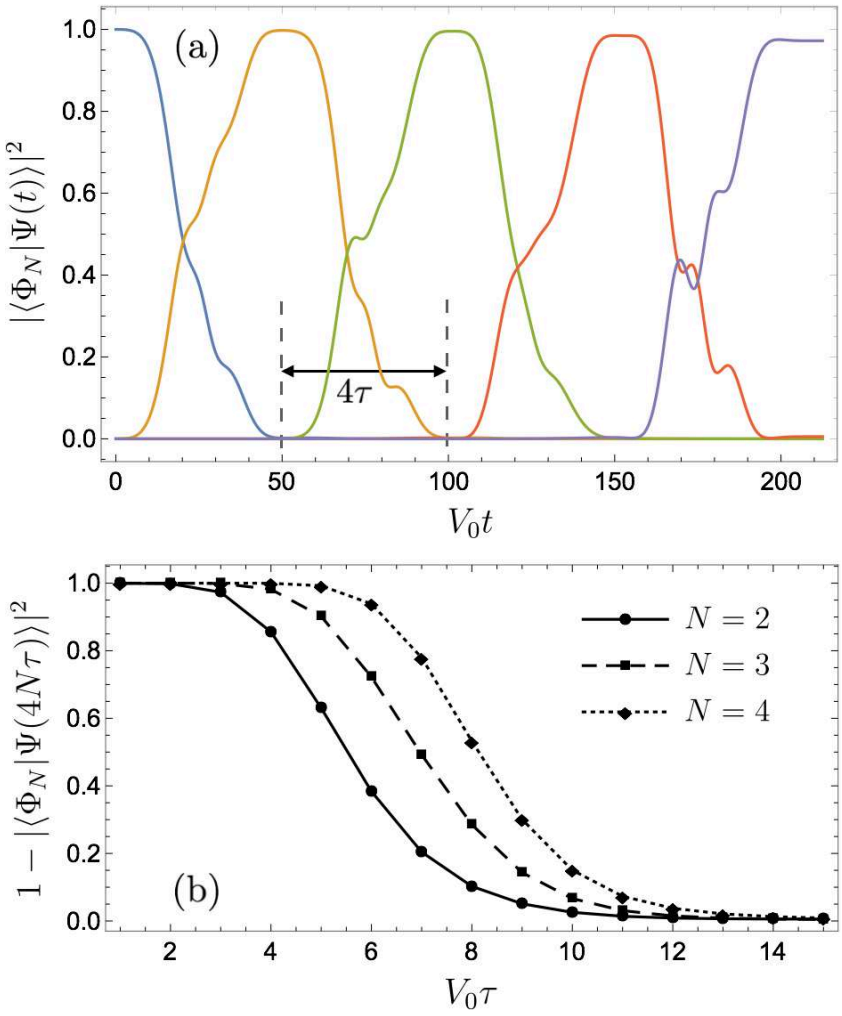

Figure 3.5: **(a)** Overlap of the system wave function $|\Psi(t)\rangle$ with each N-particle Laughlin state $|\Phi_N\rangle$ as a function of time during our driving protocol, described by Eqs. (3.6)–(3.8). Each subsequent plateau corresponds to increasing N by 1. The duration of each sweep is 4τ. As before, V_0 is the two-particle interaction energy. **(b)** Cumulative error in the final state preparation as a function of τ for three different particle numbers, with $c_\Omega = 4$, $c_\delta = 5.33$.

3.4.3 Constraint from polariton loss

We require that N_{loss}, the expected number of polaritons lost during the preparation of $|\Phi_N\rangle$, be small compared to 1. We can estimate N_{loss} by noting that the system approximately spends an interval T_L/N in a state with n polaritons, where n varies from zero to $N-1$. For a single-polariton decay rate γ, the net loss rate from an n-polariton state is $n\gamma$. Hence,

$$N_{\text{loss}} \approx T_L/N \sum_{n=0}^{N-1} n\gamma \approx N\gamma T_L/2\,. \tag{3.9}$$

Thus, our protocol can be used to prepare the N-particle Laughlin state provided $N_{\text{loss}} \ll 1$, or $V_0/\gamma \gg 20N^2 \ln N$, where we have taken $T_L = 40\,(N/V_0)\ln N$.

3.5 Quasihole generation

3.5.1 Overview

A quasiparticle or quasihole is a collective excitation with particle like properties. For example, a quasihole at location z_0 in the Laughlin state $|\Phi_N\rangle$ is described by the wavefunction $\Phi_N^{\text{o}}(\{z_j\}) \propto \prod_{i=1}^{N}(z_i - z_0)\Phi_N(\{z_j\})$ [4]. This state has all the properties of the Laughlin state, except there is a density depletion near z_0. Integrating this depletion over space yields the surprising result that exactly half a particle has been removed from this region. The wave function $\Phi_N^{\text{o}}(\{z_j\})$ is readily generalized to the case of multiple quasiholes. Thus, a state with two quasiholes at $\pm z_0$ is described by the wave function

$$\Phi_N^{\text{oo}}(\{z_j\}) \propto \prod_{i=1}^{N}(z_i - z_0)(z_i + z_0)\Phi_N(\{z_j\})\,. \tag{3.10}$$

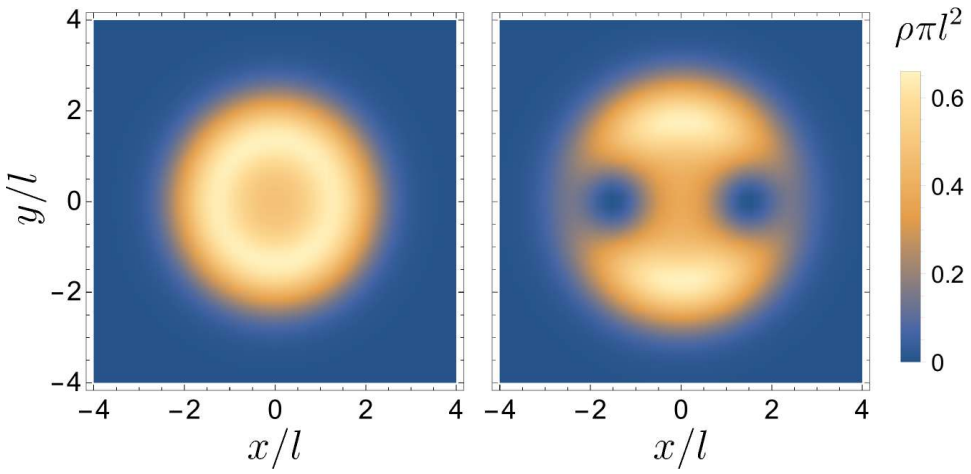

Figure 3.6: Polariton density ρ in the Laughlin state $|\Phi_{N=3}\rangle$ (left) and in a two-quasihole state $|\Phi^{oo}_{N=3}\rangle$ (right).

As shown in Fig. 3.6, the particle density in $|\Phi^{oo}_{N}\rangle$ nearly vanishes within a circle of radius $\sim l$ centered at $\pm z_0$, thus forming holes in an otherwise uniform-density background of $|\Phi_N\rangle$. Past calculations have shown that exchanging the two defects yields a Berry phase of $\phi_s = \pi/2$ in the thermodynamic limit [4–6, 22]. Thus, the quasiholes can be considered as quantum particles with fractional statistics. Here we show how to produce these defects by introducing additional laser potentials.

To produce a quasihole, we apply a localized repulsive potential just outside the Laughlin cloud and bring it radially inward through the edge. If the potential is strong enough and the radial sweep is sufficiently adiabatic, then we find that the final state will contain a quasihole bound to the potential. This procedure is more efficient than increasing the height of a potential barrier at a fixed location, as proposed in Ref. [22] for atomic systems. Experiments have demonstrated that such local potentials can be generated optically [93, 94, 117, 118], e.g., by illuminating the atoms with a laser that Stark-shifts the intermediate state in the Rydberg transitions. This illumination can be tightly focused and

moved spatially. By sweeping two such potentials through opposite sides of the Laughlin cloud, one can create a quasihole at each end, which can then be braided around one another.

3.5.2 Modeling

We model the potentials by Dirac delta functions of strength α applied at positions $\pm\vec{r}_0(t)$, where α is a constant and $\vec{r}_0(t)$ is swept radially inward along the x axis. This model is good as long as the spatial extent of the actual potential is smaller than the scaled magnetic length l. The potential energy is then described by the Hamiltonian

$$\hat{U}(t) = \alpha \int d^2r \, [\delta(\vec{r} - \vec{r}_0(t)) + \delta(\vec{r} + \vec{r}_0(t))] \hat{\psi}^\dagger(\vec{r}) \hat{\psi}(\vec{r}) \, . \tag{3.11}$$

Projecting into the LLL, we find

$$\hat{U}_{\mathrm{LLL}}(t) = U_0 \, e^{-(z_0(t))^2} \sum_{s=0}^{\infty} [z_0(t)]^{2s} \hat{Q}_{2s} \, , \tag{3.12}$$

where $z_0 \equiv r_0/l$, $\hat{Q}_s \equiv \sum_{m=0}^{s} \hat{a}_{s-m}^\dagger \hat{a}_m / \sqrt{m!(s-m)!}$, and $U_0 \equiv 2\alpha/(\pi l^2)$. Hence, the Hamiltonian conserves the particle number N but changes the total angular momentum L through the operator $\hat{Q}_s$.

The potentials must be strong enough to fully deplete the density at $\pm z_0$. If the sweep is adiabatic, the system will always be in an eigenstate of $\hat{H}_{\mathrm{LLL}} + \hat{U}_{\mathrm{LLL}}(t)$, where $\hat{H}_{\mathrm{LLL}}$ is the unperturbed Hamiltonian given by Eq. (3.4). For U_0 sufficiently large, the ground state belongs to the null space of $\hat{U}_{\mathrm{LLL}}$. This space is heavily degenerate and spanned by wavefunctions of the form $\prod_{i=1}^{N}(z_i - z_0)(z_i + z_0) f(\{z_j\})$, where f is a symmetric polynomial times a Gaussian. The two-quasihole state $|\Phi_N^{\mathrm{oo}}\rangle$ in Eq. (3.10) is the lowest-energy eigenstate

of this form in the absence of a trap ($\varepsilon = 0$). However, for $\varepsilon = 0$, the ground-state manifold is degenerate, consisting of all $f(\{z_j\}) = \Phi_N(\{z_j\})\chi(\{z_j\})$ for arbitrary symmetric polynomials χ. The harmonic trap splits the energies of different angular momentum states, thus lifting the degeneracy. For small ε, the ground state $|\Psi_g\rangle$ can be found by applying degenerate perturbation theory, which yields $1 - |\langle\Phi_N^{\text{oo}}|\Psi_g\rangle|^2 \sim \varepsilon^2/\Delta_N^2$, where Δ_N is the many-body interaction splitting shown in Fig. 3.2. Thus, $|\Phi_N^{\text{oo}}\rangle$ represents the approximate ground state. We find numerically that the overlap $|\langle\Phi_N^{\text{oo}}|\Psi_g\rangle|^2$ remains near unity as long as $\varepsilon \ll U_0$ and $\varepsilon \lesssim \Delta_N/N$.

Thus, we consider a sweep where the instantaneous ground state of the system evolves from $|\Phi_N\rangle$ when the potentials are outside the cloud to approximately $|\Phi_N^{\text{oo}}\rangle$ when they are fully inside. To produce quasiholes, the sweep must be sufficiently slow that the system resides in the instantaneous ground state at all times. Similar to the analysis in Sec. 3.4, we numerically integrate the time-dependent Schrödinger equation to evaluate the fidelity of this process. Owing to the presence of edge modes, we find that the most sensitive part of the process is when the potential moves through the edge of the cloud at $R \sim 2\sqrt{N-1}\,l$ [22]. In particular, if the motion from $r_0 = R + l$ to $r_0 = R - l$ is adiabatic, then the entire sweep is adiabatic. For simplicity, we consider linear sweeps in which r_0 is reduced at a constant rate.

The maximum allowed sweep rate $|\partial_t(r_0/l)|$ can be estimated by requiring that the rate be smaller than the energy gap ΔE between the ground state and the first excited state. When the potentials are near the edge of the cloud, the system is largely unperturbed; then ΔE is roughly the minimum of ε and $\Delta_N - N\varepsilon$ (see Fig. 3.2). The former corresponds to the lowest-energy surface waves

which increase the total angular momentum by 1 unit but do not result in any density increases. The latter corresponds to bulk excitations which increase the density and decrease the total angular momentum. To prevent exciting these modes, one must have $|\partial_t(r_0/l)| \lesssim \varepsilon, \Delta_N - N\varepsilon$. Thus, we need a small but finite trap frequency such that $0 < \varepsilon < \Delta_N/N$. This energy gap is maximized for $\varepsilon = \Delta_N/(N+1)$. However, the potentials modify the excitation spectrum as they enter the cloud. We numerically find that adiabaticity throughout the sweep requires $|\partial_t(r_0/l)| \lesssim \varepsilon \lesssim \Delta_N/(2N)$.

As a measure of adiabaticity, we plot the final overlap $|\langle\Phi_N^{\text{oo}}|\Psi_f\rangle|^2$ for $N = 3$ in Fig. 3.7(a) as a function of the sweep rate for different values of ε, with $U_0 \gg \varepsilon$. We see that the overlap approaches 1 for $|\partial_t(r_0/l)| \lesssim \varepsilon \lesssim \Delta_N/(2N)$. We show animations of the polariton density during the sweep in the Supplemental Material [116]. For nonadiabatic sweeps, the potentials excite surface modes and shape deformations in the density profile.

For smaller U_0, the ground state is not well approximated by $|\Phi_N^{\text{oo}}\rangle$. This feature is illustrated in Fig. 3.7(b), which shows the overlap following an adiabatic evolution. As expected, the overlap is near unity if $U_0 \gg \varepsilon$.

We note that a strong attractive potential ($U_0 < 0$) will also produce quasiholes. This is because the total energy is conserved and for $|U_0| \gg \varepsilon, V_0$, the dynamics get projected onto the zero-energy subspace of the applied potential, regardless of the sign of U_0.

We can calculate the time required to generate the two-quasihole state, T_h, by noting that r_0 is being swept over a distance $d \gtrsim 2l$ at a rate $|\partial_t(r_0/l)| \lesssim \Delta_N/(2N)$. Hence, $T_h \gtrsim 4N/\Delta_N$. We found earlier that Δ_N saturates at $3V_0/5$ for

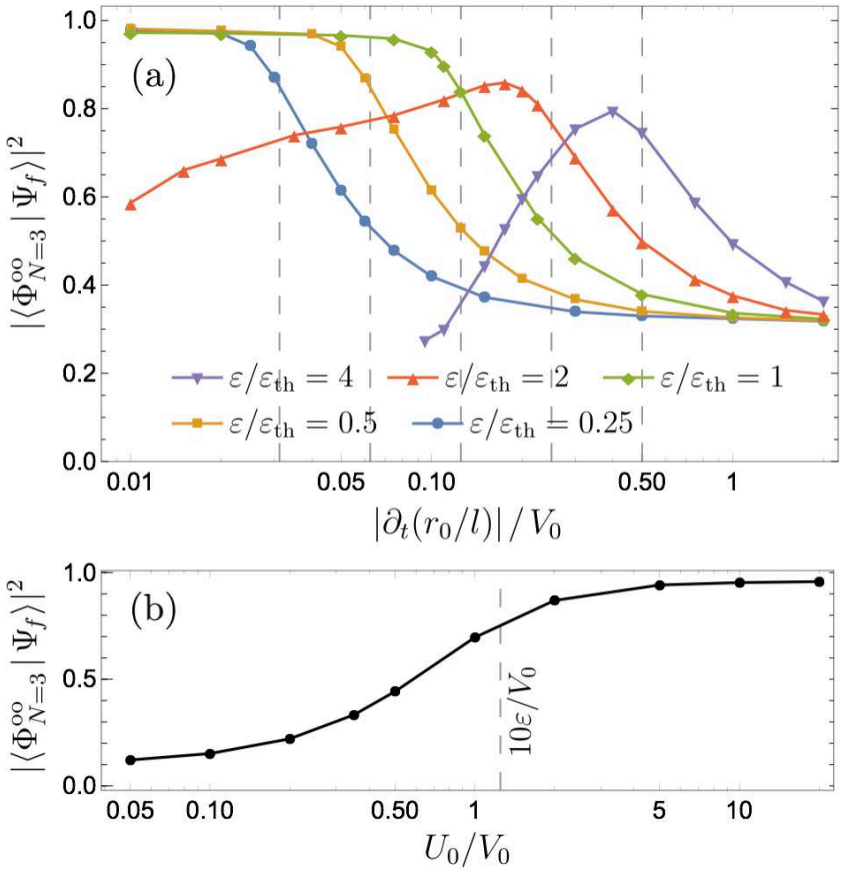

Figure 3.7: **(a)** Fidelity of the two-quasihole state preparation with a strong impurity potential ($U_0 = 20V_0$) as a function of the sweep rate $|\partial_t(r_0/l)|$ for different trap frequencies parametrized by ε. Here, r_0 is the radial distance of each pinning potential from the center and l is the scaled magnetic length. Dashed vertical lines show where $|\partial_t(r_0/l)| = \varepsilon$ for each curve. The final overlap approaches unity for $|\partial_t(r_0/l)| \lesssim \varepsilon$ provided $\varepsilon \lesssim \varepsilon_{\rm th} \equiv \Delta_N/(2N) = V_0/8$ (for $N = 3$), where Δ_N is the many-body interaction splitting shown in Fig. 3.2. To avoid visual distraction, the curve for $\varepsilon/\varepsilon_{\rm th} = 4$ is only shown for $|\partial_t(r_0/l)| > 0.1V_0$. **(b)** Fidelity of the two-quasihole state preparation as a function of the strength U_0 of the applied potential. Here, $|\partial_t(r_0/l)| = \varepsilon/2 = \varepsilon_{\rm th}/2$ (adiabatic sweep).

$N \gtrsim 5$ and $\Delta_2 = V_0$, where V_0 is the zeroth Haldane pseudopotential [Fig. 3.2(b)]. Thus, the minimum quasihole preparation time will vary from $4N/V_0$ for small N to $(20/3)N/V_0$ for $N \gtrsim 5$. This bound is much smaller than the time required to prepare the N-particle Laughlin state, $T_L \gtrsim 40(N/V_0)\ln N$ (see Sec. 3.4).

3.6 Quasihole braiding

3.6.1 Overview

In the previous section, we showed how one can create a pair of quasiholes at opposite ends of a Laughlin state, each bound to a local external potential. The same potentials can be dragged around one another to braid the two quasiholes [23]. One must move the potentials slowly enough to ensure that the quasiholes remain bound to the potentials throughout the process. The adiabaticity condition also differs for clockwise and counterclockwise motion, as the effective magnetic field breaks time-reversal symmetry. Below we investigate the conditions for an adiabatic braiding.

As we explained in the last section, the ground state $|\Psi_g\rangle$ in the presence of the applied potentials approximates the desired two-quasihole state $|\Phi_N^{\rm oo}\rangle$ in Eq. (3.10). We consider braiding these quasiholes by rotating the two potentials on a circle by an angle π. This rotation can be modeled by taking $\vec{r}_0(t) = r_0(\cos\varphi_0(t), \sin\varphi_0(t))$ in Eq. (3.11), where $\varphi_0(t)$ varies from zero to $\pm\pi$. For an infinitely slow braiding, the system follows the instantaneous ground state $|\Psi_g(t)\rangle$, which is simply the rotated version of the initial state $|\Psi_g\rangle$. Hence, in this case, the two quasiholes move with the potentials. However, for a finite

rotation speed, the overlap with the ground state is no longer unity. Then the "braiding error" can be calculated as $\eta \equiv 1 - |\langle \Psi_g | \Psi_f \rangle|^2$, where $|\Psi_f\rangle$ is the final state of the system. Since polaritons are lost in the experiment at a finite rate, our goal is to minimize the braiding duration T_b while keeping η below a cutoff η_c.

3.6.2 Modeling

For simplicity, we only consider rotations where $\varphi_0(t)$ changes at a constant rate ω_b. Then we can transform to the corotating frame where the system evolves (within the LLL) under a time-independent Hamiltonian $\hat{H}_{\text{rot}} = \hat{H}_{\text{LLL}} + \hat{U}_{\text{LLL}}(0) - \omega_b \hat{L}$, where $\hat{H}_{\text{LLL}}$ and $\hat{U}_{\text{LLL}}$ are defined in Eqs. (3.4) and (3.12). Hence, the braiding is equivalent to introducing a perturbation $\delta\hat{H} = -\omega_b \hat{L}$ for a duration $T_b = \pi/|\omega_b|$. The error η is set by the dimensionless parameters ω_b/V_0, ε/V_0, r_0/l, and U_0/V_0.

Figure 3.8 shows the error as a function of ω_b and r_0 for $\varepsilon = 0$ and $U_0/V_0 \gg 1$. If r_0 is near the edge of the cloud, the braiding can excite surface modes, resulting in braiding error. Similarly, there appear to be bulk resonances at particular radii and rotation frequencies. As more clearly illustrated by the line cuts in Fig. 3.9, this structure results in a threshold behavior, where $\eta \approx 0$ when $|\omega_b|/V_0$ is sufficiently small. The threshold for positive ω_b (counterclockwise rotations) is roughly independent of ε, while that for negative ω_b drops, and becomes sharper, as ε grows. The thresholds also move to lower values as one decreases r_0. Generally, the braiding is more adiabatic for rotations in the direction of the Lorentz force, which is counterclockwise in our case. In the Supplemental

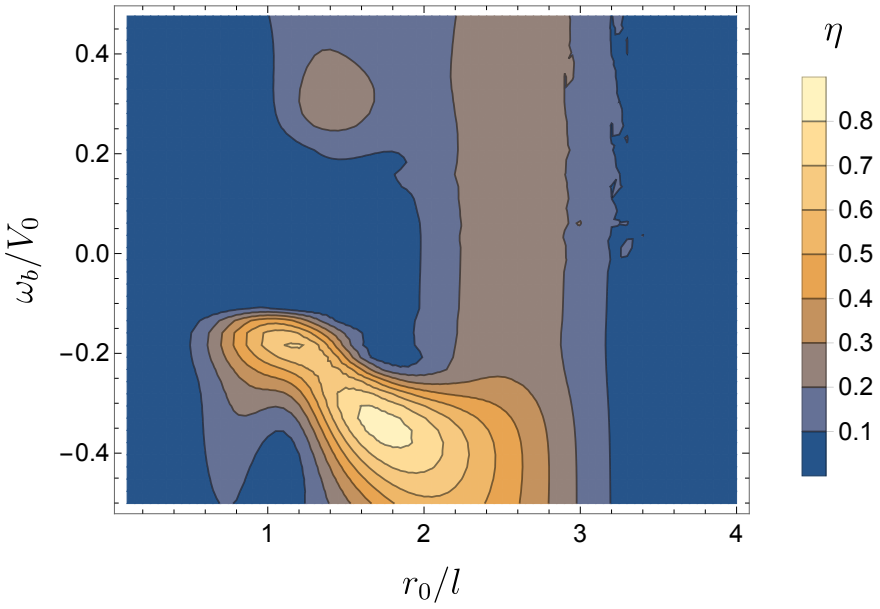

Figure 3.8: Contour plot showing the braiding error η when two strong impurity potentials ($U_0 = 100V_0$), each binding a quasihole at $\pm r_0$, are rotated by π at a constant angular speed ω_b. Here, $N = 3$ and $\varepsilon = 0$ (no trap). The vertical band centered around $r_0/l \approx 2.5$ corresponds to edge excitations. Other peaks correspond to bulk resonances. As before, l denotes the scaled magnetic length.

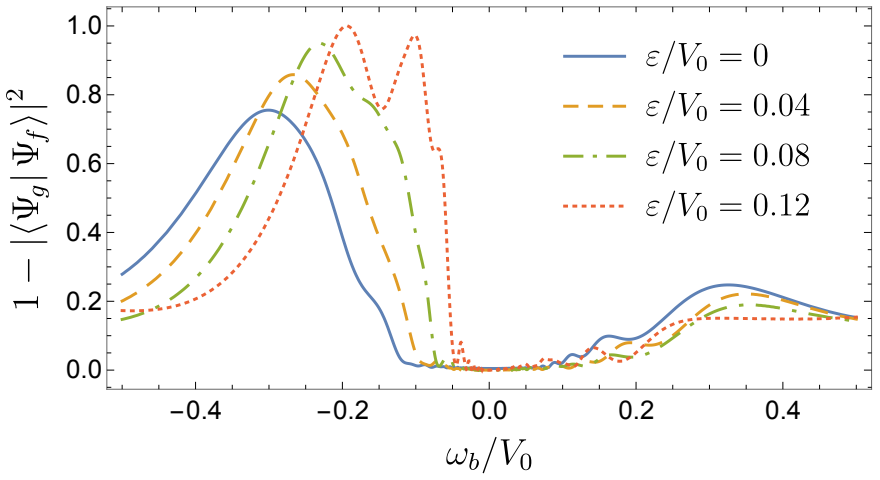

Figure 3.9: Braiding error η vs rotation rate ω_b at different trap frequencies for $N = 3$, $U_0/V_0 = 100$, and $r_0/l = 1.5$. Note that for adiabatic quasihole generation, one must have $\varepsilon \lesssim \varepsilon_{\text{th}} \equiv \Delta_N/(2N) = 0.125V_0$ [Figs. 3.7 and 3.2(b)].

Material [116], we show videos of the excitations created in the nonadiabatic regime. For $|\omega_b|/V_0 \gg 1$, the quasiholes do not have time to move, so the system remains in the initial state and $\eta \to 0$. This limit is clearly not suitable for quasihole braiding.

The threshold frequency for $\omega_b > 0$ and $N = 3$ is approximately $0.1V_0$. Thus, one can perform an adiabatic braiding of two quasiholes in a three-particle Laughlin state in a time $T_b \gtrsim 10\pi/V_0$ with vanishingly small error. This duration is much smaller than the $N = 3$ Laughlin state preparation time $T_L \gtrsim 130/V_0$ but comparable to the quasihole generation time $T_h \gtrsim 16/V_0$. One can further reduce T_b by moving the potentials in a more smooth manner [119].

3.7 Measuring anyonic statistics

3.7.1 Overview

During an adiabatic braiding of two quasiholes, the many-body wave function picks up a geometric (or Berry) phase ϕ_g, in addition to a dynamical phase ϕ_d associated with the time evolution. The geometric phase can be further decomposed into two pieces, $\phi_g = 2\phi_1 + \phi_s$, where ϕ_1 corresponds to the phase which would be acquired if one had a single quasihole and moved it through the same path. One can interpret ϕ_1 as the Aharonov-Bohm phase resulting from an effective magnetic field felt by a quasihole. The remainder, ϕ_s, is interpreted as a statistical phase which originates from exchanging the two quasiholes. Equivalently, ϕ_s can be understood as encoding how the presence of one quasihole influences the magnetic field which the other experiences. Past theoretical stud-

ies have shown that $\phi_s = \pm\pi/2$ in the thermodynamic limit (depending on the direction of rotation) [4–6, 22]. Here we examine how these "anyonic" statistics manifest for finite particle numbers and show how one can measure ϕ_s in experiments.

3.7.2 Extracting statistical phase

In the next section we describe an interferometric protocol for measuring the total many-body phase $\phi = \phi_g + \phi_d$. Given such a protocol, it is straightforward to extract ϕ_s: First, by repeating the experiment multiple times with different sweep rates, one can distinguish between ϕ_d and ϕ_g. Second, ϕ_s can be extracted from ϕ_g by comparing two experiments. In the first experiment, illustrated in Fig. 3.10(a), one rotates two quasiholes by π. In the second experiment, illustrated in Fig. 3.10(b), a single quasihole is rotated by 2π. The latter yields the same Aharonov-Bohm phase $2\phi_1$ but no statistical phase. This approach is similar to the ones suggested in Refs. [22, 47]. Figure 3.10(c) shows the value of ϕ_s which would thereby be extracted.

If the two quasiholes are too close together, they interact and it is not appropriate to interpret ϕ_s as being due to statistics. Similarly, if the quasiholes are moved outside of the bulk region, their properties are modified. Thus, in the small clouds we study, one only expects $\phi_s = \pi/2$ over a finite range of r_0 (radial position of each quasihole). As N increases, so should the bulk region. This trend is clear in Fig. 3.10(c). To calculate the curves in this figure, we took advantage of a simple relationship between the geometric phase and the total angular momentum [120, 121], which yields $\phi_s/\pi = N(N-1) + \langle \hat{L} \rangle_{\mathrm{oo}} - 2\langle \hat{L} \rangle_{\mathrm{o}}$.

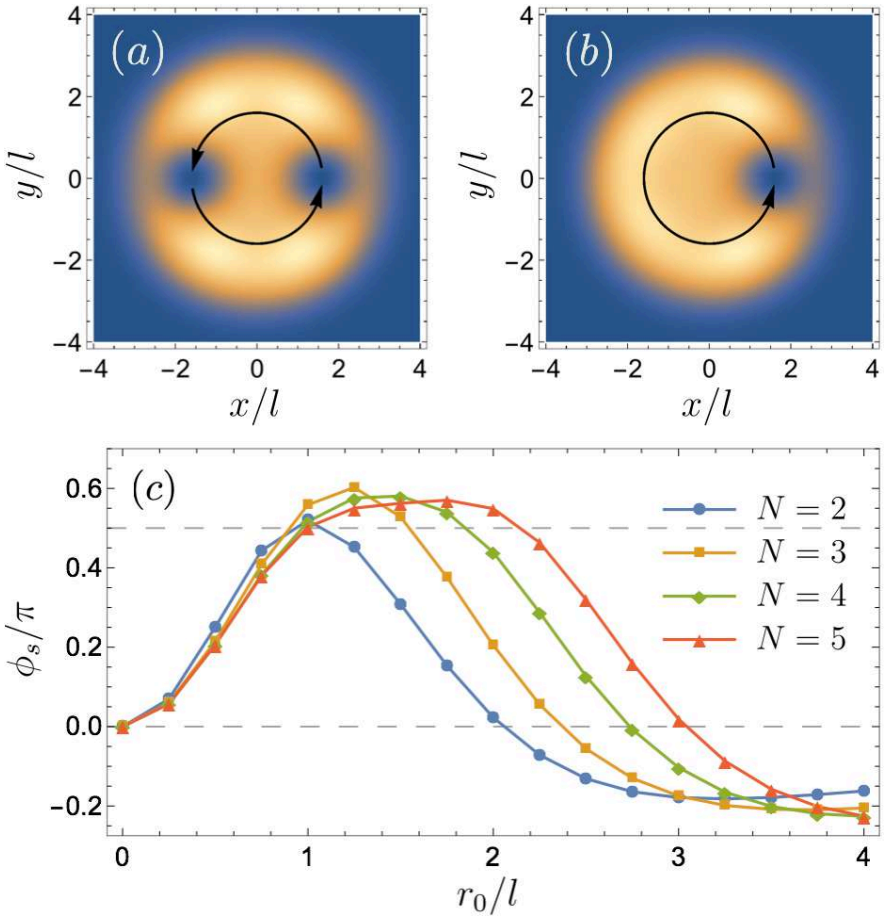

Figure 3.10: **(a,b)** Polariton density in the x–y plane for the two experiments needed to extract the statistical phase ϕ_s associated with exchanging two quasiholes. As in Fig. 3.6, brighter colors represent higher density and the dark disks correspond to quasiholes bound to potentials. Here $N = 4$. In (a) two quasiholes are exchanged while in (b) one quasihole is moved in a circle. **(c)** Statistical phase inferred from subtracting the geometric phases that would be found in these two experiments. In the thermodynamic limit, with well-separated quasiholes, one expects $\phi_s = \pi/2$. Note that r_0 denotes the radial distance of each quasihole from the center and l is the scaled magnetic length.

Here $\langle \hat{L} \rangle_{\mathrm{o}}$ and $\langle \hat{L} \rangle_{\mathrm{oo}}$ are the expectation of $\hat{L}$ in the single-quasihole and two-quasihole states, respectively.

3.7.3 Measuring total braiding phase

Our approach to measuring the total many-body phase ϕ requires being able to create a reference state $|R'\rangle$ which is unaffected by the sweep protocols that we use to fill the cavity with polaritons. That is, if we put the system in state $|R'\rangle$, then apply the manipulations in Secs. 3.4, 3.5, and 3.6, it will still be in state $|R'\rangle$. One way to generate this reference is to drive an atom into a Rydberg state $|r'\rangle$ with a large blockade radius. Then $|R'\rangle$ will represent a collective Rydberg excitation. Clearly, $|r'\rangle$ should be distinct from the state $|r\rangle$ used to produce polaritons. Blockade physics will then prevent any further excitations during our protocol [57, 75].

To measure ϕ, one first uses a $\pi/2$ pulse to prepare the system in the superposition $|0\rangle + |R'\rangle$, where $|0\rangle$ denotes all atoms being in the ground state. One then follows the procedures in Secs. 3.4 to 3.6 to create the desired Laughlin state, generate quasiholes, and braid them. Then the process is repeated backwards, removing the quasiholes and coherently converting the Laughlin state to the vacuum. During this cycle, $|R'\rangle$ is unaffected and $|0\rangle$ gains a total phase $\phi = \phi_d + \phi_g$, i.e., $|0\rangle + |R'\rangle \rightarrow e^{i\phi}|0\rangle + |R'\rangle$. Finally, a second $\pi/2$ pulse is applied to recombine the states $|0\rangle$ and $|R'\rangle$, and the phase ϕ is read out by measuring the ground-state occupation. This approach is related to the one proposed in Ref. [59] for measuring topological invariants and is similar to quantum computing protocols for measuring expectation values [122].

In order to maintain coherence, the entire experiment must be performed on a time scale that is short compared to the polariton lifetime and the lifetime of the Rydberg state $|r'\rangle$, which are typically a few tens of microseconds [92].

3.8 Summary and outlook

The rapidly growing field of many-body cavity quantum electrodynamics presents new opportunities to realize novel quantum states in a driven dissipative environment. In particular, with strong light-matter coupling and synthetic gauge fields, experiments now have the necessary ingredients to prepare fractional quantum Hall states of polaritons [56–58, 77, 80]. Here we have developed a protocol by which one can create the simplest of such states, the $\nu = 1/2$ Laughlin states, in a twisted optical cavity (Fig. 3.1). We further explained how to generate quasihole excitations and directly measure their fractional exchange statistics.

In our protocol, one sequentially drives the system between the n- and $(n+1)$-particle Laughlin states, $|\Phi_n\rangle \to |\Phi_{n+1}\rangle$. This transition requires injecting a single photon with angular momentum $2n$. We showed how the transition can be achieved by illuminating the cavity mirrors with an appropriately tuned laser and sweeping its frequency. We find that one can create a very high-fidelity N-particle Laughlin state in a time $T \propto N \ln N$ (Fig. 3.5). This can be contrasted with previous proposals for which the fidelity was exponentially small in N [47–50].

We have also shown how one can adiabatically produce and braid quasiholes in $|\Phi_N\rangle$ by moving local pinning potentials (Figs. 3.7–3.9) and extract their

anyonic statistics via interferometry (Fig. 3.10). Our results will facilitate ongoing experiments aiming to observe fractional quantum Hall physics in photonic systems [56–58].

High-fidelity preparation of Laughlin states requires a separation of energy scales between the two-particle interaction energy V_0 and the single-polariton decay rate γ. In our protocol, this condition arises from the need to maintain both adiabaticity and coherence, and takes the form $V_0/\gamma \gg 10N^2 \ln N$. While this condition is very demanding in current experiments, where $V_0/\gamma \approx 50$, this figure of merit is continually improving. Note that the bound $10N^2 \ln N$ is still much smaller than in Ref. [51], where one needs $V_0/\gamma \gtrsim 3 \times 10^4$ for $N = 3$.

Directly measuring the exchange statistics of two quasiholes in the bosonic $\nu = 1/2$ Laughlin state would be extremely impactful and would be a step towards more complicated braiding protocols. For example, at $\nu = 1$, bosons in the lowest Landau level form a paired Pfaffian state in which the quasiholes behave like Majorana fermions. Exchanging two of them rotates the system among a set of degenerate levels. At $\nu = 3/2$, the exchange statistics are sufficiently rich that one can perform arbitrary unitary gates by braiding the particles [11, 23, 24].

One fascinating feature of using optical cavities as a platform for many-body physics is that the underlying system is coupled to a highly controllable environment, which can be used to manipulate the system [51, 52, 91]. For example, one can implement a feedback stabilization mechanism where the photons emitted from the cavity are filtered by their angular momenta [51, 123] and the lost angular momentum is replenished by an appropriate drive. Despite such obvious potential, it is not yet clear how to best utilize the environment. Future studies can look deeper into this resource.

Acknowledgments

We thank Jon Simon for several illuminating discussions. This work was supported by the National Science Foundation Grant PHY-1508300 and the ARO-MURI Non-equilibrium Many-body Dynamics Grant W9111NF-14-1-0003.

BIBLIOGRAPHY FOR CHAPTER 3

[1] H. L. Stormer, D. C. Tsui, and A. C. Gossard, "The fractional quantum Hall effect," Rev. Mod. Phys. **71**, S298 (1999).

[2] H. L. Stormer, "Nobel Lecture: The fractional quantum Hall effect," Rev. Mod. Phys. **71**, 875 (1999).

[3] X.-G. Wen, "Topological orders and edge excitations in fractional quantum Hall states," Adv. Phys. **44**, 405 (1995).

[4] D. Arovas, J. R. Schrieffer, and F. Wilczek, "Fractional statistics and the quantum Hall effect," Phys. Rev. Lett. **53**, 722 (1984).

[5] B. I. Halperin, "Statistics of quasiparticles and the hierarchy of fractional quantized Hall states," Phys. Rev. Lett. **52**, 1583 (1984).

[6] A. Stern, "Anyons and the quantum Hall effect—A pedagogical review," Ann. Phys. **323**, 204 (2008).

[7] F. E. Camino, W. Zhou, and V. J. Goldman, "Realization of a Laughlin quasiparticle interferometer: Observation of fractional statistics," Phys. Rev. B **72**, 075342 (2005).

[8] R. L. Willett, L. N. Pfeiffer, and K. W. West, "Alternation and interchange of e/4 and e/2 period interference oscillations consistent with filling factor 5/2 non-Abelian quasiparticles," Phys. Rev. B **82**, 205301 (2010).

[9] S. An, P. Jiang, H. Choi, W. Kang, S. H. Simon, L. N. Pfeiffer, K. W. West, and K. W. Baldwin, "Braiding of Abelian and non-Abelian anyons in the fractional quantum Hall effect," arXiv:1112.3400 .

[10] A. Y. Kitaev, "Fault-tolerant quantum computation by anyons," Ann. Phys. **303**, 2 (2003).

[11] C. Nayak, S. H. Simon, A. Stern, M. Freedman, and S. D. Sarma, "Non-Abelian anyons and topological quantum computation," Rev. Mod. Phys. **80**, 1083 (2008).

[12] I. M. Georgescu, S. Ashhab, and F. Nori, "Quantum simulation," Rev. Mod. Phys. **86**, 153 (2014).

[13] I. Bloch, J. Dalibard, and W. Zwerger, "Many-body physics with ultracold gases," Rev. Mod. Phys. **80**, 885 (2008).

[14] M. Lewenstein, A. Sanpera, V. Ahufinger, B. Damski, A. Sen, and U. Sen, "Ultracold atomic gases in optical lattices: Mimicking condensed matter physics and beyond," Adv. Phys. **56**, 243 (2007).

[15] I. Bloch, J. Dalibard, and S. Nascimbene, "Quantum simulations with ultracold quantum gases," Nat. Phys. **8**, 267 (2012).

[16] I. Carusotto and C. Ciuti, "Quantum fluids of light," Rev. Mod. Phys. **85**, 299 (2013).

[17] C. Noh and D. G. Angelakis, "Quantum simulations and many-body physics with light," Rep. Prog. Phys. **80**, 016401 (2016).

[18] M. J. Hartmann, "Quantum simulation with interacting photons," J. Opt. **18**, 104005 (2016).

[19] A. A. Houck, H. E. Türeci, and J. Koch, "On-chip quantum simulation with superconducting circuits," Nat. Phys. **8**, 292 (2012).

[20] R. B. Laughlin, "Anomalous quantum Hall effect: An incompressible quantum fluid with fractionally charged excitations," Phys. Rev. Lett. **50**, 1395 (1983).

[21] N. K. Wilkin and J. M. F. Gunn, "Condensation of "composite bosons" in a rotating BEC," Phys. Rev. Lett. **84**, 6 (2000).

[22] B. Paredes, P. Fedichev, J. I. Cirac, and P. Zoller, "1/2-anyons in small atomic Bose-Einstein condensates," Phys. Rev. Lett. **87**, 010402 (2001).

[23] E. Kapit, P. Ginsparg, and E. Mueller, "Non-Abelian braiding of lattice bosons," Phys. Rev. Lett. **108**, 066802 (2012).

[24] N. R. Cooper, N. K. Wilkin, and J. M. F. Gunn, "Quantum phases of vortices in rotating Bose-Einstein condensates," Phys. Rev. Lett. **87**, 120405 (2001).

[25] B. Paredes, P. Zoller, and J. I. Cirac, "Fractional quantum Hall regime of a gas of ultracold atoms," Solid State Commun. **127**, 155 (2003).

[26] M. Popp, B. Paredes, and J. I. Cirac, "Adiabatic path to fractional quantum Hall states of a few bosonic atoms," Phys. Rev. A **70**, 053612 (2004).

[27] C.-C. Chang, N. Regnault, T. Jolicoeur, and J. K. Jain, "Composite fermionization of bosons in rapidly rotating atomic traps," Phys. Rev. A **72**, 013611 (2005).

[28] M. A. Baranov, K. Osterloh, and M. Lewenstein, "Fractional quantum Hall states in ultracold rapidly rotating dipolar Fermi gases," Phys. Rev. Lett. **94**, 070404 (2005).

[29] A. S. Sørensen, E. Demler, and M. D. Lukin, "Fractional quantum Hall states of atoms in optical lattices," Phys. Rev. Lett. **94**, 086803 (2005).

[30] R. N. Palmer and D. Jaksch, "High-field fractional quantum Hall effect in optical lattices," Phys. Rev. Lett. **96**, 180407 (2006).

[31] M. Hafezi, A. S. Sørensen, E. Demler, and M. D. Lukin, "Fractional quantum Hall effect in optical lattices," Phys. Rev. A **76**, 023613 (2007).

[32] R. Bhat, M. Krämer, J. Cooper, and M. J. Holland, "Hall effects in Bose-Einstein condensates in a rotating optical lattice," Phys. Rev. A **76**, 043601 (2007).

[33] S. K. Baur, K. R. A. Hazzard, and E. J. Mueller, "Stirring trapped atoms into fractional quantum Hall puddles," Phys. Rev. A **78**, 061608 (2008).

[34] G. Möller and N. R. Cooper, "Composite fermion theory for bosonic quantum Hall states on lattices," Phys. Rev. Lett. **103**, 105303 (2009).

[35] N. Gemelke, E. Sarajlic, and S. Chu, "Rotating few-body atomic systems in the fractional quantum Hall regime," arXiv:1007.2677 .

[36] E. Kapit and E. Mueller, "Exact parent Hamiltonian for the quantum Hall states in a lattice," Phys. Rev. Lett. **105**, 215303 (2010).

[37] M. Roncaglia, M. Rizzi, and J. Dalibard, "From rotating atomic rings to quantum Hall states," Sci. Rep. **1**, 43 (2011).

[38] B. Juliá-Díaz, T. Graß, N. Barberán, and M. Lewenstein, "Fractional quantum Hall states of a few bosonic atoms in geometric gauge fields," New J. Phys. **14**, 055003 (2012).

[39] A. E. B. Nielsen, G. Sierra, and J. I. Cirac, "Local models of fractional quantum Hall states in lattices and physical implementation," Nat. Commun. **4**, 2864 (2013).

[40] N. R. Cooper and J. Dalibard, "Reaching fractional quantum Hall states with optical flux lattices," Phys. Rev. Lett. **110**, 185301 (2013).

[41] J. Zhang, J. Beugnon, and S. Nascimbene, "Creating fractional quantum Hall states with atomic clusters using light-assisted insertion of angular momentum," Phys. Rev. A **94**, 043610 (2016).

[42] Y.-C. He, F. Grusdt, A. Kaufman, M. Greiner, and A. Vishwanath, "Realizing and adiabatically preparing bosonic integer and fractional quantum Hall states in optical lattices," Phys. Rev. B **96**, 201103(R) (2017).

[43] J. Cho, D. G. Angelakis, and S. Bose, "Fractional quantum Hall state in coupled cavities," Phys. Rev. Lett. **101**, 246809 (2008).

[44] A. L. C. Hayward, A. M. Martin, and A. D. Greentree, "Fractional quantum Hall physics in Jaynes-Cummings-Hubbard lattices," Phys. Rev. Lett. **108**, 223602 (2012).

[45] M. F. Maghrebi, N. Y. Yao, M. Hafezi, T. Pohl, O. Firstenberg, and A. V. Gorshkov, "Fractional quantum Hall states of Rydberg polaritons," Phys. Rev. A **91**, 033838 (2015).

[46] B. M. Anderson, R. Ma, C. Owens, D. I. Schuster, and J. Simon, "Engineering topological many-body materials in microwave cavity arrays," Phys. Rev. X **6**, 041043 (2016).

[47] R. O. Umucalılar and I. Carusotto, "Many-body braiding phases in a rotating strongly correlated photon gas," Phys. Lett. A **377**, 2074 (2013).

[48] R. O. Umucalılar, M. Wouters, and I. Carusotto, "Probing few-particle Laughlin states of photons via correlation measurements," Phys. Rev. A **89**, 023803 (2014).

[49] R. O. Umucalılar and I. Carusotto, "Fractional quantum Hall states of photons in an array of dissipative coupled cavities," Phys. Rev. Lett. **108**, 206809 (2012).

[50] M. Hafezi, M. D. Lukin, and J. M. Taylor, "Non-equilibrium fractional quantum Hall state of light," New J. Phys. **15**, 063001 (2013).

[51] R. O. Umucalilar and I. Carusotto, "Generation and spectroscopic signatures of a fractional quantum Hall liquid of photons in an incoherently pumped optical cavity," Phys. Rev. A **96**, 053808 (2017).

[52] E. Kapit, M. Hafezi, and S. H. Simon, "Induced self-stabilization in fractional quantum Hall states of light," Phys. Rev. X **4**, 031039 (2014).

[53] F. Grusdt, F. Letscher, M. Hafezi, and M. Fleischhauer, "Topological growing of Laughlin states in synthetic gauge fields," Phys. Rev. Lett. **113**, 155301 (2014).

[54] T. Ozawa, H. M. Price, A. Amo, N. Goldman, M. Hafezi, L. Lu, M. Rechtsman, D. Schuster, J. Simon, O. Zilberberg, *et al.*, "Topological photonics," arXiv:1802.04173 .

[55] D. E. Chang, V. Vuletić, and M. D. Lukin, "Quantum nonlinear optics — photon by photon," Nat. Photonics **8**, 685 (2014).

[56] N. Schine, A. Ryou, A. Gromov, A. Sommer, and J. Simon, "Synthetic Landau levels for photons," Nature (London) **534**, 671 (2016).

[57] N. Jia, N. Schine, A. Georgakopoulos, A. Ryou, A. Sommer, and J. Simon, "A strongly interacting polaritonic quantum dot," arXiv:1705.07475 .

[58] J. Ningyuan, N. Schine, A. Georgakopoulos, A. Ryou, A. Sommer, and J. Simon, "Photons and polaritons in a broken-time-reversal non-planar resonator," Phys. Rev. A **97**, 013802 (2018).

[59] F. Grusdt, N. Y. Yao, D. Abanin, M. Fleischhauer, and E. Demler, "Interferometric measurements of many-body topological invariants using mobile impurities," Nat. Commun. **7**, 11994 (2016).

[60] T. E. Northup and R. Blatt, "Quantum information transfer using photons," Nat. Photonics **8**, 356 (2014).

[61] H. J. Kimble, "The quantum internet," Nature (London) **453**, 1023 (2008).

[62] P. Kok, W. J. Munro, K. Nemoto, T. C. Ralph, J. P. Dowling, and G. J. Milburn, "Linear optical quantum computing with photonic qubits," Rev. Mod. Phys. **79**, 135 (2007).

[63] C. Monroe, "Quantum information processing with atoms and photons," Nature (London) **416**, 238 (2002).

[64] J. Klaers, J. Schmitt, F. Vewinger, and M. Weitz, "Bose-Einstein condensation of photons in an optical microcavity," Nature (London) **468**, 545 (2010).

[65] J. Marelic and R. A. Nyman, "Experimental evidence for inhomogeneous pumping and energy-dependent effects in photon Bose-Einstein condensation," Phys. Rev. A **91**, 033813 (2015).

[66] T. Damm, J. Schmitt, Q. Liang, D. Dung, F. Vewinger, M. Weitz, and J. Klaers, "Calorimetry of a Bose–Einstein-condensed photon gas," Nat. Commun. **7**, 11340 (2016).

[67] J. Marelic, L. F. Zajiczek, H. J. Hesten, K. H. Leung, E. Y. X. Ong, F. Mintert, and R. A. Nyman, "Spatiotemporal coherence of non-equilibrium multimode photon condensates," New J. Phys. **18**, 103012 (2016).

[68] T. Damm, D. Dung, F. Vewinger, M. Weitz, and J. Schmitt, "First-order spatial coherence measurements in a thermalized two-dimensional photonic quantum gas," Nat. Commun. **8**, 158 (2017).

[69] M. D. Lukin, "Colloquium: Trapping and manipulating photon states in atomic ensembles," Rev. Mod. Phys. **75**, 457 (2003).

[70] K. M. Birnbaum, A. Boca, R. Miller, A. D. Boozer, T. E. Northup, and H. J. Kimble, "Photon blockade in an optical cavity with one trapped atom," Nature (London) **436**, 87 (2005).

[71] M. Bajcsy, S. Hofferberth, V. Balic, T. Peyronel, M. Hafezi, A. S. Zibrov, V. Vuletic, and M. D. Lukin, "Efficient all-optical switching using slow light within a hollow fiber," Phys. Rev. Lett. **102**, 203902 (2009).

[72] I. Fushman, D. Englund, A. Faraon, N. Stoltz, P. Petroff, and J. Vučković, "Controlled phase shifts with a single quantum dot," Science **320**, 769 (2008).

[73] Y. Sun, Y. Yoon, M. Steger, G. Liu, L. N. Pfeiffer, K. West, D. W. Snoke, and K. A. Nelson, "Direct measurement of polariton-polariton interaction strength," Nat. Phys. **13**, 870 (2017).

[74] F. Tassone and Y. Yamamoto, "Exciton-exciton scattering dynamics in a semiconductor microcavity and stimulated scattering into polaritons," Phys. Rev. B **59**, 10830 (1999).

[75] O. Firstenberg, C. S. Adams, and S. Hofferberth, "Nonlinear quantum optics mediated by Rydberg interactions," J. Phys. B **49**, 152003 (2016).

[76] C. Lang, D. Bozyigit, C. Eichler, L. Steffen, J. M. Fink, A. A. Abdumalikov, Jr., M. Baur, S. Filipp, M. P. da Silva, A. Blais, and A. Wallraff, "Observation of resonant photon blockade at microwave frequencies using correlation function measurements," Phys. Rev. Lett. **106**, 243601 (2011).

[77] P. Roushan, C. Neill, A. Megrant, Y. Chen, R. Babbush, R. Barends, B. Campbell, Z. Chen, B. Chiaro, A. Dunsworth, *et al.*, "Chiral ground-state currents of interacting photons in a synthetic magnetic field," Nat. Phys. **13**, 146 (2017).

[78] P. Lodahl, S. Mahmoodian, S. Stobbe, A. Rauschenbeutel, P. Schneeweiss, J. Volz, H. Pichler, and P. Zoller, "Chiral quantum optics," Nature (London) **541**, 473 (2017).

[79] L. Lu, J. D. Joannopoulos, and M. Soljačić, "Topological photonics," Nat. Photonics **8**, 821 (2014).

[80] C. Owens, A. LaChapelle, B. Saxberg, B. Anderson, R. Ma, J. Simon, and D. I. Schuster, "Quarter-flux Hofstadter lattice in qubit-compatible microwave cavity array," arXiv:1708.01651 .

[81] J. Ningyuan, C. Owens, A. Sommer, D. Schuster, and J. Simon, "Time-and site-resolved dynamics in a topological circuit," Phys. Rev. X **5**, 021031 (2015).

[82] Z. Wang, Y. Chong, J. D. Joannopoulos, and M. Soljacic, "Observation of unidirectional backscattering-immune topological electromagnetic states," Nature (London) **461**, 772 (2009).

[83] M. Hafezi, S. Mittal, J. Fan, A. Migdall, and J. M. Taylor, "Imaging topological edge states in silicon photonics," Nat. Photonics **7**, 1001 (2013).

[84] M. C. Rechtsman, J. M. Zeuner, Y. Plotnik, Y. Lumer, D. Podolsky, F. Dreisow, S. Nolte, M. Segev, and A. Szameit, "Photonic Floquet topological insulators," Nature (London) **496**, 196 (2013).

[85] E. Li, B. J. Eggleton, K. Fang, and S. Fan, "Photonic Aharonov–Bohm effect in photon–phonon interactions," Nat. Commun. **5**, 3225 (2014).

[86] M. C. Rechtsman, J. M. Zeuner, A. Tünnermann, S. Nolte, M. Segev, and A. Szameit, "Strain-induced pseudomagnetic field and photonic Landau levels in dielectric structures," Nat. Photonics **7**, 153 (2013).

[87] L. D. Tzuang, K. Fang, P. Nussenzveig, S. Fan, and M. Lipson, "Non-reciprocal phase shift induced by an effective magnetic flux for light," Nat. Photonics **8**, 701 (2014).

[88] S. Mittal, J. Fan, S. Faez, A. Migdall, J. M. Taylor, and M. Hafezi, "Topologically robust transport of photons in a synthetic gauge field," Phys. Rev. Lett. **113**, 087403 (2014).

[89] A. Sommer, H. P. Büchler, and J. Simon, "Quantum crystals and Laughlin droplets of cavity Rydberg polaritons," arXiv:1506.00341 .

[90] J. Ningyuan, A. Georgakopoulos, A. Ryou, N. Schine, A. Sommer, and J. Simon, "Observation and characterization of cavity Rydberg polaritons," Phys. Rev. A **93**, 041802 (2016).

[91] R. Ma, C. Owens, A. Houck, D. I. Schuster, and J. Simon, "Autonomous stabilizer for incompressible photon fluids and solids," Phys. Rev. A **95**, 043811 (2017).

[92] See the Supplementary Information of Ref. [56].

[93] A. Hayat, C. Lange, L. A. Rozema, A. Darabi, H. M. van Driel, A. M. Steinberg, B. Nelsen, D. W. Snoke, L. N. Pfeiffer, and K. W. West, "Dynamic Stark effect in strongly coupled microcavity exciton polaritons," Phys. Rev. Lett. **109**, 033605 (2012).

[94] L. Li, Y. O. Dudin, and A. Kuzmich, "Entanglement between light and an optical atomic excitation," Nature (London) **498**, 466 (2013).

[95] E. Cancellieri, A. Hayat, A. M. Steinberg, E. Giacobino, and A. Bramati, "Ultrafast Stark-induced polaritonic switches," Phys. Rev. Lett. **112**, 053601 (2014).

[96] I. Carusotto, T. Volz, and A. Imamoğlu, "Feshbach blockade: Single-photon nonlinear optics using resonantly enhanced cavity polariton scattering from biexciton states," Europhys. Lett. **90**, 37001 (2010).

[97] A. Sommer and J. Simon, "Engineering photonic Floquet Hamiltonians through Fabry–Pérot resonators," New J. Phys. **18**, 035008 (2016).

[98] C. G. Darwin, "Free motion in the wave mechanics," Proc. R. Soc. A **117**, 258 (1927).

[99] V. Fock, "Bemerkung zur quantelung des harmonischen oszillators im magnetfeld," Z. Phys. **47**, 446 (1928).

[100] M. Fleischhauer, A. Imamoglu, and J. P. Marangos, "Electromagnetically induced transparency: Optics in coherent media," Rev. Mod. Phys. **77**, 633 (2005).

[101] M. Fleischhauer and M. D. Lukin, "Dark-state polaritons in electromagnetically induced transparency," Phys. Rev. Lett. **84**, 5094 (2000).

[102] L. Béguin, A. Vernier, R. Chicireanu, T. Lahaye, and A. Browaeys, "Direct measurement of the van der Waals interaction between two Rydberg atoms," Phys. Rev. Lett. **110**, 263201 (2013).

[103] P. Bienias, S. Choi, O. Firstenberg, M. F. Maghrebi, M. Gullans, M. D. Lukin, A. V. Gorshkov, and H. P. Büchler, "Scattering resonances and bound states for strongly interacting Rydberg polaritons," Phys. Rev. A **90**, 053804 (2014).

[104] T. Peyronel, O. Firstenberg, Q.-Y. Liang, S. Hofferberth, A. V. Gorshkov, T. Pohl, M. D. Lukin, and V. Vuletic, "Quantum nonlinear optics with single photons enabled by strongly interacting atoms," Nature (London) **487**, 57 (2012).

[105] F. D. M. Haldane, "Fractional quantization of the Hall effect: A hierarchy of incompressible quantum fluid states," Phys. Rev. Lett. **51**, 605 (1983).

[106] V. S. Malinovsky and J. L. Krause, "General theory of population transfer by adiabatic rapid passage with intense, chirped laser pulses," Eur. Phys. J. D **14**, 147 (2001).

[107] A. M. Yao and M. J. Padgett, "Orbital angular momentum: Origins, behavior and applications," Adv. Opt. Photonics **3**, 161 (2011).

[108] M. Padgett and R. Bowman, "Tweezers with a twist," Nat. Photonics **5**, 343 (2011).

[109] L. D. Landau, "A theory of energy transfer. II," Phys. Z. Sowjetunion **2**, 46 (1932).

[110] C. Zener, "Non-adiabatic crossing of energy levels," Proc. R. Soc. London A **137**, 696 (1932).

[111] N. V. Vitanov and B. M. Garraway, "Landau-Zener model: Effects of finite coupling duration," Phys. Rev. A **53**, 4288 (1996).

[112] B. W. Shore, "Coherent manipulations of atoms using laser light," Acta Phys. Slovaca **58**, 243 (2008).

[113] N. V. Vitanov, T. Halfmann, B. W. Shore, and K. Bergmann, "Laser-induced population transfer by adiabatic passage techniques," Annu. Rev. Phys. Chem. **52**, 763 (2001).

[114] A. A. Rangelov, N. V. Vitanov, and B. W. Shore, "Rapid adiabatic passage without level crossing," Opt. Commun. **283**, 1346 (2010).

[115] N. V. Vitanov and B. W. Shore, "Designer evolution of quantum systems by inverse engineering," J. Phys. B **48**, 174008 (2015).

[116] See Supplemental Material at `http://muellergroup.lassp.cornell.edu/twisted/` (if unavailable, see `https://doi.org/10.1103/PhysRevA.97.033825`) for polariton-density animations showing examples of adiabatic and nonadiabatic creation of Laughlin states, generation of quasiholes, and braiding of quasiholes.

[117] A. Amo, S. Pigeon, C. Adrados, R. Houdré, E. Giacobino, C. Ciuti, and A. Bramati, "Light engineering of the polariton landscape in semiconductor microcavities," Phys. Rev. B **82**, 081301 (2010).

[118] D. Sanvitto, S. Pigeon, A. Amo, D. Ballarini, M. De Giorgi, I. Carusotto, R. Hivet, F. Pisanello, V. G. Sala, P. S. S. Guimaraes, *et al.*, "All-optical control of the quantum flow of a polariton condensate," Nat. Photonics **5**, 610 (2011).

[119] C. Knapp, M. Zaletel, D. E. Liu, M. Cheng, P. Bonderson, and C. Nayak, "The nature and correction of diabatic errors in anyon braiding," Phys. Rev. X **6**, 041003 (2016).

[120] See the Supplementary Material of Ref. [47].

[121] R. O. Umucalilar, E. Macaluso, T. Comparin, and I. Carusotto, "Observing anyonic statistics via time-of-flight measurements," arXiv:1712.07940 .

[122] M. A. Nielsen and I. L. Chuang, *Quantum Computation and Quantum Information* (Cambridge University Press, Cambridge, 2000).

[123] A. Mair, A. Vaziri, G. Weihs, and A. Zeilinger, "Entanglement of the orbital angular momentum states of photons," Nature (London) **412**, 313 (2001).

CHAPTER 4

CONVENTION FOR BOGOLIUBOV QUASIPARTICLE OPERATORS

The goal of this chapter is to clarify the convention of the Bogoliubov quasiparticle modes which arise in the excitation spectrum of a Fermi superfluid. This will be important in the next three chapters where we will be using the Bogoliubov–de Gennes (BdG) formalism to study soliton dynamics and exotic superfluidity in Fermi gases. For a full exposition of the BdG formalism, we refer the reader to de Gennes's classic book [1].

There are at least two competing conventions in the literature for defining the Bogoliubov operators for spin-1/2 fermions: in one, the quasiparticle spectrum is symmetric for positive and negative energies, and there is only one type of Bogoliubov mode $\hat{\gamma}_j$. In the other, the spectrum has only positive energies, but there are two types of Bogoliubov modes, $\hat{\gamma}_j$ and $\hat{\zeta}_j$. We follow the first convention in Chapters 5 and 6, and the second in Chapter 7. Here we summarize both conventions and discuss how they relate to one another.

We consider a system of spin-1/2 fermions with short-ranged attractive interactions in one dimension. The formalism can be readily generalized to higher dimensions by replacing x by $\vec{r}$. The system is described by the Hamiltonian

$$\hat{H} = \int dx \Big[\sum\nolimits_{\sigma=\uparrow,\downarrow} \hat{\Psi}^\dagger_\sigma(x)(\hat{H}_0 - \mu_\sigma)\hat{\Psi}_\sigma(x) + g_{1\mathrm{D}}\hat{\Psi}^\dagger_\uparrow(x)\hat{\Psi}^\dagger_\downarrow(x)\hat{\Psi}_\downarrow(x)\hat{\Psi}_\uparrow(x)\Big], \quad (4.1)$$

where $\hat{\Psi}_\sigma(x)$ denote the fermion field operators, $\hat{H}_0$ is the single-particle Hamiltonian, $\mu_{\uparrow,\downarrow} \equiv \mu \mp h$ are the chemical potentials of the two spins, and $g_{1\mathrm{D}}$ denotes the coupling constant. Attractive interactions ($g_{1\mathrm{D}} < 0$) lead to Cooper pairing, which gives rise to the superfluid order parameter $\Delta_0(x) \equiv g_{1\mathrm{D}}\langle\hat{\Psi}_\downarrow(x)\hat{\Psi}_\uparrow(x)\rangle$. Ig-

[1] P. G. de Gennes, *Superconductivity of Metals and Alloys* (Benjamin, New York, 1966).

noring quadratic fluctuations about $\Delta_0(x)$ yields the mean-field Hamiltonian

$$\hat{H}_{\rm MF} = \int dx \left[\begin{pmatrix} \hat{\Psi}_\uparrow^\dagger(x) & \hat{\Psi}_\downarrow(x) \end{pmatrix} \begin{pmatrix} \hat{H}_0 - \mu_\uparrow & \Delta_0(x) \\ \Delta_0^*(x) & -\hat{H}_0 + \mu_\downarrow \end{pmatrix} \begin{pmatrix} \hat{\Psi}_\uparrow(x) \\ \hat{\Psi}_\downarrow^\dagger(x) \end{pmatrix} - g_{\rm 1D}^{-1} \left|\Delta_0(x)\right|^2 \right] + {\rm Tr}\left(\hat{H}_0 - \mu - h\right). \tag{4.2}$$

This Hamiltonian can be diagonalized by solving the BdG equations

$$\begin{pmatrix} \hat{H}_0 - \mu & \Delta_0(x) \\ \Delta_0^*(x) & -\hat{H}_0 + \mu \end{pmatrix} \begin{pmatrix} u_j(x) \\ v_j(x) \end{pmatrix} = \epsilon_j \begin{pmatrix} u_j(x) \\ v_j(x) \end{pmatrix}, \tag{4.3}$$

which has a symmetric spectrum: if $(u_j(x) \;\; v_j(x))^T$ is an eigenvector with eigenvalue ϵ_j, then $(-v_j^*(x) \;\; u_j^*(x))^T$ is an eigenvector with eigenvalue $-\epsilon_j$. The eigenvectors form an orthonormal set, i.e., $\int dx (u_j^*(x) u_{j'}(x) + v_j^*(x) v_{j'}(x)) = \delta_{jj'}$.

4.1 First convention

Define the Bogoliubov operators $\hat{\gamma}_j$ as

$$\begin{pmatrix} \hat{\Psi}_\uparrow(x) \\ \hat{\Psi}_\downarrow^\dagger(x) \end{pmatrix} = \sum_j \begin{pmatrix} u_j(x) \\ v_j(x) \end{pmatrix} \hat{\gamma}_j, \tag{4.4}$$

where the sum is over both positive and negative energies. The orthonormality of the eigenvectors ensures that the modes $\hat{\gamma}_j$ are fermionic, i.e., $\{\hat{\gamma}_j, \hat{\gamma}_{j'}^\dagger\} = \delta_{jj'}$. Substituting Eq. (4.4) into Eq. (4.2), we find

$$\hat{H}_{\rm MF} = \sum_j (\epsilon_j + h) \hat{\gamma}_j^\dagger \hat{\gamma}_j + {\rm Tr}\left(\hat{H}_0 - \mu - h\right) - g_{\rm 1D}^{-1} \int dx \left|\Delta_0(x)\right|^2. \tag{4.5}$$

The occupation of the modes is given by $\langle \hat{\gamma}_j^\dagger \hat{\gamma}_j \rangle = n_{\rm F}(\epsilon_j + h)$, where $n_{\rm F}$ denotes the Fermi function. Thus, at zero temperature, all quasiparticle modes with

energy $\epsilon_j < -h$ are occupied, and all other modes are empty. In particular, for $h \equiv \mu_\downarrow - \mu_\uparrow = 0$ (no spin imbalance), all negative energy modes are occupied and positive energy modes are empty. When $\mu_\downarrow > \mu_\uparrow$ ($h > 0$), one has to remove quasiparticles from the modes with energy between 0 and $-h$, resulting in a net excess of $\downarrow$-spins. Similarly, if $\mu_\uparrow > \mu_\downarrow$, one populates the modes between 0 and $|h|$, resulting in a net excess of $\uparrow$-spins.

4.2 Second convention

One arrives at the second convention by noting that Eq. (4.4) can be written as

$$\begin{aligned}
\begin{pmatrix} \hat{\Psi}_\uparrow(x) \\ \hat{\Psi}_\downarrow^\dagger(x) \end{pmatrix} &= \sum_{\epsilon_j>0} \begin{pmatrix} u_j(x) \\ v_j(x) \end{pmatrix} \hat{\gamma}_j + \sum_{\epsilon_j<0} \begin{pmatrix} u_j(x) \\ v_j(x) \end{pmatrix} \hat{\gamma}_j \\
&= \sum_{\epsilon_j>0} \begin{pmatrix} u_j(x) \\ v_j(x) \end{pmatrix} \hat{\gamma}_j + \sum_{\epsilon_j>0} \begin{pmatrix} -v_j^*(x) \\ u_j^*(x) \end{pmatrix} \hat{\zeta}_j^\dagger \\
&= \sum_{\epsilon_j>0} \begin{pmatrix} u_j(x) & -v_j^*(x) \\ v_j(x) & u_j^*(x) \end{pmatrix} \begin{pmatrix} \hat{\gamma}_j \\ \hat{\zeta}_j^\dagger \end{pmatrix}, \qquad (4.6)
\end{aligned}$$

where we have used the fact that for each state $(u_j \;\; v_j)^T$ with energy ϵ_j, there is a state $(-v_j^* \;\; u_j^*)^T$ with energy $-\epsilon_j$, and defined new fermionic operators $\hat{\zeta}_j \equiv \hat{\gamma}_j^\dagger$ for $\epsilon_j < 0$. The operators $\hat{\gamma}_j$ and $\hat{\zeta}_j$ in Eq. (4.6) represent the Bogoliubov modes in this other convention. Substituting Eq. (4.6) into Eq. (4.2), we obtain

$$\hat{H}_{\text{MF}} = \sum_{\epsilon_j>0} \left[(\epsilon_j+h)\hat{\gamma}_j^\dagger\hat{\gamma}_j + (\epsilon_j-h)\hat{\zeta}_j^\dagger\hat{\zeta}_j - (\epsilon_j-h)\right] + \text{Tr}\left(\hat{H}_0-\mu-h\right) - g_{\text{1D}}^{-1}\int dx \left|\Delta_0(x)\right|^2.$$

The occupations of the modes are given by $\langle\hat{\gamma}_j^\dagger\hat{\gamma}_j\rangle = n_{\text{F}}(\epsilon_j + h)$ and $\langle\hat{\zeta}_j^\dagger\hat{\zeta}_j\rangle = n_{\text{F}}(\epsilon_j - h)$. At zero temperature, only the $\hat{\gamma}$ modes with $\epsilon_j < -h$ and

the $\hat{\zeta}$ modes with $\epsilon_j < h$ are occupied. However $\epsilon_j > 0$, so there are no negative energy modes, which means in the balanced case ($h = 0$), all Bogoliubov modes are empty. Excess $\downarrow$-spins ($h > 0$) are incorporated by filling up only the $\hat{\zeta}$ modes with $0 < \epsilon_j < h$, whereas excess $\uparrow$-spins ($h < 0$) are incorporated by filling up only the $\hat{\gamma}$ modes with $0 < \epsilon_j < |h|$.

Equivalence

Although the two conventions yield different descriptions of a state, they are formally equivalent. This can be checked, e.g., by calculating the mean-field energy $E = \langle \hat{H}_{\text{MF}} \rangle$. In the second convention, the energy is given by

$$\begin{aligned}
\langle \hat{H}_{\text{MF}} \rangle &= \sum_{\epsilon_j > 0} \big[(\epsilon_j + h)\, n_{\text{F}}(\epsilon_j + h) + (\epsilon_j - h)\, n_{\text{F}}(\epsilon_j - h) - (\epsilon_j - h) \big] \\
&\quad + \text{Tr}\big(\hat{H}_0 - \mu - h \big) - g_{\text{1D}}^{-1} \int dx \big| \Delta_0(x) \big|^2 \\
&= \sum_{\epsilon_j > 0} \big[(\epsilon_j + h)\, n_{\text{F}}(\epsilon_j + h) + (\epsilon_j - h)\, n_{\text{F}}(-\epsilon_j + h) \big] + \text{Tr}\big(\hat{H}_0 - \mu - h \big) \\
&\quad - g_{\text{1D}}^{-1} \int dx \big| \Delta_0(x) \big|^2 \\
&= \sum_j (\epsilon_j + h)\, n_{\text{F}}(\epsilon_j + h) + \text{Tr}\big(\hat{H}_0 - \mu - h \big) - g_{\text{1D}}^{-1} \int dx \big| \Delta_0(x) \big|^2 , \qquad (4.7)
\end{aligned}$$

which is the same as the energy in the first convention.

CHAPTER 5

DYNAMICS OF A SOLITON TRAIN IN A FERMI SUPERFLUID

This chapter was adapted from "Collective Modes of a Soliton Train in a Fermi Superfluid" by Shovan Dutta and Erich J. Mueller, published in Physical Review Letters **118**, *260402 (2017).*

5.1 Abstract

We characterize the collective modes of a soliton train in a quasi-one-dimensional Fermi superfluid, using a mean-field formalism. In addition to the expected Goldstone and Higgs modes, we find novel long-lived gapped modes associated with oscillations of the soliton cores. The soliton train has an instability that depends strongly on the interaction strength and the spacing of solitons. It can be stabilized by filling each soliton with an unpaired fermion, thus forming a commensurate Fulde-Ferrell-Larkin-Ovchinnikov (FFLO) phase. We find that such a state is always dynamically stable, which paves the way for realizing long-lived FFLO states in experiments via phase imprinting.

5.2 Introduction

A unifying theme of contemporary physics is understanding emergent dynamics of many-particle systems. One motif is the appearance of persistent nonlinear structures, such as solitons [1]. Solitons arise naturally in diverse physical systems, including water waves [2–5], plasmas [6, 7], optical fibers [8–14],

conducting polymers [15–22], superconductors [23–28], Bose-Einstein condensates [29–48], DNA dynamics [49–54], quantum field theory [55–62], and early-Universe cosmology [63–68]. They are technologically important, with applications in telecommunications [69–76], information processing [28, 77–86], and matter-wave interferometry [87–96]. Moreover, cold-atom experiments can now engineer matter-wave solitons in atomic superfluids and directly observe their motion [31–48, 97–99]. Understanding the behavior of these collective objects is vital to the larger problem of forming a cohesive theory of nonequilibrium dynamics [100]. In particular, the next generation of Fermi gas experiments will be creating clouds with many of these nonlinear defects [99]. While past theoretical studies have shed light on the behavior of individual [101–116] or pairs of solitons [117–119], the behavior and even stability of soliton trains are not understood. Here, we study the linearized dynamics of a soliton train in a one-dimensional (1D) Fermi gas, finding a rich set of collective modes. We characterize these modes, finding distinct differences from Bose superfluids, which may generalize to nonlinear excitations of other systems.

We consider a two-component Fermi gas in an elongated trap with tight radial confinement so that the dynamics is effectively 1D [120]. The strong radial confinement suppresses the snake instability by which solitons decay into vortices and sound waves in three dimensions [31–34, 99, 108–114, 121–130]. To avoid the idiosyncracies of strictly 1D systems, we envision a weakly coupled array of such tubes, which have long-range superfluid order. Past experiments have studied fermionic superfluids in such geometries [131, 132]. Using phase-imprinting techniques [33–37, 97–99, 133–138], one can generate a train of solitons in the superfluid. The collective modes of the soliton train would show up as pronounced peaks in spectroscopic measurements of the pairing suscep-

tibility or in the density response of the system [139–143]. Here, we extract the collective modes by linearizing the self-consistent Bogoliubov–de Gennes (BdG) equations governing the fermion fields.

5.3 Conclusions

The soliton train has two gapless Goldstone modes, which originate from the spontaneous breaking of gauge- and translational symmetry: a "phonon" mode describing phase twists and an "elastic" mode describing oscillations in the spacing between the domain walls. The elastic mode is only well defined for wave vectors smaller than the inverse separation of the solitons, but we find a second gapped branch of oscillations, which persists to large wave vectors [Fig. 5.2(a)]. This branch is the remnant of the "Higgs" mode in a uniform superfluid [144–148].

In addition, we find a twofold degenerate gapped mode which, at small wave vectors, describes oscillations in the width and grayness of each soliton [Figs. 5.2(d)–5.2(e)]. To our knowledge, this "core" mode hasn't appeared before in the literature. It lies outside the particle-hole continua and should therefore be long lived, and hence, easier to detect in experiments than those embedded in a continuum.

However, we also find that the soliton train has two kinds of instabilities toward a uniform superfluid state: in one, pairs of neighboring solitons approach and annihilate each other [Fig. 5.2(f)], whereas in the other, the order parameter moves off into the complex plane [Fig. 5.2(g)]. Both instabilities grow at the same rate, which depends on the degree of overlap between adjacent solitons.

This overlap can be reduced by creating solitons farther apart or by increasing the attractive interaction strength to produce sharper solitons [Figs. 5.3(a)–5.3(b)]. Using either approach, one can make the instability rate much smaller compared to the frequency of the "core" modes, thus allowing them to be resolved.

One can also stabilize the train by filling each soliton with unpaired fermions, i.e., by polarizing the Fermi gas. Such a state constitutes a realization of the long-sought-after Fulde-Ferrell-Larkin-Ovchinnikov (FFLO) phase [149–161], whose experimental evidence in solid state [162] and cold gas [131, 132] systems has so far been indirect. We find that the instability rate falls with increasing polarization, vanishing for the "commensurate FFLO" (C-FFLO) phase with one excess fermion per soliton [Fig. 5.3(c)]. Thus, a C-FFLO phase is always dynamically stable, even when energetics favor a different state (Fig. 5.4). This means one can directly engineer stable FFLO states by phase imprinting, as opposed to searching for the one that minimizes the free energy. This enlarged parameter space will facilitate more direct probes of the exotic state. In the Supplemental Material [163], we briefly outline an experimental protocol for creating such states, which uses a radio-frequency sweep to selectively transfer atoms in one spin state to a third noninteracting spin state. A detailed analysis of the protocol can be found in [164].

Our results are based on a mean-field BdG formalism. Such a mean-field treatment gives a reasonably accurate description of quasi-1D Fermi gases for moderate to weak interactions, becoming quantitative in the weak-coupling limit [140, 141, 155–161, 165]. Further, past theoretical work has shown that the 1D BdG equations accurately describe the equilibrium properties of an array of

tubes [23, 24, 140].

5.4 Model

We start with the many-body Hamiltonian

$$\hat{H} = \int dx \left(\sum_{\sigma=\uparrow,\downarrow} \hat{\Psi}_\sigma^\dagger \hat{H}_\sigma^{(0)} \hat{\Psi}_\sigma + g_{1\mathrm{D}} \hat{\Psi}_\uparrow^\dagger \hat{\Psi}_\downarrow^\dagger \hat{\Psi}_\downarrow \hat{\Psi}_\uparrow \right), \tag{5.1}$$

where $\hat{\Psi}_\sigma \equiv \hat{\Psi}_\sigma(x,t)$ denotes the fermion field operators in the Heisenberg picture, and $g_{1\mathrm{D}}$ is the 1D coupling constant whose relationship to the 3D scattering length is well studied [154, 166–168]. The single-particle Hamiltonian is $\hat{H}^{(0)}_{\uparrow,\downarrow} = -\partial_x^2/2 - \epsilon_\mathrm{F} \pm h$, where ϵ_F is the Fermi energy, and h is an effective magnetic field which controls the polarization. We have set $\hbar = m = 1$, where m is the mass of each fermion. Attractive interactions ($g_{1\mathrm{D}} < 0$) lead to Cooper pairing, which we encode in the superfluid order parameter $\Delta(x,t) = g_{1\mathrm{D}} \langle \hat{\Psi}_\downarrow(x,t) \hat{\Psi}_\uparrow(x,t) \rangle$. Ignoring quadratic fluctuations about Δ yields mean-field equations of motion for $\hat{\Psi} \equiv (\hat{\Psi}_\uparrow \quad \hat{\Psi}_\downarrow^\dagger)^T$. The many-body state is formed by occupying fermionic quasiparticle modes $\hat{\gamma}_j^s$, defined by $\hat{\Psi} = \sum_{s,j} e^{isk_\mathrm{F}x} \big(U_j^s(x,t) \;\; V_j^s(x,t)\big)^T \hat{\gamma}_j^s$, where k_F is the Fermi momentum, (U,V) are coherence factors, and $s = \pm$ breaks modes into right moving and left moving. For weak interactions, only the modes near the Fermi points contribute significantly to pairing. Thus, we write $(-\partial_x^2/2 - \epsilon_\mathrm{F})[e^{\pm ik_\mathrm{F}x}(U_j^\pm, V_j^\pm)] \approx e^{\pm ik_\mathrm{F}x}[\mp ik_\mathrm{F}\partial_x (U_j^\pm, V_j^\pm)]$ (the Andreev approximation [169]), obtaining [163]

$$i\partial_t \begin{pmatrix} U_j^\pm \\ V_j^\pm \end{pmatrix} = \begin{pmatrix} \mp ik_\mathrm{F}\partial_x + h & \Delta(x,t) \\ \Delta^*(x,t) & \pm ik_\mathrm{F}\partial_x + h \end{pmatrix} \begin{pmatrix} U_j^\pm \\ V_j^\pm \end{pmatrix}, \tag{5.2}$$

$$\text{where} \quad \Delta(x,t) = g_{1\mathrm{D}} \sum_{s,j} \langle \hat{\gamma}_j^{s\dagger} \hat{\gamma}_j^s \rangle \, U_j^s V_j^{s*}. \tag{5.3}$$

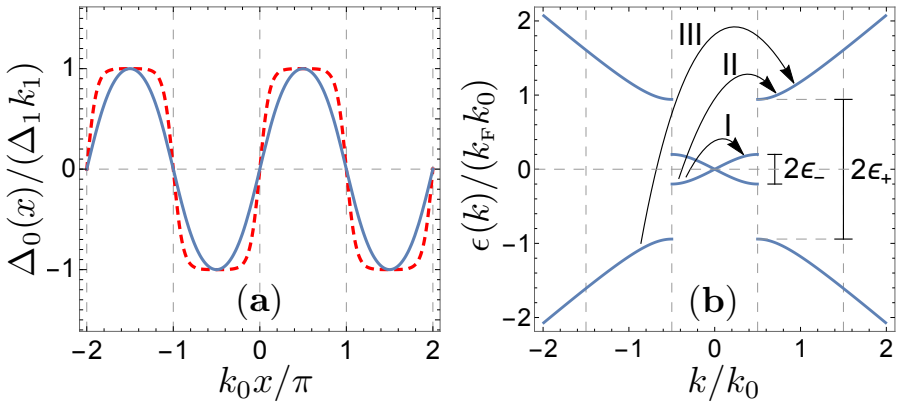

Figure 5.1: (a) Stationary soliton train profile of the order parameter with wave vector k_0 for different values of the sharpness parameter k_1. Solid: $k_1 = 0.65$, dashed: $k_1 = 0.999$. The sharpness is set by the soliton spacing, interaction strength, and spin imbalance. (b) BdG single-particle spectrum of the soliton train in the extended zone, for $k_1 = 0.65$. The arrows show three types of particle-hole excitations, which give rise to disconnected continua in the collective excitation spectrum [gray regions in Fig. 5.2(a)].

For a real stationary solution $\Delta(x,t) = \Delta_0(x)$, the coherence factors are of the form $(U_j^+, V_j^+) = (u_j(x), v_j(x))\, e^{-i(\epsilon_j + h)t}$ and $(U_j^-, V_j^-) = (u_j^*(x), v_j^*(x)) e^{-i(\epsilon_j + h)t}$, where ϵ_j represents the quasiparticle spectrum.

Prior studies have found [19–25] stationary soliton train solutions of the form $\Delta_0(x) = \Delta_1 k_1 \,\mathrm{sn}(\Delta_1 x/k_F, k_1)$, with $\Delta_1 \equiv 2k_F k_0 K(k_1)/\pi$, where $2\pi/k_0$ is the period of the train, sn is a Jacobi elliptic function [170], K is the complete elliptic integral of the first kind, and $k_1 \in (0,1)$ is a parameter controlling the sharpness of solitons, which is set by imposing self-consistency [Eq. (5.3)]. The quasiparticle spectrum has a continuum of free states for $|\epsilon| > \epsilon_+$ and a band of midgap states for $|\epsilon| < \epsilon_-$, where $\epsilon_\pm = \Delta_1(1 \pm k_1)/2$ (Fig. 5.1). The midgap band describes Andreev bound states localized at the soliton cores.

To find the collective modes, we linearize small fluctuations about the stationary solution. Thus, we write $\Delta = \Delta_0(x) + \delta\Delta(x,t)$, $U_j^+ = (u_j(x) +$

$\delta u_j^+(x,t))\, e^{-i(\epsilon_j+h)t}$, $U_j^- = (u_j^*(x) + \delta u_j^-(x,t))\, e^{-i(\epsilon_j+h)t}$, and similar expressions for $V_j^\pm$ in Eqs. (5.2) and (5.3), yielding a set of coupled equations relating $\delta u_j^\pm$, $\delta v_j^\pm$, and $\delta\Delta$. Next, we decompose the fluctuations into frequency components and use the completeness of the stationary wave functions to eliminate $\delta u_j^\pm$ and $\delta v_j^\pm$, thus arriving at an integral equation for $\delta\Delta$. In particular, we write $\delta\Delta = \mathrm{Re}(\delta_a(x)e^{i\Omega t}) + i\,\mathrm{Im}(\delta_p(x)e^{i\Omega t})$ where δ_a and δ_p describe the amplitude and phase fluctuations, respectively, and find (full derivation in Supplemental Material [163])

$$\delta_{p,a}(x) = -g_{1\mathrm{D}} \int dx' \mathcal{M}^\pm(x,x';\Omega)\, \delta_{p,a}(x')\,, \tag{5.4}$$

where, at zero temperature,

$$\mathcal{M}^\pm = \sum_{j,j'}{}' \frac{2(\epsilon_j+\epsilon_{j'})}{(\epsilon_j+\epsilon_{j'})^2-\Omega^2}(u_j^* u_{j'} \pm v_j^* v_{j'})(u_j' u_{j'}'^* \pm v_j' v_{j'}'^*). \tag{5.5}$$

Here, $\Omega \in \mathbb{C}$, the prime on the summation stands for $\epsilon_j > h$, and we have used the notation $(u,v) \equiv (u(x), v(x))$ and $(u',v') \equiv (u(x'), v(x'))$. The collective modes represent nontrivial solutions to Eq. (5.4).

Periodicity of the soliton train leads to a Brillouin zone structure for the collective modes; i.e., one can write $\delta_{p,a}(x) = e^{iqx}\sum_n C_n^\pm e^{ink_0x}$, where $-k_0/2 < q \leq k_0/2$ and $n \in \mathbb{Z}$. However, the stationary solution has an additional symmetry $\Delta_0(x+\pi/k_0) = -\Delta_0(x)$, which causes the even and odd Fourier modes to decouple in Eq. (5.4), effectively doubling the Brillouin zone [141]. Thus, we consider only odd Fourier components, with $-k_0 < q \leq k_0$. Substituting the Fourier expansion into Eq. (5.4) yields a matrix equation $C_n^\pm = -g_{1\mathrm{D}}\sum_m M_{nm}^\pm(q,\Omega)\, C_m^\pm$, where

$$M_{nm}^\pm = \frac{k_0}{2\pi}\int_{-\pi/k_0}^{\pi/k_0} dx \int dx' e^{-i(q+nk_0)x + i(q+mk_0)x'} \mathcal{M}^\pm. \tag{5.6}$$

We find the collective-mode spectrum by solving $\det\left(I + g_{1\mathrm{D}} M^\pm(q,\Omega)\right) = 0$. Note that $M^\pm(q,\Omega)$ has branch cuts on the real-Ω axis, which originate from

particle-hole excitations. Thus, while considering real frequencies (ω), we set $\Omega \to \omega + i0^+$. We find that Ω is either real or imaginary for all collective modes.

The matrices $M^{\pm}$ are related to the pairing susceptibilities $\chi^{\pm}(q,\omega)$, which describe the linear response to a pairing field, as $\chi^{\pm} = -g_{1\mathrm{D}}\mathrm{Tr}\left[(I + g_{1\mathrm{D}}M^{\pm})^{-1}M^{\pm}\right]$ (see Supplemental Material [163] for a derivation). The spectral densities, $\mathrm{Im}\,\chi^{\pm}$, contain isolated poles corresponding to collective modes, and broad particle-hole continua.

5.5 Results

The collective excitation spectrum is fully characterized by two dimensionless quantities: n_s, the number of unpaired fermions per soliton, and k_1, which describes the sharpness of the solitons. They are set by the parameters k_0/k_{F}, $k_{\mathrm{F}}a_{1\mathrm{D}}$, and h/ϵ_{F}, $a_{1\mathrm{D}}$ being the 1D scattering length ($a_{1\mathrm{D}} = -2/g_{1\mathrm{D}}$ [154, 166–168]). To a good approximation, the dependence on k_0/k_{F} and $k_{\mathrm{F}}a_{1\mathrm{D}}$ appears through the combination $w \equiv (k_0/k_{\mathrm{F}})\exp(\pi k_{\mathrm{F}}a_{1\mathrm{D}}/2)$, which measures the width of the Andreev bound states in units of the soliton spacing. For $h = 0$ and $w \lesssim 2.5$, $k_1 \approx 1 - 8e^{-4\pi/w}$ [163].

Figure 5.2(a) shows the collective-mode spectrum for $n_s = 0$, $k_0/k_{\mathrm{F}} = 0.05$, and $k_{\mathrm{F}}a_{1\mathrm{D}} = 2.6$ in the extended-zone scheme. Its structure is representative of the $n_s = 0$ case. The two-particle continuum has three separate regions, corresponding to particle-hole excitation between different bands of the quasiparticle spectrum [Fig. 5.1(b)].

We find two gapless Goldstone modes. The Goldstone phase mode is de-

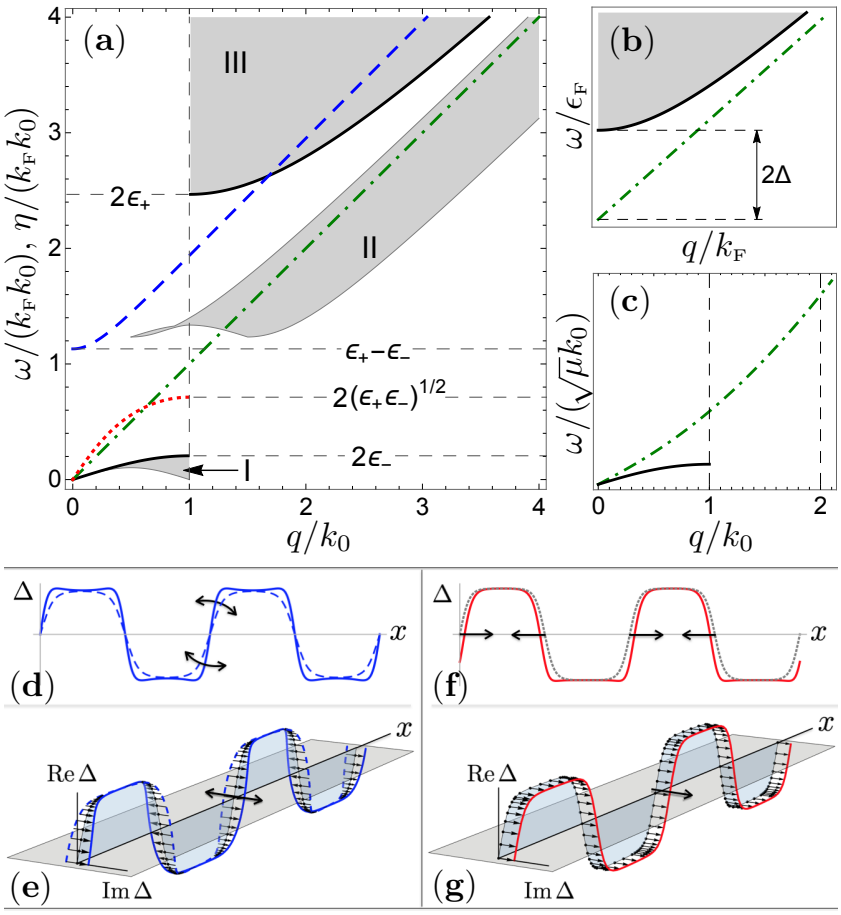

Figure 5.2: Collective-mode spectrum of (a) a soliton train in a Fermi superfluid with no spin imbalance, for $k_0/k_F = 0.05$ and $k_F a_{1D} = 2.6$, (b) a uniform Fermi superfluid, (c) a soliton train in a Bose-Einstein condensate, modeled by the Gross-Pitaevskii equation. There are two gapless Goldstone modes in (a): a "phonon" mode (dot-dashed, green) and an "elastic" mode (solid, black), which describe phase twists and elastic deformations of the order parameter, respectively. The "phonon" mode is the analog of the Anderson-Bogoliubov mode of a uniform superfluid in (b). A second gapped branch of amplitude oscillations (solid, black) forms the remnant of the "Higgs" mode in (b). Both "elastic" and "Higgs" modes in (a) reside on an edge of the two-particle continua, shaded in gray, which originate from three types of particle-hole excitations, as shown in Fig. 5.1(b). Additionally, we find novel twofold degenerate gapped modes in (a) (dashed, blue) which, for small q, describe width and grayness oscillations of each soliton, as illustrated in (d) and (e). The soliton train also has instabilities toward a uniform superfluid state, which show up as twofold degenerate unstable modes. The dotted (red) curve in (a) gives the growth rate η of these modes. The most unstable mode consists of pairs of solitons annihilating one another (f), or the order parameter moving off into the complex plane (g). In contrast, a bosonic soliton train only has two gapless Goldstone modes (c).

scribed by $\delta_p(x) \propto \Delta_0(x)e^{iqx}$ and $\omega = k_{\rm F}q$. It is the analog of the Anderson-Bogoliubov phonon mode in a uniform Fermi superfluid [171–173]. The Goldstone amplitude mode represents elastic deformations of Δ and has a second gapped branch extending to large wave vectors, which forms the analog of the "Higgs" mode in a uniform Fermi superfluid [144–148]. Both branches are expressed by $\delta_a(x) \propto u_{\frac{q}{2}}(x)\, v_{\frac{q}{2}}(x)$ and $\omega = 2\,\epsilon(\frac{q}{2})$, where $\epsilon(k)$ is the single-particle dispersion. Like the "Higgs" mode, both branches sit on the threshold for particle-hole excitations and will therefore be damped [144–146, 174–181]. In contrast, the excitation spectrum of a soliton train in a Bose superfluid, modeled by the Gross-Pitaevskii equation, is comprised only of two undamped gapless modes [Fig. 5.2(c)]. They have a similar dispersion to the fermionic case for small q, but each mode contains both amplitude and phase variations [163].

In Fig. 5.2(a), we also show a gapped mode that is not present in either a Bose superfluid or a uniform Fermi superfluid (dashed, blue curve). This mode is twofold degenerate, with a phase- and an amplitude sector. For small q, they describe oscillations in the grayness and width of each soliton [Figs. 5.2(d)–5.2(e)]. In particular, at $q = 0$, these sectors are expressed by $\delta_p(x) \propto \mathrm{cn}(\Delta_1 x/k_{\rm F}, k_1)$, $\delta_a(x) \propto \mathrm{sn}(\Delta_1 x/k_{\rm F}, k_1)\,\mathrm{dn}(\Delta_1 x/k_{\rm F}, k_1)$ and have an energy $\omega = \epsilon_+ - \epsilon_-$. Surprisingly, we find $\delta_a(x) \propto \delta_p'(x)\ \forall\, q$. Being outside the continua, these "core" modes should be long lived and hence, suitable for experimental detection. One can excite the amplitude "core" mode by a fast ramp to a different interaction strength [see Fig. 5.1(a)].

The balanced soliton train ($n_s = 0$) has dynamical instabilities toward a uniform superfluid state, which show up as two degenerate solutions to Eq. (5.4) with an imaginary frequency. The unstable amplitude mode is associated with

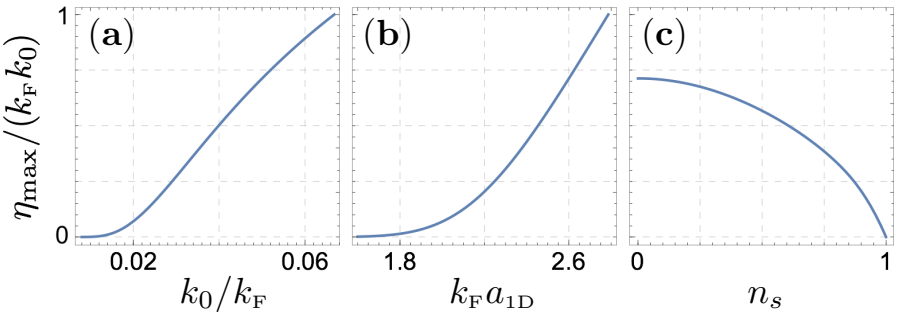

Figure 5.3: Maximum instability rate vs (a) inverse soliton separation, with $n_s = 0$, $k_F a_{1D} = 2.6$, (b) interaction strength, with $n_s = 0$, $k_0/k_F = 0.05$, and (c) spin imbalance, with $k_0/k_F = 0.05$, $k_F a_{1D} = 2.6$. By making the rate sufficiently small, one can investigate the stable collective modes.

pairs of solitons approaching one another and annihilating, whereas the unstable phase mode involves the order parameter moving off into the complex plane [Figs. 5.2(f)–5.2(g)]. The maximum instability occurs at $q = k_0$, where $\delta_a(x) \propto \mathrm{dn}^2(\Delta_1 x/k_F, k_1)$, $\delta_p(x) =$ constant, and the fluctuations grow at a rate $\eta_{\max} = 2(\epsilon_+\epsilon_-)^{1/2}$. For a given soliton spacing, $\eta_{\max}$ is highest at weak interactions, approaching $k_F k_0$. One can lower $\eta_{\max}$ by creating solitons farther apart or increasing the interaction strength [Figs. 5.3(a)–5.3(b)]. We have verified the instability by direct simulations of the BdG equations without the Andreev approximation. We find a lower bound on the soliton lifetime $\tau_{\min} \sim 8/k_F k_0$, which is saturated at weak interactions. For ^{6}Li atoms, with $\epsilon_F = 1.2$ μK (as in [131, 132]) and $k_0/k_F = 0.05$, $\tau_{\min} \approx 0.5$ ms. The instability becomes unnoticeable for $k_F a_{1D} \lesssim 2$, where adjacent solitons collide elastically, in agreement with previous findings on two-soliton collisions [117, 118]. We present the simulations in the Supplemental Material [163], along with collective-mode spectra at different interactions.

An alternate way to stabilize the soliton train is by filling solitons with unpaired fermions [114]. As we increase n_s from 0, the instability rate falls, be-

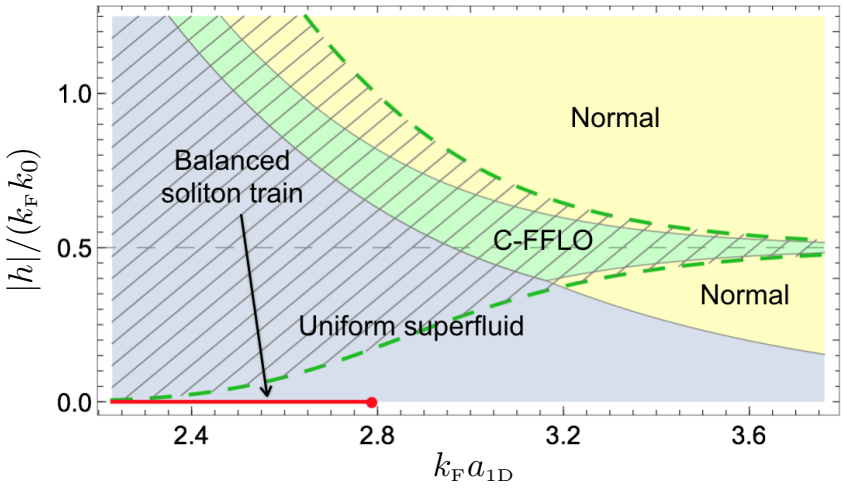

Figure 5.4: Phase diagram obtained by comparing mean-field energies of homogeneous phases, and soliton train states with $k_0/k_F = 0.05$. Solid regions show the lowest-energy states. The C-FFLO phase exists and is dynamically stable throughout the hatched region. The balanced soliton train exists above a minimum interaction strength ($w \lesssim 4$). To see where the other soliton train solutions exist, see the Supplemental Material [163].

coming zero at $n_s = 1$ for the C-FFLO phase [Fig. 5.3(c)]. The stability of the C-FFLO phase originates from the absence of zero-energy particle-hole excitations, as the chemical potentials lie within gaps in the single-particle spectrum. For $n_s > 1$, one again has instabilities (see Supplemental Material [163] for more details).

Past studies on FFLO have focused on the phase that minimizes the free energy, which occurs at specific values of k_0 within a limited region of the phase diagram [154–161]. Low-energy collective excitations of energetically stable FFLO states have been explored using different theoretical techniques [141–143, 182–186], and methods for detecting such states have been proposed [140]. However, we find that a C-FFLO phase is always dynamically stable, even when there are lower-energy states available. To see this, we compare the energies of competing states [163] to arrive at a phase diagram, shown in Fig. 5.4. Despite its large

region of stability, the C-FFLO phase has the lowest energy in a relatively small region. Moreover, the optimal value of k_0/k_F varies continuously with h, a feature not apparent in Fig. 5.4, which is concerned with a fixed value of k_0/k_F. The metastability in this system implies that energetic considerations are of less importance than how the cloud is prepared. In particular, one can engineer long-lived FFLO states by phase imprinting. In Ref. [164] we propose a simple protocol for this engineering, briefly outlined in the Supplemental Material [163].

5.6 Outlook

Our results carry over to other physical systems where solitons arise in a BdG formalism. This includes quasi-1D superconductors in a magnetic field [23–25], an electron-phonon model of conducting polymers [18–22], and Gross-Neveu models in quantum field theory [60–62]. The gapped modes describing width- and grayness oscillations of solitons could be more generic features associated with mesoscale structures; e.g., we find such modes in soliton trains described by a nonlinear Klein-Gordon equation, which also have unstable modes [163]. Although defined by pairing oscillations, these modes should be visible in many different spectroscopic channels. For example, the techniques demonstrated in [97, 98] for observing the oscillation of a single soliton are well suited for probing the "elastic" modes. The instabilities can be studied using techniques from [99, 187]. The "core" modes may be accessible through radio-frequency or modulation spectroscopy [140, 142, 188, 189]. The dynamical stability of the C-FFLO phase should pave the way to its realization via phase imprinting [163]. Other techniques might also be feasible; e.g., in Bose-Einstein condensates, soli-

ton trains spontaneously form in rapid quenches of interaction strength [38–41] or temperature [42], or when two condensates collide [43, 44]. These processes could have analogs in Fermi superfluids. There exist theoretical methods complementary to BdG, such as effective field theories [115, 116, 190, 191] and density-functional theories [113, 117], which could be extended to study soliton trains at strong interactions and finite temperatures. Our analysis provides a useful benchmark for such future investigations.

Acknowledgments

We thank Matthew Reichl for useful discussions. This work was supported by the National Science Foundation Grant PHY-1508300 and the ARO-MURI Non-equilibrium Many-body Dynamics Grant W9111NF-14-1-0003.

5.7 Supplemental Material

5.7.1 Experimental protocol for creating soliton train states

Protocol for creating balanced soliton trains

To produce a balanced soliton train, one traps equal mixtures of $\uparrow$- and $\downarrow$-fermions (e.g., two hyperfine states of ^{6}Li or ^{40}K atoms) in an array of weakly-coupled 1D tubes (Fig. 5.5). As demonstrated experimentally in [131, 132], a superfluid is formed when the atoms are cooled near a Feshbach resonance. Following the strategy used in 3D gases [97–99, 133, 134], one can create solitons

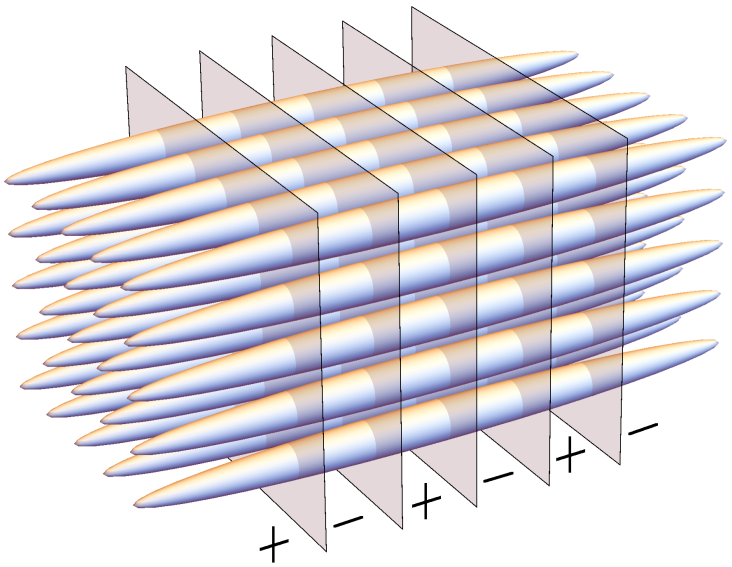

Figure 5.5: Schematic experimental setup for producing balanced soliton trains in an array of weakly coupled tubes. First, uniform superfluids are prepared in each tube by cooling attractively interacting fermions near a Feshbach resonance. Then solitons are imprinted by shining off-resonant lasers in alternate regions labeled '$-$' to reverse the sign of the local order parameter.

in these superfluids by phase imprinting, whereby one shines an off-resonant laser on selected portions of a superfluid for a short duration to rotate the phase of the local order parameter by a given amount. To generate soliton trains, one can imprint a π phase in alternate regions of each tube, as shown in Fig. 5.5.

Protocol for creating C-FFLO states

To produce a C-FFLO phase, we advocate starting with balanced soliton trains in an array of weakly-coupled tubes. As we detail in [164], one can then use radio waves to selectively break up pairs in the soliton cores, transferring spin-$\uparrow$ atoms at those locations to a third spin state $|\phi\rangle$, which does not interact with the $\uparrow$- and $\downarrow$-spin states, thus leaving behind a C-FFLO state with unpaired $\downarrow$-spins. For example, in ^{40}K one could use $|\uparrow\rangle = |9/2, -7/2\rangle$, $|\downarrow\rangle = |9/2, -9/2\rangle$,

and $|\phi\rangle = |9/2, -5/2\rangle$, where the two numbers denote the total atomic spin F and its projection $m_{\rm F}$ [192]. Unwanted bulk excitations can be eliminated by Pauli blocking if one starts with an appropriate density of $|\phi\rangle$-atoms. Even without Pauli blocking, our approach gives relatively few bulk excitations at strong enough interactions.

Within our convention for Bogoliubov operators (see Sec. 4.1), the quasiparticle spectrum of a soliton train is symmetric for positive and negative energies, with delocalized bulk modes for $|\epsilon| > \epsilon_+$, and midgap modes bound to soliton cores for $|\epsilon| < \epsilon_-$ [Fig. 5.1(b) in the main text]. All negative energy modes are occupied in a balanced soliton train. The C-FFLO state with excess $\downarrow$-spins is formed by removing all quasiparticles from the midgap modes. Our key idea is to use a Rapid Adiabatic Passage protocol which vacates the midgap modes by a radio-frequency sweep, while a preformed Fermi sea of $|\phi\rangle$-atoms prevents any bulk excitation. Adiabaticity requires that the sweep is sufficiently slow. However, the finite lifetime of the soliton train sets an upper bound on the sweep rate. Fortunately, when the interactions are sufficiently strong there is a separation of scales.

5.7.2 Stationary soliton train solution

Here we summarize the properties of the stationary soliton train solution that are relevant for examining the collective modes. For further details of derivation, we refer the reader to Refs. [19–25, 170].

We first derive the stationary BdG equations, starting from the many-body

Hamiltonian in Heisenberg picture,

$$\hat{H} = \int dx \left[\sum\nolimits_{\sigma=\uparrow,\downarrow} \hat{\Psi}^\dagger_\sigma(x,t) \hat{H}^{(0)}_\sigma \hat{\Psi}_\sigma(x,t) + g_{1\mathrm{D}} \hat{\Psi}^\dagger_\uparrow(x,t) \hat{\Psi}^\dagger_\downarrow(x,t) \hat{\Psi}_\downarrow(x,t) \hat{\Psi}_\uparrow(x,t) \right], \tag{5.7}$$

where $\hat{H}^{(0)}_{\uparrow,\downarrow} \equiv -\partial_x^2/2 - \epsilon_\mathrm{F} \pm h$. We encode superfluid pairing in the order parameter $\Delta(x,t) = g_{1\mathrm{D}} \langle \hat{\Psi}_\downarrow(x,t) \hat{\Psi}_\uparrow(x,t) \rangle$, and ignore quadratic fluctuations about Δ, yielding the mean-field Hamiltonian

$$\begin{aligned} \hat{H}_\mathrm{MF} = \int dx \Big[& \sum\nolimits_{\sigma=\uparrow,\downarrow} \hat{\Psi}^\dagger_\sigma(x,t) \hat{H}^{(0)}_\sigma \hat{\Psi}_\sigma(x,t) + \Delta(x,t) \hat{\Psi}^\dagger_\uparrow(x,t) \hat{\Psi}^\dagger_\downarrow(x,t) \\ & + \Delta^*(x,t) \hat{\Psi}_\downarrow(x,t) \hat{\Psi}_\uparrow(x,t) - g_{1\mathrm{D}}^{-1} |\Delta(x,t)|^2 \Big]. \end{aligned} \tag{5.8}$$

The Heisenberg equations of motion for the field operators, $i\partial_t \hat{\Psi}_\sigma = [\hat{H}_\mathrm{MF}, \hat{\Psi}_\sigma]$, can be expressed as

$$i\partial_t \hat{\Psi}(x,t) = \begin{pmatrix} -\partial_x^2/2 - \epsilon_\mathrm{F} + h & \Delta(x,t) \\ \Delta^*(x,t) & \partial_x^2/2 + \epsilon_\mathrm{F} + h \end{pmatrix} \hat{\Psi}(x,t), \tag{5.9}$$

where $\hat{\Psi} \equiv \begin{pmatrix} \hat{\Psi}_\uparrow & \hat{\Psi}^\dagger_\downarrow \end{pmatrix}^T$. In the Andreev approximation, we write $\hat{\Psi}(x,t)$ as a sum over right-moving and left-moving fermionic quasiparticle modes, $\hat{\Psi}(x,t) = \sum_{s=\pm,j} e^{isk_\mathrm{F}x} \begin{pmatrix} U^s_j(x,t) & V^s_j(x,t) \end{pmatrix}^T \hat{\gamma}^s_j$ where

$$\left(\partial_x^2/2 - \epsilon_\mathrm{F}\right) \left[\begin{pmatrix} U^\pm_j(x,t) \\ V^\pm_j(x,t) \end{pmatrix} e^{\pm ik_\mathrm{F}x} \right] \approx \left[\mp ik_\mathrm{F} \partial_x \begin{pmatrix} U^\pm_j(x,t) \\ V^\pm_j(x,t) \end{pmatrix} \right] e^{\pm ik_\mathrm{F}x}, \tag{5.10}$$

$$\text{and} \quad \langle \hat{\gamma}^{s\dagger}_j \hat{\gamma}^{s'}_{j'} \rangle = \delta_{ss'} \delta_{jj'} \langle \hat{\gamma}^{s\dagger}_j \hat{\gamma}^s_j \rangle. \tag{5.11}$$

Substituting this expansion into Eq. (5.9) and in the definition of the order parameter, we find the BdG equations

$$i\partial_t \begin{pmatrix} U^\pm_j(x,t) \\ V^\pm_j(x,t) \end{pmatrix} = \begin{pmatrix} \mp ik_\mathrm{F}\partial_x + h & \Delta(x,t) \\ \Delta^*(x,t) & \pm ik_\mathrm{F}\partial_x + h \end{pmatrix} \begin{pmatrix} U^\pm_j(x,t) \\ V^\pm_j(x,t) \end{pmatrix}, \tag{5.12}$$

$$\text{with} \quad \Delta(x,t) = g_{1\mathrm{D}} \sum_{s=\pm,j} \langle \hat{\gamma}^{s\dagger}_j \hat{\gamma}^s_j \rangle \, U^s_j(x,t) V^{s*}_j(x,t). \tag{5.13}$$

For a stationary solution $\Delta(x,t) = \Delta_0(x)$ with quasiparticle energies $\epsilon_j^\pm$, $\langle \hat{\gamma}_j^{\pm\dagger}\hat{\gamma}_j^\pm\rangle = n_{\rm F}(\epsilon_j^\pm + h)$ where $n_{\rm F}$ is the Fermi distribution, and $(U_j^\pm(x,t), V_j^\pm(x,t)) = (u_j^\pm(x), v_j^\pm(x))e^{-i(\epsilon_j^\pm+h)t}$. Using these expressions in Eq. (5.13), we find

$$\begin{pmatrix} \mp ik_{\rm F}\partial_x & \Delta_0(x) \\ \Delta_0^*(x) & \pm ik_{\rm F}\partial_x \end{pmatrix} \begin{pmatrix} u_j^\pm(x) \\ v_j^\pm(x) \end{pmatrix} = \epsilon_j^\pm \begin{pmatrix} u_j^\pm(x) \\ v_j^\pm(x) \end{pmatrix}, \tag{5.14}$$

$$\text{with} \quad \Delta_0(x) = g_{\rm 1D} \sum_{s=\pm,j} n_{\rm F}(\epsilon_j^s + h)\, u_j^s(x) v_j^{s*}(x)\,. \tag{5.15}$$

For real $\Delta_0(x)$, the right- and left-moving branches are related by a complex conjugation: $(u^-, v^-) = (u^+, v^+)^*$ and $\epsilon^- = \epsilon^+$. Thus we can only consider the right-moving branch, drop the superscript '+', and write

$$\begin{pmatrix} -ik_{\rm F}\partial_x & \Delta_0(x) \\ \Delta_0(x) & +ik_{\rm F}\partial_x \end{pmatrix} \begin{pmatrix} u_j(x) \\ v_j(x) \end{pmatrix} = \epsilon_j \begin{pmatrix} u_j(x) \\ v_j(x) \end{pmatrix}, \tag{5.16}$$

$$\text{with} \quad \Delta_0(x) = 2g_{\rm 1D} \sum\nolimits_j n_{\rm F}(\epsilon_j + h)\, \mathrm{Re}\big[u_j(x) v_j^*(x)\big]\,. \tag{5.17}$$

Past studies have shown that a periodic solution to Eq. (5.17) has the soliton train profile $\Delta_0(x) = \Delta_1 k_1 \mathrm{sn}(\Delta_1 x/k_{\rm F}, k_1)$, where $\Delta_1 = 2k_{\rm F}k_0K(k_1)/\pi$. Here $2\pi/k_0$ denotes the period, K denotes the complete elliptic integral of the first kind, and $k_1 \in (0,1)$ parametrizes the sharpness of the solitons.

Since $\Delta_0(x)$ is periodic, each quasiparticle wavefunction $(u(x), v(x))$ in Eq. (5.17) can be labeled by a quasimomentum k, with $-k_0/2 < k < k_0/2$ representing the first Brillouin zone. In addition, the solutions have the following properties: (i) $(-v_k, u_k)$ is a wavefunction with energy $-\epsilon_k$, and (ii) (v_k^*, u_k^*) is another wavefunction with energy ϵ_k, i.e., $(u_{-k}, v_{-k}) = (v_k^*, u_k^*)$ and $\epsilon_{-k} = \epsilon_k$. Therefore, the quasiparticle spectrum $\epsilon(k)$ is symmetric about both ϵ and k axes.

For $k \geq 0$ and $\epsilon \geq 0$, it is given by (in the extended zone representation)

$$\frac{k}{k_0} = \frac{1}{\pi}\frac{\epsilon}{\epsilon_+}\mathrm{Re}\left[\sqrt{\frac{\epsilon_-^2-\epsilon^2}{\epsilon_+^2-\epsilon^2}}\,\Pi\left(\frac{\epsilon_+^2-\epsilon_-^2}{\epsilon_+^2-\epsilon^2}, \sqrt{1-\frac{\epsilon_-^2}{\epsilon_+^2}}\right)\right], \tag{5.18}$$

where $\epsilon_\pm \equiv \frac{1}{2}(1 \pm k_1)\Delta_1$, and Π denotes the complete elliptic integral of the third kind. Figure 1(b) of the main article shows the spectrum for $k_1 = 0.65$. It has a band of Andreev bound states with $|\epsilon| \leq \epsilon_-$, and continua of free states with $|\epsilon| \geq \epsilon_+$. The dispersion is linear as $k \to 0$ and $k \to \infty$, with $\epsilon \approx k_\mathrm{F} k$ for $k \gg k_0$. Interestingly, there is no gap in the spectrum at $k = n(k_0/2)$ with $n = \pm 2, \pm 3, \ldots$. This is because $\Delta_0(x)$ presents a reflectionless potential (a 1-gap Lamé potential) to the Bogoliubov quasiparticles (see [21, 25, 170, 193–195] for more details).

Hereafter we'll use 'tilde' (˜) to denote nondimensionalized quantities, with energies rescaled by $k_\mathrm{F}k_0$, and momenta rescaled by k_0, e.g., $\tilde{\epsilon}_\pm \equiv \epsilon_\pm/(k_\mathrm{F}k_0)$, $\tilde{k} \equiv k/k_0$. The density of states is given by

$$\tilde{\rho}(\tilde{\epsilon}) \equiv \frac{1}{\pi}\frac{d\tilde{k}}{d\tilde{\epsilon}} = \frac{1}{\pi}\mathrm{Re}\left\{\frac{|\tilde{\epsilon}^2-\tilde{\epsilon}_g^2|}{[(\tilde{\epsilon}^2-\tilde{\epsilon}_-^2)(\tilde{\epsilon}^2-\tilde{\epsilon}_+^2)]^{1/2}}\right\}, \tag{5.19}$$

$$\text{where} \quad \epsilon_g^2 \equiv \epsilon_+^2\, E\left(\sqrt{1-\frac{\epsilon_-^2}{\epsilon_+^2}}\right) \Big/ K\left(\sqrt{1-\frac{\epsilon_-^2}{\epsilon_+^2}}\right). \tag{5.20}$$

Here E denotes the complete elliptic integral of the second kind. Note that the density of states diverges as $\epsilon \to \epsilon_\pm$, as expected for band edges in 1D. The energy scale ϵ_g satisfies the inequality $\epsilon_- < \epsilon_g < \epsilon_+$.

The quasiparticle wavefunctions can be expressed in terms of a "spectral parameter" $a_k \in [-\alpha, \alpha]$ where $\alpha \equiv \tilde{\epsilon}_+^{-1} K(\epsilon_-/\epsilon_+)$. The continuum of free states with $\epsilon \geq \epsilon_+$ and $k \geq k_0/2$ is described by

$$\begin{pmatrix} u_k(x) \\ v_k(x) \end{pmatrix} = \frac{e^{ikx}}{2\sqrt{L(\tilde{\epsilon}_k^2-\tilde{\epsilon}_g^2)}} \begin{pmatrix} \sum_{n\,\text{even}} \\ -i\sum_{n\,\text{odd}} \end{pmatrix} \frac{e^{ink_0x}}{\sinh(n\alpha + a_k/2)}, \tag{5.21}$$

where the momentum k and energy ϵ_k are parametrized as

$$\tilde{k} = (i/\pi)\big[\pi\,\zeta(ia_{\tilde{k}}|\pi, i\alpha) - ia_{\tilde{k}}\,\zeta(\pi|\pi, i\alpha)\big] \quad \text{and} \quad \tilde{\epsilon}_{\tilde{k}} = \sqrt{(\tilde{\epsilon}_+^2 + \tilde{\epsilon}_-^2)/3 - \wp(ia_{\tilde{k}}|\pi, i\alpha)}\,. \tag{5.22}$$

Here ζ and $\wp$ denote Weierstrass elliptic functions with half-periods π and $i\alpha$, and L in Eq. (5.21) denotes the length of the system. As k varies from $k_0/2$ to ∞, a_k decreases monotonically from α to 0, and ϵ_k grows from ϵ_+ to ∞. Similarly, the bound states with $0 \le k \le k_0/2$ and $0 \le \epsilon \le \epsilon_-$ are described by

$$\begin{pmatrix} u_k(x) \\ v_k(x) \end{pmatrix} = \frac{e^{ikx}}{2\sqrt{L(\tilde{\epsilon}_g^2 - \tilde{\epsilon}_k^2)}} \begin{pmatrix} \sum_{n\ \text{even}} \\ -i\sum_{n\ \text{odd}} \end{pmatrix} \frac{e^{ink_0x}}{\cosh(n\alpha + a_k/2)}\,, \tag{5.23}$$

with

$$\tilde{k} = (i/\pi)\big[\pi\,\zeta(\pi + ia_{\tilde{k}}|\pi, i\alpha) - (\pi + ia_{\tilde{k}})\,\zeta(\pi|\pi, i\alpha)\big]\,, \tag{5.24}$$

$$\tilde{\epsilon}_{\tilde{k}} = \sqrt{(\tilde{\epsilon}_+^2 + \tilde{\epsilon}_-^2)/3 - \wp(\pi + ia_{\tilde{k}}|\pi, i\alpha)}\,. \tag{5.25}$$

As k is varied from 0 to $k_0/2$, a_k increases monotonically from 0 to α, and ϵ_k grows from 0 to ϵ_-.

Note that the spectrum and the wavefunctions are completely specified (in rescaled coordinates) by the sharpness parameter k_1. This parameter is in turn set by k_0, k_F, h, and a_1D at zero temperature through the self-consistency condition in Eq. (5.17). To see this, we use $n_\mathrm{F}(\epsilon) = \Theta(-\epsilon)$ at zero temperature, Θ being the unit-step function, and write the self-consistency condition in terms of the quasiparticle states with $\epsilon, k \ge 0$ as

$$\Delta_0(x) = -4g_\mathrm{1D} \sum_{k\ge 0} \Theta(\epsilon_k - h)\,\mathrm{Re}\,[u_k(x)v_k^*(x)]\,. \tag{5.26}$$

Using properties of elliptic functions, one can show that $\mathrm{Re}\,[u_k(x)v_k^*(x)] = \Delta_0(x)\epsilon_k/\big[2L(\epsilon_k^2 - \epsilon_g^2)\big]\ \forall\, k \ge 0$ [25]. Substituting this result and the relation

$g_{1D} = -2/a_{1D}$ [166, 167] into Eq. (5.26), we get, in the limit $L \to \infty$,

$$\frac{2}{\pi a_{1D}} \int_0^{k_c} dk \, \frac{\Theta\big(\epsilon_k - h\big)\, \epsilon_k}{\epsilon_k^2 - \epsilon_g^2} = 1. \tag{5.27}$$

Here we have introduced an ultraviolet cutoff k_c because the integral has a logarithmic divergence at high energies, as the dispersion is linear at large k. This is an artifact of the Andreev approximation, and not present in the full model. We choose the cutoff by requiring that a uniform (BCS-type) solution to Eq. (5.17) match the known solution in the full model, as was done in Refs. [21, 25]. This procedure yields k_c/k_F as a function of $k_F a_{1D}$ (see Sec. 5.7.3). We find $k_c \approx 2k_F$ throughout the weakly-interacting regime ($k_F a_{1D} \gtrsim 1$). We have verified that the soliton train profiles obtained using this cutoff closely match the numerically obtained profiles in the full model. Further, barring the weak dependence of k_1 on k_c, the collective modes are insensitive to the choice of the cutoff. We can rewrite Eq. (5.27) as

$$\int_0^{\tilde{k}_c} d\tilde{k} \, \frac{\Theta(\tilde{\epsilon}_{\tilde{k}} - \tilde{h})\, \tilde{\epsilon}_{\tilde{k}}}{\tilde{\epsilon}_{\tilde{k}}^2 - \tilde{\epsilon}_g^2} = \frac{\pi}{2} k_F a_{1D}\,, \quad \text{or} \quad \int_{\tilde{h}}^{\tilde{\epsilon}_c} \frac{\tilde{\epsilon}\, \tilde{\rho}(\tilde{\epsilon})\, d\tilde{\epsilon}}{\tilde{\epsilon}^2 - \tilde{\epsilon}_m^2} = \frac{1}{2} k_F a_{1D}\,, \tag{5.28}$$

where $\tilde{\epsilon}_c \equiv \tilde{\epsilon}_{\tilde{k}_c}$. Substituting the expression for $\tilde{\rho}(\tilde{\epsilon})$ from Eq. (5.20), and evaluating the integral, we get

$$\mathrm{Re}\left\{ \ln \left[\frac{(\tilde{\epsilon}_c^2 - \tilde{\epsilon}_-^2)^{1/2} + (\tilde{\epsilon}_c^2 - \tilde{\epsilon}_+^2)^{1/2}}{(\tilde{\epsilon}_-^2 - \tilde{h}^2)^{1/2} + (\tilde{\epsilon}_+^2 - \tilde{h}^2)^{1/2}} \right] \right\} = \frac{\pi}{2} k_F a_{1D}\,. \tag{5.29}$$

Equation (5.29) determines k_1 for given values of k_0/k_F, $k_F a_{1D}$, and $|h|/(k_F k_0)$ at zero temperature.

The collective modes are characterized by k_1 and n_s, where n_s denotes the number of unpaired fermions per soliton. To see how n_s depends on k_0, k_F, a_{1D},

and h, we first write the expressions for the densities of up- and down-spins:

$$\langle\hat{\Psi}^\dagger_\uparrow(x)\hat{\Psi}_\uparrow(x)\rangle = 2\sum\nolimits_j n_{\rm F}(\epsilon_j+h)|u_j(x)|^2 = \sum\nolimits_j n_{\rm F}(\epsilon_j+h)\left(|u_j(x)|^2+|v_j(x)|^2\right), \tag{5.30}$$

$$\langle\hat{\Psi}^\dagger_\downarrow(x)\hat{\Psi}_\downarrow(x)\rangle = 2\sum\nolimits_j n_{\rm F}(-\epsilon_j-h)|v_j(x)|^2 = \sum\nolimits_j n_{\rm F}(-\epsilon_j-h)\left(|u_j(x)|^2+|v_j(x)|^2\right). \tag{5.31}$$

In the last step of the above equations, we have made use of the symmetry $(u_{-k}, v_{-k}) = (v_k^*, u_k^*)$ and $\epsilon_{-k} = \epsilon_k$. Thus, at zero temperature, the density of unpaired fermions is given by

$$\delta n(x) = \sum_{-|h|<\epsilon_j<|h|} |u_j(x)|^2+|v_j(x)|^2 = \sum_{0\le\epsilon_k<|h|} 2\left(|u_k(x)|^2+|v_k(x)|^2\right). \tag{5.32}$$

Here we have used $(-v_k(x), u_k(x))$ and $(u_k^*(x), -v_k^*(x))$ for the two states with energy $-\epsilon_k$. From Eqs. (5.21) and (5.23), we see that $\delta n(x+\pi/k_0) = \delta n(x)$. Thus one can find n_s by simply integrating $\delta n(x)$ over all x, then dividing by the number of solitons $N_s = L/(\pi/k_0) = k_0L/\pi$. However, $\int dx\,(|u_k(x)|^2+|v_k(x)|^2) = 1$ from normalization. Hence,

$$n_s = \frac{2\pi}{k_0L}\sum_{0\le\epsilon_k<|h|} 1 \xrightarrow{L\to\infty} \left.\frac{2k_h}{k_0}\right|_{\epsilon_{k_h}=h} = \frac{2\tilde{h}}{\pi\tilde{\epsilon}_+}\mathrm{Re}\left[\sqrt{\frac{\tilde{\epsilon}_-^2-\tilde{h}^2}{\tilde{\epsilon}_+^2-\tilde{h}^2}}\,\Pi\left(\frac{\tilde{\epsilon}_+^2-\tilde{\epsilon}_-^2}{\tilde{\epsilon}_+^2-\tilde{h}^2}, \sqrt{1-\frac{\tilde{\epsilon}_-^2}{\tilde{\epsilon}_+^2}}\right)\right], \tag{5.33}$$

where we have used Eq. (5.18) for the dispersion. Note that $\tilde{\epsilon}_\pm = (1\pm k_1)K(k_1)/\pi$. Thus Eq. (5.33) yields n_s for given values of $|h|/(k_{\rm F}k_0)$ and k_1 at zero temperature. When $h = 0$, $n_s = 0$, and we get a balanced soliton train, whereas for $\tilde{\epsilon}_- < |h|/(k_{\rm F}k_0) < \tilde{\epsilon}_+$, $n_s = 1$, and we get a commensurate FFLO (C-FFLO) state.

Equations (5.29) and (5.33) determine k_1 and n_s for given values of $k_0/k_{\rm F}$, $k_{\rm F}a_{\rm 1D}$, and $|h|/(k_{\rm F}k_0)$. In general, there can be zero, one, or multiple solutions, as the left-hand side of Eq. (5.29) is a non-monotonic function of k_1. Figure 5.6

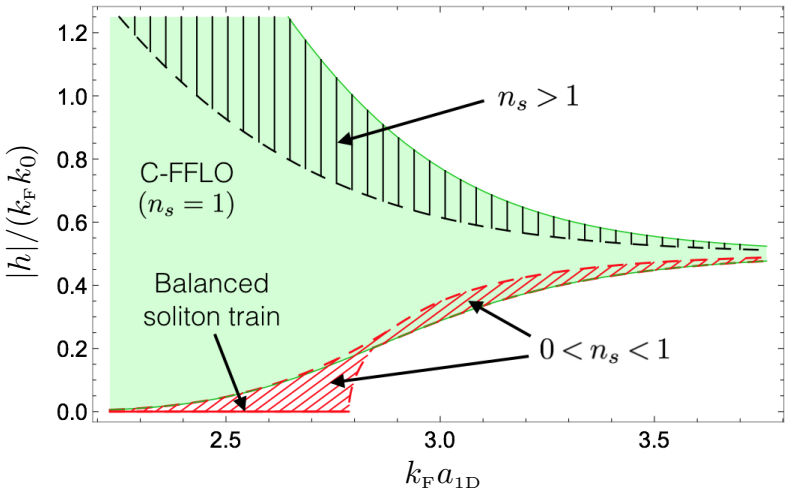

Figure 5.6: Stationary soliton train solutions in different regions of the $k_F a_{1D} - |h|/(k_F k_0)$ plane for $k_0/k_F = 0.05$. The solutions are obtained by imposing the self-consistency condition in Eq. (5.29). The states are classified in terms of n_s, the number of unpaired fermions per soliton [Eq. (5.33)]. Solid (green), vertically hatched (black), and oblique hatched (red) regions contain, respectively, a solution with $n_s = 1$, $n_s > 1$, and $0 < n_s < 1$. Overlapping regions contain multiple solutions. Figure 5.4 in the main article is similar, but shows only stable solutions for $|h| > 0$.

shows regions in the $k_F a_{1D} - |h|/(k_F k_0)$ plane where different types of solutions exist for $k_0/k_F = 0.05$. As k_0/k_F is decreased (increased), the regions remain structurally similar, but translate to weaker (stronger) interactions. In particular, the balanced soliton train with a given period exists only above a minimum interaction strength, given by $k_0/k_F \lesssim 4e^{-\frac{\pi}{2} k_F a_{1D}}$. Conversely, the C-FFLO phase exists for all values of k_0/k_F and $k_F a_{1D}$, although for very weak interactions, it is confined to a small interval of $|h|/(k_F k_0)$ near $1/2$. We also note that the C-FFLO state for a given k_0/k_F and $k_F a_{1D}$ does not vary with h, as Eqs. (5.29) and (5.33) become independent of h for $\tilde{\epsilon}_- < |h|/(k_F k_0) < \tilde{\epsilon}_+$.

5.7.3 High-energy cutoff in the Andreev approximation

In this section we find an expression for the cutoff k_c in Eq. (5.27) by requiring that a uniform superfluid solution to Eq. (5.17), $\Delta_0(x) = \Delta_{\text{BCS}}$, match the corresponding solution in the full model (at $h = 0$).

At zero temperature, the stationary BdG equations in the full model, with $\Delta_0(x) = \Delta_{\text{BCS}} \in \mathbb{R}$, are given by

$$\begin{pmatrix} -\partial_x^2/2 - \epsilon_{\text{F}} & \Delta_{\text{BCS}} \\ \Delta_{\text{BCS}} & \partial_x^2/2 + \epsilon_{\text{F}} \end{pmatrix} \begin{pmatrix} u_j(x) \\ v_j(x) \end{pmatrix} = \epsilon_j \begin{pmatrix} u_j(x) \\ v_j(x) \end{pmatrix}, \tag{5.34}$$

$$\text{with} \quad \Delta_0(x) = g_{1\text{D}} \sum\nolimits_j \Theta(-\epsilon_j)\, u_j(x) v_j^*(x)\,. \tag{5.35}$$

The Hamiltonian has plane wave eigenfunctions

$$\left(u_k^{\pm}(x), v_k^{\pm}(x)\right) = \frac{e^{ikx}}{\sqrt{2L}} \left(\left(1 + \frac{\xi_k}{\epsilon_k^{\pm}}\right)^{1/2}, \pm \left(1 - \frac{\xi_k}{\epsilon_k^{\pm}}\right)^{1/2} \right), \tag{5.36}$$

$$\text{with energies} \quad \epsilon_k^{\pm} = \pm\sqrt{\xi_k^2 + \Delta_{\text{BCS}}^2}\,, \tag{5.37}$$

where $\xi_k \equiv k^2/2 - \epsilon_{\text{F}}$. Using these expressions in the self-consistency condition in Eq. (5.35), we obtain

$$\Delta_{\text{BCS}} = -\frac{g_{1\text{D}}}{2L} \sum_k \frac{\Delta_{\text{BCS}}}{\left(\xi_k^2 + \Delta_{\text{BCS}}^2\right)^{1/2}}\,, \quad \text{or} \quad \int_0^{\infty} \frac{d\bar{k}}{\left[(\bar{k}^2 - 1)^2 + (\Delta_{\text{BCS}}/\epsilon_{\text{F}})^2\right]^{1/2}} = \frac{\pi}{2} k_{\text{F}} a_{1\text{D}}\,, \tag{5.38}$$

where $\bar{k} \equiv k/k_{\text{F}}$, and we have taken the limit $L \to \infty$. Evaluating the integral in Eq. (5.38) yields

$$\frac{1}{[1 + (\Delta_{\text{BCS}}/\epsilon_{\text{F}})^2]^{1/4}} F\left(\pi \middle| \frac{1}{2} + \frac{1}{2\,[1 + (\Delta_{\text{BCS}}/\epsilon_{\text{F}})^2]^{1/2}}\right) = \pi k_{\text{F}} a_{1\text{D}}\,, \tag{5.39}$$

where F denotes the incomplete elliptic integral of the first kind. Inverting this equation gives $\Delta_{\text{BCS}}/\epsilon_{\text{F}}$ as a function of $k_{\text{F}} a_{1\text{D}}$. In the weakly-interacting regime ($k_{\text{F}} a_{1\text{D}} \gtrsim 1$), Δ_{BCS} decays exponentially with $k_{\text{F}} a_{1\text{D}}$ as $\Delta_{\text{BCS}} \approx 8\,\epsilon_{\text{F}}\, e^{-\frac{\pi}{2} k_{\text{F}} a_{1\text{D}}}$.

Next we solve Eq. (5.17) with $\Delta_0(x) = \Delta_{\text{BCS}}$ and $h = 0$ at zero temperature to determine the cutoff k_c:

$$\begin{pmatrix} -ik_{\text{F}}\partial_x & \Delta_{\text{BCS}} \\ \Delta_{\text{BCS}} & +ik_{\text{F}}\partial_x \end{pmatrix} \begin{pmatrix} u_j(x) \\ v_j(x) \end{pmatrix} = \epsilon_j \begin{pmatrix} u_j(x) \\ v_j(x) \end{pmatrix}, \tag{5.40}$$

$$\text{with} \quad \Delta_0(x) = 2g_{1\text{D}} {\sum_j}' \Theta(-\epsilon_j)\, \text{Re}\left[u_j(x) v_j^*(x)\right], \tag{5.41}$$

where the prime on the sum stands for the cutoff. We can again solve the system in terms of plane waves

$$\left(u_k^{\pm}(x), v_k^{\pm}(x)\right) = \frac{e^{ikx}}{\sqrt{2L}} \left(\left(1 + \frac{k_{\text{F}}k}{\epsilon_k^{\pm}}\right)^{1/2}, \pm \left(1 - \frac{k_{\text{F}}k}{\epsilon_k^{\pm}}\right)^{1/2} \right), \tag{5.42}$$

$$\text{where} \quad \epsilon_k^{\pm} = \pm\sqrt{(k_{\text{F}}k)^2 + \Delta_{\text{BCS}}^2}\,. \tag{5.43}$$

Substituting these expressions in Eq. (5.41), we get

$$\Delta_{\text{BCS}} = -\frac{g_{1\text{D}}}{L} {\sum_k}' \frac{\Delta_{\text{BCS}}}{\left[(k_{\text{F}}k)^2 + \Delta_{\text{BCS}}^2\right]^{1/2}}, \quad \text{or} \quad \int_0^{\frac{k_c}{k_{\text{F}}}} \frac{d\bar{k}}{\left[\bar{k}^2 + (\Delta_{\text{BCS}}/2\epsilon_{\text{F}})^2\right]^{1/2}} = \frac{\pi}{2} k_{\text{F}} a_{1\text{D}}\,, \tag{5.44}$$

in the limit $L \to \infty$. Evaluating the integral yields

$$k_c = (\Delta_{\text{BCS}}/k_{\text{F}}) \sinh(\pi k_{\text{F}} a_{1\text{D}}/2)\,. \tag{5.45}$$

Combining Eqs. (5.39) and (5.45), we obtain k_c/k_{F} as a function of $k_{\text{F}}a_{1\text{D}}$. For $k_{\text{F}}a_{1\text{D}} \gtrsim 1$, $k_c \approx 2k_{\text{F}}$.

5.7.4 Energy of stationary states and phase diagram

Here we calculate the mean-field energy of stationary states in the Andreev approximation, which will let us compare the energies of the phases in Fig. 5.6, as well as uniform states with $\Delta_0(x) =$ constant, to arrive at a phase diagram.

We rewrite the mean-field Hamiltonian in the Eq. (5.8) for a stationary state $\Delta(x,t) = \Delta_0(x) \in \mathbb{R}$ as

$$\hat{H}_{\text{MF}} = \int dx \left[\begin{pmatrix} \hat{\Psi}^\dagger_\uparrow(x,t) & \hat{\Psi}_\downarrow(x,t) \end{pmatrix} \begin{pmatrix} -\partial_x^2/2 - \epsilon_{\text{F}} + h & \Delta_0(x) \\ \Delta_0(x) & \partial_x^2/2 + \epsilon_{\text{F}} + h \end{pmatrix} \begin{pmatrix} \hat{\Psi}_\uparrow(x,t) \\ \hat{\Psi}^\dagger_\downarrow(x,t) \end{pmatrix} \right.$$
$$\left. -\hat{\Psi}_\downarrow(x,t) \left(\frac{\partial_x^2}{2} + \epsilon_{\text{F}} + h \right) \hat{\Psi}^\dagger_\downarrow(x,t) - \hat{\Psi}^\dagger_\downarrow(x,t) \left(\frac{\partial_x^2}{2} + \epsilon_{\text{F}} + h \right) \hat{\Psi}_\downarrow(x,t) - \frac{[\Delta_0(x)]^2}{g_{\text{1D}}} \right]. \tag{5.46}$$

In the Andreev approximation, we diagonalize the Hamiltonian by the Bogoliubov transformation (see Sec. 5.7.2)

$$\begin{pmatrix} \hat{\Psi}_\uparrow(x,t) \\ \hat{\Psi}^\dagger_\downarrow(x,t) \end{pmatrix} = \sum\nolimits'_j \left[\begin{pmatrix} u_j(x) \\ v_j(x) \end{pmatrix} e^{ik_{\text{F}}x - i\epsilon_j t} \hat{\gamma}^+_j + \begin{pmatrix} u^*_j(x) \\ v^*_j(x) \end{pmatrix} e^{-ik_{\text{F}}x - i\epsilon_j t} \hat{\gamma}^-_j \right], \tag{5.47}$$

where the wavefunctions $(u_j(x) \quad v_j(x))^T$ satisfy Eq. (5.17), and the prime on the sum indicates we only include modes with energies below the high-energy cutoff. Next we use $\langle \hat{\gamma}^{s\dagger}_j \hat{\gamma}^{s'}_{j'} \rangle = n_{\text{F}}(\epsilon_j + h)\, \delta_{jj'} \delta_{ss'}$ and

$$\left(\partial_x^2/2 - \epsilon_{\text{F}}\right) \left[\begin{pmatrix} u_j(x) \\ v_j(x) \end{pmatrix} e^{ik_{\text{F}}x} \right] \approx \left[-ik_{\text{F}} \partial_x \begin{pmatrix} u_j(x) \\ v_j(x) \end{pmatrix} \right] e^{ik_{\text{F}}x} \tag{5.48}$$

in Eq. (5.46) to obtain the mean-field energy $E \equiv \langle \hat{H}_{\text{MF}} \rangle$ as

$$E = \sum\nolimits'_j \left[\int dx \left(ik_{\text{F}}\, v_j(x)\, \partial_x v^*_j(x) - ik_{\text{F}}\, v^*_j(x)\, \partial_x v_j(x) - 2h|v_j(x)|^2 \right) \right.$$
$$\left. + 2(\epsilon_j + h)\, n_{\text{F}}(\epsilon_j + h) \right] - g_{\text{1D}}^{-1} \int dx\, [\Delta_0(x)]^2 . \tag{5.49}$$

The above expression can be simplified by noting that corresponding to a state $(u_j(x) \;\; v_j(x))^T$ with energy ϵ_j, there is a state $(-u^*_j(x) \;\; v^*_j(x))^T$ with energy $-\epsilon_j$ (see Sec. 5.7.2). Therefore the terms involving derivatives in Eq. (5.49) vanish when summed over all states. Further, $(v^*_j(x) \;\; u^*_j(x))^T$ is also a state with energy ϵ_j, which lets us write

$$2 \sum\nolimits'_j \int dx\, |v_j(x)|^2 = 2 \sum\nolimits'_j \int dx\, |u_j(x)|^2 = \sum\nolimits'_j \int dx \left(|u_j(x)|^2 + |v_j(x)|^2 \right) = \sum\nolimits'_j 1 . \tag{5.50}$$

Using these results in Eq. (5.49), we find

$$E = \sum\nolimits_j{}' \left[2(\epsilon_j + h)\, n_{\rm F}(\epsilon_j + h) - h\right] - g_{\rm 1D}^{-1} \int dx\, [\Delta_0(x)]^2 \,. \tag{5.51}$$

One can show that E is an even function of h, using the identity $n_{\rm F}(-\epsilon) = 1 - n_{\rm F}(\epsilon)$ and the fact that the spectrum is symmetric for positive and negative energies. Thus we can write

$$E = \sum\nolimits_j{}' \left[2(|h| - \epsilon_j)\, n_{\rm F}(|h| - \epsilon_j) - |h|\right] - g_{\rm 1D}^{-1} \int dx\, [\Delta_0(x)]^2 \,. \tag{5.52}$$

In the limit of zero temperature and large system size ($L \to \infty$), Eq. (5.52) gives an energy density

$$\mathcal{E} \equiv \frac{E}{L} = -2 \int_{|h|}^{\epsilon_{k_c}} \epsilon\, \rho(\epsilon)\, d\epsilon - \frac{|h|}{\pi} \int_{\epsilon_k < |h|} dk - \frac{g_{\rm 1D}^{-1}}{L} \int dx\, [\Delta_0(x)]^2 \,, \tag{5.53}$$

where $\rho(\epsilon)$ represents the density of states, and we have assumed that $\Delta_0(x)$ is either uniform or periodic, such that the spectrum can be labeled by quasimomenta k, with $\epsilon_k \geq 0 \;\forall\; k$.

Next we apply Eq. (5.53) to calculate energy densities of different stationary states. We start with the Normal state where $\Delta_0(x) = 0$. The spectrum is given by $\epsilon_k = k_{\rm F}|k|$ (see Eq. (5.43)). Hence $\rho(\epsilon) \equiv (1/\pi)|dk/d\epsilon| = 1/(\pi k_{\rm F})$. Using these expressions in Eq. (5.53) yields an energy density

$$\mathcal{E}_{\rm N} = -\frac{1}{\pi k_{\rm F}} \left(k_{\rm F}^2 k_c^2 + h^2\right) = -\frac{1}{\pi k_{\rm F}} \left[\Delta_{\rm BCS}^2 \sinh^2\!\Big(\frac{\pi}{2} k_{\rm F} a_{\rm 1D}\Big) + h^2\right], \tag{5.54}$$

$$\text{or} \quad \bar{\mathcal{E}}_{\rm N} \equiv \frac{\mathcal{E}_{\rm N}}{k_{\rm F}\epsilon_{\rm F}} = -\frac{1}{2\pi} \left[(\Delta_{\rm BCS}/\epsilon_{\rm F})^2 \sinh^2\!\Big(\frac{\pi}{2} k_{\rm F} a_{\rm 1D}\Big) + (h/\epsilon_{\rm F})^2\right], \tag{5.55}$$

where we have used Eq. (5.45) for k_c, and defined a rescaled energy density $\bar{\mathcal{E}} \equiv \mathcal{E}/(k_{\rm F}\epsilon_{\rm F})$. The parameter $\Delta_{\rm BCS}/\epsilon_{\rm F}$ is a function of $k_{\rm F} a_{\rm 1D}$ as given in Eq. (5.39). Note that the dependence of $\bar{\mathcal{E}}_{\rm N}$ on the interaction strength $k_{\rm F} a_{\rm 1D}$ is a consequence of the finite cutoff k_c in the Andreev approximation. In the full model,

the normal state has an energy density $\bar{\mathcal{E}}_{\rm N}^{\rm Full} = -(2/3\pi)\big[(1+h/\epsilon_{\rm F})^{3/2} + (1-h/\epsilon_{\rm F})^{3/2}\big] = -(1/6\pi)[8+3(h/\epsilon_{\rm F})^2] - O((h/\epsilon_{\rm F})^4)$ for $|h| \le \epsilon_{\rm F}$. Thus we see that the introduction of the cutoff in the Andreev approximation renormalizes the energy of the Normal state, such that $\bar{\mathcal{E}}^{\rm Full} = \bar{\mathcal{E}} + \Lambda$, where the shift Λ depends on $k_{\rm F}a_{\rm 1D}$. We find that for $k_{\rm F}a_{\rm 1D} \gtrsim 1$ and $|h| \ll \epsilon_{\rm F}$, the energy of a uniform superfluid experiences the same renormalization, and Λ is irrelevant for comparing the energies of different states with one another. Therefore we will drop this term in the following.

For a uniform superfluid phase with $\Delta_0(x) = \Delta_u \ge 0$, the spectrum is given by $\epsilon_k = \sqrt{(k_{\rm F}k)^2 + \Delta_u^2}$. Thus,

$$\rho(\epsilon) \equiv \frac{1}{\pi}\left|\frac{dk}{d\epsilon}\right| = \frac{1}{\pi k_{\rm F}} \frac{\epsilon}{\sqrt{\epsilon^2 - \Delta_u^2}}\,\Theta(\epsilon - \Delta_u)\,. \tag{5.56}$$

Substituting this result in Eq. (5.53) and using $g_{\rm 1D} = -2/a_{\rm 1D}$, we find

$$\mathcal{E}_u = -\frac{2}{\pi k_{\rm F}} \int_{\rm Max(|h|,\Delta_u)}^{\sqrt{(k_{\rm F}k_c)^2+\Delta_u^2}} \frac{\epsilon^2 d\epsilon}{\sqrt{\epsilon^2-\Delta_u^2}} - \frac{|h|}{\pi}\int_{\sqrt{(k_{\rm F}k)^2+\Delta_u^2}<|h|} dk + \frac{\Delta_u^2 a_{\rm 1D}}{2} \tag{5.57}$$

$$= -\frac{1}{\pi k_{\rm F}}\Big\{ k_{\rm F}k_c\sqrt{(k_{\rm F}k_c)^2+\Delta_u^2} + \Delta_u^2\,\sinh^{-1}(k_{\rm F}k_c/\Delta_u) + \Big[|h|\sqrt{h^2-\Delta_u^2} - \Delta_u^2\cosh^{-1}(|h|/\Delta_u)\Big]\Theta(|h|-\Delta_u)\Big\} + \Delta_u^2 a_{\rm 1D}/2\,, \tag{5.58}$$

where $k_{\rm F}k_c = \Delta_{\rm BCS}\sinh(\pi k_{\rm F}a_{\rm 1D}/2)$ from Eq. (5.45). The stationary states correspond to local extrema of $\mathcal{E}_u$, i.e., $d\mathcal{E}_u/d\Delta_u = 0$. For $|h| < (1-e^{-\pi k_{\rm F}a_{\rm 1D}})\Delta_{\rm BCS}/2$, there is a maximum at $\Delta_u = 0$ (the Normal state) and a minimum at $\Delta_u = \Delta_{\rm BCS}$ (the "BCS" state). For $|h| > (1-e^{-\pi k_{\rm F}a_{\rm 1D}})\Delta_{\rm BCS}/2$, the Normal state turns into a minimum, and a new maximum appears at $\Delta_u = [h^2 - (\Delta_{\rm BCS} - |h|]^2\tanh^2(\pi k_{\rm F}a_{\rm 1D}/2))^{1/2}$, which represents the unstable Sarma phase. As $|h|$ is increased, the Sarma maximum approaches the BCS minimum, and the two annihilate at $|h| = \Delta_{\rm BCS}$. For larger values of $|h|$, only the Normal phase min-

imum survives. The energy of the "BCS" state can be obtained by setting $\Delta_u = \Delta_{\rm BCS} > |h|$ in Eq. (5.58), yielding

$$\mathcal{E}_{\rm BCS} = -\frac{1}{2\pi k_{\rm F}}\Delta_{\rm BCS}^2 \sinh(\pi k_{\rm F} a_{\rm 1D})\,, \quad \text{or} \quad \bar{\mathcal{E}}_{\rm BCS} = -\frac{1}{4\pi\epsilon_{\rm F}^2}\Delta_{\rm BCS}^2 \sinh(\pi k_{\rm F} a_{\rm 1D})\,. \tag{5.59}$$

Note that $\Delta_{\rm BCS}/\epsilon_{\rm F}$ only depends on $k_{\rm F}a_{\rm 1D}$ [Eq. (5.39)], so $\bar{\mathcal{E}}_{\rm BCS}$ is independent of h. Comparing Eqs. (5.54) and (5.59) we find that $\mathcal{E}_N < \mathcal{E}_{\rm BCS}$ for $h^2 > (1 - e^{-\pi k_{\rm F} a_{\rm 1D}})\Delta_{\rm BCS}^2/2$.

For a soliton train phase with period $2\pi/k_0$ and sharpness parameter k_1 (see Sec. 5.7.2),

$$\Delta_0(x) = [2k_{\rm F}k_0k_1K(k_1)/\pi]\,\mathrm{sn}\big(2K(k_1)k_0x/\pi, k_1\big)\,. \tag{5.60}$$

The quasiparticle spectrum and the density of states are given in Eqs. (5.18) and (5.20). In terms of rescaled quantities we defined earlier, the energy density in Eq. (5.53) can be expressed as

$$\bar{\mathcal{E}}_{\rm ST} = -4\,\frac{k_0^2}{k_{\rm F}^2}\bigg\{\int_{|\tilde{h}|}^{\tilde{\epsilon}_c} \tilde{\epsilon}\,\tilde{\rho}(\tilde{\epsilon})\,d\tilde{\epsilon} + \frac{1}{\pi}\,\tilde{k}_{|\tilde{h}|}|\tilde{h}| - \frac{k_{\rm F}a_{\rm 1D}}{8\pi}\,k_0\int_{-\pi/k_0}^{\pi/k_0} dx\,[\tilde{\Delta}_0(x)]^2\bigg\}. \tag{5.61}$$

Here $\bar{\mathcal{E}}_{\rm ST} \equiv \mathcal{E}_{\rm ST}/(k_{\rm F}\epsilon_{\rm F})$, $\tilde{k} \equiv k/k_0$, $(\tilde{\epsilon}, \tilde{h}, \tilde{\Delta}_0(x)) \equiv (\epsilon, h, \Delta_0(x))/(k_{\rm F}k_0)$, $\tilde{\epsilon}_c \equiv \tilde{\epsilon}_{\tilde{k}_c}$, and $k_{|h|}$ denotes the non-negative quasimomentum such that $\epsilon_{k_{|h|}} = |h|$. From Eq. (5.18) we see that

$$\tilde{k}_{|h|} = \frac{|\tilde{h}|}{\pi\tilde{\epsilon}_+}\mathrm{Re}\left[\sqrt{\frac{\tilde{\epsilon}_-^2 - \tilde{h}^2}{\tilde{\epsilon}_+^2 - \tilde{h}^2}}\,\Pi\left(\frac{\tilde{\epsilon}_+^2 - \tilde{\epsilon}_-^2}{\tilde{\epsilon}_+^2 - \tilde{h}^2}, \sqrt{1 - \frac{\tilde{\epsilon}_-^2}{\tilde{\epsilon}_+^2}}\right)\right], \tag{5.62}$$

where $\tilde{\epsilon}_\pm \equiv (1 \pm k_1)K(k_1)/\pi$. Using $\tilde{\rho}(\tilde{\epsilon})$ from Eq. (5.20) we find

$$\begin{aligned}\int_{|\tilde{h}|}^{\tilde{\epsilon}_c} \tilde{\epsilon}\,\tilde{\rho}(\tilde{\epsilon})\,d\tilde{\epsilon} = \frac{1}{2\pi}\mathrm{Re}\bigg\{&\big(\tilde{\epsilon}_+^2 + \tilde{\epsilon}_-^2 - 2\tilde{\epsilon}_g^2\big)\ln\left(\frac{(\tilde{\epsilon}_c^2 - \tilde{\epsilon}_-^2)^{\frac{1}{2}} + (\tilde{\epsilon}_c^2 - \tilde{\epsilon}_+^2)^{\frac{1}{2}}}{(\tilde{\epsilon}_-^2 - \tilde{h}^2)^{\frac{1}{2}} + (\tilde{\epsilon}_+^2 - \tilde{h}^2)^{\frac{1}{2}}}\right)\\ &+ \big[(\tilde{\epsilon}_c^2 - \tilde{\epsilon}_-^2)(\tilde{\epsilon}_c^2 - \tilde{\epsilon}_+^2)\big]^{\frac{1}{2}} + (\tilde{\epsilon}_-^2 - \tilde{h}^2)^{\frac{1}{2}}(\tilde{\epsilon}_+^2 - \tilde{h}^2)^{\frac{1}{2}}\bigg\},\end{aligned} \tag{5.63}$$

where $\tilde{\epsilon}_g^2 \equiv \tilde{\epsilon}_+^2\,E\big((1 - \tilde{\epsilon}_-^2/\tilde{\epsilon}_+^2)^{\frac{1}{2}}\big)/K\big((1 - \tilde{\epsilon}_-^2/\tilde{\epsilon}_+^2)^{\frac{1}{2}}\big)$. Finally, integrating over $[\Delta_0(x)]^2$ we find

$$k_0\int_{-\pi/k_0}^{\pi/k_0} dx\,[\tilde{\Delta}_0(x)]^2 = \frac{8}{\pi}\,K(k_1)\,\big[K(k_1) - E(k_1)\big]\,. \tag{5.64}$$

Substituting Eqs. (5.62), (5.63), and (5.64) into Eq. (5.61) yields the energy density of a soliton train phase. The stationary states with a given soliton spacing ($k_0/k_{\rm F}$) are obtained by extremizing $\bar{\mathcal{E}}_{\rm ST}$ with respect to k_1, or equivalently, by solving Eq. (5.29) (see Fig. 5.6). For the C-FFLO phase with $\tilde{\epsilon}_- < |\tilde{h}| < \tilde{\epsilon}_+$, the expression for $\bar{\mathcal{E}}_{\rm ST}$ simplifies to

$$\bar{\mathcal{E}}_{\text{C-FFLO}} = \bar{\mathcal{E}}_0 - (k_0/\pi k_{\rm F})(|h|/\epsilon_{\rm F})\,, \tag{5.65}$$

where $\bar{\mathcal{E}}_0$ is independent of h [as is k_1, see Eq. (5.29)],

$$\bar{\mathcal{E}}_0 = \frac{2}{\pi}\frac{k_0^2}{k_{\rm F}^2}\Bigg\{\left(2\tilde{\epsilon}_g^2 - \tilde{\epsilon}_+^2 - \tilde{\epsilon}_-^2\right)\ln\left(\frac{(\tilde{\epsilon}_c^2-\tilde{\epsilon}_-^2)^{\frac{1}{2}} + (\tilde{\epsilon}_c^2-\tilde{\epsilon}_+^2)^{\frac{1}{2}}}{(\tilde{\epsilon}_+^2-\tilde{\epsilon}_-^2)^{\frac{1}{2}}}\right) - \left[(\tilde{\epsilon}_c^2-\tilde{\epsilon}_-^2)(\tilde{\epsilon}_c^2-\tilde{\epsilon}_+^2)\right]^{\frac{1}{2}} + \frac{2}{\pi}k_{\rm F}a_{\rm 1D}\,K(k_1)\left[K(k_1)-E(k_1)\right]\Bigg\}. \tag{5.66}$$

For a given value of $k_0/k_{\rm F}$, both the balanced soliton train ($n_s = 0$) and the C-FFLO phase ($n_s = 1$) represent local minima of $\bar{\mathcal{E}}_{\rm ST}(k_1)$, whereas the phase with $n_s > 1$ represents a maximum lying between the C-FFLO and the Normal phase minima, thus forming an analog of the unstable Sarma phase. The incommensurate FFLO phases with $0 < n_s < 1$ come in both varieties (maximum/minimum). By comparing the energies of these phases with the uniform states [Eqs. (5.55), (5.59), and (5.61)], we arrive at the phase diagram shown in Fig. 4 of the main article.

If $k_0/k_{\rm F}$ is allowed to vary, only the "BCS," Normal, and C-FFLO phases remain as local energy minima in the higher-dimensional space. A direct comparison of their energies reveal that the ground state changes from "BCS" for $|h| < (2/\pi)\Delta_{\rm BCS}$ to C-FFLO for $|h| > (2/\pi)\Delta_{\rm BCS}$ via a second-order phase transition [21, 25]. As $|h|$ is increased further, more nodes are introduced in the C-FFLO ground state to host the excess fermions. In an exact Bethe *Ansatz* calculation, the ground state eventually changes from FFLO to a fully polarized

state for $|h| \gtrsim \epsilon_{\rm F}$ [196]. However, in the Andreev approximation, which is valid for $|h| \ll \epsilon_{\rm F}$, a fully polarized state is never the ground state. It has an energy $\mathcal{E}_P = -\left[\Delta_{\rm BCS}\sinh(\pi k_{\rm F} a_{\rm 1D}/2) + |h|\right]^2/(2\pi k_{\rm F}) \geq \mathcal{E}_N$.

5.7.5 Integral equations for collective modes

Here we derive a pair of integral equations describing the collective modes of the order parameter in the Andreev approximation [Eqs. (5.4) and (5.5) in the main article] by linearizing the dynamics about the stationary solution.

We start from the time-dependent BdG equations (see Sec. 5.7.2)

$$i\partial_t \begin{pmatrix} U_j^{\pm}(x,t) \\ V_j^{\pm}(x,t) \end{pmatrix} = \begin{pmatrix} \mp i k_{\rm F}\partial_x + h & \Delta(x,t) \\ \Delta^*(x,t) & \pm i k_{\rm F}\partial_x + h \end{pmatrix} \begin{pmatrix} U_j^{\pm}(x,t) \\ V_j^{\pm}(x,t) \end{pmatrix}, \tag{5.67}$$

$$\text{with} \quad \Delta(x,t) = g_{\rm 1D} {\sum_{s=\pm,j}}' n_{\rm F}(\epsilon_j + h)\, U_j^s(x,t) V_j^{s*}(x,t)\,, \tag{5.68}$$

where the prime on the summation imposes the high-energy cutoff. We substitute $\Delta(x,t) = \Delta_0(x) + \delta\Delta(x,t)$ and $(U_j^{\pm}(x,t), V_j^{\pm}(x,t)) = (u_j^{\pm}(x) + \delta u_j^{\pm}(x,t), v_j^{\pm}(x) + \delta v_j^{\pm}(x,t))\, e^{-i(\epsilon_j + h)t}$ into Eqs. (5.67) and (5.68), and retain terms which are linear in the fluctuations, yielding

$$i\partial_t \begin{pmatrix} \delta u_j^{\pm}(x,t) \\ \delta v_j^{\pm}(x,t) \end{pmatrix} = \begin{pmatrix} \mp i k_{\rm F}\partial_x - \epsilon_j & \Delta_0(x) \\ \Delta_0(x) & \pm i k_{\rm F}\partial_x - \epsilon_j \end{pmatrix} \begin{pmatrix} \delta u_j^{\pm}(x,t) \\ \delta v_j^{\pm}(x,t) \end{pmatrix} + \begin{pmatrix} \delta\Delta(x,t)\, v_j^{\pm}(x) \\ \delta\Delta^*(x,t)\, u_j^{\pm}(x) \end{pmatrix}, \tag{5.69}$$

$$\text{and} \quad \delta\Delta(x,t) = g_{\rm 1D} {\sum_{s=\pm,j}}' n_{\rm F}(\epsilon_j + h) \left[u_j^s(x)\, \delta v_j^{s*}(x,t) + v_j^{s*}(x)\, \delta u_j^s(x,t)\right]. \tag{5.70}$$

Next we decouple the fluctuations into frequency components by writing $\delta\Delta(x,t) = e^{-\eta t}\left[\delta\Delta_+(x)\, e^{i\omega t} + \delta\Delta_-(x)\, e^{-i\omega t}\right]$, $\delta u_j^s(x,t) = e^{-\eta t}\left[\delta u_{j,+}^s(x)\, e^{i\omega t} +\right.$

$\delta u^s_{j,-}(x)\, e^{-i\omega t}\big]$, and $\delta v^s_j(x,t) = e^{-\eta t}\big[\delta v^s_{j,+}(x)\, e^{i\omega t} + \delta v^s_{j,-}(x)\, e^{-i\omega t}\big]$ where $\eta, \omega \in \mathbb{R}$. Using these expressions in Eqs. (5.69) and (5.70), we find

$$\begin{pmatrix} -isk_{\rm F}\partial_x - \epsilon_j \pm \omega + i\eta & \Delta_0(x) \\ \Delta_0(x) & isk_{\rm F}\partial_x - \epsilon_j \pm \omega + i\eta \end{pmatrix} \begin{pmatrix} \delta u^s_{j,\pm}(x) \\ \delta v^s_{j,\pm}(x) \end{pmatrix} + \begin{pmatrix} \delta\Delta_\pm(x)\, v^s_j(x) \\ \delta\Delta^*_\mp(x)\, u^s_j(x) \end{pmatrix} = 0\,, \tag{5.71}$$

$$\text{and} \quad \delta\Delta_\pm(x) = g_{\rm 1D} \sum_{s=\pm,j}{}' n_{\rm F}(\epsilon_j + h) \left(u^s_j(x)\, \delta v^{s*}_{j,\mp}(x) + v^{s*}_j(x)\, \delta u^s_{j,\pm}(x)\right). \tag{5.72}$$

We then use the completeness of the stationary wavefunctions to express $\delta u^s_{j,\pm}(x)$ and $\delta v^s_{j,\pm}(x)$ in terms of $\delta\Delta_\pm(x)$ from Eq. (5.71). Specifically, we write $(\delta u^s_{j,\pm}(x), \delta v^s_{j,\pm}(x)) = \sum_{j'} c^s_{jj',\pm}(u^s_{j'}(x), v^s_{j'}(x))$, and use Eq. (5.15) to obtain

$$\sum_{j'} c^s_{jj',\pm}(\epsilon_{j'} - \epsilon_j \pm \omega + i\eta) \begin{pmatrix} u^s_{j'}(x) \\ v^s_{j'}(x) \end{pmatrix} + \begin{pmatrix} \delta\Delta_\pm(x)\, v^s_j(x) \\ \delta\Delta^*_\mp(x)\, u^s_j(x) \end{pmatrix} = 0\,, \tag{5.73}$$

$$\text{or} \quad c^s_{jj',\pm} = \frac{1}{\epsilon_j - \epsilon_{j'} \mp \omega - i\eta} \int dx \left(v^s_j(x)\, u^{s*}_{j'}(x)\, \delta\Delta_\pm(x) + u^s_j(x)\, v^{s*}_{j'}(x)\, \delta\Delta^*_\mp(x)\right), \tag{5.74}$$

for $s = \pm$. We have taken the inner product with $(u^{s*}_{j'}(x) \;\; v^{s*}_{j'}(x))$ from the left on Eq. (5.73), and used the orthonormality of the stationary wavefunctions to arrive at Eq. (5.74). Substituting the expression for $c^s_{jj',\pm}$ into the self-consistency condition in Eq. (5.72) yields a pair of coupled homogeneous integral equations for $\delta\Delta_\pm(x)$,

$$\delta\Delta_\pm(x) = g_{\rm 1D} \sum_{s=\pm} \sum_j{}' \sum_{j'} n_{\rm F}(\epsilon_j + h) \left(u^s_j\, v^{s*}_{j'}\, c^{s*}_{jj',\mp} + v^{s*}_j\, u^s_{j'}\, c^s_{jj',\pm}\right) \tag{5.75}$$

$$= \int dx' \left[g_{\rm 1D} \sum_{s=\pm,j}{}' \sum_{j'} n_{\rm F}(\epsilon_j + h) \left(\frac{u^s_j\, v^{s*}_{j'}\, u'^{s*}_j\, v'^s_{j'}}{\epsilon_j - \epsilon_{j'} \pm \omega + i\eta} + \frac{v^{s*}_j\, u^s_{j'}\, v'^s_j\, u'^{s*}_{j'}}{\epsilon_j - \epsilon_{j'} \mp \omega - i\eta}\right)\right] \delta\Delta_\pm(x')$$

$$+ \int dx' \left[g_{\rm 1D} \sum_{s=\pm,j}{}' \sum_{j'} n_{\rm F}(\epsilon_j + h) \left(\frac{u^s_j\, v^{s*}_{j'}\, v'^{s*}_j\, u'^s_{j'}}{\epsilon_j - \epsilon_{j'} \pm \omega + i\eta} + \frac{v^{s*}_j\, u^s_{j'}\, u'^s_j\, v'^{s*}_{j'}}{\epsilon_j - \epsilon_{j'} \mp \omega - i\eta}\right)\right] \delta\Delta^*_\mp(x')\,, \tag{5.76}$$

with the notation $(u, v) \equiv (u(x), v(x))$ and $(u', v') \equiv (u(x'), v(x'))$. Next we use two symmetries of the stationary wavefunctions: (i) if $(u_j^s(x) \quad v_j^s(x))^T$ is an eigenstate with energy ϵ_j, then $(v_j^{s*}(x) \quad u_j^{s*}(x))^T$ is also an eigenstate with energy ϵ_j, and (ii) $(u_j^-(x), v_j^-(x)) = (u_j^+(x), v_j^+(x))^*$ (see Sec. 5.7.2). These two symmetries let us write Eq. (5.76) as

$$\delta\Delta_+(x) = \int dx' \big[\mathcal{M}_1(x, x'; \Omega)\, \delta\Delta_+(x') + \mathcal{M}_2(x, x'; \Omega)\, \delta\Delta_-^*(x')\big]\,, \tag{5.77}$$

$$\text{and} \quad \delta\Delta_-^*(x) = \int dx' \big[\mathcal{M}_2(x, x'; \Omega)\, \delta\Delta_+(x') + \mathcal{M}_1(x, x'; \Omega)\, \delta\Delta_-^*(x')\big]\,, \tag{5.78}$$

where $\Omega \equiv \omega + i\eta$, and

$$\mathcal{M}_1(x, x'; \Omega) = g_{1\mathrm{D}} {\sum_j}' \sum_{j'} n_{\mathrm{F}}(\epsilon_j + h)\, \frac{2(\epsilon_j - \epsilon_{j'})}{(\epsilon_j - \epsilon_{j'})^2 - \Omega^2} \left(u_j^* v_{j'} u_j' v_{j'}'^* + v_j^* u_{j'} v_j' u_{j'}'^*\right), \tag{5.79}$$

$$\mathcal{M}_2(x, x'; \Omega) = g_{1\mathrm{D}} {\sum_j}' \sum_{j'} n_{\mathrm{F}}(\epsilon_j + h)\, \frac{2(\epsilon_j - \epsilon_{j'})}{(\epsilon_j - \epsilon_{j'})^2 - \Omega^2} \left(u_j^* v_{j'} v_j' u_{j'}'^* + v_j^* u_{j'} u_j' v_{j'}'^*\right). \tag{5.80}$$

Here all the wavefunctions refer to the right-moving branch. We can express Eqs. (5.77) and (5.78) in a simpler form by defining $\delta_{p,a}(x) \equiv \delta\Delta_+(x) \mp \delta\Delta_-^*(x)$. Note that the fluctuation of the order parameter is given by

$$\delta\Delta(x, t) = e^{-\eta t}\big[\delta\Delta_+(x)\, e^{i\omega t} + \delta\Delta_-(x)\, e^{-i\omega t}\big] = \mathrm{Re}\big(\delta_a(x) e^{i\Omega t}\big) + i\,\mathrm{Im}\big(\delta_p(x) e^{i\Omega t}\big)\,. \tag{5.81}$$

Since $\Delta_0(x)$ is real, $\delta_p(x)$ and $\delta_a(x)$ describe the phase- and amplitude-fluctuations of the order parameter, respectively. From Eqs. (5.77) and (5.78) we see that the phase and amplitude fluctuations decouple, with

$$\delta_{p,a}(x) = -g_{1\mathrm{D}} \int dx' \mathcal{M}^{\pm}(x, x'; \Omega)\, \delta_{p,a}(x')\,, \quad \text{where} \quad \mathcal{M}^{\pm} \equiv -g_{1\mathrm{D}}^{-1}(\mathcal{M}_1 \mp \mathcal{M}_2)\,. \tag{5.82}$$

Using Eqs. (5.79) and (5.80) we find

$$\begin{aligned}\mathcal{M}^{\pm}(x,x';\Omega) &= -{\sum_{j}}'\sum_{j'} n_{\mathrm{F}}(\epsilon_j+h)\frac{2\left(\epsilon_j-\epsilon_{j'}\right)}{(\epsilon_j-\epsilon_{j'})^2-\Omega^2}\left(u_j^*v_{j'}\mp v_j^*u_{j'}\right)\left(u_j'v_{j'}'^*\mp v_j'u_{j'}'^*\right),\\ &= {\sum_{j}}'\sum_{j'} n_{\mathrm{F}}(h-\epsilon_j)\frac{2\left(\epsilon_j+\epsilon_{j'}\right)}{(\epsilon_j+\epsilon_{j'})^2-\Omega^2}\left(u_j^*u_{j'}\pm v_j^*v_{j'}\right)\left(u_j'u_{j'}'^*\pm v_j'v_{j'}'^*\right).\end{aligned} \tag{5.83}$$

In Eq. (5.83) we have used the symmetry that for any eigenstate $(u_j(x)\ \ v_j(x))^T$ with energy ϵ_j, there is a corresponding eigenstate $(-v_j(x)\ \ u_j(x))^T$ with energy $-\epsilon_j$ (see Sec. 5.7.2). At zero temperature, $n_{\mathrm{F}}(h-\epsilon_j)=\Theta(\epsilon_j-h)$. Then Eq. (5.83) reduces to

$$\mathcal{M}^{\pm}(x,x';\Omega) = {\sum_{j}}'\sum_{j'}\frac{2\left(\epsilon_j+\epsilon_{j'}\right)}{(\epsilon_j+\epsilon_{j'})^2-\Omega^2}\left(u_j^*u_{j'}\pm v_j^*v_{j'}\right)\left(u_j'u_{j'}'^*\pm v_j'v_{j'}'^*\right), \tag{5.84}$$

where the prime on the j-summation now stands for the condition $h\le\epsilon_j<\epsilon_c$, ϵ_c being the high-energy cutoff. Eqs. (5.82) and (5.84) describe the collective modes of the order parameter about any stationary solution in the Andreev approximation. In particular, they apply to both a soliton train state and a uniform state.

5.7.6 Goldstone and "Higgs" modes

A soliton train spontaneously breaks both gauge- and translational-symmetries. Therefore, it has two gapless Goldstone modes: a phase mode described by $\delta_p(x)\propto\Delta_0(x)$ and an amplitude mode described by $\delta_a(x)\propto\Delta_0'(x)$ at zero energy. On the other hand, a uniform state breaks only gauge symmetry, and has only one Goldstone mode described by $\delta_p(x)\propto 1$ at zero energy. Below we show that more generally, $\delta_p(x)\propto\Delta_0(x)\,e^{iqx}$ is a collective mode with dis-

persion $\omega(q) = k_{\rm F} q$, describing Anderson-Bogoliubov phonons traveling at the Fermi velocity.

We let R represent the right-hand side of Eq. (5.82). For $\delta_p(x) = \Delta_0(x)\, e^{iqx}$ and $\Omega = k_{\rm F} q$, with Eq. (5.83),

$$R = -g_{\rm 1D} {\sum_{j}}' \sum_{j'} \left(u_j^* u_{j'} + v_j^* v_{j'}\right) \frac{2\, n_{\rm F}(h-\epsilon_j)\,(\epsilon_j + \epsilon_{j'})}{(\epsilon_j + \epsilon_{j'})^2 - (k_{\rm F} q)^2} \int dx' \left(u_j' u_{j'}'^* + v_j' v_{j'}'^*\right) \Delta_0(x') e^{iqx'}. \tag{5.85}$$

However, using the BdG equations [Eq. (5.17)] we can write

$$\begin{aligned}
&\int dx' \left(u_j' u_{j'}'^* + v_j' v_{j'}'^*\right) \Delta_0(x')\, e^{iqx'} \\
&= \int dx' u_{j'}'^* \left(\epsilon_j v_j' - i k_{\rm F} \partial_{x'} v_j'\right) e^{iqx'} + v_j' \left(\epsilon_{j'} u_{j'}'^* - i k_{\rm F} \partial_{x'} u_{j'}'^*\right) e^{iqx'} \\
&= (\epsilon_j + \epsilon_{j'} - k_{\rm F} q) \int dx' u_{j'}'^* v_j'\, e^{iqx'} - i k_{\rm F} \int dx' \partial_{x'} \left(u_{j'}'^* v_j'\, e^{iqx'}\right) \\
&= (\epsilon_j + \epsilon_{j'} - k_{\rm F} q) \int dx' u_{j'}'^* v_j'\, e^{iqx'},
\end{aligned} \tag{5.86}$$

where we have used periodic boundary conditions. Similarly, we find

$$\int dx' \left(u_j' u_{j'}'^* + v_j' v_{j'}'^*\right) \Delta_0(x')\, e^{iqx'} = (\epsilon_j + \epsilon_{j'} + k_{\rm F} q) \int dx' v_{j'}'^* u_j'\, e^{iqx'}. \tag{5.87}$$

Using Eqs. (5.86) and (5.87) in Eq. (5.85), we get

$$R = -g_{\rm 1D} {\sum_{j}}' n_{\rm F}(h-\epsilon_j) \sum\nolimits_{j'} \int dx' \left(u_j^* u_{j'} + v_j^* v_{j'}\right) \left(u_{j'}'^* v_j' + v_{j'}'^* u_j'\right) e^{iqx'}. \tag{5.88}$$

Next we substitute the completeness relations $\sum_{j'} u_{j'} u_{j'}'^* = v_{j'} v_{j'}'^* = \delta(x - x')$ and $\sum_{j'} u_{j'} v_{j'}'^* = 0$ in Eq. (5.88), and use the self-consistency of the stationary solution [Eq. (5.17)] to obtain

$$R = -g_{\rm 1D} {\sum_{j}}' n_{\rm F}(h-\epsilon_j) \left(u_j^* v_j + v_j^* u_j\right) e^{iqx} = \Delta_0(x)\, e^{iqx}. \tag{5.89}$$

This result shows that the proposed collective mode indeed satisfies the integral equation [Eq. (5.82)]. Note that in applying completeness, we use the fact that

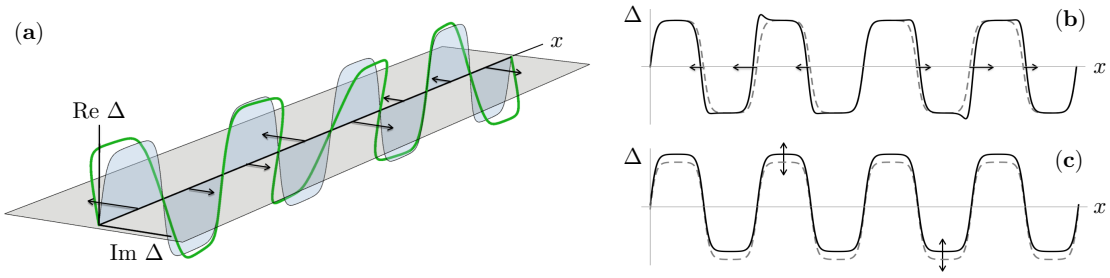

Figure 5.7: Goldstone and "Higgs" modes of a fermionic soliton train with sharpness parameter $k_1 = 0.999$: (a) Goldstone phase mode with wave-vector $q = k_0/4$, (b) Goldstone amplitude mode with $q = k_0/4$, (c) "Higgs" mode with $q = k_0$.

the sum over j' in Eq. (5.88) is unrestricted, i.e., it includes states beyond the high-energy cutoff. This is important for obtaining the correct Goldstone modes.

Similarly, we can show that $\delta_a(x) \propto \Delta_0'(x)$ represents a zero-energy collective mode for any non-uniform state. More generally, we find from numerics on the soliton train and the uniform state that $\delta_a(x) \propto u_{q/2}(x)v_{q/2}(x)$ describes a collective mode with dispersion $\omega(q) = 2\epsilon(q/2)$, where $\epsilon(k)$ denotes the single-particle spectrum. For the uniform state, this mode describes sinusoidal oscillations of the order-parameter amplitude, also known as the Higgs mode. From Eq. (5.43) we see that the "Higgs" mode has dispersion $\omega(q) = 2\sqrt{(k_{\mathrm{F}}q/2)^2 + \Delta_{\mathrm{BCS}}^2}$. For the soliton train, the mode has two branches: a gapless branch with $q < k_0$, and a gapped branch with $q > k_0$. The gapless branch represents a Goldstone amplitude mode, approaching $\delta_a(x) \propto \Delta_0'(x)$ as $q \to 0$, whereas the gapped branch represents the remnant of the "Higgs" mode. The dispersion can be found using the single-particle spectrum given in Eq. (5.18). In particular, the dispersion is linear as $q \to 0$, with a group velocity $d\omega/dq = k_{\mathrm{F}}(\epsilon_+\epsilon_-/\epsilon_g^2)$, where $\epsilon_\pm$ and ϵ_g are defined in Sec. 5.7.2. Figure 5.7 shows the fluctuations described by the Goldstone and "Higgs" modes of a soliton train.

5.7.7 Matrix equations for collective mode spectrum

Here we derive matrix equations describing the collective modes of a soliton train at zero temperature. We utilize features of the stationary solution outlined in Sec. 5.7.2 to find simplified expressions suited for numerics.

The collective modes have a Brillouin zone structure as $\Delta_0(x)$ is periodic. Further, the Brillouin zone has size $2k_0$ because of the additional symmetry $\Delta_0(x + \pi/k_0) = -\Delta_0(x)$ [141]. Thus we can write $\delta_{p,a}(x) = e^{iqx}\sum_n C_n^{\pm} e^{ink_0x}$, where n varies over odd integers, and $-k_0 \le q \le k_0$. Substituting this Fourier expansion into Eq. (5.82), we get

$$C_n^{\pm} = -g_{1D}\sum\nolimits_m M_{nm}^{\pm}(q,\Omega)\, C_m^{\pm}, \tag{5.90}$$

$$\text{where} \quad M_{nm}^{\pm}(q,\Omega) \equiv \frac{k_0}{2\pi}\int_{-\pi/k_0}^{\pi/k_0} dx \int dx' e^{-i(q+nk_0)x} e^{i(q+mk_0)x'} \mathcal{M}^{\pm}(x,x';\Omega)\,. \tag{5.91}$$

The collective modes represent non-trivial solutions to Eq. (5.90). Therefore the task is to compute the matrices $M_{nm}^{\pm}(q,\Omega)$. Using the zero-temperature expression for $\mathcal{M}^{\pm}(x,x';\Omega)$ [Eq. (5.84)] in Eq. (5.91), we find

$$M_{nm}^{\pm}(q,\Omega) = \frac{k_0}{\pi}\sum\nolimits_j{}' \sum\nolimits_{j'} \frac{\epsilon_j + \epsilon_{j'}}{(\epsilon_j+\epsilon_{j'})^2 - \Omega^2} \int_{-\pi/k_0}^{\pi/k_0} dx\, e^{-i(q+nk_0)x}\left(u_{j'}u_j^* \pm v_{j'}v_j^*\right) \times \int dx' e^{i(q+mk_0)x'}\left(u_{j'}'^* u_j' \pm v_{j'}'^* v_j'\right) \tag{5.92}$$

$$= \frac{k_0}{\pi}\sum\nolimits_k{}' \sum\nolimits_{k'} \left[\frac{\epsilon_k+\epsilon_{k'}}{(\epsilon_k+\epsilon_{k'})^2-\Omega^2} I_{kk'}^{(1)} + \frac{\epsilon_k-\epsilon_{k'}}{(\epsilon_k-\epsilon_{k'})^2-\Omega^2} I_{kk'}^{(2)}\right], \tag{5.93}$$

where

$$I_{kk'}^{(1)} \equiv \int_{-\pi/k_0}^{\pi/k_0} dx\, e^{-i(q+nk_0)x}\left(u_{k'}u_k^* \pm v_{k'}v_k^*\right)\int dx' e^{i(q+mk_0)x'}\left(u_{k'}'^* u_k' \pm v_{k'}'^* v_k'\right), \tag{5.94}$$

$$I_{kk'}^{(2)} \equiv \int_{-\pi/k_0}^{\pi/k_0} dx\, e^{-i(q+nk_0)x}\left(u_{k'}v_k^* \mp v_{k'}u_k^*\right)\int dx' e^{i(q+mk_0)x'}\left(u_{k'}'^* v_k' \mp v_{k'}'^* u_k'\right). \tag{5.95}$$

Here we have relabeled the sums over j and j' in terms of quasimomenta k and k' with $\epsilon_k, \epsilon_{k'} \ge 0$, and used the symmetry that a negative energy state with

quasimomentum k has energy $-\epsilon_k$ and wavefunction $(-\,v_k(x) \quad u_k(x))^T$. As before, the prime on the k sum in Eq. (5.93) stands for $h \le \epsilon_k < \epsilon_c$, and we consider $h \ge 0$ without loss of generality. Next we use the symmetry $\epsilon_{-k} = \epsilon_k$ and $(u_{-k}(x), v_{-k}(x)) = (v_k^*(x), u_k^*(x))\ \forall k$ in Eqs. (5.93) and (5.95) to obtain

$$M^{\pm}_{nm}(q,\Omega) = \frac{k_0}{\pi} \sum\nolimits_k{}' \sum\nolimits_{k'} \left[\frac{\epsilon_k + \epsilon_{k'}}{(\epsilon_k + \epsilon_{k'})^2 - \Omega^2}\, I^{(1)}_{kk'} + \frac{\epsilon_k - \epsilon_{k'}}{(\epsilon_k - \epsilon_{k'})^2 - \Omega^2}\, I^{(2)}_{k'k} \right]. \quad (5.96)$$

Combining Eqs. (5.93) and (5.96), we can write

$$M^{\pm}_{nm}(q,\Omega) = \frac{k_0}{\pi} \sum\nolimits^{①}_{k,k'} \frac{\epsilon_k + \epsilon_{k'}}{(\epsilon_k + \epsilon_{k'})^2 - \Omega^2}\, I^{(1)}_{kk'} + \frac{k_0}{\pi} \sum\nolimits^{②}_{k,k'} \frac{\epsilon_k - \epsilon_{k'}}{(\epsilon_k - \epsilon_{k'})^2 - \Omega^2}\, I^{(2)}_{kk'}, \quad (5.97)$$

where ① stands for the condition $\epsilon_k \in [h, \epsilon_c)$, and ② stands for the condition $\epsilon_k \in [h, \epsilon_c) \wedge \epsilon_{k'} \notin [h, \epsilon_c)$.

Next we note from Eqs. (5.94) and (5.95) that both $I^{(1)}_{kk'}$ and $I^{(2)}_{kk'}$ vanish unless $k' = k + q + rk_0$ where r is an integer, in which case $I^{(1)}_{kk'} = (2\pi/k_0 L)\left(\xi^{k',k}_{\pm,n}\right)^* \xi^{k',k}_{\pm,m}$, and $I^{(2)}_{kk'} = (2\pi/k_0 L)\left(\chi^{k',k}_{\pm,n}\right)^* \chi^{k',k}_{\pm,m}$, where

$$\xi^{k_1,k_2}_{\pm,m} \equiv \frac{k_0 L}{2\pi} \int_{-\pi/k_0}^{\pi/k_0} dx\, e^{i(q+mk_0)x} \left(u^*_{k_1}(x) u_{k_2}(x) \pm v^*_{k_1}(x) v_{k_2}(x) \right), \quad (5.98)$$

$$\text{and} \quad \chi^{k_1,k_2}_{\pm,m} \equiv \frac{k_0 L}{2\pi} \int_{-\pi/k_0}^{\pi/k_0} dx\, e^{i(q+mk_0)x} \left(u^*_{k_1}(x) v_{k_2}(x) \mp v^*_{k_1}(x) u_{k_2}(x) \right). \quad (5.99)$$

Using this result in Eq. (5.97), we obtain

$$M^{\pm}_{nm}(q,\Omega) = \frac{2}{L} \Bigg[\sum\nolimits^{①}_{r,k} \frac{\epsilon_{k+q+rk_0} + \epsilon_k}{(\epsilon_{k+q+rk_0} + \epsilon_k)^2 - \Omega^2} \left(\xi^{k+q+rk_0,k}_{\pm,n}\right)^* \xi^{k+q+rk_0,k}_{\pm,m} - \sum\nolimits^{②}_{r,k} \frac{\epsilon_{k+q+rk_0} - \epsilon_k}{(\epsilon_{k+q+rk_0} - \epsilon_k)^2 - \Omega^2} \left(\chi^{k+q+rk_0,k}_{\pm,n}\right)^* \chi^{k+q+rk_0,k}_{\pm,m} \Bigg], \quad (5.100)$$

where r varies over integers, ① stands for $\epsilon_k \in [h, \epsilon_c)$ as before, and now ②

stands for $\epsilon_k \in [h, \epsilon_c) \wedge \epsilon_{k+q+rk_0} \notin [h, \epsilon_c)$. Taking the limit $L \to \infty$, we find

$$-g_{1\mathrm{D}} M^{\pm}_{nm}(q,\Omega) = \frac{1}{\pi k_{\mathrm{F}} a_{1\mathrm{D}}} \sum_r \Bigg[\int_{①} d\tilde{k} \frac{\tilde{\epsilon}_{\tilde{k}+\tilde{q}+r} + \tilde{\epsilon}_{\tilde{k}}}{(\tilde{\epsilon}_{\tilde{k}+\tilde{q}+r} + \tilde{\epsilon}_{\tilde{k}})^2 - \tilde{\Omega}^2} \left(\xi^{\tilde{k}+\tilde{q}+r,\tilde{k}}_{\pm,n}\right)^* \xi^{\tilde{k}+\tilde{q}+r,\tilde{k}}_{\pm,m} - \int_{②} d\tilde{k} \frac{\tilde{\epsilon}_{\tilde{k}+\tilde{q}+r} - \tilde{\epsilon}_{\tilde{k}}}{(\tilde{\epsilon}_{\tilde{k}+\tilde{q}+r} - \tilde{\epsilon}_{\tilde{k}})^2 - \tilde{\Omega}^2} \left(\chi^{\tilde{k}+\tilde{q}+r,\tilde{k}}_{\pm,n}\right)^* \chi^{\tilde{k}+\tilde{q}+r,\tilde{k}}_{\pm,m} \Bigg]. \tag{5.101}$$

Here we have expressed the integrals in rescaled coordinates (see Sec. 5.7.2) and used the relation $g_{1\mathrm{D}} = -2/a_{1\mathrm{D}}$ [166, 167].

Fortunately, the $\xi^*\xi$ and $\chi^*\chi$ terms in Eq. (5.101) can be computed in closed form for the stationary wavefunctions in Eqs. (5.21) and (5.23). First we note that $u_k(x)$ has only even Fourier components if k is positive and only odd Fourier components if k is negative. For $v_k(x)$, its the other way around. Therefore, Eq. (5.98) implies that $\xi^{k+q+rk_0,k}_{\pm,m}$ will be non-zero only if k and $k+q+rk_0$ have the same sign when r and m have the same parity, and opposite sign when r and m have opposite parity. For $\chi^{k+q+rk_0,k}_{\pm,m}$, the conditions are reversed. A corollary of this result is that $M^{\pm}_{nm} = 0$ unless n and m have the same parity, which validates our premise of choosing both n and m to be odd. When the terms in Eq. (5.101) are non-zero, their computation involves evaluating the sums

$$S_{\pm}(\alpha; z_1, z_2) \equiv \sum_{n \text{ even}} \frac{1}{\sinh(n\alpha + z_1)\sinh(n\alpha + z_2)} \pm \sum_{n \text{ odd}} \frac{1}{\sinh(n\alpha + z_1)\sinh(n\alpha + z_2)}, \tag{5.102}$$

where $\alpha \in \mathbb{R}$ and $z_1, z_2 \in \mathbb{C}$. These sums can be calculated in terms of the q-digamma function $\psi_q(z)$ as [197]

$$S_+(\alpha; z_1, z_2) = \frac{4(z_2 - z_1) + \psi_{e^{2\alpha}}(\frac{z_1}{\alpha}) - \psi_{e^{2\alpha}}(\frac{z_2}{\alpha}) + \psi_{e^{2\alpha}}(1 - \frac{z_2}{\alpha}) - \psi_{e^{2\alpha}}(1 - \frac{z_1}{\alpha})}{\alpha \sinh(z_1 - z_2)}, \tag{5.103}$$

$$S_-(\alpha; z_1, z_2) = 2S_+(2\alpha; z_1, z_2) - S_+(\alpha; z_1, z_2), \tag{5.104}$$

with the understanding that for $z_1 = z_2$ one has to take the limit $z_1 \to z_2$ in Eq. (5.103). When the $\xi^*\xi$ and $\chi^*\chi$ terms in Eq. (5.101) are non-zero, they are both real and given by the expression

$$\frac{S_\pm\left(\alpha;\,(m-r)\alpha+\frac{1}{2}a_{\bar{k}}+\phi_{\bar{k}},\,\frac{1}{2}a_{\tilde{k}}+\phi_{\tilde{k}}\right)\,S_\pm\left(\alpha;\,(n-r)\alpha+\frac{1}{2}a_{\bar{k}}+\phi_{\bar{k}},\,\frac{1}{2}a_{\tilde{k}}+\phi_{\tilde{k}}\right)}{16\left(\tilde{\epsilon}_g^2-\tilde{\epsilon}_{\tilde{k}}^2\right)\left(\tilde{\epsilon}_g^2-\tilde{\epsilon}_{\tilde{k}}^2\right)}, \tag{5.105}$$

where $\bar{k} = \tilde{k}+\tilde{q}+r$, $\phi_{\tilde{k}} = (i\pi/2)\,\Theta(1/2-|\tilde{k}|)$, and $\tilde{\epsilon}_g$, $\tilde{\epsilon}_{\tilde{k}}$, $a_{\tilde{k}}$ are given in Eqs. (5.20), (5.22) and (5.25). From Eqs. (5.101) and (5.105) we see that $M^\pm_{nm} = M^\pm_{mn}$, and $M^\pm(q,\Omega^*) = [M^\pm(q,\Omega)]^*$. For computation purposes, it is most convenient to convert the integrals in Eq. (5.101) into integrals over the spectral parameter $a_{\tilde{k}}$, using the relation $d\tilde{k} = \left(\tilde{\epsilon}_g^2-\tilde{\epsilon}_{\tilde{k}}^2\right)da_{\tilde{k}}$.

The expression in Eq. (5.105) can be further simplified using properties of the q-digamma function, so that the complexity of computing the matrix grows as $O(n_{\text{max}})$, where n, m take on values from $-n_{\text{max}}$ to n_{max} in steps of 2. To speed up computation, we also truncate the infinite sums over r in Eq. (5.101) to finite sums from $-r_{\text{max}}$ to r_{max}. We find that the sums converge rapidly for $r_{\text{max}} \gtrsim n_{\text{max}}$. To evaluate $M^\pm(q,\Omega)$ for real Ω, we include a small imaginary part to avoid branch cut singularities arising from the particle-hole continua.

5.7.8 Relation between collective modes and pair susceptibility

Here we find a simple relation between the matrix derived in Sec. 5.7.7 and the pairing susceptibility. To calculate the susceptibility, we find the linear response to a small external pairing field, $\delta\hat{H} = \int dx\, f(x,t)\hat{\Psi}^\dagger_\uparrow(x,t)\hat{\Psi}^\dagger_\downarrow(x,t)$ + H.c. In the time-dependent BdG dynamics (see Sec. 5.7.5), this pairing field changes $\Delta(x,t)$ to $\Delta(x,t)+f(x,t)$ in Eq. (5.67) and $\delta\Delta(x,t)$ to $\delta\Delta(x,t)+f(x,t)$ in Eq. (5.69). We

assume the drive to be at frequency $\omega \in \mathbb{R}$, i.e.,

$$f(x,t) = f_+(x)\, e^{i\omega t} + f_-(x)\, e^{-i\omega t} \equiv \mathrm{Re}(f_a(x)\, e^{i\omega t}) + i\, \mathrm{Im}(f_p(x)\, e^{i\omega t})\,. \tag{5.106}$$

In steady-state the order-parameter fluctuations oscillate at the same frequency ω. Hence we set $\eta = 0$ or $\Omega = \omega$ in the remaining steps in Sec. 5.7.5. The inclusion of the driving terms changes $\delta\Delta_\pm(x)$ to $\delta\Delta_\pm(x) + f_\pm(x)$ in Eqs. (5.71), (5.73), and (5.74), and $\delta\Delta_\pm(x')$ to $\delta\Delta_\pm(x') + f_\pm(x')$ in the right-hand sides of Eqs. (5.76), (5.77), and (5.78). The phase and amplitude modes still decouple. However, they are now governed by an inhomogeneous integral equation,

$$\delta_{p,a}(x) = -g_{1\mathrm{D}} \int dx' \mathcal{M}^\pm(x,x';\omega) \left[\delta_{p,a}(x') + f_{p,a}(x')\right]. \tag{5.107}$$

Expanding $\delta_{p,a}(x)$ and $f_{p,a}(x)$ into Fourier components as $\delta_{p,a}(x) = e^{iqx} \sum_n C_n^\pm e^{ink_0 x}$ and $f_{p,a}(x) = e^{iqx} \sum_n F_n^\pm e^{ink_0 x}$, and substituting into Eq. (5.107) yield

$$C_n^\pm = -g_{1\mathrm{D}} \sum\nolimits_m M_{nm}^\pm(q,\omega) \left(C_m^\pm + F_m^\pm\right), \tag{5.108}$$

where the matrices $M^\pm(q,\omega)$ were studied in detail in Sec. 5.7.7. From Eq. (5.108) we can write $C_n^\pm = \sum_m X_{nm}^\pm(q,\omega)\, C_m^\pm$, where $X^\pm(q,\omega)$ represent the susceptibility matrices, given by

$$X^\pm(q,\omega) = -g_{1\mathrm{D}} \left(I + g_{1\mathrm{D}} M^\pm(q,\omega)\right)^{-1} M^\pm(q,\omega)\,. \tag{5.109}$$

We define scalar susceptibilities $\chi^\pm(q,\omega) \equiv \mathrm{Tr}\, X^\pm(q,\omega)$. In terms of the eigenvalues $\lambda_j^\pm$ of the matrices $-g_{1\mathrm{D}} M^\pm(q,\omega)$, we can write $\chi^\pm = \sum_j \lambda_j^\pm/(1-\lambda_j^\pm)$. From Eq. (5.90) we see that the collective modes with real Ω represent zeros of the eigenvalues of $I + g_{1\mathrm{D}} M^\pm(q,\omega)$. Thus they show up as isolated poles of $\chi^\pm(q,\omega)$. The branch cuts of $M^\pm(q,\omega)$, which originate from particle-hole excitations, show up as broad diffuse spectra in $\mathrm{Im}\,\chi^\pm(q,\omega)$.

An alternative derivation involves writing the susceptibility as

$$\begin{aligned}\mathcal{X} &= \begin{pmatrix} \frac{\delta\Delta(x,t)}{\delta f(x',t')} & \frac{\delta\Delta(x,t)}{\delta f^*(x',t')} \\ \frac{\delta\Delta^*(x,t)}{\delta f(x',t')} & \frac{\delta\Delta^*(x,t)}{\delta f^*(x',t')} \end{pmatrix} \\ &= -g_{1\mathrm{D}} \begin{pmatrix} \frac{\delta\langle\hat{\Psi}_\downarrow(x,t)\hat{\Psi}_\uparrow(x,t)\rangle}{\delta f(x',t')} & \frac{\delta\langle\hat{\Psi}_\downarrow(x,t)\hat{\Psi}_\uparrow(x,t)\rangle}{\delta f^*(x',t')} \\ \frac{\delta\langle\hat{\Psi}^\dagger_\uparrow(x,t)\hat{\Psi}^\dagger_\downarrow(x,t)\rangle}{\delta f(x',t')} & \frac{\delta\langle\hat{\Psi}^\dagger_\uparrow(x,t)\hat{\Psi}^\dagger_\downarrow(x,t)\rangle}{\delta f^*(x',t')} \end{pmatrix}_0 \\ &\quad - g_{1\mathrm{D}} \int dx''dt'' \begin{pmatrix} \frac{\delta\langle\hat{\Psi}_\downarrow(x,t)\hat{\Psi}_\uparrow(x,t)\rangle}{\delta\Delta(x'',t'')} & \frac{\delta\langle\hat{\Psi}_\downarrow(x,t)\hat{\Psi}_\uparrow(x,t)\rangle}{\delta\Delta^*(x'',t'')} \\ \frac{\delta\langle\hat{\Psi}^\dagger_\uparrow(x,t)\hat{\Psi}^\dagger_\downarrow(x,t)\rangle}{\delta\Delta(x'',t'')} & \frac{\delta\langle\hat{\Psi}^\dagger_\uparrow(x,t)\hat{\Psi}^\dagger_\downarrow(x,t)\rangle}{\delta\Delta^*(x'',t'')} \end{pmatrix} \begin{pmatrix} \frac{\delta\Delta(x'',t'')}{\delta f(x',t')} & \frac{\delta\Delta(x'',t'')}{\delta f^*(x',t')} \\ \frac{\delta\Delta^*(x'',t'')}{\delta f(x',t')} & \frac{\delta\Delta^*(x'',t'')}{\delta f^*(x',t')} \end{pmatrix}, \end{aligned} \tag{5.110}$$

where the first term on the right is the response neglecting self-consistency and the second term gives the correction from self-consistency. We define

$$\mathcal{M} \equiv \begin{pmatrix} \frac{\delta\langle\hat{\Psi}_\downarrow(x,t)\hat{\Psi}_\uparrow(x,t)\rangle}{\delta f(x',t')} & \frac{\delta\langle\hat{\Psi}_\downarrow(x,t)\hat{\Psi}_\uparrow(x,t)\rangle}{\delta f^*(x',t')} \\ \frac{\delta\langle\hat{\Psi}^\dagger_\uparrow(x,t)\hat{\Psi}^\dagger_\downarrow(x,t)\rangle}{\delta f(x',t')} & \frac{\delta\langle\hat{\Psi}^\dagger_\uparrow(x,t)\hat{\Psi}^\dagger_\downarrow(x,t)\rangle}{\delta f^*(x',t')} \end{pmatrix}_0 = \begin{pmatrix} \frac{\delta\langle\hat{\Psi}_\downarrow(x,t)\hat{\Psi}_\uparrow(x,t)\rangle}{\delta\Delta(x',t')} & \frac{\delta\langle\hat{\Psi}_\downarrow(x,t)\hat{\Psi}_\uparrow(x,t)\rangle}{\delta\Delta^*(x',t')} \\ \frac{\delta\langle\hat{\Psi}^\dagger_\uparrow(x,t)\hat{\Psi}^\dagger_\downarrow(x,t)\rangle}{\delta\Delta(x',t')} & \frac{\delta\langle\hat{\Psi}^\dagger_\uparrow(x,t)\hat{\Psi}^\dagger_\downarrow(x,t)\rangle}{\delta\Delta^*(x',t')} \end{pmatrix}. \tag{5.111}$$

In the Fourier domain Eq. (5.110) has the same form as Eq. (5.109). A straightforward application of linear response theory [198] confirms that in the Andreev approximation, Eq. (5.111) reduces to $\mathcal{M} = \begin{pmatrix} \mathcal{M}_1 & \mathcal{M}_2 \\ \mathcal{M}_2 & \mathcal{M}_1 \end{pmatrix}$, where $\mathcal{M}_1$ and $\mathcal{M}_2$ are defined in Eqs. (5.79) and (5.80).

5.7.9 Spectra at different interactions and spin imbalance

In this section we present additional figures showing the variation of the collective mode spectrum of a soliton train with spin imbalance and interaction strength.

Figure 5.8 shows how the spectrum changes as the number of unpaired

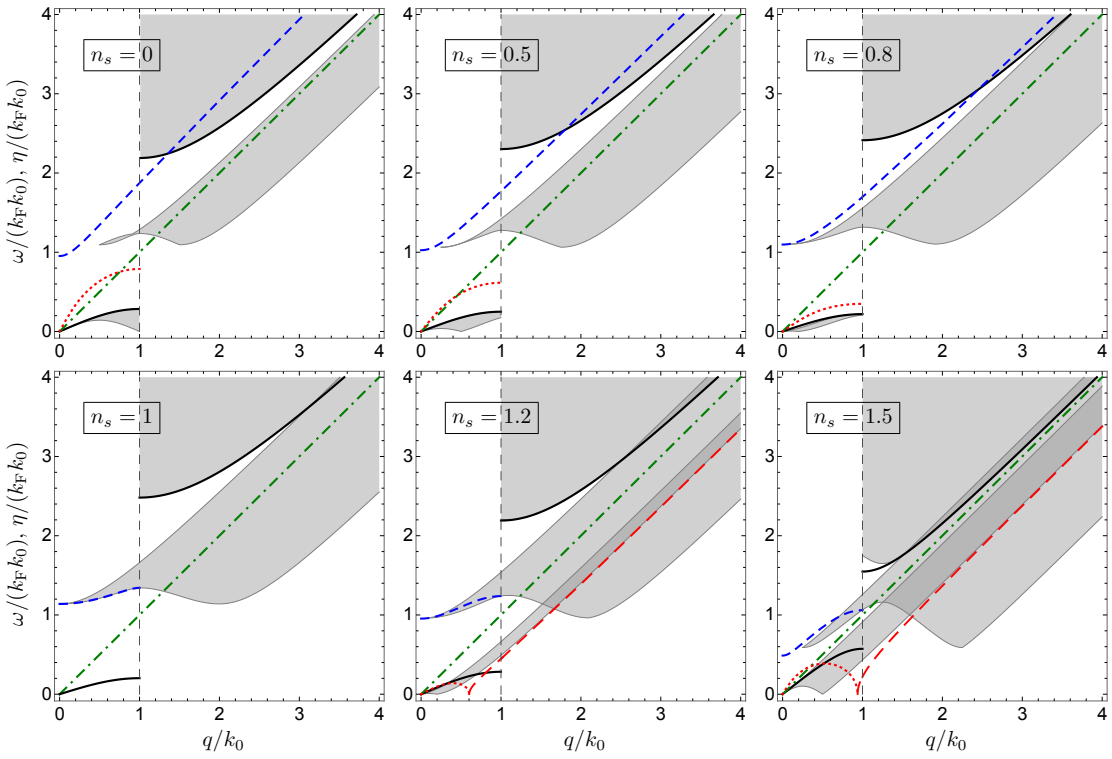

Figure 5.8: Collective excitation spectra of a fermionic soliton train at different spin imbalance in the extended zone representation, for $k_0/k_F = 0.05$ and $k_F a_{1D} = 2.65$. Gray regions show particle-hole continua, dot-dashed (green) curves show the Goldstone phase (phonon) mode, while dashed (blue) curves represent the doubly-degenerate "core" modes. The Goldstone amplitude ("elastic") mode with $q \leq k_0$, as well as the "Higgs" mode with $q \geq k_0$, are shown by solid (black) lines. The dotted (red) curves give the growth rate η of the two-fold degenerate unstable modes. For $n_s > 1$, the unstable modes are connected via a cusp to a new branch of stable modes, shown as wide-dashed (red) curves.

fermions per soliton (n_s) is varied. As n_s is increased from 0, the instability rate falls toward zero, and vanishes for the C-FFLO phase with $n_s = 1$. Since a change in n_s comes about from altering the chemical potentials, it also affects the allowed particle-hole excitations, so the two-particle continua are modified. In the limit $n_s \to 1$, the degenerate "core" modes merge with the neighboring continuum, and the Goldstone amplitude mode becomes undamped. For $n_s \geq 1$, the "core" modes (dashed, blue lines in Fig. 5.8) are confined to wave-vectors

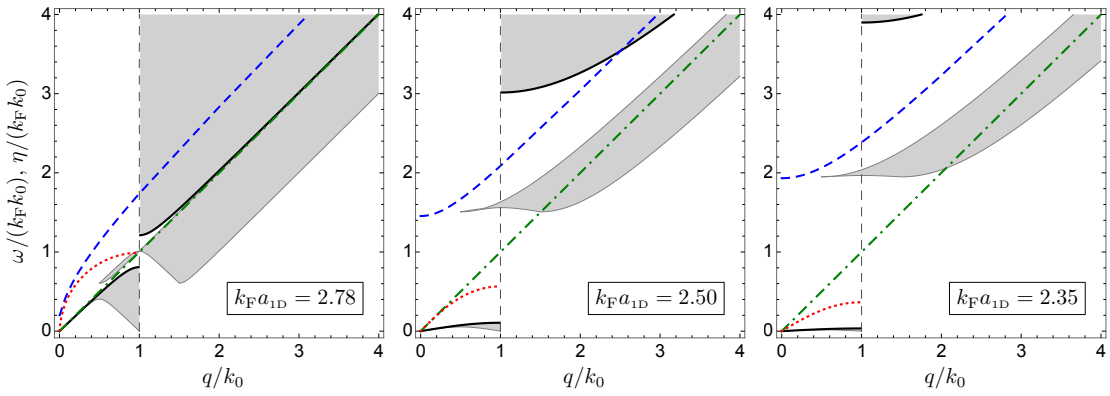

Figure 5.9: Collective excitation spectra of a fermionic soliton train at different interaction strengths in the extended zone representation, for $k_0/k_F = 0.05$ and $n_s = 0$. Conventions for the curves/regions are the same as in Fig. 5.8.

$q \leq k_0$. This is different from the $n_s < 1$ case, when the "core" modes extend to arbitrarily large q. As described in the main article, the amplitude and phase branches of the "core" modes are related as $\delta_a(x) \propto \delta_p'(x)\ \forall\ q$. At $q = 0$, they are described by $\delta_p(x) \propto \mathrm{cn}(\Delta_1 x/k_F, k_1)$ and $\omega = \Delta_1 k_1$. For $n_s \geq 1$, the end-point of the "core" spectrum at $q = k_0$ also has a simple form: there we find $\delta_p(x) \propto \mathrm{dn}(\Delta_1 x/k_F, k_1)$ and $\omega = \Delta_1$ [Note that $\Delta_1 \equiv 2k_F k_0 K(k_1)/\pi$]. The state with $n_s > 1$ is an analog of the unstable Sarma phase (see Sec. 5.7.4). It has zero-energy particle-hole excitations, and we again find dynamical instabilities. As before, there are two degenerate unstable modes which reduce to $\delta_p(x) \propto \Delta_0(x)$ and $\delta_a(x) \propto \Delta_0'(x)$ at $q = 0$, shown as dotted red lines in Fig. 5.8. However, the maximum instability occurs at a wave-vector $q < k_0$, and the unstable modes are connected, via a cusp at $q = q_0 \leq k_0$, to a doubly degenerate stable mode which extends to large wave-vectors, shown as dashed red lines. As n_s is increased, the maximum instability rate grows, and q_0 moves toward k_0. In addition, more of the low-energy "Higgs" modes become undamped. A soliton train solution exists as long as $n_s < n_s^{\max} = [1 + (4\tilde{\epsilon}_c^2 - 1)\, e^{-\pi k_F a_{1D}}]^{1/2}$. In the limit $n_s \to n_s^{\max}$, the soliton train reduces to a sinusoid of vanishingly small amplitude.

Figure 5.9 shows the variation in the spectrum with interaction strength. Stronger interactions (smaller $k_{\rm F}a_{\rm 1D}$) increase the band-gap between the bound states and free states in the single-particle spectrum (see Fig. 1 of the main article), which leads to a larger separation of energy scales in the collective mode spectrum. In particular, the "Higgs" mode and the "core" modes move to higher frequencies, while the Goldstone amplitude mode moves to a lower frequency. Stronger interactions also produce sharp, well-separated solitons, thus reducing the instability rate. In the next section, we present simulations of the full time-dynamics of a two-soliton system without the Andreev apprximation, which show that the instabilities become unnoticeable for $k_{\rm F}a_{\rm 1D} \lesssim 2$.

5.7.10 Simulation of the full dynamics of a two-soliton system

We simulate the full BdG dynamics [Eq. (5.9)] of two solitons on a ring without the Andreev approximation, using a split-step algorithm. We start from the stationary solution $\Delta_0(x)$, with two domain walls located at $x = \pm\pi/(2k_0)$, and apply a small perturbation $\delta\hat{H} = \int dx\, f(x,t)\hat{\Psi}^\dagger_\uparrow(x,t)\hat{\Psi}^\dagger_\downarrow(x,t)$ + H.c. where $f(x,t) = -(0.01/k_0)|\Delta_0'(x)|e^{-5tk_{\rm F}k_0}\Theta(t)$. The perturbation is short-lived compared to the dynamical timescales. However, it causes the two solitons to start moving toward each other. Figure 5.10 shows the ensuing dynamics for different interaction strengths and spin imbalance. The dark bands represent the location of the domain walls [where $\Delta(x,t) = 0$] as a function of time. For weak interactions and no spin imbalance, the system has dynamical instabilities: the solitons approach one another and annihilate, then repeatedly reform and annihilate. At stronger interactions, it takes longer for the solitons to merge, during which they exhibit a rich oscillatory motion. For very strong interactions

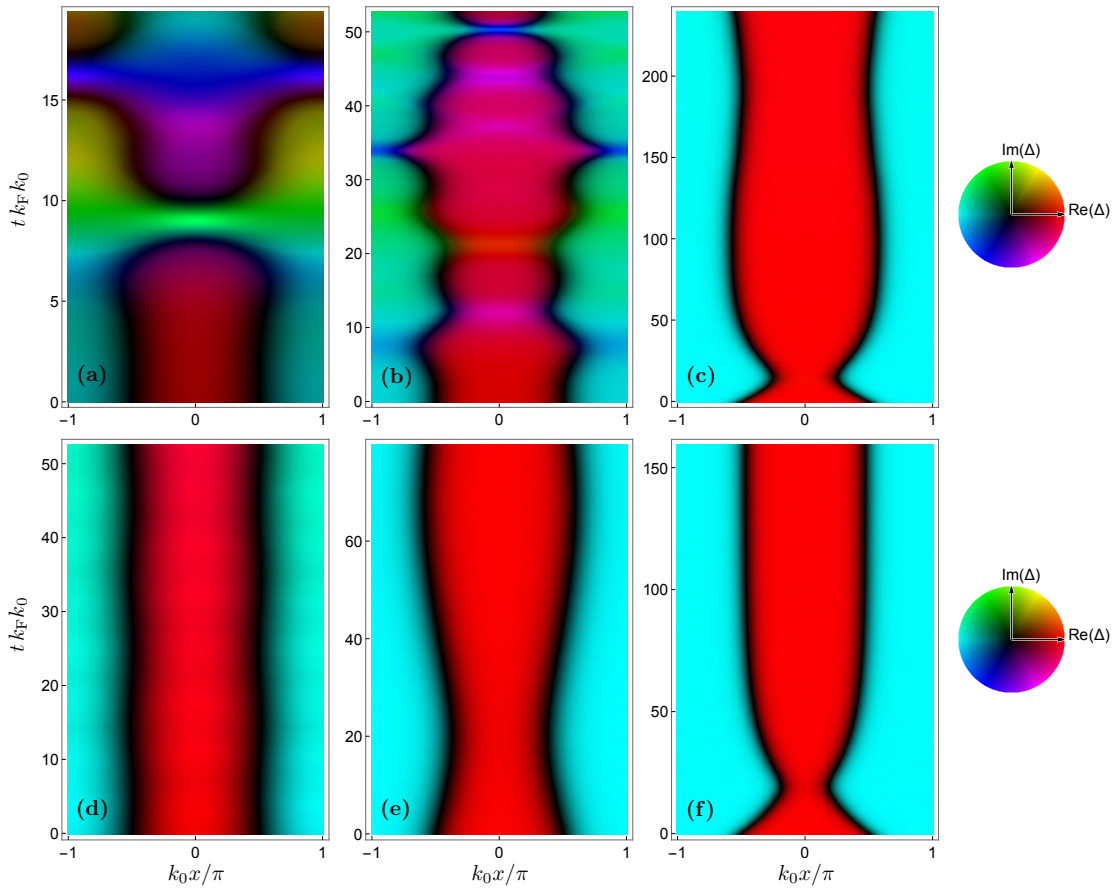

Figure 5.10: Full dynamics of two solitons with periodic boundary conditions, for $k_0/k_F = 0.05$. The absolute magnitude of Δ is proportional to the brightness, so dark bands represent the location of domain walls. The color wheels on the right show how the phase of Δ is encoded. Upper row: no spin imbalance, with (a) $k_F a_{1D} = 2.75$, (b) $k_F a_{1D} = 2.4$, and (c) $k_F a_{1D} = 2$. Lower row: with spin imbalance, and (d) $k_F a_{1D} = 2.75$, (e) $k_F a_{1D} = 2.4$, and (f) $k_F a_{1D} = 2$.

($k_F a_{1D} \lesssim 2$ for $k_0/k_F = 0.05$), we no longer see a merging of the solitons. Instead, they collide elastically off one another, and the domain walls undergo slow oscillations. This increase in stability with interaction strength is in agreement with the variation of the collective-mode spectrum of a soliton train in Fig. 5.9. Figures 5.10(d)-(f) show the dynamics in the presence of spin imbalance, such that the chemical potential difference $|h|$ is larger then the energy of the Andreev bound states, but smaller than the energy of all free quasiparticle states. This situation corresponds to the C-FFLO state of a soliton train,

which we found earlier to be dynamically stable (see Fig. 5.8). Similarly we find here that the domain walls undergo stable oscillations. The oscillation timescale corresponds to the frequency of the "elastic" modes in Fig 5.8, which become slower at stronger interactions. The initial response to the perturbation is larger for stronger interactions.

5.7.11 Soliton train in the Gross-Pitaevskii equation

Here we find the collective modes of a soliton train in a 1D Bose superfluid modeled by the Gross-Pitaevskii (GP) equation. We first set up the equations for a general stationary state, then consider the special case of a soliton train.

The GP equation describes the dynamics of the macroscopic wavefunction of the superfluid, $\psi(x,t)$, as

$$i\,\partial_t \psi(x,t) = \big(-\,\partial_x^2/2 - \mu + g\,|\psi(x,t)|^2\big)\,\psi(x,t)\,, \tag{5.112}$$

where μ denotes the chemical potential, and g is the coupling constant. Thus, a stationary state $\psi_0(x) \in \mathbb{R}$ satisfies

$$\big\{-\,\partial_x^2/2 - \mu + g\,[\psi_0(x)]^2\big\}\,\psi_0(x) = 0\,. \tag{5.113}$$

To find the collective modes, we linearize Eq. (5.112) for small fluctuations $\delta\psi(x,t)$ about $\psi_0(x)$, obtaining

$$i\,\partial_t \delta\psi(x,t) = (-\partial_x^2/2 - \mu)\,\delta\psi(x,t) + g\,[\psi_0(x)]^2\,(2\delta\psi(x,t) + \delta\psi^*(x,t))\,. \tag{5.114}$$

Next we decompose $\delta\psi$ into amplitude and phase fluctuations, $\delta\psi(x,t) = \mathrm{Re}\big(\delta\psi_a(x)\,e^{i\Omega t}\big) + i\,\mathrm{Im}\big(\delta\psi_p(x)\,e^{i\Omega t}\big)$ where $\delta\psi_a(x), \delta\psi_p(x), \Omega \in \mathbb{C}$. Comparing real

and imaginary parts in Eq. (5.114), we find

$$-\Omega\,\delta\psi_p(x) = \left\{-\partial_x^2/2 - \mu + g\,[\psi_0(x)]^2\right\}\delta\psi_a(x)\,, \tag{5.115}$$

$$\text{and} \quad -\Omega\,\delta\psi_a(x) = \left\{-\partial_x^2/2 - \mu + 3g\,[\psi_0(x)]^2\right\}\delta\psi_p(x)\,. \tag{5.116}$$

Equations (5.115) and (5.116) describe the collective modes. Note that the amplitude and phase modes are coupled, unlike the fermionic case [Eq. (5.82)]. We also see that Ω^2 is an eigenvalue of a Hermitian operator. Thus Ω^2 must be real, which means Ω is either real or imaginary. For a soliton train phase (as well as a uniform state), we find Ω is real for all collective modes, i.e., there is no dynamical instability.

A soliton train solution to Eq. (5.113) with period $2\pi/k_0$ exists for $0 < \kappa < 1$, where $\kappa \equiv k_0^2/(2\mu)$ is a measure of the ratio of kinetic energy to interaction energy. The soliton train profile is given by

$$\psi_0(x) = \sqrt{2\kappa n_0}\,[2k_1K(k_1)/\pi]\,\mathrm{sn}\big(2K(k_1)k_0x/\pi, k_1\big)\,, \tag{5.117}$$

where $n_0 \equiv \mu/g$, and k_1 is a sharpness parameter set by the equation $2(1 + k_1^2)^{1/2}K(k_1) = \pi/\sqrt{\kappa}$. For $\kappa \to 0$, $k_1 \to 1$, and $\psi_0(x)$ describes an array of sharp domain walls separating uniform regions with $\psi_0 = \pm\sqrt{n_0}$. Conversely, for $\kappa \to 1$, $k_1 \to 0$, and $\psi_0(x)$ reduces to a sinusoid of vanishing amplitude. Note that $\psi_0(x)$ in Eq. (5.117) has the same spatial variation as a soliton train in a Fermi superfluid [Eq. (5.60)].

To obtain the collective mode spectrum, we write $\delta\psi_{p,a}(x) = e^{iqx}\sum_n A_n^{p,a}e^{ink_0x}$ in Eqs. (5.115) and (5.116), and use

$$[\psi_0(x)]^2 = 2\kappa n_0\left\{\left(\frac{2K(k_1)}{\pi}\right)^2\left(1 - \frac{E(k_1)}{K(k_1)}\right) - 4\sum_{n=1}^{\infty}\frac{n\cos(2nk_0x)}{\sinh\left[n\pi K\left(\sqrt{1-k_1^2}\right)/K(k_1)\right]}\right\} \tag{5.118}$$

to yield a matrix equation for the coefficients $A_n^{p,a}$. The eigenvalues of this matrix give the frequencies of collective oscillations. The collective modes are characterized by the parameter κ. Figure 5.2(c) in the main article shows the spectrum for $\kappa = 0.7$. The spectrum only contains two gapless Goldstone modes which arise from the spontaneous breaking of gauge and translational symmetry. In contrast, the fermionic soliton train has a much richer spectrum [Figs. 5.8 and 5.9]. In the limit $\kappa \to 0$ (sharp well-separated solitons) and $q \to 0$, the mode with unbounded spectrum is described by $(\delta\psi_p(x), \delta\psi_a(x)) \propto (\psi_0(x), 0)$ and $\Omega = \sqrt{\mu}\, q$, whereas the mode with bounded spectrum is described by $(\delta\psi_p(x), \delta\psi_a(x)) \propto (0, \psi_0'(x))$ and $\Omega \approx 0$. In other words, the two modes become pure phase ("phonon") and pure amplitude ("elastic") modes, respectively. In the opposite limit $\kappa \to 1$, the phase and amplitude oscillations are strongly mixed. For $q \to 0$, both modes are given by $(\delta\psi_p(x), \delta\psi_a(x)) \propto (\psi_0(x), i\psi_0'(x))$ and $\Omega = \sqrt{2\mu}\, q$.

5.7.12 Soliton train in a nonlinear Klein-Gordon equation

Here we study the collective modes of an "order parameter" $\phi(x,t)$ governed by the nonlinear Klein-Gordon equation

$$-(\partial_t^2/2)\phi(x,t) = v^2\big(-\partial_x^2/2 - \mu + g\,|\phi(x,t)|^2\big)\,\phi(x,t)\,, \tag{5.119}$$

where μ, g, and v are phenamenological parameters playing the role of chemical potential, interaction strength, and speed of sound, respectively. The motivation for studying such an equation is twofold. First, it presents a simple "fermionic analog" of the GP equation [Eq. (5.112)]. The stationary solutions of the GP equation and Eq. (5.119) are identical. However, Eq. (5.119) is second-order in

time, which causes phase and amplitude collective modes to decouple, as is the case in a Fermi superfluid [Eq. (5.82)]. Further, Eq. (5.119) reproduces several features of the collective modes in a Fermi superfluid, in particular, analogs of Goldstone and "Higgs" modes, as well as soliton "core" modes and dynamical instabilities. This similarity suggests that the features could arise more generically in mesoscopic nonlinear systems, which might allow their broad characterization in terms of effective coarse-grained models.

To study the collective modes, we linearize Eq. (5.119) about a stationary solution $\phi_0(x) \in \mathbb{R}$, yielding

$$\left[\partial_t^2/(2v^2) - \partial_x^2/2 - \mu\right] \delta\phi(x,t) + g\left[\phi_0(x)\right]^2 \left(2\delta\phi(x,t) + \delta\phi^*(x,t)\right) = 0\,. \tag{5.120}$$

Substituting $\delta\phi(x,t) = \mathrm{Re}\big(\delta\phi_a(x)\, e^{i\Omega t}\big) + i\,\mathrm{Im}\big(\delta\phi_p(x)\, e^{i\Omega t}\big)$ and comparing real and imaginary parts, we find

$$(\Omega/v)^2\, \delta\phi_p(x) = 2\left\{-\partial_x^2/2 - \mu + g\left[\phi_0(x)\right]^2\right\} \delta\phi_p(x)\,, \tag{5.121}$$

$$\text{and} \quad (\Omega/v)^2\, \delta\phi_a(x) = 2\left\{-\partial_x^2/2 - \mu + 3g\left[\phi_0(x)\right]^2\right\} \delta\phi_a(x)\,. \tag{5.122}$$

Thus the amplitude and phase oscillations decouple, and Ω^2 is given by an eigenvalue of a Hermitian operator. Thus, Ω must be either real or imaginary for any collective mode.

For a uniform stationary solution, $\phi_0(x) = \sqrt{\mu/g}$, there is a Goldstone phase mode arising from the spontaneous breaking of gauge symmetry, described by $\delta\phi_p(x) \propto e^{iqx}$ and $\Omega = vq$. It is similar to the Anderson-Bogoliubov phonon mode of a uniform Fermi superfluid. There is also an amplitude mode described by $\delta\phi_a(x) \propto e^{iqx}$ and $\Omega = v\,(q^2 + 4\mu)^{1/2}$, which is analogous to the "Higgs" mode in a uniform Fermi superfluid (see Sec. 5.7.6).

A stationary soliton train has the same profile as in Eq. (5.117), $\phi_0(x) =$

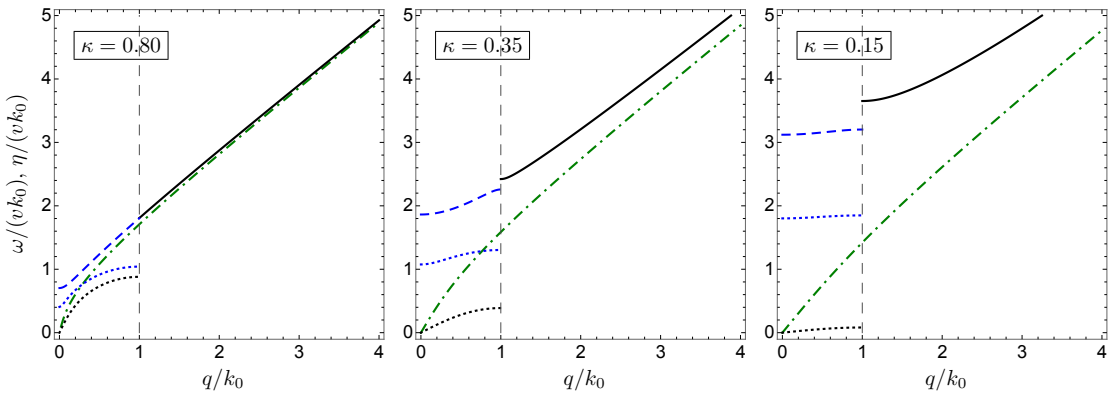

Figure 5.11: Collective mode spectra of a soliton train described by a nonlinear Klein-Gordon equation [Eq. (5.119)] for different values of $\kappa \equiv k_0^2/(2\mu)$. There are three stable modes: a Goldstone phase mode, a Higgs-like amplitude mode, and a "core" mode describing width oscillations of solitons. These are represented by dot-dashed (green), solid (black), and dashed (blue) curves, respectively. The dotted curves give the growth rate of two unstable modes: a gapless Goldstone amplitude mode (shown in black), and a "core" mode describing grayness oscillations of solitons (shown in blue).

$\sqrt{2\kappa n_0}\, k_1 \nu\, \mathrm{sn}(\nu k_0 x, k_1)$ where $\nu \equiv 2K(k_1)/\pi$, $\kappa \equiv k_0^2/(2\mu)$, and $n_0 \equiv \sqrt{\mu/g}$. Its collective modes are characterized by κ. Figure 5.11 shows the spectrum for different values of κ in the extended zone scheme. Comparing with Figs. 5.8 and 5.9, we find a number of similarities, as well as some differences, with the spectrum in a Fermi superfluid. Like a fermionic soliton train, we find a Goldstone phase mode with an unbounded spectrum, which in the limit $q \to 0$, is given by $\delta\phi_p(x) \propto \phi_0(x)$. However, the Goldstone amplitude mode here is unstable with imaginary frequency. At $q = 0$, the mode describes a uniform translation, $\delta\phi_a(x) \propto \phi_0'(x)$, whereas at $q = k_0$, it describes a fluctuation $\delta\phi_a(x) \propto 1 - \varepsilon_- \,\mathrm{sn}^2(\nu k_0 x, k_1)$ growing at a rate $\eta = \Gamma_-$, where $\varepsilon_\pm \equiv \big[1 \pm (1 - 3\kappa^2 k_1^2 \nu^4)^{1/2}\big]/(\kappa\nu^2)$ and $\Gamma_\pm \equiv v k_0 \big[1 \pm 2(1 - 3\kappa^2 k_1^2 \nu^4)^{1/2}\big]^{1/2}/\sqrt{\kappa}$. This instability is similar to the one we had found in the fermionic soliton train, where neighboring solitons approach and annihilate one another [see Fig. 5.2(f) in the main article]. There we also had an instability where the entire soliton

train moves off into the complex plane. Such an instability is only present here in the limit $\kappa \to 1$. In general, the maximum instability comes from a gapped unstable phase mode at $q = k_0$, where a fluctuation $\delta\phi_p(x) \propto \mathrm{dn}(\nu k_0 x, k_1)$ grows at a rate $\eta_{\max} = v k_0 (1/\kappa - k_1^2 \nu^2)^{1/2}$. In the limit $\kappa \to 1$, $\mathrm{dn}(\nu k_0 x, k_1) \to 1$ and $\eta_{\max} = v k_0$. At $q = 0$, the unstable phase mode describes a fluctuation $\delta\phi_p(x) \propto \mathrm{cn}(\nu k_0 x, k_1)$ growing at a rate $\eta_{\max} = v k_0 (1/\kappa - \nu^2)^{1/2}$. This fluctuation, in fact, has the same functional form as the "core" mode which described grayness oscillations of each soliton in the fermionic soliton train [Fig. 5.2(e) in the main article]. Thus, the phase branch of the "core" modes has turned into an unstable mode. In contrast, the amplitude branch, describing oscillations in the soliton widths, is still present, but only for $q \leq k_0$. At $q = 0$, it is given by $\delta\phi_a(x) \propto \mathrm{sn}(\nu k_0 x, k_1)\,\mathrm{dn}(\nu k_0 x, k_1)$ and $\Omega = \sqrt{3 k_1 \nu}$, whereas at $q = k_0$, it is given by $\delta\phi_a(x) \propto \mathrm{sn}(\nu k_0 x, k_1)\,\mathrm{cn}(\nu k_0 x, k_1)$ and $\Omega = \sqrt{3\nu}$. In addition, we have the analog of the "Higgs" mode for $q \geq k_0$. At $q = k_0$, it describes an amplitude oscillation similar to the one in a fermionic soliton train shown in Fig. 5.7(c), given by $\delta\phi_a(x) \propto 1 - \varepsilon_+ \,\mathrm{sn}^2(\nu k_0 x, k_1)$ and $\Omega = \Gamma_+$. Since κ measures the ratio of kinetic to interaction energy, decreasing κ correspond to stronger interactions, or smaller values of $k_{\mathrm{F}} a_{1\mathrm{D}}$ in Fig. 5.9.

BIBLIOGRAPHY FOR CHAPTER 5

[1] T. Dauxois and M. Peyrard, *Physics of Solitons* (Cambridge University Press, Cambridge, 2006).

[2] N. J. Zabusky and M. D. Kruskal, "Interaction of solitons in a collisionless plasma and the recurrence of initial states," Phys. Rev. Lett. **15**, 240 (1965).

[3] A. Chabchoub, O. Kimmoun, H. Branger, N. Hoffmann, D. Proment, M. Onorato, and N. Akhmediev, "Experimental observation of dark solitons on the surface of water," Phys. Rev. Lett. **110**, 124101 (2013).

[4] S. Trillo, G. Deng, G. Biondini, M. Klein, G. F. Clauss, A. Chabchoub, and M. Onorato, "Experimental observation and theoretical description of multisoliton fission in shallow water," Phys. Rev. Lett. **117**, 144102 (2016).

[5] T. B. Sisan and S. Lichter, "Solitons transport water through narrow carbon nanotubes," Phys. Rev. Lett. **112**, 044501 (2014).

[6] E. A. Kuznetsov, A. M. Rubenchik, and V. E. Zakharov, "Soliton stability in plasmas and hydrodynamics," Phys. Rep. **142**, 103 (1986).

[7] P. K. Shukla and B. Eliasson, "Formation and dynamics of dark solitons and vortices in quantum electron plasmas," Phys. Rev. Lett. **96**, 245001 (2006).

[8] Y. S. Kivshar and G. Agrawal, *Optical Solitons: From Fibers to Photonic Crystals* (Academic press, San Diego, 2003).

[9] Y. S. Kivshar and B. Luther-Davies, "Dark optical solitons: Physics and applications," Phys. Rep. **298**, 81 (1998).

[10] L. F. Mollenauer and J. P. Gordon, *Solitons in Optical Fibers: Fundamentals and Applications* (Academic Press, Boston, 2006).

[11] L. F. Mollenauer, R. H. Stolen, and J. P. Gordon, "Experimental observation of picosecond pulse narrowing and solitons in optical fibers," Phys. Rev. Lett. **45**, 1095 (1980).

[12] F. M. Mitschke and L. F. Mollenauer, "Experimental observation of interaction forces between solitons in optical fibers," Opt. Lett. **12**, 355 (1987).

[13] A. Hasegawa, "Generation of a train of soliton pulses by induced modulational instability in optical fibers," Opt. Lett. **9**, 288 (1984).

[14] P. D. Drummond, R. M. Shelby, S. R. Friberg, and Y. Yamamoto, "Quantum solitons in optical fibres," Nature (London) **365**, 307 (1993).

[15] Y. Lu, *Solitons and Polarons in Conducting Polymers* (World Scientific, Singapore, 1988).

[16] A. J. Heeger, S. Kivelson, J. R. Schrieffer, and W.-P. Su, "Solitons in conducting polymers," Rev. Mod. Phys. **60**, 781 (1988).

[17] W. P. Su, J. R. Schrieffer, and A. J. Heeger, "Solitons in polyacetylene," Phys. Rev. Lett. **42**, 1698 (1979).

[18] H. Takayama, Y. R. Lin-Liu, and K. Maki, "Continuum model for solitons in polyacetylene," Phys. Rev. B **21**, 2388 (1980).

[19] S. A. Brazovskii, S. A. Gordyunin, and N. N. Kirova, "An exact solution of the Peierls model with an arbitrary number of electrons in the unit cell," JETP Lett. **31**, 456 (1980), [Pis'ma v Zh. Eksp. Teor. Fiz. **31**, 486 (1980)].

[20] B. Horovitz, "Soliton lattice in polyacetylene, spin-Peierls systems, and two-dimensional sine-Gordon systems," Phys. Rev. Lett. **46**, 742 (1981).

[21] J. Mertsching and H. J. Fischbeck, "The incommensurate Peierls phase of the quasi-one-dimensional Fröhlich model with a nearly half-filled band," Phys. Status Solidi (B) **103**, 783 (1981).

[22] S. A. Brazovskii, N. N. Kirova, and S. I. Matveenko, "Peierls effect in conducting polymers," Sov. Phys. JETP **59**, 434 (1984), [Zh. Eksp. Teor. Fiz. **86**, 743 (1984)].

[23] A. I. Buzdin and V. V. Tugushev, "Phase diagrams of electronic and superconducting transitions to soliton lattice states," Sov. Phys. JETP **58**, 428 (1983), [Zh. Eksp. Teor. Fiz. **85**, 735 (1983)].

[24] A. I. Buzdin and S. V. Polonskii, "Nonuniform state in quasi-1D superconductors," Sov. Phys. JETP **66**, 422 (1987), [Zh. Eksp. Teor. Fiz. **93**, 747 (1987)].

[25] K. Machida and H. Nakanishi, "Superconductivity under a ferromagnetic molecular field," Phys. Rev. B **30**, 122 (1984).

[26] S. A. Kivelson, D. S. Rokhsar, and J. P. Sethna, "Topology of the resonating valence-bond state: Solitons and high-T_c superconductivity," Phys. Rev. B **35**, 8865 (1987).

[27] Y. Tanaka, "Soliton in two-band superconductor," Phys. Rev. Lett. **88**, 017002 (2001).

[28] A. Dienst, E. Casandruc, D. Fausti, L. Zhang, M. Eckstein, M. Hoffmann, V. Khanna, N. Dean, M. Gensch, S. Winnerl, *et al.*, "Optical excitation of

Josephson plasma solitons in a cuprate superconductor," Nat. Mater. **12**, 535 (2013).

[29] D. J. Frantzeskakis, "Dark solitons in atomic Bose–Einstein condensates: From theory to experiments," J. Phys. A **43**, 213001 (2010).

[30] P. G. Kevrekidis, D. J. Frantzeskakis, and R. Carretero-González, *Emergent Nonlinear Phenomena in Bose-Einstein Condensates: Theory and Experiment* (Springer, Berlin, 2007).

[31] Z. Dutton, M. Budde, C. Slowe, and L. V. Hau, "Observation of quantum shock waves created with ultra-compressed slow light pulses in a Bose-Einstein condensate," Science **293**, 663 (2001).

[32] S. Donadello, S. Serafini, M. Tylutki, L. P. Pitaevskii, F. Dalfovo, G. Lamporesi, and G. Ferrari, "Observation of solitonic vortices in Bose-Einstein condensates," Phys. Rev. Lett. **113**, 065302 (2014).

[33] S. Burger, K. Bongs, S. Dettmer, W. Ertmer, K. Sengstock, A. Sanpera, G. V. Shlyapnikov, and M. Lewenstein, "Dark solitons in Bose-Einstein condensates," Phys. Rev. Lett. **83**, 5198 (1999).

[34] B. P. Anderson, P. C. Haljan, C. A. Regal, D. L. Feder, L. A. Collins, C. W. Clark, and E. A. Cornell, "Watching dark solitons decay into vortex rings in a Bose-Einstein condensate," Phys. Rev. Lett. **86**, 2926 (2001).

[35] J. Denschlag, J. E. Simsarian, D. L. Feder, C. W. Clark, L. A. Collins, J. Cubizolles, L. Deng, E. W. Hagley, K. Helmerson, W. P. Reinhardt, *et al.*, "Generating solitons by phase engineering of a Bose-Einstein condensate," Science **287**, 97 (2000).

[36] C. Becker, S. Stellmer, P. Soltan-Panahi, S. Dörscher, M. Baumert, E.-M. Richter, J. Kronjäger, K. Bongs, and K. Sengstock, "Oscillations and interactions of dark and dark–bright solitons in Bose–Einstein condensates," Nat. Phys. **4**, 496 (2008).

[37] S. Stellmer, C. Becker, P. Soltan-Panahi, E.-M. Richter, S. Dörscher, M. Baumert, J. Kronjäger, K. Bongs, and K. Sengstock, "Collisions of dark solitons in elongated Bose-Einstein condensates," Phys. Rev. Lett. **101**, 120406 (2008).

[38] L. Khaykovich, F. Schreck, G. Ferrari, T. Bourdel, J. Cubizolles, L. Carr, Y. Castin, and C. Salomon, "Formation of a matter-wave bright soliton," Science **296**, 1290 (2002).

[39] K. E. Strecker, G. B. Partridge, A. G. Truscott, and R. G. Hulet, "Formation and propagation of matter-wave soliton trains," Nature (London) **417**, 150 (2002).

[40] J. H. V. Nguyen, D. Luo, and R. G. Hulet, "Formation of matter-wave soliton trains by modulational instability," Science **356**, 422 (2017).

[41] P. J. Everitt, M. A. Sooriyabandara, M. Guasoni, P. B. Wigley, C. H. Wei, G. D. McDonald, K. S. Hardman, P. Manju, J. D. Close, C. C. N. Kuhn, *et al.*, "Observation of a modulational instability in Bose-Einstein condensates," Phys. Rev. A **96**, 041601(R) (2017).

[42] G. Lamporesi, S. Donadello, S. Serafini, F. Dalfovo, and G. Ferrari, "Spontaneous creation of Kibble-Zurek solitons in a Bose-Einstein condensate," Nat. Phys. **9**, 656 (2013).

[43] A. Weller, J. P. Ronzheimer, C. Gross, J. Esteve, M. K. Oberthaler, D. J. Frantzeskakis, G. Theocharis, and P. G. Kevrekidis, "Experimental observation of oscillating and interacting matter wave dark solitons," Phys. Rev. Lett. **101**, 130401 (2008).

[44] I. Shomroni, E. Lahoud, S. Levy, and J. Steinhauer, "Evidence for an oscillating soliton/vortex ring by density engineering of a Bose–Einstein condensate," Nat. Phys. **5**, 193 (2009).

[45] K. Bongs, S. Burger, D. Hellweg, M. Kottke, S. Dettmer, T. Rinkleff, L. Cacciapuoti, J. Arlt, K. Sengstock, and W. Ertmer, "Spectroscopy of dark soliton states in Bose–Einstein condensates," J. Opt. B **5**, S124 (2003).

[46] R. G. Scott, A. M. Martin, T. M. Fromhold, S. Bujkiewicz, F. W. Sheard, and M. Leadbeater, "Creation of solitons and vortices by Bragg reflection of Bose-Einstein condensates in an optical lattice," Phys. Rev. Lett. **90**, 110404 (2003).

[47] G. Theocharis, A. Weller, J. P. Ronzheimer, C. Gross, M. K. Oberthaler, P. G. Kevrekidis, and D. J. Frantzeskakis, "Multiple atomic dark solitons in cigar-shaped Bose-Einstein condensates," Phys. Rev. A **81**, 063604 (2010).

[48] C. Becker, K. Sengstock, P. Schmelcher, P. G. Kevrekidis, and R. Carretero-González, "Inelastic collisions of solitary waves in anisotropic Bose-Einstein condensates: Sling-shot events and expanding collision bubbles," New J. Phys. **15**, 113028 (2013).

[49] E. W. Prohofsky, "Solitons hiding in DNA and their possible significance in RNA transcription," Phys. Rev. A **38**, 1538 (1988).

[50] V. Muto, A. C. Scott, and P. L. Christiansen, "Thermally generated solitons in a Toda lattice model of DNA," Phys. Lett. A **136**, 33 (1989).

[51] A. Scott, "Davydov's soliton," Phys. Rep. **217**, 1 (1992).

[52] L. V. Yakushevich, A. V. Savin, and L. I. Manevitch, "Nonlinear dynamics of topological solitons in DNA," Phys. Rev. E **66**, 016614 (2002).

[53] M. Vanitha and M. Daniel, "Internal nonlinear dynamics of a short lattice DNA model in terms of propagating kink-antikink solitons," Phys. Rev. E **85**, 041911 (2012).

[54] M. Peyrard, "Nonlinear dynamics and statistical physics of DNA," Nonlinearity **17**, R1 (2004).

[55] R. Rajaraman, *Solitons and Instantons* (North Holland, Amsterdam, 1982).

[56] G. Başar and G. V. Dunne, "Self-consistent crystalline condensate in chiral Gross-Neveu and Bogoliubov–de Gennes systems," Phys. Rev. Lett. **100**, 200404 (2008).

[57] G. V. Dunne and M. Thies, "Time-dependent Hartree-Fock solution of Gross-Neveu models: Twisted-kink constituents of baryons and breathers," Phys. Rev. Lett. **111**, 121602 (2013).

[58] G. V. Dunne and M. Thies, "Full time-dependent Hartree-Fock solution of large N Gross-Neveu models," Phys. Rev. D **89**, 025008 (2014).

[59] V. Schön and M. Thies, "Emergence of the Skyrme crystal in Gross-Neveu and 't Hooft models at finite density," Phys. Rev. D **62**, 096002 (2000).

[60] M. Thies, "From relativistic quantum fields to condensed matter and back again: Updating the Gross–Neveu phase diagram," J. Phys. A **39**, 12707 (2006).

[61] M. Thies, "Analytical solution of the Gross-Neveu model at finite density," Phys. Rev. D **69**, 067703 (2004).

[62] D. K. Campbell and A. R. Bishop, "Soliton excitations in polyacetylene and relativistic field theory models," Nucl. Phys. B **200**, 297 (1982).

[63] T. W. B. Kibble, "Topology of cosmic domains and strings," J. Phys. A **9**, 1387 (1976).

[64] P. Sikivie, "Axions, domain walls, and the early universe," Phys. Rev. Lett. **48**, 1156 (1982).

[65] J. A. Frieman, G. B. Gelmini, M. Gleiser, and E. W. Kolb, "Primordial origin of nontopological solitons," Phys. Rev. Lett. **60**, 2101 (1988).

[66] A. Kusenko, "Solitons in the supersymmetric extensions of the standard model," Phys. Lett. B **405**, 108 (1997).

[67] K. D. Lozanov and M. A. Amin, "End of inflation, oscillons, and matter-antimatter asymmetry," Phys. Rev. D **90**, 083528 (2014).

[68] E. J. Weinberg, *Classical Solutions in Quantum Field Theory* (Cambridge University Press, Cambridge, 2012).

[69] H. A. Haus and W. S. Wong, "Solitons in optical communications," Rev. Mod. Phys. **68**, 423 (1996).

[70] M. Nakazawa, "Soliton transmission in telecommunication networks," IEEE Commun. Mag. **32**, 34 (1994).

[71] A. Hasegawa, Y. Kodama, and A. Maruta, "Recent progress in dispersion-managed soliton transmission technologies," Opt. Fiber Technol. **3**, 197 (1997).

[72] V. E. Zakharov and S. Wabnitz, eds., *Optical Solitons: Theoretical Challenges and Industrial Perspectives* (Springer-Verlag, Berlin, 1999).

[73] M. Nakazawa, H. Kubota, K. Suzuki, E. Yamada, and A. Sahara, "Recent progress in soliton transmission technology," Chaos **10**, 486 (2000).

[74] A. Hasegawa, "Soliton-based optical communications: An overview," IEEE J. Sel. Top. Quantum Electron. **6**, 1161 (2000).

[75] S. K. Turitsyn, B. G. Bale, and M. P. Fedoruk, "Dispersion-managed solitons in fibre systems and lasers," Phys. Rep. **521**, 135 (2012).

[76] P. Rohrmann, A. Hause, and F. Mitschke, "Solitons beyond binary: Possibility of fibre-optic transmission of two bits per clock period," Sci. Rep. **2**, 866 (2012).

[77] J. Scheuer and M. Orenstein, "All-optical gates facilitated by soliton interactions in a multilayered Kerr medium," J. Opt. Soc. Am. B **22**, 1260 (2005), and references therein.

[78] U. Al Khawaja, S. M. Al-Marzoug, and H. Bahlouli, "All-optical switches, unidirectional flow, and logic gates with discrete solitons in waveguide arrays," Opt. Express **24**, 11062 (2016).

[79] K. Steiglitz and D. Rand, "Photon trapping and transfer with solitons," Phys. Rev. A **79**, 021802 (2009).

[80] K. Steiglitz, "Soliton-guided phase shifter and beam splitter," Phys. Rev. A **81**, 033835 (2010).

[81] K. Steiglitz, "Making beam splitters with dark soliton collisions," Phys. Rev. A **82**, 043831 (2010).

[82] M. H. Jakubowski, K. Steiglitz, and R. Squier, "Computing with solitons: A review and prospectus," in *Collision-Based Computing*, edited by A. Adamatzky (Springer, London, 2002) Chap. 10, p. 277.

[83] W.-X. Yang, J.-M. Hou, and R.-K. Lee, "Ultraslow bright and dark solitons in semiconductor quantum wells," Phys. Rev. A **77**, 033838 (2008).

[84] M. Pang, W. He, X. Jiang, and P. S. J. Russell, "All-optical bit storage in a fibre laser by optomechanically bound states of solitons," Nat. Photonics **10**, 454 (2016).

[85] S. Bonetti, R. Kukreja, Z. Chen, F. Macià, J. M. Hernàndez, A. Eklund, D. Backes, J. Frisch, J. Katine, G. Malm, *et al.*, "Direct observation and imaging of a spin-wave soliton with p-like symmetry," Nat. Commun. **6**, 8889 (2015).

[86] A. Janutka, "Quantum-like information processing using vector solitons," J. Phys. A **41**, 375202 (2008).

[87] G. D. McDonald, C. C. N. Kuhn, K. S. Hardman, S. Bennetts, P. J. Everitt, P. A. Altin, J. E. Debs, J. D. Close, and N. P. Robins, "Bright solitonic matter-wave interferometer," Phys. Rev. Lett. **113**, 013002 (2014).

[88] B. Gertjerenken, T. P. Billam, C. L. Blackley, C. R. Le Sueur, L. Khaykovich, S. L. Cornish, and C. Weiss, "Generating mesoscopic Bell states via col-

lisions of distinguishable quantum bright solitons," Phys. Rev. Lett. **111**, 100406 (2013).

[89] J. L. Helm, S. L. Cornish, and S. A. Gardiner, "Sagnac interferometry using bright matter-wave solitons," Phys. Rev. Lett. **114**, 134101 (2015).

[90] R. G. Scott, T. E. Judd, and T. M. Fromhold, "Exploiting soliton decay and phase fluctuations in atom chip interferometry of Bose-Einstein condensates," Phys. Rev. Lett. **100**, 100402 (2008).

[91] J. Polo and V. Ahufinger, "Soliton-based matter-wave interferometer," Phys. Rev. A **88**, 053628 (2013).

[92] A. Negretti and C. Henkel, "Enhanced phase sensitivity and soliton formation in an integrated BEC interferometer," J. Phys. B **37**, L385 (2004).

[93] N. Veretenov, Y. Rozhdestvensky, N. Rosanov, V. Smirnov, and S. Fedorov, "Interferometric precision measurements with Bose–Einstein condensate solitons formed by an optical lattice," Eur. Phys. J. D **42**, 455 (2007).

[94] J. Cuevas, P. G. Kevrekidis, B. A. Malomed, P. Dyke, and R. G. Hulet, "Interactions of solitons with a Gaussian barrier: Splitting and recombination in quasi-one-dimensional and three-dimensional settings," New J. Phys. **15**, 063006 (2013).

[95] A. D. Martin and J. Ruostekoski, "Quantum dynamics of atomic bright solitons under splitting and recollision, and implications for interferometry," New J. Phys. **14**, 043040 (2012).

[96] H. Sakaguchi and B. A. Malomed, "Matter-wave soliton interferometer based on a nonlinear splitter," New J. Phys. **18**, 025020 (2016).

[97] T. Yefsah, A. T. Sommer, M. J. Ku, L. W. Cheuk, W. Ji, W. S. Bakr, and M. W. Zwierlein, "Heavy solitons in a fermionic superfluid," Nature (London) **499**, 426 (2013).

[98] M. J. H. Ku, W. Ji, B. Mukherjee, E. Guardado-Sanchez, L. W. Cheuk, T. Yefsah, and M. W. Zwierlein, "Motion of a solitonic vortex in the BEC-BCS crossover," Phys. Rev. Lett. **113**, 065301 (2014).

[99] M. J. H. Ku, B. Mukherjee, T. Yefsah, and M. W. Zwierlein, "Cascade of solitonic excitations in a superfluid Fermi gas: From planar solitons to vortex rings and lines," Phys. Rev. Lett. **116**, 045304 (2016).

[100] D. A. Takahashi, "Bogoliubov–de Gennes soliton dynamics in unconventional Fermi superfluids," Phys. Rev. B **93**, 024512 (2016).

[101] J. Dziarmaga and K. Sacha, "Gap soliton in superfluid Fermi gas at zero and finite temperature," Laser Phys. **15**, 674 (2005).

[102] M. Antezza, F. Dalfovo, L. P. Pitaevskii, and S. Stringari, "Dark solitons in a superfluid Fermi gas," Phys. Rev. A **76**, 043610 (2007).

[103] R. Liao and J. Brand, "Traveling dark solitons in superfluid Fermi gases," Phys. Rev. A **83**, 041604 (2011).

[104] R. G. Scott, F. Dalfovo, L. P. Pitaevskii, and S. Stringari, "Dynamics of dark solitons in a trapped superfluid Fermi gas," Phys. Rev. Lett. **106**, 185301 (2011).

[105] A. Spuntarelli, L. D. Carr, P. Pieri, and G. C. Strinati, "Gray solitons in a strongly interacting superfluid Fermi gas," New J. Phys. **13**, 035010 (2011).

[106] D. K. Efimkin and V. Galitski, "Moving solitons in a one-dimensional fermionic superfluid," Phys. Rev. A **91**, 023616 (2015).

[107] A. R. Hammer and A. B. Vorontsov, "Bound collective modes in nonuniform superconductors," Phys. Rev. B **93**, 014503 (2016).

[108] A. Cetoli, J. Brand, R. G. Scott, F. Dalfovo, and L. P. Pitaevskii, "Snake instability of dark solitons in fermionic superfluids," Phys. Rev. A **88**, 043639 (2013).

[109] W. Wen, C. Zhao, and X. Ma, "Dark-soliton dynamics and snake instability in superfluid Fermi gases trapped by an anisotropic harmonic potential," Phys. Rev. A **88**, 063621 (2013).

[110] M. D. Reichl and E. J. Mueller, "Vortex ring dynamics in trapped Bose-Einstein condensates," Phys. Rev. A **88**, 053626 (2013).

[111] P. Scherpelz, K. Padavić, A. Rançon, A. Glatz, I. S. Aranson, and K. Levin, "Phase imprinting in equilibrating Fermi gases: The transience of vortex rings and other defects," Phys. Rev. Lett. **113**, 125301 (2014).

[112] A. Munoz Mateo and J. Brand, "Chladni solitons and the onset of the snaking instability for dark solitons in confined superfluids," Phys. Rev. Lett. **113**, 255302 (2014).

[113] A. Bulgac, M. McNeil Forbes, M. M. Kelley, K. J. Roche, and G. Wlazłowski, "Quantized superfluid vortex rings in the unitary Fermi gas," Phys. Rev. Lett. **112**, 025301 (2014).

[114] M. D. Reichl and E. J. Mueller, "Core filling and snaking instability of dark solitons in spin-imbalanced superfluid Fermi gases," Phys. Rev. A **95**, 053637 (2017).

[115] S. N. Klimin, J. Tempere, and J. T. Devreese, "Finite-temperature effective field theory for dark solitons in superfluid Fermi gases," Phys. Rev. A **90**, 053613 (2014).

[116] G. Lombardi, W. Van Alphen, S. N. Klimin, and J. Tempere, "Soliton-core filling in superfluid Fermi gases with spin imbalance," Phys. Rev. A **93**, 013614 (2016).

[117] A. Bulgac, Y.-L. Luo, and K. J. Roche, "Quantum shock waves and domain walls in the real-time dynamics of a superfluid unitary Fermi gas," Phys. Rev. Lett. **108**, 150401 (2012).

[118] R. G. Scott, F. Dalfovo, L. P. Pitaevskii, S. Stringari, O. Fialko, R. Liao, and J. Brand, "The decay and collisions of dark solitons in superfluid Fermi gases," New J. Phys. **14**, 023044 (2012).

[119] W. Wen and G. Huang, "Dynamics of dark solitons in superfluid Fermi gases in the BCS-BEC crossover," Phys. Rev. A **79**, 023605 (2009).

[120] X.-W. Guan, M. T. Batchelor, and C. Lee, "Fermi gases in one dimension: From Bethe ansatz to experiments," Rev. Mod. Phys. **85**, 1633 (2013).

[121] A. E. Muryshev, H. B. van Linden van den Heuvell, and G. V. Shlyapnikov, "Stability of standing matter waves in a trap," Phys. Rev. A **60**, R2665 (1999).

[122] D. L. Feder, M. S. Pindzola, L. A. Collins, B. I. Schneider, and C. W. Clark, "Dark-soliton states of Bose-Einstein condensates in anisotropic traps," Phys. Rev. A **62**, 053606 (2000).

[123] J. Brand and W. P. Reinhardt, "Solitonic vortices and the fundamental

modes of the "snake instability": Possibility of observation in the gaseous Bose-Einstein condensate," Phys. Rev. A **65**, 043612 (2002).

[124] S. Komineas and N. Papanicolaou, "Solitons, solitonic vortices, and vortex rings in a confined Bose-Einstein condensate," Phys. Rev. A **68**, 043617 (2003).

[125] P. G. Kevrekidis, G. Theocharis, D. J. Frantzeskakis, and A. Trombettoni, "Avoiding infrared catastrophes in trapped Bose-Einstein condensates," Phys. Rev. A **70**, 023602 (2004).

[126] A. M. Kamchatnov and L. P. Pitaevskii, "Stabilization of solitons generated by a supersonic flow of Bose-Einstein condensate past an obstacle," Phys. Rev. Lett. **100**, 160402 (2008).

[127] A. V. Mamaev, M. Saffman, and A. A. Zozulya, "Propagation of dark stripe beams in nonlinear media: Snake instability and creation of optical vortices," Phys. Rev. Lett. **76**, 2262 (1996).

[128] V. Tikhonenko, J. Christou, B. Luther-Davies, and Y. S. Kivshar, "Observation of vortex solitons created by the instability of dark soliton stripes," Opt. Lett. **21**, 1129 (1996).

[129] E. A. Kuznetsov and S. K. Turitsyn, "Instability and collapse of solitons in media with a defocusing nonlinearity," Sov. Phys. JETP **67**, 1583 (1988), [Zh. Eksp. Teor. Fiz. **94**, 119 (1988)].

[130] C. Josserand and Y. Pomeau, "Generation of vortices in a model of superfluid ^{4}He by the Kadomtsev-Petviashvili instability," Europhys. Lett. **30**, 43 (1995).

[131] Y.-a. Liao, A. S. C. Rittner, T. Paprotta, W. Li, G. B. Partridge, R. G. Hulet, S. K. Baur, and E. J. Mueller, "Spin-imbalance in a one-dimensional Fermi gas," Nature (London) **467**, 567 (2010).

[132] M. C. Revelle, J. A. Fry, B. A. Olsen, and R. G. Hulet, "1D to 3D crossover of a spin-imbalanced fermi gas," Phys. Rev. Lett. **117**, 235301 (2016).

[133] K. Sacha and D. Delande, "Proper phase imprinting method for a dark soliton excitation in a superfluid Fermi mixture," Phys. Rev. A **90**, 021604 (2014).

[134] T. Karpiuk, M. Brewczyk, and K. Rzazewski, "Solitons and vortices in ultracold fermionic gases," J. Phys. B **35**, L315 (2002).

[135] Ł. Dobrek, M. Gajda, M. Lewenstein, K. Sengstock, G. Birkl, W. Ertmer, *et al.*, "Optical generation of vortices in trapped Bose-Einstein condensates," Phys. Rev. A **60**, R3381 (1999).

[136] S. Burger, L. D. Carr, P. Öhberg, K. Sengstock, and A. Sanpera, "Generation and interaction of solitons in Bose-Einstein condensates," Phys. Rev. A **65**, 043611 (2002).

[137] C. K. Law, "Dynamic quantum depletion in phase-imprinted generation of dark solitons," Phys. Rev. A **68**, 015602 (2003).

[138] B. Wu, J. Liu, and Q. Niu, "Controlled generation of dark solitons with phase imprinting," Phys. Rev. Lett. **88**, 034101 (2002).

[139] H. Moritz, T. Stöferle, M. Köhl, and T. Esslinger, "Exciting collective oscillations in a trapped 1D gas," Phys. Rev, Lett. **91**, 250402 (2003).

[140] R. M. Lutchyn, M. Dzero, and V. M. Yakovenko, "Spectroscopy of the soliton lattice formation in quasi-one-dimensional fermionic superfluids with population imbalance," Phys. Rev. A **84**, 033609 (2011).

[141] J. M. Edge and N. R. Cooper, "Signature of the Fulde-Ferrell-Larkin-Ovchinnikov phase in the collective modes of a trapped ultracold Fermi gas," Phys. Rev. Lett. **103**, 065301 (2009).

[142] J. M. Edge and N. R. Cooper, "Collective modes as a probe of imbalanced Fermi gases," Phys. Rev. A **81**, 063606 (2010).

[143] M. O. J. Heikkinen and P. Törmä, "Collective modes and the speed of sound in the Fulde-Ferrell-Larkin-Ovchinnikov state," Phys. Rev. A **83**, 053630 (2011).

[144] D. Pekker and C. M. Varma, "Amplitude/Higgs modes in condensed matter physics," Annu. Rev. Condens. Matter Phys. **6**, 269 (2015).

[145] P. B. Littlewood and C. M. Varma, "Amplitude collective modes in superconductors and their coupling to charge-density waves," Phys. Rev. B **26**, 4883 (1982).

[146] R. Matsunaga, Y. I. Hamada, K. Makise, Y. Uzawa, H. Terai, Z. Wang, and R. Shimano, "Higgs amplitude mode in the BCS superconductors $Nb_{1-x}Ti_xN$ induced by terahertz pulse excitation," Phys. Rev. Lett. **111**, 057002 (2013).

[147] P. W. Anderson, "Superconductivity: Higgs, Anderson and all that," Nat. Phys. **11**, 93 (2015).

[148] R. Matsunaga, N. Tsuji, H. Fujita, A. Sugioka, K. Makise, Y. Uzawa, H. Terai, Z. Wang, H. Aoki, and R. Shimano, "Light-induced collective

pseudospin precession resonating with Higgs mode in a superconductor," Science **345**, 1145 (2014).

[149] P. Fulde and R. A. Ferrell, "Superconductivity in a strong spin-exchange field," Phys. Rev. **135**, A550 (1964).

[150] A. I. Larkin and I. U. N. Ovchinnikov, "Nonuniform state of superconductors," Sov. Phys. JETP **20**, 762 (1965), [Zh. Eksp. Teor. Fiz. **47**, 1136 (1964)].

[151] R. Casalbuoni and G. Nardulli, "Inhomogeneous superconductivity in condensed matter and QCD," Rev. Mod. Phys. **76**, 263 (2004).

[152] Y. Matsuda and H. Shimahara, "Fulde–Ferrell–Larkin–Ovchinnikov state in heavy fermion superconductors," J. Phys. Soc. Jpn. **76**, 051005 (2007).

[153] G. Zwicknagl and J. Wosnitza, "Breaking translational invariance by population imbalance: The Fulde–Ferrell–Larkin–Ovchinnikov states," Int. J. Mod. Phys. B **24**, 3915 (2010).

[154] S. Dutta and E. J. Mueller, "Dimensional crossover in a spin-imbalanced Fermi gas," Phys. Rev. A **94**, 063627 (2016), and references therein.

[155] X.-J. Liu, H. Hu, and P. D. Drummond, "Fulde-Ferrell-Larkin-Ovchinnikov states in one-dimensional spin-polarized ultracold atomic Fermi gases," Phys. Rev. A **76**, 043605 (2007).

[156] X.-J. Liu, H. Hu, and P. D. Drummond, "Finite-temperature phase diagram of a spin-polarized ultracold Fermi gas in a highly elongated harmonic trap," Phys. Rev. A **78**, 023601 (2008).

[157] M. M. Parish, S. K. Baur, E. J. Mueller, and D. A. Huse, "Quasi-one-

dimensional polarized Fermi superfluids," Phys. Rev. Lett. **99**, 250403 (2007).

[158] T. Mizushima, K. Machida, and M. Ichioka, "Direct imaging of spatially modulated superfluid phases in atomic fermion systems," Phys. Rev. Lett. **94**, 060404 (2005).

[159] K. Sun and C. J. Bolech, "Oscillatory pairing amplitude and magnetic compressible-incompressible transitions in imbalanced fermionic superfluids in optical lattices of elongated tubes," Phys. Rev. A **85**, 051607 (2012).

[160] L. Radzihovsky and D. E. Sheehy, "Imbalanced Feshbach-resonant Fermi gases," Rep. Prog. Phys. **73**, 076501 (2010).

[161] L. O. Baksmaty, H. Lu, C. J. Bolech, and H. Pu, "A Bogoliubov–de Gennes study of trapped spin-imbalanced unitary Fermi gases," New J. Phys. **13**, 055014 (2011).

[162] G. Koutroulakis, H. Kühne, J. A. Schlueter, J. Wosnitza, and S. E. Brown, "Microscopic study of the Fulde-Ferrell-Larkin-Ovchinnikov state in an all-organic superconductor," Phys. Rev. Lett. **116**, 067003 (2016), and references therein. Also see references in Ref. [154].

[163] See Supplemental Material (Sec. 5.7), which includes Refs. [192–198] for an outline of a protocol to generate C-FFLO states, analytic results, collective-mode spectra at different interactions and spin imbalance, simulations showing instability, and collective modes of a soliton train in the Gross-Pitaevskii and a nonlinear Klein-Grodon equation.

[164] S. Dutta and E. J. Mueller, "Protocol to engineer Fulde-Ferrell-Larkin-Ovchinnikov states in a cold Fermi gas," Phys. Rev. A **96**, 023612 (2017).

[165] Y. Xu, L. Mao, B. Wu, and C. Zhang, "Dark solitons with Majorana fermions in spin-orbit-coupled Fermi gases," Phys. Rev. Lett. **113**, 130404 (2014).

[166] M. Olshanii, "Atomic scattering in the presence of an external confinement and a gas of impenetrable bosons," Phys. Rev. Lett. **81**, 938 (1998).

[167] T. Bergeman, M. G. Moore, and M. Olshanii, "Atom-atom scattering under cylindrical harmonic confinement: Numerical and analytic studies of the confinement induced resonance," Phys. Rev. Lett. **91**, 163201 (2003).

[168] E. Haller, M. J. Mark, R. Hart, J. G. Danzl, L. Reichsöllner, V. Melezhik, P. Schmelcher, and H.-C. Nägerl, "Confinement-induced resonances in low-dimensional quantum systems," Phys. Rev. Lett. **104**, 153203 (2010).

[169] A. F. Andreev, "The thermal conductivity of the intermediate state in superconductors," Sov. Phys. JETP **19**, 1228 (1964), [Zh. Eksp. Teor. Fiz. **46**, 1823 (1964)].

[170] E. T. Whittaker and G. N. Watson, *A Course of Modern Analysis* (Cambridge University Press, Cambridge, 1996).

[171] N. N. Bogoljubov, V. V. Tolmachov, and D. V. Širkov, "A new method in the theory of superconductivity," Fortschr. Phys. **6**, 605 (1958).

[172] P. W. Anderson, "Random-phase approximation in the theory of superconductivity," Phys. Rev. **112**, 1900 (1958).

[173] Y. Nambu, "Quasi-particles and gauge invariance in the theory of superconductivity," Phys. Rev. **117**, 648 (1960).

[174] A. F. Volkov and S. M. Kogan, "Collisionless relaxation of the energy gap in superconductors," Sov. Phys. JETP **38**, 1018 (1974), [Zh. Eksp. Teor. Fiz. **65**, 2038 (1973)].

[175] R. A. Barankov and L. S. Levitov, "Synchronization in the BCS pairing dynamics as a critical phenomenon," Phys. Rev. Lett. **96**, 230403 (2006).

[176] R. A. Barankov, L. S. Levitov, and B. Z. Spivak, "Collective Rabi oscillations and solitons in a time-dependent BCS pairing problem," Phys. Rev. Lett. **93**, 160401 (2004).

[177] T. Cea, C. Castellani, G. Seibold, and L. Benfatto, "Nonrelativistic dynamics of the amplitude (Higgs) mode in superconductors," Phys. Rev. Lett. **115**, 157002 (2015).

[178] D. Podolsky, A. Auerbach, and D. P. Arovas, "Visibility of the amplitude (Higgs) mode in condensed matter," Phys. Rev. B **84**, 174522 (2011).

[179] T. Cea and L. Benfatto, "Nature and Raman signatures of the Higgs amplitude mode in the coexisting superconducting and charge-density-wave state," Phys. Rev. B **90**, 224515 (2014).

[180] X. Han, B. Liu, and J. Hu, "Observability of Higgs mode in a system without Lorentz invariance," Phys. Rev. A **94**, 033608 (2016).

[181] D. Sherman, U. S. Pracht, B. Gorshunov, S. Poran, J. Jesudasan, M. Chand, P. Raychaudhuri, M. Swanson, N. Trivedi, A. Auerbach, *et al.*, "The Higgs mode in disordered superconductors close to a quantum phase transition," Nat. Phys. **11**, 188 (2015).

[182] A. E. Feiguin and D. A. Huse, "Spectral properties of a partially spin-polarized one-dimensional Hubbard/Luttinger superfluid," Phys. Rev. B **79**, 100507(R) (2009).

[183] K. V. Samokhin, "Goldstone modes in Larkin-Ovchinnikov-Fulde-Ferrell superconductors," Phys. Rev. B **81**, 224507 (2010).

[184] K. V. Samokhin, "Spectrum of Goldstone modes in Larkin-Ovchinnikov-Fulde-Ferrell superfluids," Phys. Rev. B **83**, 094514 (2011).

[185] L. Radzihovsky and A. Vishwanath, "Quantum liquid crystals in an imbalanced Fermi gas: Fluctuations and fractional vortices in Larkin-Ovchinnikov states," Phys. Rev. Lett. **103**, 010404 (2009).

[186] L. Radzihovsky, "Fluctuations and phase transitions in Larkin-Ovchinnikov liquid-crystal states of a population-imbalanced resonant Fermi gas," Phys. Rev. A **84**, 023611 (2011).

[187] L. M. Aycock, H. M. Hurst, D. K. Efimkin, D. Genkina, H.-I. Lu, V. M. Galitski, and I. B. Spielman, "Brownian motion of solitons in a Bose–Einstein condensate," Proc. Natl. Acad. Sci. U.S.A. **114**, 2503 (2017).

[188] P. Törmä, "Physics of ultracold Fermi gases revealed by spectroscopies," Phys. Scr. **91**, 043006 (2016).

[189] M. Endres, T. Fukuhara, D. Pekker, M. Cheneau, P. Schauß, C. Gross, E. Demler, S. Kuhr, and I. Bloch, "The 'Higgs' amplitude mode at the two-dimensional superfluid/Mott insulator transition," Nature **487**, 454 (2012).

[190] S. Simonucci, P. Pieri, and G. C. Strinati, "Vortex arrays in neutral trapped Fermi gases through the BCS-BEC crossover," Nat. Phys. **11**, 941 (2015).

[191] S. N. Klimin, J. Tempere, G. Lombardi, and J. T. Devreese, "Finite temperature effective field theory and two-band superfluidity in Fermi gases," Eur. Phys. J. B **88**, 122 (2015).

[192] Y. Sagi, T. E. Drake, R. Paudel, R. Chapurin, and D. S. Jin, "Breakdown of the Fermi liquid description for strongly interacting fermions," Phys. Rev. Lett. **114**, 075301 (2015).

[193] E. D. Belokolos, J. C. Eilbeck, V. Z. Enolskii, and M. Salerno, "Exact energy bands and Fermi surfaces of separable Abelian potentials," J. Phys. A **34**, 943 (2001).

[194] F. Cooper, A. Khare, and U. Sukhatme, "Supersymmetry and quantum mechanics," Phys. Rep. **251**, 267 (1995).

[195] S. Novikov, S. V. Manakov, L. P. Pitaevskii, and V. E. Zakharov, *Theory of Solitons* (Plenum, New York, 1984).

[196] G. Orso, "Attractive Fermi gases with unequal spin populations in highly elongated traps," Phys. Rev. Lett. **98**, 070402 (2007).

[197] R. Askey, "The q-Gamma and q-Beta functions," Applicable Analysis **8**, 125 (1978).

[198] M. Plischke and B. Bergersen, *Equilibrium Statistical Physics* (World Scientific, Singapore, 2006).

CHAPTER 6

ENGINEERING FULDE-FERRELL-LARKIN-OVCHINNIKOV STATES IN A FERMI GAS

This chapter was adapted from "Protocol to engineer Fulde-Ferrell-Larkin-Ovchinnikov states in a cold Fermi gas" by Shovan Dutta and Erich J. Mueller, published in Physical Review A **96**, *023612 (2017).*

6.1 Abstract

We propose a two-step experimental protocol to directly engineer Fulde-Ferrell-Larkin-Ovchinnikov (FFLO) states in a cold two-component Fermi gas loaded into a quasi-one-dimensional trap. First, one uses phase imprinting to create a train of domain walls in a superfluid with equal number of ↑- and ↓-spins. Second, one applies a radio-frequency sweep to selectively break Cooper pairs near the domain walls and transfer the ↑-spins to a third spin state which does not interact with the ↑- and ↓-spins. The resulting FFLO state has exactly one unpaired ↓-spin in each domain wall and is stable for all values of domain-wall separation and interaction strength. We show that the protocol can be implemented with high fidelity at sufficiently strong interactions for a wide range of parameters available in present-day experimental conditions.

6.2 Introduction

Ever since Fulde and Ferrell [1] and Larkin and Ovchinnikov [2] (FFLO) predicted translational symmetry breaking in superconductors with magnetic impurities, there has been an intense search for physical examples of the phenomenon [3]. Although thermodynamic evidence has been found in certain heavy-fermion superconductors [4–13], layered organic superconductors [14–24], and cold Fermi gases in elongated traps [25, 26], the phase space for the FFLO state is generically small. As we suggested in a recent Letter [27], one can enlarge this parameter space by circumventing thermodynamics, and directly engineering the FFLO state. There we argued that such an engineered FFLO superfluid would be long-lived. Here we give a detailed protocol for this engineering, thereby greatly extending the ability to produce and study the FFLO phase.

In a two-component system of fermions, superconductivity typically occurs when spin-$\uparrow$ particles form Cooper pairs with spin-$\downarrow$ particles. Magnetic impurities can change the relative chemical potentials of the $\uparrow$- and $\downarrow$-spins, breaking pairs and frustrating superconductivity. In cold Fermi gases, where the spin-relaxation time exceeds the timescale of the experiment, similar physics occurs when more $\downarrow$-spins than $\uparrow$-spins are placed in a trap, making an imbalanced (or spin-imbalanced) gas. In 1964, Fulde and Ferrell [1] argued that one could find exotic pairing in such systems, where the Cooper pairs condense into a state with finite momentum, $\Delta_0(x) \sim e^{ik_0 x}$. At the same time, Larkin and Ovchinnikov [2] proposed that such systems will have an oscillatory order parameter, $\Delta_0(x) \sim \cos k_0 x$, an ansatz that is energetically more favorable. Subsequent work found that one generally expects a train of domain walls (soli-

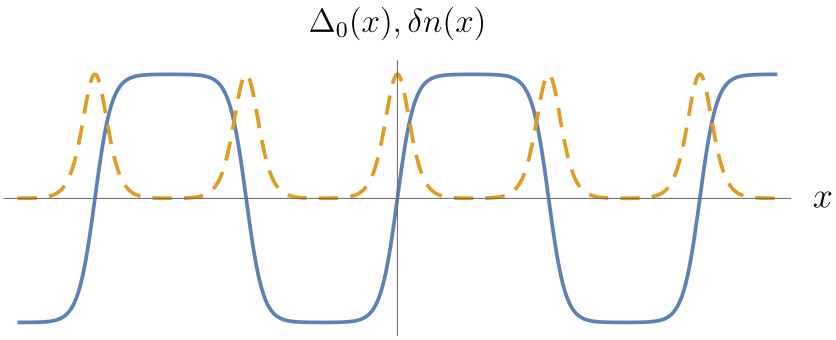

Figure 6.1: Spatial variation in the FFLO state. Solid blue curve shows the order parameter or pair wave function $\Delta_0(x)$. Dashed yellow curve shows the density of unpaired fermions, $\delta n(x) \equiv |n_\uparrow(x) - n_\downarrow(x)|$. The unpaired fermions are localized near the domain walls.

tons), where the order parameter periodically changes sign [28–34]. Larkin and Ovchinnikov's wave function is viewed as a special case, where the width of the domain walls is comparable to their separation. In all cases the spin imbalance is concentrated near the order-parameter nodes, where the density of pairs vanishes (Fig. 6.1). These FFLO states have been predicted to occur in a wide range of physical systems, including heavy-fermion superconductors [35], organic supercoductors [36–39], ultracold Fermi superfluids [40–49], and high-density quark matter [50–56].

In this paper, we present a simple and robust approach to generating an FFLO state in a superfluid of cold fermionic atoms. We build upon the fact that experimentalists routinely produce superfluids of fermionic lithium or potassium atoms [57], control their environment through optical traps [26], control their spin states with radio waves and microwaves [58], and tune their interactions through Feshbach resonance [59]. After engineering these exotic superfluids, they can probe the order parameter using both in-situ techniques [25, 26] and time-of-flight imaging [60–62].

Our approach differs from the conventional method of simply cooling an

imbalanced gas into the FFLO phase. By coherently driving the system into this state, we overcome the hysteresis and metastability issues which can thwart the traditional prescriptions [45].

6.3 Overview

We envision a two-component gas of fermionic atoms (two hyperfine states of ^{6}Li or ^{40}K) with attractive interactions, loaded into a quasi-one-dimensional (quasi-1D) optical trap consisting of an array of weakly coupled 1D tubes (Fig. 6.2). The 1D nature of each tube leads to Fermi-surface nesting, stabilizing the FFLO states [42–45]. The small intertube tunneling helps establish long-range superfluid order [46, 47]. To produce FFLO states in each tube, we propose a two-step protocol. In the first step, one creates an array of domain walls (solitons) in a balanced superfluid. To this end, one loads an equal mixture of $\uparrow$- and $\downarrow$-fermions into the trap and cools the system near a Feshbach resonance to form a superfluid, as demonstrated experimentally in Refs. [25, 26]. One can create solitons in these superfluids by phase imprinting [60–68], whereby one shines an off-resonant laser pulse on selected portions of the superfluid, which rotates the local phase of the order parameter by π. Working in a 3D geometry, past experiments [60–62] have demonstrated that one can create solitons in Fermi superfluids by phase imprinting. The same technique has been used extensively in Bose gases [69–73]. A train of solitons can be formed in each tube by imprinting a π phase in alternate regions of the trap, as illustrated in Fig. 6.2. The tight radial confinement in each tube will prevent the solitons from decaying into vortices and sound waves via the snake instability [62, 74–77]. This first step is straightforward and we do not model it in detail.

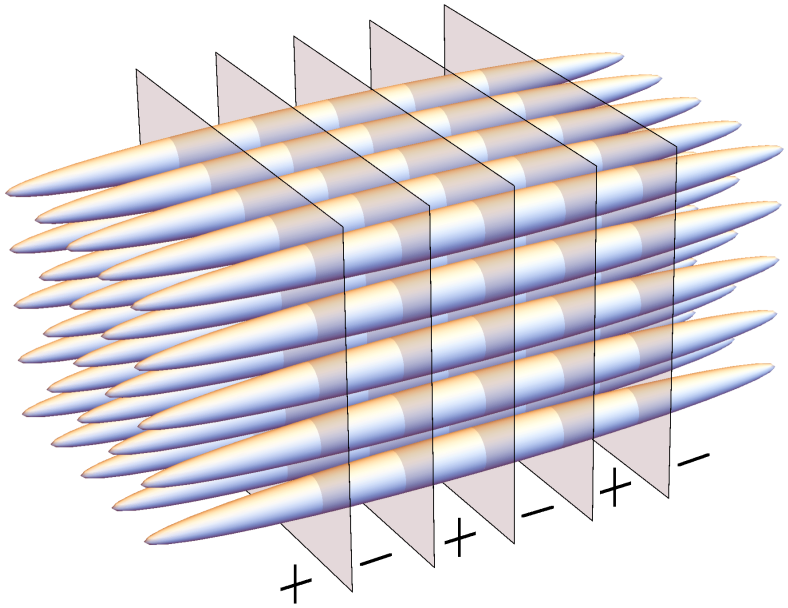

Figure 6.2: Schematic experimental setup for producing balanced soliton trains in an array of weakly coupled tubes. First, uniform superfluids are prepared in each tube by cooling an equal number of attractively interacting ↑- and ↓-fermions near a Feshbach resonance. Then solitons (domain walls) are imprinted by shining off-resonant lasers in alternate regions labeled "$-$" to reverse the sign of the local order parameter.

The subject of this paper is analyzing the second step. Once the domain walls (solitons) are formed, we propose using radio waves to selectively break up Cooper pairs in the soliton cores, transferring spin-↑ atoms at these locations to a third spin state $|\phi\rangle$ which does not interact with the $|\uparrow\rangle$ and $|\downarrow\rangle$ spin states, thus leaving behind an FFLO state with unpaired ↓-spins at the nodes. For example, in ^{40}K one could use $|\uparrow\rangle = |\frac{9}{2}, -\frac{7}{2}\rangle$, $|\downarrow\rangle = |\frac{9}{2}, -\frac{9}{2}\rangle$, and $|\phi\rangle = |\frac{9}{2}, -\frac{5}{2}\rangle$, where the two numbers denote the total atomic spin F and its projection $m_{\rm F}$ [78]. The frequencies for the atomic transitions are sensitive to the local environment, and, as we will show, one can select frequencies such that the transitions only occur near the cores of the domain walls.

In a recent paper [27], we showed that when each soliton in a given tube is filled with exactly one unpaired fermion, the resulting commensurate FFLO (C-

FFLO) phase is stable for all values of soliton spacing and interaction strength. In this paper, we will demonstrate that one can produce such long-lived C-FFLO states in a controlled manner by shining radio waves on a balanced soliton train and performing a frequency sweep.

As we describe in Sec. 6.4, a soliton train has gapped bulk modes that are delocalized, and gapless bound states that are localized in the soliton cores. Our protocol utilizes the separation of energy scales between these localized and bulk excitations. The C-FFLO state differs from a balanced soliton train only in the occupation of the bound states. In our protocol we change these occupations by sweeping the energy of radio waves which couple the $|\uparrow\rangle$ and $|\phi\rangle$ states. As in other applications of Rapid Adiabatic Passage ideas [79–84], the sweep rate must be slow enough to satisfy adiabaticity. However, the sweep duration is limited by the finite lifetime of the balanced soliton train [27]. This lifetime increases sharply with interactions. Therefore, one can achieve higher fidelities when the interactions are stronger. Unwanted bulk excitations caused by the sweep can be eliminated by Pauli blocking if one starts with an appropriate density of $|\phi\rangle$-atoms. Even without Pauli blocking, our approach gives relatively few bulk excitations when the bulk gap is large. A larger bulk gap also yields a higher critical temperature [31–34], thus reducing thermal fluctuations. These arguments further suggest that it is beneficial to work in the strongly interacting regime. We analyze this protocol in detail in Sec. 6.5, showing that current experiments are in a parameter range where one can generate long-lived C-FFLO states with high fidelity.

Our results are based on a mean-field self-consistent Bogoliubov de-Gennes (BdG) formalism which gives an accurate description of quasi-1D Fermi gases

for moderate to weak interactions, and is semiquantitative for stronger interactions [40, 43, 85–94]. In addition, past theoretical studies have shown that 1D BdG equations correctly model the equilibrium properties of an array of tubes [33, 34, 90]. As we will show, our protocol depends primarily on a separation of energy scales between the localized and bulk excitations of a soliton train. It is not contingent on the quantitative details.

The rest of the paper is organized as follows. In Sec. 6.4 we describe the Bogoliubov modes of a train of solitons (or domain walls) and show how the generation of a C-FFLO state from a balanced soliton train is equivalent to changing the mode occupations. In Sec. 6.5, we model the radio-frequency sweep which implements this change. We carefully analyze different processes that could affect the generation of the C-FFLO state, finding parameter regimes where the protocol has high fidelity. We conclude with a summary and outlook in Sec. 6.6.

6.4 Quasiparticle modes

In this section, we cast the problem of generating the C-FFLO state from a balanced soliton train in terms of the occupation of the Bogoliubov modes. This formalism is convenient for modeling the population transfer by the radio-frequency sweep.

We first summarize a few important features of the fermionic quasiparticle spectrum of a soliton train that are relevant for analyzing the effect of a radio-frequency sweep. We will also establish the connection between the occupation of the Bogoliubov modes with the generation of C-FFLO states. Further details on the spectrum of a soliton train can be found in Refs. [27–34].

Following our approach in Ref. [27] we use the Andreev approximation [95], whereby one linearizes the dispersion about the Fermi points and considers right-moving and left-moving modes separately. With this approximation one can solve the BdG equations analytically, which is particularly useful to obtain a qualitative understanding of the physics and estimating the variation of physical quantites, such as the bulk gap, with the experimental parameters. However, this approximation is strictly valid only for weak interactions where pairing is limited to the vicinity of each Fermi point. As we will see in Sec. 6.5, the validity of our protocol does not depend on making the Andreev approximation. It only rests on a few generic features, such as a separation of energy scales between localized and bulk excitations, that are also present in the full model. We will only use the Andreev approximation to estimate the range of parameters over which the protocol has high fidelity. We find good numerical agreement of these estimates with the full BdG equations.

The BdG equations for the coherence factors in a 1D tube can be expressed as

$$\begin{pmatrix} -\partial_x^2/2 - \epsilon_{\mathrm{F}} & \Delta_0(x) \\ \Delta_0^*(x) & \partial_x^2/2 + \epsilon_{\mathrm{F}} \end{pmatrix} \begin{pmatrix} u_j(x) \\ v_j(x) \end{pmatrix} = \epsilon_j \begin{pmatrix} u_j(x) \\ v_j(x) \end{pmatrix}, \tag{6.1}$$

where we have set $\hbar = m = 1$, m being the mass of each fermion. For sufficiently weak interactions, only the modes near the Fermi points contribute to pairing. Thus, as already explained, we make the Andreev approximation, where we write the fermion fields as a sum over right-moving and left-moving Bogoliubov modes $\hat{\gamma}_j^{\pm}$,

$$\begin{pmatrix} \hat{\Psi}_\uparrow(x) \\ \hat{\Psi}_\downarrow^\dagger(x) \end{pmatrix} = \sum_{s=\pm,j} e^{isk_{\mathrm{F}}x} \begin{pmatrix} u_j^s(x) \\ v_j^s(x) \end{pmatrix} \hat{\gamma}_j^s, \tag{6.2}$$

where

$$\left(-\frac{\partial_x^2}{2}-\epsilon_{\rm F}\right)\left[\begin{pmatrix}u_j^{\pm}(x)\\ v_j^{\pm}(x)\end{pmatrix}e^{\pm ik_{\rm F}x}\right]\approx\left[\mp ik_{\rm F}\partial_x\begin{pmatrix}u_j^{\pm}(x)\\ v_j^{\pm}(x)\end{pmatrix}\right]e^{\pm ik_{\rm F}x} \tag{6.3}$$

and $\{\hat{\gamma}_j^s,\hat{\gamma}_{j'}^{s'\dagger}\}=\delta_{ss'}\delta_{jj'}$ where $k_{\rm F}$ is the Fermi momentum. The BdG equations for the right-moving and left-moving Bogoliubov modes can be obtained be substituting $(u_j(x),v_j(x))=(u_j^{\pm}(x),v_j^{\pm}(x))\,e^{\pm ik_{\rm F}x}$ in Eq. (6.1) and using Eq. (6.3), which yield

$$\begin{pmatrix}\mp ik_{\rm F}\partial_x & \Delta_0(x)\\ \Delta_0^*(x) & \pm ik_{\rm F}\partial_x\end{pmatrix}\begin{pmatrix}u_j^{\pm}(x)\\ v_j^{\pm}(x)\end{pmatrix}=\epsilon_j^{\pm}\begin{pmatrix}u_j^{\pm}(x)\\ v_j^{\pm}(x)\end{pmatrix}, \tag{6.4}$$

$$\text{where}\;\;\Delta_0(x)=g_{\rm 1D}\sum_{s=\pm,j}n_{\rm F}(\epsilon_j^s+h)\,u_j^s(x)v_j^{s*}(x)\,. \tag{6.5}$$

For real $\Delta_0(x)$, the right- and left-moving branches are related by a complex conjugation: $(u^-,v^-)=(u^+,v^+)^*$ and $\epsilon^-=\epsilon^+=\epsilon$. Thus we can rewrite Eq. (6.5) as

$$\Delta_0(x)=2g_{\rm 1D}\sum\nolimits_j n_{\rm F}(\epsilon_j+h)\,{\rm Re}\left[u_j^+(x)v_j^{+*}(x)\right]. \tag{6.6}$$

A periodic solution to Eqs. (6.4) and (6.6) has the soliton train profile $\Delta_0(x)=\Delta_1 k_1{\rm sn}(\Delta_1 x/k_{\rm F},k_1)$, where $\Delta_1=2k_{\rm F}k_0K(k_1)/\pi$ [28–34]. Here $2\pi/k_0$ denotes the period, sn is a Jacobi elliptic function [96], K denotes the complete elliptic integral of the first kind, and $k_1\in(0,1)$ parametrizes the sharpness of each soliton. The modes are characterized by the parameter k_1 which is in turn set by the self-consistency condition in Eq. (6.6). Many of our results are conveniently expressed in terms of $w\equiv(k_0/k_{\rm F})\exp(\pi k_{\rm F}a_{\rm 1D}/2)$ where $a_{\rm 1D}$ denotes the 1D scattering length ($a_{\rm 1D}=-2/g_{\rm 1D}$ [97]). The parameter w corresponds to the width of each soliton in units of the separation between solitons (k_0^{-1}). This ratio quantifies the effects of interactions in a soliton train. The width of a soliton is determined by the interaction strength, and for fixed k_0, decreasing the interactions

increases w (recall, $g_{1D} < 0$). If the interactions become too weak, the superfluid becomes too frail to support the soliton train and the system is driven normal. Thus for balanced soliton trains ($h = 0$) one must have $w \lesssim 4$. For $w \lesssim 1$, one enters the strongly interacting regime.

Since $\Delta_0(x)$ is periodic, each Bogoliubov mode can be labeled by a quasi-momentum lying in the first Brillouin zone. The energy spectrum $\epsilon(k)$ is most conveniently expressed in the extended zone representation as

$$\frac{k}{k_0} = \pm\frac{1}{\pi}\frac{\epsilon}{\epsilon_+}\mathrm{Re}\left[\sqrt{\frac{\epsilon_-^2-\epsilon^2}{\epsilon_+^2-\epsilon^2}}\,\Pi\left(\frac{\epsilon_+^2-\epsilon_-^2}{\epsilon_+^2-\epsilon^2}, \sqrt{1-\frac{\epsilon_-^2}{\epsilon_+^2}}\right)\right], \tag{6.7}$$

where $\epsilon_\pm \equiv \frac{1}{2}(1 \pm k_1)\Delta_1$ and Π denotes the complete elliptic integral of the third kind. As per our convention (see Sec. 4.1), the spectrum is symmetric for positive and negative energies. It has a continuum of bulk modes with $|\epsilon| > \epsilon_+$ and a band of midgap modes for with $|\epsilon| < \epsilon_-$, as seen in the boxed region of Fig. 6.3(a). Describing the region outside the box requires going beyond the Andreev approximation. Those modes are not relevant to the processes which we are studying. For sufficiently strong interactions ($w \lesssim 2$), $\epsilon_+ \approx 4k_\mathrm{F}k_0/w$ and $\epsilon_- \approx 16k_\mathrm{F}k_0 w^{-1}e^{-4\pi/w} \ll \epsilon_+$. Hence, the bulk gap increases as $1/w$.

The mode wave functions are of the Bloch form, labeled by a quasimomentum $p \in [-k_0/2, k_0/2)$ and an energy ϵ. The positive and negative energy modes are related by a particle-hole transformation: $(u(x), v(x)) \leftrightarrow (-v(x), u(x))$. In addition, one has the symmetry $(u^\pm_{-p}(x), v^\pm_{-p}(x)) = (v^{\pm *}_p(x), u^{\pm *}_p(x))$ for modes with the same energy. The midgap modes represent Andreev bound states which are localized in the soliton cores [98, 99]. For strong enough interactions ($w \lesssim 3$), they are given by (for $\epsilon, p > 0$)

$$\begin{pmatrix} u_p^+(x) \\ v_p^+(x) \end{pmatrix} \approx \sqrt{\frac{\xi}{L}} \begin{pmatrix} \sum_{n\,\mathrm{even}} \\ -i\sum_{n\,\mathrm{odd}} \end{pmatrix} \frac{e^{i(p+nk_0)x}}{\cosh\left(2\xi(n+\frac{p}{k_0})\right)}, \tag{6.8}$$

where L denotes the length of the system, and $\xi = \pi w/16$ represents the width of a bound state around a soliton core: to a good approximation, $|u_p^+(x)|^2, |v_p^+(x)|^2 \propto \exp(-(k_0 x/\sqrt{2}\xi)^2)$ for $|k_0 x| < \pi/2$.

The higher-energy bulk modes are relatively unaffected by pairing. Hence, they are well described by plane waves. The lowest-energy bulk mode ($|\epsilon| = \epsilon_+$) is the one most affected. For $w \lesssim 2$, this mode is given by (for $\epsilon, p > 0$)

$$\begin{pmatrix} u^+(x) \\ v^+(x) \end{pmatrix} \approx \frac{w}{8\sqrt{L}} \begin{pmatrix} \sum_{n \text{ even}} \\ -i \sum_{n \text{ odd}} \end{pmatrix} \frac{e^{i(n+1/2)k_0 x}}{\sinh\left(\frac{\pi w}{8}(n+\frac{1}{2})\right)}. \tag{6.9}$$

Note that the coherence factors $u_p^+(x)$ [and $v_p^+(x)$] for both midgap modes and bulk modes can be written in the form $u_p^+(x) = (1/\sqrt{L}) \sum_n \bar{u}_{p,n}^j e^{i(p+2nk_0)x}$ where n is an integer and $-k_0 \le p < k_0$. This is because the soliton train has an additional symmetry, $\Delta_0(x + \pi/k_0) = -\Delta_0(x)$, which decouples the even and odd Fourier modes in the BdG equations, effectively doubling the size of the Brillouin zone [27, 91].

For $h \neq 0$, the number of excess fermions per soliton n_s is simply related to the spectrum $\epsilon(k)$ in Eq. (6.7) as $n_s = 2|k_h|/k_0$ where $\epsilon(k_h) = h$. Hence, the C-FFLO state, with $n_s = 1$, is formed when $\epsilon_- < |h| < \epsilon_+$ [see Fig. 6.3(a)]; i.e., when the chemical potentials lie in the gap between bulk modes and midgap modes. Since $\mu_{\uparrow,\downarrow} \equiv \epsilon_F \mp h$, a C-FFLO state with excess $\downarrow$-spins is formed when $\epsilon_- < h < \epsilon_+$, whereas the one with excess $\uparrow$-spins is formed when $-\epsilon_+ < h < -\epsilon_-$.

In our convention, detailed in Chapter 4, the occupation of a Bogoliubov mode $\hat{\gamma}_j$ at zero temperature is given by $\langle \hat{\gamma}_j^\dagger \hat{\gamma}_j \rangle = \Theta(-\epsilon_j - h)$, where Θ denotes the unit step function. Therefore, a balanced soliton train ($h = 0$) is formed by

filling up all the negative energy modes. In a C-FFLO state with excess ↓-spins, only the negative energy bulk modes, with $\epsilon < -\epsilon_+$, are occupied. Therefore, one can produce such a state by vacating all the occupied midgap modes in a balanced soliton train. Conversely, to produce a C-FFLO state with excess ↑-spins, one needs to fill all the unoccupied midgap modes. This change of occupation can be achieved by a radio-frequency sweep, which we model in the next section.

6.5 Generation of C-FFLO states

Here we model the process of generating a C-FFLO state from a balanced soliton train by a radio-frequency sweep. We describe in detail the physics behind the protocol in Sec. 6.5.1. In Sec. 6.5.2 through 6.5.7 we explore various processes which could interfere with producing the FFLO state, explaining how to choose parameters. We show that the protocol can be implemented with high fidelity in present-day experimental conditions.

Our strategy is to use radio waves to selectively break up pairs in the soliton cores, and convert the spin-↑ atoms to a third noninteracting spin state $|\phi\rangle$. As we described in the last section, a balanced soliton train differs from a C-FFLO state in the occupation of the Bogoliubov modes. In our convention, the quasiparticle spectrum of a soliton train is symmetric for positive and negative energies, with delocalized bulk modes for $|\epsilon| > \epsilon_+$ and localized midgap modes for $|\epsilon| < \epsilon_-$ [Fig. 6.3(a)]. All negative energy modes are occupied in a balanced soliton train. The C-FFLO state with excess ↓-spins is formed by removing all quasiparticles from the midgap modes. Our key idea is to use a Rapid Adia-

batic Passage protocol which uses a radio-frequency (RF) sweep to vacate these midgap modes by transferring the spin-$\uparrow$ atoms to the $|\phi\rangle$ state. A preformed Fermi sea of $|\phi\rangle$-atoms prevents any bulk excitation, though even without the Fermi sea the number of bulk excitations can be small.

6.5.1 Modeling the radio-frequency sweep

We model the coupling of the atoms to radio waves by

$$\hat{H}_{\text{RF}} = \Omega \int dx\, \hat{\Phi}^\dagger(x)\, \hat{\Psi}_\uparrow(x)\, e^{-i\int dt\, \omega(t)} + \text{h.c.}\,, \tag{6.10}$$

where $\hat{\Phi}^\dagger(x)$ creates a fermion at position x in the spin state $|\phi\rangle$, Ω is the coupling strength, and $\omega(t)$ is the frequency of the radio waves. In our protocol one sweeps ω over a small frequency range (a few kHz) around $\Delta\epsilon_{\text{hf}}$, where $\Delta\epsilon_{\text{hf}}$ is the internal energy difference of the $|\uparrow\rangle$ and $|\phi\rangle$ states (hundreds of MHz). Throughout the sweep the coupling is far-off-resonant for the spin-$\downarrow$ atoms. We can write Eq. (6.10) in terms of the Bogoliubov operators $\hat{\gamma}_j$ as

$$\hat{H}_{\text{RF}} = \Omega \sum_j \int dx\, \hat{\Phi}^\dagger(x)\, u_j(x) \hat{\gamma}_j\, e^{-i\int dt\, \omega(t)} + \text{h.c.}\,. \tag{6.11}$$

As can be seen, within our convention, the RF coupling removes quasiparticles from the superfluid while creating particles in the $|\phi\rangle$ state, and *vice-versa*. There are right-moving and left-moving Bogoliubov modes centered at the two Fermi points [Fig. 6.3(a)]. They respond equally to the applied field, so we will only consider the right-moving modes. As we showed in Sec. 6.4, each right-moving mode can be labeled by a quasimomentum $p \in [-k_0, k_0)$, and an energy ϵ indexed by j, with wave functions of the form $u_p^j(x) = (1/\sqrt{L}) \sum_n \bar{u}_{p,n}^j e^{i(k_{\text{F}}+p+2nk_0)x}$ where n is an integer. The noninteracting state $|\phi\rangle$ is composed of plane-wave

eigenstates, $\hat{\Phi}^\dagger(x) = (1/\sqrt{L})\sum_k e^{-ikx}\hat{\phi}^\dagger_k$. As a result, radio waves only couple $|\phi\rangle$ states with momentum $k_\mathrm{F} + k$ to Bogoliubov modes with quasimomentum p_k such that $p_k + 2n_k k_0 = k$ for some integer n_k, or $p_k = k - 2k_0\lfloor k/2k_0 + 1/2\rfloor$. Thus we can rewrite Eq. (6.11) as

$$\hat{H}^+_\mathrm{RF} = \Omega \sum_k \sum_j \bar{u}^j_k \hat{\phi}^\dagger_{k_\mathrm{F}+k} \hat{\gamma}^j_{p_k} e^{-i\int dt\,\omega(t)} + \text{h.c.}\,, \tag{6.12}$$

where the superscript '+' indicates that we are working with the right-moving Bogoliubov modes, the k-summation is over all momenta, the j-summation is over different modes with the same quasimomentum p_k, and $\bar{u}^j_k \equiv \bar{u}^j_{p_k,n_k}$.

The effect of the coupling in Eq. (6.12) is best understood in a repeated-zone representation of the Bogoliubov modes. This is shown by the blue curves in Fig. 6.3(b) where we also plot the spectrum of the $|\phi\rangle$ states shifted down by ω (red curve). Near the Fermi point, the $|\phi\rangle$ spectrum is linear with slope k_F. In this repeated-zone picture, a $|\phi\rangle$ state is coupled to the quasiparticle states at the same momentum, and the coupling is on resonance where the red curve intersects a blue curve. In the experiment, one sweeps ω over a small range from ω_max to ω_min such that all the occupied midgap modes come on resonance at least once, as in Fig. 6.3(b). If the sweep is sufficiently adiabatic, the RF coupling will vacate these modes, while populating the resonantly coupled $|\phi\rangle$ states [Fig. 6.3(c)]. Since the $|\phi\rangle$-atoms are noninteracting, or very weakly interacting, their momentum distribution cannot change appreciably over the sweep duration, so there is no possibility of refilling any of the unoccupied midgap modes.

There may also be transitions from the bulk modes. These unwanted transitions can be entirely eliminated if all of the $|\phi\rangle$ states below an energy threshold ϵ_ϕ are initially occupied, so that the available $|\phi\rangle$ states are far-off-resonant with

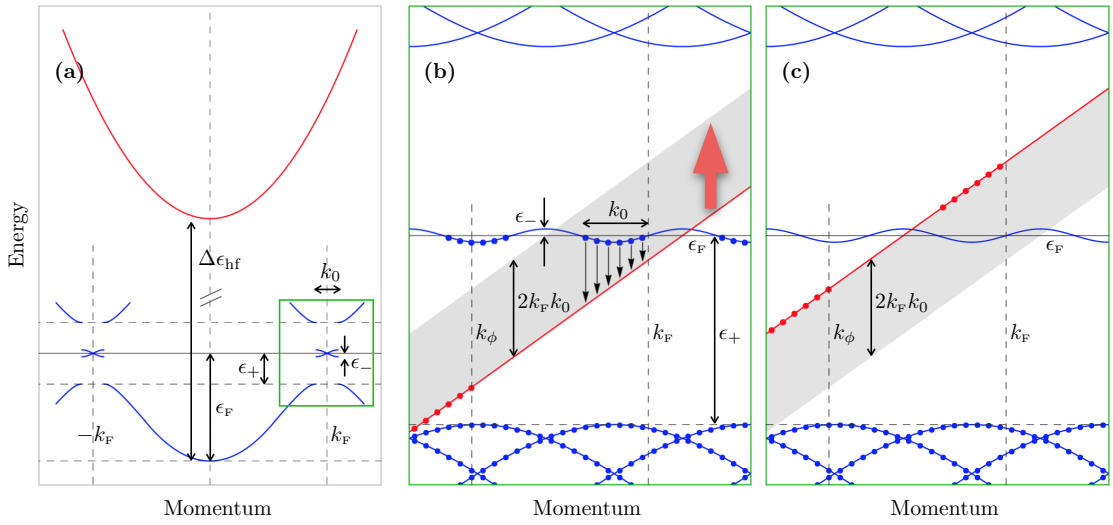

Figure 6.3: Bogoliubov mode occupations during a radio frequency sweep which drives a balanced soliton train into an FFLO state. **(a)** Blue curves show the Bogoliubov spectrum of a soliton train, containing bulk modes with $|\epsilon| > \epsilon_+$ and midgap modes with $|\epsilon| < \epsilon_-$, where ϵ is measured from the Fermi level $\epsilon_{\rm F}$. Red curve shows the quadratic dispersion of a noninteracting spin state $|\phi\rangle$. The internal energy difference is large compared to the Fermi energy, $\Delta\epsilon_{\rm hf} \gg \epsilon_{\rm F}$. **(b,c)** Blue curves show the right-moving Bogoliubov modes [boxed in **(a)**] in the repeated-zone representation. Red line shows the $|\phi\rangle$ dispersion shifted by the radio frequency ω, which is swept from $\omega_{\rm max} = \Delta\epsilon_{\rm hf} + k_{\rm F}k_0/2$ [in **(b)**] to $\omega_{\rm min} = \Delta\epsilon_{\rm hf} - 3k_{\rm F}k_0/2$ [in **(c)**]. Small dots indicate occupied states. The RF sweep couples a filled quasiparticle state with an empty $|\phi\rangle$ state at the same momentum and *vice versa*. If the coupling is sufficiently adiabatic (see Sec. 6.5.2), the sweep will transfer all particles from the midgap modes to the resonantly coupled $|\phi\rangle$ states [as in **(c)**]. If all $|\phi\rangle$ states below a suitable momentum $k_\phi \equiv \sqrt{2\epsilon_\phi}$ are initially occupied, the sweep does not affect the bulk modes or the vacant midgap modes.

the bulk modes [Fig. 6.3(b)]. As we show below, this can be achieved for a wide range of parameters. Alternatively, if it is inconvenient to pre-fill the trap with $|\phi\rangle$-atoms, one can tune the sweep rate so that it is adiabatic for the midgap modes, but diabatic for the bulk modes, thus only causing transition from the midgap modes. This latter approach requires a separation of scales in the coherence factors $|\bar{u}^j_k|$ in Eq. (6.12) between the bulk and the midgap modes. As we will show, this separation of scales exists and becomes larger at stronger

interactions.

6.5.2 Adiabaticity requirements for midgap modes

We model a linear frequency sweep with ω decreasing from $\omega_{\text{max}} = \Delta\epsilon_{\text{hf}} + k_{\text{F}}k_0/2$ to $\omega_{\text{min}} = \Delta\epsilon_{\text{hf}} - 3k_{\text{F}}k_0/2$ at a rate ν, as depicted in Figs. 6.3(b) and 6.3(c). During this evolution, each midgap mode is swept through resonance with a $|\phi\rangle$ state with $k \in [-k_0, 0]$. The coherence factors $|\bar{u}_k^g|$ ('g' refers to midgap modes) in this interval are larger than those in any other interval. For each value of $k \in [-k_0, 0]$, the RF coupling in Eq. (6.12) is well-approximated by a two-level finite duration Landau-Zener problem between a midgap state and a $|\phi\rangle$ state [83, 84]. In order for the transfer probability to be unity, one needs both that the sweep rate is sufficiently small, and that the frequency range of the sweep is sufficiently large. For our system, these two requirements yield

$$k_{\text{F}}k_0 \gtrsim 10\,\Omega\,|\bar{u}_k^g| \;\text{ and }\; \Omega\,|\bar{u}_k^g| \gtrsim \sqrt{\nu} \;\text{ for all }\; k \in [-k_0, 0]\,. \tag{6.13}$$

In Sec. **??** we showed that for sufficiently strong interactions ($w \lesssim 3$, where $w \equiv (k_0/k_{\text{F}})\exp(\pi k_{\text{F}} a_{1\text{D}}/2)$), $|\bar{u}_k^g|$ is well-approximated by $|\bar{u}_k^g| \approx \sqrt{\xi}\,\text{sech}(2\xi k/k_0)$, where $\xi = \pi w/16$ measures the spatial width of a midgap state around a soliton core. Thus we can rewrite the conditions in Eq. (6.13) in terms of w as

$$k_{\text{F}}k_0 \gtrsim 10\,\Omega\sqrt{\xi} \;\text{ and }\; \Omega\sqrt{\xi} \gtrsim \sqrt{\nu}\cosh(2\xi)\,, \tag{6.14}$$

$$\text{where }\; \xi(w) \approx \pi w/16\,. \tag{6.15}$$

Note that $\Omega\sqrt{\xi}$ acts as the effective coupling strength. This is sensible because the coupling strength involves the inner product of a midgap state and a plane wave, which is indeed proportional to the square root of the width ξ of the midgap state.

6.5.3 Eliminating bulk excitations by Pauli blocking

As previously explained, if one starts with a Fermi sea of $|\phi\rangle$-atoms, Pauli blocking prevents any excitation from the occupied bulk modes. This requires that the Fermi energy ϵ_ϕ is sufficiently large. However, if it is too large, one may transfer atoms from the $|\phi\rangle$ states to the vacant quasiparticle modes. Here we calculate the bounds on ϵ_ϕ. We find that the lower and upper bounds are well separated for strong enough interactions.

We can estimate a lower bound on ϵ_ϕ by calculating the effect on the bulk mode b^* with the smallest detuning from resonance, which occurs at $k_\mathrm{F} + k = k_\phi \equiv \sqrt{2\epsilon_\phi}$ when $\omega = \omega_\mathrm{max}$ [Fig. 6.3(b)]. The finite duration Landau-Zener problem gives negligible transfer probability if

$$\epsilon_\mathrm{F} - \epsilon_\phi \lesssim \epsilon_+ - k_\mathrm{F} k_0/2 - 10\,\Omega \left|\bar{u}^{b^*}_{k_\phi - k_\mathrm{F}}\right|. \tag{6.16}$$

Similarly, the upper bound on ϵ_ϕ is set by requiring that no particle is transferred from a filled $|\phi\rangle$ state to an empty midgap state. The smallest detuning for such a coupling occurs at $k = k_\phi - k_\mathrm{F}$ when $\omega = \omega_\mathrm{min}$ [Fig. 6.3(c)]. The transfer probability approaches zero if

$$\epsilon_\mathrm{F} - \epsilon_\phi \gtrsim \epsilon_- + 3k_\mathrm{F} k_0/2 + 10\,\Omega \left|\bar{u}^{g}_{k_\phi - k_\mathrm{F}}\right|. \tag{6.17}$$

The conditions in Eqs. (6.16) and (6.17) simplify for $w \lesssim 2$, where $\epsilon_- \approx 0$, $\epsilon_+ \approx 4k_\mathrm{F}k_0/w$, $|\bar{u}^g_k| \approx \sqrt{\xi}\,\mathrm{sech}(2\xi k/k_0)$, and $|\bar{u}^{b^*}_k| \approx |k_0/\pi k|$ for $k < -k_0/2$ (details in Sec. **??**). Combining these estimates with Eq. (6.14) and using the inequality $k_\mathrm{F} - k_\phi \gtrsim (\epsilon_\mathrm{F} - \epsilon_\phi)/k_\mathrm{F} > 0$, we can write

$$\Omega \left|\bar{u}^{g}_{k_\phi - k_\mathrm{F}}\right| < \Omega\sqrt{\xi} \lesssim 0.1\, k_\mathrm{F} k_0, \quad \text{and} \tag{6.18}$$

$$\Omega \left|\bar{u}^{b^*}_{k_\phi - k_\mathrm{F}}\right| \lesssim \frac{1}{\pi}\frac{\Omega\, k_\mathrm{F} k_0}{\epsilon_\mathrm{F} - \epsilon_\phi} \lesssim \frac{0.1}{\pi\sqrt{\xi}}\frac{(k_\mathrm{F}k_0)^2}{\epsilon_\mathrm{F} - \epsilon_\phi} \approx \frac{0.4}{\pi^{\frac{3}{2}}\sqrt{w}}\frac{(k_\mathrm{F}k_0)^2}{\epsilon_\mathrm{F} - \epsilon_\phi}. \tag{6.19}$$

Substituting these upper bounds into Eqs. (6.16) and (6.17), we find that the inequalities will be satisfied if

$$(5/2)\,k_{\rm F}k_0 \lesssim \epsilon_{\rm F} - \epsilon_\phi \lesssim \left(4/w - 1/2 - \sqrt{w}/\pi^{3/2}\right) k_{\rm F}k_0\,. \tag{6.20}$$

Note that Eq. (6.20) gives only sufficient, not necessary, conditions on the energy threshold ϵ_ϕ. In practice, the bounds on ϵ_ϕ would be less stringent than in Eq. (6.20).

6.5.4 Bulk excitations without Pauli blocking

If all $|\phi\rangle$ states are initially empty, the RF coupling will excite particles from the occupied bulk modes to these empty $|\phi\rangle$ states. Here we estimate an upper bound on the probability P_b of such excitations.

The coherence factors $|\bar{u}_k^j|$ in Eq. (6.12) fall off as one moves away from the Fermi point. Thus P_b is maximum for the bulk mode b_+ which is resonantly coupled to a $|\phi\rangle$ state at the smallest magnitude of k, which occurs for $(k_{\rm F}+k)^2/2 \approx \epsilon_{\rm F} - \epsilon_+$ [Figs. 6.3(b) and 6.3(c)], or $k \approx \sqrt{2(\epsilon_{\rm F}-\epsilon_+)} - k_{\rm F} \lesssim k_+ \equiv -\epsilon_+/k_{\rm F}$. For $w \lesssim 2$, $k_+ \approx 4k_0/w$ (see Sec. 6.4). The corresponding coherence factor is given by $|\bar{u}_{k_+}^{b_+}| \approx |k_0/\pi k_+| \approx w/(4\pi)$, which is linear in w. In contrast, the coherence factors for resonantly coupled midgap modes (see Sec. 6.5.2) are given by $|\bar{u}_k^g| \gtrsim \sqrt{\pi w/16}\,\mathrm{sech}(\pi w/8) \sim \mathcal{O}(\sqrt{w})$ for small w. Hence the coherence factors for bulk excitations fall off much faster with stronger interactions (smaller w), which means one can tune the coupling strength Ω so that the RF sweep is adiabatic for midgap modes, but diabatic for bulk modes.

In particular, at the lower bound of the coupling strength for adiabaticity in

Eq. (6.14), a Landau-Zener analysis for the bulk mode b_+ gives

$$P_b \lesssim 1 - e^{-2\pi \left|\bar{u}_{k_+}^{b_+}\right|^2 \Omega^2/\nu} \approx 1 - e^{-(2w/\pi^2)\cosh^2(\pi w/8)}\,, \tag{6.21}$$

which falls toward zero as interactions are increased. For $w = 2$, $P_b \lesssim 0.5$, and for $w = 1$, $P_b \lesssim 0.2$. Thus even without Pauli blocking, one excites a small fraction of the bulk modes at strong enough interactions.

6.5.5 Condition for dynamical stability

In Ref. [27] we showed that a balanced soliton train has dynamical instabilities toward a uniform superfluid phase. The instability consists of neighboring solitons approaching one another and annihilating after a characteristic lifetime set by the maximum instability rate η_{max}. For our protocol to work properly, the sweep duration τ_{sw} must be short compared to this lifetime, i.e., $\tau_{\text{sw}} \ll \eta_{\text{max}}^{-1}$, as otherwise the soliton train would decay before the sweep is completed. In Ref. [27] we found an upper bound on η_{max} in the full BdG dynamics, $\eta_{\text{max}} \lesssim 2\sqrt{\epsilon_+\epsilon_-}$. For $w \lesssim 2$, this upper bound can be expressed as (see Sec. 6.4)

$$\eta_{\text{max}} \lesssim 2\sqrt{\epsilon_+\epsilon_-} \approx k_{\text{F}} k_0 f(w)\,, \tag{6.22}$$

$$\text{where} \quad f(w) \approx 16\, w^{-1} e^{-2\pi/w}\,. \tag{6.23}$$

Note that η_{max} decreases sharply with w, as stronger interactions stabilize the soliton train. The sweep duration is given by $\tau_{\text{sw}} = 2k_{\text{F}}k_0/\nu$. Hence, the condition $\tau_{\text{sw}} \ll \eta_{\text{max}}^{-1}$ will be satisfied if

$$1/f(w) \gg 2(k_{\text{F}}k_0)^2/\nu\,. \tag{6.24}$$

Note that Eq. (6.24) is again a sufficient condition, not a necessary one.

6.5.6 Implication for interaction strength

Combining the adiabaticity requirements in Eq. (6.14) and the stability condition in Eq. (6.24), we obtain

$$\frac{1}{f(w)} \gg \frac{2(k_F k_0)^2}{\nu} \gtrsim 200 \frac{\Omega^2 \xi(w)}{\nu} \gtrsim 200 \cosh^2(2\xi(w)) \tag{6.25}$$

[Recall, w parametrizes the interaction strength, $f(w)$ is given by Eq. (6.23), and $\xi(w)$ is given by Eq. (6.15)]. To satisfy this inequality, one must have $1/f(w) \gg 200 \cosh^2(2\xi(w))$, which occurs for $w < 3/4$, i.e., in the strongly interacting regime. Quantitative calculations in this regime may require going beyond the Andreev approximation. Nevertheless, our estimates should be robust. Firstly, the procedure itself rests on very generic features which do not depend on the specifics of the model, such as (i) the principle of Rapid Adiabatic Passage to transfer particles between two states [79–84], (ii) a separation of energy scales between the localized and bulk quasiparticle modes, and (iii) symmetry properties of a soliton train. Therefore Eqs. (6.14), (6.16), (6.17), and (6.24) remain valid in the full model. We have only invoked the Andreev approximation in writing down expressions for $\xi(w)$ and $f(w)$ in Eqs. (6.15) and (6.23), and in estimating the bounds in Eqs. (6.20) and (6.21). By numerically solving the full BdG equations, we find good agreement with these estimates at strong interactions. Further, as we discussed earlier, stronger interactions yield a large bulk gap, which increases the critical temperature of the superfluid [31–34], thus reducing the effect of thermal fluctuations which we have ignored. Hence, our protocol will have a high fidelity in the strongly interacting regime. Note that experimentalists routinely tune the atomic interactions from very small to very large values using a Feshbach resonance [59].

6.5.7 Typical experimental parameters

As a specific example, suppose we would like to create a C-FFLO state where adjacent domain walls are separated by $\pi/k_0 \sim 10$ μm. This lengthscale is compatible with phase imprinting, where achievable lengthscales are ultimately limited by diffraction. We consider the parameters in Ref. [25] where ^{6}Li atoms were trapped in quasi-1D tubes with $\epsilon_{\rm F} = 1.2$ μK, or $k_{\rm F} = 5.4 \times 10^6$ m^{-1}. Then a 10 μm soliton spacing corresponds to $k_0/k_{\rm F} \approx 0.05$. To ensure the soliton train is stable thoughout the sweep, we require $\eta_{\rm max}\tau_{\rm sw} \approx 1/20$. Then Eq. (6.25) gives

$$\frac{1}{f(w)} \gg \frac{40(k_{\rm F}k_0)^2}{\nu} \gtrsim 4000\,\frac{\Omega^2\xi(w)}{\nu} \gtrsim 4000\cosh^2(2\xi(w)). \tag{6.26}$$

Comparing the first and last terms, we get $w \lesssim 0.54$ or $k_{\rm F}a_{\rm 1D} \lesssim 1.5$, which could be set by tuning a magnetic field around a Feshbach resonance [59]. For comparison, in Ref. [25] $k_{\rm F}a_{\rm 1D} \approx 0.6$. For $k_{\rm F}a_{\rm 1D} = 1.5$, the instability rate is $\eta_{\rm max} \lesssim k_{\rm F}k_0 f(w) \approx 3.8$ s^{-1}, which gives a sweep duration $\tau_{\rm sw} \sim 1/(20\eta_{\rm max}) \approx 13$ ms. During this interval the frequency is to be varied over a range $\Delta\omega = 2k_{\rm F}k_0 \approx 5$ kHz, at a rate $\nu \approx 3.8 \times 10^5$ Hz/s. Equating the middle terms in Eq. (6.26) yields a Rabi frequency $\Omega \sim k_{\rm F}k_0/(10\sqrt{\xi}) \approx 0.77$ kHz. To suppress unwanted quasiparticle excitations, one can fill up all $|\phi\rangle$ states with energy below ϵ_ϕ where, from Eq. (6.20), 0.4 μK $\lesssim \epsilon_\phi \lesssim$ 0.9 μK. These numbers are well within reach of present-day experiments. Even if one starts with no $|\phi\rangle$-atoms, from Eq. (6.21) we find that the sweep will only excite less than 11% of the bulk modes.

6.6 Summary and outlook

We have described a simple experimental protocol to engineer long-lived FFLO states in a two-component gas of cold fermionic atoms loaded in a quasi-1D trap. The protocol consists of first preparing a train of domain walls in a balanced superfluid by phase imprinting, then using a radio-frequency sweep to selectively transfer the spin-↑ atoms near the domain walls to a third noninteracting spin state $|\phi\rangle$, leaving behind an FFLO state with exactly one unpaired fermion per domain wall. Prior work has shown that this engineered configuration is stable [27]. By analyzing the different limiting factors, we have shown that the protocol can be implemented with high fidelity for sufficiently strong interactions which are readily attainable in current experimental set-ups. It provides a route to directly produce FFLO states in experiments in a controlled manner and study their properties. Such a direct approach complements the thermodynamic search of the exotic state and contributes to the larger goal of engineering many-body quantum states.

In describing the protocol, we have analyzed the case where the frequency is swept over an interval $\Delta\omega = 2k_{\mathrm{F}}k_0$ [Figs. 6.3(b) and 6.3(c)], as this is the shortest sweep which is expected to transfer all of the particles from the localized modes. One can also sweep over larger frequency intervals, but the analysis would have to be repeated to ensure the broader sweep did not excite bulk modes.

Our procedure yields an FFLO state in the presence of a gas of $|\phi\rangle$ atoms. Since the $|\phi\rangle$-atoms are very weakly interacting, they should not affect the dynamics of the soliton train. Alternatively, one could remove all $|\phi\rangle$-atoms after the sweep by a resonant optical pulse [100].

The generated FFLO state can be probed using a variety of techniques that have been proposed in the literature [87, 90–92, 101–109]. For example, one can excite collective modes by ramping to a different interaction strength. If the ramp is fast compared to the bulk gap $\epsilon_+ \approx 4k_{\mathrm{F}}k_0/w$, the domain walls will not have time to adjust their shape, which will excite a novel collective mode where the width of each domain wall oscillates in time [27]. The collective modes could be detected using spectroscopic or imaging techniques [61, 62, 90–92, 110, 111].

Our protocol could be generalized to create incommensurate FFLO states which have less than one excess fermion per soliton, for example, by sweeping over smaller frequency intervals such that only a fraction of the midgap modes are resonantly driven during a sweep. However, since the midgap modes are contiguous in energy, it would be more challenging to control the number of unpaired fermions per soliton.

Finally, a recent study has shown that domain walls are also stabilized in 3D when filled with unpaired fermions [74], which could offer ways of extending our protocol to higher dimensions.

Acknowledgments

This work was supported by the National Science Foundation Grant PHY-1508300.

BIBLIOGRAPHY FOR CHAPTER 6

[1] P. Fulde and R. A. Ferrell, "Superconductivity in a strong spin-exchange field," Phys. Rev. **135**, A550 (1964).

[2] A. I. Larkin and I. U. N. Ovchinnikov, "Nonuniform state of superconductors," Sov. Phys. JETP **20**, 762 (1965), [Zh. Eksp. Teor. Fiz. **47**, 1136 (1964)].

[3] R. Casalbuoni and G. Nardulli, "Inhomogeneous superconductivity in condensed matter and QCD," Rev. Mod. Phys. **76**, 263 (2004).

[4] G. Koutroulakis, M. D. Stewart, Jr., V. F. Mitrović, M. Horvatić, C. Berthier, G. Lapertot, and J. Flouquet, "Field evolution of coexisting superconducting and magnetic orders in $CeCoIn_5$," Phys. Rev. Lett. **104**, 087001 (2010).

[5] K. Cho, B. E. Smith, W. A. Coniglio, L. E. Winter, C. C. Agosta, and J. A. Schlueter, "Upper critical field in the organic superconductor $\beta'' - (ET)_2 SF_5CH_2CF_5SO_3$: Possibility of Fulde-Ferrell-Larkin-Ovchinnikov state," Phys. Rev. B **79**, 220507(R) (2009).

[6] M. Kenzelmann, T. Strässle, C. Niedermayer, M. Sigrist, B. Padmanabhan, M. Zolliker, A. D. Bianchi, R. Movshovich, E. D. Bauer, J. L. Sarrao, *et al.*, "Coupled superconducting and magnetic order in $CeCoIn_5$," Science **321**, 1652 (2008).

[7] C. F. Miclea, M. Nicklas, D. Parker, K. Maki, J. L. Sarrao, J. D. Thompson, G. Sparn, and F. Steglich, "Pressure dependence of the Fulde-Ferrell-Larkin-Ovchinnikov state in $CeCoIn_5$," Phys. Rev. Lett. **96**, 117001 (2006).

[8] K. Kumagai, M. Saitoh, T. Oyaizu, Y. Furukawa, S. Takashima, M. Nohara, H. Takagi, and Y. Matsuda, "Fulde-Ferrell-Larkin-Ovchinnikov state in a

perpendicular field of quasi-two-dimensional $CeCoIn_5$," Phys. Rev. Lett. **97**, 227002 (2006).

[9] K. Kakuyanagi, M. Saitoh, K. Kumagai, S. Takashima, M. Nohara, H. Takagi, and Y. Matsuda, "Texture in the superconducting order parameter of $CeCoIn_5$ revealed by nuclear magnetic resonance," Phys. Rev. Lett. **94**, 047602 (2005).

[10] T. Watanabe, Y. Kasahara, K. Izawa, T. Sakakibara, Y. Matsuda, C. J. Van der Beek, T. Hanaguri, H. Shishido, R. Settai, and Y. Onuki, "High-field state of the flux-line lattice in the unconventional superconductor $CeCoIn_5$," Phys. Rev. B **70**, 020506(R) (2004).

[11] C. Capan, A. Bianchi, R. Movshovich, A. Christianson, A. Malinowski, M. F. Hundley, A. Lacerda, P. G. Pagliuso, and J. L. Sarrao, "Anisotropy of thermal conductivity and possible signature of the Fulde-Ferrell-Larkin-Ovchinnikov state in $CeCoIn_5$," Phys. Rev. B **70**, 134513 (2004).

[12] H. A. Radovan, N. A. Fortune, T. P. Murphy, S. T. Hannahs, E. C. Palm, S. W. Tozer, and D. Hall, "Magnetic enhancement of superconductivity from electron spin domains," Nature (London) **425**, 51 (2003).

[13] A. Bianchi, R. Movshovich, C. Capan, P. G. Pagliuso, and J. L. Sarrao, "Possible Fulde-Ferrell-Larkin-Ovchinnikov superconducting state in $CeCoIn_5$," Phys. Rev. Lett. **91**, 187004 (2003).

[14] G. Koutroulakis, H. Kühne, J. A. Schlueter, J. Wosnitza, and S. E. Brown, "Microscopic study of the Fulde-Ferrell-Larkin-Ovchinnikov state in an all-organic superconductor," Phys. Rev. Lett. **116**, 067003 (2016).

[15] H. Mayaffre, S. Krämer, M. Horvatić, C. Berthier, K. Miyagawa, K. Kanoda, and V. F. Mitrović, "Evidence of Andreev bound states as a hallmark of the FFLO phase in κ-(BEDT-TTF)$_2$Cu(NCS)$_2$," Nat. Phys. **10**, 928 (2014).

[16] C. C. Agosta, J. Jin, W. A. Coniglio, B. E. Smith, K. Cho, I. Stroe, C. Martin, S. W. Tozer, T. P. Murphy, E. C. Palm, *et al.*, "Experimental and semiempirical method to determine the Pauli-limiting field in quasi-two-dimensional superconductors as applied to κ-(BEDT-TTF)$_2$Cu(NCS)$_2$: Strong evidence of a FFLO state," Phys. Rev. B **85**, 214514 (2012).

[17] S. Uji, K. Kodama, K. Sugii, T. Terashima, Y. Takahide, N. Kurita, S. Tsuchiya, M. Kimata, A. Kobayashi, B. Zhou, *et al.*, "Magnetic torque studies on FFLO phase in magnetic-field-induced organic superconductor λ-(BETS)$_2$FeCl$_4$," Phys. Rev. B **85**, 174530 (2012).

[18] B. Bergk, A. Demuer, I. Sheikin, Y. Wang, J. Wosnitza, Y. Nakazawa, and R. Lortz, "Magnetic torque evidence for the Fulde-Ferrell-Larkin-Ovchinnikov state in the layered organic superconductor κ-(BEDT-TTF)$_2$Cu(NCS)$_2$," Phys. Rev. B **83**, 064506 (2011).

[19] J. A. Wright, E. Green, P. Kuhns, A. Reyes, J. Brooks, J. Schlueter, R. Kato, H. Yamamoto, M. Kobayashi, and S. E. Brown, "Zeeman-driven phase transition within the superconducting state of κ-(BEDT-TTF)$_2$Cu(NCS)$_2$," Phys. Rev. Lett. **107**, 087002 (2011).

[20] S. Yonezawa, S. Kusaba, Y. Maeno, P. Auban-Senzier, C. Pasquier, K. Bechgaard, and D. Jérome, "Anomalous in-plane anisotropy of the onset of superconductivity in (TMTSF)$_2$ClO$_4$," Phys. Rev. Lett. **100**, 117002 (2008).

[21] R. Lortz, Y. Wang, A. Demuer, P. H. M. Böttger, B. Bergk, G. Zwicknagl,

Y. Nakazawa, and J. Wosnitza, "Calorimetric evidence for a Fulde-Ferrell-Larkin-Ovchinnikov superconducting state in the layered organic superconductor κ-(BEDT-TTF)$_2$Cu(NCS)$_2$," Phys. Rev. Lett. **99**, 187002 (2007).

[22] S. Uji, T. Terashima, M. Nishimura, Y. Takahide, T. Konoike, K. Enomoto, H. Cui, H. Kobayashi, A. Kobayashi, H. Tanaka, *et al.*, "Vortex dynamics and the Fulde-Ferrell-Larkin-Ovchinnikov state in a magnetic-field-induced organic superconductor," Phys. Rev. Lett. **97**, 157001 (2006).

[23] J. A. Symington, J. Singleton, M.-S. Nam, A. Ardavan, M. Kurmoo, and P. Day, "Evidence for the Fulde–Ferrell–Larkin–Ovchinnikov state in the organic superconductor κ-(BEDT-TTF)$_2$Cu(NCS)$_2$," Physica B **294**, 418 (2001).

[24] J. Singleton, J. A. Symington, M. S. Nam, A. Ardavan, M. Kurmoo, and P. Day, "Observation of the Fulde-Ferrell-Larkin-Ovchinnikov state in the quasi-two-dimensional organic superconductor κ-(BEDT-TTF)$_2$Cu(NCS)$_2$ (BEDT-TTF=bis(ethylene-dithio)tetrathiafulvalene)," J. Phys. Condens. Matter **12**, L641 (2000).

[25] Y.-a. Liao, A. S. C. Rittner, T. Paprotta, W. Li, G. B. Partridge, R. G. Hulet, S. K. Baur, and E. J. Mueller, "Spin-imbalance in a one-dimensional Fermi gas," Nature (London) **467**, 567 (2010).

[26] M. C. Revelle, J. A. Fry, B. A. Olsen, and R. G. Hulet, "1D to 3D crossover of a spin-imbalanced fermi gas," Phys. Rev. Lett. **117**, 235301 (2016).

[27] S. Dutta and E. J. Mueller, "Collective modes of a soliton train in a Fermi superfluid," Phys. Rev. Lett. **118**, 260402 (2017).

[28] S. A. Brazovskii, S. A. Gordyunin, and N. N. Kirova, "An exact solution of the Peierls model with an arbitrary number of electrons in the unit cell," JETP Lett. **31**, 456 (1980), [Pis'ma v Zh. Eksp. Teor. Fiz. **31**, 486 (1980)].

[29] B. Horovitz, "Soliton lattice in polyacetylene, spin-Peierls systems, and two-dimensional sine-Gordon systems," Phys. Rev. Lett. **46**, 742 (1981).

[30] S. A. Brazovskii, N. N. Kirova, and S. I. Matveenko, "The Peierls effect in conducting polymers," Sov. Phys. JETP **59**, 434 (1984), [Zh. Eksp. Teor. Fiz. **86**, 743 (1984)].

[31] J. Mertsching and H. J. Fischbeck, "The incommensurate Peierls phase of the quasi-one-dimensional Fröhlich model with a nearly half-filled band," Phys. Status Solidi (B) **103**, 783 (1981).

[32] K. Machida and H. Nakanishi, "Superconductivity under a ferromagnetic molecular field," Phys. Rev. B **30**, 122 (1984).

[33] A. I. Buzdin and V. V. Tugushev, "Phase diagrams of electronic and superconducting transitions to soliton lattice states," Sov. Phys. JETP **58**, 428 (1983), [Zh. Eksp. Teor. Fiz. **85**, 735 (1983)].

[34] A. I. Buzdin and S. V. Polonskii, "Nonuniform state in quasi-1D superconductors," Sov. Phys. JETP **66**, 422 (1987), [Zh. Eksp. Teor. Fiz. **93**, 747 (1987)].

[35] Y. Matsuda and H. Shimahara, "Fulde–Ferrell–Larkin–Ovchinnikov state in heavy fermion superconductors," J. Phys. Soc. Jpn. **76**, 051005 (2007).

[36] R. Beyer and J. Wosnitza, "Emerging evidence for FFLO states in layered organic superconductors," Low Temp. Phys. **39**, 225 (2013).

[37] H. Shimahara, "Fulde-Ferrell-Larkin-Ovchinnikov state and field-induced superconductivity in an organic superconductor," J. Phys. Soc. Jpn. **71**, 1644 (2002).

[38] M. Houzet, A. Buzdin, L. Bulaevskii, and M. Maley, "New superconducting phases in field-induced organic superconductor λ-$(BETS)_2FeCl_4$," Phys. Rev. Lett. **88**, 227001 (2002).

[39] H. Burkhardt and D. Rainer, "Fulde-Ferrell-Larkin-Ovchinnikov state in layered superconductors," Ann. Phys. (Berlin) **506**, 181 (1994).

[40] L. Radzihovsky and D. E. Sheehy, "Imbalanced Feshbach-resonant Fermi gases," Rep. Prog. Phys. **73**, 076501 (2010).

[41] X.-W. Guan, M. T. Batchelor, and C. Lee, "Fermi gases in one dimension: From Bethe ansatz to experiments," Rev. Mod. Phys. **85**, 1633 (2013).

[42] S. Dutta and E. J. Mueller, "Dimensional crossover in a spin-imbalanced Fermi gas," Phys. Rev. A **94**, 063627 (2016).

[43] M. M. Parish, S. K. Baur, E. J. Mueller, and D. A. Huse, "Quasi-one-dimensional polarized Fermi superfluids," Phys. Rev. Lett. **99**, 250403 (2007).

[44] M. Casula, D. M. Ceperley, and E. J. Mueller, "Quantum Monte Carlo study of one-dimensional trapped fermions with attractive contact interactions," Phys. Rev. A **78**, 033607 (2008).

[45] L. O. Baksmaty, H. Lu, C. J. Bolech, and H. Pu, "Concomitant modulated superfluidity in polarized Fermi gases," Phys. Rev. A **83**, 023604 (2011).

[46] E. Zhao and W. V. Liu, "Theory of quasi-one-dimensional imbalanced Fermi gases," Phys. Rev. A **78**, 063605 (2008).

[47] K. Yang, "Inhomogeneous superconducting state in quasi-one-dimensional systems," Phys. Rev. B **63**, 140511 (2001).

[48] Y. L. Loh and N. Trivedi, "Detecting the elusive Larkin-Ovchinnikov modulated superfluid phases for imbalanced Fermi gases in optical lattices," Phys. Rev. Lett. **104**, 165302 (2010).

[49] M. Rizzi, M. Polini, M. A. Cazalilla, M. R. Bakhtiari, M. P. Tosi, and R. Fazio, "Fulde-Ferrell-Larkin-Ovchinnikov pairing in one-dimensional optical lattices," Phys. Rev. B **77**, 245105 (2008).

[50] A. Sedrakian and D. H. Rischke, "Phase diagram of chiral quark matter: From weakly to strongly coupled Fulde-Ferrell phase," Phys. Rev. D **80**, 074022 (2009).

[51] M. G. Alford, A. Schmitt, K. Rajagopal, and T. Schäfer, "Color superconductivity in dense quark matter," Rev. Mod. Phys. **80**, 1455 (2008).

[52] L. He, M. Jin, and P. Zhuang, "Pion condensation in baryonic matter: From Sarma phase to Larkin-Ovchinnikov-Fudde-Ferrell phase," Phys. Rev. D **74**, 036005 (2006).

[53] I. Giannakis, D.-f. Hou, and H.-C. Ren, "A neutral two-flavor LOFF color superconductor," Phys. Lett. B **631**, 16 (2005).

[54] R. Casalbuoni, M. Ciminale, M. Mannarelli, G. Nardulli, M. Ruggieri, and R. Gatto, "Effective gap equation for the inhomogeneous Larkin-Ovchinnikov-Fulde-Ferrel superconductive phase," Phys. Rev. D **70**, 054004 (2004).

[55] J. A. Bowers and K. Rajagopal, "Crystallography of color superconductivity," Phys. Rev. D **66**, 065002 (2002).

[56] M. Alford, J. A. Bowers, and K. Rajagopal, "Crystalline color superconductivity," Phys. Rev. D **63**, 074016 (2001).

[57] M. W. Zwierlein, "Superfluidity in ultracold atomic Fermi gases," in *Novel Superfluids: Volume 2*, edited by K.-H. Bennemann and J. B. Ketterson (Oxford University Press, Oxford, 2014) Chap. 18, p. 269.

[58] G. B. Partridge, W. Li, R. I. Kamar, Y.-a. Liao, and R. G. Hulet, "Pairing and phase separation in a polarized Fermi gas," Science **311**, 503 (2006).

[59] C. Chin, R. Grimm, P. Julienne, and E. Tiesinga, "Feshbach resonances in ultracold gases," Rev. Mod. Phys. **82**, 1225 (2010).

[60] T. Yefsah, A. T. Sommer, M. J. Ku, L. W. Cheuk, W. Ji, W. S. Bakr, and M. W. Zwierlein, "Heavy solitons in a fermionic superfluid," Nature (London) **499**, 426 (2013).

[61] M. J. H. Ku, W. Ji, B. Mukherjee, E. Guardado-Sanchez, L. W. Cheuk, T. Yefsah, and M. W. Zwierlein, "Motion of a solitonic vortex in the BEC-BCS crossover," Phys. Rev. Lett. **113**, 065301 (2014).

[62] M. J. H. Ku, B. Mukherjee, T. Yefsah, and M. W. Zwierlein, "Cascade of solitonic excitations in a superfluid Fermi gas: From planar solitons to vortex rings and lines," Phys. Rev. Lett. **116**, 045304 (2016).

[63] K. Sacha and D. Delande, "Proper phase imprinting method for a dark soliton excitation in a superfluid Fermi mixture," Phys. Rev. A **90**, 021604 (2014).

[64] C. K. Law, "Dynamic quantum depletion in phase-imprinted generation of dark solitons," Phys. Rev. A **68**, 015602 (2003).

[65] T. Karpiuk, M. Brewczyk, and K. Rzazewski, "Solitons and vortices in ultracold fermionic gases," J. Phys. B **35**, L315 (2002).

[66] S. Burger, L. D. Carr, P. Öhberg, K. Sengstock, and A. Sanpera, "Generation and interaction of solitons in Bose-Einstein condensates," Phys. Rev. A **65**, 043611 (2002).

[67] B. Wu, J. Liu, and Q. Niu, "Controlled generation of dark solitons with phase imprinting," Phys. Rev. Lett. **88**, 034101 (2002).

[68] Ł. Dobrek, M. Gajda, M. Lewenstein, K. Sengstock, G. Birkl, W. Ertmer, *et al.*, "Optical generation of vortices in trapped Bose-Einstein condensates," Phys. Rev. A **60**, R3381 (1999).

[69] S. Stellmer, C. Becker, P. Soltan-Panahi, E.-M. Richter, S. Dörscher, M. Baumert, J. Kronjäger, K. Bongs, and K. Sengstock, "Collisions of dark solitons in elongated Bose-Einstein condensates," Phys. Rev. Lett. **101**, 120406 (2008).

[70] C. Becker, S. Stellmer, P. Soltan-Panahi, S. Dörscher, M. Baumert, E.-M. Richter, J. Kronjäger, K. Bongs, and K. Sengstock, "Oscillations and interactions of dark and dark–bright solitons in Bose–Einstein condensates," Nat. Phys. **4**, 496 (2008).

[71] B. P. Anderson, P. C. Haljan, C. A. Regal, D. L. Feder, L. A. Collins, C. W. Clark, and E. A. Cornell, "Watching dark solitons decay into vortex rings in a Bose-Einstein condensate," Phys. Rev. Lett. **86**, 2926 (2001).

[72] J. Denschlag, J. E. Simsarian, D. L. Feder, C. W. Clark, L. A. Collins, J. Cubizolles, L. Deng, E. W. Hagley, K. Helmerson, W. P. Reinhardt, *et al.*, "Generating solitons by phase engineering of a Bose-Einstein condensate," Science **287**, 97 (2000).

[73] S. Burger, K. Bongs, S. Dettmer, W. Ertmer, K. Sengstock, A. Sanpera, G. V. Shlyapnikov, and M. Lewenstein, "Dark solitons in Bose-Einstein condensates," Phys. Rev. Lett. **83**, 5198 (1999).

[74] M. D. Reichl and E. J. Mueller, "Core filling and snaking instability of dark solitons in spin-imbalanced superfluid Fermi gases," Phys. Rev. A **95**, 053637 (2017).

[75] A. Bulgac, M. McNeil Forbes, M. M. Kelley, K. J. Roche, and G. Wlazłowski, "Quantized superfluid vortex rings in the unitary Fermi gas," Phys. Rev. Lett. **112**, 025301 (2014).

[76] A. Cetoli, J. Brand, R. G. Scott, F. Dalfovo, and L. P. Pitaevskii, "Snake instability of dark solitons in fermionic superfluids," Phys. Rev. A **88**, 043639 (2013).

[77] W. Wen, C. Zhao, and X. Ma, "Dark-soliton dynamics and snake instability in superfluid Fermi gases trapped by an anisotropic harmonic potential," Phys. Rev. A **88**, 063621 (2013).

[78] Y. Sagi, T. E. Drake, R. Paudel, R. Chapurin, and D. S. Jin, "Breakdown of the Fermi liquid description for strongly interacting fermions," Phys. Rev. Lett. **114**, 075301 (2015).

[79] N. V. Vitanov, T. Halfmann, B. W. Shore, and K. Bergmann, "Laser-

induced population transfer by adiabatic passage techniques," Annu. Rev. Phys. Chem. **52**, 763 (2001).

[80] D. Møller, L. B. Madsen, and K. Mølmer, "Quantum gates and multiparticle entanglement by Rydberg excitation blockade and adiabatic passage," Phys. Rev. Lett. **100**, 170504 (2008).

[81] A. A. Rangelov, N. V. Vitanov, L. P. Yatsenko, B. W. Shore, T. Halfmann, and K. Bergmann, "Stark-shift-chirped rapid-adiabatic-passage technique among three states," Phys. Rev. A **72**, 053403 (2005).

[82] V. S. Malinovsky and J. L. Krause, "General theory of population transfer by adiabatic rapid passage with intense, chirped laser pulses," Eur. Phys. J. D **14**, 147 (2001).

[83] N. V. Vitanov and B. M. Garraway, "Landau-Zener model: Effects of finite coupling duration," Phys. Rev. A **53**, 4288 (1996).

[84] J. R. Rubbmark, M. M. Kash, M. G. Littman, and D. Kleppner, "Dynamical effects at avoided level crossings: A study of the Landau-Zener effect using Rydberg atoms," Phys. Rev. A **23**, 3107 (1981).

[85] X.-J. Liu, H. Hu, and P. D. Drummond, "Fulde-Ferrell-Larkin-Ovchinnikov states in one-dimensional spin-polarized ultracold atomic Fermi gases," Phys. Rev. A **76**, 043605 (2007).

[86] X.-J. Liu, H. Hu, and P. D. Drummond, "Finite-temperature phase diagram of a spin-polarized ultracold Fermi gas in a highly elongated harmonic trap," Phys. Rev. A **78**, 023601 (2008).

[87] T. Mizushima, K. Machida, and M. Ichioka, "Direct imaging of spatially

modulated superfluid phases in atomic fermion systems," Phys. Rev. Lett. **94**, 060404 (2005).

[88] L. O. Baksmaty, H. Lu, C. J. Bolech, and H. Pu, "A Bogoliubov–de Gennes study of trapped spin-imbalanced unitary Fermi gases," New J. Phys. **13**, 055014 (2011).

[89] K. Sun and C. J. Bolech, "Oscillatory pairing amplitude and magnetic compressible-incompressible transitions in imbalanced fermionic superfluids in optical lattices of elongated tubes," Phys. Rev. A **85**, 051607 (2012).

[90] R. M. Lutchyn, M. Dzero, and V. M. Yakovenko, "Spectroscopy of the soliton lattice formation in quasi-one-dimensional fermionic superfluids with population imbalance," Phys. Rev. A **84**, 033609 (2011).

[91] J. M. Edge and N. R. Cooper, "Signature of the Fulde-Ferrell-Larkin-Ovchinnikov phase in the collective modes of a trapped ultracold Fermi gas," Phys. Rev. Lett. **103**, 065301 (2009).

[92] J. M. Edge and N. R. Cooper, "Collective modes as a probe of imbalanced Fermi gases," Phys. Rev. A **81**, 063606 (2010).

[93] Y. Xu, L. Mao, B. Wu, and C. Zhang, "Dark solitons with Majorana fermions in spin-orbit-coupled Fermi gases," Phys. Rev. Lett. **113**, 130404 (2014).

[94] D. K. Efimkin and V. Galitski, "Moving solitons in a one-dimensional fermionic superfluid," Phys. Rev. A **91**, 023616 (2015).

[95] A. F. Andreev, "The thermal conductivity of the intermediate state in superconductors," Sov. Phys. JETP **19**, 1228 (1964), [Zh. Eksp. Teor. Fiz. **46**, 1823 (1964)].

[96] E. T. Whittaker and G. N. Watson, *A Course of Modern Analysis* (Cambridge University Press, Cambridge, 1996).

[97] M. Olshanii, "Atomic scattering in the presence of an external confinement and a gas of impenetrable bosons," Phys. Rev. Lett. **81**, 938 (1998).

[98] M. Antezza, F. Dalfovo, L. P. Pitaevskii, and S. Stringari, "Dark solitons in a superfluid Fermi gas," Phys. Rev. A **76**, 043610 (2007).

[99] R. G. Scott, F. Dalfovo, L. P. Pitaevskii, S. Stringari, O. Fialko, R. Liao, and J. Brand, "The decay and collisions of dark solitons in superfluid Fermi gases," New J. Phys. **14**, 023044 (2012).

[100] X. Du, L. Luo, B. Clancy, and J. E. Thomas, "Observation of anomalous spin segregation in a trapped Fermi gas," Phys. Rev. Lett. **101**, 150401 (2008).

[101] H. Lu, L. O. Baksmaty, C. J. Bolech, and H. Pu, "Expansion of 1D polarized superfluids: The Fulde-Ferrell-Larkin-Ovchinnikov state reveals itself," Phys. Rev. Lett. **108**, 225302 (2012).

[102] H. Hu and X.-J. Liu, "Josephson effect in an atomic Fulde-Ferrell-Larkin-Ovchinnikov superfluid," Phys. Rev. A **83**, 013631 (2011).

[103] M. Swanson, Y. L. Loh, and N. Trivedi, "Proposal for interferometric detection of the topological character of modulated superfluidity in ultracold Fermi gases," New J. Phys. **14**, 033036 (2012).

[104] M. R. Bakhtiari, M. J. Leskinen, and P. Törmä, "Spectral signatures of the Fulde-Ferrell-Larkin-Ovchinnikov order parameter in one-dimensional optical lattices," Phys. Rev. Lett. **101**, 120404 (2008).

[105] A. Korolyuk, F. Massel, and P. Törmä, "Probing the Fulde-Ferrell-Larkin-Ovchinnikov phase by double occupancy modulation spectroscopy," Phys. Rev. Lett. **104**, 236402 (2010).

[106] J. Kajala, F. Massel, and P. Törmä, "Expansion dynamics of the Fulde-Ferrell-Larkin-Ovchinnikov state," Phys. Rev. A **84**, 041601(R) (2011).

[107] V. Gritsev, E. Demler, and A. Polkovnikov, "Interferometric probe of paired states," Phys. Rev. A **78**, 063624 (2008).

[108] T. Roscilde, M. Rodríguez, K. Eckert, O. Romero-Isart, M. Lewenstein, E. Polzik, and A. Sanpera, "Quantum polarization spectroscopy of correlations in attractive fermionic gases," New J. Phys. **11**, 055041 (2009).

[109] A. Lüscher, R. M. Noack, and A. M. Läuchli, "Fulde-Ferrell-Larkin-Ovchinnikov state in the one-dimensional attractive Hubbard model and its fingerprint in spatial noise correlations," Phys. Rev. A **78**, 013637 (2008).

[110] P. Törmä, "Physics of ultracold Fermi gases revealed by spectroscopies," Phys. Scripta **91**, 043006 (2016).

[111] M. Endres, T. Fukuhara, D. Pekker, M. Cheneau, P. Schauß, C. Gross, E. Demler, S. Kuhr, and I. Bloch, "The 'Higgs' amplitude mode at the two-dimensional superfluid/Mott insulator transition," Nature **487**, 454 (2012).

CHAPTER 7

DIMENSIONAL CROSSOVER IN A SPIN-IMBALANCED FERMI GAS

This chapter, apart from the Supplement in Sec. 7.7, was adapted from "Dimensional crossover in a spin-imbalanced Fermi gas" by Shovan Dutta and Erich J. Mueller, published in Physical Review A **94**, *063627 (2016).*

7.1 Abstract

We model the one-dimensional (1D) to three-dimensional (3D) crossover in a cylindrically trapped Fermi gas with attractive interactions and spin imbalance. We calculate the mean-field phase diagram and study the relative stability of exotic superfluid phases as a function of interaction strength and temperature. For weak interactions and low density, we find 1D-like behavior, which repeats as a function of the chemical potential as new channels open. For strong interactions, mixing of single-particle levels gives 3D-like behavior at all densities. Furthermore, we map the system to an effective 1D model, finding significant density dependence of the effective 1D scattering length.

7.2 Introduction

Spin-imbalanced Fermi gases are predicted to display an array of exotic superconducting phases, where the order parameter has nontrivial structure [1–82]. Mean-field theories predict that these states occupy a very small fraction of the phase diagram in 3D, but are ubiquitous in 1D [1–16, 18–20], with the caveat

that quantum fluctuations prevent long-range order in 1D [83, 84]. Indeed, cold-atom experiments in 3D [85–90] have found no sign of the exotic Fulde-Ferrell-Larkin-Ovchinnikov (FFLO) phase [91, 92], while experiments on 1D tubes [21, 22] found thermodynamic evidence for a fluctuating version [23–44] of FFLO but were unable to measure the order parameter. One avenue for directly observing these exotic superfluid states is to use highly anisotropic quasi-1D geometries where they should be robust [41, 93–103]. A competing approach is to study fermions in optical lattices, which also stabilizes the FFLO phase [104–106]. Here we solve the Bogoliubov–de Gennes (BdG) equations in a quasi-1D geometry. We find large regions of the phase diagram in which the FFLO finite-momentum-pairing state is stable. We also find a stable breached-pair (BP) state where pairs coexist with a Fermi surface [2–4, 107–110]. Our analysis provides a much needed narrative for thinking about the 1D-to-3D crossover, going beyond the existing single-band models [93, 100, 102, 111–115] and studies of finite systems [96–98, 103]. While we focus on cold atoms, these considerations are also relevant to nuclear, astrophysical [110, 116–128], and condensed-matter systems [116, 129–163]. Evidence of the FFLO phase has recently been found in a quasi-two-dimensional (2D) superconductor [129], and there are ongoing attempts to see related physics in 2D atomic systems [164–172].

We consider a harmonic oscillator potential of frequency $\omega_\perp$ which confines the motion of the atoms in the x-y plane. The atoms are free to move in the z direction, have mass m, and interact via s-wave collisions, characterized by a scattering length a_s (tunable via a Feshbach resonance [45, 173]). We consider the "Bardeen-Cooper-Schrieffer (BCS) side" of resonance where $a_s < 0$, and calculate the mean-field phase diagram in the μ-h plane, where $\mu \equiv (\mu_\uparrow + \mu_\downarrow)/2$ and $h \equiv (\mu_\uparrow - \mu_\downarrow)/2$ denote, respectively, the average chemical potential and

the chemical potential difference of the two spins. Prior work on this model have examined the low-density (small-μ) limit, where the transverse motion of the atoms is confined to the lowest oscillator level [20–23, 93, 111–113], and the system maps onto an effective 1D model [174, 175]. Conversely, when μ is large, the atoms can access many energy levels of the trap, and the system is locally three dimensional. Here we investigate the crossover between these regimes. In the Supplement (Sec. 7.7), we extend our modeling to Fermi gases trapped in an array of tubes produced by a 2D optical lattice, which more closely resembles the experimental setup in Refs. [21, 22]. In addition to the crossover with μ, we also explore the transition from 1D to 3D as one increases the coupling between tubes by lowering the lattice depth.

The exact 1D phase diagram contains three phases which are fluctuating analogs of the BCS superfluid, the FFLO state, and a fully polarized (FP) gas [20–24]. Since interaction effects in 1D are stronger at low densities, pairs are more stable at smaller μ, and the slope $\gamma \equiv d\mu/dh$ of the line separating the BCS and FFLO phases is negative. The analogous phase boundary in 3D has a positive slope, providing a convenient distinction between 1D-like and 3D-like behavior. In 3D there is also a partially polarized Normal (N) state [2–4].

For weak interactions and $\mu < 2\hbar\omega_\perp$, we find 1D-like behavior, in that $\gamma < 0$. The critical field h_c, at which the BCS-to-FFLO transition occurs, jumps whenever a new channel opens (near $\mu \sim n\hbar\omega_\perp$), but after this jump we again find $\gamma < 0$ [Fig. 7.1(a)]. Once many channels are occupied we find 3D-like behavior with $\gamma > 0$. Each 1D-like interval hosts a large FFLO region. In the 3D regime, these regions merge to form a single domain. As interactions are increased, the crossover to 3D-like behavior moves to smaller μ [Fig. 7.2(a)]. For

very strong interactions near unitarity ($a_s \to -\infty$), the harmonic oscillator levels are strongly mixed, and we always find $\gamma > 0$ [Fig. 7.2(b)]. Regardless, we find that the FFLO phase occupies much of the phase diagram for all interaction strengths. Moreover, at sufficiently strong interactions, we find a BP region, nestled between the BCS and the FFLO phases. Such a (zero-temperature) BP phase is stable in 3D only for negative μ in the deep Bose-Einstein condensate (BEC) side of resonance ($a_s > 0$) [1–13, 110, 176]. These results suggest that exotic superfluids will be observable in quasi-1D experiments.

We study the temperature variation of the phase diagrams (Figs. 7.4 and 7.5). The FFLO and BP phases shrink much faster with temperature than the BCS phase as they have much smaller pairing energies. For weak interactions, the BCS phase survives in isolated pockets, which disappear sequentially with temperature. The critical temperatures grow with interactions, as interactions favor pairing.

In addition to directly solving the 3D BdG equations, we map the system to an effective 1D model in the single-channel limit $\mu < 2\hbar\omega_\perp$. We find that the effective 1D coupling constant $g_{1\mathrm{D}}$ becomes more strongly attractive at larger μ. Our mapping reduces to that in [174, 175] in the low-density limit, but has previously unexplored correction terms at higher densities. These become more important at stronger interactions [Eq. (7.10)].

We use the BdG mean-field formalism. This approach does not include a Hartree self-energy [16]. This deficiency is typically unimportant for weak interactions but becomes significant as one approaches unitarity. It may also be important for studying the competition between phases with similar energies. Unfortunately the literature contains no convenient way to incorporate the Hartree

term. The technical difficulty is that the bare coupling constant for contact interactions has an ultraviolet divergence. Renormalizing this divergence causes the Hartree term to identically vanish, and there is active debate about the significance of those terms [16]. At unitarity, one can circumvent this problem by imposing universality on the equation of state and constructing a regularized energy functional [17, 103, 177, 178]. However, there is no equivalent scheme at intermediate interactions, as the proper set of constraints is unknown. Along with self-energy corrections, quantum fluctuations also become significant at stronger interactions [179–182]. Thus we do not expect our results to be accurate in the unitary regime. In fact, two recent experiments with ^{6}Li atoms, performed near unitarity, found the behavior of the system to be 1D-like at low densities [21, 22], whereas our model predicts 3D-like physics there. We believe the physics neglected in the BdG approach largely renormalizes a_s, and that our unitary results should agree with experiments for $a_s > 0$. Finally, we cannot rule out other phases not considered here, e.g., deformed Fermi surface pairing [46, 47], or an incoherent mixture of paired and unpaired fermions [48, 49].

Despite these limitations, our simple model lets us make concrete predictions and provides insight into the nature of the dimensional crossover. In particular, we find that the phase diagram changes dramatically with interaction strength (Figs. 7.1 and 7.2). These phase diagrams, and even the equation of state, can be probed in experiments [1, 2, 42–44, 46–49, 51, 94, 95, 100, 101, 104–107, 183–201].

7.3 Model

Our starting point is the many-body Hamiltonian

$$\hat{H} = \int d^3r \left[\sum_{\sigma=\uparrow,\downarrow} \hat{\psi}^\dagger_\sigma(\vec{r}) \big(\hat{H}^{\rm sp} - \mu_\sigma\big) \hat{\psi}_\sigma(\vec{r}) + g\, \hat{\psi}^\dagger_\uparrow(\vec{r}) \hat{\psi}^\dagger_\downarrow(\vec{r}) \hat{\psi}_\downarrow(\vec{r}) \hat{\psi}_\uparrow(\vec{r}) \right], \tag{7.1}$$

where $\hat{\psi}_\sigma(\vec{r})$ denote the fermion field operators, $\hat{H}^{\rm sp}$ is the single-particle Hamiltonian, $\hat{H}^{\rm sp} = -\hbar^2\nabla^2/(2m) + (1/2)m\omega_\perp^2(x^2+y^2)$, and g is the "bare" coupling constant describing interactions between an $\uparrow$ spin and a $\downarrow$ spin. We can relate g to a_s by the Lippmann-Schwinger equation $1/g = m/(4\pi\hbar^2 a_s) - \int d^3k\, m/(8\pi^3\hbar^2k^2)$ [202]. We define the pairing field $\Delta(\vec{r}) = g\langle\hat{\psi}_\downarrow(\vec{r})\hat{\psi}_\uparrow(\vec{r})\rangle$, and ignore quadratic fluctuations, arriving at the mean-field Hamiltonian

$$\begin{aligned} \hat{H}^{\rm MF} = & \int d^3r \begin{pmatrix} \hat{\psi}_\uparrow(\vec{r}) \\ \hat{\psi}^\dagger_\downarrow(\vec{r}) \end{pmatrix}^\dagger \begin{pmatrix} \hat{H}^{\rm sp} - \mu_\uparrow & \Delta(\vec{r}) \\ \Delta^*(\vec{r}) & \mu_\downarrow - \hat{H}^{\rm sp} \end{pmatrix} \begin{pmatrix} \hat{\psi}_\uparrow(\vec{r}) \\ \hat{\psi}^\dagger_\downarrow(\vec{r}) \end{pmatrix} \\ & + \sum_n \left(\varepsilon^{\rm sp}_n - \mu_\downarrow\right) - g^{-1} \int d^3r\, |\Delta(\vec{r})|^2 \,, \end{aligned} \tag{7.2}$$

where $\varepsilon^{\rm sp}_n$ denote the single-particle energies. We diagonalize $\hat{H}^{\rm MF}$ by a Bogoliubov transformation (see convention in Sec. 4.2), obtaining $\hat{H}^{\rm MF} = \sum_n [(E_n - h)\hat{\gamma}^\dagger_{n_\uparrow}\hat{\gamma}_{n_\uparrow} + (E_n + h)\hat{\gamma}^\dagger_{n_\downarrow}\hat{\gamma}_{n_\downarrow} + (\varepsilon_n - E_n)] - g^{-1}\int d^3r|\Delta(\vec{r})|^2$. Here $\varepsilon_n \equiv \varepsilon^{\rm sp}_n - \mu$, $\hat{\gamma}_{n_{\uparrow,\downarrow}}$ represent the Bogoliubov quasiparticle annihilation operators, and the eigenvalues E_n ($\geqslant 0$) are determined from the equation

$$\begin{pmatrix} \hat{H}^{\rm sp} - \mu & \Delta(\vec{r}) \\ \Delta^*(\vec{r}) & \mu - \hat{H}^{\rm sp} \end{pmatrix} \begin{pmatrix} u(\vec{r}) \\ v(\vec{r}) \end{pmatrix} = E \begin{pmatrix} u(\vec{r}) \\ v(\vec{r}) \end{pmatrix}. \tag{7.3}$$

In the zero-temperature ground state, all quasiparticle states with a negative energy are filled, and others are empty, which yields a total energy

$$\mathcal{E} = \sum_n [\alpha(E_n - h) + \varepsilon_n - E_n] - g^{-1} \int d^3r\, |\Delta(\vec{r})|^2 \,, \tag{7.4}$$

where $\alpha(x) \equiv x$ for $x < 0$, and 0 for $x > 0$. The ground-state solution is found by minimizing $\mathcal{E}$ as a functional of $\Delta(\vec{r})$ for a given μ and h.

To simplify calculations, we take the *ansatz* $\Delta(\vec{r}) = \Delta_0 e^{iqz} \exp[-(x^2+y^2)/\xi^2]$, and minimize Eq. (7.4) with respect to Δ_0, ξ, and q. The $\exp(iqz)$ factor describes Fulde-Ferrell (FF) pairing at wave vector q. The *ansatz* (with $q = 0$) also encompasses the BCS and the BP phases and, when $\Delta_0 = 0$, includes the Normal phase. A Larkin-Ovchinnikov (LO) *ansatz*, in which $\exp(iqz)$ is replaced by $\cos(qz)$, produces very similar results. Based on prior calculations, one expects that further *ansätze*, such as the liquid crystal phases in [82], will also give similar boundaries. While we label regions of the phase diagram as FFLO, the exact nature of the order is uncertain.

We diagonalize Eq. (7.3) by expanding $u(\vec{r})$ and $v(\vec{r})$ in the single-particle states with energies lower than a cutoff E_c. We exactly solve this finite-dimensional low-energy sector and calculate the contribution of higher-energy states perturbatively. We write Eq. (7.3) in the bra-ket notation, and express $|v\rangle$ in terms of $|u\rangle$ to obtain $(\hat{H}^{\text{sp}} - \mu)|u\rangle + \hat{\Delta}(\hat{H}^{\text{sp}} + E - \mu)^{-1}\hat{\Delta}^\dagger|u\rangle = E|u\rangle$. The second term acts as a perturbation, yielding $E_n - \varepsilon_n = \langle n|\hat{\Delta}(\hat{H}^{\text{sp}} + \varepsilon_n^{\text{sp}} - 2\mu)^{-1}\hat{\Delta}^\dagger|n\rangle$, where $|n\rangle$ is the corresponding single-particle state. Using completeness of the single-particle states, we write this as $E_n - \varepsilon_n = \int_0^\infty d\tau e^{-2\mu\tau}\langle n|e^{-\hat{H}^{\text{sp}}\tau}\hat{\Delta}e^{-\hat{H}^{\text{sp}}\tau}\hat{\Delta}^\dagger|n\rangle$, which can be expanded in powers of ε_n^{-1} using the Hadamard lemma. Since ε_n is large, we only retain the first term, which is $\langle n|\hat{\Delta}\hat{\Delta}^\dagger|n\rangle/(2\varepsilon_n)$. Thus we rewrite Eq. (7.4) as

$$\mathcal{E} = \mathcal{E}_{\text{ex}} - \sum \langle n|\hat{\Delta}\hat{\Delta}^\dagger|n\rangle/(2\varepsilon_n) - g^{-1}\int d^3r|\Delta(\vec{r})|^2, \tag{7.5}$$

where $\mathcal{E}_{\text{ex}}$ denotes the exact-diagonalized part, and the sum is over n with $\varepsilon_n^{\text{sp}} > E_c$. We take $|n\rangle = |n_x, n_y, k\rangle$, where (n_x, n_y) labels harmonic oscillator states in

the x-y plane, and k labels plane waves along z. Then $\varepsilon_n^{\rm sp} = (n_x + n_y + 1)\hbar\omega_\perp + \hbar^2 k^2/(2m)$, and $\langle n|\hat{\Delta}\hat{\Delta}^\dagger|n\rangle = \Delta_0^2\xi^2/(4\pi d_\perp^2\sqrt{n_x n_y})$ for large n_x, n_y, where $d_\perp \equiv \sqrt{\hbar/(m\omega_\perp)}$. Thus the energy per unit length along z is

$$\tilde{\mathcal{E}} = \tilde{\mathcal{E}}_{\rm ex} + \frac{\tilde{\Delta}_0^2\tilde{\xi}^2}{4\pi}\Big\{\tilde{k}_c\big[1 + f\big((1-\tilde{\mu})/\tilde{k}_c^2\big)\big] - \pi/(2\tilde{a}_s)\Big\}, \tag{7.6}$$

where $\tilde{k}_c \equiv [2(\tilde{E}_c - 1)]^{1/2}$, $f(x) \equiv \sqrt{2x}\,\tan^{-1}\sqrt{2x}$, and the tildes denote nondimensionalized quantities, with energies rescaled by $\hbar\omega_\perp$ and lengths rescaled by $d_\perp$. We perform calculations with $\tilde{E}_c = 10$. We verified that our results are unchanged if $\tilde{E}_c$ is made larger. Our approach to including high-energy modes eliminates the ultraviolet divergence associated with the contact interaction. It is similar to the approach in [16], where higher modes are included via a local-density approximation. Other regularization schemes have also been successful [203–205].

7.4 Results of the full model

Figure 7.1(a) shows the phase diagram at weak interactions. For small h the ground state is a fully paired BCS state. Increasing h drives a first-order transition to an FFLO or a Normal region. As described earlier, in this weak-coupling limit, the phase boundary is reminiscent of 1D, with a structure that repeats with μ as various channels open. The FFLO state is most stable when μ is just above $n\hbar\omega_\perp$ for integer n. The length ξ over which $\Delta(\vec{r})$ falls off increases with μ. The FFLO wave vector q grows with h. The FFLO-Normal and FFLO-FP transitions are second order, with the amplitude $\Delta_0 \to 0$ as the boundary is approached.

Figure 7.2 shows how the phase diagram changes at stronger interactions. As interactions favor pairing, we find superfluidity over a larger area. However,

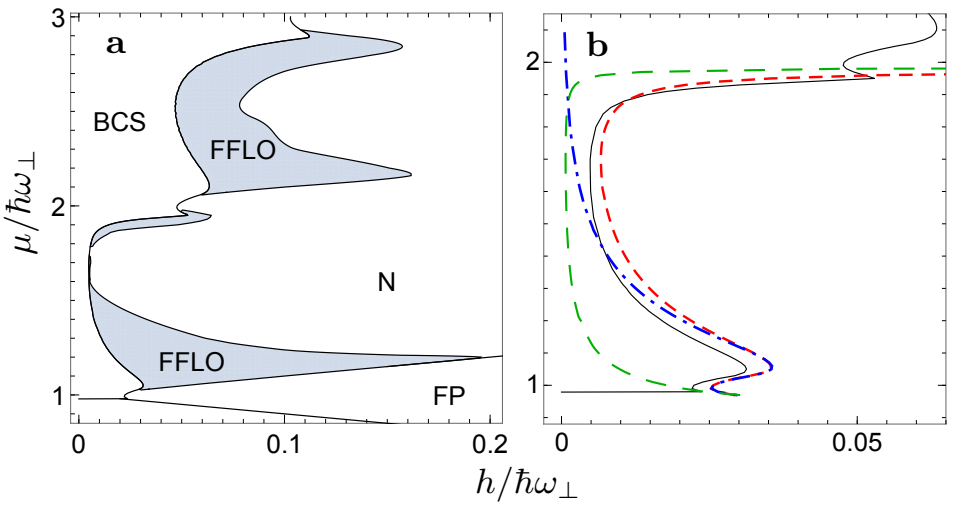

Figure 7.1: Zero-temperature phase diagram of a two-component Fermi gas in a 2D harmonic trap of frequency $\omega_\perp$. Here $d_\perp/a_s = -3$, where a_s is the 3D scattering length, and $d_\perp \equiv (\hbar/m\omega_\perp)^{1/2}$. (a) Phase boundaries calculated using 3D BdG equations. (b) BCS critical field of the full model (solid curve) and of various effective 1D models (dashed curves). Short-dashed (red) line, 1D BdG with the mapping in Eq. (7.10); dot-dashed (blue) line, 1D BdG with Olshanii's mapping [174, 175]; and long-dashed (green) line, Bethe *Ansatz* with Eq. (7.10).

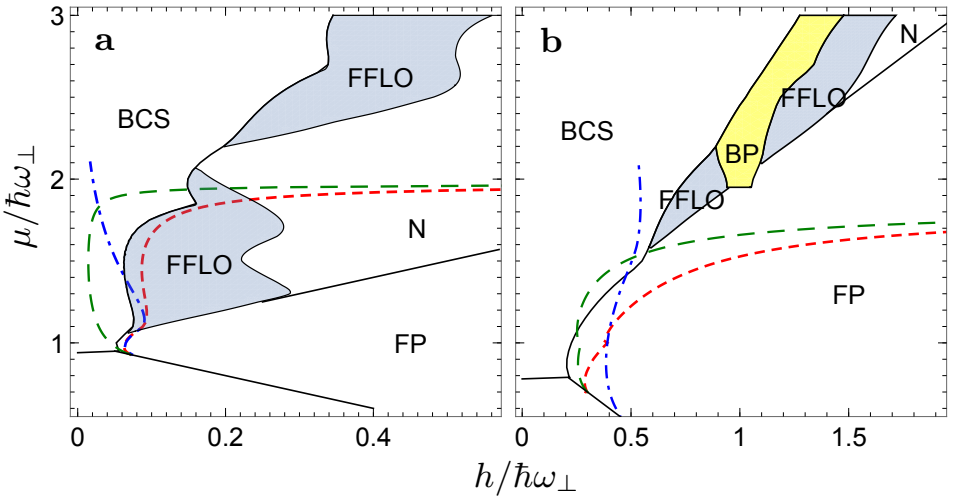

Figure 7.2: Zero-temperature phase diagram of the full model for (a) $d_\perp/a_s = -3/2$ and (b) $d_\perp/a_s = 0$. Dashed curves plot the BCS critical field predicted by effective 1D models. Conventions for the curves are the same as in Fig. 7.1.

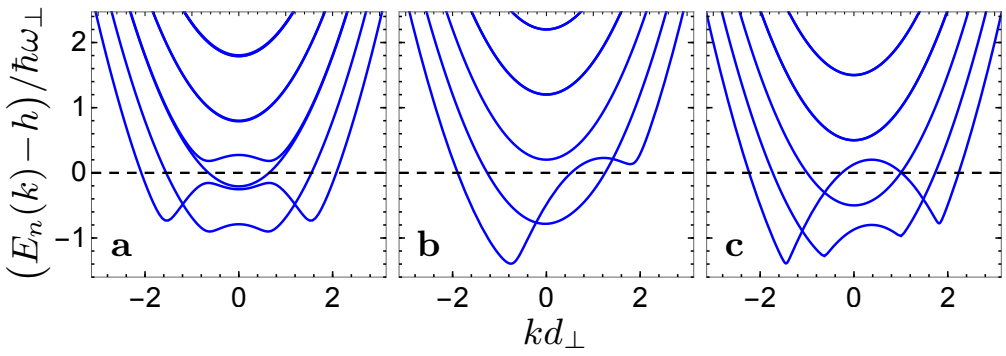

Figure 7.3: Quasiparticle dispersion at unitarity for (a) the BP phase at $(\tilde{\mu}, \tilde{h}) = (2.2, 1)$, (b) the FFLO phase at $(\tilde{\mu}, \tilde{h}) = (2, 0.8)$, and (c) the FFLO phase at $(\tilde{\mu}, \tilde{h}) = (2.35, 1.15)$. Different curves denote different transverse modes.

the phase diagram becomes more 3D-like, and the relative stabilities of different superfluid phases change. In particular, we see the appearance of a stable BP phase near unitarity. As seen in the excitation spectra in Fig. 7.3(a), the BP state is a gapless superfluid with a uniform order parameter (in the z direction), which contains both paired and unpaired modes. The unpaired fermions fill the sea of negative energy states. The literature (mostly on isotropic systems) distinguishes between BP states by the topology of the Fermi sea [107, 110, 176]. For a given transverse quantum number, the Fermi sea in Fig. 7.3(a) is connected, making our state analogous to the "BP1" state in [107]. We do not find BP states where a Fermi sea is broken into disjoint momentum intervals (cf. [1–13, 50, 96, 108, 110, 176, 206–211]). However, we do find FFLO states of both varieties [Figs. 7.3(b) and 7.3(c)]. The BCS-BP transition as well as the BP-FFLO transition are first order, accompanied by jumps in the polarization.

We show the phase diagrams at finite temperature in Figs. 7.4 and 7.5. Here we include thermal fluctuations at temperature T by minimizing the mean-field free energy $F = \mathcal{E} - TS$, where S denotes the entropy. This has the effect of changing the sum in Eq. (7.4) to $(-1/\beta)\sum_n \ln\left(1 + e^{-\beta(E_n - h)}\right) + \sum_n(\varepsilon_n + h)$,

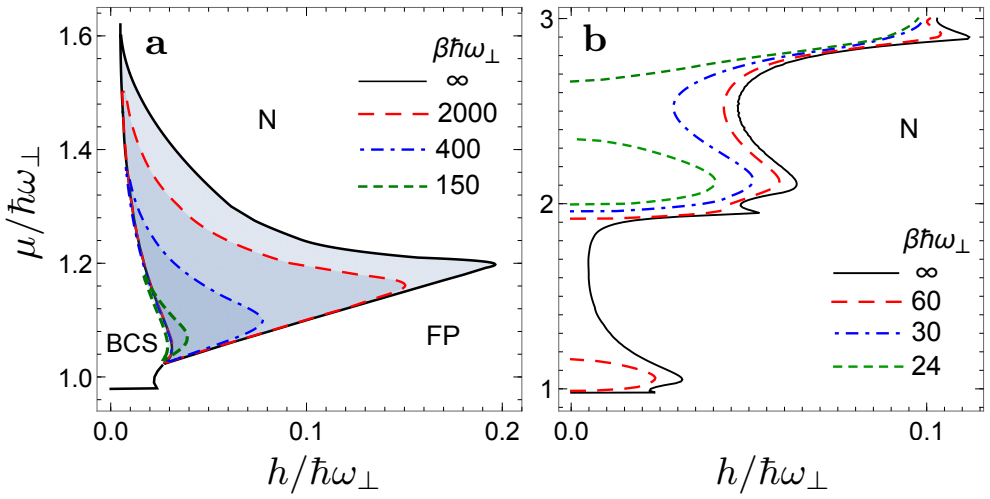

Figure 7.4: Variation of the superfluid regions with temperature for $d_\perp/a_s = -3$. (a) FFLO region. (b) BCS region(s). The BCS phase is stable to the left of the curve(s) at a given temperature.

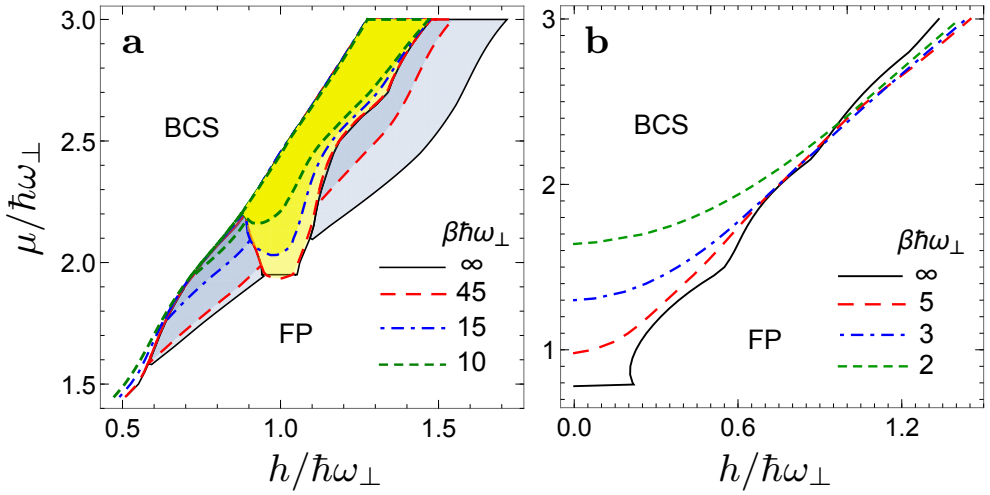

Figure 7.5: Variation of the superfluid regions with temperature for $d_\perp/a_s = 0$. (a) FFLO region. (b) BCS region.

where $\beta \equiv 1/(k_B T)$, and E_n takes on both positive and negative values. Such a mean-field approach ignores the contribution of noncondensed pairs and overestimates the critical temperature [1, 5, 6, 52–56, 179–182, 212]. However, we expect the qualitative features in Figs. 7.4 and 7.5 to be valid. In particular, we find vastly different critical temperatures for the FFLO and BCS phases, requiring separate figures to show the behavior. This separation of scales is rea-

sonable, as the pairing energy of the gapped BCS phase is much larger than the gapless FFLO or BP phases. The critical temperatures grow with the interaction strength since the pairing energy is increased. The BCS phase acquires polarization at finite T, which causes Δ_0 to decrease with h, making the BCS-Normal transition second order at small $\tilde{\mu}$. At sufficiently high temperature the BP and BCS phases merge and become indistinguishable. The most striking feature of the weak-coupling phase diagram (Fig. 7.4) is that the BCS region breaks up into a series of disconnected lobes which disappear one by one at higher temperatures.

7.5 Derivation of and comparison with an effective 1D model

To further understand this system, we take $q = 0$ and map it onto an effective 1D model for $\tilde{\mu} < 2$. We project Eq. (7.3) into the harmonic oscillator basis, treating $\Delta_{\vec{m},\vec{n}} \equiv \langle \vec{m}|\hat{\Delta}|\vec{n}\rangle$ as a perturbation if $\vec{n}$ or $\vec{m} \neq \vec{0}$ [where $\vec{n} \equiv (n_x, n_y)$]. This yields a 1D BdG equation for the $\vec{n} = \vec{0}$ mode. Neglecting the influence of higher modes on the lowest mode yields an energy per unit length

$$\tilde{\mathcal{E}} = \frac{\tilde{\Delta}^2\tilde{\xi}^2}{16\pi^2}\int \frac{d^3\tilde{k}}{\tilde{k}^2} - {\sum_{\vec{m},\vec{n}}}' \tilde{\Delta}^2_{\vec{m},\vec{n}} \int \frac{d\tilde{k}}{4\pi} \frac{\tilde{\varepsilon}_{\vec{m}}/\tilde{\varepsilon}_{\vec{m},+} + \tilde{\varepsilon}_{\vec{n}}/\tilde{\varepsilon}_{\vec{n},+}}{\tilde{\varepsilon}_{\vec{m},+} + \tilde{\varepsilon}_{\vec{n},+}}$$
$$- \frac{\tilde{\Delta}^2\tilde{\xi}^2}{8\tilde{a}_s} + \int \frac{d\tilde{k}}{2\pi}\big[\tilde{\varepsilon}_{\vec{0}} - \tilde{\varepsilon}_{\vec{0},+} + \alpha\big(\tilde{\varepsilon}_{\vec{0},+} - \tilde{h}\big)\big], \tag{7.7}$$

where the integrals are over all $\tilde{k}$, and the prime on the sum stands for $(\vec{m},\vec{n}) \neq (\vec{0},\vec{0})$. Here $\varepsilon_{\vec{0},+} = \big(\varepsilon^2_{\vec{0}} + \Delta^2_{\vec{0},\vec{0}}\big)^{\frac{1}{2}}$, and $\varepsilon_{\vec{n},+} = \varepsilon_{\vec{n}}$ for $\vec{n} \neq \vec{0}$, with $\tilde{\varepsilon}_{\vec{n}} = n_x + n_y + \tilde{k}^2/2 + 1 - \tilde{\mu}$. The first two terms in Eq. (7.7) separately diverge, but their sum is finite. This expression for $\tilde{\mathcal{E}}$ maps to that of a purely 1D mean-field model provided we identify the effective 1D order parameter $\Delta_{1\mathrm{D}}$ and the coupling constant $g_{1\mathrm{D}}$

as $\Delta_{1\mathrm{D}} = \Delta_{\vec{0},\vec{0}} = \Delta_0\tilde{\xi}^2/(\tilde{\xi}^2+1)$ and

$$\frac{1}{\tilde{g}_{1\mathrm{D}}} = \frac{(\tilde{\xi}^2+1)^2}{8\tilde{\xi}^2 a_s} - \lim_{n_c\to\infty}\left[\frac{(\tilde{\xi}^2+1)^2}{8\tilde{\xi}^2}\sqrt{2n_c - 2\tilde{\mu}+3}\right. \\ \left. - {\sum_{\vec{m},\vec{n}}}' \mathcal{C}_{m_x n_x}\mathcal{C}_{m_y n_y}\int\frac{d\tilde{k}}{4\pi}\frac{\tilde{\varepsilon}_{\vec{m}}/\tilde{\varepsilon}_{\vec{m},+} + \tilde{\varepsilon}_{\vec{n}}/\tilde{\varepsilon}_{\vec{n},+}}{\tilde{\varepsilon}_{\vec{m},+}+\tilde{\varepsilon}_{\vec{n},+}}\right]. \quad (7.8)$$

Here $\tilde{g}_{1\mathrm{D}} \equiv g_{1\mathrm{D}}/(d_\perp\hbar\omega_\perp)$, and

$$\mathcal{C}_{mn} \equiv \frac{1}{\pi m!n!}\left(\frac{2}{\tilde{\xi}^2+1}\right)^{m+n}\left[\Gamma\left(\frac{1+m+n}{2}\right){}_2F_1\left(-m,-n;\frac{1-m-n}{2};\frac{\tilde{\xi}^2+1}{2}\right)\right]^2 \quad (7.9)$$

when $m+n$ is even and 0 otherwise, where ${}_2F_1$ is a hypergeometric function and Γ is the Gamma function. The prime on the sum in Eq. (7.8) stands for the condition $2 \leqslant m_x + n_x + m_y + n_y \leqslant 2n_c$ and the limit converges as $n_c^{-3/2}$. The effective coupling constant $g_{1\mathrm{D}}$ is weakly dependent on $\Delta(\vec{r})$, and its structure is best understood by taking $\tilde{\Delta}_0 \to 0$, $\tilde{\xi}\to 1$, for which

$$\frac{1}{\tilde{g}_{1\mathrm{D}}} = \frac{1}{2\tilde{a}_s} + \frac{\zeta(\frac{1}{2},2-\tilde{\mu})}{2\sqrt{2}} - \frac{\sqrt{2}}{\pi}\Theta(\tilde{\mu}-1)\sum_{j=1}^{\infty}\frac{2^{-2j}}{\sqrt{j+1-\tilde{\mu}}}\tan^{-1}\sqrt{\frac{\tilde{\mu}-1}{j+1-\tilde{\mu}}}\,, \quad (7.10)$$

where ζ denotes the Hurwitz zeta function, and Θ is the unit step function. At $\tilde{\mu}=1$, $1/\tilde{g}_{1\mathrm{D}} = 1/(2\tilde{a}_s) + \zeta(1/2)/(2\sqrt{2})$, which is Olshanii's two-particle result [174, 175]. As $\tilde{\mu}$ grows, $\tilde{g}_{1\mathrm{D}}$ decreases, approaching $-\infty$ as $\tilde{\mu}\to 2$. This divergence is unphysical and signals a breakdown of the mapping to 1D when more channels open.

In Fig. 7.1(b) we evaluate the validity of this mapping by plotting the critical field of the BCS phase, h_c, from the effective 1D model. It closely follows the critical field obtained from the full model for nearly all $\tilde{\mu} < 2$. We also plot h_c using Olshanii's mapping [174, 175], which agrees with the full model at small $\tilde{\mu}$, but becomes less accurate as $\tilde{\mu}$ increases. Furthermore, we show the prediction of the Bethe *Ansatz* with the mapping in Eq. (7.10), which illustrates the

difference between an exact and a mean-field analysis in 1D [20]. The mapping to 1D becomes less accurate at stronger interactions due to mixing of the trap levels, as seen in Fig. 7.2.

7.6 Outlook

Achieving the temperatures required to directly observe the FFLO state at weak coupling is extremely challenging. The numbers near unitarity are more promising, but the accuracy of our mean-field theory is questionable there. The 1D thermodynamic measurements [21, 22] are promising: the measured equation of state agrees with the thermodynamic Bethe *Ansatz*, which contains a fluctuating version of the FFLO phase. Time-dependent BdG calculations suggest the FFLO domain walls will be observable in time-of-flight expansion of 1D gases [101]. Density-matrix renormalization-group simulations on very small systems are more ambiguous [201]. This signature should be even more robust in the geometries we have been studying. There are also interesting connections to experiments on domain walls in highly elongated traps [213–215]. It is likely that these various research directions will converge in the near future.

Acknowledgments

We thank Randy Hulet and Ben Olsen for useful discussions. This work was supported by the National Science Foundation Grant PHY-1508300.

7.7 Supplement: Fermi gas in array of coupled tubes

Here, we extend our analysis to model experiments where a spin-imbalanced Fermi gas is loaded into an array of 1D tubes by turning on a lattice in the transverse plane, as in Refs. [21, 22]. We calculate the mean-field phase diagram taking into account all energy bands of the lattice. The 1D-to-3D crossover occurs in two different ways depending on whether the lattice depth is decreased or the interactions are increased. Lowering the lattice depth increases tunneling between the tubes, making the system more three dimensional, as was observed in Ref. [22]. On the other hand, stronger interactions mix the energy bands, enabling more transverse degrees of freedom and promoting 3D-like behavior, as we found for a single tube in the main text.

We consider a square lattice in the x–y plane and choose units such that the single-particle Hamiltonian is given by $\hat{H}^{\rm sp} = -\vec{\nabla}^2 + V_0(\sin^2 x + \sin^2 y - 1)$. The eigenstates of $\hat{H}^{\rm sp}$ can be expressed as $\phi_{\vec{k}}(\vec{r}) = \left(1/\sqrt{\mathcal{V}}\right) e^{ik_z z}\chi_{k_x}(x)\chi_{k_y}(y)$, where $\mathcal{V}$ is the volume, (k_x, k_y) are the quasimomenta in the extended-zone representation, and the Bloch functions $\chi_k(x)$ can be computed exactly as

$$\chi_k(x) = \frac{1}{\sqrt{\pi}}\left[C\left(a_k\left(\frac{V_0}{4}\right), \frac{V_0}{4}, x+\frac{\pi}{2}\right) + i\,\mathrm{sgn}(k)\,S\left(a_k\left(\frac{V_0}{4}\right), \frac{V_0}{4}, x+\frac{\pi}{2}\right)\right], \quad (7.11)$$

where C and S denote, respectively, the Mathieu cosine and Mathieu sine functions with period π and characteristic value a [216]. The single-particle spectrum is given by $\varepsilon^{\rm sp}(\vec{k}) = k_z^2 + a_{k_x}(V_0/4) + a_{k_y}(V_0/4)$.

We consider a generalized Fulde-Ferrell *ansatz* for the pair wave function,

$$\Delta(\vec{r}) = \Delta_0\, e^{iqz} \sum_{j_x, j_y} \exp\left[-\frac{(x - j_x\pi)^2 + (y - j_y\pi)^2}{\xi^2}\right], \quad (7.12)$$

where Δ_0, q, and ξ are variational parameters. As before, the mean-field energy $\mathcal{E}$ can be calculated from Eq. (7.4) after diagonalizing the BdG Hamiltonian. We

perform this diagonalization numerically for states below an energy cutoff E_c and include the higher-energy states perturbatively, yielding [see Eq. (7.5)]

$$\mathcal{E} = \mathcal{E}_{\text{ex}} - \sum\nolimits_{\vec{k}}{}' \frac{\int d^3r\, |\Delta(\vec{r})|^2\, |\phi_{\vec{k}}(\vec{r})|^2}{2\big[\varepsilon^{\text{sp}}(\vec{k}) - \mu\big]} - \frac{1}{g}\int d^3r\, |\Delta(\vec{r})|^2, \tag{7.13}$$

where $\mathcal{E}_{\text{ex}}$ is the exact-diagonalized part and the primed sum is over states with $\varepsilon^{\text{sp}}(\vec{k}) > E_c \gg \mu$. For such states, $\phi_{\vec{k}}(\vec{r}) \approx \big(1/\sqrt{\mathcal{V}}\big)\, e^{i\vec{k}.\vec{r}}$ and $\varepsilon^{\text{sp}}(\vec{k}) \approx k^2$. Using this approximation in Eq. (7.13), we find the energy per unit volume

$$\frac{\mathcal{E}}{\mathcal{V}} = \frac{\mathcal{E}_{\text{ex}}}{\mathcal{V}} - \frac{1}{\mathcal{V}}\int d^3r\, |\Delta(\vec{r})|^2 \left[\frac{1}{g} + \frac{1}{2\mathcal{V}}\sum\nolimits_{\vec{k}} \frac{\Theta(k^2 - E_c)}{k^2 - \mu}\right], \tag{7.14}$$

where Θ is the unit step function. This expression can be simplified further by substituting the *ansatz* for $\Delta(\vec{r})$ from Eq. (7.12) and writing g in terms of the scattering length a_s using the Lippmann-Schwinger equation, which yields

$$\begin{aligned}\frac{\mathcal{E}}{\mathcal{V}} &= \frac{\mathcal{E}_{\text{ex}}}{\mathcal{V}} + \frac{\Delta_0^2\xi^2}{2\pi}\left[\vartheta_3\Big(0, e^{-\pi^2/(2\xi^2)}\Big)\right]^2 \left\{-\frac{1}{8\pi a_s} + \frac{1}{2}\int \frac{d^3k}{(2\pi)^3}\left[\frac{1}{k^2} - \frac{\Theta(k^2 - E_c)}{k^2 - \mu}\right]\right\} \\ &= \frac{\mathcal{E}_{\text{ex}}}{\mathcal{V}} + \frac{\Delta_0^2\xi^2}{8\pi^3}\left[\vartheta_3\Big(0, e^{-\pi^2/(2\xi^2)}\Big)\right]^2 \left(-\frac{\pi}{2a_s} + \sqrt{E_c} - \sqrt{\mu}\,\tanh^{-1}\sqrt{\frac{\mu}{E_c}}\right), \end{aligned} \tag{7.15}$$

where ϑ_3 denotes a Jacobi theta function [216]. We find the phase diagram by minimizing the energy density with respect to Δ_0, ξ, and q.

Figure 7.6 shows the phase diagram in the μ–h plane for $V_0 = 5$ and $a_s = -1$. As in a single tube, we find the FFLO phase is stable over a significant range of parameters. Generically, as h is increased from zero, the fully paired BCS phase becomes unstable to a partially polarized phase at a critical imbalance h_c through a first-order phase transition. As we discussed in Sec. 7.2, the variation of h_c with μ provides a convenient distinction between 1D-like and 3D-like behavior. In 3D, pairing is favored at higher density, which increases the stability of the BCS state, resulting in a larger critical field h_c. Thus, $dh_c/d\mu > 0$. In 1D, the effect is reversed and $dh_c/d\mu < 0$. We find that $h_c(\mu)$ has a positive slope in

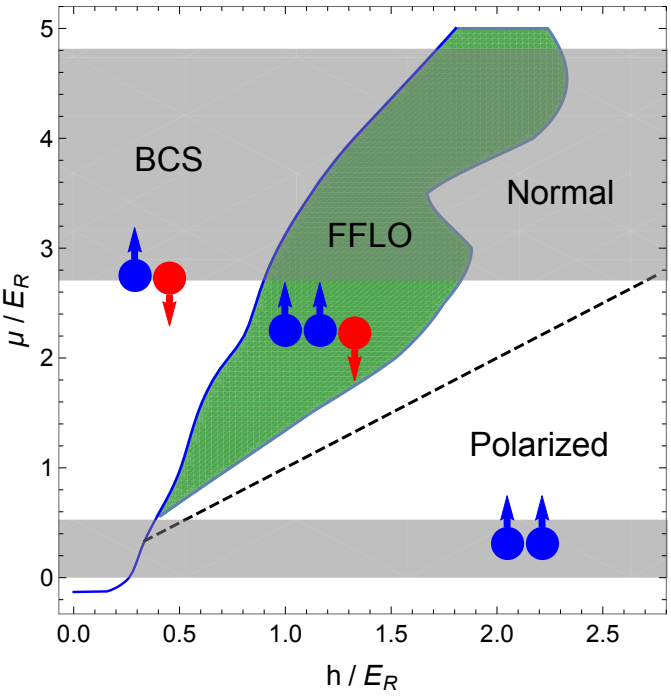

Figure 7.6: Mean-field phase diagram of a spin-imbalanced Fermi gas loaded into an array of coupled tubes by turning on a square lattice in the transverse plane, with $V_0/E_R = 5$ and $\pi a_s/a = -1$. Here μ and h denote the average chemical potential and chemical potential difference between the two spin components, respectively, E_R is the recoil energy, V_0 is the lattice depth, a is the lattice spacing, and a_s is the s-wave scattering length. The gray shaded regions show the locations of the energy bands of the lattice.

Fig. 7.6 (solid blue curve). This is because the interactions are sufficiently strong to mix the energy bands of the lattice and produce 3D-like kinematics.

Figure 7.7 shows how the curve $h_c(\mu)$ changes as the interactions are reduced. At weaker interactions, there is less mixing between the energy bands. Consequently, if the chemical potential μ lies in the gap between two low-lying energy bands, the transverse motion is frozen out and the phase diagram is 1D like. The system exhibits 3D-like behavior when μ is inside an energy band or when sufficiently many bands are occupied. The 1D-like regions shrink with stronger interactions. This variation with the interaction strength is similar to what we found for a Fermi gas in a single tube [see Figs. 7.1 and 7.2].

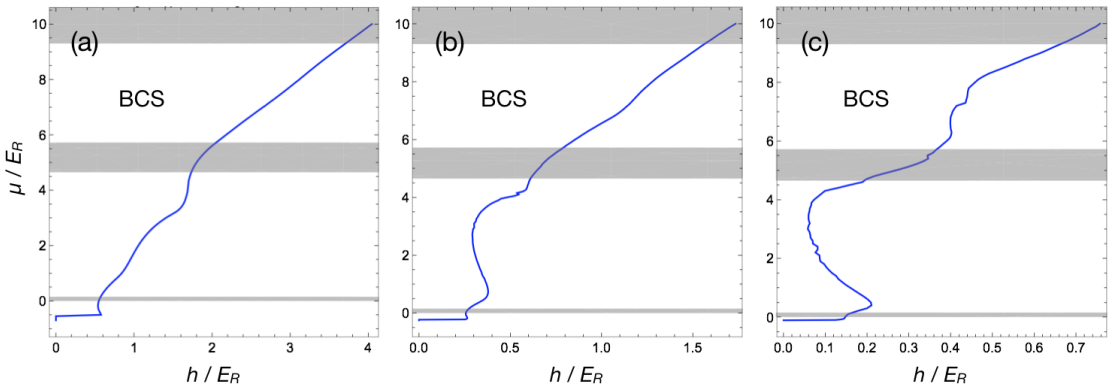

Figure 7.7: Variation of the critical imbalance curve, $h_c(\mu)$, with the interaction strength, for $V_0/E_R = 10$. (a) $\pi a_s/a = -1$, (b) $\pi a_s/a = -0.4$, (c) $\pi a_s/a = -0.25$. As in Fig. 7.6, gray shaded regions show the energy bands of the lattice.

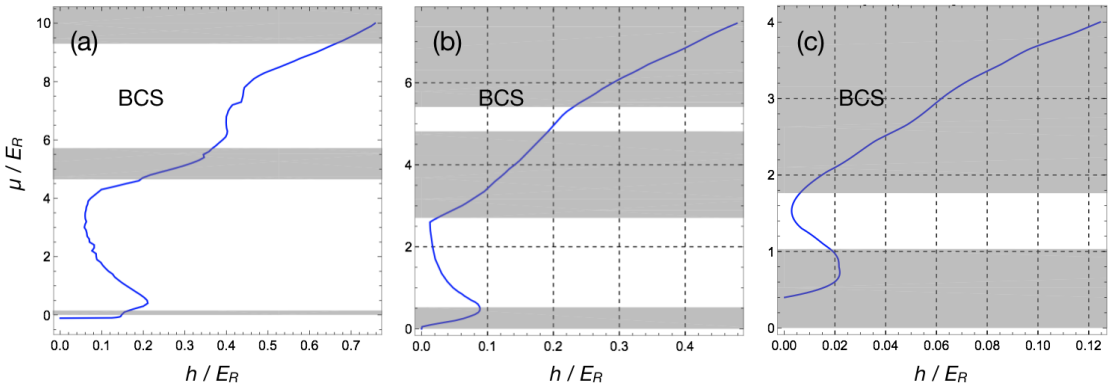

Figure 7.8: Variation of the critical imbalance curve with the lattice depth, for $\pi a_s/a = -0.25$. (a) $V_0/E_R = 10$, (b) $V_0/E_R = 5$, (c) $V_0/E_R = 2.5$. As before, gray shaded regions show where the energy bands of the lattice are located.

Tuning the lattice depth V_0 provides another means of probing the 1D-to-3D crossover. In the limit $V_0 \to \infty$, the tubes are isolated from one another and each can be modeled by a 2D harmonic trap, which we studied in the main text. Figure 7.8 shows how the phase diagram changes as the lattice depth is varied. For a large but finite V_0, the particles can tunnel between the tubes and the energy bands have a finite width that scales with the tunneling. In particular, the lower-energy bands are well separated from each other and we find 1D-like behavior between the first and second band. As V_0 is decreased, the energy bands get wider and eventually overlap, making the system fully three dimensional.

BIBLIOGRAPHY FOR CHAPTER 7

[1] M. M. Parish, F. M. Marchetti, A. Lamacraft, and B. D. Simons, "Finite-temperature phase diagram of a polarized Fermi condensate," Nat. Phys. **3**, 124 (2007).

[2] D. E. Sheehy and L. Radzihovsky, "BEC-BCS crossover in "magnetized" Feshbach-resonantly paired superfluids," Phys. Rev. Lett. **96**, 060401 (2006).

[3] T. N. De Silva and E. J. Mueller, "Profiles of near-resonant population-imbalanced trapped Fermi gases," Phys. Rev. A **73**, 051602(R) (2006).

[4] W. Yi and L.-M. Duan, "Phase diagram of a polarized Fermi gas across a Feshbach resonance in a potential trap," Phys. Rev. A **74**, 013610 (2006).

[5] W. Yi and L.-M. Duan, "Trapped fermions across a Feshbach resonance with population imbalance," Phys. Rev. A **73**, 031604(R) (2006).

[6] X.-J. Liu and H. Hu, "BCS-BEC crossover in an asymmetric two-component Fermi gas," Europhys. Lett. **75**, 364 (2006).

[7] D. E. Sheehy and L. Radzihovsky, "BEC–BCS crossover, phase transitions and phase separation in polarized resonantly-paired superfluids," Ann. Phys. **322**, 1790 (2007).

[8] L. Radzihovsky and D. E. Sheehy, "Imbalanced Feshbach-resonant Fermi gases," Rep. Prog. Phys. **73**, 076501 (2010).

[9] L. M. Jensen, J. Kinnunen, and P. Törmä, "Non-BCS superfluidity in trapped ultracold Fermi gases," Phys. Rev. A **76**, 033620 (2007).

[10] M. Mannarelli, G. Nardulli, and M. Ruggieri, "Evaluating the phase diagram of superconductors with asymmetric spin populations," Phys. Rev. A **74**, 033606 (2006).

[11] L. He, M. Jin, and P. Zhuang, "LOFF pairing vs breached pairing in asymmetric fermion superfluids," Phys. Rev. B **73**, 214527 (2006).

[12] C.-H. Pao, S.-T. Wu, and S.-K. Yip, "Superfluid stability in the BEC-BCS crossover," Phys. Rev. B **73**, 132506 (2006), Erratum-*ibid.* **74**, 189901 (2006).

[13] A. Mishra and H. Mishra, "LOFF and breached pairing with cold atoms," Eur. Phys. J. D **53**, 75 (2009).

[14] N. Yoshida and S.-K. Yip, "Larkin-Ovchinnikov state in resonant Fermi gas," Phys. Rev. A **75**, 063601 (2007).

[15] H. Hu and X.-J. Liu, "Mean-field phase diagrams of imbalanced Fermi gases near a Feshbach resonance," Phys. Rev. A **73**, 051603(R) (2006).

[16] X.-J. Liu, H. Hu, and P. D. Drummond, "Mean-field thermodynamics of a spin-polarized spherically trapped Fermi gas at unitarity," Phys. Rev. A **75**, 023614 (2007).

[17] A. Bulgac and M. M. Forbes, "Unitary Fermi supersolid: The Larkin-Ovchinnikov phase," Phys. Rev. Lett. **101**, 215301 (2008).

[18] X.-J. Liu, H. Hu, and P. D. Drummond, "Finite-temperature phase diagram of a spin-polarized ultracold Fermi gas in a highly elongated harmonic trap," Phys. Rev. A **78**, 023601 (2008).

[19] X.-W. Guan, M. T. Batchelor, and C. Lee, "Fermi gases in one dimension: From Bethe ansatz to experiments," Rev. Mod. Phys. **85**, 1633 (2013).

[20] X.-J. Liu, H. Hu, and P. D. Drummond, "Fulde-Ferrell-Larkin-Ovchinnikov states in one-dimensional spin-polarized ultracold atomic Fermi gases," Phys. Rev. A **76**, 043605 (2007).

[21] Y.-a. Liao, A. S. C. Rittner, T. Paprotta, W. Li, G. B. Partridge, R. G. Hulet, S. K. Baur, and E. J. Mueller, "Spin-imbalance in a one-dimensional Fermi gas," Nature (London) **467**, 567 (2010).

[22] M. C. Revelle, J. A. Fry, B. A. Olsen, and R. G. Hulet, "1D to 3D crossover of a spin-imbalanced fermi gas," Phys. Rev. Lett. **117**, 235301 (2016).

[23] G. Orso, "Attractive Fermi gases with unequal spin populations in highly elongated traps," Phys. Rev. Lett. **98**, 070402 (2007).

[24] H. Hu, X.-J. Liu, and P. D. Drummond, "Phase diagram of a strongly interacting polarized Fermi gas in one dimension," Phys. Rev. Lett. **98**, 070403 (2007).

[25] G. G. Batrouni, M. H. Huntley, V. G. Rousseau, and R. T. Scalettar, "Exact numerical study of pair formation with imbalanced fermion populations," Phys. Rev. Lett. **100**, 116405 (2008).

[26] E. Zhao, X.-W. Guan, W. V. Liu, M. T. Batchelor, and M. Oshikawa, "Analytic thermodynamics and thermometry of Gaudin-Yang Fermi gases," Phys. Rev. Lett. **103**, 140404 (2009).

[27] M. Tezuka and M. Ueda, "Density-Matrix Renormalization Group study of trapped imbalanced Fermi condensates," Phys. Rev. Lett. **100**, 110403 (2008).

[28] M. Tezuka and M. Ueda, "Ground states and dynamics of population-imbalanced Fermi condensates in one dimension," New J. Phys. **12**, 055029 (2010).

[29] J.-S. He, A. Foerster, X.-W. Guan, and M. T. Batchelor, "Magnetism and quantum phase transitions in spin-1/2 attractive fermions with polarization," New J. Phys. **11**, 073009 (2009).

[30] P. Kakashvili and C. Bolech, "Paired states in spin-imbalanced atomic Fermi gases in one dimension," Phys. Rev. A **79**, 041603(R) (2009).

[31] M. J. Wolak, V. G. Rousseau, C. Miniatura, B. Grémaud, R. T. Scalettar, and G. G. Batrouni, "Finite-temperature quantum monte carlo study of the one-dimensional polarized fermi gas," Phys. Rev. A **82**, 013614 (2010).

[32] F. Heidrich-Meisner, G. Orso, and A. E. Feiguin, "Phase separation of trapped spin-imbalanced Fermi gases in one-dimensional optical lattices," Phys. Rev. A **81**, 053602 (2010).

[33] F. Heidrich-Meisner, A. E. Feiguin, U. Schollwöck, and W. Zwerger, "BCS-BEC crossover and the disappearance of Fulde-Ferrell-Larkin-Ovchinnikov correlations in a spin-imbalanced one-dimensional Fermi gas," Phys. Rev. A **81**, 023629 (2010).

[34] G. Xianlong and R. Asgari, "Spin-density-functional theory for imbalanced interacting Fermi gases in highly elongated harmonic traps," Phys. Rev. A **77**, 033604 (2008).

[35] B. Wang and L.-M. Duan, "Suppression or enhancement of the Fulde-Ferrell-Larkin-Ovchinnikov order in a one-dimensional optical lattice with particle-correlated tunneling," Phys. Rev. A **79**, 043612 (2009).

[36] A. E. Feiguin and F. Heidrich-Meisner, "Pairing states of a polarized Fermi gas trapped in a one-dimensional optical lattice," Phys. Rev. B **76**, 220508(R) (2007).

[37] A. E. Feiguin and D. A. Huse, "Spectral properties of a partially spin-polarized one-dimensional Hubbard/Luttinger superfluid," Phys. Rev. B **79**, 100507(R) (2009).

[38] A.-H. Chen and G. Xianlong, "Pure Fulde-Ferrell-Larkin-Ovchinnikov state in optical lattices," Phys. Rev. B **85**, 134203 (2012).

[39] E. Zhao and W. V. Liu, "An effective field theory for one-dimensional polarized Fermi gases," J. Low Temp. Phys. **158**, 36 (2010).

[40] J. Y. Lee and X.-W. Guan, "Asymptotic correlation functions and FFLO signature for the one-dimensional attractive spin-1/2 Fermi gas," Nucl. Phys. B **853**, 125 (2011).

[41] M. Rizzi, M. Polini, M. A. Cazalilla, M. R. Bakhtiari, M. P. Tosi, and R. Fazio, "Fulde-Ferrell-Larkin-Ovchinnikov pairing in one-dimensional optical lattices," Phys. Rev. B **77**, 245105 (2008).

[42] M. Casula, D. M. Ceperley, and E. J. Mueller, "Quantum Monte Carlo study of one-dimensional trapped fermions with attractive contact interactions," Phys. Rev. A **78**, 033607 (2008).

[43] S. K. Baur, J. Shumway, and E. J. Mueller, "Fulde-Ferrell-Larkin-Ovchinnikov versus Bose-Fermi mixture in a polarized one-dimensional Fermi gas at a Feshbach resonance: A three-body study," Phys. Rev. A **81**, 033628 (2010).

[44] A. Lüscher, R. M. Noack, and A. M. Läuchli, "Fulde-Ferrell-Larkin-Ovchinnikov state in the one-dimensional attractive Hubbard model and its fingerprint in spatial noise correlations," Phys. Rev. A **78**, 013637 (2008).

[45] K. B. Gubbels and H. T. C. Stoof, "Imbalanced Fermi gases at unitarity," Phys. Rep. **525**, 255 (2013).

[46] H. Müther and A. Sedrakian, "Spontaneous breaking of rotational symmetry in superconductors," Phys. Rev. Lett. **88**, 252503 (2002).

[47] A. Sedrakian, J. Mur-Petit, A. Polls, and H. Müther, "Pairing in a two-component ultracold Fermi gas: Phases with broken-space symmetries," Phys. Rev. A **72**, 013613 (2005).

[48] P. F. Bedaque, H. Caldas, and G. Rupak, "Phase separation in asymmetrical fermion superfluids," Phys. Rev. Lett. **91**, 247002 (2003).

[49] H. Caldas, "Cold asymmetrical fermion superfluids," Phys. Rev. A **69**, 063602 (2004).

[50] T.-L. Dao, M. Ferrero, A. Georges, M. Capone, and O. Parcollet, "Polarized superfluidity in the attractive Hubbard model with population imbalance," Phys. Rev. Lett. **101**, 236405 (2008).

[51] L. Radzihovsky, "Fluctuations and phase transitions in Larkin-Ovchinnikov liquid-crystal states of a population-imbalanced resonant Fermi gas," Phys. Rev. A **84**, 023611 (2011).

[52] C.-C. Chien, Q. Chen, Y. He, and K. Levin, "Intermediate-temperature superfluidity in an atomic Fermi gas with population imbalance," Phys. Rev. Lett. **97**, 090402 (2006).

[53] C.-C. Chien, Q. Chen, Y. He, and K. Levin, "Superfluid phase diagrams of trapped Fermi gases with population imbalance," Phys. Rev. Lett. **98**, 110404 (2007).

[54] C.-C. Chien, Q. Chen, Y. He, and K. Levin, "Finite temperature effects in trapped Fermi gases with population imbalance," Phys. Rev. A **74**, 021602(R) (2006).

[55] Y. He, C.-C. Chien, Q. Chen, and K. Levin, "Single-plane-wave Larkin-Ovchinnikov-Fulde-Ferrell state in BCS-BEC crossover," Phys. Rev. A **75**, 021602(R) (2007).

[56] Q. Chen, Y. He, C.-C. Chien, and K. Levin, "Stability conditions and phase diagrams for two-component Fermi gases with population imbalance," Phys. Rev. A **74**, 063603 (2006).

[57] F. Chevy and C. Mora, "Ultra-cold polarized Fermi gases," Rep. Prog. Phys. **73**, 112401 (2010).

[58] A. Bulgac, M. M. Forbes, and A. Schwenk, "Induced p-wave superfluidity in asymmetric Fermi gases," Phys. Rev. Lett. **97**, 020402 (2006).

[59] K. Machida, T. Mizushima, and M. Ichioka, "Generic phase diagram of fermion superfluids with population imbalance," Phys. Rev. Lett. **97**, 120407 (2006).

[60] K. B. Gubbels, M. W. J. Romans, and H. T. C. Stoof, "Sarma phase in trapped unbalanced Fermi gases," Phys. Rev. Lett. **97**, 210402 (2006).

[61] T. D. Cohen, "Phase separation and an upper bound for a generalized superfluid gap for cold Fermi fluids in the unitary regime," Phys. Rev. Lett. **95**, 120403 (2005).

[62] F. Chevy, "Density profile of a trapped strongly interacting Fermi gas with unbalanced spin populations," Phys. Rev. Lett. **96**, 130401 (2006).

[63] M. Iskin and C. A. R. S. De Melo, "Two-species fermion mixtures with population imbalance," Phys. Rev. Lett. **97**, 100404 (2006).

[64] J. Carlson and S. Reddy, "Asymmetric two-component fermion systems in strong coupling," Phys. Rev. Lett. **95**, 060401 (2005).

[65] T. K. Koponen, T. Paananen, J.-P. Martikainen, and P. Törmä, "Finite-temperature phase diagram of a polarized Fermi gas in an optical lattice," Phys. Rev. Lett. **99**, 120403 (2007).

[66] S. Pilati and S. Giorgini, "Phase separation in a polarized Fermi gas at zero temperature," Phys. Rev. Lett. **100**, 030401 (2008).

[67] P. Castorina, M. Grasso, M. Oertel, M. Urban, and D. Zappalà, "Nonstandard pairing in asymmetric trapped Fermi gases," Phys. Rev. A **72**, 025601 (2005).

[68] J.-P. Martikainen, "Ultracold polarized Fermi gas at intermediate temperatures," Phys. Rev. A **74**, 013602 (2006).

[69] D. T. Son and M. A. Stephanov, "Phase diagram of a cold polarized Fermi gas," Phys. Rev. A **74**, 013614 (2006).

[70] F. Chevy, "Universal phase diagram of a strongly interacting Fermi gas with unbalanced spin populations," Phys. Rev. A **74**, 063628 (2006).

[71] A. Bulgac and M. M. Forbes, "Zero-temperature thermodynamics of asymmetric Fermi gases at unitarity," Phys. Rev. A **75**, 031605(R) (2007).

[72] W.-C. Su, "Analytical results for cold asymmetrical fermion superfluids at the mean-field level," Phys. Rev. A **74**, 063627 (2006).

[73] Z. Zhang, H.-H. Hung, C. M. Ho, E. Zhao, and W. V. Liu, "Modulated pair condensate of p-orbital ultracold fermions," Phys. Rev. A **82**, 033610 (2010).

[74] Z. Cai, Y. Wang, and C. Wu, "Stable Fulde-Ferrell-Larkin-Ovchinnikov pairing states in two-dimensional and three-dimensional optical lattices," Phys. Rev. A **83**, 063621 (2011).

[75] X.-W. Guan, M. T. Batchelor, C. Lee, and M. Bortz, "Phase transitions and pairing signature in strongly attractive Fermi atomic gases," Phys. Rev. B **76**, 085120 (2007).

[76] C. H. Pao and S. K. Yip, "Asymmetric Fermi superfluid in a harmonic trap," J. Phys. Condens. Matter **18**, 5567 (2006).

[77] R. Combescot, "BCS superfluidity in ultracold gases with unequal atomic populations," Europhys. Lett. **55**, 150 (2001).

[78] T. Koponen, J. Kinnunen, J.-P. Martikainen, L. M. Jensen, and P. Törmä, "Fermion pairing with spin-density imbalance in an optical lattice," New J. Phys. **8**, 179 (2006).

[79] T.-L. Ho and H. Zhai, "Homogeneous fermion superfluid with unequal spin populations," J. Low Temp. Phys. **148**, 33 (2007).

[80] L. Radzihovsky, "Quantum liquid-crystal order in resonant atomic gases," Physica C **481**, 189 (2012).

[81] A. Koga and P. Werner, "Polarized superfluidity in the imbalanced attractive Hubbard model," J. Phys. Soc. Jpn. **79**, 064401 (2010).

[82] L. Radzihovsky and A. Vishwanath, "Quantum liquid crystals in an imbalanced Fermi gas: Fluctuations and fractional vortices in Larkin-Ovchinnikov states," Phys. Rev. Lett. **103**, 010404 (2009).

[83] P. C. Hohenberg, "Existence of long-range order in one and two dimensions," Phys. Rev. **158**, 383 (1967).

[84] N. D. Mermin and H. Wagner, "Absence of ferromagnetism or antiferromagnetism in one-or two-dimensional isotropic Heisenberg models," Phys. Rev. Lett. **17**, 1133 (1966).

[85] M. W. Zwierlein, A. Schirotzek, C. H. Schunck, and W. Ketterle, "Fermionic superfluidity with imbalanced spin populations," Science **311**, 492 (2006).

[86] G. B. Partridge, W. Li, R. I. Kamar, Y.-a. Liao, and R. G. Hulet, "Pairing and phase separation in a polarized Fermi gas," Science **311**, 503 (2006).

[87] M. W. Zwierlein, C. H. Schunck, A. Schirotzek, and W. Ketterle, "Direct observation of the superfluid phase transition in ultracold Fermi gases," Nature (London) **442**, 54 (2006).

[88] Y.-i. Shin, C. H. Schunck, A. Schirotzek, and W. Ketterle, "Phase diagram of a two-component Fermi gas with resonant interactions," Nature (London) **451**, 689 (2008).

[89] G. B. Partridge, W. Li, Y. A. Liao, R. G. Hulet, M. Haque, and H. T. C. Stoof, "Deformation of a trapped Fermi gas with unequal spin populations," Phys. Rev. Lett. **97**, 190407 (2006).

[90] Y. Shin, M. W. Zwierlein, C. H. Schunck, A. Schirotzek, and W. Ketterle, "Observation of phase separation in a strongly interacting imbalanced Fermi gas," Phys. Rev. Lett. **97**, 030401 (2006).

[91] P. Fulde and R. A. Ferrell, "Superconductivity in a strong spin-exchange field," Phys. Rev. **135**, A550 (1964).

[92] A. I. Larkin and I. U. N. Ovchinnikov, "Nonuniform state of superconductors," Sov. Phys. JETP **20**, 762 (1965), [Zh. Eksp. Teor. Fiz. **47**, 1136 (1964)].

[93] M. M. Parish, S. K. Baur, E. J. Mueller, and D. A. Huse, "Quasi-one-dimensional polarized Fermi superfluids," Phys. Rev. Lett. **99**, 250403 (2007).

[94] H. Hu and X.-J. Liu, "Josephson effect in an atomic Fulde-Ferrell-Larkin-Ovchinnikov superfluid," Phys. Rev. A **83**, 013631 (2011).

[95] M. Swanson, Y. L. Loh, and N. Trivedi, "Proposal for interferometric detection of the topological character of modulated superfluidity in ultracold Fermi gases," New J. Phys. **14**, 033036 (2012).

[96] D.-H. Kim, J. J. Kinnunen, J.-P. Martikainen, and P. Törmä, "Exotic superfluid states of lattice fermions in elongated traps," Phys. Rev. Lett. **106**, 095301 (2011).

[97] L. O. Baksmaty, H. Lu, C. J. Bolech, and H. Pu, "Concomitant modulated superfluidity in polarized Fermi gases," Phys. Rev. A **83**, 023604 (2011).

[98] L. O. Baksmaty, H. Lu, C. J. Bolech, and H. Pu, "A Bogoliubov–de Gennes study of trapped spin-imbalanced unitary Fermi gases," New J. Phys. **13**, 055014 (2011).

[99] X. Cui and Y. Wang, "Polarized Fermi gases in asymmetric optical lattices," Phys. Rev. A **81**, 023618 (2010).

[100] R. M. Lutchyn, M. Dzero, and V. M. Yakovenko, "Spectroscopy of the soliton lattice formation in quasi-one-dimensional fermionic superfluids with population imbalance," Phys. Rev. A **84**, 033609 (2011).

[101] H. Lu, L. O. Baksmaty, C. J. Bolech, and H. Pu, "Expansion of 1D polarized superfluids: The Fulde-Ferrell-Larkin-Ovchinnikov state reveals itself," Phys. Rev. Lett. **108**, 225302 (2012).

[102] R. Mendoza, M. Fortes, and M. A. Solís, "Collective excitations of an imbalanced fermion gas in a 1D optical lattice," J. Low Temp. Phys. **175**, 265 (2014).

[103] J. C. Pei, J. Dukelsky, and W. Nazarewicz, "Competition between normal superfluidity and Larkin-Ovchinnikov phases of polarized Fermi gases in elongated traps," Phys. Rev. A **82**, 021603(R) (2010).

[104] Y. L. Loh and N. Trivedi, "Detecting the elusive Larkin-Ovchinnikov modulated superfluid phases for imbalanced Fermi gases in optical lattices," Phys. Rev. Lett. **104**, 165302 (2010).

[105] T. K. Koponen, T. Paananen, J.-P. Martikainen, M. R. Bakhtiari, and P. Törmä, "FFLO state in 1-, 2- and 3-dimensional optical lattices combined with a non-uniform background potential," New J. Phys. **10**, 045014 (2008).

[106] J. Gukelberger, S. Lienert, E. Kozik, L. Pollet, and M. Troyer, "Fulde-Ferrell-Larkin-Ovchinnikov pairing as leading instability on the square lattice," Phys. Rev. B **94**, 075157 (2016).

[107] W. Yi and L.-M. Duan, "Detecting the breached-pair phase in a polarized ultracold Fermi gas," Phys. Rev. Lett. **97**, 120401 (2006).

[108] G. Sarma, "On the influence of a uniform exchange field acting on the spins of the conduction electrons in a superconductor," J. Phys. Chem. Solids **24**, 1029 (1963).

[109] W. V. Liu and F. Wilczek, "Interior gap superfluidity," Phys. Rev. Lett. **90**, 047002 (2003).

[110] E. Gubankova, A. Schmitt, and F. Wilczek, "Stability conditions and Fermi surface topologies in a superconductor," Phys. Rev. B **74**, 064505 (2006).

[111] E. Zhao and W. V. Liu, "Theory of quasi-one-dimensional imbalanced Fermi gases," Phys. Rev. A **78**, 063605 (2008).

[112] K. Sun and C. J. Bolech, "Pair tunneling, phase separation, and dimensional crossover in imbalanced fermionic superfluids in a coupled array of tubes," Phys. Rev. A **87**, 053622 (2013).

[113] K. Sun and C. J. Bolech, "Oscillatory pairing amplitude and magnetic compressible-incompressible transitions in imbalanced fermionic superfluids in optical lattices of elongated tubes," Phys. Rev. A **85**, 051607(R) (2012).

[114] K. Yang, "Inhomogeneous superconducting state in quasi-one-dimensional systems," Phys. Rev. B **63**, 140511(R) (2001).

[115] A. E. Feiguin and F. Heidrich-Meisner, "Pair correlations of a spin-imbalanced Fermi gas on two-leg ladders," Phys. Rev. Lett. **102**, 076403 (2009).

[116] R. Casalbuoni and G. Nardulli, "Inhomogeneous superconductivity in condensed matter and QCD," Rev. Mod. Phys. **76**, 263 (2004).

[117] E. Gubankova, W. V. Liu, and F. Wilczek, "Breached pairing superfluidity: Possible realization in QCD," Phys. Rev. Lett. **91**, 032001 (2003).

[118] M. Alford, J. Berges, and K. Rajagopal, "Gapless color superconductivity," Phys. Rev. Lett. **84**, 598 (2000).

[119] L. He, M. Jin, and P. Zhuang, "Pion condensation in baryonic matter: From Sarma phase to Larkin-Ovchinnikov-Fudde-Ferrell phase," Phys. Rev. D **74**, 036005 (2006).

[120] J. A. Bowers and K. Rajagopal, "Crystallography of color superconductivity," Phys. Rev. D **66**, 065002 (2002).

[121] M. Alford, J. A. Bowers, and K. Rajagopal, "Crystalline color superconductivity," Phys. Rev. D **63**, 074016 (2001).

[122] R. Casalbuoni, M. Ciminale, M. Mannarelli, G. Nardulli, M. Ruggieri, and R. Gatto, "Effective gap equation for the inhomogeneous Larkin-Ovchinnikov-Fulde-Ferrel superconductive phase," Phys. Rev. D **70**, 054004 (2004).

[123] K. Rajagopal and A. Schmitt, "Stressed pairing in conventional color superconductors is unavoidable," Phys. Rev. D **73**, 045003 (2006).

[124] A. Sedrakian and D. H. Rischke, "Phase diagram of chiral quark matter: From weakly to strongly coupled Fulde-Ferrell phase," Phys. Rev. D **80**, 074022 (2009).

[125] I. Boettcher, T. K. Herbst, J. M. Pawlowski, N. Strodthoff, L. von Smekal, and C. Wetterich, "Sarma phase in relativistic and non-relativistic systems," Phys. Lett. B **742**, 86 (2015).

[126] I. Giannakis, D.-f. Hou, and H.-C. Ren, "A neutral two-flavor LOFF color superconductor," Phys. Lett. B **631**, 16 (2005).

[127] I. Shovkovy and M. Huang, "Gapless two-flavor color superconductor," Phys. Lett. B **564**, 205 (2003).

[128] M. Kitazawa, D. H. Rischke, and I. A. Shovkovy, "Stable gapless superconductivity at strong coupling," Phys. Lett. B **637**, 367 (2006).

[129] H. Mayaffre, S. Krämer, M. Horvatić, C. Berthier, K. Miyagawa, K. Kanoda, and V. F. Mitrović, "Evidence of Andreev bound states as a hallmark of the FFLO phase in κ-(BEDT-TTF)$_2$Cu(NCS)$_2$," Nat. Phys. **10**, 928 (2014).

[130] H. A. Radovan, N. A. Fortune, T. P. Murphy, S. T. Hannahs, E. C. Palm, S. W. Tozer, and D. Hall, "Magnetic enhancement of superconductivity from electron spin domains," Nature (London) **425**, 51 (2003).

[131] M. Kenzelmann, T. Strässle, C. Niedermayer, M. Sigrist, B. Padmanabhan, M. Zolliker, A. D. Bianchi, R. Movshovich, E. D. Bauer, J. L. Sarrao, *et al.*, "Coupled superconducting and magnetic order in CeCoIn$_5$," Science **321**, 1652 (2008).

[132] A. I. Buzdin and S. V. Polonskii, "Nonuniform state in quasi-1D superconductors," Sov. Phys. JETP **66**, 422 (1987), [Zh. Eksp. Teor. Fiz. **93**, 747 (1987)].

[133] L. W. Gruenberg and L. Gunther, "Fulde-Ferrell effect in type-II superconductors," Phys. Rev. Lett. **16**, 996 (1966).

[134] K. Kakuyanagi, M. Saitoh, K. Kumagai, S. Takashima, M. Nohara, H. Takagi, and Y. Matsuda, "Texture in the superconducting order parameter of $CeCoIn_5$ revealed by nuclear magnetic resonance," Phys. Rev. Lett. **94**, 047602 (2005).

[135] C. F. Miclea, M. Nicklas, D. Parker, K. Maki, J. L. Sarrao, J. D. Thompson, G. Sparn, and F. Steglich, "Pressure dependence of the Fulde-Ferrell-Larkin-Ovchinnikov state in $CeCoIn_5$," Phys. Rev. Lett. **96**, 117001 (2006).

[136] A. Bianchi, R. Movshovich, C. Capan, P. G. Pagliuso, and J. L. Sarrao, "Possible Fulde-Ferrell-Larkin-Ovchinnikov superconducting state in $CeCoIn_5$," Phys. Rev. Lett. **91**, 187004 (2003).

[137] G. Koutroulakis, M. D. Stewart, Jr., V. F. Mitrović, M. Horvatić, C. Berthier, G. Lapertot, and J. Flouquet, "Field evolution of coexisting superconducting and magnetic orders in $CeCoIn_5$," Phys. Rev. Lett. **104**, 087001 (2010).

[138] K. Kumagai, M. Saitoh, T. Oyaizu, Y. Furukawa, S. Takashima, M. Nohara, H. Takagi, and Y. Matsuda, "Fulde-Ferrell-Larkin-Ovchinnikov state in a perpendicular field of quasi-two-dimensional $CeCoIn_5$," Phys. Rev. Lett. **97**, 227002 (2006).

[139] S. Uji, T. Terashima, M. Nishimura, Y. Takahide, T. Konoike, K. Enomoto, H. Cui, H. Kobayashi, A. Kobayashi, H. Tanaka, *et al.*, "Vortex dynamics and the Fulde-Ferrell-Larkin-Ovchinnikov state in a magnetic-field-induced organic superconductor," Phys. Rev. Lett. **97**, 157001 (2006).

[140] R. Lortz, Y. Wang, A. Demuer, P. H. M. Böttger, B. Bergk, G. Zwicknagl, Y. Nakazawa, and J. Wosnitza, "Calorimetric evidence for a Fulde-Ferrell-

Larkin-Ovchinnikov superconducting state in the layered organic superconductor κ-(BEDT-TTF)$_2$Cu(NCS)$_2$," Phys. Rev. Lett. **99**, 187002 (2007).

[141] S. Yonezawa, S. Kusaba, Y. Maeno, P. Auban-Senzier, C. Pasquier, K. Bechgaard, and D. Jérome, "Anomalous in-plane anisotropy of the onset of superconductivity in (TMTSF)$_2$ClO$_4$," Phys. Rev. Lett. **100**, 117002 (2008).

[142] T. Kontos, M. Aprili, J. Lesueur, and X. Grison, "Inhomogeneous superconductivity induced in a ferromagnet by proximity effect," Phys. Rev. Lett. **86**, 304 (2001).

[143] Y. L. Loh, N. Trivedi, Y. M. Xiong, P. W. Adams, and G. Catelani, "Origin of excess low-energy states in a disordered superconductor in a Zeeman field," Phys. Rev. Lett. **107**, 067003 (2011).

[144] S. K. Sinha, G. W. Crabtree, D. G. Hinks, and H. Mook, "Study of coexistence of ferromagnetism and superconductivity in single-crystal ErRh$_4$B$_4$," Phys. Rev. Lett. **48**, 950 (1982).

[145] H. Burkhardt and D. Rainer, "Fulde-Ferrell-Larkin-Ovchinnikov state in layered superconductors," Ann. Phys. (Berlin) **506**, 181 (1994).

[146] K. Machida and H. Nakanishi, "Superconductivity under a ferromagnetic molecular field," Phys. Rev. B **30**, 122 (1984).

[147] M. Houzet and A. Buzdin, "Structure of the vortex lattice in the Fulde-Ferrell-Larkin-Ovchinnikov state," Phys. Rev. B **63**, 184521 (2001).

[148] N. Dupuis, "Larkin-Ovchinnikov-Fulde-Ferrell state in quasi-one-dimensional superconductors," Phys. Rev. B **51**, 9074 (1995).

[149] A. G. Lebed and S. Wu, "Larkin-Ovchinnikov-Fulde-Ferrell phase in the superconductor $(TMTSF)_2ClO_4$: Theory versus experiment," Phys. Rev. B **82**, 172504 (2010).

[150] H. Shimahara, "Fulde-Ferrell state in quasi-two-dimensional superconductors," Phys. Rev. B **50**, 12760 (1994).

[151] T. Watanabe, Y. Kasahara, K. Izawa, T. Sakakibara, Y. Matsuda, C. J. Van der Beek, T. Hanaguri, H. Shishido, R. Settai, and Y. Onuki, "High-field state of the flux-line lattice in the unconventional superconductor $CeCoIn_5$," Phys. Rev. B **70**, 020506(R) (2004).

[152] C. Capan, A. Bianchi, R. Movshovich, A. Christianson, A. Malinowski, M. F. Hundley, A. Lacerda, P. G. Pagliuso, and J. L. Sarrao, "Anisotropy of thermal conductivity and possible signature of the Fulde-Ferrell-Larkin-Ovchinnikov state in $CeCoIn_5$," Phys. Rev. B **70**, 134513 (2004).

[153] B. Bergk, A. Demuer, I. Sheikin, Y. Wang, J. Wosnitza, Y. Nakazawa, and R. Lortz, "Magnetic torque evidence for the Fulde-Ferrell-Larkin-Ovchinnikov state in the layered organic superconductor κ-$(BEDT\text{-}TTF)_2Cu(NCS)_2$," Phys. Rev. B **83**, 064506 (2011).

[154] S. Uji, K. Kodama, K. Sugii, T. Terashima, Y. Takahide, N. Kurita, S. Tsuchiya, M. Kimata, A. Kobayashi, B. Zhou, *et al.*, "Magnetic torque studies on FFLO phase in magnetic-field-induced organic superconductor λ-$(BETS)_2FeCl_4$," Phys. Rev. B **85**, 174530 (2012).

[155] K. Cho, B. E. Smith, W. A. Coniglio, L. E. Winter, C. C. Agosta, and J. A. Schlueter, "Upper critical field in the organic superconductor $\beta'' -$

$(ET)_2SF_5CH_2CF_5SO_3$: Possibility of Fulde-Ferrell-Larkin-Ovchinnikov state," Phys. Rev. B **79**, 220507(R) (2009).

[156] Y. Matsuda and H. Shimahara, "Fulde–Ferrell–Larkin–Ovchinnikov state in heavy fermion superconductors," J. Phys. Soc. Jpn. **76**, 051005 (2007).

[157] M. Nicklas, C. F. Miclea, J. L. Sarrao, J. D. Thompson, G. Sparn, and F. Steglich, "Antiferromagnetic fluctuations and the Fulde?Ferrell?Larkin?Ovchinnikov state in $CeCoIn_5$," J. Phys. Soc. Jpn. **76**, 128 (2007).

[158] S. Yonezawa, S. Kusaba, Y. Maeno, P. Auban-Senzier, C. Pasquier, and D. Jérome, "Magnetic-field variations of the pair-breaking effects of superconductivity in $(TMTSF)_2ClO_4$," J. Phys. Soc. Jpn. **77**, 054712 (2008).

[159] I. T. Padilha and M. A. Continentino, "Pressure induced FFLO instability in multi-band superconductors," J. Phys. Condens. Matter **21**, 095603 (2009).

[160] J. Singleton, J. A. Symington, M. S. Nam, A. Ardavan, M. Kurmoo, and P. Day, "Observation of the Fulde-Ferrell-Larkin-Ovchinnikov state in the quasi-two-dimensional organic superconductor κ-$(BEDT\text{-}TTF)_2Cu(NCS)_2$ (BEDT-TTF=bis(ethylene-dithio)tetrathiafulvalene)," J. Phys. Condens. Matter **12**, L641 (2000).

[161] J. A. Symington, J. Singleton, M.-S. Nam, A. Ardavan, M. Kurmoo, and P. Day, "Evidence for the Fulde–Ferrell–Larkin–Ovchinnikov state in the organic superconductor κ-$(BEDT\text{-}TTF)_2Cu(NCS)_2$," Physica B **294**, 418 (2001).

[162] G. Zwicknagl and J. Wosnitza, "Breaking translational invariance by population imbalance: The Fulde–Ferrell–Larkin–Ovchinnikov states," Int. J. Mod. Phys. B **24**, 3915 (2010).

[163] G. Koutroulakis, H. Kühne, J. A. Schlueter, J. Wosnitza, and S. E. Brown, "Microscopic study of the Fulde-Ferrell-Larkin-Ovchinnikov state in an all-organic superconductor," Phys. Rev. Lett. **116**, 067003 (2016).

[164] Z. Koinov, R. Mendoza, and M. Fortes, "Rotonlike Fulde-Ferrell collective excitations of an imbalanced Fermi gas in a two-dimensional optical lattice," Phys. Rev. Lett. **106**, 100402 (2011).

[165] W. Ong, C. Cheng, I. Arakelyan, and J. E. Thomas, "Spin-imbalanced quasi-two-dimensional Fermi gases," Phys. Rev. Lett. **114**, 110403 (2015).

[166] M. M. Parish and J. Levinsen, "Highly polarized Fermi gases in two dimensions," Phys. Rev. A **87**, 033616 (2013).

[167] J. P. A. Devreese, S. N. Klimin, and J. Tempere, "Resonant enhancement of the Fulde-Ferell-Larkin-Ovchinnikov state in three dimensions by a one-dimensional optical potential," Phys. Rev. A **83**, 013606 (2011).

[168] J. P. A. Devreese, M. Wouters, and J. Tempere, "Controlling the pair momentum of the Fulde-Ferrell-Larkin-Ovchinnikov state in a three-dimensional Fermi gas through a one-dimensional periodic potential," Phys. Rev. A **84**, 043623 (2011).

[169] S. Yin, J.-P. Martikainen, and P. Törmä, "Fulde-Ferrell states and Berezinskii-Kosterlitz-Thouless phase transition in two-dimensional imbalanced Fermi gases," Phys. Rev. B **89**, 014507 (2014).

[170] A. V. Samokhvalov, A. S. Mel'nikov, and A. I. Buzdin, "Fulde-Ferrell-Larkin-Ovchinnikov states and quantum oscillations in mesoscopic superconductors and superfluid ultracold Fermi gases," Phys. Rev. B **82**, 174514 (2010).

[171] T. N. De Silva, "Population imbalanced Fermi gases in quasi two dimensions," J. Phys. B **42**, 165301 (2009).

[172] D. E. Sheehy, "Fulde-Ferrell-Larkin-Ovchinnikov state of two-dimensional imbalanced Fermi gases," Phys. Rev. A **92**, 053631 (2015).

[173] C. Chin, R. Grimm, P. Julienne, and E. Tiesinga, "Feshbach resonances in ultracold gases," Rev. Mod. Phys. **82**, 1225 (2010).

[174] M. Olshanii, "Atomic scattering in the presence of an external confinement and a gas of impenetrable bosons," Phys. Rev. Lett. **81**, 938 (1998).

[175] T. Bergeman, M. G. Moore, and M. Olshanii, "Atom-atom scattering under cylindrical harmonic confinement: Numerical and analytic studies of the confinement induced resonance," Phys. Rev. Lett. **91**, 163201 (2003).

[176] R. Dasgupta, "Stability of the breached pair state for a two-species fermionic system in the presence of Feshbach resonance," Phys. Rev. A **80**, 063623 (2009).

[177] S. An, P. Jiang, H. Choi, W. Kang, S. H. Simon, L. N. Pfeiffer, K. W. West, and K. W. Baldwin, "The Asymmetric Superfluid Local Density Approximation (ASLDA)," arXiv:0808.1436 .

[178] A. Bulgac, M. M. Forbes, and P. Magierski, "The unitary Fermi gas: From Monte Carlo to density functionals," in *The BCS-BEC Crossover and the*

Unitary Fermi Gas, edited by W. Zwerger (Springer, Berlin, Heidelberg, 2012) Chap. 9, p. 305.

[179] A. Perali, P. Pieri, L. Pisani, and G. C. Strinati, "BCS-BEC crossover at finite temperature for superfluid trapped Fermi atoms," Phys. Rev. Lett. **92**, 220404 (2004).

[180] J. Tempere, S. N. Klimin, and J. T. Devreese, "Phase separation in imbalanced fermion superfluids beyond the mean-field approximation," Phys. Rev. A **78**, 023626 (2008).

[181] I. Boettcher, J. Braun, T. K. Herbst, J. M. Pawlowski, D. Roscher, and C. Wetterich, "Phase structure of spin-imbalanced unitary Fermi gases," Phys. Rev. A **91**, 013610 (2015).

[182] E. J. Mueller, "Evolution of the pseudogap in a polarized Fermi gas," Phys. Rev. A **83**, 053623 (2011).

[183] M. R. Bakhtiari, M. J. Leskinen, and P. Törmä, "Spectral signatures of the Fulde-Ferrell-Larkin-Ovchinnikov order parameter in one-dimensional optical lattices," Phys. Rev. Lett. **101**, 120404 (2008).

[184] C. Sanner, E. J. Su, A. Keshet, W. Huang, J. Gillen, R. Gommers, and W. Ketterle, "Speckle imaging of spin fluctuations in a strongly interacting Fermi gas," Phys. Rev. Lett. **106**, 010402 (2011).

[185] J. M. Edge and N. R. Cooper, "Signature of the Fulde-Ferrell-Larkin-Ovchinnikov phase in the collective modes of a trapped ultracold Fermi gas," Phys. Rev. Lett. **103**, 065301 (2009).

[186] T. Mizushima, K. Machida, and M. Ichioka, "Direct imaging of spatially

modulated superfluid phases in atomic fermion systems," Phys. Rev. Lett. **94**, 060404 (2005).

[187] A. Korolyuk, F. Massel, and P. Törmä, "Probing the Fulde-Ferrell-Larkin-Ovchinnikov phase by double occupancy modulation spectroscopy," Phys. Rev. Lett. **104**, 236402 (2010).

[188] G. M. Bruun, B. M. Andersen, E. Demler, and A. S. Sørensen, "Probing spatial spin correlations of ultracold gases by quantum noise spectroscopy," Phys. Rev. Lett. **102**, 030401 (2009).

[189] J. Kinnunen, L. M. Jensen, and P. Törmä, "Strongly interacting Fermi gases with density imbalance," Phys. Rev. Lett. **96**, 110403 (2006).

[190] K. Yang, "Realization and detection of Fulde-Ferrell-Larkin-Ovchinnikov superfluid phases in trapped atomic fermion systems," Phys. Rev. Lett. **95**, 218903 (2005).

[191] K. Yang, "Realization, characterization, and detection of novel superfluid phases with pairing between unbalanced fermion species," in *Pairing in Fermionic Systems*, edited by A. Sedrakian, J. W. Clark, and M. Alford (World Scientific, 2006) p. 253.

[192] J. Kajala, F. Massel, and P. Törmä, "Expansion dynamics of the Fulde-Ferrell-Larkin-Ovchinnikov state," Phys. Rev. A **84**, 041601(R) (2011).

[193] V. Gritsev, E. Demler, and A. Polkovnikov, "Interferometric probe of paired states," Phys. Rev. A **78**, 063624 (2008).

[194] E. Altman, E. Demler, and M. D. Lukin, "Probing many-body states of ultracold atoms via noise correlations," Phys. Rev. A **70**, 013603 (2004).

[195] T. Paananen, T. K. Koponen, P. Törmä, and J.-P. Martikainen, "Noise correlations of the ultracold Fermi gas in an optical lattice," Phys. Rev. A **77**, 053602 (2008).

[196] Y.-P. Shim, R. A. Duine, and A. H. MacDonald, "Fulde-Ferrell-Larkin-Ovchinnikov vortex lattice states in fermionic cold-atom systems," Phys. Rev. A **74**, 053602 (2006).

[197] M. O. J. Heikkinen and P. Törmä, "Collective modes and the speed of sound in the Fulde-Ferrell-Larkin-Ovchinnikov state," Phys. Rev. A **83**, 053630 (2011).

[198] J. T. Stewart, J. P. Gaebler, and D. S. Jin, "Using photoemission spectroscopy to probe a strongly interacting Fermi gas," Nature (London) **454**, 744 (2008).

[199] K. Eckert, O. Romero-Isart, M. Rodriguez, M. Lewenstein, E. S. Polzik, and A. Sanpera, "Quantum non-demolition detection of strongly correlated systems," Nat. Phys. **4**, 50 (2008).

[200] T. Roscilde, M. Rodriguez, K. Eckert, O. Romero-Isart, M. Lewenstein, E. Polzik, and A. Sanpera, "Quantum polarization spectroscopy of correlations in attractive fermionic gases," New J. Phys. **11**, 055041 (2009).

[201] C. J. Bolech, F. Heidrich-Meisner, S. Langer, I. P. McCulloch, G. Orso, and M. Rigol, "Long-time behavior of the momentum distribution during the sudden expansion of a spin-imbalanced Fermi gas in one dimension," Phys. Rev. Lett. **109**, 110602 (2012).

[202] H. T. C. Stoof, K. B. Gubbels, and D. B. M. Dickerscheid, *Ultracold Quantum Fields* (Springer, Dordrecht, 2009).

[203] G. Bruun, Y. Castin, R. Dum, and K. Burnett, "BCS theory for trapped ultracold fermions," Eur. Phys. J. D **7**, 433 (1999).

[204] A. Bulgac and Y. Yu, "Renormalization of the Hartree-Fock-Bogoliubov equations in the case of a zero range pairing interaction," Phys. Rev. Lett. **88**, 042504 (2002).

[205] M. Grasso and M. Urban, "Hartree-Fock-Bogoliubov theory versus local-density approximation for superfluid trapped fermionic atoms," Phys. Rev. A **68**, 033610 (2003).

[206] M. M. Forbes, E. Gubankova, W. V. Liu, and F. Wilczek, "Stability criteria for breached-pair superfluidity," Phys. Rev. Lett. **94**, 017001 (2005).

[207] S.-T. Wu and S. Yip, "Superfluidity in the interior-gap states," Phys. Rev. A **67**, 053603 (2003).

[208] P. Hořava, "Stability of Fermi surfaces and K theory," Phys. Rev. Lett. **95**, 016405 (2005).

[209] Y. X. Zhao and Z. D. Wang, "Topological classification and stability of Fermi surfaces," Phys. Rev. Lett. **110**, 240404 (2013).

[210] J. L. Mañes, F. Guinea, and M. A. Vozmediano, "Existence and topological stability of Fermi points in multilayered graphene," Phys. Rev. B **75**, 155424 (2007).

[211] G. E. Volovik, "Quantum phase transitions from topology in momentum space," in *Quantum Analogues: From Phase Transitions to Black Holes and Cosmology*, edited by W. Unruh and R. Schützhold (Springer, Berlin, Heidelberg, 2007) p. 31.

[212] Y. He, C.-C. Chien, Q. Chen, and K. Levin, "Thermodynamics and superfluid density in BCS-BEC crossover with and without population imbalance," Phys. Rev. B **76**, 224516 (2007).

[213] M. J. H. Ku, W. Ji, B. Mukherjee, E. Guardado-Sanchez, L. W. Cheuk, T. Yefsah, and M. W. Zwierlein, "Motion of a solitonic vortex in the BEC-BCS crossover," Phys. Rev. Lett. **113**, 065301 (2014).

[214] T. Yefsah, A. T. Sommer, M. J. H. Ku, L. W. Cheuk, W. Ji, W. S. Bakr, and M. W. Zwierlein, "Heavy solitons in a fermionic superfluid," Nature (London) **499**, 426 (2013).

[215] M. J. H. Ku, B. Mukherjee, T. Yefsah, and M. W. Zwierlein, "Cascade of solitonic excitations in a superfluid Fermi gas: From planar solitons to vortex rings and lines," Phys. Rev. Lett. **116**, 045304 (2016).

[216] M. Abramowitz and I. A. Stegun, *Handbook of Mathematical Functions with Formulas, Graphs, and Mathematical Tables* (Dover, New York, 1974).

CHAPTER 8

KINETICS OF BOSE-EINSTEIN CONDENSATION IN A DIMPLE TRAP

This chapter was adapted from "Kinetics of Bose-Einstein condensation in a dimple potential" by Shovan Dutta and Erich J. Mueller, published in Physical Review A **91**, *013601 (2015).*

8.1 Abstract

We model the dynamics of condensation in a bimodal trap consisting of a large reservoir region and a tight "dimple" whose depth can be controlled. Experimental investigations have found that such dimple traps provide an efficient means of achieving condensation. In our kinetic equations, we include two- and three-body processes. The two-body processes populate the dimple and lead to loss when one of the colliding atoms is ejected from the trap. The three-body processes produce heating and loss. We explain the principal trends, give a detailed description of the dynamics, and provide quantitative predictions for the time scales and condensate yields. From these simulations, we extract optimal parameters for future experiments.

8.2 Introduction

8.2.1 Overview

Cold atom physics faces ever-increasing challenges related to kinetics. Experimentalists are trying to produce ever-more complicated states of matter which

are intrinsically difficult to cool [1–5]. To further complicate matters, the techniques used to produce these states add mechanisms for heating. One paradigm for addressing these challenges is to divide the system into two parts: a "reservoir" which can readily be cooled, coupled to a smaller subsystem which has interesting properties [6–15]. The prototypical example of such a separation are the "dimple traps" pioneered by Pinkse *et al.* [7] and more recently explored by several other groups [6, 8–11]. The key to such programs is an understanding of the kinetic processes through which energy and particles move between the two subsystems. Here we model the loading and equilibration of a dimple trap in a gas of weakly interacting Bosons.

The initial dimple experiments were motivated by a desire to reduce the complexity of cooling atomic gases and explore fundamental questions of condensate growth [16–35]. Dimples have been key to proposals to study atom lasers [11, 36, 37]. They also have promising applications in atom interferometry [38], quantum tweezers for atoms [39], controlling soliton-sound interaction [40], ultraslow light propagation [41], and studying analogs of cosmological physics [42–45].

Stellmer *et al.* describe a typical dimple experiment in Ref. [46]. They precool a cloud of bosonic atoms to hundreds of nanokelvin and trap them in a large but shallow optical trap. At this point, the phase space density is well below the threshold for condensation. Next, a laser beam focused in a small region near the trap center creates a strongly attractive dimple potential, causing a great increase in the local atom density without much change in temperature. As the density in the dimple grows, they see the development of a condensate. Theoretical steps have been taken to understand Bose condensation by this method

[10, 16, 47–53] (see Sec. 8.2.2 for a brief review). However, a detailed quantitative study of how the condensate fraction, the temperature, and the characteristic time scales depend on the trap parameters and the initial conditions is, to our knowledge, still lacking. Here, we take a simple quantum kinetic approach toward achieving this goal.

Since in experiments like Stellmer *et al.*'s, the phase space density in the reservoir stays small, we model it as a classical Boltzmann gas in a three-dimensional (3D) harmonic well. We assume that the collision rate in the reservoir is fast compared to the condensation dynamics so that the reservoir is always in quasi-thermal equilibrium: the occupation of a mode of energy ε is $n_\varepsilon^r(t) = e^{-(\varepsilon-\mu_r(t))/k_B T_r(t)}$, where the temperature T_r and the chemical potential μ_r depend on time. Many cold atom experiments are described by such a quasiequilibrium [6, 7, 10]. For simplicity we assume that the harmonic well is isotropic. We model the dimple as a 3D square well and consider the case where it is turned on suddenly at $t = 0$. This is a prototypical protocol for turning on the dimple [10, 16, 20, 49]. In Sec. 8.3.1, we outline the physical parameters relevant to the dynamics. In Sec. 8.3.2, we analyze the two-body scattering processes responsible for the transfer of atoms from the reservoir to the dimple and their redistribution among the momentum states of the dimple. In particular, the dimple is populated via two-body collisions: one particle enters the dimple, transferring energy to the second. This permits us to write down rate equations for the populations of the dimple states. Due to the symmetry of kinetic processes, the population of a dimple state depends only on its energy. Since in most present-day experiments the dimple contains thousands of energy levels [10, 11], we describe their populations by a continuous distribution function $f(E, t)$, treating the ground state occupation N_0 separately. As the collision pro-

cesses also change the number of atoms N_r and the energy E_r in the reservoir, we arrive at coupled rate equations for $f(E,t)$, N_0, N_r, and E_r.

In Sec. 8.4.1, we discuss the short-time dynamics after turning on the dimple. We find that energy levels near half the dimple depth start filling up first. When the atom density in the dimple becomes comparable to that in the reservoir, particle scattering between energy levels initiates thermalization. Denoting the collisional mean free time in the reservoir by τ_{coll}, we find that for $t \gtrsim 8\tau_{\text{coll}}$, $f(E,t)$ is well approximated by a thermal distribution. The states in the high-energy tail take longer to thermalize than those near the bottom of the dimple. During thermalization, for large enough dimple depths, we notice that $f(E,t)$ passes through a bimodal shape, which should show up in time-of-flight images in experiments. We find that $N_0(t)$ grows slowly at first until it becomes sufficiently large that Bose stimulation takes over. This gives rise to an onset time τ_{on} after which the condensate grows rapidly. This effect was studied for condensation by evaporative cooling in harmonic traps [20, 27–29], and has been observed in recent experiments on dimples [10, 11]. Our estimates of thermalization time scales are similar to those found in a wide range of experiments [20, 24, 25, 27, 46, 54, 55].

We consider both the cases of an infinite trap depth and a finite trap depth. In the former situation, we allow particles in the reservoir to have arbitrarily high energies, whereas in the latter, we eject particles which recoil from a collision with an energy greater than the trap depth. In Sec. 8.4.2, we discuss the infinite trap depth case. In practice, this is equivalent to a trap whose depth is large compared to the dimple depth and the initial thermal energy. The reservoir temperature rises as particles are scattered into the dimple. In the absence

of inelastic losses, the dimple population grows monotonically, saturating after a time τ_{sat} at a value limited by the amount of heating. Guided by the result that the dimple thermalizes fast compared to the population growth rates, we introduce a simplified model where we assume that $f(E,t)$ is given by a thermal Bose-Einstein distribution. This method reproduces all features of the full model for $t \gtrsim 10\tau_{\text{coll}}$ and requires fewer computational resources to simulate. We only use this approximation in Sec. 8.4.2, returning to the full kinetic equations in later sections. We provide detailed results of how the final populations, the final temperature, the entropy gain, τ_{on}, and τ_{sat} vary with the dimple depth ε_d, the initial phase space density ρ_i, the ratio of the reservoir volume to the dimple volume Ω, and the initial temperature T_{r0}. In particular, the atoms do not condense if ε_d is smaller than $|\mu_r(t=0)|$. As ε_d is increased, the final condensate fraction F_0 grows and attains a maximum for an optimal depth ε_d^*, which is set by ρ_i, Ω, and T_{r0}. With further increase in ε_d, F_0 falls off due to increased heating. Such a nonmonotonic variation was observed in a recent experiment [10]. In addition to maximizing F_0, $\varepsilon_d = \varepsilon_d^*$ also minimizes τ_{on}. Both F_0 and ε_d^* increase with ρ_i and Ω. We find that $\Omega\tau_{\text{coll}}$ sets the typical time scale for saturation. The dynamics become more nonadiabatic and takes longer to saturate at larger dimple depths.

We add inelastic losses to our model in Sec. 8.4.3. Here we consider the case for ^{87}Rb where three-body recombination dominates the loss [56]. In this process three atoms collide to produce a molecule in an excited state, thereby releasing a large amount of energy which causes all three atoms to escape. As a result, the condensate fraction decays toward zero after reaching a peak value F_0^{peak} at $t = \tau_{\text{peak}}$. Thus, three-body loss gives a finite condensate lifetime Δt_{lf} [11]. We find that F_0^{peak} exhibits a nonmonotonic dependence on ε_d, similar to

F_0. However, the maximum condensate fraction is smaller by almost an order of magnitude due to the large three-body loss rate in the dimple, where the density becomes large. We find that three-body loss also lowers the optimal dimple depth, in agreement with recent findings [10]. Smaller dimples result in higher local densities, which increase the loss rate. We therefore find an optimal volume ratio Ω^*. Similarly, there is an optimal initial phase space density ρ_i^*. The three-body rate grows faster with T_{r0} than the two-body collision rate. Thus, F_0^{peak} falls off with T_{r0}. We find that Δt_{lf} increases with Ω and decreases with ε_d, ρ_i, and T_{r0}. Since the three-body loss rate varies with the s-wave scattering length a as $|a|^4$ [57], one can influence it by using a different species of atoms or exploiting Feshbach resonances [8]. However, such manipulations may introduce other inelastic channels or hydrodynamic losses [58] and one should be careful to take that into account.

In Sec. 8.4.4, we discuss how our results change when the reservoir trap has a finite depth ε_t. Here, we eject any atom which gains sufficient energy from a collision to have a total energy $\varepsilon > \varepsilon_t$. Such a model correctly describes a trapped gas in the Knudsen regime: the collisional mean free path is larger than the size of the reservoir, which is true in most experiments on trapped gases [25]. We assume that the atom energies in the reservoir follow a Boltzmann distribution truncated at $\varepsilon = \varepsilon_t$. Previous numerical studies have shown that this assumption accurately describes evaporative cooling [25–27]. The effect of finite trap depth on the dynamics becomes appreciable when ε_t is no longer larger than ε_d and $k_B T_{r0}$. We find that lower trap depths yield lower final temperatures and increase the condensate growth rate. This leads to a higher condensate fraction F_0^{peak} and a longer lifetime Δt_{lf}. However, when ε_t becomes very small, the increased evaporation rate of the reservoir limits the rise of Δt_{lf}. We summarize

our findings and suggest future work in Sec. 8.5.

To keep the problem computationally tractable, we have made some simplifying approximations. First, we have not included the mean-field interactions between the condensate and the thermal cloud [10, 28–30, 34, 35, 47, 59–61]. This mean field changes the effective potential experienced by the atoms by an amount proportional to the condensate density, in effect changing the dimple depth. This effect causes a repulsion between the condensate and thermal cloud [29, 59] and also lowers the critical temperature [60]. It can be compensated by making the dimple parameters time-dependent and is unimportant for the short-time dynamics. We do not model quantum fluctuations of the condensate [27, 34, 47, 60], although our model does include thermal fluctuations. The modifications due to quantum fluctuations should be much smaller than that of the mean field [27, 60]. We use the infinite square well energy eigenstates for the dimple. The kinetics do not depend on the exact model of the dimple potential as long as it contains many energy levels, which is true for present-day experiments [10, 11]. In modeling the condensation kinetics, we neglect two kinds of elastic collisions: First, we neglect collisions internal to the dimple where there is no exchange of atoms with the reservoir. These processes serve to equilibrate the dimple. Within our approximations, we find that the dimple thermalizes within $\tau_{\text{th}} \approx 8\tau_{\text{coll}}$, and these processes can at most speed up thermalization. For $t > \tau_{\text{th}}$, these neglected collisions play no role. Second, we neglect collisions in which an atom from a low-energy state in the dimple and an atom from the reservoir collide, leaving two atoms in the dimple. Such collisions can become important for deep dimples when the condensate fraction becomes appreciable and can subsequently enhance the dimple population rate. They can be included in a future refinement of our model and might alter some quantitative

details such as the time to reach saturation. However, we do not expect that these processes will change any of the qualitative features our model captures [28].

8.2.2 Review of past theoretical studies

In order to put our work in context, here we briefly summarize previous theoretical studies of related problems. Much of the theoretical groundwork was developed in Refs. [27–30], largely in the context of modeling evaporative cooling. Our approach closely follows that quantum kinetic formalism. Alternative formalisms have also been developed. For example, Stoof and Bijlsma developed a field theoretical approach [31, 47], while Holland and collaborators developed another form of the quantum Boltzmann equation [32, 34]. The general problem is complex: the system is spatially inhomogeneous, out of equilibrium, and experiencing time-dependent forces. Moreover, the possible parameter space is huge. Any two studies may be distinguished by the system geometry, the formalism used, and the range of parameters studied. Below we give further details about the most relevant studies.

As already introduced, we consider the case of a small impurity at the center of a three-dimensional cloud. This system can be contrasted, for example, to the work of Garrett et al. in which the "dimple potential" spans the waist of an elongated cloud [10]. They found that in such large and inhomogeneous impurities, three-body collisions are relatively unimportant. This is in striking contrast to our geometry.

In Ref. [16], Comparat *et al.* consider a geometry closer to ours, but a very

different experimental protocol. They envisage an experiment where the dimple is first loaded with thermal atoms from a large reservoir. Then one removes the reservoir trap and ramps down the dimple depth to induce condensation. Such a forced evaporation in a cigar-shaped dimple led to the first realization of a ^{133}Cs condensate [8]. They analyze the evolution using classical kinetic theory and optimize elements of their protocol. The also pay close attention to the details of the trapping potential, such as the influence of gravity. The same experiment was studied by Ma *et al.* using a different classical kinetic approach [48]. They used a Monte Carlo simulation to integrate the Boltzmann equation. They carefully study the dependence on the dimple size and the differences between using ^{133}Cs and ^{85}Rb.

While not a kinetic theory, Uncu *et al.* carried out some modeling of adiabatic dimple loading by considering conservation of entropy. They used a simple model for the dimple, parametrized solely by the depth and location [50–52].

Finally, Stoof and collaborators conducted a number of kinetic simulations using their stochastic field theory approach [47, 49]. One feature of this approach is that it allowed them to model the case where the reservoir is partially condensed and describe the collective excitations of the reservoir. They restricted their studies to 1D clouds.

8.3 Formalism

8.3.1 Physical parameters of the dimple potential

In this subsection, we describe our model for the reservoir and the dimple and develop some useful notation.

We model the reservoir as an isotropic harmonic well of frequency ω, truncated at the trap depth ε_t, and assume a truncated Boltzmann distribution. We can relate the number of atoms N_r and the energy E_r in the reservoir to ε_t, the inverse temperature $\beta_r = 1/k_B T_r$, and the fugacity $z_r = e^{\beta_r \mu_r}$ by integrating over the phase space:

$$N_r = \int' \frac{d^3p d^3r}{h^3} \exp\Big[-\beta_r \Big(\frac{p^2}{2m} + \frac{1}{2} m\omega^2 r^2 - \mu_r \Big) \Big]. \tag{8.1}$$

Here, m denotes the mass of an atom. The prime stands for the condition that any atom in the reservoir has a total energy less than ε_t, i.e., $\frac{p^2}{2m} + \frac{1}{2} m\omega^2 r^2 < \varepsilon_t$. Eq. (8.1) can be simplified to obtain

$$N_r = \frac{z_r}{(\beta_r \hbar\omega)^3} \frac{1}{2} \gamma(3, \beta_r \varepsilon_t) \ , \tag{8.2}$$

where γ denotes the lower incomplete gamma function. Similarly, we find for the energy,

$$\begin{aligned} E_r &= \int' \frac{d^3p d^3r}{h^3} \Big(\frac{p^2}{2m} + \frac{1}{2} m\omega^2 r^2 \Big) \ e^{-\beta_r (\frac{p^2}{2m} + \frac{1}{2} m\omega^2 r^2 - \mu_r)} \\ &= \frac{1}{\beta_r} \frac{z_r}{(\beta_r \hbar\omega)^3} \frac{1}{2} \gamma(4, \beta_r \varepsilon_t) \ . \end{aligned} \tag{8.3}$$

After turning on the dimple, N_r, E_r, β_r, and z_r change as functions of time. We define $f_r(t)$ and $e_r(t)$ as the ratio of $N_r(t)$ and $E_r(t)$ to their initial values $\mathcal{N}$

and $\mathcal{E}$, respectively. Thus,

$$f_r \equiv \frac{N_r}{\mathcal{N}} = \frac{\tilde{z}_r}{\tilde{\beta}_r^3}\frac{\gamma(3,\tilde{\beta}_r\tilde{\varepsilon}_t)}{\gamma(3,\tilde{\varepsilon}_t)} \ , \tag{8.4}$$

$$e_r \equiv \frac{E_r}{\mathcal{E}} = \frac{\tilde{z}_r}{\tilde{\beta}_r^4}\frac{\gamma(4,\tilde{\beta}_r\tilde{\varepsilon}_t)}{\gamma(4,\tilde{\varepsilon}_t)} \ , \tag{8.5}$$

where $\tilde{z}_r \equiv z_r/z_{r0}$, $\tilde{\beta}_r \equiv \beta_r/\beta_{r0}$, and $\tilde{\varepsilon}_t \equiv \beta_{r0}\varepsilon_t$. The zeros in the subscripts refer to the respective values at $t = 0$. In our simulation of the kinetics, we use Eqs. (8.4) and (8.5) to extract the instantaneous values of $\tilde{z}_r$ and $\tilde{\beta}_r$ from a knowledge of f_r and e_r.

The spatial density of atoms in the reservoir can be found as

$$\begin{aligned} n_r(\vec{r}) &= \int' \frac{d^3p}{h^3} \ \exp\Big[-\beta_r\Big(\frac{p^2}{2m} + \frac{1}{2}m\omega^2r^2 - \mu_r\Big)\Big] \\ &= \frac{z_r}{\lambda_r^3}\frac{2}{\sqrt{\pi}}\gamma\Big(\frac{3}{2}, \beta_r\varepsilon_t - \frac{1}{2}\beta_r m\omega^2r^2\Big) \ e^{-\frac{1}{2}\beta_r m\omega^2r^2}. \end{aligned} \tag{8.6}$$

Here, $\lambda_r = (2\pi\hbar^2\beta_r/m)^{1/2}$ denotes the thermal de Broglie wavelength. We see that n_r and hence the phase space density fall off with distance from the center of the well. We define the "initial phase space density" ρ_i to be

$$\rho_i \equiv n_{r0}(\vec{0})\lambda_{r0}^3 = z_{r0} \ \frac{2}{\sqrt{\pi}}\gamma(3/2,\tilde{\varepsilon}_t) \ , \tag{8.7}$$

which corresponds to the phase space density near the dimple at $r = 0$.

The "collisional mean-free time" τ_{coll} is the average time between successive collisions among the atoms in the reservoir near $r = 0$. We can estimate τ_{coll} at $t = 0$ as $\tau_{\text{coll}} = (n\sigma v)^{-1}$, where $n = n_{r0}(\vec{0})$, $\sigma = 8\pi a^2$ is the scattering cross section for weakly interacting bosons [62], and v denotes the average initial speed of the reservoir atoms near $r = 0$. One can find v as

$$\begin{aligned} v &= \frac{1}{n_{r0}(\vec{0})}\int' \frac{d^3p}{h^3}\frac{p}{m}\exp\Big[-\beta_{r0}\Big(\frac{p^2}{2m} - \mu_{r0}\Big)\Big] \\ &= \Big(\frac{8}{\pi m\beta_{r0}}\Big)^{1/2}\frac{\sqrt{\pi}/2}{\gamma(3/2,\tilde{\varepsilon}_t)}\gamma(2,\tilde{\varepsilon}_t) \ . \end{aligned} \tag{8.8}$$

Therefore,

$$\tau_{\text{coll}} = \frac{(m\beta_{r0})^{1/2}}{16\sqrt{2\pi}a^2 n_{r0}(\vec{0})} \frac{2}{\sqrt{\pi}} \frac{\gamma(3/2, \tilde{\varepsilon}_t)}{\gamma(2, \tilde{\varepsilon}_t)} \ . \tag{8.9}$$

We define an effective volume V_r of the reservoir as $V_r \equiv N_r/n_r(\vec{0})$. At $t = 0$, this volume has the value

$$V_{r0} = \mathcal{N}/n_{r0}(\vec{0}) = \Big(\frac{2\pi}{\beta_0 m\omega^2}\Big)^{3/2} \frac{\sqrt{\pi}}{4} \frac{\gamma(3, \tilde{\varepsilon}_t)}{\gamma(3/2, \tilde{\varepsilon}_t)} \ , \tag{8.10}$$

where we have substituted from Eqs. (8.2) and (8.6). The incomplete gamma functions become quite insensitive to $\tilde{\varepsilon}_t$ for $\tilde{\varepsilon}_t \gtrsim 5$, where $\gamma(\nu, \tilde{\varepsilon}_t) \approx \Gamma(\nu)$. Then, ρ_i and V_{r0} are just functions of the trap frequency, the initial temperature, and the total number of trapped atoms. When $\tilde{\varepsilon}_t \lesssim 1$, the truncated Boltzmann distribution may no longer be a good model for the reservoir.

We model the dimple as a square well of depth ε_d and length l_d. We find that the condensation dynamics depends on the ratio of V_{r0} to the dimple volume l_d^3. Thus, we define the "volume ratio" $\Omega \equiv V_{r0}/l_d^3$. Using Eqs. (8.7) and (8.10), one can write

$$\Omega \equiv \frac{V_{r0}}{l_d^3} = \frac{\mathcal{N}\lambda_{r0}^3}{l_d^3\, \rho_i} = \frac{\mathcal{N}}{\tilde{l}_d^3} \frac{1}{z_{r0}} \frac{\sqrt{\pi}/2}{\gamma(3/2, \tilde{\varepsilon}_t)} \ , \tag{8.11}$$

where $\tilde{l}_d \equiv l_d/\lambda_{r0}$.

We assume that the eigenstates of the dimple coincide with those for the "particle-in-a-box" model, i.e., they are plane wave states of definite momenta:

$$\psi_{\vec{n}}(\vec{r}) = l_d^{-3/2} e^{i\frac{2\pi}{l_d}\vec{n}.\vec{r}} \ , \tag{8.12}$$

where $\vec{n}$ is a triplet of integers. Such a state has energy

$$\varepsilon_n \equiv -\varepsilon_d + E_n = -\varepsilon_d + \frac{2\pi^2\hbar^2}{m l_d^2} n^2 \ , \tag{8.13}$$

with $n = (n_1^2 + n_2^2 + n_3^2)^{1/2}$. We can estimate the total number of such states, M, by applying the condition that ε_n must be negative, which gives $M \approx$

$(1/6\pi^2)(2ml_d^2\varepsilon_d/\hbar^2)^{3/2}$. For typical magnitudes of ε and l_d in present-day experiments, M is very large [10, 46]. Multiplying Eq. (8.13) by β_{r0}, we can express it in the tilde notation as

$$\tilde{\varepsilon}_n \equiv -\tilde{\varepsilon}_d + \tilde{E}_n = -\tilde{\varepsilon}_d + (\pi/\tilde{l}_d^2)n^2 \ . \tag{8.14}$$

Other models for the dimple (such as a harmonic oscillator) yield similar results for the dynamics.

8.3.2 Kinetic model for condensation in the dimple

To model the nonequilibrium dynamics after the dimple is turned on, we consider the two different kinds of two-body elastic collisions which dominate the energy and particle transport between the reservoir and the dimple. These are illustrated in Fig. 8.1. In the first kind, a collision between two atoms in the reservoir transfers one of the atoms to the dimple, while the other atom gains energy. The second atom can leave the reservoir if its total energy exceeds the trap depth ε_t. However, when ε_t is large compared to ε_d, it is more likely that the second atom will stay in the reservoir and cause heating. Collisions of this kind lead to the growth of the dimple population and increase the local phase space density. In the second kind of collision, an atom in the reservoir collides with an atom in the dimple and transfers it to another energy state in the dimple. The first atom can then either remain in the reservoir or leave, depending on the amount of energy it gains or loses in the process. Collisions of this second kind serve to thermalize the dimple by redistributing its atom population among the various energy levels. In the following, we analyze these two kinds of collisions (and their reverse processes) in detail to derive the equations of motion for the dynamics.

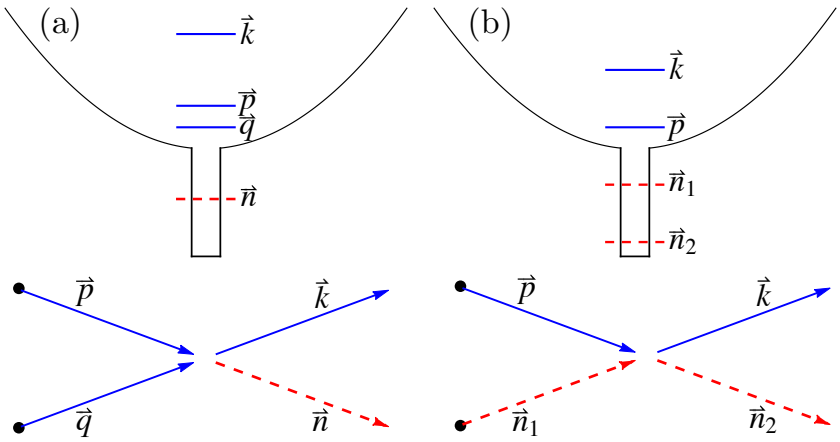

Figure 8.1: Two body collisions responsible for the growth and redistribution of the dimple population: (a) Two atoms from the reservoir collide and one of them enters a dimple state, transferring energy to the other. (b) A reservoir atom exchanges energy with an atom in the dimple, transferring it to a different energy state.

Growth of dimple population

Here we consider the process shown in Fig 8.1(a). Two reservoir atoms with momenta $\vec{p}$ and $\vec{q}$ collide with each other. One of the atoms enters the $\vec{n}$-th state in the dimple and the other atom recoils with momentum $\vec{k}$. The rate of this process depends on the following factors: (i) It is proportional to the occupations of the momentum states $\vec{p}$ and $\vec{q}$ at the origin, which give rise to the Boltzmann factor $\exp[-\beta_r((p^2+q^2)/2m - 2\mu_r)]$. (ii) Due to the quantum-mechanical symmetry of identical bosons, the likelihood of scattering into the $\vec{n}$-th state is enhanced by a factor of $N_{\vec{n}}$, the number of bosons already present in the $\vec{n}$-th state. This effect gives rise to a Bose stimulation factor $1 + N_{\vec{n}}$. (iii) The rate is proportional to U_0^2, where $U_0 = 4\pi\hbar^2 a/m$ is the scattering amplitude for weakly interacting bosons, a being the s-wave scattering length [62]. This factor originates from the overlap of initial and final states in Fermi's golden rule. Since all four single-particle states involved in the collision have definite momenta, the overlap also pro-

duces a delta function which imposes conservation of momentum. Finally, we must conserve energy. Combining these factors, we can write down the total rate at which atoms enter the $\vec{n}$-th dimple state via such processes:

$$\left(\frac{dN_{\vec{n}}}{dt}\right)^g_{in} = \frac{2\pi}{\hbar}U_0^2(1+N_{\vec{n}})\int' \frac{d^3pd^3q}{(2\pi\hbar)^6}\, e^{-\beta_r(\frac{p^2+q^2}{2m}-2\mu_r)} \times \delta\left\{\frac{p^2+q^2-[\vec{p}+\vec{q}-(2\pi\hbar/l_d)\vec{n}]^2}{2m}-\varepsilon_n\right\}. \tag{8.15}$$

Here, the prime restricts the initial momenta $\vec{p}$ and $\vec{q}$ to regions where $p^2, q^2 < 2m\varepsilon_t$.

In the reverse process, a reservoir atom collides with an atom in the $\vec{n}$-th dimple state and both enter the reservoir. The rate at which such processes decrease $N_{\vec{n}}$ can be written using similar reasoning as above:

$$\left(\frac{dN_{\vec{n}}}{dt}\right)^g_{out} = -\frac{2\pi}{\hbar}U_0^2N_{\vec{n}}\int' \frac{d^3pd^3q}{(2\pi\hbar)^6}\, e^{-\beta_r(\frac{p^2+q^2}{2m}-\varepsilon_n-\mu_r)} \times \delta\left\{\frac{p^2+q^2-[\vec{p}+\vec{q}-(2\pi\hbar/l_d)\vec{n}]^2}{2m}-\varepsilon_n\right\}. \tag{8.16}$$

The net growth rate of $N_{\vec{n}}$ can now be found by summing Eqs. (8.15) and (8.16).

In the forward process described by Eq. (8.15), when the atom recoiling with momentum $\vec{k}$ has energy exceeding ε_t, i.e., $k^2/2m = (p^2+q^2)/2m + \varepsilon_d - E_n > \varepsilon_t$, it is lost from the trap. We call such collisions "one-way collisions" since they do not have any reverse process. Whereas collisions in which $k^2/2m < \varepsilon_t$ can happen both ways. We call such collisions "two-way collisions." A one-way collision reduces the number of atoms in the reservoir (N_r) by 2, whereas a two-way collision reduces N_r by 1. Thus, we write

$$\left(\frac{dN_{\vec{n}}}{dt}\right)^g = \left(\frac{dN_{\vec{n}}}{dt}\right)^g_1 + \left(\frac{dN_{\vec{n}}}{dt}\right)^g_2, \tag{8.17}$$

$$\left(\frac{dN_r}{dt}\right)^g = -\sum_{\vec{n}}\left[2\left(\frac{dN_{\vec{n}}}{dt}\right)^g_1 + \left(\frac{dN_{\vec{n}}}{dt}\right)^g_2\right], \tag{8.18}$$

with explicit expressions for these terms given in Appendix 8.6.

In a two-way collision, the reservoir energy E_r increases by $\varepsilon_d - E_n$, which leads to heating. The net rate of increase of E_r due to two-way collisions can be written as

$$\left(\frac{dE_r}{dt}\right)^g_2 = \sum_{\vec{n}} (\varepsilon_d - E_n) \left(\frac{dN_{\vec{n}}}{dt}\right)^g_2 . \tag{8.19}$$

On the other hand, in a one-way collision between two atoms of momenta $\vec{p}$ and $\vec{q}$, their total energy $(p^2+q^2)/2m$ is lost from the reservoir. Depending on whether this energy is greater or less than twice the average particle energy in the reservoir, such a collision cools down or heats up the reservoir. We can obtain the rate at which E_r decreases due to one-way collisions which populate the $\vec{n}$-th dimple state by using arguments similar to those preceding Eq. (8.15):

$$\begin{aligned}\left(\frac{dE_r}{dt}\right)^g_{1,\vec{n}} = &- \frac{2\pi}{\hbar} U_0^2 (1+N_{\vec{n}}) \int'' \frac{d^3p d^3q}{(2\pi\hbar)^6}\, e^{-\beta_r(\frac{p^2+q^2}{2m} - 2\mu_r)} \\ &\times \frac{p^2+q^2}{2m}\, \delta\left\{ \frac{p^2+q^2 - [\vec{p}+\vec{q} - (2\pi\hbar/l_d)\vec{n}]^2}{2m} - \varepsilon_n \right\}. \end{aligned} \tag{8.20}$$

Here, the double prime indicates that the initial momenta satisfy $p^2, q^2 < 2m\varepsilon_t$ and $p^2+q^2 > 2m(\varepsilon_t - \varepsilon_d + E_n)$. In Appendix 8.6, we reduce Eq. (8.20) to a lower dimensional integral. The net rate of change of E_r is given by

$$\left(\frac{dE_r}{dt}\right)^g = \left(\frac{dE_r}{dt}\right)^g_2 + \sum_{\vec{n}} \left(\frac{dE_r}{dt}\right)^g_{1,\vec{n}} . \tag{8.21}$$

Due to symmetry, the population of the dimple states depend only on their energy, as can be verified from Eqs. (8.46) and (8.47). This feature allows us to describe them by a continuous distribution function in energy $f(\tilde{E},t)$: the number of atoms in the energy interval $d\tilde{E}$ at time t equals $\mathcal{N} f(\tilde{E},t) d\tilde{E}$. Using this definition we can relate $f(\tilde{E},t)$ to $N_{\vec{n}}(t)$ via the density of states $D(\tilde{E})$: $f(\tilde{E},t) = D(\tilde{E}) N_{\vec{n}}(t)/\mathcal{N}$, where $\tilde{E}_n = \tilde{E}$. The density of states $D(\tilde{E})$ can be obtained by

noting that $\tilde{E}_n = (\pi/\tilde{l}_d^2)n^2$ [Eq. (8.14)], which yields $D(\tilde{E}) = 2\tilde{l}_d^3(\tilde{E}/\pi)^{1/2}$. We can then express Eq. (8.17) as equations of motion for $f(\tilde{E},t)$. The characteristic time in these equations is $\tau_{\text{coll}}\Omega$, the product of the collision time and the volume ratio of the reservoir to the dimple.

To account for condensation, we treat $N_{\vec{0}}(t)$ separately from $f(\tilde{E},t)$ and define $f_0(t) \equiv N_{\vec{0}}(t)/\mathcal{N}$ as the condensate fraction. Eqs. (8.15) and (8.16) then give equations of motion for $f_0(t)$, which can be written in terms of one- and two-way collisions.

The reservoir fraction $f_r(t)$ defined in Eq. (8.4) then evolves according to

$$\left(\frac{df_r}{dt}\right)^g = -2\left(\frac{df_0}{dt}\right)_1^g - \left(\frac{df_0}{dt}\right)_2^g - \int_0^{\tilde{\varepsilon}_d} d\tilde{E}\left\{2\left[\frac{\partial f(\tilde{E},t)}{\partial t}\right]_1^g + \left[\frac{\partial f(\tilde{E},t)}{\partial t}\right]_2^g\right\}, \tag{8.22}$$

and similar expressions hold for the relative energy in the reservoir $e_r(t)$ defined in Eq. (8.5).

Redistribution of dimple population

Here, we examine two-body collisions of the kind illustrated in Fig 8.1(b), where a reservoir atom of momentum $\vec{p}$ exchanges energy with a dimple atom in state $\vec{n}_1$, sending it to a different state $\vec{n}_2$. The rate of such processes can be calculated using reasoning similar to that outlined at the beginning of section 8.3.2:

$$\begin{aligned}\frac{dN_{\vec{n}_1\to\vec{n}_2}}{dt} =& \frac{2\pi}{\hbar}U_0^2 N_{\vec{n}_1}(1+N_{\vec{n}_2})\frac{1}{l_d^3}\int' \frac{d^3p}{(2\pi\hbar)^3}\, e^{-\beta_r(\frac{p^2}{2m}-\mu_r)} \\ &\times \delta\left\{\frac{p^2}{2m} + E_{n_1} - \frac{[\vec{p}+(2\pi\hbar/l_d)(\vec{n}_1-\vec{n}_2)]^2}{2m} - E_{n_2}\right\},\end{aligned} \tag{8.23}$$

where the prime denotes the condition $p^2 < 2m\varepsilon_t$. The net rate of change of $N_{\vec{n}}$ due to such collisions is given by

$$\left(\frac{dN_{\vec{n}}}{dt}\right)^r = \sum_{\vec{n}' \neq \vec{n}} \frac{dN_{\vec{n}' \to \vec{n}}}{dt} - \frac{dN_{\vec{n} \to \vec{n}'}}{dt} \ . \tag{8.24}$$

Once again there are one- and two-way collisions. In Eq. (8.23), if the final energy of the reservoir atom is sufficiently large, $p^2/2m + E_{n_1} - E_{n_2} > \varepsilon_t$, it is lost from the trap. Such one-way collisions happen only when the dimple atom is transferred to a much lower energy level. As in our prior sections, collisions in which the above condition is not satisfied happen both ways. These do not change the number of atoms in the reservoir (N_r), but can change their average energy, thus changing the reservoir temperature T_r. Denoting the rates of one- and two-way collisions by $R^{(1)}_{\vec{n},\vec{n}'}$ and $R^{(2)}_{\vec{n},\vec{n}'}$, respectively, we write

$$\left(\frac{dN_{\vec{n}}}{dt}\right)^r = \sum_{\vec{n}' \neq \vec{n}} R^{(1)}_{\vec{n},\vec{n}'} + R^{(2)}_{\vec{n},\vec{n}'} \ , \tag{8.25}$$

$$\left(\frac{dN_r}{dt}\right)^r = - \sum_{\substack{\vec{n}',\vec{n} \\ E_{n'} > E_n}} R^{(1)}_{\vec{n},\vec{n}'} \ . \tag{8.26}$$

In a one-way collision, the energy in the reservoir (E_r) decreases by an amount $p^2/2m$. Therefore, we obtain the net rate of change of E_r due to one-way collisions as

$$\left(\frac{dE_r}{dt}\right)^r_1 = \sum_{\substack{\vec{n}',\vec{n} \\ E_{n'} > E_n}} \left(\frac{dE_r}{dt}\right)^r_{1,\vec{n}' \to \vec{n}} \ , \tag{8.27}$$

where

$$\left(\frac{dE_r}{dt}\right)^r_{1,\vec{n}' \to \vec{n}} = - \frac{2\pi z_r}{\hbar l_d^3} U_0^2 N_{\vec{n}'}(1 + N_{\vec{n}}) \int'' \frac{d^3p}{(2\pi\hbar)^3} \, e^{-\beta_r \frac{p^2}{2m}} \times \frac{p^2}{2m} \delta \left\{ \frac{p^2}{2m} + E_{n'} - \frac{\left[\vec{p} + (2\pi\hbar/l_d)(\vec{n}_1 - \vec{n}_2)\right]^2}{2m} - E_n \right\} . \tag{8.28}$$

Here, the double prime imposes the condition $2m(\varepsilon_t + E_n - E_{n'}) < p^2 < 2m\varepsilon_t$. Conversely, when a two-way collision transfers a dimple atom from state $\vec{n}'$ to state $\vec{n}$, the reservoir energy changes by $E_{n'} - E_n$. Thus,

$$\left(\frac{dE_r}{dt}\right)_2^r = \sum_{\substack{\vec{n}',\vec{n} \\ E_{n'}>E_n}} (E_{n'} - E_n)\, R^{(2)}_{\vec{n},\vec{n}'} \ . \tag{8.29}$$

The total change in E_r is then found by adding the two contributions [Eqs. (8.27) and (8.29)].

Describing the dimple states in terms of a continuous distribution function $f(\tilde{E}, t)$, as defined in section 8.3.2, we can express Eq. (8.25) as

$$\left[\frac{\partial f(\tilde{E},t)}{\partial t}\right]^r = \int_0^{\tilde{\varepsilon}_d} d\tilde{E}' \left[\mathcal{R}_1(\tilde{E},\tilde{E}') + \mathcal{R}_2(\tilde{E},\tilde{E}')\right] \ , \tag{8.30}$$

where $\mathcal{R}_1(\tilde{E},\tilde{E}')$ and $\mathcal{R}_2(\tilde{E},\tilde{E}')$ are given in Appendix 8.7. As would be expected, we find that the characteristic time for these processes is the collision time τ_{coll}. The rate equations for the condensate fraction f_0, the reservoir fraction f_r, and the relative energy in the reservoir e_r can be obtained likewise from Eqs. (8.25)$-$(8.29).

To simulate the overall dynamics incorporating both the growth and the redistribution process, we add the corresponding equations of motion describing the two processes. In the next section, we present our numerical results. Three-body processes will be discussed in Sec. 8.4.3.

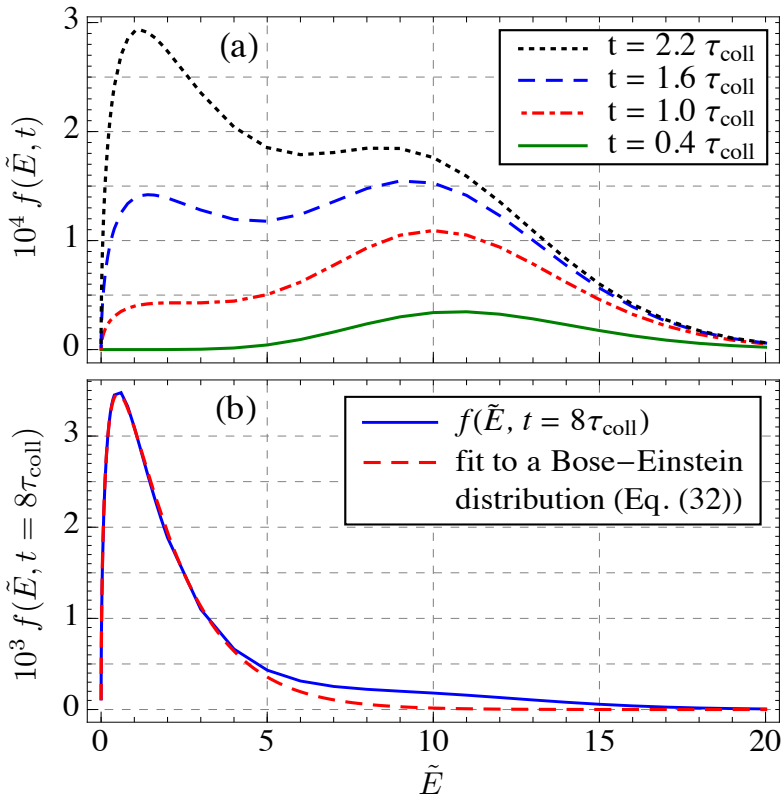

Figure 8.2: Time evolution of the atom distribution in the dimple, $f(\tilde{E}, t)$, for $0 < t \lesssim 10\tau_{\text{coll}}$, where $\tilde{E} \equiv E/k_B T_{r0}$ is the energy measured from the bottom of the dimple scaled by the initial reservoir temperature. (a) Initial population growth occurs near $\tilde{E} = \tilde{\varepsilon}_d/2$. These atoms are quickly transferred to lower energy states, giving rise to a hump near $\tilde{E} = 0$, which grows rapidly. Around $t \approx 1.6\tau_{\text{coll}}$, $f(\tilde{E}, t)$ has a bimodal shape for $\tilde{\varepsilon}_d \gtrsim 8$, which should show up in time-of-flight experiments. (b) $f(\tilde{E}, t = 8\tau_{\text{coll}})$ is well fit by a thermal Bose-Einstein distribution given by Eq. (8.31). Parameter values used for plotting are $\rho_i = 0.05$, $\Omega = 2000$, $\tilde{\varepsilon}_d = 20$, $\tilde{\varepsilon}_t = 10$, and $\tilde{l}_d = 100$. At $T_{r0} = 1\,\mu$K, these parameters give $\tau_{\text{coll}} \approx 11$ ms for ^{87}Rb.

8.4 Results

8.4.1 Initial dynamics and thermalization

Figure 8.2 shows how the particle distribution in the dimple $f(\tilde{E}, t)$ evolves for $0 < t \lesssim 10\tau_{\text{coll}}$ after the dimple is turned on at $t = 0$. Although the plots cor-

respond to specific initial conditions stated in the caption, we observe the same general features for other choices of parameters. We find that the reservoir particles predominantly scatter into states whose energies are near half the dimple depth, creating a hump in $f(\tilde{E},t)$. Such a highly nonequilibrium distribution does not last for long. Within a few $\tau_{\rm coll}$, the processes in Fig. 8.1(b) transfer these atoms to lower energy states near the bottom of the dimple. This generates a hump in $f(\tilde{E},t)$ near $\tilde{E}=0$, which grows and soon overtakes the hump near $\tilde{E}=\tilde{\varepsilon}_d/2$. As a result, around $t\sim 1.6\tau_{\rm coll}$, $f(\tilde{E},t)$ has a bimodal shape. The peaks are more distinct for larger dimple depths and are hard to resolve when $\tilde{\varepsilon}_d \lesssim 8$. This nonequilibrium stage lasts for a few collision times. For ^{87}Rb with $\rho_i = 0.05$ and $T_{r0} = 1\,\mu$K, the collision time is $\tau_{\rm coll}\approx 11$ ms, sufficiently long that one can experimentally resolve these dynamics. In time-of-flight imaging, the bimodal shape of $f(\tilde{E},t)$ should produce two expanding shells of atoms.

For $t \gtrsim 8\tau_{\rm coll}$, we find that $f(\tilde{E},t)$ is well approximated by a thermal distribution. This is seen in Fig. 8.2(b) where we fit $f(\tilde{E},t=8\tau_{\rm coll})$ to a Bose-Einstein distribution truncated at $\tilde{E}=\tilde{\varepsilon}_d$:

$$f(\tilde{E}) = \frac{D(\tilde{E})/\mathcal{N}}{e^{\beta_d(-\varepsilon_d+E-\mu_d)}-1} = \frac{1}{\rho_i\Omega}\frac{2(\tilde{E}/\pi)^{1/2}}{e^{\tilde{\beta}_d(-\tilde{\varepsilon}_d+\tilde{E}-\tilde{\mu}_d)}-1}\,. \tag{8.31}$$

Here $\beta_d \equiv \tilde{\beta}_d\beta_{r0} = 1/k_BT_d$ and $\mu_d \equiv \tilde{\mu}_d/\beta_{r0}$ denote the inverse temperature and chemical potential of the dimple. The high-energy tail of $f(\tilde{E},t)$ takes a little longer to thermalize. Once the density in the dimple exceeds that of the reservoir, the time scales for redistribution become much shorter than those for growth. Thus we find quasi-thermal equilibrium inside the dimple for $t\gtrsim 8\tau_{\rm coll}$, though β_d and μ_d change with time.

We find that the condensate fraction f_0 grows very slowly at first until it becomes large enough that Bose stimulation can take over. This gives rise to

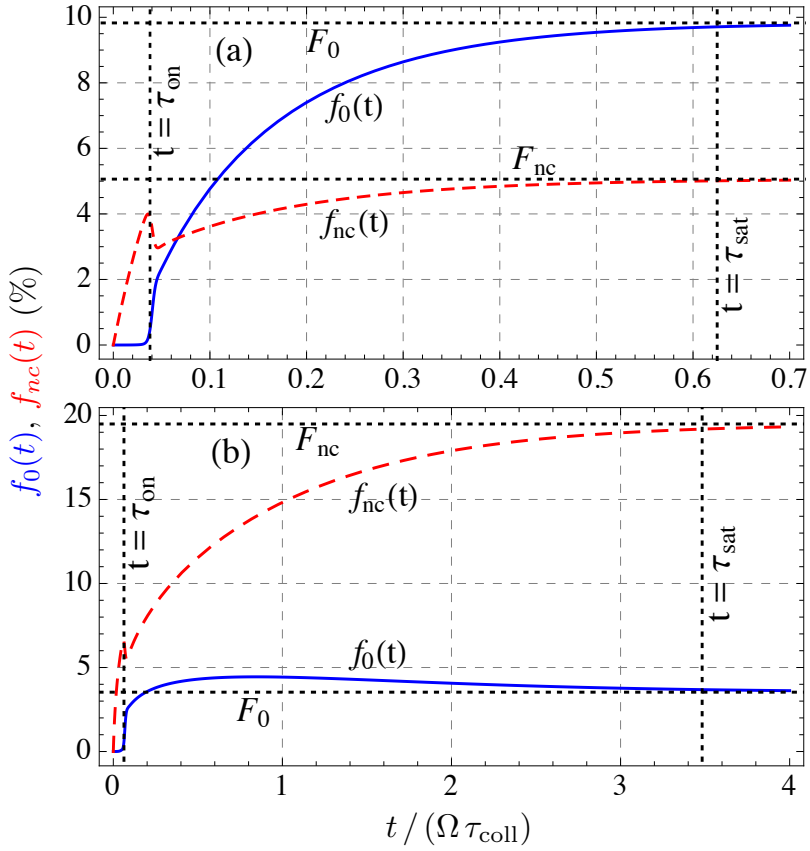

Figure 8.3: Evolution of the condensate fraction f_0 (solid blue) and the non-condensed fraction f_{nc} (dashed red) in the dimple for $\rho_i = 0.05$, $\Omega = 2000$, and $\tilde{l}_d = 20$, assuming no three-body loss. The condensate fraction $f_0(t)$ grows slowly at first until Bose stimulation takes over at the onset time $\tau_{\rm on}$. The populations reach equilibrium at a much later time $\tau_{\rm sat}$: F_0 and F_{nc} denote the saturation values of f_0 and f_{nc}, respectively. (a) $\tilde{\varepsilon}_d = 7$: when the dimple depth is small, $f_0(t)$ monotonically increases toward F_0. (b) $\tilde{\varepsilon}_d = 28$: at large dimple depths, $f_0(t)$ overshoots F_0 after $t = \tau_{\rm on}$ before coming down again.

a noticeable time delay in the onset of condensation, marked as $\tau_{\rm on}$ in Fig. 8.3 where we plot $f_0(t)$ for two different sets of parameter values. Figure 8.3 also shows the evolution of the total noncondensate fraction in the dimple $f_{nc}(t) = \int_0^{\tilde{\varepsilon}_d} d\tilde{E} f(\tilde{E}, t)$. After $t = \tau_{\rm on}$, $f_0(t)$ grows rapidly due to Bose enhancement. Part of this enhanced growth comes from atoms in low-lying excited states scattering to the ground state via two-body collisions with reservoir atoms. This redistribution causes a sudden dip in $f_{nc}(t)$ just after $t = \tau_{\rm on}$. In

the absence of three-body loss, $f_0(t)$ and $f_{nc}(t)$ reach their respective saturation values F_0 and F_{nc} at a much later time $t = \tau_{\text{sat}}$. When $\tilde{\varepsilon}_d$ is small, $f_0(t)$ monotonically approaches F_0 from below [Fig. 8.3(a)], whereas for large dimple depths, $f_0(t)$ overshoots F_0 shortly after $t = \tau_{\text{on}}$ [Fig. 8.3(b)]. In both cases, however, the reservoir fraction $f_r(t)$ monotonically decreases from 1 toward its saturation value F_r.

8.4.2 Results for infinite trap depth

When the trap is sufficiently deep, no particles can be lost. Therefore only two-way collisions are present and we have the relation $f_r(t) + f_0(t) + f_{nc}(t) = 1$. We can simplify the calculation further by noting our previous observation that the dimple thermalizes very quickly compared to the growth rate of its atom population. Thus, we assume that $f(\tilde{E}, t)$ is always described by a thermal distribution as given in Eq. (8.31), where the temperature (T_d) and the chemical potential (μ_d) of the dimple vary with time. This approximation allows us to rapidly simulate the dynamics for a wide range of parameter values and reproduces all features of the full model for $t \gtrsim 10\tau_{\text{coll}}$.

Long time behavior

Figure 8.4 shows the variation of F_0 with $\tilde{\varepsilon}_d$ for different values of the initial phase space density ρ_i and the volume ratio Ω. The different features in the plots can be explained by the following model: as particles are scattered into the negative energy states of the dimple, those remaining in the reservoir have a higher total energy. Therefore the temperature T_r increases and the chemical

potential μ_r drops [see Eqs. (8.2) and (8.3)]. In equilibrium, $T_r = T_d \equiv T_f$ and $\mu_r = \mu_d \equiv \mu_f \leq -\varepsilon_d$, since we are considering bosonic atoms. At a given temperature T_f, there is an upper limit to the number of noncondensed particles the dimple can hold, which occurs when $\mu_f = -\varepsilon_d$:

$$f_{nc}^{max} \approx \frac{1}{\rho_i \Omega} \int_0^\infty d\tilde{E}\, \frac{2(\tilde{E}/\pi)^{1/2}}{e^{\tilde{\beta}_f \tilde{E}} - 1} = \frac{\zeta(3/2)}{\rho_i \Omega \tilde{\beta}_f^{3/2}}\,, \tag{8.32}$$

where $\beta_f \equiv 1/k_B T_f$. Consequently, only if $1 - F_r \geq f_{nc}^{max}$ will we get condensation. The condensate fraction will be $F_0 = 1 - F_r - f_{nc}^{max}$ and the chemical potential will be $\mu_f = -\varepsilon_d$. The chemical potential of the reservoir must monotonically decrease as particles scatter into the dimple. Thus we only find condensation if $\ln(\rho_i) = \tilde{\mu}_{r0} > -\tilde{\varepsilon}_d$. This behavior is illustrated in Fig. 8.4. As $\tilde{\varepsilon}_d$ increases from this threshold, the condensate fraction grows. This growth occurs because the lower final chemical potential implies a lower density of the reservoir atoms (and hence, a larger number of atoms in the dimple). However, deeper dimples also lead to more heating of the reservoir. If $\tilde{\varepsilon}_d$ is too large, this heating prevents condensation. Thus F_0 is nonmonotonic, and there exists an optimal dimple depth, $\tilde{\varepsilon}_d^*$, for which F_0 is maximum. The F_0 vs $\tilde{\varepsilon}_d$ curves for different ρ_i and Ω can be well reproduced by assuming $\mu_f = -\varepsilon_d$ and imposing conservation of energy and particle number. When $k_B T_f$ is small relative to ε_d, this yields

$$F_r \tilde{T}_f - \frac{\tilde{\varepsilon}_d}{3}(1 - F_r) + f_{nc}^{max} \tilde{T}_f \frac{\zeta(5/2)}{2\zeta(3/2)} = 1\,, \tag{8.33}$$

with $F_r = e^{-\tilde{\beta}_f \tilde{\varepsilon}_d}/\rho_i \tilde{\beta}_f^3$ and f_{nc}^{max} given by Eq. (8.32). Solving Eq. (8.33) for $\tilde{T}_f$ one finds a very weak dependence on ρ_i and virtually no dependence on Ω for sufficiently large Ω. Therefore, choosing a higher volume ratio does not change the reservoir fraction F_r but decreases the maximum fraction of noncondensed particles in the dimple f_{nc}^{max}. In other words, increasing the ratio of the reservoir size to the dimple size increases the local atom density without altering the final

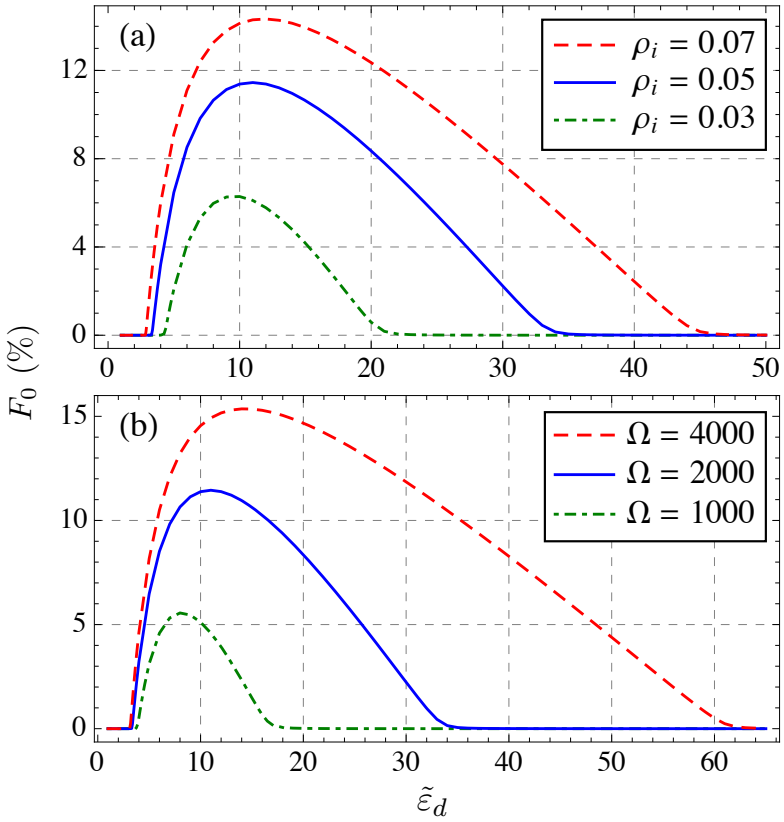

Figure 8.4: Variation of the final condensate fraction F_0 with the dimple depth $\tilde{\varepsilon}_d \equiv \varepsilon_d / k_B T_{r0}$ for different choices of the initial phase space density ρ_i and the volume ratio Ω when the trap depth is infinite and there is no three-body loss. In (a), $\Omega = 2000$ and in (b), $\rho_i = 0.05$. When $\tilde{\varepsilon}_d < |\tilde{\mu}_{r0}| = |\ln(\rho_i)|$, the atoms do not condense. As $\tilde{\varepsilon}_d$ is increased beyond this threshold, the atom density in the dimple grows, producing a larger F_0. However, atoms scattering into a deeper dimple also cause more heating, which prevents condensation at large $\tilde{\varepsilon}_d$. Consequently, there exists an optimal dimple depth $\tilde{\varepsilon}_d^*$ which yields the maximum condensate fraction. Larger ρ_i and Ω increase the atom density in the dimple without causing much change in the final temperature, hence give a larger F_0. The optimal dimple depth $\tilde{\varepsilon}_d^*$ also grows with both ρ_i and Ω.

temperature, thus producing a larger condensate fraction. Similarly, a large ρ_i decreases both F_r and f_{nc}^{max}, hence increasing F_0, as one would expect intuitively. This explains why the F_0 vs $\tilde{\varepsilon}_d$ curves in Fig. 8.4 are higher for greater values of Ω and ρ_i. We also find that the optimal dimple depth $\tilde{\varepsilon}_d^*$ increases with both Ω and ρ_i.

Figures 8.5(a) and 8.5(b) show that the final temperature rises linearly with the dimple depth when $\tilde{\varepsilon}_d$ is large. We can understand this behavior by considering the limit of very large $\tilde{\varepsilon}_d$, where F_0 is vanishingly small and the dimple population can be treated classically. Using Eqs. (8.4) and (8.31), one can write $F_r = ze^{-\tilde{\beta}_f\tilde{\varepsilon}_d}/\rho_i\tilde{\beta}_f^3$ and $F_{nc} \approx z/\rho_i\Omega\tilde{\beta}_f^3$, with $z = \exp\left[\beta_f(\varepsilon_d + \mu_f)\right]$. Conservation of both energy and particle number then yields

$$F_r = \frac{\tilde{\beta}_f\tilde{\varepsilon}_d + 3\tilde{\beta}_f - 3/2}{\tilde{\beta}_f\tilde{\varepsilon}_d + 3/2} = \frac{1}{1 + \tilde{\beta}_f^{3/2}e^{\tilde{\beta}_f\tilde{\varepsilon}_d}/\Omega}\,. \tag{8.34}$$

To approximate the solution to this transcendental equation, we replace the right-hand side with a step function. The value of $\tilde{\beta}_f$ at the center of the step [and hence, our approximate solution to Eq. (8.34)] is found by setting $1/(1 + \tilde{\beta}_f^{3/2}e^{\tilde{\beta}_f\tilde{\varepsilon}_d}/\Omega) = 1/2$. This gives $\tilde{\beta}_f = 1.5\,\tilde{\varepsilon}_d^{-1}\,W\big((2^{1/3}/3)\,\tilde{\varepsilon}_d\Omega^{2/3}\big)$, where W denotes the Lambert W function. Since W increases only logarithmically for large arguments, $\tilde{T}_f$ rises linearly with $\tilde{\varepsilon}_d$ when $\tilde{\varepsilon}_d$ is large. Substituting this result into the left-hand size of Eq. (8.34), we see that for large $\tilde{\varepsilon}_d$, $F_r \sim A + B/\tilde{\varepsilon}_d$, where A and B depend logarithmically on $\tilde{\varepsilon}_d$. This structure is apparent in Fig. 8.5(c) as a saturation of F_{nc}. At smaller dimple depths, F_{nc} equals f_{nc}^{max}, which grows with $\tilde{\varepsilon}_d$ as $\tilde{\beta}_f$ decreases.

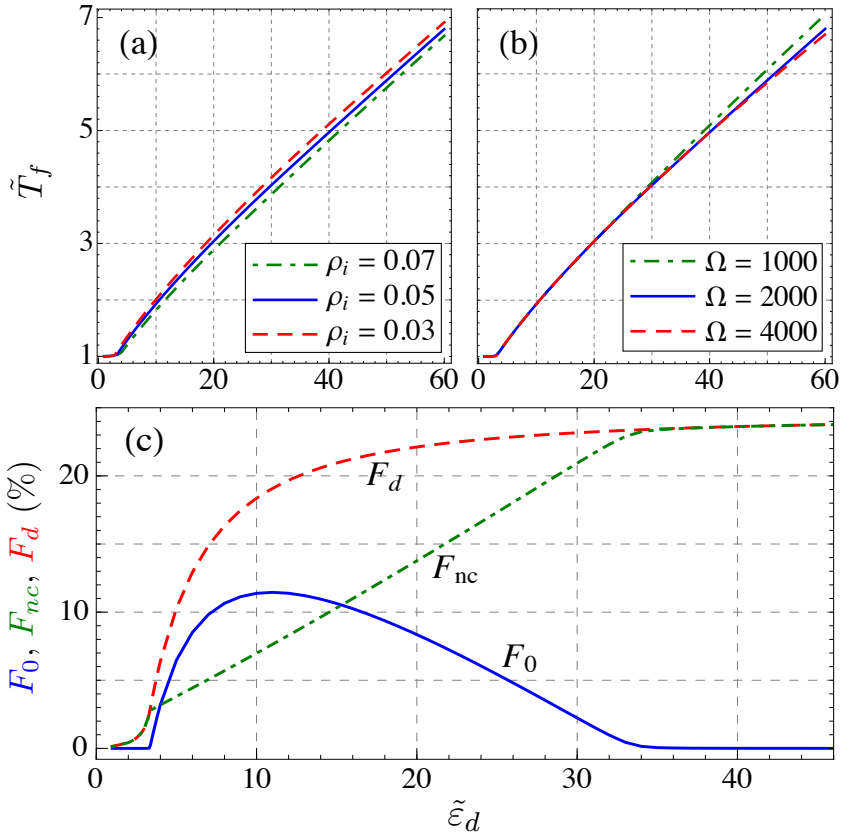

Figure 8.5: (a, b) Variation of the final temperature $\tilde{T}_f \equiv T_f/T_{r0}$ with the dimple depth $\tilde{\varepsilon}_d \equiv \varepsilon_d/k_B T_{r0}$ for different choices of ρ_i and Ω. In (a), $\Omega = 2000$ and in (b), $\rho_i = 0.05$. When $\tilde{\varepsilon}_d < |\tilde{\mu}_{r0}|$, very few atoms scatter into the dimple and $T_f \approx T_{r0}$. As $\tilde{\varepsilon}_d$ is increased, atoms scattering into the dimple cause more heating of the reservoir. Thus, $\tilde{T}_f$ increases monotonically with $\tilde{\varepsilon}_d$. (c) Variation of the final condensate fraction F_0 (solid blue), the final non-condensate fraction F_{nc} (dot-dashed green), and their sum F_d (dashed red) with the dimple depth $\tilde{\varepsilon}_d$ for $\rho_i = 0.05$ and $\Omega = 2000$. When $\mu_{r0} < -\varepsilon_d$, no condensation occurs and $F_0 = 0$. At larger dimple depths, the phase space density in the dimple becomes large enough to reach condensation. In this regime, the final chemical potential lies at the bottom of the dimple, $\mu_f \approx -\varepsilon_d$, and the noncondensed fraction in the dimple follows the standard expression for a Bose gas, $F_{nc} = \zeta(3/2)/\rho_i \Omega \tilde{\beta}_f^{3/2} \propto \tilde{\varepsilon}_d$. Deeper dimples give a larger $\tilde{T}_f$, causing F_{nc} to grow monotonically. When $\tilde{\varepsilon}_d$ becomes very large, excessive heating prevents condensation. Thereafter μ_f decreases below $-\varepsilon_d$, causing F_{nc} to saturate.

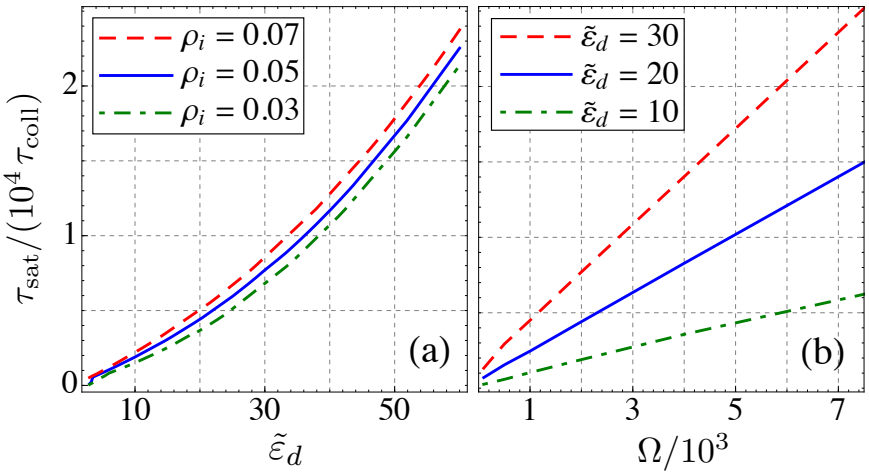

Figure 8.6: (a) Variation of the saturation time $\tau_{\rm sat}$ with the dimple depth $\tilde{\varepsilon}_d$ for different values of ρ_i when $\Omega = 2000$. The rate of particle scattering into the dimple falls with increasing $\tilde{\varepsilon}_d$ due of smaller overlap between the initial and final states. This results in a larger $\tau_{\rm sat}$. Changing the initial phase space density ρ_i alters the collision time $\tau_{\rm coll}$, however $\tau_{\rm sat}/\tau_{\rm coll}$ remains essentially unchanged. This is expected since the dimple is populated via two-body collisions. (b) Variation of $\tau_{\rm sat}$ with the volume ratio Ω at different dimple depths when $\rho_i = 0.05$. $\tau_{\rm sat}$ grows almost linearly with Ω because a larger Ω increases the total particle number without changing the scattering rate into the dimple. Thus $\Omega\tau_{\rm coll}$ sets the typical timescale for saturation.

Timescales

As seen from Fig. 8.3, the condensation dynamics are well characterized by two time scales: the time needed for the populations to saturate, $\tau_{\rm sat}$, and the time which marks the onset of condensation, $\tau_{\rm on}$.

Chemical equilibrium is reached when the reservoir chemical potential μ_r crosses below the dimple bottom and merges with the dimple chemical potential μ_d. This is accompanied by the reservoir fraction $f_r(t)$ approaching F_r from above. For concreteness, we define the saturation time $\tau_{\rm sat}$ as the time required for $f_r(t)$ to equal $1.002\,F_r$. In Fig. 8.6(a), we plot $\tau_{\rm sat}$ vs $\tilde{\varepsilon}_d$ for different choices of ρ_i. The collapse of the curves for different ρ_i indicates that $\tau_{\rm sat}$ is proportional to

τ_{coll}. This is expected since the dimple is populated via two-body collisions. Additionally, the rate of these two-body collisions decreases as the dimple is made deeper due to reduced overlap between the initial and final states, causing τ_{sat} to rise monotonically. Fig 8.6(b) shows the variation of τ_{sat} with the volume ratio Ω for different values of the dimple depth. As evident from the plots, $\Omega\tau_{\text{coll}}$ sets the typical time scale for saturation. This is because a larger Ω increases the total number of atoms $\mathcal{N}$ without changing the particle scattering rate into the dimple. Thus it takes longer for the dimple population to reach a given fraction of $\mathcal{N}$.

For suitable initial conditions, μ_d quickly reaches the bottom of the dimple, signaling the onset of condensation. Thereafter $f_0(t)$ grows rapidly due to Bose stimulation. We define the onset time τ_{on} as the time when the growth rate of f_0 increases at the maximum rate, i.e., $d^3 f_0/dt^3|_{t=\tau_{\text{on}}} = 0$ (see Fig. 8.3). Figure 8.7 shows how τ_{on} varies with $\tilde{\varepsilon}_d$, ρ_i, Ω, and $\tilde{l}_d$. For very small or very large dimple depths, we do not find any condensation, so $f_0(t)$ is never macroscopic and it is not sensible to quote an onset time. Interestingly, there are ranges of large $\tilde{\varepsilon}_d$ where $F_0 \approx 0$ but $f_0(t)$ rises to significant values before falling to 0. Thus, τ_{on} is well-defined even for some parameters where F_0 is vanishingly small. In the window of $\tilde{\varepsilon}_d$ where F_0 is significant, we find that τ_{on} is minimum near the optimal dimple depth $\tilde{\varepsilon}_d^*$. Therefore, choosing $\tilde{\varepsilon}_d = \tilde{\varepsilon}_d^*$ both minimizes the onset time and yields the maximum condensate fraction. As $\tilde{\varepsilon}_d$ is decreased below $\tilde{\varepsilon}_d^*$, $f_0(t)$ takes longer and longer to take off, but saturates more quickly. Thus, τ_{on} rises while τ_{sat} diminishes, until at a particular dimple depth $\tilde{\varepsilon}_d^>$, the two time scales become equal. For lower $\tilde{\varepsilon}_d$, the atoms do not condense. This phenomenon shows up in the τ_{on} vs $\tilde{\varepsilon}_d$ curve as an apparent singularity at $\tilde{\varepsilon}_d = \tilde{\varepsilon}_d^>$. Increasing either ρ_i or Ω favors condensation and lowers τ_{on}.

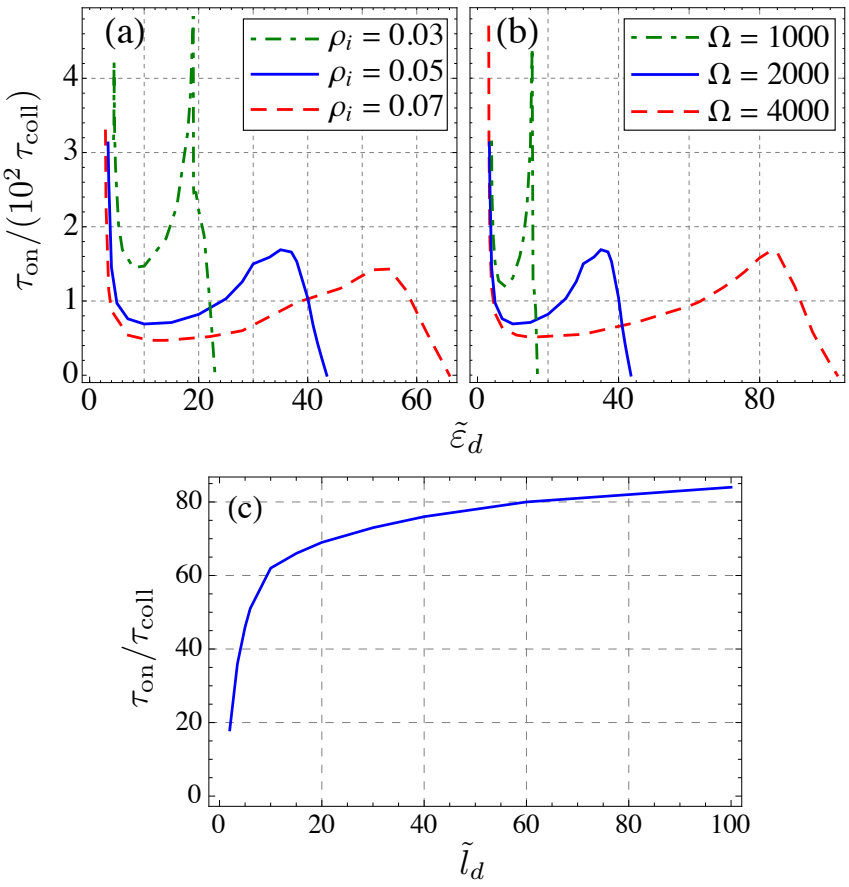

Figure 8.7: (a, b) Variation of the onset time τ_{on} with the dimple depth $\tilde{\varepsilon}_d$ for different choices of ρ_i and Ω when the dimple size $\tilde{l}_d \equiv l_d/\lambda_{r0} = 20$, where λ_{r0} is the initial thermal wavelength. In (a), $\Omega = 2000$ and in (b), $\rho_i = 0.05$. Within the range of $\tilde{\varepsilon}_d$ where the saturation condensate fraction F_0 is significant, τ_{on} is minimum near the optimal dimple depth $\tilde{\varepsilon}_d^*$ which maximizes F_0 (see Fig. 8.4). As $\tilde{\varepsilon}_d$ is lowered below $\tilde{\varepsilon}_d^*$, τ_{on} grows and τ_{sat} falls until they become equal at $\tilde{\varepsilon}_d = \tilde{\varepsilon}_d^> \approx -\tilde{\mu}_{r0}$. For smaller dimple depths, condensation does not occur and $F_0 = 0$. F_0 also becomes vanishingly small when $\tilde{\varepsilon}_d$ exceeds a large value $\tilde{\varepsilon}_d^<$. However, for a range of $\tilde{\varepsilon}_d > \tilde{\varepsilon}_d^<$, the condensate fraction rises to significant values before falling to 0. Thus τ_{on} is well defined in this range. (c) Variation of τ_{on} with $\tilde{l}_d$ for $\rho_i = 0.05$, $\Omega = 2000$, and $\tilde{\varepsilon}_d = 10$. Since the initial growth rate of the condensate fraction is proportional to $1/\tilde{l}_d^3$, τ_{on} increases with $\tilde{l}_d$, saturating when $\tilde{l}_d$ becomes sufficiently large.

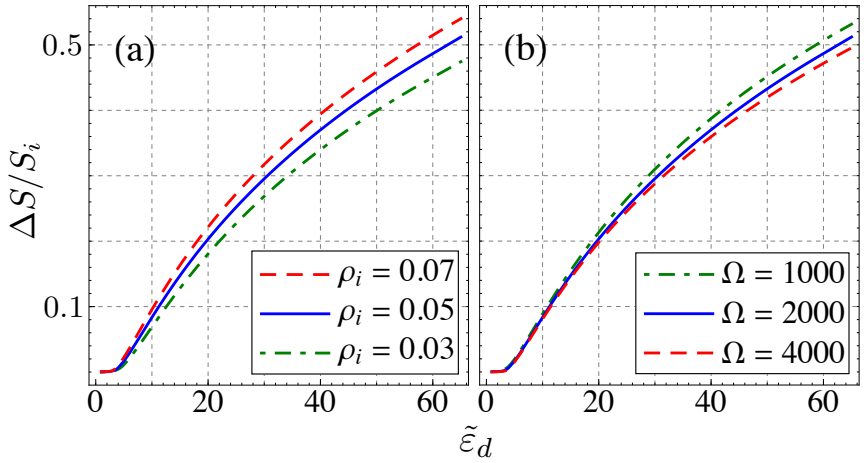

Figure 8.8: Relative increase of the total entropy of the reservoir and the dimple, $\Delta S/S_i$, as a function of the dimple depth $\tilde{\varepsilon}_d$ for different values of ρ_i and Ω. In (a), $\Omega = 2000$ and in (b), $\rho_i = 0.05$. The entropy grows because the dimple is turned on suddenly, leading to nonadiabatic dynamics. The dimple loading is more nonadiabatic when $\tilde{\varepsilon}_d$ is large, causing a higher entropy gain. $\Delta S/S_i$ also grows as ρ_i is increased or Ω is decreased, although this dependence is weak.

The initial growth rate of f_0 is proportional to the inverse volume of the dimple measured in units of the thermal wavelength, $1/\tilde{l}_d^3$ [see Eqs. (8.57) and (8.58)]. Therefore, a higher $\tilde{l}_d$ leads to a smaller onset time. This trend is seen in Fig. 8.7(c) which shows how τ_{on} varies with $\tilde{l}_d$ when ρ_i, Ω, and $\tilde{\varepsilon}_d$ are held fixed. $\tilde{l}_d$ does not affect other features of the dynamics. For large $\tilde{l}_d$, where most experiments operate, τ_{on} also becomes independent of $\tilde{l}_d$. When $\tilde{l}_d \tilde{\varepsilon}_d^{1/2} \lesssim 1$, the continuum approximation for the dimple states is not expected to hold [see Eq. (8.14)] and the kinetics should be modeled via a discrete spectrum.

We have considered a sudden turn on of the dimple. Hence the dimple loading is nonadiabatic. A measure of the nonadiabaticity is given by the percentage increase in the total entropy, which we plot in Fig. 8.8. As expected, we find that the dynamics are more nonadiabatic for deeper dimples, with the entropy increasing by 50% when $\tilde{\varepsilon}_d \approx 60$. The entropy gain also shows a weak dependence on ρ_i and Ω, increasing slowly as ρ_i is increased or Ω is decreased.

8.4.3 Effect of three-body loss

Here we incorporate three-body loss into our kinetics model. The loss introduces an additional timescale to the dynamics which depends on the particular atomic species. We will consider the case of ^{87}Rb.

At low temperatures the rate of three-body recombinations is, to a good approximation, proportional to the probability of finding three particles at the same point [62]. Thus the loss rate of the total atom density $n(\vec{r})$ is

$$\left[\frac{dn(\vec{r})}{dt}\right]^l = -L\langle[\hat{\Psi}^\dagger(\vec{r})]^3[\hat{\Psi}(\vec{r})]^3\rangle\,, \tag{8.35}$$

where L denotes the loss coefficient which was measured experimentally for ^{87}Rb as $L = 1.8\times10^{-29}$ cm^6 s^{-1} [56]. We write $\hat{\Psi}(\vec{r})$ as the sum of a condensate mean field $\psi_0(\vec{r})$ and a field $\hat{\psi}_{th}(\vec{r})$ representing thermal fluctuations. Substituting this decomposition into Eq. (8.35) and using Wick's theorem to expand, we find [10, 62, 63]

$$\left[\frac{dn(\vec{r})}{dt}\right]^l = -L\left[n_0^3(\vec{r}) + 9\,n_0^2(\vec{r})\,n_{ex}(\vec{r}) + 18\,n_0(\vec{r})\,n_{ex}^2(\vec{r}) + 6n_{ex}^3(\vec{r})\right]\,, \tag{8.36}$$

where $n_0(\vec{r}) = |\psi_0(\vec{r})|^2$ and $n_{ex}(\vec{r}) = \langle\hat{\psi}_{th}^\dagger(\vec{r})\hat{\psi}_{th}(\vec{r})\rangle$ denote the densities of the condensate and excited-state atoms respectively. $n_{ex}(\vec{r})$ is further decomposed into $n_{nc}(\vec{r})$, the density of the non-condensate atoms in the dimple, and $n_r(\vec{r})$, the density of reservoir atoms from Eq. (8.6). We then derive the decay rates of the individual densities and how these decays contribute to the kinetics (see Appendix 8.8). In particular, we find that the condensate fraction $f_0(t)$ evolves as

$$\left[\frac{df_0(t)}{dt}\right]^l = -L\frac{\rho_i^2\Omega^2}{\lambda_{r0}^6}f_0\Big[f_0^2 + 6f_0f' + 6f'^2\Big], \tag{8.37}$$

where $f' \equiv f_{nc} + (\tilde{z}_r/\Omega\tilde{\beta}_r^{3/2})[\gamma(3/2,\tilde{\beta}_r\tilde{\varepsilon}_t)/\gamma(3/2,\tilde{\varepsilon}_t)]$ and γ denotes the lower incomplete gamma function.

Results for the case $\varepsilon_t \gg k_B T_{r0}, \varepsilon_d$

As with the discussion in Sec. 8.4.2, we consider the limit of infinite trap depth $\varepsilon_t \gg k_B T_{r0}, \varepsilon_d$. Here we have loss, and the total number of atoms in the system decays monotonically toward zero. The decay rate depends explicitly on the particle density. The more general case of finite trap depth will be discussed in Sec. 8.4.4.

As before, we find that the condensate fraction $f_0(t)$ grows slowly at first until Bose stimulation causes it to take off at the onset time $t = \tau_{\text{on}}$. Since $f_0(t)$ is very small for $t < \tau_{\text{on}}$, the three-body loss of condensate atoms is negligible at these early times. Thus the onset time is largely unaffected by the presence of three-body recombination. For $t > \tau_{\text{on}}$, $f_0(t)$ grows rapidly, greatly increasing the particle density and enhancing the three-body loss rate. The condensate fraction attains its maximum value F_0^{peak} at $t = \tau_{\text{peak}}$ when the condensate decay rate balances the rate of particle scattering into the condensate. Thereafter, $f_0(t)$ decreases due to three-body loss. Since the condensate holds a macroscopic number of particles, the atom density in the condensate far exceeds that of any of the excited states. Therefore, $f_0(t)$ decays much faster than either the non-condensate fraction in the dimple $f_{nc}(t)$ or the reservoir fraction $f_r(t)$. The preferential ejection of low-energy atoms via three-body recombination leads to evaporative heating. This heating, along with the particle loss, ultimately results in the death of the condensate. Thus we get a finite condensate lifetime, Δt_{lf}, defined as the duration for which $f_0(t)$ is larger than half its maximum value. These general features are illustrated in Fig. 8.9 where we plot $f_0(t)$ for a specific set of parameter values. In the following we discuss how F_0^{peak}, Δt_{lf}, τ_{peak}, and τ_{on} vary with the different parameters.

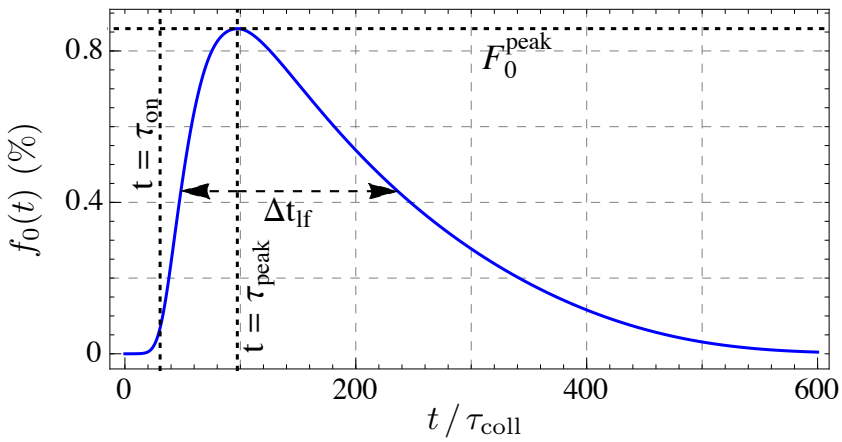

Figure 8.9: Time evolution of the condensate fraction f_0 in the presence of three-body loss for $\tilde{\varepsilon}_d = 8$, $\Omega = 2000$, $\rho_i = 0.2$, and $T_{r0} = 0.1$ μK. f_0 takes off at $t = \tau_{\rm on}$ due to Bose stimulation. As the dimple population grows, the atom density in the dimple increases, which leads to a higher three-body recombination rate. At $t = \tau_{\rm peak}$, the three-body decay rate of f_0 balances the two-body scattering rate into the condensate, and f_0 reaches its peak value $F_0^{\rm peak}$. As more particles scatter into the dimple, the temperature continues to increase. Three-body losses further heat the system by ejecting more low-energy particles. This heating, combined with the particle loss, causes the chemical potential to drop which decreases f_0. Thus we get a finite condensate lifetime $\Delta t_{\rm lf}$.

Figure 8.10 shows the variation of the peak condensate fraction and the three timescales with the dimple depth $\tilde{\varepsilon}_d$ when other parameters are held fixed. Similar to Fig. 8.4, we find that the variation of $F_0^{\rm peak}$ with $\tilde{\varepsilon}_d$ is non-monotonic. However, the maximum value as well as the optimal dimple depth $\tilde{\varepsilon}_d^*$ are significantly reduced by three-body loss. When $\varepsilon_d < |\mu_{r0}|$, the initial chemical potential lies below the dimple bottom, and the atoms do not condense, so $F_0^{\rm peak}$ vanishes. At larger dimple depths, the population of the condensate is governed by the competition between two-body collisions scattering particles into the condensate and three-body recombinations causing particles to leave the condensate. The condensate fraction reaches its peak when the two-body and three-body rates balance each other. As ε_d is increased beyond the threshold $|\mu_{r0}|$, the two-body rate climbs as the phase space density increases, then falls

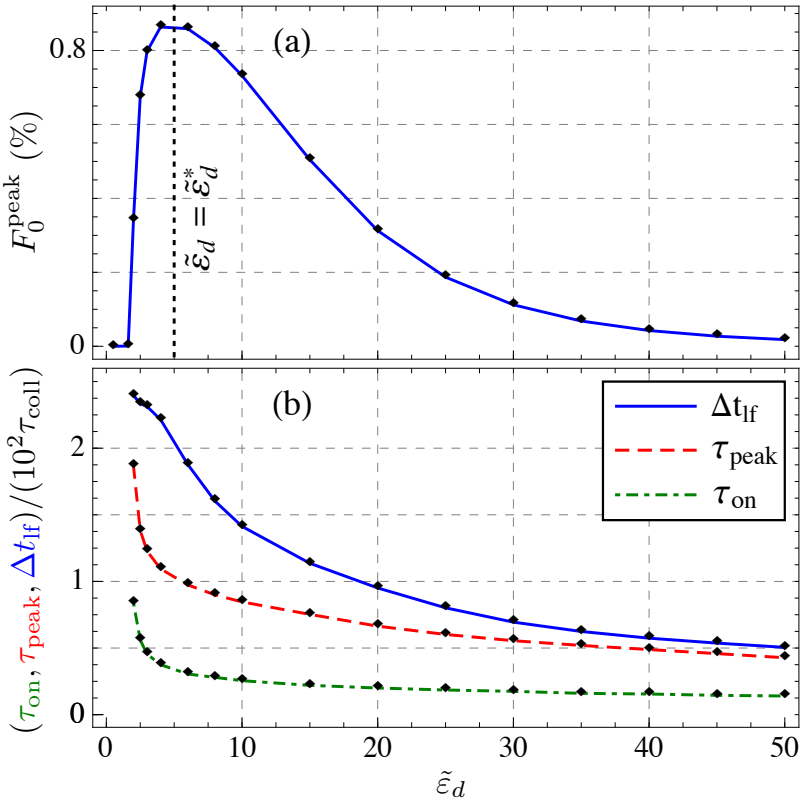

Figure 8.10: Variation of (a) the peak condensate fraction $F_0^{\rm peak}$, (b) the onset time $\tau_{\rm on}$ (dot-dashed green), the peak time $\tau_{\rm peak}$ (dashed red), and the condensate lifetime $\Delta t_{\rm lf}$ (solid blue) with the dimple depth $\tilde{\varepsilon}_d \equiv \beta_{r0}\varepsilon_d$ for $\Omega = 2000$, $\rho_i = 0.2$, and $T_{r0} = 0.1$ μK. For $\tilde{\varepsilon}_d < |\tilde{\mu}_{r0}|$, the atoms do not condense. As $\tilde{\varepsilon}_d$ is increased, the two-body scattering rate into the condensate grows rapidly at first, then falls off at large $\tilde{\varepsilon}_d$. The peak condensate fraction is reached when the three body loss rate balances the two-body scattering rate. Since the three-body rate depends only on the atom density, the non-monotonic variation of the two-body rate shows up in the variation of $F_0^{\rm peak}$ with $\tilde{\varepsilon}_d$. The growth of the two-body rate above the condensation threshold decreases $\tau_{\rm on}$ and $\tau_{\rm peak}$. These vary little at large $\tilde{\varepsilon}_d$ since both $F_0^{\rm peak}$ and the two-body rate fall off. At large $\tilde{\varepsilon}_d$, three-body loss is dominated by collisions between the non-condensed dimple atoms and the condensate atoms. The number of such non-condensed atoms grows with $\tilde{\varepsilon}_d$, yielding shorter lifetimes.

due to increased heating and a reduced overlap between the initial and final states. The three-body rate only depends on the density, so the $F_0^{\rm peak}$ vs $\tilde{\varepsilon}_d$ curve follows the variation of the two-body scattering rate. The rapid increase of the two-body rate with ε_d just above the threshold leads to a sharp decrease in the

onset time, τ_{on}, and the time required to reach peak condensate fraction, τ_{peak}. At large dimple depths, τ_{peak} decrease very slowly because both F_0^{peak} and the two-body rate fall off. We also find that the condensate lifetime Δt_{lf} decreases monotonically with $\tilde{\varepsilon}_d$. For large $\tilde{\varepsilon}_d$, the condensate loss is dominated by collisions between the non-condensed dimple atoms and the condensate. The number of such non-condensed dimple atoms grows with $\tilde{\varepsilon}_d$, yielding the shorter lifetimes.

In Fig. 8.11(a) we plot the variation of F_0^{peak} with the volume ratio Ω. Decreasing Ω reduces the total number of atoms ($\mathcal{N}$), without changing the maximum number of non-condensed atoms in the dimple. Therefore, when Ω becomes very small, the atoms in the dimple no longer condense, as seen experimentally in Ref. [46]. As Ω is increased, the condensate fraction increases rapidly until Ω reaches an optimal value Ω^*, beyond which F_0^{peak} falls off due to increased three-body loss. We see a similar variation of F_0^{peak} with ρ_i in Fig. 8.12(a). When ρ_i is very small, few atoms populate the dimple and no condensation takes place. As one increases ρ_i, F_0^{peak} rises rapidly at first, then falls for $\rho_i > \rho_i^*$. The increase of the condensate fraction with Ω and ρ_i was also seen in Fig. 8.4 where no inelastic loss was assumed. The fall-off at large Ω or large ρ_i can be explained as follows: As Ω or ρ_i is increased, the total particle number $\mathcal{N}$ and the condensate population N_0 grows, however, the number of non-condensed atoms in the dimple (N_{nc}) does not change. Therefore at large Ω or ρ_i, $N_0 \gg N_{nc}$. The non-condensate population merely acts as a medium to transfer particles from the reservoir to the condensate. In addition, three-body loss principally occurs in the dimple, resulting from collisions among the densely packed condensate atoms. Thus the dynamics are governed by the simplified

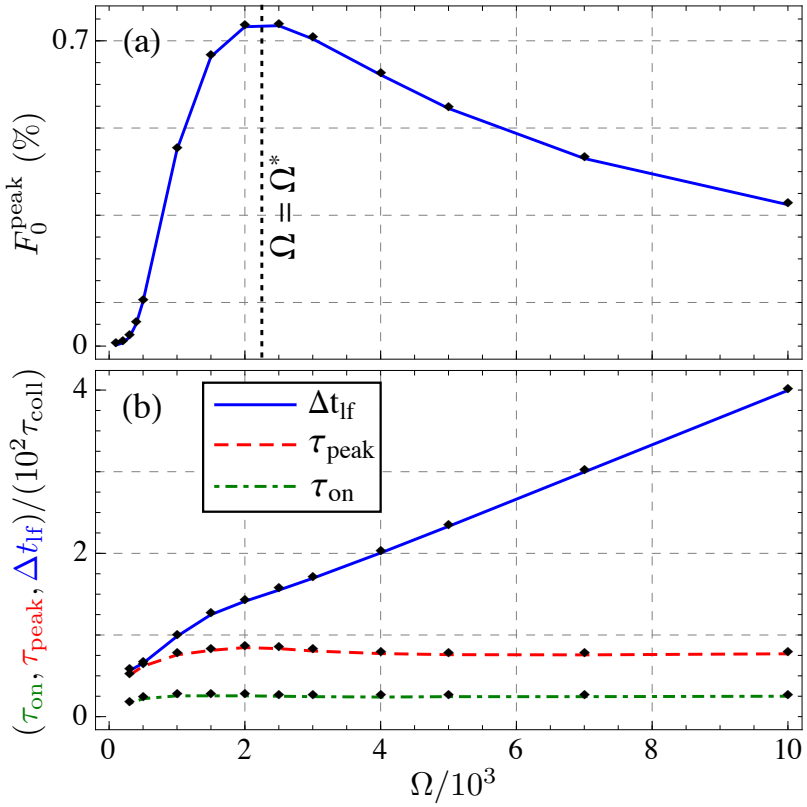

Figure 8.11: Variation of (a) $F_0^{\rm peak}$, (b) $\tau_{\rm on}$ (dot-dashed green), $\tau_{\rm peak}$ (dashed red), and $\Delta t_{\rm lf}$ (solid blue) with the volume ratio Ω for $\tilde{\varepsilon}_d = 10$, $\rho_i = 0.2$, and $T_{r0} = 0.1$ μK. When Ω is very small, the total atom number $\mathcal{N}$ is small and the dimple can hold its entire population in the excited states, so condensation does not occur. As Ω is increased, $F_0^{\rm peak}$ grows rapidly at first, then falls off when Ω becomes larger than an optimal value Ω^*. At large Ω, the condensate population N_0 far exceeds the non-condensate population in the dimple, and three-body loss is dominated by collisions among the condensate atoms. Balancing the two-body growth rate and the three-body decay rate gives a peak condensate size $N_0^{\rm peak}$ which is independent of Ω. Since $\mathcal{N} \propto \Omega$, $F_0^{\rm peak}$ falls off as $1/\Omega$. The condensate lifetime is set by the depletion rate of the reservoir. When Ω is large, the condensate size and hence the loss rate becomes independent of Ω. Thus it takes longer to empty a larger reservoir, causing $\Delta t_{\rm lf}$ to grow linearly. We also find that $\tau_{\rm on}$ and $\tau_{\rm peak}$ are mostly independent of Ω.

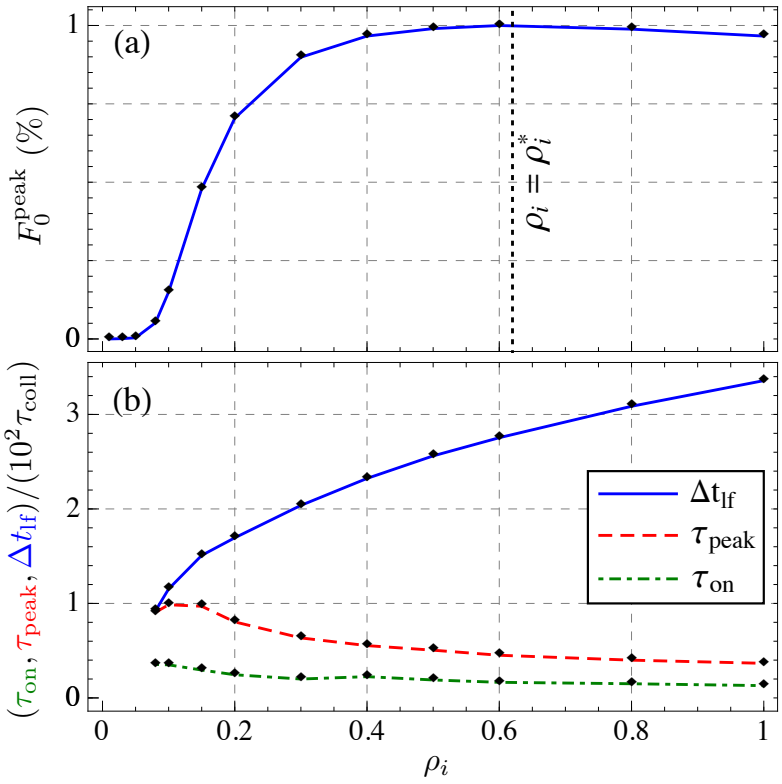

Figure 8.12: Variation of (a) $F_0^{\rm peak}$, (b) $\tau_{\rm on}$ (dot-dashed green), $\tau_{\rm peak}$ (dashed red), and $\Delta t_{\rm lf}$ (solid blue) with the initial phase space density ρ_i for $\tilde{\varepsilon}_d = 10$, $\Omega = 3000$, and $T_{r0} = 0.1$ μK. When ρ_i is very small, the atoms do not condense. As ρ_i is increased, $F_0^{\rm peak}$ rises rapidly at first, then falls at large ρ_i because the three-body decay rate of the condensate fraction grows faster than the two-body growth rate. Thus we get an optimal phase space density ρ_i^* which yields the largest condensate, although this peak is much less pronounced compared to the peaks seen when one varies $\tilde{\varepsilon}_d$ (Fig. 8.10) or Ω (Fig. 8.11). The increased three-body decay rate at larger ρ_i also leads to a smaller condensate lifetime: $\Delta t_{\rm lf}$ falls off as $\rho_i^{-1/2}$ for large ρ_i. However, since $\tau_{\rm coll}$ diminishes more rapidly as $1/\rho_i$, $\Delta t_{\rm lf}/\tau_{\rm coll}$ grows as $\sqrt{\rho_i}$. We find that $\tau_{\rm on}/\tau_{\rm coll}$ and $\tau_{\rm peak}/\tau_{\rm coll}$ decrease slowly with ρ_i.

rate equations

$$\dot{N}_0 = c_1 n N_0 - c_2 N_0^3\,, \quad \text{and} \quad \dot{n} = -(c_1/V_r)\, n N_0\,, \tag{8.38}$$

where V_r is the reservoir volume and n is the density of reservoir particles. The rate coefficients c_1 and c_2 represent two-particle collisions which fill the dimple, and three-body losses respectively. They depend on the reservoir temperature but do not depend explicitly on Ω or ρ_i. From our full model we find that the

temperature does not vary much ($\sim 25\%$) during the condensate lifetime, and depends very weakly on Ω and ρ_i (also seen in Fig. 8.5). Thus we treat c_1 and c_2 as constants in solving Eq. (8.38). N_0 attains its peak value when $\dot{N}_0 = 0$. Thus $N_0^{\text{peak}} = (c_1 n(\tau_{\text{peak}})/c_2)^{1/2}$. From Figs. 8.11(b) and 8.12(b) we see that when Ω or ρ_i is large, the condensate reaches its peak size very quickly, then decays gradually. For $0 < t < \tau_{\text{peak}}$, the change in n is negligible. Hence $N_0^{\text{peak}} \approx (c_1 n(0)/c_2)^{1/2} \propto \rho_i^{1/2}$, and $F_0^{\text{peak}} \equiv N_0^{\text{peak}}/\mathcal{N} = N_0^{\text{peak}}/(\rho_i \Omega \tilde{l}_d^3) \propto \Omega^{-1}\rho_i^{-1/2}$. This accounts for the reduction of F_0^{peak} at large Ω or ρ_i. To calculate the lifetime we note that the transfer of one atom from the reservoir to the condensate decreases n by $1/V_r \ll n(0)$. Therefore, as the growth rate of N_0 declines after $t = \tau_{\text{peak}}$, the decay rate also falls to maintain $\dot{N}_0 \approx 0$, or $N_0(t) \approx (c_1 n(t)/c_2)^{1/2}$. Thus the lifetime is set by the time required for the reservoir to be depleted [46]. Using the above expression for $N_0(t)$ in the other equation, we find $1/N_0(t) = 1/N_0^{\text{peak}} + c_1 t/2V_r$, which gives a lifetime $\Delta t_{\text{lf}} \approx 2V_r/(c_1 N_0^{\text{peak}}) \propto \Omega \rho_i^{-1/2}$. Since τ_{coll} falls off with ρ_i as $1/\rho_i$ [Eq. (8.9)], $\Delta t_{\text{lf}}/\tau_{\text{coll}} \propto \Omega \rho_i^{1/2}$. Such variation of the lifetime is illustrated in Figs. 8.11(b) and 8.12(b). We find that τ_{on} and τ_{peak} vary little with Ω. As was true without three-body collisions, $\tau_{\text{on}}/\tau_{\text{coll}}$ decreases slowly with ρ_i. $\tau_{\text{peak}}/\tau_{\text{coll}}$ also falls with ρ_i, following the variation of $\tau_{\text{on}}/\tau_{\text{coll}}$.

Figure 8.13 shows how F_0^{peak}, Δt_{lf}, τ_{peak}, and τ_{on} vary with the initial reservoir temperature T_{r0}. To understand the features, we note that the growth and redistribution of the dimple population occur via two-body collisions. Thus the rates of these processes are set by $1/\tau_{\text{coll}}$ which is proportional to T_{r0}^2 [see Eqs. (8.7) and (8.9)]. However, from Eq. (8.37) we find that the three-body loss rate is proportional to T_{r0}^3. Therefore, a higher initial temperature increases the strength of three-body decay processes relative to two-body elastic processes. This reduces the peak condensate fraction as well as the condensate lifetime. We find

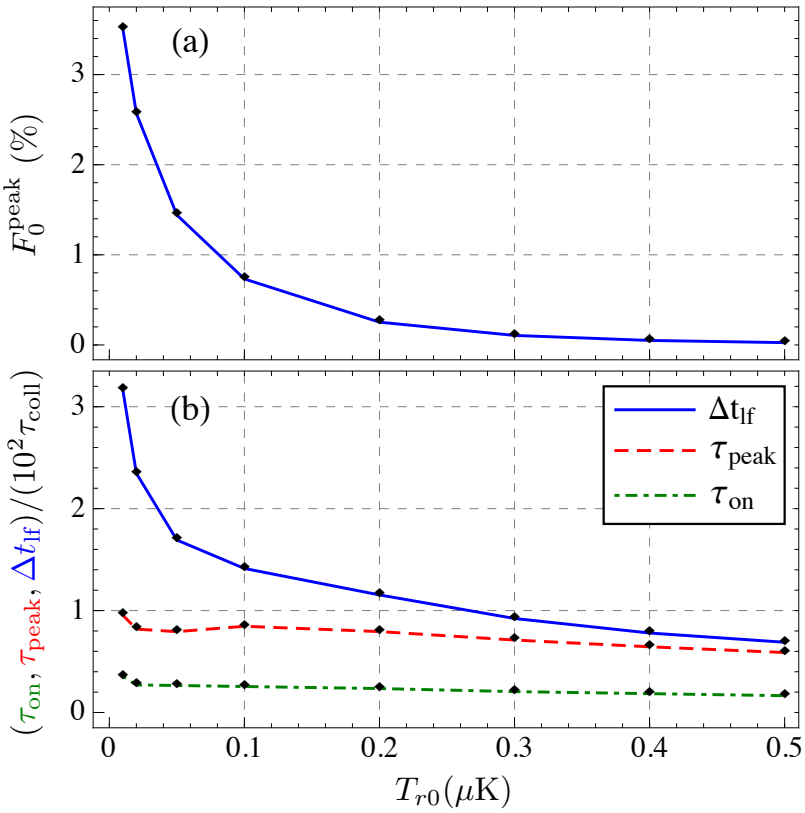

Figure 8.13: Variation of (a) $F_0^{\rm peak}$, (b) $\tau_{\rm on}$ (dot-dashed green), $\tau_{\rm peak}$ (dashed red), and $\Delta t_{\rm lf}$ (solid blue) with the initial reservoir temperature T_{r0} for $\tilde{\varepsilon}_d = 10$, $\Omega = 2000$, and $\rho_i = 0.2$. The rate of two-body collisions which populate the dimple is set by $1/\tau_{\rm coll} \propto T_{r0}^2$, whereas the three-body loss rate grows as T_{r0}^3. Thus a higher T_{r0} increases the three-body loss rate relative to the two-body scattering rate, causing both $F_0^{\rm peak}$ and $\Delta t_{\rm lf}/\tau_{\rm coll}$ to decrease. $\Delta t_{\rm lf}/\tau_{\rm coll}$ diverges as $1/T_{r0}$ for small T_{r0}. Since $F_0^{\rm peak}$ is smaller at larger T_{r0}, it takes fewer two-body collisions to reach this value, so $\tau_{\rm peak}/\tau_{\rm coll}$ decreases slowly with T_{r0}. The onset of condensation is not affected much by three-body loss, thus $\tau_{\rm on}/\tau_{\rm coll}$ is nearly independent of T_{r0}.

that $\Delta t_{\rm lf}/\tau_{\rm coll}$ diverges as $1/T_{r0}$ for small T_{r0}. Since $F_0^{\rm peak}$ is smaller for larger T_{r0}, it takes fewer two-body collisions to reach the peak condensate fraction. Consequently, $\tau_{\rm peak}/\tau_{\rm coll}$ decreases slowly with T_{r0}. We also notice that $\tau_{\rm on}/\tau_{\rm coll}$ stays essentially constant as T_{r0} is varied because the onset of condensation is governed by two-body processes alone.

8.4.4 Effect of finite trap depth

Here we discuss how the above results are altered when the reservoir trap has a finite depth ε_t. First we remind the reader that we have modeled the growth and redistribution of the dimple population by two kinds of elastic collisions, as illustrated in Fig. 8.1. Both processes can be either one-way or two-way: if the recoiling reservoir atom has a total energy greater than ε_t, it escapes from the trap. Such a collision has no reverse process and happens only one-way. Other collisions happen both ways.

When $\tilde{\varepsilon}_t \equiv \beta_{r0}\varepsilon_t \to \infty$, only two-way collisions are present. After the dimple is turned on, two-way growth processes start populating the dimple. Such processes reduce the number of reservoir atoms N_r, but increase their total energy E_r, thus heating up the reservoir. When the atom density in the dimple becomes comparable to that in the reservoir, two-way redistribution processes transfer atoms to the lower energy dimple states, leading to thermalization (see Fig. 8.2). These redistribution processes do not change N_r, but increase E_r, causing heating. Three-body recombinations also cause evaporative heating. Thus the reservoir temperature T_r increases monotonically, as shown by the solid blue curve in Fig. 8.14. When $\tilde{\varepsilon}_t$ is finite, both one-way and two-way collisions are present. In a one-way growth process, the colliding atoms are removed from the reservoir. Since the dimple is located at the trap center, the average energy of a colliding atom is less than the average energy per particle in the reservoir. Therefore, one-way growth processes (and for the same reason, one-way redistribution processes) contribute to heating. Thus we find that T_r always increases just after turning on the dimple. When the atom density in the dimple becomes large enough, redistribution processes start operating. At first, both one-way

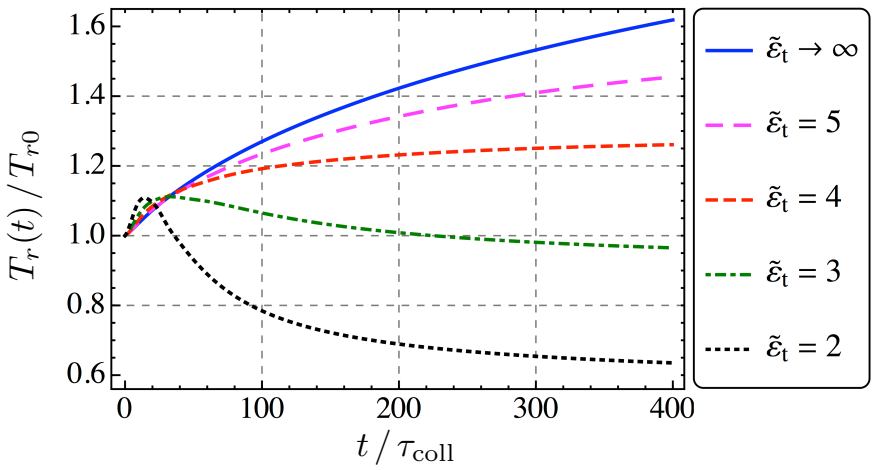

Figure 8.14: Time evolution of the reservoir temperature T_r for different values of the trap depth $\tilde{\varepsilon}_t \equiv \beta_{r0}\varepsilon_t$ with $\tilde{\varepsilon}_d = 10$, $\Omega = 2000$, $\rho_i = 0.2$, and $T_{r0} = 0.1\ \mu$K. When $\tilde{\varepsilon}_t \to \infty$ (solid blue line), particle transfer from the reservoir to the dimple and their redistribution from the higher-energy to the lower-energy dimple states heat the reservoir. Along with evaporative heating by three-body loss, this causes T_r to rise monotonically. When $\tilde{\varepsilon}_t$ is finite (dashed and dotted lines), a reservoir atom can recoil from a collision with a total energy greater than ε_t and leave the trap. The average initial energy of this atom is less than the average particle energy in the reservoir since the dimple is located at the trap center. Therefore such one-way collisions contribute to heating at short times. When the atom density in the dimple becomes sufficiently large, both one-way and two-way collisions initiate thermalization by transferring atoms from the higher to the lower-energy dimple states. However, the one-way transfer soon results in an excess of particles in the low-energy states. Two-way collisions now transfer these extra particles to higher-energy states and thus cool the reservoir. The cooling rate increases as $\tilde{\varepsilon}_t$ is lowered. Thus lower trap depths yield lower final temperatures.

and two-way collisions cause a net transfer of atoms from the higher energy to the lower energy dimple states. However, the one way particle transfer soon overcompensates thermalization, resulting in an excess of atoms in the low-energy states. This imbalance flips the direction of the two-way traffic, which now transfers atoms to the higher energy states. Such two-way collisions decrease E_r without changing N_r, thus cooling the reservoir. A smaller $\tilde{\varepsilon}_t$ results in a larger imbalance of the atom distribution, which increases the cooling rate. Thus we see in Fig. 8.14 that T_r decreases after the initial growth when $\tilde{\varepsilon}_t$ is

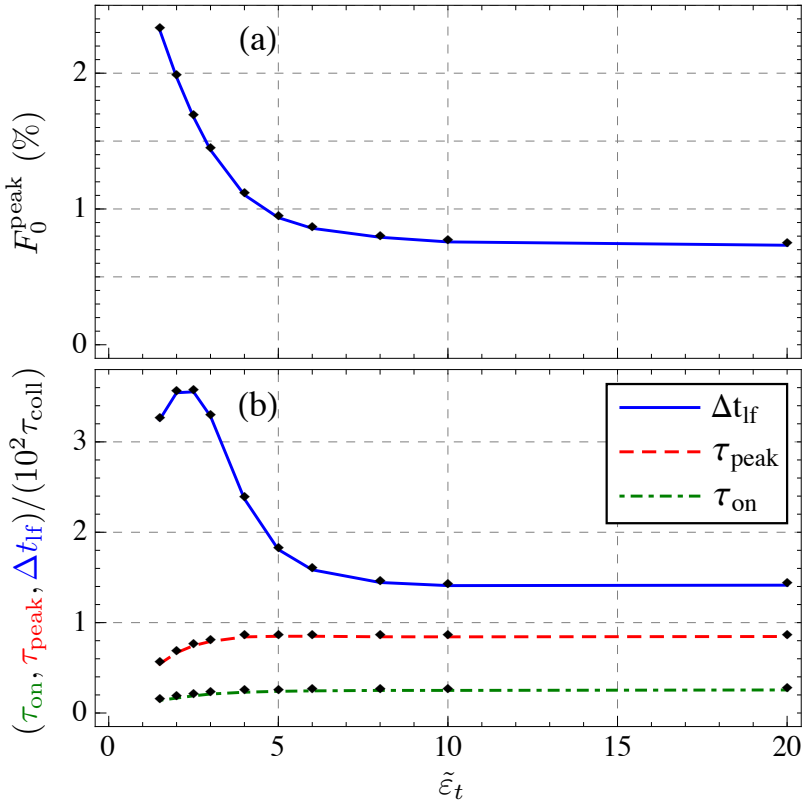

Figure 8.15: Variation of (a) $F_0^{\rm peak}$, (b) $\tau_{\rm on}$ (dot-dashed green), $\tau_{\rm peak}$ (dashed red), and $\Delta t_{\rm lf}$ (solid blue) with the trap depth $\tilde{\varepsilon}_t \equiv \beta_{r0}\varepsilon_t$ for $\tilde{\varepsilon}_d = 10$, $\Omega = 2000$, $\rho_i = 0.2$, and $T_{r0} = 0.1\ \mu$K. As $\tilde{\varepsilon}_t$ is decreased, the rate of one-way redistribution processes which transfer atoms from the higher-energy to the lower-energy dimple states increases. This gives rise to a faster growth of the condensate, which increases $F_0^{\rm peak}$ and decreases $\tau_{\rm on}$ and $\tau_{\rm peak}$. A smaller trap depth also causes more cooling, which reduces the non-condensate fraction f_{nc} and thus the three-body decay rate of the condensate. Hence we get a larger condensate lifetime. However, when $\tilde{\varepsilon}_t$ becomes very small, the increased evaporation rate of the reservoir limits the growth of $\Delta t_{\rm lf}/\tau_{\rm coll}$.

sufficiently small compared to $\tilde{\varepsilon}_d$.

In Fig. 8.15 we plot the variation of the peak condensate fraction $F_0^{\rm peak}$ and the timescales with the trap depth $\tilde{\varepsilon}_t$. As $\tilde{\varepsilon}_t$ is decreased, one-way redistribution processes become stronger, leading to a faster growth of the condensate. Consequently, a higher condensate density has to be reached before the three-body decay rate can balance the growth rate. Thus $F_0^{\rm peak}$ grows as the trap is made

shallower. The larger growth rate also reduces the onset time τ_{on} and the time required to reach the peak, τ_{peak}. A smaller trap depth causes less heating and reduces the non-condensate fraction f_{nc}, which in turn decreases the three-body decay rate of the condensate. Combined with the faster growth rate, this yields a larger condensate lifetime Δt_{lf}. However, as the trap depth is lowered, the evaporation rate of the reservoir atoms also increases, and eventually becomes comparable to the decay rate of the condensate. As the number of reservoir atoms falls, so does the rate of particle transfer from the reservoir to the dimple, and hence the growth rate of the condensate. This limits the rise of $\Delta t_{\text{lf}}/\tau_{\text{coll}}$. Additionally, τ_{coll} grows at small $\tilde{\varepsilon}_t$ [Eq. (8.9)], causing $\Delta t_{\text{lf}}/\tau_{\text{coll}}$ to decrease.

8.5 Summary and outlook

In this work we have studied the condensation kinetics of weakly interacting Bosons in a dimple potential using quantum kinetic rate equations. We have modeled the growth and redistribution of the dimple population by two-body elastic collisions. We have incorporated three-body inelastic losses for ^{87}Rb, and varied the reservoir trap depth ε_t to study the effects of evaporation. The dynamics are controlled by the dimple depth ε_d, the ratio of the reservoir volume to the dimple volume Ω, the initial phase space density ρ_i, and the initial temperature T_{r0}. The absolute size of the dimple does not matter as long as it is much larger than the thermal wavelength. We have presented detailed results for condensate fraction, the temperature, and the different timescales. Our results are consistent with features observed in recent experiments, and should provide a useful guide for more efficient production of condensates in the future.

We find that the initial growth of the dimple population is dominated by states whose energy is near half the dimple depth. However, scattering between levels quickly transfers these particles to the low-energy states, giving rise to a bimodal particle distribution at $t \approx 2\tau_{\text{coll}}$ when $\varepsilon_d \gtrsim 8k_BT_{r0}$. The dimple attains quasi-thermal equilibrium in about $8\tau_{\text{coll}}$ after it is turned on. Comparable thermalization timescales were reported in previous studies [20, 24, 25, 27, 46, 54, 55]. The condensate grows slowly at first until Bose stimulation can take over. This results in a time-delay τ_{on} before the onset of condensation, as was seen in Refs. [10, 11]. When $\varepsilon_t \gg \varepsilon_d$ and k_BT_{r0}, particle scattering into the dimple causes heating in the reservoir. In the absence of three-body loss, the dimple population saturates at a value limited by this heating. The saturation time is proportional to both τ_{coll} and Ω, and increases monotonically with ε_d. When ε_d is small such that the initial chemical potential is below the dimple bottom, we do not get condensation. As ε_d is increased beyond this threshold, the saturation condensate fraction F_0 grows rapidly at first, then falls off due to increased heating. This gives rise to an optimal dimple depth ε_d^* which yields the largest condensate fraction. The onset time τ_{on} is also minimized at $\varepsilon_d = \varepsilon_d^*$. We find that ε_d^* scales with k_BT_{r0}. The non-monotonic behavior of the condensate fraction was observed in a recent experiment [10]. A larger ρ_i or Ω both favor condensation, increasing F_0 and ε_d^*, while decreasing τ_{on}. The reduction of τ_{on} was seen in Ref. [46]. The dynamics become more non-adiabatic at larger ε_d, with the entropy growing by 20% when $\varepsilon_d \approx 20k_BT_{r0}$. Typical experiments have ε_d ranging from a few k_BT_{r0} to $\sim 10k_BT_{r0}$ [10, 11].

We find that three-body loss plays an important role for ^{87}Rb, reducing the maximum condensate fraction to a few percent for $T_{r0} = 100$ nK. It also limits the condensate lifetime Δt_{lf}. The condensate fraction now decays toward zero

after reaching a peak value F_0^{peak} at $t = \tau_{\text{peak}}$. F_0^{peak} varies non-monotonically with ε_d similar to F_0. However, both its maximum value and the optimal dimple depth ε_d^* are significantly reduced by three-body loss, in agreement with similar modeling in Ref. [10]. When ρ_i or Ω is very small, condensation does not occur, as seen experimentally in Ref. [11]. As ρ_i or Ω is increased, F_0^{peak} grows rapidly at first, then falls due to increased loss rate resulting from higher local densities. Thus there exist an optimal volume ratio Ω^* and an optimal initial phase space density ρ_i^* which yield maximum condensate fraction. We find that the peak at $\rho_i = \rho_i^*$ is much flatter than either of those at $\Omega = \Omega^*$ or $\varepsilon_d = \varepsilon_d^*$. The three-body decay rate grows much faster with T_{r0} than the rate of two-body collisions, causing F_0^{peak} to drop. We find that $\Delta t_{\text{lf}}/\tau_{\text{coll}}$ increases with ρ_i and Ω, and decreases with ε_d and T_{r0}. We also find that τ_{peak} follows the variation of τ_{on}, falling off with ε_d, ρ_i, and T_{r0}, while being almost independent of Ω. When the trap depth is finite, particles recoiling with sufficiently high energies from elastic collisions escape from the trap. This leads to cooling. Lower trap depths yield lower final temperatures and enhance the condensate growth rate, producing larger and longer-lived condensates. However, at very small trap depths, the increased evaporation rate of the reservoir limits the condensate lifetime.

Several of our predictions are amenable to testing in future experiments. The bimodal shape of $f(\tilde{E}, t)$ at $t \approx 2\tau_{\text{coll}}$ should show up in time-of-flight images as two expanding shells of atoms, though their actual shape would depend on the trap geometry. Our predictions for condensate fractions can readily be checked using the techniques in Refs. [6, 8–11].

Our model can be readily generalized to study experiments where the dimple is turned on gradually, making the loading process more adiabatic [6–8, 10].

A gradual turn-on is likely to increase the condensate fraction, although recent experiments suggest that it does not affect the dynamics at large times [46]. One can also make the reservoir trap anisotropic [10, 11], or vary the location of the dimple [51]. Dimples located off-center in a harmonic trap should have smaller filling rates due to lower particle density, but can assist in evaporative cooling since the particles would have higher energies. In Ref. [11], Stellmer *et al.* employed a novel technique where the reservoir is continuously laser cooled while the dimple particles are rendered transparent to the cooling photons by a blue-detuned laser beam. This prevents heating of the reservoir and significantly increases the condensate lifetime. It would be valuable to study how this technique alters the kinetics in future theory work. One could also explore the loading of arrays of dimples. Our framework can be naturally extended to model such experiments. Dimple methods can also be applied to Fermions [12] or Boson-Fermion mixtures.

In modeling the kinetics, we have made a few simplifying assumptions to reduce the computational complexity. In particular, we have not included mean-field interactions between the condensate and the thermal cloud [10, 28–30, 34, 35, 46, 47, 59–61], and we have neglected two kinds of elastic collisions, as described in the last paragraph in Sec. 8.2.1. These can be incorporated in future refinements of our model. They might alter some quantitative predictions by factors of 2, but we do not expect them to change any of the qualitative features [7, 28, 29, 32].

Acknowledgments

We thank Mukund Vengalattore and his students for illuminating discussions. This work was supported by the National Science Foundation Grant PHY-1068165 and the ARO-MURI Non-equilibrium Many-body Dynamics grant 63834-PH-MUR.

8.6 Appendix A: Rate equations for population growth

The rate of inflow of particles to the $\vec{n}$-th dimple state is given by [Eq. (8.15)]

$$\left(\frac{dN_{\vec{n}}}{dt}\right)^{g}_{in} = \frac{2\pi}{\hbar} U_0^2 z_r^2 (1+N_{\vec{n}}) \int' \frac{d^3p\, d^3q}{(2\pi\hbar)^6}\, e^{-\beta_r(\frac{p^2+q^2}{2m})} \times \delta\left\{ \frac{p^2+q^2-\left[\vec{p}+\vec{q}-(2\pi\hbar/l_d)\vec{n}\right]^2}{2m} - \varepsilon_n \right\}, \tag{8.39}$$

where the prime on the integral symbol denotes the condition that the initial momenta of the colliding particles must satisfy $p^2, q^2 < 2m\varepsilon_t$. To simplify Eq. (8.39) we write it in terms of $\vec{\tilde{p}}, \vec{\tilde{q}} \equiv (\beta_r/4m)^{1/2}(\vec{p} \pm \vec{q})$ and use the dispersion of the dimple modes, Eq. (8.14). This gives

$$\left(\frac{dN_{\vec{n}}}{dt}\right)^{g}_{in} = \frac{2ma^2 z_r^2}{\pi^3\hbar^3\beta_r^2} (1+N_{\vec{n}}) \int' d^3\tilde{p}\, d^3\tilde{q}\, e^{-(\tilde{p}^2+\tilde{q}^2)} \times \delta\left[\tilde{q}^2 + \beta_r\varepsilon_d - \tilde{p}^2 - 2\beta_r E_n + 2(2\beta_r E_n)^{1/2}\, \vec{\tilde{p}}.\hat{n}\right], \tag{8.40}$$

where $\hat{n} \equiv \vec{n}/n$ and in the new variables, the prime stands for the constraint $\tilde{p}^2 + \tilde{q}^2 \pm 2\vec{\tilde{p}}.\vec{\tilde{q}} < 2\beta_r\varepsilon_t$. Dividing the integration region into separate parts we can express Eq. (8.40) as

$$\left(\frac{dN_{\vec{n}}}{dt}\right)^{g}_{in} = \tilde{G}\frac{\tilde{z}_r^2}{\tilde{\beta}_r^2}(1+N_{\vec{n}}) \sum_{i=1,2} \mathscr{G}_i(\tilde{\beta}_r\tilde{\varepsilon}_t, \tilde{\beta}_r\tilde{\varepsilon}_d, \tilde{\beta}_r\tilde{E}_n), \tag{8.41}$$

where $\tilde{G} \equiv 16\sqrt{2}\ (a/\lambda_{r0})^2(z_{r0}^2/\beta_{r0}\hbar)$ and

$$\mathscr{G}_1(\tilde{\varepsilon}_t, \tilde{\varepsilon}_d, \tilde{E}) \equiv \frac{1}{\sqrt{\tilde{E}}}\left[\iint\limits_{IA,C} d\tilde{p}\, d\tilde{q}\, \tilde{p}\, \tilde{q}^2\, e^{-(\tilde{p}^2+\tilde{q}^2)} + \iint\limits_{IB,C} d\tilde{p}\, d\tilde{q}\, \tilde{q} \left(\tilde{\varepsilon}_t - \frac{\tilde{p}^2+\tilde{q}^2}{2} \right) e^{-(\tilde{p}^2+\tilde{q}^2)} \right], \tag{8.42}$$

$$\mathscr{G}_2(\tilde{\varepsilon}_t, \tilde{\varepsilon}_d, \tilde{E}) \equiv \frac{1}{\sqrt{\tilde{E}}} \iint\limits_{II,C} d\tilde{p}\, d\tilde{q}\, \tilde{p}\, \tilde{q}^2\, e^{-(\tilde{p}^2+\tilde{q}^2)}\ . \tag{8.43}$$

Here the labels under the integrals denote the following conditions on $\tilde{p}$ and $\tilde{q}$:

$$\begin{aligned}
IA &: \ \tilde{p}^2+\tilde{q}^2 \geq \tilde{\varepsilon}_t - \tilde{\varepsilon}_d + \tilde{E} \text{ and } \tilde{p}+\tilde{q} < (2\tilde{\varepsilon}_t)^{1/2} \\
IB &: \ \tilde{p}+\tilde{q} \geq (2\tilde{\varepsilon}_t)^{1/2} \text{ and } \tilde{p}^2+\tilde{q}^2 < 2\tilde{\varepsilon}_t \\
II &: \ \tilde{p}^2+\tilde{q}^2 < \tilde{\varepsilon}_t - \tilde{\varepsilon}_d + \tilde{E} \\
C &: \ \left[\tilde{p} - (2\tilde{E})^{1/2}\right]^2 \leq \tilde{q}^2 + \tilde{\varepsilon}_d \leq \left[\tilde{p} + (2\tilde{E})^{1/2}\right]^2
\end{aligned}$$

Conditions IA and IB correspond to the range of initial momenta for which the atom recoiling back to the reservoir gains sufficient energy from the collision to escape from the trap. Such collisions happen only one-way: they do not have any reverse process. Whereas if condition II is satisfied, no atom is lost from the trap, giving rise to two-way collisions. Condition C ensures that both momentum and energy are conserved in the process.

Similarly, we simplify Eq. (8.16) describing the rate of particle flow out of the $\vec{n}$-th dimple state to obtain

$$\left(\frac{dN_{\vec{n}}}{dt}\right)^g_{out} = -\tilde{G}\frac{\tilde{z}_r}{z_{r0}\tilde{\beta}_r^2} N_{\vec{n}}\, e^{-\tilde{\beta}_r(\tilde{\varepsilon}_d - \tilde{E}_n)} \mathscr{G}_2(\tilde{\beta}_r\tilde{\varepsilon}_t, \tilde{\beta}_r\tilde{\varepsilon}_d, \tilde{\beta}_r\tilde{E}_n). \tag{8.44}$$

The net growth rate of $N_{\vec{n}}(t)$ is then found by adding Eqs. (8.41) and (8.44). We write this as a sum of contributions from one-way and two-way collisions:

$$\left(\frac{dN_{\vec{n}}}{dt}\right)^g = \left(\frac{dN_{\vec{n}}}{dt}\right)^g_1 + \left(\frac{dN_{\vec{n}}}{dt}\right)^g_2, \tag{8.45}$$

where

$$\left(\frac{dN_{\vec{n}}}{dt}\right)^{g}_{1} = \tilde{G}\frac{\tilde{z}_r^2}{\tilde{\beta}_r^2}(1+N_{\vec{n}})\,\mathscr{G}_1(\tilde{\beta}_r\tilde{\varepsilon}_t,\tilde{\beta}_r\tilde{\varepsilon}_d,\tilde{\beta}_r\tilde{E}_n)\,, \tag{8.46}$$

$$\left(\frac{dN_{\vec{n}}}{dt}\right)^{g}_{2} = \tilde{G}\frac{\tilde{z}_r^2}{\tilde{\beta}_r^2}\left\{1-N_{\vec{n}}\left[\frac{1}{z_r}e^{\tilde{\beta}_r(\tilde{\varepsilon}_d-\tilde{E}_n)}-1\right]\right\} \times \mathscr{G}_2(\tilde{\beta}_r\tilde{\varepsilon}_t,\tilde{\beta}_r\tilde{\varepsilon}_d,\tilde{\beta}_r\tilde{E}_n)\,. \tag{8.47}$$

Each one-way collision reduces the number of atoms in the reservoir (N_r) by 2, whereas every two-way collision changes N_r by 1. Hence we write

$$\left(\frac{dN_r}{dt}\right)^{g} = -\sum_{\vec{n}}\left[2\left(\frac{dN_{\vec{n}}}{dt}\right)^{g}_{1}+\left(\frac{dN_{\vec{n}}}{dt}\right)^{g}_{2}\right]. \tag{8.48}$$

In a one-way collision, the total energy of the colliding particles is lost from the reservoir. Therefore, the rate at which one-way collisions decrease the total energy in the reservoir (E_r) can be written as [Eq. (8.20)]

$$\left(\frac{dE_r}{dt}\right)^{g}_{1} = -\frac{2\pi}{\hbar}U_0^2 z_r^2\sum_{\vec{n}}(1+N_{\vec{n}})\int''\frac{d^3p\,d^3q}{(2\pi\hbar)^6}\;e^{-\beta_r(\frac{p^2+q^2}{2m})} \times\frac{p^2+q^2}{2m}\,\delta\left\{\frac{p^2+q^2-[\vec{p}+\vec{q}-(2\pi\hbar/l_d)\vec{n}]^2}{2m}-\varepsilon_n\right\}, \tag{8.49}$$

where the double prime restricts the initial momenta to regions where $p^2, q^2 < 2m\varepsilon_t$ and $p^2+q^2 > 2m(\varepsilon_t-\varepsilon_d+E_n)$. To simplify Eq. (8.49) we apply the same operations as we did on Eq. (8.39). This yields

$$\left(\frac{dE_r}{dt}\right)^{g}_{1} = -\tilde{G}\frac{\tilde{z}_r^2}{\beta_r\tilde{\beta}_r^2}\sum_{\vec{n}}(1+N_{\vec{n}})\,\mathscr{C}_g(\tilde{\beta}_r\tilde{\varepsilon}_t,\tilde{\beta}_r\tilde{\varepsilon}_d,\tilde{\beta}_r\tilde{E}_n)\,, \tag{8.50}$$

where

$$\mathscr{C}_g(\tilde{\varepsilon}_t,\tilde{\varepsilon}_d,\tilde{E}) \equiv \frac{1}{\sqrt{\tilde{E}}}\left[\iint_{IA,C}d\tilde{p}\,d\tilde{q}\,\tilde{p}\,\tilde{q}^2(\tilde{p}^2+\tilde{q}^2)\,e^{-(\tilde{p}^2+\tilde{q}^2)} + \iint_{IB,C}d\tilde{p}\,d\tilde{q}\,\tilde{q}\,(\tilde{p}^2+\tilde{q}^2)\left(\tilde{\varepsilon}_t-\frac{\tilde{p}^2+\tilde{q}^2}{2}\right)e^{-(\tilde{p}^2+\tilde{q}^2)}\right]. \tag{8.51}$$

A two-way collision which scatters a particle to the $\vec{n}$-th state increases E_r by $\varepsilon_d - E_n$. Therefore,

$$\left(\frac{dE_r}{dt}\right)_2^g = \sum_{\vec{n}} (\varepsilon_d - E_n)\left(\frac{dN_{\vec{n}}}{dt}\right)_2^g . \tag{8.52}$$

Since the occupation of a dimple state depends only on its energy [Eqs. (8.46) and (8.47)], the dimple population can be described by a continuous distribution function $f(\tilde{E},t) = D(\tilde{E})N_{\vec{n}}(t)/\mathcal{N}$ with $\tilde{E}_n = \tilde{E}$, where $D(\tilde{E}) = 2\tilde{l}_d^3(\tilde{E}/\pi)^{1/2}$ denotes the density of states. Using this definition in Eqs. (8.45)−(8.47) we find the growth rate of $f(\tilde{E},t)$:

$$\left[\frac{\partial f(\tilde{E},t)}{\partial t}\right]^g = \left[\frac{\partial f(\tilde{E},t)}{\partial t}\right]_1^g + \left[\frac{\partial f(\tilde{E},t)}{\partial t}\right]_2^g , \tag{8.53}$$

where

$$\left[\frac{\partial f(\tilde{E},t)}{\partial t}\right]_1^g = G\frac{\tilde{z}_r^2}{\tilde{\beta}_r^2}\left[2\left(\frac{\tilde{E}}{\pi}\right)^{\frac{1}{2}} + \rho_i\Omega f(\tilde{E},t)\right]\mathscr{G}_1(\tilde{\beta}_r\tilde{\varepsilon}_t, \tilde{\beta}_r\tilde{\varepsilon}_d, \tilde{\beta}_r\tilde{E}) , \tag{8.54}$$

$$\left[\frac{\partial f(\tilde{E},t)}{\partial t}\right]_2^g = G\frac{\tilde{z}_r^2}{\tilde{\beta}_r^2}\mathscr{G}_2(\tilde{\beta}_r\tilde{\varepsilon}_t, \tilde{\beta}_r\tilde{\varepsilon}_d, \tilde{\beta}_r\tilde{E})\left\{2\left(\frac{\tilde{E}}{\pi}\right)^{\frac{1}{2}} - \rho_i\Omega f(\tilde{E},t)\left[\frac{1}{z_r}e^{-\tilde{\beta}_r(\tilde{\varepsilon}_d-\tilde{E})} - 1\right]\right\}, \tag{8.55}$$

with the "rate constant" G given by

$$G \equiv \frac{\tilde{G}}{\rho_i\Omega} = \frac{16\sqrt{2}}{\beta_{r0}\hbar}\left(\frac{a}{\lambda_{r0}}\right)^2\frac{\rho_i}{\Omega}\frac{\pi/4}{[\gamma(3/2,\tilde{\varepsilon}_t)]^2} = \frac{1}{\tau_{\text{coll}}\Omega}\frac{\sqrt{\pi/2}}{\gamma(2,\tilde{\varepsilon}_t)\gamma(3/2,\tilde{\varepsilon}_t)} . \tag{8.56}$$

Here we have substituted from Eqs. (8.7), (8.9), and (8.11). We note that the characteristic timescale for the growth of the dimple population is $\tau_{\text{coll}}\Omega$.

Condensation occurs when a macroscopic number of particles reside in the ground state. The condensate fraction is defined as $f_0(t) \equiv N_{\vec{0}}(t)/\mathcal{N}$. Using Eqs. (8.45)−(8.47) we obtain

$$\left(\frac{df_0}{dt}\right)_1^g = G\frac{\tilde{z}_r^2}{\tilde{\beta}_r^2}\left(\frac{1}{\tilde{l}_d^3} + \rho_i\Omega f_0\right)\mathscr{G}_1(\tilde{\beta}_r\tilde{\varepsilon}_t, \tilde{\beta}_r\tilde{\varepsilon}_d, 0) , \tag{8.57}$$

$$\left(\frac{df_0}{dt}\right)_2^g = G\frac{\tilde{z}_r^2}{\tilde{\beta}_r^2}\left[\frac{1}{\tilde{l}_d^3} - \rho_i\Omega f_0\left(\frac{1}{z_r}e^{-\tilde{\beta}_r\tilde{\varepsilon}_d} - 1\right)\right]\mathscr{G}_2(\tilde{\beta}_r\tilde{\varepsilon}_t, \tilde{\beta}_r\tilde{\varepsilon}_d, 0) . \tag{8.58}$$

Similarly, Eqs. (8.48), (8.50), and (8.52) yield the growth rates of the reservoir fraction $f_r \equiv N_r/\mathcal{N}$ and of $\tilde{e}_r \equiv e_r\big(\gamma(4,\tilde{\varepsilon}_t)/\gamma(3,\tilde{\varepsilon}_t)\big) = (E_r/\mathcal{E})[\gamma(4,\tilde{\varepsilon}_t)/\gamma(3,\tilde{\varepsilon}_t)]$:

$$\left(\frac{df_r}{dt}\right)^g = -2\left(\frac{df_0}{dt}\right)_1^g - \left(\frac{df_0}{dt}\right)_2^g - \int_0^{\tilde{\varepsilon}_d} d\tilde{E}\left\{2\left[\frac{\partial f(\tilde{E},t)}{\partial t}\right]_1^g + \left[\frac{\partial f(\tilde{E},t)}{\partial t}\right]_2^g\right\}, \tag{8.59}$$

$$\left(\frac{d\tilde{e}_r}{dt}\right)_1^g = -G\frac{\tilde{z}_r^2}{\tilde{\beta}_r^3}\left\{\left(\frac{1}{\tilde{l}_d^3} + \rho_i\Omega f_0\right)\mathscr{C}_g(\tilde{\beta}_r\tilde{\varepsilon}_t, \tilde{\beta}_r\tilde{\varepsilon}_d, 0) + \int_0^{\tilde{\varepsilon}_d} d\tilde{E}\left[2\left(\frac{\tilde{E}}{\pi}\right)^{\frac{1}{2}} + \rho_i\Omega f(\tilde{E},t)\right]\mathscr{C}_g(\tilde{\beta}_r\tilde{\varepsilon}_t, \tilde{\beta}_r\tilde{\varepsilon}_d, \tilde{\beta}_r\tilde{E})\right\}, \tag{8.60}$$

$$\left(\frac{d\tilde{e}_r}{dt}\right)_2^g = \tilde{\varepsilon}_d\left(\frac{df_0}{dt}\right)_2^g + \int_0^{\tilde{\varepsilon}_d} d\tilde{E}\,(\tilde{\varepsilon}_d - \tilde{E})\left[\frac{\partial f(\tilde{E},t)}{\partial t}\right]_2^g. \tag{8.61}$$

8.7 Appendix B: Rate equations for population redistribution

The rate at which particles are scattered from state $\vec{n}_1$ to state $\vec{n}_2$ of the dimple is given by [Eq. (8.23)]

$$\frac{dN_{\vec{n}_1\to\vec{n}_2}}{dt} = \frac{2\pi}{\hbar}U_0^2\,\frac{z_r}{l_d^3}N_{\vec{n}_1}(1+N_{\vec{n}_2})\int'\frac{d^3p}{(2\pi\hbar)^3}\,e^{-\beta_r\frac{p^2}{2m}} \times\,\delta\left\{\frac{p^2}{2m} + E_{n_1} - \frac{\left[\vec{p}+(2\pi\hbar/l_d)(\vec{n}_1-\vec{n}_2)\right]^2}{2m} - E_{n_2}\right\}, \tag{8.62}$$

where the prime restricts the initial energy of the reservoir particle below the trap depth: $p^2 < 2m\varepsilon_t$. We can write Eq. (8.62) more simply in terms of $\vec{\tilde{p}} \equiv (\beta_r/2m)^{1/2}\vec{p}$:

$$\frac{dN_{\vec{n}_1\to\vec{n}_2}}{dt} = \tilde{R}\frac{\tilde{z}_r}{\tilde{\beta}_r}\frac{N_{\vec{n}_1}(1+N_{\vec{n}_2})\int^\star d\tilde{p}\,2\tilde{p}\,e^{-\tilde{p}^2}}{\left[\tilde{E}_{n_1}+\tilde{E}_{n_2}-2(\tilde{E}_{n_1}\tilde{E}_{n_2})^{1/2}\,\hat{n}_1.\hat{n}_2\right]^{1/2}}, \tag{8.63}$$

where $\hat{n}_i \equiv \vec{n}_i/n_i$, $\tilde{R} \equiv (4\pi a^2 z_{r0}/l_d^3)\sqrt{2/m\beta_{r0}}$, and the asterisk imposes the condition $\beta_r E_{n_2}\cos^2\theta(\vec{n}_2, \vec{n}_1-\vec{n}_2) < \tilde{p}^2 < \beta\varepsilon_t$, $\theta(\vec{n}_2, \vec{n}_1-\vec{n}_2)$ being the angle between $\vec{n}_2$ and $\vec{n}_1-\vec{n}_2$. The lower limit on $\tilde{p}$ arises from conservation of energy and momentum. When $E_{n_2} < E_{n_1}$, the reservoir particle recoils with a higher energy. If

$\tilde{p}^2 > \beta_r(\varepsilon_t - E_{n_1} + E_{n_2})$, its energy exceeds ε_t and it is lost from the trap. Such collisions have no reverse process. Whereas for $\tilde{p}^2 < \beta_r(\varepsilon_t - E_{n_1} + E_{n_2})$, no particle is lost and collisions happen both ways. When $E_{n_2} > E_{n_1}$, every scattering event which transfers a particle from state $\vec{n}_1$ to state $\vec{n}_2$ can happen backward as well. Thus we can identify the contributions of one-way and two-way collisions in Eq. (8.63):

$$\left(\frac{dN_{\vec{n}_1\to\vec{n}_2}}{dt}\right)_1 = \tilde{R}\frac{\tilde{z}_r}{\tilde{\beta}_r}N_{\vec{n}_1}(1+N_{\vec{n}_2})\frac{\alpha\left(e^{-\max\{\tilde{\beta}_r\tilde{E}_{n_2}\cos^2\theta(\vec{n}_2,\vec{n}_1-\vec{n}_2),\,\tilde{\beta}_r(\tilde{\varepsilon}_t-\tilde{E}_{n_1}+\tilde{E}_{n_2})\}}-e^{-\tilde{\beta}_r\tilde{\varepsilon}_t}\right)}{\left[\tilde{E}_{n_1}+\tilde{E}_{n_2}-2(\tilde{E}_{n_1}\tilde{E}_{n_2})^{1/2}\,\hat{n}_1.\hat{n}_2\right]^{1/2}}\,, \tag{8.64}$$

$$\left(\frac{dN_{\vec{n}_1\to\vec{n}_2}}{dt}\right)_2 = \tilde{R}\frac{\tilde{z}_r}{\tilde{\beta}_r}N_{\vec{n}_1}(1+N_{\vec{n}_2})\frac{\alpha\left(e^{-\tilde{\beta}_r\tilde{E}_{n_2}\cos^2\theta(\vec{n}_2,\vec{n}_1-\vec{n}_2)}-e^{-\min\{\tilde{\beta}_r\tilde{\varepsilon}_t,\,\tilde{\beta}_r(\tilde{\varepsilon}_t-\tilde{E}_{n_1}+\tilde{E}_{n_2})\}}\right)}{\left[\tilde{E}_{n_1}+\tilde{E}_{n_2}-2(\tilde{E}_{n_1}\tilde{E}_{n_2})^{1/2}\,\hat{n}_1.\hat{n}_2\right]^{1/2}}\,, \tag{8.65}$$

where α denotes the ramp function: $\alpha(x) = x$ for $x > 0$, and $\alpha(x) = 0$ for $x < 0$. The overall rate of change of $N_{\vec{n}}$ due to particle transfer from other states can then be written as

$$\left(\frac{dN_{\vec{n}}}{dt}\right)^r = \sum_{\vec{n}'\neq\vec{n}} R^{(1)}_{\vec{n},\vec{n}'} + R^{(2)}_{\vec{n},\vec{n}'}\,, \tag{8.66}$$

where

$$R^{(i)}_{\vec{n},\vec{n}'} \equiv \left(\frac{dN_{\vec{n}'\to\vec{n}}}{dt}\right)_i - \left(\frac{dN_{\vec{n}\to\vec{n}'}}{dt}\right)_i, \quad i = 1, 2. \tag{8.67}$$

Two-way collisions do not alter the number of particles in the reservoir (N_r), whereas each one-way collision removes one particle from the reservoir. Therefore,

$$\left(\frac{dN_r}{dt}\right)^r = -\sum_{\substack{\vec{n}',\vec{n}\\ E_{n'}>E_n}} R^{(1)}_{\vec{n},\vec{n}'}\,. \tag{8.68}$$

In a one-way collision, the reservoir particle is lost from the trap. This reduces the energy in the reservoir (E_r) by $p^2/2m$. The expression for the net rate

of decrease of E_r looks similar to Eq. (8.62) and is given in Eq. (8.28). To simplify we perform the same substitutions as in Eq. (8.62), thus obtaining

$$\left(\frac{dE_r}{dt}\right)^r_1 = -\tilde{R}\frac{\tilde{z}_r}{\beta_r\tilde{\beta}_r}\sum_{\substack{\vec{n}',\vec{n}\\ E_{n'}>E_n}} N_{\vec{n}'}(1+N_{\vec{n}})\times \frac{\xi\big(\max\{\tilde{\beta}_r\tilde{E}_n\cos^2\theta(\vec{n},\vec{n}'-\vec{n}),\tilde{\beta}_r(\tilde{\varepsilon}_t-\tilde{E}_{n'}+\tilde{E}_n)\},\tilde{\beta}_r\tilde{\varepsilon}_t\big)}{\big[\tilde{E}_n+\tilde{E}_{n'}-2(\tilde{E}_n\tilde{E}_{n'})^{1/2}\,\hat{n}.\hat{n}'\big]^{1/2}}, \tag{8.69}$$

where $\xi(a,b)\equiv\big[(1+a)\,e^{-a}-(1+b)\,e^{-b}\big]\,\Theta(b-a)$, Θ being the Heaviside step function: $\Theta(x)=1$ for $x>0$, and $\Theta(x)=0$ for $x<0$.

A two-way collision which transfers a particle from state $\vec{n}'$ to state $\vec{n}$ increases E_r by $E_{n'}-E_n$. Hence,

$$\left(\frac{dE_r}{dt}\right)^r_2 = \sum_{\substack{\vec{n}',\vec{n}\\ E_{n'}>E_n}} (E_{n'}-E_n)\,R^{(2)}_{\vec{n},\vec{n}'}\,. \tag{8.70}$$

Due to symmetry, $N_{\vec{n}}$ depends only on E_n [Eqs. (8.64)–(8.67)]. Thus we describe the discrete states in the dimple by a continuous density of states $D(\tilde{E})=2\tilde{l}_d^3(\tilde{E}/\pi)^{1/2}$ and their occupations by a distribution function $f(\tilde{E},t)\equiv D(\tilde{E})N_{\vec{n}}(t)/\mathcal{N}$ where $\tilde{E}_n=\tilde{E}$. Then Eqs. (8.64)−(8.67) give

$$\left[\frac{\partial f(\tilde{E},t)}{\partial t}\right]^r = \int_0^{\tilde{\varepsilon}_d} d\tilde{E}'\big[\mathcal{R}_1(\tilde{E},\tilde{E}')+\mathcal{R}_2(\tilde{E},\tilde{E}')\big]\,, \tag{8.71}$$

where $\mathcal{R}_i(\tilde{E}',\tilde{E})=-\mathcal{R}_i(\tilde{E},\tilde{E}')$ and for $\tilde{E}'>\tilde{E}$,

$$\mathcal{R}_1(\tilde{E},\tilde{E}')\equiv R\frac{\tilde{z}_r}{\tilde{\beta}_r^{1/2}}f(\tilde{E}',t)\left[2\left(\frac{\tilde{E}}{\pi}\right)^{\frac{1}{2}}+\rho_i\Omega f(\tilde{E},t)\right]\mathcal{I}_A^{(1)}(\tilde{\beta}_r\tilde{\varepsilon}_t,\tilde{\beta}_r\tilde{E},\tilde{\beta}_r\tilde{E}')\,, \tag{8.72}$$

$$\begin{aligned}\mathcal{R}_2(\tilde{E},\tilde{E}')\equiv R\frac{\tilde{z}_r}{\tilde{\beta}_r^{1/2}}\Bigg\{&f(\tilde{E}',t)\left[2\left(\frac{\tilde{E}}{\pi}\right)^{\frac{1}{2}}+\rho_i\Omega f(\tilde{E},t)\right]\\ &-f(\tilde{E},t)\left[2\left(\frac{\tilde{E}'}{\pi}\right)^{\frac{1}{2}}+\rho_i\Omega f(\tilde{E}',t)\right]e^{-\tilde{\beta}_r(\tilde{E}'-\tilde{E})}\Bigg\}\\ &\times\mathcal{I}_A^{(2)}(\tilde{\beta}_r\tilde{\varepsilon}_t,\tilde{\beta}_r\tilde{E},\tilde{\beta}_r\tilde{E}')\,,\end{aligned} \tag{8.73}$$

where the "rate constant" R has the expression

$$R = \frac{2\sqrt{\pi}}{\beta_{r0}\hbar}\Big(\frac{a}{\lambda_{r0}}\Big)^2 \rho_i \frac{\sqrt{\pi}/2}{\gamma(3/2,\tilde{\varepsilon}_t)} = \frac{\sqrt{\pi}\,\gamma(2,\tilde{\varepsilon}_t)}{8\,\tau_{\rm coll}}\,, \tag{8.74}$$

and the functions $\mathcal{I}_A^{(1)}$ and $\mathcal{I}_A^{(2)}$ are given by

$$\mathcal{I}_A^{(1)}(\tilde{\varepsilon}_t,\tilde{E},\tilde{E}') \equiv \int_{-1}^{1} du\, \frac{\alpha\Big(e^{-\max\left\{\tilde{E}\frac{(\sqrt{\tilde{E}'}u-\sqrt{\tilde{E}})^2}{\tilde{E}+\tilde{E}'-2\sqrt{\tilde{E}\tilde{E}'}u},\,\tilde{\varepsilon}_t-\tilde{E}'+\tilde{E}\right\}} - e^{-\tilde{\varepsilon}_t}\Big)}{\big(\tilde{E}+\tilde{E}'-2\sqrt{\tilde{E}\tilde{E}'}u\big)^{1/2}}\,, \tag{8.75}$$

$$\mathcal{I}_A^{(2)}(\tilde{\varepsilon}_t,\tilde{E},\tilde{E}') \equiv \int_{-1}^{1} du\, \frac{\alpha\Big(e^{-\tilde{E}\frac{(\sqrt{\tilde{E}'}u-\sqrt{\tilde{E}})^2}{\tilde{E}+\tilde{E}'-2\sqrt{\tilde{E}\tilde{E}'}u}} - e^{-(\tilde{\varepsilon}_t-\tilde{E}'+\tilde{E})}\Big)}{\big(\tilde{E}+\tilde{E}'-2\sqrt{\tilde{E}\tilde{E}'}u\big)^{1/2}}\,. \tag{8.76}$$

We note that the characteristic timescale in Eqs. (8.72) and (8.73) is $\tau_{\rm coll}$. Thus we expect $\tau_{\rm coll}$ to set the thermalization time scale.

The equation of motion for the condensate fraction $f_0(t) \equiv N_{\vec{0}}(t)/\mathcal{N}$ can be obtained likewise:

$$\left(\frac{df_0}{dt}\right)^r_1 = R\frac{\tilde{z}_r}{\tilde{\beta}_r^{1/2}}\left(\frac{1}{\tilde{l}_d^3}+\rho_i\Omega f_0\right)\int_0^{\tilde{\varepsilon}_d} d\tilde{E} f(\tilde{E},t)\,\mathcal{I}_A^{(1)}(\tilde{\beta}_r\tilde{\varepsilon}_t,0,\tilde{\beta}_r\tilde{E})\,, \tag{8.77}$$

$$\left(\frac{df_0}{dt}\right)^r_2 = \int_0^{\tilde{\varepsilon}_d} d\tilde{E}\,\mathcal{R}_0(\tilde{E})\,, \tag{8.78}$$

where

$$\begin{aligned}\mathcal{R}_0(\tilde{E}) \equiv\; & R\frac{\tilde{z}_r}{\tilde{\beta}_r^{1/2}}\left\{f(\tilde{E},t)\left(\frac{1}{\tilde{l}_d^3}+\rho_i\Omega f_0\right) - f_0\left[2\left(\frac{\tilde{E}}{\pi}\right)^{\frac{1}{2}}+\rho_i\Omega f(\tilde{E},t)\right]e^{-\tilde{\beta}_r\tilde{E}}\right\} \\ & \times \mathcal{I}_A^{(2)}(\tilde{\beta}_r\tilde{\varepsilon}_t,0,\tilde{\beta}_r\tilde{E})\,.\end{aligned} \tag{8.79}$$

Similarly, the continuum limit of Eqs. (8.68)−(8.70) yields

$$\left(\frac{df_r}{dt}\right)^r = -\left(\frac{df_0}{dt}\right)^r_1 - \int_0^{\tilde{\varepsilon}_d} d\tilde{E}\int_{\tilde{E}}^{\tilde{\varepsilon}_d} d\tilde{E}'\,\mathcal{R}_1(\tilde{E},\tilde{E}')\,, \tag{8.80}$$

$$\begin{aligned}\left(\frac{d\tilde{e}_r}{dt}\right)^r_1 = -R\frac{\tilde{z}_r}{\tilde{\beta}_r^{3/2}}\Bigg\{ & \left(\frac{1}{\tilde{l}_d^3}+\rho_i\Omega f_0\right)\mathscr{C}_r(\tilde{\beta}_r,\tilde{\varepsilon}_t,0,t) \\ & + \int_0^{\tilde{\varepsilon}_d} d\tilde{E}\left[2\left(\frac{\tilde{E}}{\pi}\right)^{\frac{1}{2}}+\rho_i\Omega f(\tilde{E})\right]\mathscr{C}_r(\tilde{\beta}_r,\tilde{\varepsilon}_t,\tilde{E},t)\Bigg\},\end{aligned} \tag{8.81}$$

$$\left(\frac{d\tilde{e}_r}{dt}\right)^r_2 = \int_0^{\tilde{\varepsilon}_d} d\tilde{E}'\left[\tilde{E}'\mathcal{R}_0(\tilde{E}') + \int_0^{\tilde{E}'}(\tilde{E}'-\tilde{E})\mathcal{R}_2(\tilde{E},\tilde{E}')\right], \tag{8.82}$$

where $\tilde{e}_r \equiv e_r\big(\gamma(4,\tilde{\varepsilon}_t)/\gamma(3,\tilde{\varepsilon}_t)\big)$ [Eq. (8.5)] and

$$\begin{aligned}&\mathscr{C}_r(\tilde{\beta}_r,\tilde{\varepsilon}_t,\tilde{E},t)\\&\equiv\int_{\tilde{E}}^{\tilde{\varepsilon}_d}d\tilde{E}'f(\tilde{E}',t)\int_{-1}^{1}du\frac{\xi\Big(\tilde{\beta}_r\max\Big\{\tilde{E}\frac{(\sqrt{\tilde{E}'}u-\sqrt{\tilde{E}})^2}{\tilde{E}+\tilde{E}'-2\sqrt{\tilde{E}\tilde{E}'}u},\,\tilde{\varepsilon}_t-\tilde{E}'+\tilde{E}\Big\},\tilde{\beta}_r\tilde{\varepsilon}_t\Big)}{\tilde{\beta}_r^{1/2}\big(\tilde{E}+\tilde{E}'-2\sqrt{\tilde{E}\tilde{E}'}u\big)^{1/2}}.\end{aligned}\tag{8.83}$$

8.8 Appendix C: Rate equations for three-body loss

Because of three-body loss the overall particle density decays as [Eq. (8.36)] [10, 62, 63]

$$\left[\frac{dn(\vec{r})}{dt}\right]^l=-L\Big[n_0^3(\vec{r})+9\,n_0^2(\vec{r})\,n_{ex}(\vec{r})+18\,n_0(\vec{r})\,n_{ex}^2(\vec{r})+6n_{ex}^3(\vec{r})\Big],\tag{8.84}$$

where $n_0(\vec{r})$ and $n_{ex}(\vec{r})$ are the densities of the condensate and the excited-state atoms respectively, and L denotes the loss coefficient which for ^{87}Rb equals $L = 1.8\times10^{-29}$ cm^6 s^{-1} [56]. The exponents in Eq. (8.84) arise from the number of atoms participating in the recombination process: the first term results from recombination of three condensate atoms, whereas the second term originates from events where two condensate atoms recombine with a higher-energy atom etc. Further, an excited-state atom can either be a member of the non-condensate population in the dimple or reside in the reservoir. Thus $n_{ex}(\vec{r}) = n_{nc}(\vec{r}) + n_r(\vec{r})$ with $n_r(\vec{r})$ given in Eq. (8.6). Keeping these in mind we write down the decay rates of the individual densities

$$\left(\frac{dn_0}{dt}\right)^l = -L\,n_0\big(n_0^2+6n_0n_{ex}+6n_{ex}^2\big),\tag{8.85}$$

$$\left(\frac{dn_{nc}}{dt}\right)^l = -3\,L\,n_{nc}\big(n_0^2+4n_0n_{ex}+2n_{ex}^2\big),\tag{8.86}$$

$$\left(\frac{dn_r}{dt}\right)^l = -3\,L\,n_r\big(n_0^2+4n_0n_{ex}+2n_{ex}^2\big).\tag{8.87}$$

We model the densities in the dimple as $n_0(\vec{r}) = \mathcal{N} f_0/l_d^3 = (\rho_i\Omega/\lambda_{r0}^3) f_0$ and $n_{nc}(\vec{r}) = \mathcal{N} f_{nc}/l_d^3 = (\rho_i\Omega/\lambda_{r0}^3) f_{nc}$. Outside the dimple we take $n_0(\vec{r}) = n_{nc}(\vec{r}) = 0$. In addition, since the dimple is many times smaller than the reservoir, the reservoir density can be taken as uniform inside the dimple: $n_r(\vec{r}) \approx n_r(\vec{0}) = (\rho_i \tilde{z}_r/\lambda_{r0}^3 \tilde{\beta}_r^{3/2})[\gamma(3/2, \tilde{\beta}_r\tilde{\varepsilon}_t)/\gamma(3/2, \tilde{\varepsilon}_t)]$ for points inside the dimple [Eqs. (8.6) and (8.7)]. Using these expressions in Eqs. (8.85) and (8.86) we find

$$\left(\frac{df_0}{dt}\right)^l = -L\frac{\rho_i^2\Omega^2}{\lambda_{r0}^6} f_0(f_0^2 + 6f_0 f' + 6f'^2)\,, \tag{8.88}$$

$$\left(\frac{df_{nc}}{dt}\right)^l = -3L\frac{\rho_i^2\Omega^2}{\lambda_{r0}^6} f_{nc}(f_0^2 + 4f_0 f' + 2f'^2)\,, \tag{8.89}$$

where $f' \equiv f_{nc} + (\tilde{z}_r/\Omega\tilde{\beta}_r^{3/2})[\gamma(3/2, \tilde{\beta}_r\tilde{\varepsilon}_t)/\gamma(3/2, \tilde{\varepsilon}_t)]$. In terms of the particle distribution $f(\tilde{E}, t)$ in the excited states of the dimple, $f_{nc} = \int_0^{\tilde{\varepsilon}_d} d\tilde{E} f(\tilde{E}, t)$. Under the assumption that double or higher occupancy of the excited states in negligible, it follows from Eq. (8.89) that

$$\left[\frac{\partial f(\tilde{E}, t)}{\partial t}\right]^l = -3L\frac{\rho_i^2\Omega^2}{\lambda_{r0}^6} f(\tilde{E}, t)(f_0^2 + 4f_0 f' + 2f'^2)\,. \tag{8.90}$$

The three-body decay rate of the reservoir fraction $f_r = (1/\mathcal{N})\int d^3r\, n_r(\vec{r})$ can be obtained by substituting $n_r(\vec{r})$ from Eq. (8.6) and the above expressions for n_0 and n_{nc} into Eq. (8.87). This yields

$$\begin{aligned}\left(\frac{df_r}{dt}\right)^l = &-3L\frac{\rho_i^2\tilde{z}_r\Omega}{\lambda_{r0}^6\tilde{\beta}_r^{3/2}}\frac{\gamma(3/2, \tilde{\beta}_r\tilde{\varepsilon}_t)}{\gamma(3/2, \tilde{\varepsilon}_t)}\left[f_0^2 + 4f_0 f' + 2f_{nc}^2 + 4\frac{f_{nc}\tilde{z}_r}{\Omega\tilde{\beta}_r^{3/2}}\frac{\gamma(3/2, \tilde{\beta}_r\tilde{\varepsilon}_t)}{\gamma(3/2, \tilde{\varepsilon}_t)}\right] \\ &- \frac{48L}{\pi\gamma(3, \tilde{\varepsilon}_t)[\gamma(3/2, \tilde{\varepsilon}_t)]^2}\frac{\rho_i^2\tilde{z}_r^3}{\lambda_{r0}^6\tilde{\beta}_r^6}\int_0^{\tilde{\beta}_r\tilde{\varepsilon}_t} dx\,\sqrt{x}\,e^{-3x}[\gamma(3/2, \tilde{\beta}_r\tilde{\varepsilon}_t - x)]^3.\end{aligned} \tag{8.91}$$

The total energy in the reservoir (E_r) also decays because of three-body loss. We can find the decay rate as $(dE_r/dt)^l = -\int d^3r\, u_r(\vec{r})(dn_r/dt)^l$, where $u_r(\vec{r})$ denotes the average energy of a reservoir particle at position $\vec{r}$. To calculate

$u_r(\vec{r})$ we integrate over the phase space, finding

$$u_r(\vec{r}) = \frac{1}{\beta_r}\frac{\gamma(5/2, \beta_r\varepsilon_t - \beta_r m\omega^2 r^2/2)}{\gamma(3/2, \beta_r\varepsilon_t - \beta_r m\omega^2 r^2/2)} + \frac{1}{2}m\omega^2 r^2 \,. \tag{8.92}$$

When $\varepsilon_t \rightarrow \infty$, this reduces to the familiar expression $(3/2)k_B T_r + (1/2)m\omega^2 r^2$. Using Eqs. (8.87) and (8.92) we obtain the decay rate of $\tilde{e}_r \equiv (E_r/\mathcal{E})[\gamma(4,\tilde{\varepsilon}_t)/\gamma(3,\tilde{\varepsilon}_t)]$ as

$$\begin{aligned}\left(\frac{d\tilde{e}_r}{dt}\right)^l = &-3L\frac{\rho_i^2\tilde{z}_r\Omega}{\lambda_{r0}^6\tilde{\beta}_r^{5/2}}\frac{\gamma(5/2,\tilde{\beta}_r\tilde{\varepsilon}_t)}{\gamma(3/2,\tilde{\varepsilon}_t)}\left[f_0^2 + 4f_0 f' + 2f_{nc}^2 + 4\frac{f_{nc}\tilde{z}_r}{\Omega\tilde{\beta}_r^{3/2}}\frac{\gamma(3/2,\tilde{\beta}_r\tilde{\varepsilon}_t)}{\gamma(3/2,\tilde{\varepsilon}_t)}\right] \\ &- \frac{48L}{\pi\gamma(3,\tilde{\varepsilon}_t)[\gamma(3/2,\tilde{\varepsilon}_t)]^2}\frac{\rho_i^2\tilde{z}_r^3}{\lambda_{r0}^6\tilde{\beta}_r^7} \\ &\times\int_0^{\tilde{\beta}_r\tilde{\varepsilon}_t} dx\sqrt{x}e^{-3x}[\gamma(3/2,\tilde{\beta}_r\tilde{\varepsilon}_t - x)]^3\left[\frac{\gamma(5/2,\tilde{\beta}_r\tilde{\varepsilon}_t - x)}{\gamma(3/2,\tilde{\beta}_r\tilde{\varepsilon}_t - x)} + x\right].\end{aligned} \tag{8.93}$$

BIBLIOGRAPHY FOR CHAPTER 8

[1] D. C. McKay and B. DeMarco, "Cooling in strongly correlated optical lattices: Prospects and challenges," Rep. Prog. Phys. **74**, 054401 (2011).

[2] I. Bloch, J. Dalibard, and W. Zwerger, "Many-body physics with ultracold gases," Rev. Mod. Phys. **80**, 885 (2008).

[3] S. K. Baur, K. R. A. Hazzard, and E. J. Mueller, "Stirring trapped atoms into fractional quantum Hall puddles," Phys. Rev. A **78**, 061608 (2008).

[4] T.-L. Ho and Q. Zhou, "Squeezing out the entropy of fermions in optical lattices," Proc. Natl. Acad. Sci. USA **106**, 6916 (2009).

[5] T.-L. Ho and Q. Zhou, "Intrinsic heating and cooling in adiabatic processes for bosons in optical lattices," Phys. Rev. Lett. **99**, 120404 (2007).

[6] D. M. Stamper-Kurn, H.-J. Miesner, A. P. Chikkatur, S. Inouye, J. Stenger, and W. Ketterle, "Reversible formation of a Bose-Einstein condensate," Phys. Rev. Lett. **81**, 2194 (1998).

[7] P. W. H. Pinkse, A. Mosk, M. Weidemüller, M. W. Reynolds, T. W. Hijmans, and J. T. M. Walraven, "Adiabatically changing the phase-space density of a trapped Bose gas," Phys. Rev. Lett. **78**, 990 (1997).

[8] T. Weber, J. Herbig, M. Mark, H.-C. Nägerl, and R. Grimm, "Bose-Einstein condensation of cesium," Science **299**, 232 (2003).

[9] D. Jacob, E. Mimoun, L. De Sarlo, M. Weitz, J. Dalibard, and F. Gerbier, "Production of sodium Bose–Einstein condensates in an optical dimple trap," New J. Phys. **13**, 065022 (2011).

[10] M. C. Garrett, A. Ratnapala, E. D. Van Ooijen, C. J. Vale, K. Weegink, S. K. Schnelle, O. Vainio, N. R. Heckenberg, H. Rubinsztein-Dunlop, and M. J. Davis, "Growth dynamics of a Bose-Einstein condensate in a dimple trap without cooling," Phys. Rev. A **83**, 013630 (2011).

[11] S. Stellmer, B. Pasquiou, R. Grimm, and F. Schreck, "Laser cooling to quantum degeneracy," Phys. Rev. Lett. **110**, 263003 (2013).

[12] J.-S. Bernier, C. Kollath, A. Georges, L. De Leo, F. Gerbier, C. Salomon, and M. Köhl, "Cooling fermionic atoms in optical lattices by shaping the confinement," Phys. Rev. A **79**, 061601 (2009).

[13] T.-L. Ho and Q. Zhou, "Universal cooling scheme for quantum simulation," arXiv:0911.5506 .

[14] F. Heidrich-Meisner, S. R. Manmana, M. Rigol, A. Muramatsu, A. E. Feiguin, and E. Dagotto, "Quantum distillation: Dynamical generation of low-entropy states of strongly correlated fermions in an optical lattice," Phys. Rev. A **80**, 041603 (2009).

[15] C. Grenier, A. Georges, and C. Kollath, "Peltier cooling of fermionic quantum gases," Phys. Rev. Lett. **113**, 200601 (2014).

[16] D. Comparat, A. Fioretti, G. Stern, E. Dimova, B. L. Tolra, and P. Pillet, "Optimized production of large Bose-Einstein condensates," Phys. Rev. A **73**, 043410 (2006).

[17] M. H. Anderson, J. R. Ensher, M. R. Matthews, C. E. Wieman, and E. A. Cornell, "Observation of Bose-Einstein condensation in a dilute atomic vapor," Science **269**, 198 (1995).

[18] C. C. Bradley, C. A. Sackett, J. J. Tollett, and R. G. Hulet, "Evidence of Bose-Einstein condensation in an atomic gas with attractive interactions," Phys. Rev. Lett. **75**, 1687 (1995).

[19] K. B. Davis, M.-O. Mewes, M. R. Andrews, N. J. Van Druten, D. S. Durfee, D. M. Kurn, and W. Ketterle, "Bose-Einstein condensation in a gas of sodium atoms," Phys. Rev. Lett. **75**, 3969 (1995).

[20] H.-J. Miesner, D. M. Stamper-Kurn, M. R. Andrews, D. S. Durfee, S. Inouye, and W. Ketterle, "Bosonic stimulation in the formation of a Bose-Einstein condensate," Science **279**, 1005 (1998).

[21] E. A. Donley, N. R. Claussen, S. L. Cornish, J. L. Roberts, E. A. Cornell, and C. E. Wieman, "Dynamics of collapsing and exploding Bose–Einstein condensates," Nature (London) **412**, 295 (2001).

[22] M. Köhl, M. J. Davis, C. W. Gardiner, T. W. Hänsch, and T. Esslinger, "Growth of Bose-Einstein condensates from thermal vapor," Phys. Rev. Lett. **88**, 080402 (2002).

[23] M. Erhard, H. Schmaljohann, J. Kronjäger, K. Bongs, and K. Sengstock, "Bose-Einstein condensation at constant temperature," Phys. Rev. A **70**, 031602 (2004).

[24] S. Ritter, A. Öttl, T. Donner, T. Bourdel, M. Köhl, and T. Esslinger, "Observing the formation of long-range order during Bose-Einstein condensation," Phys. Rev. Lett. **98**, 090402 (2007).

[25] O. J. Luiten, M. W. Reynolds, and J. T. M. Walraven, "Kinetic theory of the evaporative cooling of a trapped gas," Phys. Rev. A **53**, 381 (1996).

[26] K. B. Davis, M.-O. Mewes, and W. Ketterle, "An analytical model for evaporative cooling of atoms," Appl. Phys. B **60**, 155 (1995).

[27] C. W. Gardiner, P. Zoller, R. J. Ballagh, and M. J. Davis, "Kinetics of Bose-Einstein condensation in a trap," Phys. Rev. Lett. **79**, 1793 (1997).

[28] C. W. Gardiner, M. D. Lee, R. J. Ballagh, M. J. Davis, and P. Zoller, "Quantum kinetic theory of condensate growth: Comparison of experiment and theory," Phys. Rev. Lett. **81**, 5266 (1998).

[29] M. D. Lee and C. W. Gardiner, "Quantum kinetic theory. VI. The growth of a Bose-Einstein condensate," Phys. Rev. A **62**, 033606 (2000).

[30] M. J. Davis, C. W. Gardiner, and R. J. Ballagh, "Quantum kinetic theory. VII. The influence of vapor dynamics on condensate growth," Phys. Rev. A **62**, 063608 (2000).

[31] H. T. C. Stoof, "Initial stages of Bose-Einstein condensation," Phys. Rev. Lett. **78**, 768 (1997).

[32] M. Holland, J. Williams, and J. Cooper, "Bose-Einstein condensation: Kinetic evolution obtained from simulated trajectories," Phys. Rev. A **55**, 3670 (1997).

[33] C. W. Gardiner and P. Zoller, "Quantum kinetic theory: A quantum kinetic master equation for condensation of a weakly interacting Bose gas without a trapping potential," Phys. Rev. A **55**, 2902 (1997).

[34] R. Walser, J. Williams, J. Cooper, and M. Holland, "Quantum kinetic theory for a condensed bosonic gas," Phys. Rev. A **59**, 3878 (1999).

[35] M. J. Bijlsma, E. Zaremba, and H. T. C. Stoof, "Condensate growth in trapped Bose gases," Phys. Rev. A **62**, 063609 (2000).

[36] M.-O. Mewes, M. R. Andrews, D. M. Kurn, D. S. Durfee, C. G. Townsend, and W. Ketterle, "Output coupler for Bose-Einstein condensed atoms," Phys. Rev. Lett. **78**, 582 (1997).

[37] I. Bloch, T. W. Hänsch, and T. Esslinger, "Atom laser with a cw output coupler," Phys. Rev. Lett. **82**, 3008 (1999).

[38] A. D. Cronin, J. Schmiedmayer, and D. E. Pritchard, "Optics and interferometry with atoms and molecules," Rev. Mod. Phys. **81**, 1051 (2009).

[39] R. B. Diener, B. Wu, M. G. Raizen, and Q. Niu, "Quantum tweezer for atoms," Phys. Rev. Lett. **89**, 070401 (2002).

[40] N. G. Parker, N. P. Proukakis, M. Leadbeater, and C. S. Adams, "Soliton-sound interactions in quasi-one-dimensional Bose-Einstein condensates," Phys. Rev. Lett. **90**, 220401 (2003).

[41] D. Tarhan and H. Uncu, "Effect of dimple potential on ultraslow light in a Bose-Einstein condensate," Acta Phys. Pol. A **121**, 141 (2012).

[42] T. W. B. Kibble, "Topology of cosmic domains and strings," J. Phys. A **9**, 1387 (1976).

[43] A. H. Guth, "Inflationary universe: A possible solution to the horizon and flatness problems," Phys. Rev. D **23**, 347 (1981).

[44] A. D. Linde, "A new inflationary universe scenario: A possible solution of the horizon, flatness, homogeneity, isotropy and primordial monopole problems," Phys. Lett. B **108**, 389 (1982).

[45] W. H. Zurek, "Cosmological experiments in superfluid helium?" Nature (London) **317**, 505 (1985).

[46] See the Supplementary Material of Ref. [11].

[47] H. T. C. Stoof and M. J. Bijlsma, "Dynamics of fluctuating Bose–Einstein condensates," J. Low Temp. Phys. **124**, 431 (2001).

[48] Z.-Y. Ma, C. J. Foot, and S. L. Cornish, "Optimized evaporative cooling using a dimple potential: An efficient route to Bose–Einstein condensation," J. Phys. B **37**, 3187 (2004).

[49] N. P. Proukakis, J. Schmiedmayer, and H. T. C. Stoof, "Quasicondensate growth on an atom chip," Phys. Rev. A **73**, 053603 (2006).

[50] H. Uncu, D. Tarhan, E. Demiralp, and Ö. E. Müstecaplıoğlu, "Bose-Einstein condensate in a harmonic trap decorated with Dirac δ functions," Phys. Rev. A **76**, 013618 (2007).

[51] H. Uncu, D. Tarhan, E. Demiralp, and Ö. Müstecaplıoglu, "Bose-Einstein condensate in a harmonic trap with an eccentric dimple potential," Laser Phys. **18**, 331 (2008).

[52] H. Uncu and D. Tarhan, "Bose–Einstein condensate in a linear trap with a dimple potential," Commun. Theor. Phys. **59**, 629 (2013).

[53] M. C. Aydin, H. Uncu, and C. Deniz, "A parabolic model for dimple potentials," Phys. Scr. **88**, 035006 (2013).

[54] D. W. Snoke and J. P. Wolfe, "Population dynamics of a Bose gas near saturation," Phys. Rev. B **39**, 4030 (1989).

[55] Y. M. Kagan, B. V. Svistunov, and G. V. Shlyapnikov, "Erratum: Kinetics of Bose condensation in an interacting Bose gas," Sov. Phys. JETP **75**, 387 (1992), [Zh. Eksp. Teor. Fiz. **102**, 719 (1992)].

[56] J. Söding, D. Guéry-Odelin, P. Desbiolles, F. Chevy, H. Inamori, and J. Dalibard, "Three-body decay of a rubidium Bose–Einstein condensate," Appl. Phys. B **69**, 257 (1999).

[57] B. D. Esry, C. H. Greene, and J. P. Burke, Jr., "Recombination of three atoms in the ultracold limit," Phys. Rev. Lett. **83**, 1751 (1999).

[58] K. M. R. Van Der Stam, R. Meppelink, J. M. Vogels, and P. van der Straten, "Reaching the hydrodynamic regime in a Bose-Einstein condensate by suppression of avalanches," Phys. Rev. A **75**, 031602 (2007).

[59] F. Gerbier, J. H. Thywissen, S. Richard, M. Hugbart, P. Bouyer, and A. Aspect, "Experimental study of the thermodynamics of an interacting trapped Bose-Einstein condensed gas," Phys. Rev. A **70**, 013607 (2004).

[60] M. Houbiers, H. T. C. Stoof, and E. A. Cornell, "Critical temperature of a trapped Bose gas: Mean-field theory and fluctuations," Phys. Rev. A **56**, 2041 (1997).

[61] F. Dalfovo, S. Giorgini, L. P. Pitaevskii, and S. Stringari, "Theory of Bose-Einstein condensation in trapped gases," Rev. Mod. Phys. **71**, 463 (1999).

[62] C. J. Pethick and H. Smith, *Bose-Einstein Condensation in Dilute Gases* (Cambridge University Press, Cambridge, 2002).

[63] Y. Kagan, B. V. Svistunov, and G. V. Shlyapnikov, "Effect of Bose condensation on inelastic processes in gases," JETP Lett. **42**, 209 (1985), [Pis'ma Zh. Eksp. Teor. Fiz. **42**, 169 (1985)].

CHAPTER 9

THERMALIZATION IN A QUASI-ONE-DIMENSIONAL TRAP

9.1 Abstract

We model thermalization in a quantum gas loaded into an array of weakly coupled parallel one-dimensional tubes produced by turning on a lattice in the transverse plane. We study quantum kinetic rate equations for the momentum distribution along the tubes by analyzing binary elastic collisions. For small intertube coupling J, the rate of thermalization grows as $J^2 \ln J$. We show that the equilibration times in two recent experiments [Nature **467**, 567 (2010)] and [Nature **440**, 900 (2006)] differ hugely from one another, which provides justification for their apparently conflicting observations. We highlight the qualitative differences in the approach to equilibrium after an adiabatic and a sudden turn on of the lattice. In particular, we find that for a sudden turn on, the momentum distribution develops isolated peaks at short times, which can be probed in future experiments.

9.2 Introduction

The remarkable progress in trapping and cooling atoms in recent years has enabled the experimental study of many-body quantum systems in different dimensions [1]. In particular, using a suitable laser configuration it is now possible to trap atoms in highly elongated tubes, effectively confining their motion to one dimension (1D) [2–7]. Reducing the dimensionality of a system enhances

correlation effects among the particles, and can lead to exotic quantum phases not present in higher dimensions. A prime example of such a phase is the modulated superconducting phase (also known as FFLO) in a population-imbalanced two-component Fermi gas with attractive interactions [5, 8–14]. When the two spin components ($\uparrow$,$\downarrow$) have equal populations, an $\uparrow$ spin forms a Cooper pair with a $\downarrow$ spin, leading to Bardeen-Cooper-Schrieffer (BCS) superconductivity with a uniform order parameter. However, when they have unequal populations, their Fermi surfaces mismatch, which destabilizes the BCS phase. It was predicted from theory that the ground state of such a system in 1D is a partially spin-polarized superconducting phase with an order parameter that oscillates in space. Such a partially polarized phase was indeed observed in a recent experiment at Rice with ^{6}Li atoms [5]. The experimental data fit very well with the phase diagram calculated from the thermodynamic Bethe ansatz. However, the theoretical model assumes that the system is in thermal equilibrium. But it is well known that an isolated 1D system cannot thermalize due to kinematic constraints [6, 15–18]. In higher dimensions, thermalization occurs via elastic collisions among the particles, which redistribute their momenta, thus allowing the system to ergodically sample all momentum states. However, in 1D, conservation of both momentum and energy implies that particles can only exchange momenta in a binary collision. Therefore no new momentum states are occupied and the system fails to thermalize. This feature was observed in another experiment [6], where Kinoshita *et al.* prepared bosonic ^{87}Rb atoms in a highly elongated trap in an out-of-equilibrium state. The system did not thermalize even after thousands of collisions. The resolution to the apparent conflict between the two experiments rests in the fact that real setups are not perfectly 1D. The particles still have some leftover degrees of freedom to move in the other

two dimensions, which allows the system to thermalize at long times. Here we model thermalization in such quasi-1D systems.

In a typical experiment such as [5], the experimentalists first prepare atoms of mass m in a three-dimensional (3D) harmonic trap. Then they turn on a deep lattice potential in the x-y plane. As a result, the atoms are captured in an array of elongated tubes along the z direction. In a deep lattice, the potential near a lattice site is well approximated by a harmonic well of frequency ω. This transverse confinement frequency is typically 2-3 orders of magnitude larger than the axial trapping frequency. Thus the particles are essentially free to move along the tubes in the z direction. The state of the atoms after the lattice is turned on depends on how fast the lattice is turned on compared to the collision rate among particles. In both Refs. [5] and [6], the lattice turn-on time is large compared to the collision time, allowing the system to relax to the lowest band. Since the atom energies are much smaller than the band gap $\hbar\omega$, the subsequent dynamics are confined to the lowest band. We first discuss thermalization under such conditions. One can also imagine experiments where the lattice is turned on suddenly. Then the atoms will also populate higher bands. We model this situation in the latter part of the paper and find that it gives rise to qualitatively different dynamics en route to equilibrium.

We focus on thermalization resulting from the exchange of energy between longitudinal and transverse degrees of freedom via two-body elastic collisions. In particular, we do not model second-order virtual excitations which can also contribute to thermal relaxation [19, 20]. We treat the interactions as a perturbation which induces transitions among the single-particle states, and do not model the mean-field energy shift of such states [21]. We also ignore three-

body loss processes which can become important for strongly interacting bosons [22, 23]. Thus, our formalism is valid when the interactions do not fundamentally alter the nature of the dynamics [24]. Such interaction effects could be explored in future studies.

9.3 Particles in the lowest band

When the particles are confined to the lowest band, the single-particle Hamiltonian reduces to the tight-binding model, which is characterized by a tunneling amplitude J that describes particle hopping between adjacent tubes. The dynamics depend on the dimensionless ratio $\tilde{J} \equiv \pi^2(J/E_R)$, where E_R is the lattice recoil energy. J/E_R decreases with the depth of the lattice. For an infinitely deep lattice, $\tilde{J} = 0$, so the motion is strictly 1D and no thermalization occurs. Here we study the case where $\tilde{J}$ is small but non-zero, which allows the system to equilibrate. In our model, equilibration occurs through redistribution of momenta resulting from two-body elastic collisions. In an ultracold experimental setting, collisions are predominantly s-wave, parametrized by a scattering length a_s that can be tuned via a Feshbach resonance [25]. We find that, in units of $m\omega^2 a_s^2$, the thermalization rate grows with $\tilde{J}$ as $J^2(a - b\ln\tilde{J})$, where a and b are set by the initial occupations of the momentum states. For the experimental conditions in [6], our numerics suggest a thermalization time ~ 20 min, which is large compared to the duration of the experiment (~ 0.4 s). This justifies the observed lack of thermalization. In the other experiment [5], the tunneling parameter $\tilde{J}$ is much larger. We estimate an upper bound for the thermalization time of a few μs, which is 3 orders of magnitude smaller than the observation time scale, explaining why the measurements agree so well with

thermodynamic calculations. Below we outline our analysis in further detail.

We consider a two-component Fermi gas (labeled by spin $\sigma = \uparrow, \downarrow$) loaded into a two-dimensional (2D) optical lattice potential with unit lattice spacing, $V_{\text{lat}}(x, y) = V_0[\sin^2(\pi x) + \sin^2(\pi y)]$. We consider a deep lattice with $V_0 \gg E_R$, where E_R is the recoil energy, $E_R = \pi^2\hbar^2/(2m)$. The system is described by the Hamiltonian

$$\hat{H} = \hat{H}_0 + \hat{H}_{\text{int}} \ , \tag{9.1}$$

where the kinetic and interaction parts are given by

$$\hat{H}_0 = \int d^3r \sum_\sigma \hat{\psi}^\dagger_\sigma(\vec{r}) \left[-\frac{\hbar^2}{2m}\nabla^2 + V_{\text{lat}}(x, y) \right] \hat{\psi}_\sigma(\vec{r}) \ , \tag{9.2}$$

$$\hat{H}_{\text{int}} = \frac{4\pi\hbar^2 a_s}{m} \int d^3r \ \hat{\psi}^\dagger_\uparrow(\vec{r})\hat{\psi}^\dagger_\downarrow(\vec{r})\hat{\psi}_\downarrow(\vec{r})\hat{\psi}_\uparrow(\vec{r}) \ . \tag{9.3}$$

Here $\hat{\psi}_\sigma(\vec{r})$ denotes the fermion field operator, and $\hat{H}_{\text{int}}$ describes interactions among the particles by a short-range pseudopotential characterized by the s-wave scattering length a_s. We will treat $\hat{H}_{\text{int}}$ as a perturbation which induces transitions among the single-particle eigenstates via two-body elastic collisions.

When the dynamics are confined to the lowest band, we can label the single-particle eigenstates by quasimomenta k_x and k_y in the x–y plane and momentum k_z along the z direction:

$$\psi_{k_x,k_y,k_z}(\vec{r}) = \frac{1}{\sqrt{L}} e^{ik_z z} \phi_{k_x}(x)\phi_{k_y}(y) \tag{9.4}$$

$$= \frac{1}{N\sqrt{L}} e^{ik_z z} \sum_{j_x,j_y} e^{i(k_x j_x + k_y j_y)} w_{j_x}(x) w_{j_y}(y) \tag{9.5}$$

Here L denotes the length over which the particles can move along the z direction and ϕ_k denotes the Bloch state with momentum k, which we have expanded in terms of the N Wannier states w_j localized at the N lattice sites j. We will consider the limit $L \to \infty$. For deep lattices, the Wannier state $w_j(x)$ is a Gaussian

centered at site j: $w_j(x) = \pi^{-1/4} d^{-1/2} \exp\left(-(x-j)^2/(2d^2)\right)$, where $d \equiv \sqrt{\hbar/(m\omega)}$, ω being the transverse confinement frequency, $\omega = (2E_R/\hbar)\sqrt{V_0/E_R}$. The single-particle state in Eq. (9.4) has energy

$$\varepsilon(k_x, k_y, k_z) = -2J(\cos k_x + \cos k_y) + \hbar^2 k_z^2/(2m) \ , \tag{9.6}$$

where J is the tunneling amplitude in the tight-binding model corresponding to the Hamiltonian H_0. The tunneling decreases exponentially with V_0/E_R for large lattice depths, $J \approx (4E_R/\sqrt{\pi})(V_0/E_R)^{3/4} \exp(-2\sqrt{V_0/E_R})$ [26].

We consider the growth of the $\uparrow$-spin population $n^{\uparrow}(\vec{k})$ in state $\psi_{\vec{k}}$, where $\vec{k}$ denotes (k_x, k_y, k_z). This occurs by means of elastic collisions between an $\uparrow$ spin and a $\downarrow$ spin, which scatter the $\uparrow$ spin into the state $\psi_{\vec{k}}$. In such a process, the total energy and z-momentum are conserved and quasimomenta along x and y are conserved up to one reciprocal lattice constant, 2π. The rate of such a process is proportional to the populations of the initial states $n^{\uparrow}(\vec{k}_1)$ and $n^{\downarrow}(\vec{k}_2)$. In addition, the exclusion principle for fermions prohibits the process if the final states $\psi_{\vec{k}}$ and $\psi_{\vec{k}_3}$ are already occupied by an $\uparrow$ spin and a $\downarrow$ spin respectively. This gives rise to the Pauli blocking factors $1-n^{\uparrow}(\vec{k})$ and $1-n^{\downarrow}(\vec{k}_3)$. The collision rate is also proportional to the transition probability between the initial and the final states. We calculate this probability using Fermi's golden rule, which yields the factor $|\langle\psi_{\vec{k}_1}\psi_{\vec{k}_2}|\hat{H}_{\text{int}}|\psi_{\vec{k}}\psi_{\vec{k}_3}\rangle|^2$. Combining all these terms, we arrive the kinetic

rate equation

$$\begin{aligned}\frac{dn^{\uparrow}(\vec{k})}{dt} = &\frac{16\pi}{\hbar} m\omega^2 a_s^2 \int_{-\infty}^{\infty} \frac{dk_{z_1}}{2\pi} \int_{-\infty}^{\infty} \frac{dk_{z_2}}{2\pi} \int_{-\pi}^{\pi} \frac{dk_{x_1}}{2\pi} \int_{-\pi}^{\pi} \frac{dk_{y_1}}{2\pi} \int_{-\pi}^{\pi} \frac{dk_{x_2}}{2\pi} \int_{-\pi}^{\pi} \frac{dk_{y_2}}{2\pi} \\ &\times \Big\{ n^{\uparrow}(\vec{k}_1) n^{\downarrow}(\vec{k}_2) \big[1 - n^{\uparrow}(\vec{k})\big] \big[1 - n^{\downarrow}(\vec{k}_1 + \vec{k}_2 - \vec{k})\big] \\ &\quad - \big[1 - n^{\uparrow}(\vec{k}_1)\big] \big[1 - n^{\downarrow}(\vec{k}_2)\big] n^{\uparrow}(\vec{k}) n^{\downarrow}(\vec{k}_1 + \vec{k}_2 - \vec{k}) \Big\} \\ &\times \delta\Big(k_z^2 + (k_{z1} + k_{z2} - k_z)^2 - k_{z_1}^2 - k_{z_2}^2 \\ &\quad + 2\tilde{J}\big[\cos k_{x_1} + \cos k_{x_2} - \cos k_x - \cos\left(k_{x_1} + k_{x_2} - k_x\right) \\ &\qquad + \cos k_{y_1} + \cos k_{y_2} - \cos k_y - \cos\left(k_{y_1} + k_{y_2} - k_y\right)\big] \Big). \end{aligned} \tag{9.7}$$

Hereafter we assume that the energy distribution of the particles has a width much larger than J, so that all quasimomentum states are equally populated, i.e., $n^{\sigma}(k_x, k_y, k_z) \approx n^{\sigma}(k_z)$. This is a valid approximation in most quasi-1D experiments [5, 6] and significantly reduces the computational cost. Then the integral $\int n^{\sigma}(k_z) dk_z$ gives the linear density of spin-σ particles along the z direction at each lattice site. For simplicity, we limit our analysis to the case where the $\uparrow$- and $\downarrow$- spins are equally distributed among the momentum states, i.e., $n^{\sigma}(k_z) = n(k_z)$. We have studied the case of unequal populations and found that the main features remain unaltered as long as the imbalance is not too large. In addition, making this assumption also allows us to apply our formalism to spinless bosons [6]. As opposed to fermions, bosons have a greater likelihood of scattering into a state k_z that is already occupied. Hence, we will have a Bose enhancement factor $[1 + n(k_z)]$ in place of the Pauli blocking factor $[1 - n(k_z)]$. With these considerations, we can simplify Eq. (9.7) to obtain (see Appendix 9.6

for details)

$$\frac{dn(k)}{d\tau} = \int_{-\infty}^{\infty} dp \int_{-\infty}^{\infty} dq\ f(pq) \times \Big\{ n\big(k+\tilde{J}^{\frac{1}{2}}p\big)\, n\big(k+\tilde{J}^{\frac{1}{2}}q\big) \big[1+\zeta n(k)\big] \big[1+\zeta n\big(k+\tilde{J}^{\frac{1}{2}}(p+q)\big)\big] - \big[1+\zeta n\big(k+\tilde{J}^{\frac{1}{2}}p\big)\big] \big[1+\zeta n\big(k+\tilde{J}^{\frac{1}{2}}q\big)\big]\, n(k)\, n\big(k+\tilde{J}^{\frac{1}{2}}(p+q)\big) \Big\}, \quad (9.8)$$

where $\tau = 2m\omega^2 a_s^2/(\pi\hbar)$, $k \equiv k_z$, and $\zeta = +1$ for bosons and -1 for fermions. The function f results from integrating out the delta function in Eq. (9.7) over the quasimomenta and is given by

$$f(\xi) = \frac{1}{2\pi} \int_{-\infty}^{\infty} du\ e^{i\xi u} \left[{}_2F_3\left(\frac{1}{2}, \frac{1}{2}; 1, 1, 1; -4u^2\right)\right]^2, \quad (9.9)$$

where ${}_2F_3$ is a hypergeometric function. Plotting the right-hand side of Eq. (9.9) reveals that $f(\xi)$ is peaked about $\xi = 0$ and vanishes for $|\xi| > 8$.

Since we are interested in quasi-1D experiments where $\tilde{J}$ is small, it is useful to expand Eq. (9.8) in powers of $\tilde{J}$. However, a direct Taylor expansion proves difficult because although the product $\tilde{J}pq$ is restricted to small values, either of $\tilde{J}^{1/2}p$ or $\tilde{J}^{1/2}q$ can be very large. Physically, this means that there are two kinds of energy-conserving collisions which populate state k: (i) collisions where both particles have momenta close to k and (ii) collisions where one particle has momentum very different from k and the other particle has momentum $\approx k$. The difficulty in obtaining an asymptotic expansion is bypassed if one transforms Eq. (9.8) into the Fourier domain $\tilde{n}(x)$. We carry out the expansion in the Fourier domain and then perform an inverse transform to get the following expressions (see Appendix 9.7 for details)

$$\dot{n}(k) = \big[\dot{n}(k)\big]_{\text{cl}} + \big[\dot{n}(k)\big]_{\text{qu}} + O(\tilde{J}^4 \ln \tilde{J})\ , \quad (9.10)$$

with

$$\left[\dot{n}(k)\right]_{\rm cl} = \tilde{J}^2\Big\{\left[(3-\ln\tilde{J})I_2 - I_{2l}\right]\mathcal{F}_1[n(k)] + I_2\mathcal{F}_2[n(k)]\Big\}, \tag{9.11}$$

$$\left[\dot{n}(k)\right]_{\rm qu} = \zeta\tilde{J}^2\Big\{\left[(3-2\gamma+\ln 4-\ln\tilde{J})I_2 - I_{2l}\right]\mathcal{F}_3[n(k)] + I_2\mathcal{F}_4[n(k)]\Big\}. \tag{9.12}$$

Here $\dot{n}(k) \equiv dn(k)/d\tau$, $I_2 = \int_0^\infty d\xi\ \xi^2 f(\xi) \approx 2$, $I_{2l} = \int_0^\infty d\xi\ \xi^2 \ln\xi\ f(\xi) \approx 2.18$, and γ denotes the Euler's constant ≈ 0.577. Equation (9.10) shows that the net dynamics can be broken up into a classical part $\left[\dot{n}(k)\right]_{\rm cl}$ and a quantum part $\left[\dot{n}(k)\right]_{\rm qu}$. Here $\zeta = +1$ for bosons, -1 for fermions, and 0 for distinguishable particles. The expressions for the functionals $\mathcal{F}_i[n(k)]$, $i = 1,2,3,4$ are given in Eqs. (9.25)–(9.28) in Appendix 9.7. We have simulated the dynamics using both the full rate equation [Eq. (9.8)] as well as the asymptotic expressions in Eqs. (9.10)–(9.12), and found excellent agreement between the two for $\tilde{J} \lesssim 0.01$.

From Eqs. (9.11) and (9.12) we see that the thermalization rate, in units of $m\omega^2 a_s^2/\hbar$, grows with $\tilde{J}$ as $\tilde{J}^2(a - b\ln\tilde{J})$ where the coefficients a and b are set by $n(k)$. In Fig. 9.1 we show how $n(k)$ evolves with time for $\tilde{J} = 0.001$, after starting from a double-peaked nonequilibrium profile $n(k, t=0) = \frac{1}{2}\left[\exp\left(-8(k+1)^2\right) + \exp(-8k^2) + \exp\left(-8(k-1)^2\right)\right]$, corresponding to a linear density of ≈ 0.47 in units of the lattice spacing. We plot $n(k,t)$ for bosons and fermions. We see that bosons thermalize faster than fermions. This trend is expected since bosons experience Bose enhancement which assists two-body collisions, whereas fermions experience Pauli blocking which reduces the collision rate. However, for states with occupation $\lesssim 0.5$, we find that both classes of particles exhibit similar dynamics. To quantify the approach toward a thermal state, we calculate the mismatch between the momentum distribution $n(k,t)$ and its thermal fit $n_{\rm th}(k,t)$, $\delta(t) \equiv \int[n(k,t) - n_{\rm th}(k,t)]^2/[\int n(k)dk]^2$. We plot this mismatch in Fig. 9.2. We find that the particle distribution monotonically ap-

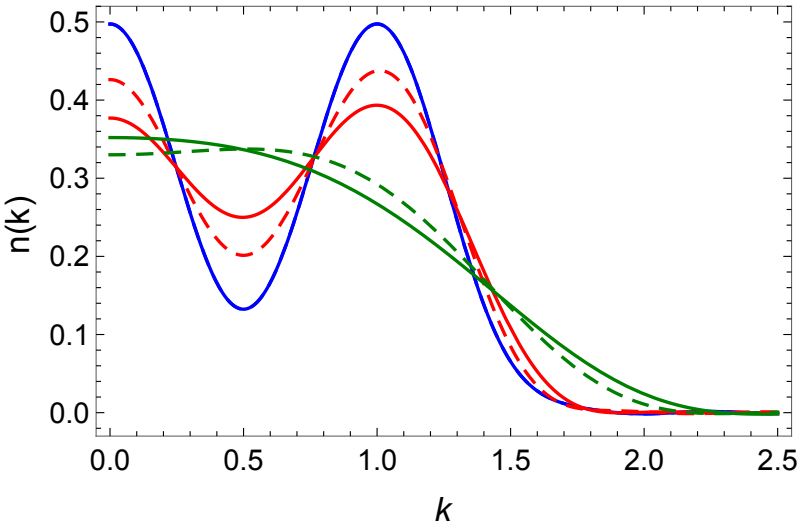

Figure 9.1: Time evolution of the momentum distribution $n(k)$ for $\tilde{J} = 0.001$. The blue, red, and green curves correspond to $t/t_0 = 0$, 200, and 4500, respectively, where $t_0 = \pi\hbar/(2m\omega^2 a_s^2)$. Solid lines: bosons, dashed lines: fermions.

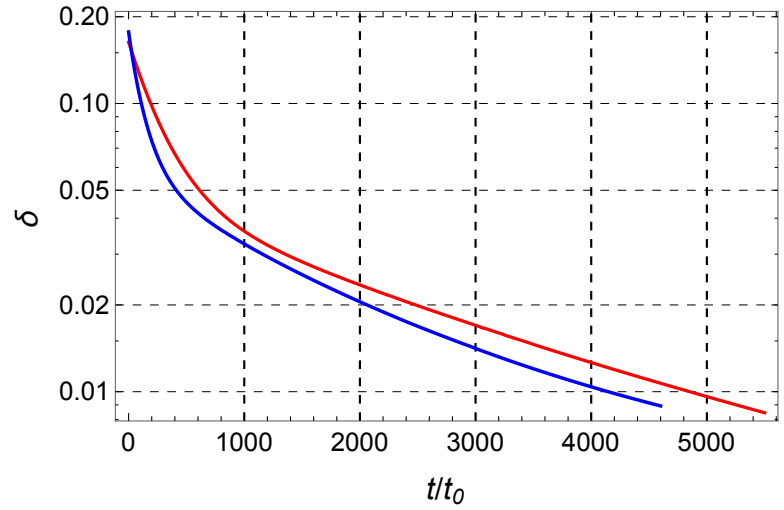

Figure 9.2: Mismatch δ (defined in text) between $n(k)$ and its thermal fit, plotted as a function of time. Blue curve: bosons, red curve: fermions.

proaches a thermal state at long times. Taking a cutoff of 0.01 for δ, we obtain a thermalization time $t_{\rm th} \sim 5 \times 10^3 t_0$, where $t_0 = \pi\hbar/(2m\omega^2 a_s^2)$.

We now estimate the thermalization times for the experimental setups in Refs. [5] and [6]. In Ref. [6], Kinoshita *et al.* prepare a gas of ^{87}Rb atoms having

scattering length $a_s = 5.3$ nm in highly elongated tubes with a transverse confinement frequency $\omega = 2\pi \times 67$ kHz, which gives $t_0 \approx 0.23$ ms. They use a deep lattice in the x–y plane with a lattice spacing $a = 386.5$ nm. Using ω and a we can calculate $V_0/E_R = [\hbar\omega/(2E_R)]^2 \approx 76$ and therefore the tunneling amplitude $\tilde{J} \approx 4\pi^{3/2}(V_0/E_R)^{3/4}\exp(-2\sqrt{V_0/E_R}) = 1.5 \times 10^{-5}$. The linear density of ^{87}Rb atoms in the experiment is $\sim 5 \times 10^6 \text{m}^{-1} \approx 1.93/a$. Comparing these values with the ones used in Figs. 9.1 and 9.2, we find that although the linear density is about 4 times larger in the experiment, the tunneling amplitude $\tilde{J}$ is about 66 times smaller. Since we have seen that for small $\tilde{J}$, the thermalization rate grows as $\tilde{J}^2 \ln \tilde{J}$ [Eqs. (9.10)-(9.12)] and we expect the rate to grow linearly with the density, we conclude that the thermalization time t_{th} for the experimental system in Ref. [6] would be much larger than $5 \times 10^3 t_0 = 1.15$ s. As a rough estimate, we get $t_{\text{th}} \sim (1/4)(66^2)(1.15 \text{ s}) \sim 20$ min, which explains why no signature of thermalization was observed within the experimental duration of ~ 0.4 s.

On the other hand, in Ref. [5], Liao *et al.* load ^{6}Li atoms into a 2D array of elongated tubes with a transverse confinement frequency $\omega = 4\pi \times 10^5$ Hz. They perform their experiment close to a Feshbach resonance. Hence, the ^{6}Li atoms have a large scattering length, $a_s \approx -484$ nm. Using these parameters, we get $t_0 \approx 45$ ns. The lattice spacing in the x–y plane is $a = 532$ nm, which yields $V_0/E_R \approx 11.6$, and $\tilde{J} \approx 0.15$. The linear density of particles along the tubes near $z = 0$ is $\sim 10^7 \text{ cm}^{-1} \approx 5/a$. We see that both the density and the tunneling amplitude are much larger than those used in Figs. 9.1 and 9.2. Therefore, the thermalization time t_{th} would be much smaller than $5 \times 10^3 t_0 = 0.22$ ms. Since the experiment occurs in the strongly interacting regime, one would need to modify our kinetic equations to get an accurate measure for t_{th}. However, based on the order of magnitudes involved, we can safely say that that the system

would equilibrate within a few μs, which is about a thousand times smaller than the time scale of observations. Thus, it is not surprising that the measurements agree with thermodynamic calculations.

In summary, a finite tunneling amplitude $\tilde{J}$ allows the particles to hop between adjacent tubes. This motional degree of freedom in the x–y plane allows the redistribution of the z-momenta via two-body elastic collisions, eventually leading to thermalization. In the limit of small $\tilde{J}$, the momentum occupations evolve in a diffusive manner [Eqs. (9.8)–(9.12)]. The initial nonequilibrium profile "spreads out" gradually and monotonically approaches a thermal distribution, as in Figs. (9.1)–(9.2). The thermalization rate is proportional to $m\omega^2 a_s^2$ and increases with $\tilde{J}$ and the particle density. It vanishes at $\tilde{J} = 0$ and grows as $\tilde{J}^2(a - b \ln \tilde{J}) + O(\tilde{J}^4)$ for small $\tilde{J}$, where a and b are set by $n(k)$.

9.4 Particles in discrete energy levels

In the last section, we considered the situation where the particles are free to move along each tube in the z direction, but their transverse motion is confined to the lowest band of the lattice in the x–y plane. Such a scenario arises in experiments where the lattice is turned on adiabatically, i.e, slowly compared to the rate of collisions between the particles. This is true in both Refs. [5] and [6]. However, one can envision an experiment where the particles are first collected in a 3D harmonic trap, then a lattice potential is turned on suddenly in the x–y plane. Here, the particles would not have sufficient time to relax to the lowest band during the turn on. In the following, we model the subsequent dynamics toward thermalization under such conditions.

We consider a situation where the lattice depth is large, $V_0/E_R \gg 1$, so the low-lying energy bands reduce to a series of equispaced energy levels. This amounts to assuming zero tunneling between adjacent tubes and replacing the lattice potential at each tube by a harmonic trap with frequency ω. The atoms will then populate several of these harmonic oscillator states after the lattice is turned on. The reason for making the harmonic approximation is two fold. First, it simplifies the analysis and keeps the problem computationally tractable. Second, it allows us to study the qualitative differences in the approach to equilibrium between two limits, one where the transverse degrees of freedom originate from a set of discrete energy levels and the other where they originate from a continuum set of states within a band.

We label the single-particle states by n_x, n_y, and k_z, where (n_x, n_y) denotes the eigenstates of a 2D harmonic oscillator and k_z labels the z-momentum. The wave function ϕ and energy ε of such a state are given by $\phi_{n_x,n_y,k_z}(\vec{r}) = (Ld^2)^{-\frac{1}{2}}\,\chi_{n_x}(x/d)\,\chi_{n_y}(y/d)\exp(ik_z z)$ and $\varepsilon_{n_x,n_y,k_z} = (n_x+n_y+1)\hbar\omega + \hbar^2 k_z^2/(2m)$, where d is the harmonic oscillator length, $d \equiv \sqrt{\hbar/(m\omega)}$ and $\chi_n(x) = e^{-x^2/2}H_n(x)/\sqrt{2^n n!\sqrt{\pi}}$, H_n being the Hermite polynomial of degree n.

By analyzing the rate of two-body elastic collisions in the same way as presented in the last section, we arrive at a rate equation for the state occupations:

$$\frac{dn_{\vec{n}}(k)}{d\tau} = \sum_{\vec{n}_1,\vec{n}_2,\vec{n}_3} \mathcal{C}(n_x, n_{x_1}, n_{x_2}, n_{x_3})\,\mathcal{C}(n_y, n_{y_1}, n_{y_2}, n_{y_3}) \times \int' \frac{dp}{q}\Big\{ n_{\vec{n}_1}(p+q) n_{\vec{n}_2}(p-q)\big[1+\zeta n_{\vec{n}}(k)\big]\big[1+\zeta n_{\vec{n}_3}(2p-k)\big] - \big[1+\zeta n_{\vec{n}_1}(p+q)\big]\big[1+\zeta n_{\vec{n}_2}(p-q)\big] n_{\vec{n}}(k) n_{\vec{n}_3}(2p-k)\Big\}, \quad (9.13)$$

where $\vec{n} \equiv (n_x, n_y)$, $k \equiv k_z d$, $\tau = [4m\omega^2 a_s^2/(\pi^3\hbar)]t$,

$$q = \sqrt{(p-k)^2 + n_x + n_{x_3} - n_{x_1} - n_{x_2} + n_y + n_{y_3} - n_{y_1} - n_{y_2}}\,, \quad (9.14)$$

and the prime over the integration symbol restricts the integral over regions where q is real. The coefficient $\mathcal{C}$ is defined as the overlap $\mathcal{C}(n, n_1, n_2, n_3) \equiv 2\pi^2 \left| \int_{-\infty}^{\infty} dx \chi_n(x)\chi_{n_1}(x)\chi_{n_2}(x)\chi_{n_3}(x) \right|^2$, which vanishes if $n + n_1 + n_2 + n_3$ is odd and otherwise has the expression

$$\mathcal{C}(n, n_1, n_2, n_3) = \frac{1}{n!n_1!n_2!n_3!} \left[\frac{\Gamma(\frac{n+n_3+n_1-n_2+1}{2})\Gamma(\frac{n-n_3+n_1+n_2+1}{2})}{\Gamma(\frac{n-n_3+n_1-n_2+1}{2})} \right]^2 \times \left[{}_3F_2 \left(\begin{matrix} -n, & -n_1, & \frac{-n+n_3-n_1+n_2+1}{2}; \\ \frac{-n-n_3-n_1+n_2+1}{2}, & & \frac{-n+n_3-n_1-n_2+1}{2}; \end{matrix} 1 \right) \right]^2 . \quad (9.15)$$

As before, $\zeta = +1$ for bosons, -1 for fermions, and 0 for distinguishable particles in Eq. (9.13). In the following we limit our consideration to fermions. As we discussed in the last section, the qualitative features do not change with statistics unless the occupation numbers are large.

We simulate the dynamics using Eq. (9.13) from out-of-equilibrium initial states where the k distribution is narrow compared to $1/d$. This is because in experiments, prior to the lattice turn on, the trapped atoms are at a temperature T which is small compared to the band gap $\hbar\omega$. We find three different time scales in the resulting dynamics. The different states within a given energy level, $n_x + n_y = M$, attain equal populations within a few collision times. It takes longer for the total populations in different energy levels to reach a thermal distribution. The slowest time scale in the dynamics is the equilibration of the z-momentum states (k), which takes several hundred collision times. We calculate the collision time τ_{coll} by fitting the initial distribution to a thermal one and using the thermal fit to compute $\tau_{\text{coll}} = 1/(4\pi a_s^2 n v)$, where n and v denote the average 3D density and the average speed of the particles, respectively.

Since the states within a given energy level quickly reach equal population, we can simplify the full dynamics in Eq. (9.13) by assuming that they are always

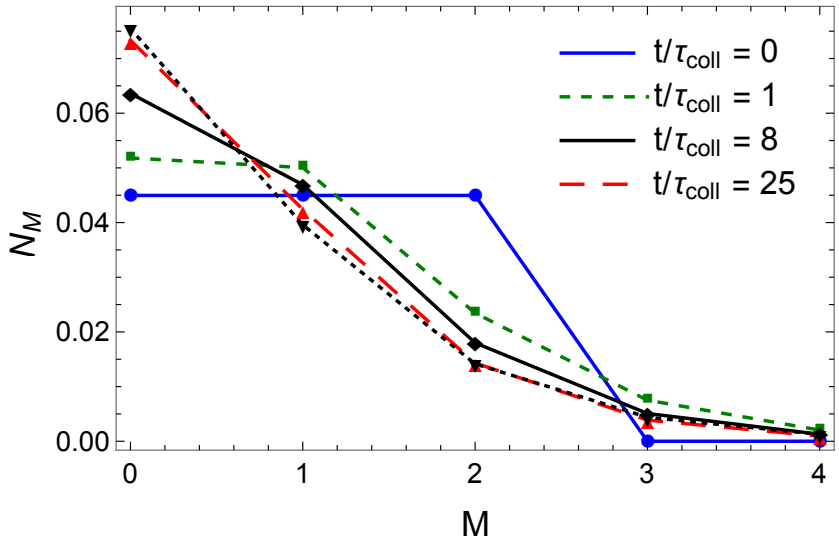

Figure 9.3: Evolution of the total populations in different energy levels of the transverse harmonic trap. The dotted black line shows the thermal distribution with the same total energy and particle number, and $\tau_{\rm coll}$ is the collision time.

equally populated, i.e., $n_{\vec{n}}(k) = n_M(k)$, where $n_x + n_y = M$. Thus, we obtain the following rate equation for $n_M(k)$:

$$\frac{dn_M(k)}{d\tau} = \frac{1}{M+1} \sum_{M_1,M_2,M_3=0}^{\infty} F(M,M_1,M_2,M_3) \times \int' \frac{dp}{q} \Big\{ n_{M_1}(p+q) n_{M_2}(p-q) \big[1+\zeta n_M(k)\big] \big[1+\zeta n_{M_3}(2p-k)\big] - \big[1+\zeta n_{M_1}(p+q)\big] \big[1+\zeta n_{M_2}(p-q)\big] n_M(k) n_{M_3}(2p-k) \Big\}, \quad (9.16)$$

where

$$F(M_0,M_1,M_2,M_3) = \prod_{j=0}^{3} \sum_{n_j=0}^{M_j} \mathcal{C}(n_0,n_1,n_2,n_3)\, \mathcal{C}(M_0-n_0, M_1-n_1, M_2-n_2, M_3-n_3). \quad (9.17)$$

Figure 9.3 shows how the band populations $N_M(t) = (M+1)\int n_M(k,t)dk$ evolve, starting from $n_M(k,t=0) = \frac{0.4}{M+1}\big[\tanh\big(20(k+0.1)\big) - \tanh\big(20(k-0.1)\big)\big]$ for $M = 0,1,2$, and zero otherwise. Note that k is expressed in units of $1/d$. In Fig. 9.4, we plot the evolution of the total momentum-state occupations $N(k) =$

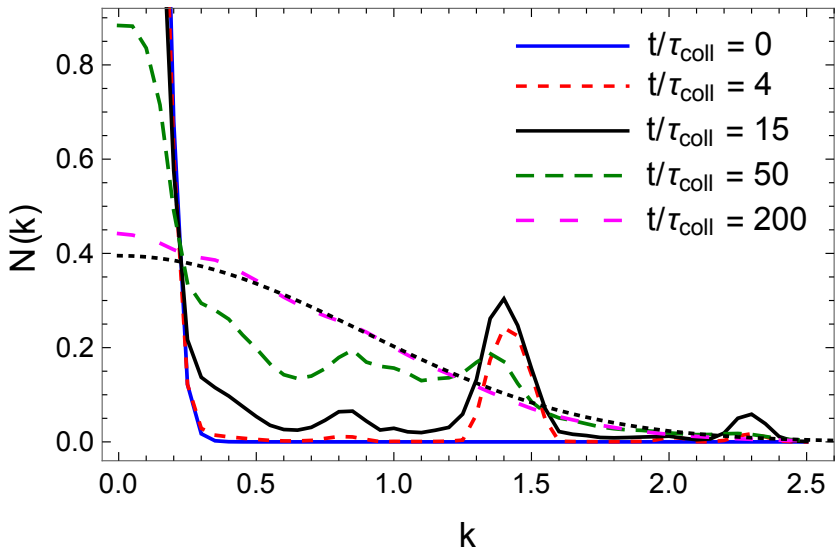

Figure 9.4: Evolution of the z-momentum distribution along each tube, $N(k)$. As in Fig. 9.3, the dotted black line shows the thermal distribution with the same total energy and particle number, and τ_{coll} denotes the collision time.

$\sum_M (M+1) n_M(k)$. We see that N_M reaches a thermal profile within ~ 30 collision times, whereas it takes ~ 200 collision times for $N(k)$ to thermalize. We have tested different initial distributions and found that the equilibration times do not vary appreciably as long as more than one energy level is populated initially.

More interestingly, we see from Fig. 9.4 that the nature of thermalization for $N(k)$ is qualitatively different from all the other cases discussed so far. In contrast to the slow diffusion-like behavior Fig. 9.1, here we find that at short times, $N(k)$ develops a secondary peak around $k = \sqrt{2}$. As time passes, this peak grows gradually and new tertiary peaks appear at $k \approx 0.87$ and $k \approx 2.3$. With time, these peaks spread out in either directions and overlap with one another, leading eventually to a thermal profile. We can explain the appearance of these peaks by examining the redistribution of momenta in two-body elastic collisions. Let us consider a collision between two particles with initial states $(M_1, p+q)$, $(M_2, p-q)$ and final states (M, k), $(M_3, 2p-k)$. We can write the

conservation of energy, in units of $\hbar\omega$, as $k^2 + (2p - k)^2 = 2(p^2 + q^2) + 2\Delta M$, where $\Delta M = M + M_3 - M_1 - M_2$. The index ΔM quantifies the exchange of energy between longitudinal and transverse directions. It can only assume even integer values, $0, \pm 2, \pm 4, \ldots$, as the overlap factor F in Eqs. (9.16)–(9.17) vanishes unless $M + M_1 - M_2 - M_3$ is even. This selection rule originates from the alternating parity of the successive harmonic oscillator levels. Initially, all particles in the trap have momenta close to zero. Thus, $p, q \approx 0$ and the dominant process which populate high-momentum states comes from $\Delta M = 2$, for which we get $k = \sqrt{2}$. This process gives rise to the secondary peak at short times in Fig. 9.4. Once a particle has scattered into the $k = \sqrt{2}$ state, it can then collide with a $k = 0$ particle. The dominant redistribution process for such a collision again comes from $\Delta M = 2$, which yields the new set of momenta at $k \approx 0.87$ and 2.3. Thus, we find tertiary peaks around these values in Fig. 9.4. These peaks are small because the population at $k = \sqrt{2}$ is much smaller than at $k = 0$. The distinct momentum values generated in binary collisions soon proliferate, which cause the different peaks to overlap and eventually form a thermal profile. Future experiments can probe this multi-peaked momentum distribution which can be resolved for a duration of about $50\tau_{\text{coll}}$.

9.5 Conclusions

We have modeled thermalization in a quantum gas loaded in a quasi-1D trap using kinetic rate equations. In such an experiment, particles are captured in an array of elongated tubes oriented along the z direction by turning on a deep lattice in the x–y plane. We have considered two different scenarios. In one, the lattice is turned on adiabatically, as in Refs. [5, 6], and in the other, it is turned

on suddenly. In the first case, the particles are confined to the lowest band. Here, thermalization occurs because the different Bloch states within the band have slightly different energies, measured by the the tunneling amplitude $\tilde{J}$. In a binary elastic collision, the colliding particles can change their z-momenta by small amounts by scattering into different Bloch states. This redistribution allows the particles to reach all momentum states after sufficiently many collisions, which leads to thermal equilibrium. In the limit of small $\tilde{J}$, we find that the momentum occupations evolve according to a diffusion-like equation [Eqs. (9.10)–(9.12)] and gradually approaches a thermal profile (Fig. 9.1). The thermalization rate is given by $m\omega^2 a_s^2 \tilde{J}^2(a - b\ln\tilde{J}) + O(\tilde{J}^4 \ln\tilde{J})$ where m is the particle mass, ω is the transverse confinement frequency, a_s is the scattering length, and the coefficients a and b grow with the particle density. From our numerics we estimate that the equilibration times in the experiments [5] and [6] are, respectively, much smaller and much larger than the measurement time scales, which explains the agreement with thermodynamic calculations in the former and the lack of thermalization observed in the latter.

If instead the lattice potential is turned on suddenly, the particles will be excited to several higher bands. We consider the case of a deep lattice and model the subsequent dynamics by replacing the bands by discrete energy levels of a 2D harmonic confinement. We find three different time scales in the dynamics. The degenerate states within a level attain equal populations within a few collision times (τ_{coll}). The different energy levels thermalize with one another in $\sim 30\tau_{\text{coll}}$ and the z-momentum states take the longest to equilibrate ($\sim 200\tau_{\text{coll}}$). The evolution of the momentum distribution $N(k)$ in this case is qualitatively different from that in an gradual turn on. Instead of slowly spreading out like a diffusion, $N(k)$ develops isolated peaks which grow and eventually merge with

one another to form a thermal profile (Fig. 9.4). This behavior originates from the discreteness of the energy levels which causes the z-momenta of the colliding particles to change in a discontinuous manner. Future experiments can probe this nonequilibrium multi-peaked momentum distribution.

Acknowledgments

I thank Profs. Erich Mueller and Mukund Vengalattore for useful discussions.

9.6 Appendix A: Simplifying the rate equation

When the particles are confined to the lowest band, the full rate equation governing the occupations of the momentum states is given by Eq. (9.7). With $n^\sigma(\vec{k}) = n(k)$, we can write

$$\begin{aligned}
\frac{dn(k)}{d\tau} &= \int_{-\pi}^{\pi} \frac{dk_x}{2\pi} \int_{-\pi}^{\pi} \frac{dk_y}{2\pi} \frac{dn(\vec{k})}{d\tau} \\
&= \frac{1}{\tilde{J}} \int_{-\infty}^{\infty} dp \int_{-\infty}^{\infty} dq \, \Big\{ n(k+p)\, n(k+q) \big[1+\zeta n(k)\big] \big[1+\zeta n(k+p+q)\big] \\
&\qquad\qquad - \big[1+\zeta n(k+p)\big] \big[1+\zeta n(k+q)\big] n(k)\, n(k+p+q) \Big\} \\
&\quad \times \int_{-\pi}^{\pi} \frac{dk_x}{2\pi} \int_{-\pi}^{\pi} \frac{dk_{x_1}}{2\pi} \int_{-\pi}^{\pi} \frac{dk_{x_2}}{2\pi} \int_{-\pi}^{\pi} \frac{dk_y}{2\pi} \int_{-\pi}^{\pi} \frac{dk_{y_1}}{2\pi} \int_{-\pi}^{\pi} \frac{dk_{y_2}}{2\pi} \\
&\qquad \delta\Big(\frac{pq}{\tilde{J}} + \cos k_{x_1} + \cos k_{x_2} - \cos k_x - \cos\left(k_{x_1} + k_{x_2} - k_x\right) \\
&\qquad\quad + \cos k_{y_1} + \cos k_{y_2} - \cos k_x - \cos\left(k_{y_1} + k_{y_2} - k_y\right) \Big),
\end{aligned} \tag{9.18}$$

where $\tau = 2m\omega^2 a_s^2/(\pi\hbar)$. Using the integral representation of the delta function we can write the six-dimensional integration over the quasimomenta as

$$f\Big(\frac{pq}{\tilde{J}}\Big) = \frac{1}{2\pi}\int_{-\infty}^{\infty} e^{i\frac{pq}{\tilde{J}}u}[g(u)]^2, \tag{9.19}$$

where

$$\begin{aligned}
g(u) &= \int_{-\pi}^{\pi}\frac{dx}{2\pi}\int_{-\pi}^{\pi}\frac{dy}{2\pi}\int_{-\pi}^{\pi}\frac{dz}{2\pi}\, e^{iu[\cos x+\cos y-\cos z-\cos(x+y-z)]} \\
&= \int_{-\pi}^{\pi}\frac{dx}{2\pi}\int_{-\pi}^{\pi}\frac{dy}{2\pi}\int_{-\pi}^{\pi}\frac{dz}{2\pi}\int_{-\infty}^{\infty}\frac{d\alpha}{2\pi}\int_{-\infty}^{\infty} d\beta\, e^{i[\beta(x+y-z-\alpha)+u(\cos x+\cos y-\cos z-\cos\alpha)]} \\
&= \int_{-\infty}^{\infty} d\beta \sum_{n=-\infty}^{\infty} e^{2\pi i n\beta}\left|\int_{-\infty}^{\infty}\frac{dx}{2\pi}e^{i(u\cos x+\beta x)}\right|^4 \\
&= \int_{-\infty}^{\infty} d\beta \sum_{n=-\infty}^{\infty} \delta(\beta-n)\left|\int_{-\infty}^{\infty}\frac{dx}{2\pi}e^{i(u\cos x+\beta x)}\right|^4 \\
&= \sum_{n=-\infty}^{\infty}\left|\int_{-\infty}^{\infty}\frac{dx}{2\pi}e^{i(u\cos x+nx)}\right|^4 = \sum_{n=-\infty}^{\infty}[J_n(u)]^4 = {}_2F_3\Big(\frac{1}{2},\frac{1}{2};1,1,1;-4u^2\Big).
\end{aligned} \tag{9.20}$$

Here, J_n denotes the Bessel function and ${}_2F_3$ is a hypergeometric function. Substituting Eq. (9.20) into Eq. (9.18) and rescaling the momenta p and q to $\tilde{J}^{\frac{1}{2}}p$ and $\tilde{J}^{\frac{1}{2}}q$, respectively, yield the expressions in Eqs. (9.8) and (9.9).

9.7 Appendix B: Aysmptotic expansion of the rate equation

Fourier transforming both sides of Eq. (9.8) we get

$$\dot{\tilde{n}}(x) = \big[\dot{\tilde{n}}(x)\big]_{\text{cl}} + \big[\dot{\tilde{n}}(x)\big]_{\text{qu}}, \tag{9.21}$$

where $\dot{\tilde{n}}(x) \equiv d\tilde{n}(x)/d\tau$ and

$$\left[\dot{\tilde{n}}(x)\right]_{\rm cl} = \frac{2}{\pi}\int_{-\infty}^{\infty} d\xi \int_{-\infty}^{\infty} dy\, f(\xi)\,\tilde{n}(y)\,\tilde{n}(x-y)\,{\rm Re}\left[K_0\left(2\sqrt{\xi\tilde{J}y(x-y)}\right) - K_0\left(2\sqrt{\xi\tilde{J}y^2}\right)\right], \tag{9.22}$$

$$\left[\dot{\tilde{n}}(x)\right]_{\rm qu} = \frac{\zeta}{\pi^2}\int_{-\infty}^{\infty} d\xi f(\xi) \int_{-\infty}^{\infty} dx_1 \int_{-\infty}^{\infty} dx_2\, \tilde{n}(x_1)\,\tilde{n}(x_2)\,\tilde{n}(x-x_1-x_2)$$
$$\times\, {\rm Re}\left[K_0\left(2\sqrt{\xi\tilde{J}x_1x_2}\right) + K_0\left(2\sqrt{\xi\tilde{J}(x-x_1)(x-x_2)}\right) - 2K_0\left(2\sqrt{\xi\tilde{J}x_1(x-x_2)}\right)\right]. \tag{9.23}$$

Here, K_0 denotes the modifies Bessel function and ${\rm Re}$ denotes the real part. Since we have assumed that the momentum distribution $n(k)$ has a width large compared to $\tilde{J}^{\frac{1}{2}}$, its Fourier transform $\tilde{n}(x)$ will have a width smaller than $1/\tilde{J}^{\frac{1}{2}}$. In addition, we note that $\tilde{J}$ is small and the function $f(\xi)$ is significant only for $-8 \lesssim \xi \lesssim 8$. Therefore, all arguments of K_0 in the above equations are small. Thus, we can expand Eq. (9.23) in powers of $\tilde{J}$ using

$$K_0(\sqrt{z}) + {\rm Re}\, K_0(i\sqrt{z}) = -2\gamma - \ln(z/4) + (z^2/64)[3 - 2\gamma - \ln(z/4)] + O(z^4) \tag{9.24}$$

for small positive z, where γ is the Euler's constant. We then perform an inverse Fourier transform to obtain the asymptotic expansion in Eqs. (9.10)–(9.12),

where the functionals $\mathcal{F}_i[n(k)]$ ($i = 1, 2, 3, 4$) are given by

$$\mathcal{F}_1[n(k)] = [n''(k)]^2 - n(k)\, n^{(4)}(k)\ , \tag{9.25}$$

$$\begin{aligned}\mathcal{F}_2[n(k)] = {} & n(k) \int_0^\infty dp \ln p \left[n^{(5)}(k+p) - n^{(5)}(k-p)\right] \\ & - n''(k) \int_0^\infty dp \ln p \left[n^{(3)}(k+p) - n^{(3)}(k-p)\right],\end{aligned} \tag{9.26}$$

$$\mathcal{F}_3[n(k)] = -\frac{n(k)}{3}\left\{6[n''(k)]^2 + 16 n'(k)\, n^{(3)}(k) + 5 n(k)\, n^{(4)}(k)\right\}, \tag{9.27}$$

$$\begin{aligned}\mathcal{F}_4[n(k)] = {} & 2(\ln 2 - \gamma)\, \partial_k^2 \left\{[n(k)]^2\, n^{(3)}(k) - 2\,[n'(k)]^3 - 2\, n(k)\, n'(k)\, n''(k)\right\} \\ & + \partial_k^2 \left\{ [n(k)]^2 \int_0^\infty dp \ln p \left[n^{(4)}(k+p) - n^{(4)}(k-p)\right] \right. \\ & \left. - n'(k)\ \partial_k^3 \int_0^\infty dp \ln p \left[\big(n(k+p)\big)^2 - \big(n(k-p)\big)^2\right] \right\},\end{aligned} \tag{9.28}$$

where ∂_k denotes the derivative with respect to k and $n^{(i)}(k) \equiv \partial_k^i n(k)$.

BIBLIOGRAPHY FOR CHAPTER 9

[1] I. Bloch, J. Dalibard, and W. Zwerger, "Many-body physics with ultracold gases," Rev. Mod. Phys. **80**, 885 (2008).

[2] B. Paredes, A. Widera, V. Murg, O. Mandel, S. Fölling, I. Cirac, G. V. Shlyapnikov, T. W. Hänsch, and I. Bloch, "Tonks–Girardeau gas of ultracold atoms in an optical lattice," Nature (London) **429**, 277 (2004).

[3] H. Moritz, T. Stöferle, M. Köhl, and T. Esslinger, "Exciting collective oscillations in a trapped 1D gas," Phys. Rev. Lett. **91**, 250402 (2003).

[4] H. Moritz, T. Stöferle, K. Günter, M. Köhl, and T. Esslinger, "Confinement induced molecules in a 1D Fermi gas," Phys. Rev. Lett. **94**, 210401 (2005).

[5] Y.-a. Liao, A. S. C. Rittner, T. Paprotta, W. Li, G. B. Partridge, R. G. Hulet, S. K. Baur, and E. J. Mueller, "Spin-imbalance in a one-dimensional Fermi gas," Nature (London) **467**, 567 (2010).

[6] T. Kinoshita, T. Wenger, and D. S. Weiss, "A quantum Newton's cradle," Nature (London) **440**, 900 (2006).

[7] M. A. Cazalilla, A. F. Ho, and T. Giamarchi, "Interacting Bose gases in quasi-one-dimensional optical lattices," New J. Phys. **8**, 158 (2006).

[8] G. Orso, "Attractive Fermi gases with unequal spin populations in highly elongated traps," Phys. Rev. Lett. **98**, 070402 (2007).

[9] X.-J. Liu, H. Hu, and P. D. Drummond, "Fulde-Ferrell-Larkin-Ovchinnikov states in one-dimensional spin-polarized ultracold atomic Fermi gases," Phys. Rev. A **76**, 043605 (2007).

[10] M. Casula, D. M. Ceperley, and E. J. Mueller, "Quantum Monte Carlo study of one-dimensional trapped fermions with attractive contact interactions," Phys. Rev. A **78**, 033607 (2008).

[11] E. Zhao and W. V. Liu, "Theory of quasi-one-dimensional imbalanced Fermi gases," Phys. Rev. A **78**, 063605 (2008).

[12] K. Yang, "Inhomogeneous superconducting state in quasi-one-dimensional systems," Phys. Rev. B **63**, 140511(R) (2001).

[13] P. Kakashvili and C. J. Bolech, "Paired states in spin-imbalanced atomic Fermi gases in one dimension," Phys. Rev. A **79**, 041603(R) (2009).

[14] X.-W. Guan, M. T. Batchelor, and C. Lee, "Fermi gases in one dimension: From Bethe ansatz to experiments," Rev. Mod. Phys. **85**, 1633 (2013).

[15] M. Rigol, "Breakdown of thermalization in finite one-dimensional systems," Phys. Rev. Lett. **103**, 100403 (2009).

[16] M. Rigol, "Quantum quenches and thermalization in one-dimensional fermionic systems," Phys. Rev. A **80**, 053607 (2009), Erratum-*ibid.* **87**, 029902 (2013).

[17] M. Rigol, V. Dunjko, and M. Olshanii, "Thermalization and its mechanism for generic isolated quantum systems," Nature (London) **452**, 854 (2008).

[18] A. Polkovnikov, K. Sengupta, A. Silva, and M. Vengalattore, "Colloquium: Nonequilibrium dynamics of closed interacting quantum systems," Rev. Mod. Phys. **83**, 863 (2011).

[19] I. E. Mazets, T. Schumm, and J. Schmiedmayer, "Breakdown of integrability in a quasi-1D ultracold bosonic gas," Phys. Rev. Lett. **100**, 210403 (2008).

[20] I. E. Mazets and J. Schmiedmayer, "Thermalization in a quasi-one-dimensional ultracold bosonic gas," New J. Phys. **12**, 055023 (2010).

[21] D. Guéry-Odelin, "Mean-field effects in a trapped gas," Phys. Rev. A **66**, 033613 (2002).

[22] J. Söding, D. Guéry-Odelin, P. Desbiolles, F. Chevy, H. Inamori, and J. Dalibard, "Three-body decay of a rubidium Bose–Einstein condensate," Appl. Phys. B **69**, 257 (1999).

[23] S. Dutta and E. J. Mueller, "Kinetics of Bose-Einstein condensation in a dimple potential," Phys. Rev. A **91**, 013601 (2015).

[24] R. Nandkishore and D. A. Huse, "Many-body localization and thermalization in quantum statistical mechanics," Annu. Rev. Condens. Matter Phys. **6**, 15 (2015).

[25] C. Chin, R. Grimm, P. Julienne, and E. Tiesinga, "Feshbach resonances in ultracold gases," Rev. Mod. Phys. **82**, 1225 (2010).

[26] D. Jaksch, C. Bruder, J. I. Cirac, C. W. Gardiner, and P. Zoller, "Cold bosonic atoms in optical lattices," Phys. Rev. Lett. **81**, 3108 (1998).